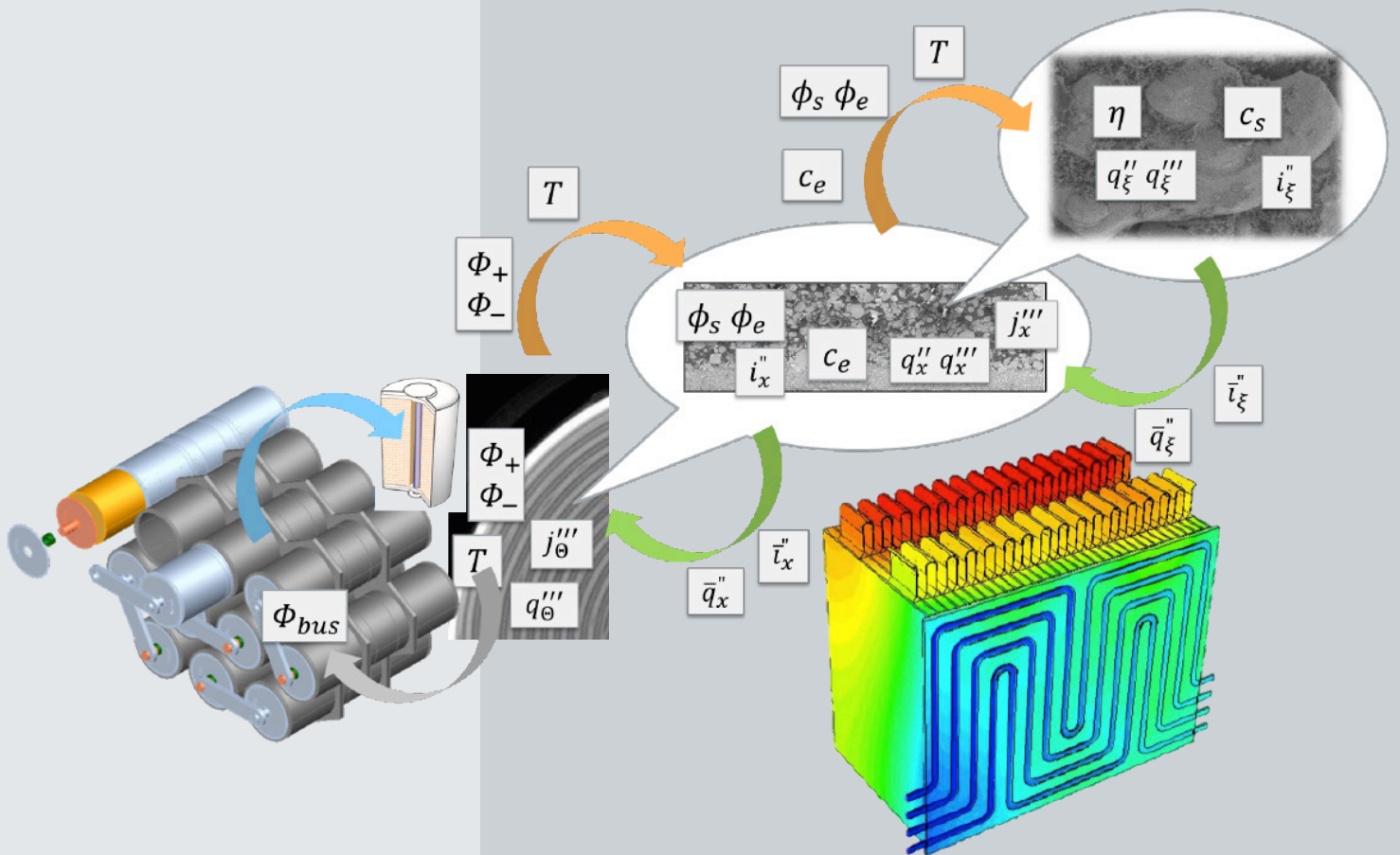


Energy Storage

2015 Annual Report

Vehicle Technologies Office



CONTENTS

I. Introduction	1
I.A Vehicle Technologies Office Overview	1
I.B Vehicle Technologies Battery R&D Overview	1
I.B.1 DOE Battery R&D Goals and Technical Targets	1
I.B.2 DOE Battery R&D Plans.....	2
I.B.3 Energy Storage R&D Programmatic Structure.....	3
I.B.4 Recent <i>EV Everywhere</i> Highlights	5
I.B.5 Organization of this Report	10
II. Advanced Battery Development	11
II.A USABC Battery Development Projects	15
II.A.1 High Energy Lithium Batteries for Electric Vehicles (Envia Systems)	15
II.A.2 Development of a High Energy Density Cell and Module for EV Applications (LG Chem Power, Inc.)	20
II.A.3 Advanced High-Performance Batteries for Electric Vehicle (EV) Applications (Amprius).....	24
II.A.4 EV Technology Assessment Program (Seeo)	32
II.A.5 PHEV Battery Development (Xerion ABC)	43
II.A.6 Development of Advanced High-Performance Batteries for 12V Start-Stop Vehicle Applications (Maxwell Technologies)	50
II.A.7 A 12V Start-Stop Li Polymer Battery Pack (LG Chem Power, Inc.).....	57
II.A.8 Development of 12V Start-stop Microhybrid Batteries (Saft).....	61
II.A.9 Advanced Polyolefin Separators for Li-Ion Batteries Used in Vehicle Applications (AMTEK Research).....	68
II.B Advanced Lithium Battery Cell Technology	74
II.B.1 Development of Large Format Lithium-ion Cells with Higher Energy Density (XALT Energy)	74
II.B.2 Innovative Cell Materials and Designs for 300 Mile Range EVs (OneD Material)	81
II.B.3 Advanced High Energy Li-ion Cell for PHEV and EV (3M Company)	95
II.B.4 Development of High-Energy Lithium-Sulfur Battery Cells (PSU).....	105
II.B.5 Stand Alone Battery Thermal System (DENSO)	111
II.C Low-cost Processing Research	118
II.C.1 Cells or Battery Packs with Significant Cost Improvement (JCI)	118
II.C.2 Utilization of UV Curing Technology to Significantly Reduce the Manufacturing Cost of LIB Electrodes (Miltec UV International)	129
II.C.3 High Capacity Alloy Anodes (Applied Materials)	133
II.C.4 Innovative Manufacturing and Materials for Low Cost Lithium-ion Batteries (Optodot Corporation).....	141

II.C.5 Dry Process Electrode Fabrication (Navitas Advanced Solutions Group, LLC)	147
II.D Small Business Innovative Research (SBIR) Projects.....	152
III. Battery Testing, Analysis, and Design.....	154
III.A Cost Assessments and Requirements Analysis.....	155
III.A.1 BatPaC Model Development (ANL)	155
III.A.2 Battery Production and Recycling Materials Issues (ANL).....	163
III.A.3 Battery Leasing & Standardization for Medium-Duty Hybrid Electric Vehicle (NREL)	172
III.B Battery Testing.....	179
III.B.1 Battery Performance and Life Testing (ANL)	179
III.B.2 Electrochemical Performance Testing (INL)	183
III.B.3 Battery Safety Testing (SNL)	190
III.B.4 Battery Thermal Analysis and Characterization Activities (NREL)	198
III.C Battery Analysis and Design Activities	204
III.C.1 Battery Multiscale Multidomain Framework & Modeling (NREL)	204
III.C.2 Computer Aided Engineering of Batteries – CAEBAT (NREL).....	212
III.C.3 Open Architecture Software for CAEBAT (ORNL)	222
III.C.4 Coupling Mechanical with Electrochemical-Thermal Models Batteries under Abuse (NREL).....	228
III.C.5 Mechanistic Modeling Framework for Predicting Extreme Battery Response (SNL)	239
III.C.6 Efficient Safety and Degradation Modeling of Automotive Li-ion Cells and Pack (EC Power, Penn State U)	245
III.C.7 Significant Enhancement of Computational Efficiency in Nonlinear Multiscale Battery Model for Computer-Aided Engineering (NREL).....	249
III.C.8 Crash Propagation in Automotive Batteries: Simulations and Validation (NREL)	256
IV. Applied Battery Research for Transportation.....	264
IV.A Introduction.....	264
IV.B Core and Enabling Support Facilities.....	267
IV.B.1 Cell Analysis, Modeling, and Prototyping (CAMP) Facility Research Activities (ANL)	267
IV.B.2 Materials Benchmarking Activities for CAMP Facility (ANL)	297
IV.B.3 Abuse Tolerance Improvements (SNL)	307
IV.B.4 Post-Test Diagnostic Facility Activities	313
IV.C Critical Barrier Focus —Enabling High Energy, High Voltage Li-ion Batteries	318
IV.C.1 Enabling High-Energy/Voltage Lithium-Ion Cells for Transportation Applications – Part 1: Baseline Protocols and Analysis (ANL)	318
IV.C.2 Enabling High-Energy/Voltage Lithium-Ion Cells for Transportation Applications – Part 2: Materials (ANL).....	331
IV.C.3 Enabling High-Energy/Voltage Lithium-Ion Cells for Transportation Applications – Part 3: Electrochemistry (ANL).....	343

IV.D Next-Generation Li-ion Chemistries: “Improvements in Cell Chemistry, Composition, and Processing”	364
IV.D.1. New High Energy Electrochemical Couple for Automotive Applications (ANL)	364
IV.D.2 High Energy Novel Cathode / Alloy Automotive Cell (3M)	372
IV.D.3 High Energy Density Li-Ion Cells for EVs Based on Novel, High Voltage Cathode Material Systems (Farasis Energy, Inc.)	379
IV.D.4 High Energy Lithium Batteries for PHEV Applications (Envia, LBNL, ORNL, GM)	383
IV.D.5 High Energy, Long Cycle Life Lithium-Ion Batteries for EV Application (PSU)	400
IV.D.6 High Energy High Power Battery Exceeding PHEV40 Requirements (TIAX LLC)	420
IV.E Process Development and Manufacturing R&D at National Laboratories	431
IV.E.1 Process Development and Scale up of Advanced Active Battery Materials (ANL)	431
IV.E.2 Process R&D and Scale up of Critical Battery Materials (ANL)	444
IV.E.3 Electrode Coating Defect Analysis and Processing NDE for High-Energy Lithium-Ion Batteries (ORNL).....	456
IV.E.4 Thick Low-Cost, High-Power Lithium-Ion Electrodes via Aqueous Processing (ORNL)	466
IV.E.5 Development of Industrially Viable Electrode Coatings (NREL)	474
IV.F Process Development and Manufacturing R&D with U.S. Industry	481
IV.F.1 Low Cost, Structurally Advanced Novel Electrode and Cell Manufacturing (24M Technologies)	481
IV.F.2 Advanced Drying Process for Low Cost Manufacturing of Electrodes (Lambda Technologies)	484
IV.F.3 Dramatically Improve the Safety Performance of Li Ion Battery Separators and Reduce the Manufacturing Cost using Ultraviolet Curing and High Precision Coating Technologies (Miltec UV International)	496
IV.F.4 A Commercially Scalable Process for Silicon Anode Prelithiation (Amprius)	501
IV.F.5 A Disruptive Concept for a Whole Family of New Battery Systems (Parthian Energy)	506
IV.F.6 Low Cost, High Capacity Non-Intercalation Chemistry Automotive Cells (Sila Nanotechnologies)	513
V. Advanced Battery Materials Research (BMR)	520
V.A Introduction	520
V.B Advanced Electrode Architectures	523
V.B.1 Physical, Chemical, and Electrochemical Failure Analysis of Electrodes and Cells (LBNL)	523
V.B.2 Electrode Architecture-Assembly of Battery Materials and Electrodes (HydroQuebec)	528
V.B.3 Design and Scalable Assembly of High Density Low Tortuosity Electrodes (MIT)	533
V.B.4 Hierarchical Assembly of Inorganic/Organic Hybrid Si Negative Electrodes (LBNL)	537
V.B.5 Studies in Advanced Electrode Fabrication (LBNL).....	545
V.C Silicon Anode Research	550
V.C.1 Development of Si-Based High-Capacity Anodes (PNNL)	550

V.C.2 Pre-Lithiation of Silicon Anode for High Energy Li Ion Batteries (Stanford U)	560
V.C.3 Atomic Layer Deposition for Stabilization of Silicon Anodes (NREL).....	566
V.D High Energy Density Cathodes for Advanced Lithium-ion Batteries	572
V.D.1 Studies on High Capacity Cathodes for Advanced Lithium-Ion (ORNL)	572
V.D.2 High Energy Density Lithium Battery (Binghamton U).....	581
V.D.3 Development of High-Energy Cathode Materials (PNNL)	586
V.D.4 <i>In situ</i> Solvothermal Synthesis of Novel High Capacity Cathodes (BNL)	593
V.D.5 Novel Cathode Materials and Processing Methods (ANL)	604
V.D.6 Novel Cathode Materials for High-Energy Lithium Batteries (UTA).....	609
V.D.7 Lithium-Bearing Mixed Polyanion Glasses as Cathode Materials (ORNL).....	616
V.D.8 Design of High Performance, High Energy Cathode Materials (LBNL)	622
V.D.9 Lithium Batteries with higher Capacity and Voltage (UTA).....	630
V.D.10 Exploiting Co and Ni Spinels in Structurally-Integrated Composite Electrodes (ANL)	638
V.E Electrolytes for High Voltage, High Energy Lithium-ion Batteries	642
V.E.1 Fluorinated Electrolyte for 5-V Li-ion Chemistry (ANL)	642
V.F Diagnostics	656
V.F.1 Design and Synthesis of Advanced High-Energy Cathode Materials (LBNL).....	656
V.F.2 Interfacial Processes – Diagnostics (LBNL).....	663
V.F.3 Advanced in situ Diagnostic Techniques for Battery Materials (BNL)	671
V.F.4 NMR and Pulse Field Gradient Studies of SEI and Electrode Structure (U Cambridge).....	679
V.F.5 Optimization of Ion Transport in High-Energy Composite Electrodes (UCSD)	687
V.F.6 Analysis of Film Formation Chemistry on Silicon Anodes by Advanced In Situ and Operando Vibrational Spectroscopy (UC Berkeley, LBNL).....	696
V.F.7 Microscopy Investigation on the Fading Mechanism of Electrode Materials (PNNL)	701
V.F.8 Characterization Studies of High Capacity Composite Electrode Structures (ANL).....	706
V.G Modeling Advanced Electrode Materials.....	711
V.G.1 Electrode Materials Design and Failure Prediction (LBNL)	711
V.G.2 Predicting and Understanding Novel Electrode Materials from First Principles (LBNL)	717
V.G.3 First Principles Calculations of Existing and Novel Electrode Materials (MIT).....	721
V.G.4 First Principles Modeling of SEI Formation on Bare and Surface/Additive Modified Silicon Anode (TAMU)	726
V.G.5 A Combined Experimental and Modeling Approach for the Design of High Current Efficiency Si Electrodes (GM, MSU).....	736
V.G.6 Predicting Microstructure and Performance for Optimal Cell Fabrication (BYU).....	742
V.H Metallic Lithium and Solid Electrolytes	749
V.H.1 Mechanical Properties at the Protected Lithium Interface (ORNL)	749
V.H.2 Solid electrolytes for solid-state and lithium-sulfur batteries (University of Michigan).....	754

V.H.3 Composite Electrolytes to Stabilize Metallic Lithium Anodes (ORNL)	758
V.H.4 Overcoming Interfacial Impedance in Solid-State Batteries (University of Maryland).....	763
V.H.5 Nanoscale Interfacial Engineering for Stable Lithium Metal Anodes (Stanford University)	771
V.H.6 Lithium Dendrite Suppression for Lithium-Ion Batteries (PNNL).....	781
V.H.7 Daikin Advanced Lithium Ion Battery Technology – High Voltage Electrolyte (Daikin America).....	793
V.H.8 Novel Non-Carbonate Based Electrolytes for Silicon Anodes (Wildcat Discovery Technologies)	806
V.I Lithium Sulfur Batteries.....	813
V.I.1 New Lamination and doping Concepts for Enhanced Li-S Battery Performance (U Pittsburgh)	813
V.I.2 Simulations and X-ray Spectroscopy of Li-S Chemistry (LBNL).....	824
V.I.3 Novel Chemistry: Lithium-Selenium and Selenium-Sulfur Couple (ANL)	832
V.I.4 Multi-Functional Cathode Additives (BNL)	841
V.I.5 Development of High Energy Lithium Sulfur Batteries (PNNL).....	852
V.I.6 Nanostructured Design of Sulfur Cathodes for High Energy Lithium-Sulfur Batteries (Stanford U).....	857
V.I.7 Addressing Internal “Shuttle” Effect: Electrolyte Design and Cathode Morphology Evolution in Li-S Batteries (TAMU).....	862
V.J Lithium-Air Batteries.....	872
V.J.1 Rechargeable Lithium-Air Batteries (PNNL)	872
V.J.2 Efficient Rechargeable Li/O ₂ Batteries Utilizing Stable Inorganic Molten Salt Electrolytes (Liox Power, Inc.).....	880
V.J.3. Li-Air Batteries (ANL)	887
V.J.4 Overcome the Obstacles for the Rechargeable Li-air Batteries (BNL/UWM)	893
V.K Sodium-Ion Batteries	899
V.K.1 Exploratory Studies of Novel Sodium-Ion Battery Systems (BNL).....	899
Appendix A: List of Contributors.....	906
Appendix B: List of Acronyms	913

FIGURES

Figure I- 1: Battery advancements needed to enable a large market penetration of PEVs	2
Figure I- 2: Comparative capacity per unit area of cells using 24M electrodes (shaded area) vs. traditional cells (curves shown near 2 and 4 mAh/cm ² , both plotted as a function of current density, or cell discharge power. The 24M cells range in capacity from .003Ah to 2Ah.....	6
Figure I- 3: Cycle life testing for battery cells show identical performance of battery electrodes dried with VFM (Lambda) or dried with IR/Convection dryer (Navitas).....	6

Figure I- 4: Discharge capacity of $\text{Li}_{1.25}\text{Nb}_{0.25}\text{Mn}_{0.5}\text{O}_2$. vs. Li metal half cells cycled at 55 °C and room temperature versus cycle number 7

Figure I- 5: Top: Components of ISC device that can be placed anywhere in a cylindrical or prismatic cell. Bottom images left to right: a Li-Ion cell with ISC device, a few minutes after melting the wax, and going into thermal runaway 7

Figure I- 6: (a) Schematic representation of $\text{Li}_x\text{Si-Li}_2\text{O}$ NPs synthesis method. (b) STEM image of $\text{Li}_x\text{Si-Li}_2\text{O}$ NPs. (c) 1st cycle voltage profiles of Si NPs/ $\text{Li}_x\text{Si-Li}_2\text{O}$ and Si NPs show that the incorporation of $\text{Li}_x\text{Si-Li}_2\text{O}$ NPs compensates the 1st cycle capacity loss of Si NPs 8

Figure II- 1: Development areas and partners 16

Figure II- 2: Projected cell development timeline 17

Figure II- 3: Cycle life improvement of coated Si- SiO_x -C anode 18

Figure II- 4: Cycle life from down-selected lithium-rich cathode (C#24) 18

Figure II- 5: CC-CV cycling of baseline 21Ah pouch cells 19

Figure II- 6: Effect of ALD coating on the cyclability of Mn-rich NCM. The numbers refer to different coating conditions 21

Figure II- 7: Effect of ALD coating Ni-rich NCM cathode. The numbers refer to different coating conditions 22

Figure II- 8: Comparison of the expansion of various Si-based electrodes. The data are for cells after the 50th charge 22

Figure II- 9: Effect of SiO electrode porosity on cycle-life 22

Figure II- 10: Comparison of the cycle-life of Si-alloy and SiO-based full cells at room temperature and 0.3C rate 23

Figure II- 11: Comparison of the adhesion force of two cathode binders 23

Figure II- 12: Capacities of Amprius’ 18 Silicon-LCO Cells 26

Figure II- 13: Energies of Amprius’ 18 Silicon-LCO Cells 26

Figure II- 14: Energy Densities of Amprius’ 18 Silicon-LCO Cells 27

Figure II- 15: Specific Energies of Amprius’ 18 Silicon-LCO Cells 27

Figure II- 16: Amprius’ cells continue to cycle. Amprius’ Silicon-NCM cells continue to exhibit stable cycling past 400 cycles. Amprius’ Silicon-LCO cells also continue to exhibit stable cycling past 100 cycles 28

Figure II- 17: Voltage and Current Profiles from the HPPC Test, which Amprius’ Silicon-NCM Cells Passed 28

Figure II- 18: Potential-Capacity Curves from the HPPC Test, which Amprius’ Silicon-NCM Cells Passed 29

Figure II- 19: Amprius identified solvent compositions that extend the cycle lives of cells with silicon nanowire anodes 29

Figure II- 20: Amprius identified electrolyte additives that extend the cycle lives of cells with silicon nanowire anodes 30

Figure II- 21: Amprius’ design for the interim, Year 2 cells, with a target capacity of at least 10 Ah 30

Figure II- 22: (left) Seo 1.8 kWh module. (right) Seo Single-Module Thermal Chamber (SMTC) 33

Figure II- 23: Constant-current rate test discharge curves for Seo modules. 80°C internal temperature, 30°C ambient environment 34

Figure II- 24: Discharge capacities for all characterization data reported by ANL (modules 1, 2 and 3) and Seeo (modules 4, 5 and 6). Modules were tested with internal temperatures of 80°C, while in 30°C ambient environments.....	35
Figure II- 25: Peak Power results for module 1 at beginning of life (BOL), from 0% DOD to 90% DOD in 10% increments. Internal temperature was 80°C, external temperature was 30°C.....	36
Figure II- 26: DST ₂₂₅ cycle life RPT results – C ₃ /3 and DST ₂₂₅ capacity and energy.....	37
Figure II- 27: DST ₂₂₅ cycle life RPT results – peak power at 80% DOD	37
Figure II- 28: Peak power capability showing extrapolation towards the EOL limit (red line). Internal temperature was 80°C, external temperature was 30°C.....	38
Figure II- 29: USABC Seeo vehicle US06 drive cycle profile.. The reference power is scaled by the value on the y-axis. For instance, at 5600 W, the max discharge is 5600 W and the max regeneration power is 2883 W.....	39
Figure II- 30: US06 full discharge at 438 W/kg (module). Internal temperature was 80°C, external temperature was 30°C	39
Figure II- 31: Stand test fixture (STF) for a single module	40
Figure II- 32: C/3 discharges before (orange, baseline) and after (blue) a 15-day stand test using the module’s internal power for heating. Internal temperature was 80°C, external temperature was 30°C	41
Figure II- 33: Conceptual 32.4 kWh pack design with 18 modules in a 2S9P configuration that would retain 50% of the pack energy after 30 days at 80°C using internal power	41
Figure II- 34: Large format StructurePore™ carbon scaffold	44
Figure II- 35: LMO from aqueous bath.....	45
Figure II- 36: a) Charge/discharge curve, and b) power curve data for aqueous LMO.....	45
Figure II- 37: Non-aqueous spinel LMO on StructurePore™ Cathode.....	46
Figure II- 38: a) XRD of LiMn ₂ O ₄ deposited by electroplating in a non-aqueous bath. The red curve is experimental data and the blue lines are the expected peak locations of a single phase spinel. b) Voltage curve for non-aqueous LMO	46
Figure II- 39: Porous carbon composite anode (a) power and (b) cycle life data. Electrode areal charge density is 1 mAh/cm ²	47
Figure II- 40: Twenty layer ultrasonic electrode weld	48
Figure II- 41: a) Characteristic voltage curves for initial LMO pouch cells from non-aqueous bath. b) Cycle life for same pouch cell. Electrode areal charge density is 2mAh/cm ²	48
Figure II- 42: Power curves for LMO pouch cell. Electrode areal charge density is 2mAh/cm ²	49
Figure II- 43: Initial LMO pouch cell from non-aqueous bath (left) and charged high power graphite negative electrode (right). Cathode dimension: 16 mm X 23 mm X 0.12 mm. Anode dimension: 18 mm X 25 mm X 0.08 mm. Separator thickness: 0.02 mm	49
Figure II- 44: The baseline POC module design.....	51
Figure II- 45: The baseline POC module deliverable	51
Figure II- 46: The Simulink model of the hybrid system	52
Figure II- 47: The Simulink model predictions of cold crank performance.....	52
Figure II- 48: Warm and cold discharge resistances for three A123 cells performance.....	53
Figure II- 49: POC 9 built with the 20Ah Gen3 A123 cells.....	53
Figure II- 50: The voltage trace during cold crank on POC 9.....	54

Figure II- 51: Cap fade testing of Baseline cells 54

Figure II- 52: Gassing reduction with additive 55

Figure II- 53: The prototype CAD model 56

Figure II- 54: Effect of cathode materials surface area on the discharge resistance. Cathode 1) Baseline; Cathode 2) surface area: 30% more than baseline; Cathode 3) Surface area: 80% more than baseline 58

Figure II- 55: Effect of cathode porosity on cell resistance. Cathode 1) Baseline; Cathode 2) 13% lower porosity than baseline; Cathode 3) 25% lower porosity than baseline..... 59

Figure II- 56: Effect of porosity on electrode adhesion 59

Figure II- 57: Effect of cathode porosity on cold-cranking power. Cathode 1) Baseline; Cathode 2) 13% lower porosity than baseline; Cathode 3) 25% lower porosity than baseline 59

Figure II- 58: Simulation data for the pack temperatures when stored at a 75°C ambient for 4 hours 60

Figure II- 59: Cylindrical vs Prismatic module design..... 63

Figure II- 60: Gassing rates of different electrolytes..... 64

Figure II- 61: Comparison of gassing between LTO and LMO electrodes 65

Figure II- 62: Discharge curves of positive electrode blends 66

Figure II- 63: Cold crank curves of positive electrode blends 67

Figure II- 64: Optical images of selected samples from base sheet optimization trials 70

Figure II- 65: SEM images of samples from optimization trials 70

Figure II- 66: SEM images (20k magnification) of selected samples from the base sheet optimization trials 71

Figure II- 67: Effect of corona treatment intensity level on wetting. Wetting data collected 5 minutes after applying solvent 72

Figure II- 68: Effect of corona treatment on dielectric breakdown voltage 72

Figure II- 69: Optical images (transmitted light) of corona treated samples at varying intensity levels 73

Figure II- 70: TEM images of uncoated, TiO₂ coated, and Al₂O₃ coated electrodes prior to cycling 77

Figure II- 71: EIS analysis of uncoated, TiO₂ coated (red), and Al₂O₃ coated (green) cathode electrodes shows similar impedance profiles prior to cycling..... 77

Figure II- 72: Rate capability testing of uncoated, 4 layer TiO₂, 8 layer TiO₂, 4 layer Al₂O₃, and 8 layer Al₂O₃ coatings 77

Figure II- 73: Peak power discharge testing of uncoated, 4 layer TiO₂, 8 layer TiO₂, 4 layer Al₂O₃, and 8 layer Al₂O₃ coatings..... 78

Figure II- 74: Cycle life testing at 1C-1C from 3.0-4.3V of uncoated, 4 layer TiO₂, 8 layer TiO₂, 4 layer Al₂O₃, and 8 layer Al₂O₃ coatings..... 78

Figure II- 75: Cycle life testing at C/3-C/3 from 3.0-4.3V of uncoated, 4 layer TiO₂, 8 layer TiO₂, 4 layer Al₂O₃, and 8 layer Al₂O₃ coatings..... 78

Figure II- 76: TEM images of uncoated, TiO₂ coated, and Al₂O₃ coated electrodes post 1C-1C cycling. Images on the left are brightfield images while images on the right are high resolution images..... 79

Figure II- 77: EIS analysis of uncoated, TiO₂ coated (red), and Al₂O₃ coated (green) cathode electrodes post 1C-1C cycling. The Al₂O₃ coated cathode shows less impedance growth with cycling..... 79

Figure II- 78: Plot of optimized cell energy density based on adjustable design parameters and manufacturing constraints.....	80
Figure II- 79: Baseline SiNANODE/LCO full cell.....	83
Figure II- 80: Voltage hysteresis of SiNANODE and Si powder-graphite full cells.....	83
Figure II- 81: SiNANODE half cell with 700~1000mAh/g.....	84
Figure II- 82: >1600mAh/g SiNANODE's voltage profile.....	84
Figure II- 83: Uniform Si Nanowire distribution on graphite powders for 700mAh/g (Left) and >1600mAh/g (Right).....	84
Figure II- 84: Voltage profiles and rate capabilities of cathode candidates	85
Figure II- 85: Cathode cyclability vs. different electrolyte	85
Figure II- 86: Cycle life at 0.3C rate (80% DOD)	85
Figure II- 87: (a) 1200mAh/g SiNANODE cyclability in half cell; (b) 1400mAh/g SiNANODE cyclability in half cell	86
Figure II- 88: Discharge voltage profiles of various cathode materials.....	87
Figure II- 89: Cycle life of the pouch cell using 600 mAh/g SiNANODE at 0.5C rate (DOD 100)	87
Figure II- 90: Thickness change of High Energy Density Pouch Cells: SiNANODE/NCA.....	88
Figure II- 91: 600mAh/g SiNANODE/NCA full cell cyclability.....	88
Figure II- 92: 1100mAh/g SiNANODE/NCA pouch cell performance.....	88
Figure II- 93: Low temperature performance of SiNANODE/NCA cell	89
Figure II- 94: Pouch Cell Specific Power of SiNANODE vs. Graphite	89
Figure II- 95: New electrolyte enables better cycling performance	90
Figure II- 96: Si Nanowire grown on larger graphite powders (Left) and smaller graphite powders (Right) for >800mAh/g	91
Figure II- 97: Calendered SiNANODE Anode (Left) and Graphite Anode (Right) with 1.5g/cm ³	91
Figure II- 98: Winding on 0.9 mm diameter pin.....	92
Figure II- 99: Cell thickness reduction vs. Si% in the anode diameter pin	92
Figure II- 100: 32%SiNANODE/LCO pouch cell: discharged at C/10.....	93
Figure II- 101: 32%SiNANODE/LCO pouch cell: discharged at C/10.....	93
Figure II- 102: dQ/dV comparison of original Si alloy and the new version of Si alloy with improved microstructure.....	97
Figure II- 103: Cycle life comparison of original Si alloy and the new version of Si alloy with improved microstructure. 18650 cells with improved microstructure show lower fade than the 18650 cells with the original Si alloy	97
Figure II- 104: Half cell cycling of pitch coated V11 annealed at 500°C, pitch amounts are listed in the legend	98
Figure II- 105: SEM and EDS mapping results of 0.5 mol% LaPO ₄ coated NMC622 materials (T2696).....	99
Figure II- 106: Coin-cell comparison results for 3M (P0357) and Umicore materials (T2696)	99
Figure II- 107: Effect of voltage window on the cycle life performance.....	100
Figure II- 108: Effect of different electrolyte on cycle life performance	101
Figure II- 109: Cycle life at 30 °C at C/3 between 2.81 V and 4.29 V corresponding to 5-95% of SOC, and defining 4.4-2.5 V as the 100% SOC	102
Figure II- 110: Rate Capability testing at 25 °C between 4.4-2.5 V.....	102

Figure II- 111: Cell Thickness Expansion versus % CV7 Silicon Alloy in Anode 104

Figure II- 112: Voltage changing with (a) Li deposition amount (mAh) to LiP electrode and (b) Li dissolution amount (mAh) from LiP electrode at the 36th cycle in LiP / Li foil coin cells..... 107

Figure II- 113: Cycling efficiency of LiP electrode in LiP / Li foil coin cells, varying with cycle number..... 107

Figure II- 114: Nyquist plots of electrochemical impedance spectra measured at (a) 0% Li deposition (b) 50% Li deposition to LiP electrode at cycle 2 in LiP / Li foil coin cells 108

Figure II- 115: (a) R_{ohmic} and (b) $R_{interface}$ obtained from Nyquist plots varying with Li deposition amount to LiP electrode at cycle 2 in LiP / Li foil coin cells 108

Figure II- 116: Voltage profile for a pouch cell made with PSU-7 cathode, LiP anod, and ANL’s electrolyte 109

Figure II- 117: The (a) capacity and (b) discharge specific energy for a pouch cell with PSU-7 cathode, LiP anode, and ANL’s electrolyte. The cells were cycled at C/20 in the first 2 cycles, then at C/10 in subsequent cycles 109

Figure II- 118: Battery Simulation Compared to Actual Vehicle Results..... 112

Figure II- 119: PTC and Heat Pump Heating Performance Compared 113

Figure II- 120: Comparing Heating System Power Consumption..... 113

Figure II- 121: COP Comparision of PTC and Heat Pumps 114

Figure II- 122: Thermal System Energy Usage at -20C Driving Conditions 114

Figure II- 123: Time to Cool the Battery Pack from Hot Soak 114

Figure II- 124: Study of passive heating and cooling; most benifit is found in mild ambient like Seattle 115

Figure II- 125: Relative Capacity of Battery Pack during Battery Life 115

Figure II- 126: Battery Pack Capacity Can Be Reduced 5% and Achive Life Requirements 115

Figure II- 127: -20°C to 0°C Warm Up Test 116

Figure II- 128: 43°C to 30°C Cooling Test Comparison 116

Figure II- 129: US06 Drive Cycle starting at 43°C soak..... 117

Figure II- 130: Davis Dam Test starting at 43°C soak 117

Figure II- 131: Cost Down Is Achived If AC Compressor Is Common With Cabin Cooling..... 117

Figure II- 132: Comparison of DC impedance of dry processed electrodes..... 119

Figure II- 133: Rate capability – dry process electrodes 119

Figure II- 134: Profiles of 5C continuous discharges with the dry process electrodes 120

Figure II- 135: 1C/1C 100% DOD cycle life (3~4.2V) at 45°C 120

Figure II- 136: Calendar life test at 60°C for 1 month 120

Figure II- 137: Wetting balance test results for the Maxwell dry-coated electrodes. Wetting rates are shown for all past samples and the final Build 6. Anode kinetics were similar to the highest wetting rates observed. Cathode kinetics were somewhat below historical values though the absolute values of the wetting rates for Build 6 cathode are higher than the anode. Testing was done in a baseline 3:7 EC:EMC solution with 1.2M LiPF6 for all samples 121

Figure II- 138: Porosity of Maxwell dry-coated samples as determined by Hg porosimetry. Cathode porosity was improved for Build 6 relative to Build 3 samples..... 121

Figure II- 139: Thickness of laminates as a function of machine direction thickness using ENTEK calendaring equipment for 15Ah final deliverables..... 122

Figure II- 140: 3Ah Pouch Cell Rate Performance	123
Figure II- 141: 3Ah Pouch Cell HPPC Performance (5C Gen, 10 sec).....	123
Figure II- 142: 3Ah Pouch Cell Cycle Life Performance (1C/1C Full Swing).....	123
Figure II- 143: The surface SEM images of aqueous cathode: (a) New mix processed aqueous cathode, (b) Old mix processed aqueous cathode	125
Figure II- 144: The ASI thru HPPC test (5C/3.75C, 10sec pulse).....	125
Figure II- 145: Cycle life results (2C charging / 5C discharging, 100% DOD from 3 to 4.2V).....	126
Figure II- 146: Calendar life results at SOC100% and 60°C	126
Figure II- 147: Technology-dependent processes impacting cost estimates – aqueous, dry coating and laminated separator.....	126
Figure II- 148: Cycle life results (2C charging / 5C discharging, 100% DOD from 3 to 4.2V).....	127
Figure II- 149: Separator cost reduction estimate for the laminated separator	127
Figure II- 150: Formation cost reduction	128
Figure II- 151: Cost comparison for the integration of proposed solutions (excluding formation effect).....	128
Figure II- 152: Cost comparison for the integration of proposed solutions (including the formation effect).....	128
Figure II- 153: Capacity over 50 cycles of the 90-5-5 sample (NMC:carbon:binder) cured at 328 fpm (100 meter per minute) under 3 lamps.....	130
Figure II- 154: Capacity over 50 cycles of the 90-7-3 sample (NMC:carbon:binder) cured at 100 fpm (~ 30 meters per minute) under 3 UV lamps.....	131
Figure II- 155: AC impedance comparison of cathode with 5% PVDF and UV binder taken at -10°C.....	131
Figure II- 156: Cathode with 5% UV binder demonstrated better capacity retention (by ~7%) than cathode with 5% PVDF binder	131
Figure II- 157: Schematic diagram of process flows for manufacturing baseline cells, interim cells and final cells with 3D current collector and alloy anodes (introducing Stabilized Lithium Metal Powder (SLMP) is optional)	135
Figure II- 158: Effect of decreasing irreversible capacity loss (ICL) from 25 to 10% with increasing cell capacity (current loading from 2 to 5 mAh/cm ²) on the interim cell energy parameters (3DCuSnFe / NMC design model)	135
Figure II- 159: 3D Current collector baseline cells 3, 4 and 5 with 1000 cycles at 86-88% capacity retention	136
Figure II- 160: 3DCuSnFe/Graphite alloy anode capacity retention at high C-rates allows charging time improvement vs. Graphite anode.....	136
Figure II- 161: 3DCuSnFe-binder electrode bending test over various diameter rolls	137
Figure II- 162: 3DCuSnFe-Graphite/NMC(111) interim cell with 985 cycles at 80% capacity retention	137
Figure II- 163: 3D electrode energy density with different Si alloy material content at 3%, 6%, 9%; and 2-3 mAh/cm ² 3DCuSnFe-Si-Graphite/NMC(532) cells cycled 200 cycles at >80% retention in coin cell assemblies	137
Figure II- 164: The voltage profiles and differential capacity curves of final half cells with different 3DCuSnFe versions during formation cycle	138
Figure II- 165: Rate capability of final full cells with different 3DCuSnFe porous versions of substrates.....	139

Figure II- 166: Dual side simultaneous separator slot die coating.....	143
Figure II- 167: Experimental matrix for selection of the appropriate release liner	144
Figure II- 168: Schematic of lamination process for making the anode laminated stacks	145
Figure II- 169: Formation cycling for 2 Ah cell with the anode laminated stack	145
Figure II- 170: Cycle life study of dry process cathodes in full DLP cells; loading of 3.3mAh/cm ² ; cut off voltage 4.2-2.7V; charged and discharged at 0.5C.....	149
Figure II- 171: ARC data overlay of heat-wait-see tests of pure NCM wet processed 2Ahr cells with that of dry processed 50:50 & 25:75 LMFP:NCM 2Ahr Cells	149
Figure II- 172: Cycle life of low-solvent processed anode in full Li ion cells with dry-processed cathode	150
Figure II- 173: Slot-die coated low solvent anode with loading of 4 mAh/cm ²	151
Figure II- 174: 4Ah cells are DST cycled 100 times to 80% DoD Each 100 cycles, they are checked for C/3 discharge capacity to 100% DoD and DST discharge capacity to 100% DoD. They are also tested for peak power capability, and then they begin another 100 DST cycles to 80% DoD.....	151
Figure III- 1: Schematic of a NMP Recovery Process.....	157
Figure III- 2: Schematic of the Air Processing for a Dry Room	158
Figure III- 3: Effect of the Size of the Heat Exchanger on the Energy Demand and Cost of Dry Room Operations	159
Figure III- 4: Schematic of the Production Process for NMC Cathode Material	160
Figure III- 5: Rate capability study on NMC622/Gr pouch cells of increasing areal capacities shown as a function of C-rate (a) and current density (b). Dashed lines represent differing values of $\gamma = 0.3, 0.6, \text{ and } 0.9$. Open symbols of blue (LFP/Gr) and red (NMC333/Gr) transformed from Zheng et al. <i>ENREF_9 Electrochim Acta</i> 71 258 (2012)	161
Figure III- 6: Battery price for a 45 kWh use and 90 kWh net 360 V as a function of volumetric capacity of the advanced Li-ion negative electrode	161
Figure III- 7: Cradle-to-gate energy consumption for batteries with different cathode materials (NMC= $\text{LiNi}_{0.4}\text{Co}_{0.2}\text{Mn}_{0.4}\text{O}_2$, LMR-NMC= $0.5\text{Li}_2\text{MnO}_3 \cdot 0.5\text{LiNi}_{0.44}\text{Co}_{0.25}\text{Mn}_{0.31}\text{O}_2$, LCO= LiCoO_2 , LFP= LiFePO_4 , HT=hydrothermal preparation, SS=solid state)	165
Figure III- 8: Schematic of Processes Avoided by Recycling.....	166
Figure III- 9: Comparison of element values to cathode price.....	167
Figure III- 10: Energy required to produce battery	167
Figure III- 11: Batteries contribute a significant fraction of life-cycle sulfur emissions. Pioneer plant energy intensity based on Ellingsen et al. Nth plant assembly energy intensity based on Dunn et al. (2012) and reflects mature, high-throughput battery assembly facilities	168
Figure III- 12: Cathodes made from recycled materials minimize sulfur emissions	168
Figure III- 13: Fuel cycle and vehicle cycle total energy consumption for BEVs, PHEV50s, and ICVs. The PHEV50 (km) is modelled as being in charge-depleting (CD) and charge-sustaining (CS) modes during 47.5% and 52.5% of operation, respectfully. The PHEV50 is assumed to have a fuel economy of 3.2 and 8.5 gasoline equivalent L/100 km in CD and CS modes, respectively. The BEV is assumed to have a fuel economy of 2.9 gasoline equivalent L/100 km mpgge while the ICV operates at 23 mpg. The liquid	

fuel used by the ICV and the PHEV30 during CS mode is conventional gasoline, 4% of which derives from oil sands recovered via in-situ production.....	169
Figure III- 14: Relative performance of BEV (NMC cathode) and PHEV50 (LMO cathode) as compared to ICV. Green, orange, black, red, blue, and purple points represent results for vehicles powered with the average U.S. grid, North East Power Coordinating Council regional grid, the California grid, exclusively natural gas-fired power plants, exclusively coal-fired power plants, and hydropower plants, respectively. Hollow and full points represent results generated with the at capacity and low-throughput battery assembly energies, respectively.....	169
Figure III- 15: Lithium loss from cathodes under varied conditions	169
Figure III- 16: Impact of individual standardization strategies on battery cost (positive is cost reduction).....	176
Figure III- 17: Average change in relative capacity vs. time for the three cycling protocols used in the experiments. The markers represent the data, and the solid curves, the least squares fit. The values of r^2 for these fits was 0.99. The error bars represent the standard deviation at that point ($\pm 1\sigma$). If $1\sigma \leq \sim 5\%$ of the reported value, the error bar will not be visible	181
Figure III- 18: Increase in average, relative change in resistance vs. time for the cells tested using the USABC and QC/T 743 (pulse) protocols. The values from the former method were calculated at two values of %DOD and using two pulse widths to facilitate comparison with the values from QC/T 743 (pulse). The values of r^2 were typically 0.99. The error bars represent the standard deviation at that point ($\pm 1\sigma$). If $1\sigma \leq \sim 5\%$ of the reported value, the error bar will not be visible	181
Figure III- 19: Capacity fade as a function of testing length. The solid line represents the BLE fit based on data from RPT 67.....	187
Figure III- 20: Life estimation determined using capacity fade, resistance growth and power fade as a function of aging	188
Figure III- 21: New EV Voltage Definitions and Key Concepts	188
Figure III- 22: Cell temperature and voltage during a thermal ramp test of a COTS 18650 cell.....	192
Figure III- 23: Cell temperature and voltage during a modified hotbox test of a COTS 18650 cell	192
Figure III- 24: Cell temperatures during a propagation test of a 1S10P LiCoO ₂ battery	193
Figure III- 25: Cell temperatures during a propagation test of a 1S10P LiFePO ₄ battery with cells connected with Ni tab.....	193
Figure III- 26: Cell temperatures during a propagation test of a 1S10P LiFePO ₄ battery with cells connected with a copper bus bar	194
Figure III- 27: (Right) force and displacement during crush tests (red and blue traces) and a crush simulation (orange trace) of a 1S12P battery. (Left) Images from the simulation showing the buckling of the electrode layers in a sandwich model	194
Figure III- 28: Computed tomography image of a 1S12P battery after a crush test using a cylindrical impactor.....	195
Figure III- 29: Sandwich model of a 12S1P battery crush test using a cylindrical impactor	195
Figure III- 30: Heat released (kJ) as a function of % capacity fade and %DOD for aged and fresh COTS cells	196
Figure III- 31: Peak heating rate (W) as a function of % capacity fade and %DOD for aged and fresh COTS cells.....	196
Figure III- 32: Efficiency of cells tested at 30°C in NREL’s calorimeter during FY15	199

Figure III- 33: Efficiency of LTO cell tested at 30°C under a full charge/discharge 200

Figure III- 34: Efficiency of LTO cell tested at 30°C under a full and partial charge..... 200

Figure III- 35: Efficiency of LTO cell at different temperatures under a partial discharge 201

Figure III- 36: Entropic heating of LTO cell at 30°C and 0°C..... 201

Figure III- 37: Efficiency comparison of PHEV/EV cell under full and partial discharge 202

Figure III- 38: PHEV cell heat generation under US06 drive cycle 202

Figure III- 39: Infrared image of PHEV cell at the end of a 2C discharge 203

Figure III- 40: Modular Multiscale Model Framework of MSMD 206

Figure III- 41: Standard MSMD input file structure 207

Figure III- 42: From left to right (top to bottom) the parameters summarized are: i_0 , D_s , E_{act} , surface area, radius 1, volume fraction 1. With respect to optimization there are only 2 or 3 free parameters: Cells labeled 4,5,7,8 are clearly correlated, so they represent only one actual choice by the optimizer. Except for outliers, V_9 attains only one value. V_6 appears uncorrelated with the other parameters..... 211

Figure III- 43: Battery simulation through ANSYS Battery Design Tool (ABDT) 215

Figure III- 44: Comparison of transient simulation results (1.8 million unknowns)..... 216

Figure III- 45: Comparison of transient simulation results (0.41 million unknowns)..... 216

Figure III- 46: Flow distribution along the cooling channels 217

Figure III- 47: Pack level validation overview..... 217

Figure III- 48: Electrical system model for a unit in a production-intent battery pack..... 217

Figure III- 49: Thermal system model for a unit in a production-intent battery pack..... 218

Figure III- 50: Thermal system model for a unit in a production-intent battery pack..... 218

Figure III- 51: ANSYS website describes the battery simulation capabilities developed under the CAEBAT project 220

Figure III- 52: Automated mesh generation from cell to pack level with corresponding results of thermal solution..... 223

Figure III- 53: Von Mises stress distribution in different domains of a pouch cell under external mechanical loading 224

Figure III- 54: Temperature distribution in a module with asymmetric cooling..... 225

Figure III- 55: Calculated volumetric heat source using loosely and tightly coupled scenarios 225

Figure III- 56: CAEBAT-ICE workflow environment for simulation setup, job launch and data post-processing 226

Figure III- 57: Interactions among the mechanical, EM, and thermal solvers for the simultaneously coupled modeling approach 230

Figure III- 58: (a) Cross-sectional view of a pouch cell and schematic of an RS: the pouch cell is represented by a single RS that explicitly represents the thickness proportions of each individual component. (b) Schematic and dimensions of the single RS indentation model: a quarter of the actual domain is utilized in the finite-element model based on symmetry. (c) Schematic of electrical connections for the single RS model and full pouch cell model: in this work, scaled electrical conductivity properties are utilized for each individual component of the single RS model to theoretically match the overall Joule heat..... 232

Figure III- 59: Experimental measurement of material properties..... 233

Figure III- 60: (a) Correlation of numerically predicted and experimentally measured force-strain curves for the small-punch indentation test and numerically predicted deformation of the separator and active materials at the instant of the cell fracture. The crack in the separator layer propagates along the y-direction, consistent with the experimental observation. (b) Comparison of the numerically predicted and experimentally measured force-strain responses for three different indentation tests and the numerically predicted deformation of the battery cell at the instant of the cell fracture. With an increase in indenter diameter, the maximum indentation depth at the moment of the fracture increases, indicating that the larger-punch test results in a delayed failure of the cell	235
Figure III- 61: Evolution of average current (A) across the active material before and after short circuit at the electrical contact area, and isotropic-view of the current density (A/m ²) distribution in the battery cell for the three different indentation tests: (a) small punch, (b) medium punch and (c) large punch.....	236
Figure III- 62: Comparisons of high current cantrilbat calculations against Mao et al., using the OCV fitting capability, the generalized Butler-Volmer implementation, and Surface Damkoeler limiter within Cantera	241
Figure III- 63: Corresponding Cathode Temperature vs. time. Temperatures were relatively flat across cell structure	242
Figure III- 64: Geometry and mesh of the simulated cylindrical cell	242
Figure III- 65: Sample results for cylindrical cell (temperature on the left and the electrical potential on the right).....	242
Figure III- 66: Simulated transport through a reconstructed composite cathode.....	243
Figure III- 67: Simulated thermal response from an internal short in an 18650 cell.....	243
Figure III- 68: Methods of upscaling of heat generation tables are being evaluated.....	244
Figure III- 69: Charge voltage and SOC of Li-ion cell with Si alloy based anode with and without swelling effect accounted for in computational model.....	246
Figure III- 70: Calendar and cycle life ageing of 26650 LFP/Graphite cell with new ageing models (temperature in degrees Celsius); data taken from Delacourt et al., <i>Journal of the Electrochemical Society</i> , 159 (8) A1283-A1291 (2012)	247
Figure III- 71: Nondimensional temperature and voltage data acquired from one single cell and one multi-cell nail penetration tests; data being used for validation of model	247
Figure III- 72: GH-MSMD significantly improves the computational speed of nonlinear multiscale battery model without compromising accuracy.....	250
Figure III- 73: Comparison of electrical and thermal response of a battery for a mid-size sedan plug-in hybrid electric vehicle (PHEV10) on the US06 20-minute driving power profile from the GH-MSMD and the original MSMD.....	251
Figure III- 74: Comparison of the original MSMD and the GH-MSMD framework structure and main changes in the GH-MSMD.....	252
Figure III- 75: A-SVM verification and benchmark results against various MSMD/GH-MSMD models.....	253
Figure III- 76: Custom GUI of GH-MSMD set up in ANSYS/Fluent.....	254
Figure III- 77: NREL's custom implementation of GH-MSMD in Fluent is verified. Solid lines are the cell voltage response of NREL custom GH-MSMD model simulations, and the symbols are corresponding outputs from the Fluent MSMD Battery Simulation Module.....	254

Figure III- 78: CAD image of a 20 cell module complete with packaging and heat-exchange fins (geometry courtesy of Ford): the hardware uses the same 15 Ah cells and has more than 800 small parts meshing of which results in more than 16 million elements, making it challenging to run efficient simulations..... 258

Figure III- 79: Illustration of obtaining parameters in the constitutive models by calibration against component-level test data. This information is then used as input to the cell-level and larger scale simulations 258

Figure III- 80: a) Comparison of experimental and simulated geometry showing no breach of packaging material under the impact load conditions tested; the model results for this test case compare well with the EUCAR-2 response observed in the tests. b) A detailed comparison of the force vs time shows that the test data suffer from oscillations of the indenter upon impact. The simulation results do not capture this because the models do not account for factors such as elasticity of the indenter material and fixtures to hold the cell..... 259

Figure III- 81: Electrical and thermal responses of the cell: a) Model predictions (solid line) vs experimental data from high-speed imagery (dots), b) Comparison of the experimentally observed maxima for the surface temperatures (dots) against the model predictions (bars). In general, the experimental results are consistent with the simulation: the initial voltage drop varies directly as a function of contact time with the load and the maximum temperature decreases with a decrease in the contact duration 260

Figure III- 82: (a) Experimental test set up for X-plane crush of a cell string and (b) Sample simulation results comparing deformation with and without the packaging 260

Figure III- 83: a) Simulation conditions for the module showing the different orientations of the test article subjected to crush; b) Sample simulation results for impact along the x-plane; (c) Sample simulation results for impact along the z-plane..... 262

Figure IV- 1: Representative lithiation and delithiation voltage profiles of Li//various silicon content Si-Gr coin cells at room temperature. The cells were cycled from at ~C/10 from 1.5 to 0.005V (LCV) using the electrolyte 1.2 M LiPF₆ in EC:EMC (3:7 wt.%) with 10 wt.% FEC additive..... 271

Figure IV- 2: Representative delithiation capacities of Li//Si-Gr coin cells at room temperature. The cells were cycled from at ~C/10 from 1.5V to various lower voltage cutoffs (LCV) 271

Figure IV- 3: Average cycling performance of various positive electrodes//Si-Gr coin cells at room temperature, following the initial formation procedure. The cells were cycled from 3.0 to 4.1V at a C/5, with the exceptions of 5V spinel (3.5 to 4.7V) and HE5050 (3.0 to 4.4V). The error bars represent 2σ standard deviation..... 272

Figure IV- 4: Average coulombic efficiency during cycling of various positive electrodes//Si-Gr coin cells at room temperature, following the formation procedure (see plot above). The cells were cycled from 3.0 to 4.1V at a C/5, with the exceptions of 5V spinel (3.5 to 4.7V) and HE5050 (3.0 to 4.4V). Error bars not included 272

Figure IV- 5: Simple modeling plot showing the capacity retention based on various coulombic efficiencies during cycling of a hypothetical cell 273

Figure IV- 6: Average cycling performance of NCM523//Si-Gr coin cells at room temperature. The cells were cycled from 3.0 to 4.1V at a C/3 rate with RPT's (C/24 cycle and HPPC) occurring at the beginning and at cycle 97. The error bars represent 2σ standard deviation 274

Figure IV- 7: Average coulombic efficiency during cycling (see the prior figure) of NCM523//Si-Gr coin cells at room temperature. Error bars represent 2σ standard deviation	274
Figure IV- 8: Representative area specific impedance (ASI) vs. cell voltage for NCM523//Si-Gr coin cells at room temperature, before (filled symbols) and after (open symbols) aging cycles. The ASI data shown were obtained with a 3C discharge pulse.....	275
Figure IV- 9: Anodes fabricated by the CAMP Facility and their matching cathode couple for xx3450 pouch cell evaluation. Refer to the nomenclature on the left for reference to the figures that follow.....	276
Figure IV- 10: Average cycling performance of various generations of the NCM523//Si-Gr xx3450 pouch cells at 30°C, with complementary NCM523//Gr xx3450 pouch cells representing baseline data, following the initial formation procedure. The cells were cycled at a $\sim C/3$ rate. The error bars represent 2σ standard deviation	277
Figure IV- 11: Average coulombic efficiency of various generations of the NCM523//Si-Gr xx3450 pouch cells at 30°C, with complementary NCM523//Gr xx3450 pouch cells representing baseline data, following the initial formation procedure. The cells were cycled at a $\sim C/3$ rate	277
Figure IV- 12: Photo of electrodes from xx3450 pouch cells that have been disassembled in various states of charges (SOC). The top row is from graphite only electrodes with PVDF binder. The bottom is from 5wt.% silicon-based electrode with LiPAA binder. The electrodes to the far right are representative cathodes	277
Figure IV- 13: Summary of electrode thickness changes as a function of state of charge for various electrodes with differing amounts of silicon present in the electrode.....	278
Figure IV- 14: Third cycle capacity (1.5-0.0 V) per g of active material for graphite-Si (0-15 wt%) electrodes as measured with a 0.085 mA-cm ⁻² current in coin cells with a Li-metal counter electrode and Gen2 + 10 % FEC electrolyte. Silicon, graphite, and C-45 are included in the active material weight	278
Figure IV- 15: Plots from graphite-Si//NCM523 full cells with Gen2 + 10% FEC electrolyte cycled between 2.5 and 4.1 V and 0.05 mA cm ⁻² current ($\sim C/20$ rate) for 0-15 wt% Si-content. The (a) charge-discharge profiles, and (b) differential capacity plots as a function of cell voltage shown, are from the second cycle	279
Figure IV- 16: HPPC test data from full cells with either the mixed graphite-15 wt% Si electrode (15 wt% Si) or graphite-only electrode (0 wt% Si), NCM523 positive electrode, and Gen2 + 10 wt% FEC electrolyte. The data were measured in a three-electrode setup, and deconvolutes contributions from the positive and negative electrodes to the full cell impedance, after formation cycling	279
Figure IV- 17: Capacity as a function of cycle number of Si-graphite // NCM523 full cells (0-15 wt% Si) with Gen2 + 10% FEC electrolyte, cycled in a 2.5-4.1 V voltage window using 0.05 mA cm ⁻² ($\sim C/20$, first 3 and last 3 cycles) and 0.33 mA cm ⁻² (C/3, intermediate cycles) currents. The specific capacity refers to g of the oxide active material. Data shown are from duplicate cells prepared from each electrode	280
Figure IV- 18: AC impedance spectra after formation cycling for 15 wt% Si-graphite electrodes, obtained with a Li _x Sny micro-reference electrode, in cells containing different electrolyte compositions.....	280
Figure IV- 19: Discharge capacity retention after 100 cycles for graphite-15 wt% Si // NCM523 cells, containing various electrolyte compositions, cycled in a 2.5-4.1 V voltage window. Data shown are from duplicate cells prepared for each electrolyte composition	281

Figure IV- 20: Effect of cycling range on (a) discharge capacity and (b) coulombic efficiency, over 100 cycles for graphite-15 wt% Si // NCM523 cells containing Gen2 +10 wt% FEC electrolyte 281

Figure IV- 21: Full cell (top), positive electrode (middle), and negative electrode (bottom) potentials, obtained with a Li metal reference, from graphite-15 wt% Si // NCM523 cells with Gen2 + 10% FEC electrolyte cycled in various voltage windows (0.06 mAh cm² current) 282

Figure IV- 22: 10-s discharge DC impedance as a function of cell voltage, before (BOL) and after (EOL) 50 cycles, from graphite-15 wt.% Si // NCM523 cells, measured with a Li_xSn_y reference in a three-electrode setup 283

Figure IV- 23: Intercalation electrochemical model equations, grouped according to electronic and ionic transport through cell sandwich and solid-state diffusion in active material 283

Figure IV- 24: NMC-532 half-cell voltage during a GITT 13m C/21 current pulse and 120m relaxation 284

Figure IV- 25: Lithium diffusion coefficients for the bulk NMC-532 as a function of the fraction of lithium in the material (i.e. lithium concentration over maximum lithium concentration)..... 285

Figure IV- 26: Positive electrode results from 10s 3C discharge current pulse on NMC-532/Graphite cell (full cell at 3.788v) with a LiSn micro-reference electrode..... 285

Figure IV- 27: Baseline electrodes developed for ABR High Energy-High Voltage Project 287

Figure IV- 28: Electrodes made with alumina-coated NCM523 developed for ABR High Energy-High Voltage Project 289

Figure IV- 29: 1st and 3rd cycle capacity of A12 graphite (left) and NCM523 (right) with various ALD coating cycles..... 289

Figure IV- 30: Photo depicting degree of curling of electrodes from Table 4 upon application of electrolyte drops 290

Figure IV- 31: Organizations that have utilized the CAMP Facility’s resources 292

Figure IV- 32: ABR-Amine-FOA cathode (Left) and anode (Right) composition and specifications fabricated at the CAMP Facility for the interim xx3450 pouch cell build 292

Figure IV- 33: (Left) Formation voltage profile of the FCG//graphite xx3450 pouch cells tested at 30°C. (Right) Formation capacities of the FCG//graphite xx3450 pouch cells tested at 30°C 293

Figure IV- 34: Cathode (Left) and anode (Right) compositions and specifications fabricated at the CAMP Facility and used for the baseline, interim, and final ABR-Zhang-FOA xx3450 pouch cell builds 293

Figure IV- 35: (Left, Middle, Right) Representative Baseline, Interim, and Final formation voltage profiles (excluding the 15 minute tap charge and 12 hour rest), respectively, of the graphite//5V spinel xx3450 single-layer pouch cells tested at 30°C 294

Figure IV- 36: Rate performance of Li/Si half cell with various PAA binders 299

Figure IV- 37: SBR effect on the integrity of silicon electrode 299

Figure IV- 38: Electrochemical performance of silicon electrode with PAA/SBR binder 300

Figure IV- 39: FEC effect on the silicon electrode in Li/Si half cells 300

Figure IV- 40: SEM images of Si/Gn electrodes after the initial cycles at 0.1C with no FEC (left) and 10wt% FEC (right)..... 301

Figure IV- 41: Elemental concentrations measured by EDX at least four different positions for Si-Gn electrode after initial cycles with and without FEC..... 301

Figure IV- 42: FEC effect on thermal stability of fully lithiated Si-Gn electrode	302
Figure IV- 43: SEM image of Lithium Powder (SMLP)	302
Figure IV- 44: Capacity retention of Si/NCA cell w/ and w/o prelithiation.....	303
Figure IV- 45: Coulombic efficiency of Si/NCA cell w/ and w/o prelithiation	303
Figure IV- 46: SEM Images Polyethylene Separator with and without Ceramic Coating.....	303
Figure IV- 47: Heat shrinkage of ceramic coated PE separator	303
Figure IV- 48: ASI of A12/NCA cell	304
Figure IV- 49: Cycle performance of A12/NCA cell	304
Figure IV- 50: Flow chart of the operating procedure	304
Figure IV- 51: 1st formation (left) and rate test (right) of A12 graphite/NCM523 full cell with various separators. Color code: black/PP:PE:PP; red/PP only; green/coated PP; and blue/alumina-coated PE.....	305
Figure IV- 52: Photo of separators after cycling	305
Figure IV- 53: Normalized heating rate ($^{\circ}\text{C}/\text{min}$) as a function of temperature measured by accelerating rate calorimetry (ARC) for LMR-NMC, NMC 523/graphite, NMC523/Si-C, NMC 111, and LFP 18650 cells	308
Figure IV- 54: A plot of cell voltage and discharge capacity for NMC523 cells with different electrolytes	309
Figure IV- 55: A plot of electrolyte conductivity vs. temperature for various electrolytes	309
Figure IV- 56: Normalized discharge capacity as a function of cycle number for NMC cells with various electrolytes.....	310
Figure IV- 57: Rate capability plotted as normalized discharge capacity for discharge rates from $\text{C}/10$ to 2C	310
Figure IV- 58: Normalized heating rate as a function of temperature for ARC measurements of NMC cells with different electrolytes (expanded view on the right side)	310
Figure IV- 59: Cell voltage and temperature as a function of SOC during 1C overcharge testing of NMC cells with various electrolytes. measurements.....	311
Figure IV- 60: Still images during flammability tests of various electrolytes in NMC cells	312
Figure IV- 61: (a) Photograph of an 18650-sized cell being dismantled using traditional methods. The hand saw cut into the electrode material, causing a short circuit. (b) Photograph of cell materials harvested using a tubing cutter, showing that materials were removed intact.....	314
Figure IV- 62: Average, normalize resistance vs. charge time, charging method and charging rate. FC=fast charge.....	315
Figure IV- 63: Change in relative resistance vs. $i2R\Delta t$ and charge rate for the full-charged cells	315
Figure IV- 64: Change in relative resistance vs. $i2R\Delta t$ and charge rate for the fast-charged cells	315
Figure IV- 65: Optical photographs of anodes from full-charged cells	316
Figure IV- 66: Optical photographs of anodes from fast-charged cells	316
Figure IV- 67: SEM micrographs of anodes from fast-charged cells.....	316
Figure IV- 68: (a) Curling of single-sided anode (left) and cathode (right) laminates due to uneven strain. (b) Flat laminates after vacuum drying wound on metal cylinder. (c) and (d) Laminates being wound on metal cylinder to counter natural curvature.....	320

Figure IV- 69: (a)-(c) show the first 4 cycles between 4.25-3.0 V (C/10) for NMC-532/graphite cells having different cathode to anode areas. (d) Shows an example of two cells (14/14 bad 1&2) with purposely misaligned electrodes 320

Figure IV- 70: First 4 cycles between 4.25-3.0 V for NMC-532/graphite cells after flattening curled electrodes 321

Figure IV- 71: (a) First 4 cycles and (b) first-cycle dQ/dV of the top performing cells from each group shown in the previous figure 322

Figure IV- 72: Extended cycling results (4.25-3.0 V) for cells with increasing anode:cathode areas. (a) Average discharge capacity for three cells of each anode:cathode area. (b) Average Coulombic efficiency for three cells of each anode:cathode area 322

Figure IV- 73: Formation cycling voltage profiles of baseline NMC-532/graphite cells with electrolyte volumes from 1.7x to 8.7x the calculated, total pore volume as given in the previous table. Shown in each figure are data from 4 separate cells with the same total electrolyte volume as labeled 324

Figure IV- 74: Comparison of formation-cycling voltage profiles (left) and cycle performance (right) for the best two performing cells of each electrolyte volume group, 1.7-8.7x, shown in the previous figure 324

Figure IV- 75: First HPPC discharge ASI vs. depth of discharge (%) for the best performing cells in the electrolyte volume groups listed in a previous table 325

Figure IV- 76: (a) Discharge capacity and (b) discharge capacity retention for the best 2 performing cells of each group, 1.7-8.7x, as a function of cycle number. 100% is taken as the discharge capacity of the last formation cycle (i.e. cycle 4)..... 325

Figure IV- 77: (a) Average discharge capacity vs. cycle number and (b) Coulombic efficiency for 4 cells from the 2.7, 4.7, and 8.7x electrolyte volume study. Error bars are 2 standard deviations..... 326

Figure IV- 78: Cycling performance and Coulombic efficiencies (inset) for 30, identically-prepared NMC-532/graphite, baseline cells..... 326

Figure IV- 79: Expanded view of cycling data shown in the previous figure for 30, identically-prepared NMC-532/graphite baseline cells. HPPC diagnostic cycles appear as breaks in the data 327

Figure IV- 80: Expanded view of the first 4, formation cycles of the cells shown in the previous two figures. The red and blue dashed lines represent 2 and 3 standard deviations of the 30 cell set, respectively, on cycles 1 and 4 327

Figure IV- 81: Propagated error in capacity from a ± 0.2 mg error in materials weighing 327

Figure IV- 82: (a) Discharge energies and (b) Coulombic efficiencies on the last formation cycle (cycle 4) for individual cells of the 30-cell NMC-532/graphite set. Red boxes show the cells identified as outliers 328

Figure IV- 83: Probability map used as a gate for small data sets. Shaded areas correspond to probability regions that give an estimate of the likelihood that the mean cycle-3 Coulombic efficiency for a sample of size N is different than the mean for the baseline data 329

Figure IV- 84: Average Coulombic efficiencies for two, 10-cell sets of NMC-532/graphite using either a current cutoff (black) or a time cutoff (red) at the top of each charge (4.25-3.0V, C/3, 30°C). Error bars are 2 standard deviations 330

Figure IV- 85: SEM picture of 523 as provided by CAMP (Trask, ANL). The samples appear as approximately 8 μm spheres composed of platy primary particles 332

Figure IV- 86: Unit cell volume vs annealing temperature for 2 wt% Al₂O₃ on NCM523 333

Figure IV- 87: ^{27}Al MAS-NMR spectrum for LiAlO_2 and alumina	334
Figure IV- 88: ^{27}Al NMR of NCM523 coated with 2 wt% Al_2O_3 at various annealing temperatures for 8h.....	334
Figure IV- 89: ^7Li MAS NMR of pristine and alumina coated NCM 523	335
Figure IV- 90: Cycling data for NCM523 coated with alumina by various methods	335
Figure IV- 91: Cycling data for NCM523 coated with alumina annealed at different temperatures	336
Figure IV- 92: Pristine structure of NMC 622, showing the transition metal only. Ni is in green, Co in pink, Mn in purple, and O in red. Ni-rich domains are visible	336
Figure IV- 93: NMC532 All Li removed AIMD+DFT. Left panel: view along the TM planes. O-O bonds are shown in blue. O is in red, Ni in green, Co in pink, and Mn in gray. Right panel: view along the c-axis perpendicular to the TM planes	337
Figure IV- 94: NMC333 (001) stoichiometric Li-O terminated lowest energy surface (1.39 J/m^2). (a) View along [100]. (b) View along [001] perpendicular to the surface, the atom sizes have been increased to show the line ordering of Li vacancies (Li shown in purple)	337
Figure IV- 95: Ternary phase diagram for the system $\text{LiCoO}_2\text{-LiMnO}_2\text{-LiNiO}_2$	339
Figure IV- 96: (a) XRD patterns of LiNiO_2 synthesized under two different atmospheres, (b) Cycling performance of the oxygen cycled material cycled to 4.7V, (c) first cycle CV of the two samples.....	340
Figure IV- 97: (a) CV cycling data for 0.5 $\text{LiCoO}_2\text{-0.5 LiNiO}_2$, (b) XRD patterns of 0.5 $\text{LiCoO}_2\text{-0.5 LiNiO}_2$	341
Figure IV- 98: Implemented protocol for electrochemical testing	345
Figure IV- 99: Discharge capacity (a), discharge voltage (b), discharge energy (c) and coulombic efficiency (d) for NCA (28 cells) and NCM523 (30 cells) full cells. A darker shade indicates a higher density of cells, i.e., in (c) there is a high density of cells near the top of the NCA band	346
Figure IV- 100: Initial and final impedance values derived from HPPC measurements for the two baseline chemistries.....	347
Figure IV- 101: Performance ellipses for discharge energy (a) and HPPC impedance (b) for baseline chemistries NCA and NCM. Arrows indicate general directions for improvement, viz. a shift in the performance ellipse. The ellipses are based off a 1.85 standard deviation in (a) and 2.00 in (b).....	348
Figure IV- 102: Correlation plot for coulombic efficiency and energy retention.....	349
Figure IV- 103: Bootstrap analysis of coulombic efficiency	349
Figure IV- 104: Voltage–capacity plots, and (b) voltage–normalized capacity plots for half-cells with pristine and harvested positive electrodes cycled between 3-4.5 V, at a $\sim\text{C}/10$ rate and 30°C . (c) Voltage–capacity plots, and (d) voltage–normalized capacity plots for half-cells with pristine and harvested negative electrodes cycled between 1.5-0.0 V, at a $\sim\text{C}/10$ rate and 30°C ; the inset in (d) shows an expanded view of the data between 0.0 and 0.4 V. The captions H1 (210-10) and H2 (212-16) refer to coin cells that were the source of the harvested electrodes	351
Figure IV- 105: AC impedance data (30°C , 100 kHz - 5 mHz) from positive (POS) and negative (NEG) electrodes, after initial cycling and after 100 aging cycles. (a) and (c) are data from NCM523//Graphite cells, whereas (b) and (d) are data from NCA//Graphite cells	352
Figure IV- 106: Initial cycling (30°C) of an NCM523//Gr cell with a Li-metal reference electrode. (a) The cycling includes a 2h rest, a 15 min tap charge to 1.5 V full cell voltage	

followed by a 4h rest, and four $\sim C/10$ cycles. (b) close-up of the first 20h, and (c) is a close-up of cycle 2..... 353

Figure IV- 107: Full cell, positive electrode, and negative electrode, area specific impedance data (30°C) from HPPC tests, conducted on a NCM523//Gr cell with a Li-Sn reference electrode, after formation cycling and after 100 aging-cycles (3-4.4 V). The data are from (a) 3C, 10-s discharge pulses; (b) 2.25C, 10-s charge pulses..... 354

Figure IV- 108: Intercalation electrochemical model equations, grouped according to electronic and ionic transport through cell sandwich and solid-state diffusion in active material 355

Figure IV- 109: Average and surface active material particle lithium concentration (electrode midpoint) in coin cells with matched electrodes and oversized anode. (a) Matched electrodes at top of charge. (b) Oversized anode at top of charge. (c) Matched electrodes at bottom of discharge. (d) Oversized anode at bottom of discharge 356

Figure IV- 110: Average active material particle lithium concentration (electrode midpoint) in coin cells with oversized anode at top of a C/3 charge at the indicated cycle. (a) Anode. (b) Cathode..... 357

Figure IV- 111: Current efficiency of oversized anode and matched electrode coin cells during C/3 cycling after a C/15 discharge 357

Figure IV- 112: Average active material particle lithium concentration (electrode midpoint) in coin cells with oversized anode at bottom of discharge at the indicated cycle. (a) Anode. (b) Cathode..... 357

Figure IV- 113: Assumed open circuit voltage curves for the bulk active material and surface layer as a function of the fraction of lithium in the material (i.e. lithium concentration over maximum lithium concentration) 358

Figure IV- 114: Simulation of half-cell C/10 discharge curve 359

Figure IV- 115: Comparison of half-cell C/10 discharge simulation to the assumed open circuit voltage curves for the bulk active material (a) and surface layer (b) as a function of the fraction of lithium in the respective materials 359

Figure IV- 116: Change in fraction of lithium in the bulk active material and surface layer as a function of discharge capacity during the half-cell C/10 discharge simulation..... 360

Figure IV- 117: Electrolyte additive reaction and diffusion model equations 360

Figure IV- 118: SEI reaction and transport electrochemical model equations 361

Figure IV- 119: Comparison of positive electrode EIS studies taken with a micro-reference electrode cell (100 kHz-10 mHz) 362

Figure IV- 120: Electron probe micro-analysis showing a gradient composition across the particle of FCG $\text{LiNi}_{0.6}\text{Mn}_{0.2}\text{Co}_{0.2}\text{O}_2$ 366

Figure IV- 121: (a) Initial charge and discharge capacities with different calcination temperature and (b) capacity vs. rate at different calcination temperatures of FCG $\text{LiNi}_{0.6}\text{Mn}_{0.2}\text{Co}_{0.2}\text{O}_2$ cathode..... 366

Figure IV- 122: (a) Initial charge and discharge capacities of FCG (6:2:2) cathode and baseline cathode and (b) capacity vs. cycle number of FCG and baseline cathode..... 367

Figure IV- 123: Cycling performance of FCG cathode at 55°C 367

Figure IV- 124: TR-XRD/MS of FCG (6:2:2) and NMC (6:2:2) baseline 368

Figure IV- 125: Ni L-edge soft XAS for baseline NMC (6:2:2) (left) and FCG (6:2:2) (right) using fluorescence detection (FY mode, bulk probing)..... 369

Figure IV- 126: Ni L-edge soft XAS for baseline NMC (6:2:2) (left) and FCG (6:2:2) (right) using partial electron yield detection (PEY mode, surface probing)..... 369

Figure IV- 127: Structure of conductive binder developed by LBNL.....	370
Figure IV- 128: Cycling performance of cell based on 5%PFM binder, 15% C-65 carbon additive, 60% SiO-Sn _x Co _y C _z , and 20% MAG anode using conductive binder (PFM)	370
Figure IV- 129: Cycling performance of cells based on SiO-Sn _x Co _y C _z and MAG anode using (a) 5% PAA binder and (b) 4% LiPAA binder.....	370
Figure IV- 130: Cycling performance of a cell based on SiO-Sn _x Co _y C _z and MAG anode using 5% LiPAA binder	370
Figure IV- 131: In-situ volume change of CV7-containing pouch cells as a function of time. The slow cycle is can be seen every 50 cycles	374
Figure IV- 132: Voltage and in-situ volume change during formation for cells listed in the adjacent table	375
Figure IV- 133: BOL Wh/L with different coated NMC cathode	375
Figure IV- 134: Advanced Cathode formulation for the roll to roll coating run	376
Figure IV- 135: Viscosity and density of the cathode dispersion within target specification.....	376
Figure IV- 136: Rate test of the 18650 cell with advanced electrochemical couple.....	377
Figure IV- 137: Comparison of NCM stabilization approaches. “ST” = Surface Treated NCM, “BD” = Bulk Doped NCM, “Control” = as-synthesized NCM. Cycling conditions: CCCV Charge: C/5 to 4.6 V, C/50 cutoff; Discharge: C/3 to 2.5 V; Li metal anode, LiPF ₆ in EC/EMC electrolyte	381
Figure IV- 138: Comparison of rate capability of HE-NCM materials. Cycling conditions: Charge to 4.4 V at rate indicated in table; Discharge to 2 V at rate indicated in table; Li metal anode, LiPF ₆ in EC/EMC electrolyte	381
Figure IV- 139: Stabilized NCM and HV stable electrolytes work together to improve cycle life. (a) Cycling conditions: CCCV Charge: C/2 to 4.4 V, C/20 cutoff; Discharge: C/2 to 3 V; C/20 cycle every 20 cycles; 2 Ah NCM//Graphite 18650 cells. (b) Cycling conditions: CC Charge: C/3 to 4.4 V; Discharge: C/3 to 3 V; C/20 cycle every 20 cycles; 1.4 Ah NCM//Graphite pouch cells	382
Figure IV- 140: Ternary-phase diagram for Envia Systems’ HCMR TM class of cathode materials.....	385
Figure IV- 141: DC-R profiles for HCMRTM-XE, HCMRTM-XLE and Carbon-coated HCMRTM-XLE materials in pouch-cell vs graphite anode.....	386
Figure IV- 142: Overview for HCMR TM material development and surface modifications by addressing root causes for DC-R.....	387
Figure IV- 143: (1) Energy of HCMRTM-XLE2 coated materials at different discharge rates with varying LiPON sputtering deposition time measured in half-cells. (2) DC-R profiles of baseline, 1 hr, and 3 hr LiPON sputtering on HCMRTM-XLE2 cells vs graphite after 1 and 125 1C cycles between 4.4-2.0V	388
Figure IV- 144: STEM images of baseline and Al ₂ O ₃ coated HCMR TM - materials via ALD evidencing a growth in ALD-coating thickness as a function of reaction cycle number.....	388
Figure IV- 145: Rate capability of HCMR TM -XE2 baseline, heat-treated (HT) under Argon, and HT with 2 and 5 reaction cycles of Al ₂ O ₃ ALD coating.....	388
Figure IV- 146: DC-R profile for HT-ALD coated HCMR TM -XE2 materials on the 1 st cycle and after 25 1C cycles.....	389
Figure IV- 147: DC-R profile for the HCMR TM -XLE1 material coated with Conduction Polymer #1 on the 1 st cycle and after 25 1C cycles between 4.4-2.0V	390

Figure IV- 148: EIS response of HCMRTM-XE2 cathode as a function of cycle-life 391

Figure IV- 149: Raman spectroscopy for (1) HCMRTM-XLE2 cathode (5 and 100 cycles) and (2) HCMRTM-XE2 cathode (5 and 50 cycles)..... 392

Figure IV- 150: Ni oxidation number distribution for (1) HCMRTM-XLE2 cathode and (2) HCMRTM-XE2 cathode 393

Figure IV- 151: (1) STEM image HCMRTM-XLE2 and (2) Electron Diffraction patterns of cycled HCMRTM-XLE2 393

Figure IV- 152: STEM images of HCMRTM-XP cathode (1) surface and (2) bulk structure 394

Figure IV- 153: Conducting polymeric binder development (1) PFM binder showing high peel strength, (2) comparison of Eniva’s binder with the PFM binder, (3) exploring the effect of binder on other forms of Si-anode 395

Figure IV- 154: Sizing calculations at different charging voltages targeting to meet the ABR project goals for both specific energy and energy density 396

Figure IV- 155: Typical discharge curve for the HCMRTM-XE based baseline cells vs. Si-SiO-C anode 397

Figure IV- 156: HPPC studies for the HCMRTM-XE based baseline cells vs. Si-SiO-C anode 398

Figure IV- 157: Cycling performance for the HCMRTM-XE based baseline cells vs. Si-SiO-C anode 398

Figure IV- 158: (a) and (b) Cycling performance, and (c) coulombic efficiency (from the 22nd cycle) of the PSU Si electrodes with 1000 mAh/g targeted capacity based on the whole electrode 402

Figure IV- 159: Cycling performance (a) and coulombic efficiency (b) of the full cell in coin cell format constructed of the fresh Si anode and NCM cathode..... 402

Figure IV- 160: Cycling performance (a) and coulombic efficiency (b) of full cells in coin cell format constructed of different precycled Si anodes and NCM cathodes 403

Figure IV- 161: Visualization of the surface electrochemical degradation of NCM71515 electrodes (18–20 μm) after 100 cycles at room temperature. Upper: HAADF-STEM images showing the local structure at the primary particle surface; the scale bars are 400, 20, 2, and 2 nm from left to right; lower: TOF-SIMS mappings demonstrating the composite electrode surface with cathode secondary particles, additive carbon, and polymeric binder; the scale bar is 10 μm..... 404

Figure IV- 162: TOF-SIMS depth profiles of various chemical species from the surface of LiNi_{0.7}Co_{0.15}Mn_{0.15}O₂ composite electrodes (18–20 μm) after 100 cycles at room temperature. Upper: processed data referenced with the pristine electrode (not shown here); and lower: raw data (left) with the evolution of the corresponding secondary ion mass spectra as a function of sputtering time (right) 404

Figure IV- 163: Powder X-ray diffraction patterns of Li₂ZrO₃-coated LiNi_{0.7}Co_{0.15}Mn_{0.15}O₂ samples prepared by sol-gel and precipitation methods 405

Figure IV- 164: Cross sectional SEM-EDX mapping of the Zr element in the Li₂ZrO₃-coated LiNi_{0.7}Co_{0.15}Mn_{0.15}O₂ samples prepared by sol-gel and precipitation methods 406

Figure IV- 165: Capacity retention of the Li₂ZrO₃-coated LiNi_{0.7}Co_{0.15}Mn_{0.15}O₂ cathodes prepared by sol-gel and precipitation methods. Cycling conditions: 3.0 – 4.5 V, C/3 rate, 25 °C..... 406

Figure IV- 166: Scanning electron microscopy (SEM) images of (a) the bare and (b) double-coated sample with lithium-rich layered oxide and AlF₃ (20LNM-ALF sample). (c) High-resolution transmission electron microscopy (HR-TEM) images and (d) the energy-dispersive X-ray spectroscopy (EDS) profile of the surface of the 20LNM-ALF sample..... 407

Figure IV- 167: High-resolution transmission electron micrograph of (a) the cross-sectional view and (b) the interface between core and shell of 20LNM-ALF. (Inset figure of (b) indicates a pattern of fast Fourier transform of the green square). (c) High angle annular dark field (HAADF) image and (d) the filtered image of the green square region in (b). (e) Simulated crystal structure of Li_2MnO_3 (C2/m) along rhombohedral [2 1 0] direction. (The balls with yellow, green, and grey respectively indicate transition metals, oxygen, and lithium ions)	407
Figure IV- 168: Cycling performances of two concentration-gradient samples and constant-concentration sample with same transition-metal composition ($\text{LiNi}_{0.75}\text{Co}_{0.1}\text{Mn}_{0.15}\text{O}_2$)	408
Figure IV- 169: Loading and storage effect (in air) on CG sample. Low-loading: 4 mg/cm^2 ; high-loading: 20 mg/cm^2 ; storage time: 6 months	408
Figure IV- 170: SEM and EDS profiles of the newly prepared CG sample and electrochemical performance with different lithiation temperature	408
Figure IV- 171: First two charge/discharge curves of the coin-type full cell with graphite anode with different negative and positive electrode energy density ratios of (a) 0.95 and (b) 1.05. All cells were charged to 4.4 V and then discharged to 2.5 V with a constant current of C/10 rate	409
Figure IV- 172: Comparison of the long-term cycle performances of coin-type full cells with different N/P ratios. All cells were charged to 4.4 V and then discharged to 2.5 V with a constant current of C/3 rate	410
Figure IV- 173: First two charge/discharge curves of the pouch-type full cell with a graphite anode with negative and positive electrode energy density ratios of 1.1. The cell was charged to 4.4 V and then discharged to 2.5 V with a constant current of C/10 rate.....	410
Figure IV- 174: Comparison of the long-term cycle performances of pouch-type full cells with N/P ratio of 1.1. Cell was charged to 4.4 V and then discharged to 2.5 V with a constant current of C/3 rate	410
Figure IV- 175: The SEM morphology of (a), (b) SLMP coated anode surface after pressure activation and (c), (d) after immersing in electrolyte for 48 hours. The coating here uses 3% SBR solution	410
Figure IV- 176: Photo images of SLMP suspension in 1% PS, 1%SBR and 0.5% PS with 0.5% SBR binder solution and rest for 0 second (a), 30 seconds (b) and 120 seconds (c). The photo images of SLMP loading on large piece of graphite anode surface with 1% PS (d), 1% SBR (e) and 0.5% PS with 0.5% SBR (f) binder solution	411
Figure IV- 177: The SEM images of SLMP loading on graphite surface before, after calendaring and after immersing in electrolyte for 48 hours with 1% PS (a, d, g), 1% SBR (b, e, h) and 0.5% PS with 0.5% SBR (c, f, i) binder solution	412
Figure IV- 178: SEM characterization of pristine Si anode from PSU. (a) PSU_600_60. (b) PSU_600_80. (c) PSU_800_60 and (d) PSU_800_80.....	412
Figure IV- 179: Capacity retention and coulombic efficiency of PSU anode cathode /Li cells with baseline electrolyte (a) PSU_600_60 and PSU_600_80. (b) PSU_800_60 and PSU_800_80	413
Figure IV- 180: Capacity retention and coulombic efficiency of PSU_600_80 cells with baseline electrolyte and additive	413
Figure IV- 181: Electrochmeial performance for the $\text{LiNi}_{0.5}\text{Mn}_{0.3}\text{Co}_{0.2}\text{O}_2/\text{Li}$ half cell. (a) Voltage profiles for the half cells in Gen 2 electrolyte in different cut off voltage (b) cycle life at 4.2V cut off voltage (c) cycle life at 4.4V cut off voltage (d) cycle life at 4.6V cut off voltage.....	414

Figure IV- 182: Cycling performance of $\text{LiNi}_{0.5}\text{Mn}_{0.3}\text{Co}_{0.2}\text{O}_2$ /Graphite cell in different cut off voltages 414

Figure IV- 183: Molecular structures of triethyl phosphite (TEP) and tris(2,2,2,-trifluoroethyl)phosphite (TTFP) 415

Figure IV- 184: Cycling performance of the NCM523/Graphite cells with TEP and TTFP as additives..... 415

Figure IV- 185: SEM images of (a) pristine electrode, (b) cycled with baseline electrolyte, (c) 1% TEP containing and (d) 1% TTFP containing..... 416

Figure IV- 186: Molecular structures of fluorinated linear carbonate solvents 416

Figure IV- 187: Voltage profiles for NCM523/graphite cells in (a) baseline electrolyte and (b) 1.0 M LiPF_6 in FEC/HF-DEC in 1/1 volume ratio with 1% LiDFOB..... 417

Figure IV- 188: Room temperature cycling of baseline CAM-7/Graphite 18650 cells between 2.7 and 4.1V. C/2 charge - 1C discharge; 1C discharge from 4.2V every 150 cycles. Note that cycling between 2.7 and 4.1V corresponds to 90% SOC swing. Cells fabricated at TIAX 422

Figure IV- 189: Room temperature cycling of baseline CAM-7/Graphite 18650 cells over the full DOD range. C/2 charge - 1C discharge, 4.2 to 2.7V; C/3 and C/2 discharge every 50 cycles. Cells fabricated at TIAX..... 422

Figure IV- 190: 45°C storage of baseline CAM-7/Graphite 18650 cells at 4.1V. (a) Intermittent C/20, C/3, C/2, and 1C discharge between 4.2 to 2.7V and (b) 1C 10s HPPC rate characterization at RT 422

Figure IV- 191: Impact of (a) dopants and (b) synthesis modification on high temperature impedance rise. Accelerated cycle life testing at 45°C using high rate charge and discharge cycles with intermittent 1C/1C characterization cycles at 45°C between 4.2V and 2.7V. CAM-7/Graphite coin cells with $\sim 2\text{mAh/cm}^2$ loading. CV charge time used as an impedance characterization metric 423

Figure IV- 192: Table above shows the discharge capacity of the baseline and higher capacity CAM-7 cathode materials measured in half cells with Li metal anode (3.0-4.3V). The bottom figure shows cycle life of the higher capacity CAM-7 at room temperature with graphite anode (2.7-4.2V, 1C/1C) 424

Figure IV- 193: Capacity retention and coulombic efficiencies of Si-based anodes evaluated in coin cells with Li metal counter electrode. Materials tested with 75% active (except C-1 with 60%) content electrodes 425

Figure IV- 194: Representative example for capacity retention and coulombic efficiencies of blended Si-based anodes with graphite evaluated in coin cells with Li metal counter electrode 426

Figure IV- 195: Impact of pre-lithiation and anode over-sizing on full cell cycling of silicon/carbon composite anode paired with CAM-7 cathode in coin cells. Discharge capacity normalized by cathode active material weight 427

Figure IV- 196: Cycle life of CAM-7-based cathode paired with a blended Graphite/Si-containing anode evaluated in coin cells. (A:C ~ 1 and no pre-lithiation) 427

Figure IV- 197: Impact of electrode design on projected 18650 cell power and energy. Power based on HPPC measurements in coin cells using graphite anodes (ASI vs. SOC for 10s 3C pulse). Energy based on 1C discharge from 4.2V. Cell engineering model used to scale coin cell measurements to 18650 cells 428

Figure IV- 198: Impact of 18650 hardware modifications on cell power capability. Baseline 18650 cell design with CAM-7 cathode and graphite anode with $\sim 2\text{mAh/cm}^2$ active material loading. HPPC power testing done using 5A 10s Discharge.....	428
Figure IV- 199: HPPC testing shows that the Gen 1 CAM-7/Si cells can provide comparable power while providing higher energy density than the baseline 18650 cells. Si: 5A 10s Discharge, 3.75A 10s Charge. $V_{\text{min}} = 2.0\text{V}$, $V_{\text{max}} = 4.3\text{V}$ for HPPC power calculation. Graphite: 5A 10s Discharge, 3.6A 10s Charge. $V_{\text{min}} = 2.6\text{V}$, $V_{\text{max}} = 4.3\text{V}$ for HPPC power calculation.....	429
Figure IV- 200: Comparison of cell power capability and 2.7-4.1V C/2 - 1C room temperature cycle life for baseline and improved CAM-7/Graphite cells with equivalent design (equal electrode length with $\sim 2\text{mAh/cm}^2$ active material loading). HPPC power testing done using 5A 10s Discharge, 3.6A 10s Charge. $V_{\text{min}} = 2.6\text{V}$, $V_{\text{max}} = 4.3\text{V}$ for HPPC power calculation.....	429
Figure IV- 201: Flow chart of material scale-up	432
Figure IV- 202: Coin cell result of preliminary synthesized layered layered material	433
Figure IV- 203: Statistical design of experiments (DoE).....	433
Figure IV- 204: Main effects plot of process variables.....	434
Figure IV- 205: ANOVA and response surface regression	434
Figure IV- 206: Outgoing inspection data sheet of scaled layered layered material.....	435
Figure IV- 207: Coin cell result of preliminary synthesized layered layered spinel material.....	436
Figure IV- 208: SEM images of layered layered spinel materials with different spinel content.....	436
Figure IV- 209: C/13 cycling result of layered layered spinel materials.....	437
Figure IV- 210: Rate performance of layered layered spinel materials	437
Figure IV- 211: Taylor vortex reactor system.....	438
Figure IV- 212: Voltage profiles of layered latered materials produced by 3 processes.....	439
Figure IV- 213: Cyclability of layered latered materials produced by 3 processes	440
Figure IV- 214: SEM images of pristine and AlF_3 -coated materials.....	440
Figure IV- 215: ICP-MS analysis of AlF_3 -coated materials	441
Figure IV- 216: Cycle performance of AlF_3 -coated materials.....	441
Figure IV- 217: Capacity retention of AlF_3 -coated materials	442
Figure IV- 218: ICP-MS, SEM and particle size analysis results of bench-scale FCG material.....	442
Figure IV- 219: Synthesis of PFPBO-LiF complex.....	446
Figure IV- 220: Improved Synthesis of F-DEC.....	446
Figure IV- 221: Improved Synthesis of F-EMC.....	446
Figure IV- 222: Crosslinking vs. % residual Chloride	447
Figure IV- 223: 3% crosslinked	447
Figure IV- 224: 24% crosslinked	447
Figure IV- 225: 50 nm silicon coated with 10% w/w PFM (before milling); PSA of wet-blended Si-PFM/Nano-Si after milling.....	448
Figure IV- 226: PSA of Si-PFM/Nano-Si	448
Figure IV- 227: Freeze-dried PFM powder	448
Figure IV- 228: Cell performance of LBNL binder vs. non-treated Si	449
Figure IV- 229: Self-Discharge Current.....	450

Figure IV- 230: Cycling behavior of LiFSI from different commercial vendors 451

Figure IV- 231: Rapid capacity fade in cells formulated with electrolyte A1-5..... 452

Figure IV- 232: Self-discharge current in calendar life aging experiments 452

Figure IV- 233: An example of an erratic triplicate cells and photomicrograph of imperfections in Al-clad coin cell casing 453

Figure IV- 234: Cycling behavior of electrolytes prepared from selected LiFSI samples in NCA//Gr pouch cells 453

Figure IV- 235: Synthesis of 3rd Generation Si-Binder..... 454

Figure IV- 236: Comparison between gravimetric capacity-fading results for the baseline and defective NMC 532 electrodes at 2C and 5C current rates (triplicate full coin cells)..... 458

Figure IV- 237: Gravimetric and total cell capacity before and after 200 charge-discharge cycles at 2C (a) and 5C (b) discharge rates. Capacity retention values after 200 cycles for the baseline and defective electrodes at the 2C discharge rate and at the 5C discharged rate (c)..... 459

Figure IV- 238: Scanning electron micrographs and elemental EDS maps (Mn, Ni, Co, C, O) from (a) the baseline NMC 532 electrode and (b) a defective electrode with large agglomerates 461

Figure IV- 239: (a–c) Cross-sectional SEM images of the baseline NMC 532 electrodes, (d–g) cross-sectional SEM images from an electrode having missing coating strips (i.e. “1X defect” or “3X defects”)..... 462

Figure IV- 240: (a) Temperature distribution of A12_SBR anode; (b) Temperature profiles along line L1 for two anodes, and two cathodes..... 463

Figure IV- 241: Standing wave comparison with experiment for NMC cathodes (a: model, b: experiment); standing wave comparison with experiment anode (c: model, d: experiment)..... 464

Figure IV- 242: Modeling results of hypothetical anodes (offsetting properties) 465

Figure IV- 243: Correlation of Tmax to electrode porosity range 465

Figure IV- 244: Surface energy of various substrates and contact angles of NMC532 slurry on various substrates 468

Figure IV- 245: NMC532 cathode on C-coated and corona treated Al foils demonstrate better rate performance (left) and lower interfacial impedance (right) 468

Figure IV- 246: Rate performance (left) and cyclability (right) of baseline (conventional PVDF/NMP) pouch cells 469

Figure IV- 247: Rate performance (left) and capacity retention (right) of pouch cells with all-aqueous processed electrodes 469

Figure IV- 248: Comparison of pouch cell performance with ORNL baseline electrodes, ORNL all-aqueous processed electrodes, and aqueous processed cathodes with industry formulation; capacity retention under accelerated degradation (left); rate capability (right) 470

Figure IV- 249: Comparison between calendered and non-calendered pouch cells cycled at high-rate accelerated testing conditions 471

Figure IV- 250: F 1s and O 1s signals from XPS of ConocoPhillips natural graphite anode washed by DMC..... 472

Figure IV- 251: F 1s and O 1s signals from XPS of NMC 532 cathode washed by DMC..... 472

Figure IV- 252: Standard “static” ALD chamber reactor 475

Figure IV- 253: Conceptual example of a spatial “in-line” ALD reactor	475
Figure IV- 254: Computer rendering of “drum-in-drum” reactor format.....	476
Figure IV- 255: Example schematic of “drum-in-drum” design showing configuration of gas introduction and exhaust channels	476
Figure IV- 256: Photographs of a flexible metal coated plastic film before loading (A) into the rotary reactor and (B) after deposition of ~ 650 nm of alumina	477
Figure IV- 257: Thickness measurement for alumina coatings deposited across metal coated plastic sample.....	477
Figure IV- 258: Plot of measured alumina film thickness as a function of number of ALD cycles, which is equivalent to the number of reactor rotations	477
Figure IV- 259: Measured ALD growth rate for alumina as a function of reactor rotation rate.....	478
Figure IV- 260: Schematic of anodic aluminum oxide samples	478
Figure IV- 261: Plot of normalized Zn concentration EDX signal across porous AAO sample structure.....	479
Figure IV- 262: Plot of normalized Zn concentration EDX signal across AAO samples with varied porosity	479
Figure IV- 263: Plot of cathode average weights and thicknesses for cells used for Phase 1 deliverable	483
Figure IV- 264: Plot of anode average weights and thicknesses for cells used for Phase 1 deliverable	483
Figure IV- 265: ADP Prototype configured for installation at Navitas	486
Figure IV- 266: Digital Image of Process Module placed on the left and Power Module configured on the right at Lambda.....	487
Figure IV- 267: Schematic of the Process Module to be integrated in the pilot coating line. The Power Module will be actually placed behind the Process Module for this particular set up.....	487
Figure IV- 268: (a) Digital image of the ADP Prototype installed at Navitas. The Process Module is in front while the Power Module is placed behind the Process Module, shown below it. (b) Digital image of the Power Module placed behind the Process Module delivering VFM power through the waveguide connecting both modules	488
Figure IV- 269: Solvent content (moisture) analysis for anode electrodes (water based binder) dried using standard and ADP samples	489
Figure IV- 270: Electrochemical performance results for anode electrodes dried using standard and ADP methods. (a) First formation cycle (0.01-1.0V @ 0.1C) (b) rate capability (lithiated at 0.1C and delithiated at 0.1, 0.2, 0.5, 1.0 and 2.0C currents)	490
Figure IV- 271: Electrochemical performance results for cathode electrodes dried using standard and ADP approaches. (a) First formation cycle (3.0-4.2V @ 0.1C) (b) rate capability (lithiated at 0.1C and delithiated at 0.1, 0.2, 0.5, 1.0 and 2.0C currents)	491
Figure IV- 272: Formation voltage vs. specific capacity plots for (a) Lambda-cathode (with Navitas anode) and (b) Lambda-anode (with Navitas cathode) against Navitas’ baseline. Cycles were run from 3.0 to 4.2V at C/10 current.....	492
Figure IV- 273: Rate capability results for (a) Lambda-cathode (with Navitas anode) and (b) Lambda-anode (with Navitas cathode) against Navitas baseline. All cell were charged at C/10 and then discharge at 0.1, 0.2, 0.5, 1.0 and 2.0C currents between 2.7 and 4.2 V	492

Figure IV- 274: Cycle life testing for single layer pouch cells for Navitas cathode (NMP based binder) matched with ADP dried anode (water based binder) compared to Navitas baseline cell. The baseline cells were dried with conventional drying methods..... 493

Figure IV- 275: Digital images showing result from wet adhesion test for aqueous anode dried using ADP under (a) continuous (0.5m/min) and (b) static drying 493

Figure IV- 276: Moisture analysis shows the solvent content after static and continuous ADP drying. For both cases the values are lower than the target (< 5000 ppm) 494

Figure IV- 277: Half-cell electrochemical performance results for anode electrodes dried under static and continuous ADP (a) first formation cycle at C/20 0.01V to 1.0V and (b) rate capability lithiated at C/10 and delithiated at 0.1, 0.2, 0.5, 1.0 and 2.0C 494

Figure IV- 278: 4 μm thick UV ceramic Coating reduced shrinkage..... 498

Figure IV- 279: 4 μm thick UV ceramic Coating reduced shrinkage..... 498

Figure IV- 280: 4 μm thick UV ceramic Coating reduced shrinkage..... 498

Figure IV- 281: Results for NMC half cells and higher voltages with ceramic coatings made with UV and acrylic coatings 499

Figure IV- 282: UV Ceramic Coatings Cycling In 4.8 V Cell 499

Figure IV- 283: Silicon anodes consume and trap significant amounts of lithium, reducing first cycle efficiency and cell-level energy. Current lab-scale prelithiation methods add extra lithium and address first cycle loss – but are not scalable 502

Figure IV- 284: Prelithiation formulations increase capacity by about 3%..... 504

Figure IV- 285: “In cell” prelithiation increased cell capacity, but by less than “ex situ” prelithiation increased cell capacity 505

Figure IV- 286: Scell concept: The perpendicular anode-cathode structure of S-cell with silicon anode (slow discharge, fast charging) and lithium anode (fast discharge, slow charging). The geometry enables in-situ lithiation of non-lithiated cathode and anode materials. Each of the two anode materials has a separate electrical tab. The cathode is perforated plates of commercial cathode electrodes. Note that each of the rods can consist a bundle of micro or nano sized features, such as nano or micro rods..... 507

Figure IV- 287: Early prototypes of Scell, before the start of the project. Perforated cathode plates (commercial LiCoO₂ films, two-sides) and copper anode rods (lithium deposited on copper rods from the cathode)..... 507

Figure IV- 288: Proposed Scell may deliver 125 Wh (10.2, 10.2, 1.2 cm) (300 gr). 100 units of this S-cell may power a mid-size PEV to run for 50 miles (Total system: 20 L, 40 kg). Assumption: NCA, 640 mAh/cm³ and Silicon-Carbon 1000 mAh/cm³. Each of the rods consists of a bundle of micro or nano rods with silicon particles on them (deposition methods) or between them (slurry injecting methods). This micro-nano structure accommodates the large shape changes of silicon lithiation-delithiation; it also results in short charges paths for higher rate capabilities. In this project we have focused on rods with 0.5 mm diameter and 0.5 mm height. The distance between the rods depends on the ratio of the anode to cathode capacity and thus on the voltage-capacity range of silicon-carbon anode 508

Figure IV- 289: Fabrication process for Si rod T4. A: Stretched Cu wire substrate. B: Stretched Cu wire substrate coated with some sections coated with Si slurry. C: Final cut Si T-4 rod. Six strands of thin Cu wire were stretched on a fixture and coated with Si slurry in 2.5 cm long sections. The strands of Cu wire were allowed to dry overnight. When dried, the Cu strands were cut to appropriate length 509

Figure IV- 290: SEM image of two types of silicon powder tested 509

Figure IV- 291: Left: T4-micro-silicon rod, center: Micro-silicon anode in coin cell structure. Right: Thick Rod-Micro-silicon anode.....	510
Figure IV- 292: Left: Si30-SC-rod. Right: Si30-SC-coin cell	510
Figure IV- 293: Equivalent electrical circuit	510
Figure IV- 294: Template mask for separator-solid electrolyte coating	512
Figure IV- 295: (a,d) The charge and discharge profiles of the nanocomposite MFx –based Li half cells in three electrolytes in the initial 2 cycles; (b) The first cycle cyclic voltammetry diagrams of the nanocomposite FeF ₂ /C – Li cells; (c) The 5 cycles cyclic voltammetry diagrams of the nanocomposite half cells in electrolyte #3	515
Figure IV- 296: Charge capacities and coulombic efficiencies of nanocomposite MFx cathode half cells in different electrolytes	516
Figure IV- 297: Charge capacity and coulombic efficiency of nanocomposite nanocomposite MFx cathode half cells in electrolyte #3 for 1000 cycles. Previously reported performances of similar materials are compared	516
Figure IV- 298: Charge-discharge profiles of nanocomposite MFx cathode half cells in electrolytes # 1 and #3 during 5th, 20th, 50th, and 100th cycles	517
Figure IV- 299: Average charge and discharge voltages of nanocomposite MFx cathode half cells in electrolytes # 1, #2 and #3 during the first 100 cycles	517
Figure IV- 300: High resolution XPS spectra of MFx nanocomposite cathode cycled in different electrolytes: (a) C _{1s} ; (b) O _{1s} ; (c) F _{1s} ; (d) S _{2p}	518
Figure IV- 301: (a-d) SEM of original Li foil (a) and Li foil cycled in electrolytes (b) #1, (c) #2 and (d) #3	519
Figure V- 1: BMR approach overview	520
Figure V- 2: Areas of focus in the BMR program with materials discovery aided by modeling and diagnostics	521
Figure V- 3: Cycling performance of NCM (left), LCO (center), and HV-LCO (right) between 2.8 and 4.3 V at C/10 charge and C/2 discharge.....	525
Figure V- 4: Average voltage on charge and on discharge of LCO (left) and HV-LCO (right) in half cells. Charge was performed at C/10 and discharge at C/2.....	525
Figure V- 5: Capacity versus cycle number of a half cell of NCM cycled between 2.8 and 4.5 v with baseline electrolyte (left) and high-voltage electrolyte (right).....	526
Figure V- 6: Superimposed voltage curves for baseline electrolyte (left) and high-voltage electrolyte (right)	526
Figure V- 7: MCMB/NCM full cells cycled with baseline electrolyte (left and high-voltage electrolyte (right)	527
Figure V- 8: MCMB/NCM full cells cycled with baseline electrolyte (left and high-voltage electrolyte (right)	527
Figure V- 9: Cycle life of Li/Si cells at 40% DoD with different loading levels (a) 0.45 mg/cm ² , (b) 0.75 mg/cm ² , (c) 0.99 mg/cm ² , (d) 1.26 mg/cm ² and (e) 1.96 mg/cm ²	529
Figure V- 10: Photos of anode slurries obtained from (a) nano-Si, (b) PAA surface coated nano-Si powder	530
Figure V- 11: Photos of anode powders (a) nano-Si, (b) nano-Si/PAA/C composite and (c) the cross-section of nano-Si/PAA/C composite	530
Figure V- 12: Photo of anode electrode of nano-Si/PAA/C composite with polyimide binder	531

Figure V- 13: Cycle life of Si/PAA/C composite with different loading: 2mils of $\sim 1.5\text{mg}/\text{cm}^2$, 3mils of $\sim 2\text{mg}/\text{cm}^2$, 5mils of $\sim 3\text{mg}/\text{cm}^2$ 531

Figure V- 14: Photos of anode slurry (a) nano-Si in H₂O with pH7.5, (b) nano-Si in H₂O with pH 4 and (c) the electrodes of slurry (a) left and of slurry (b) right 531

Figure V- 15: (a) Photos of cell nano-Si/PAA/C composite/EC-DEC-FEC LiPF₆/ NCM and (b) charge/discharge voltage profile between 4.4V and 2.5V at RT 532

Figure V- 16: Cross sections of graphite anodes formulated with CMC binder and freeze-cast at the cooling rates indicated. Electrodes were lyophilized to retain structure. Total porosity is 58-60 vol% 534

Figure V- 17: Galvanostatic discharge voltage vs. capacity for 800 μm thick electrode sectioned from sample directionally freeze-cast at 7.5°C/min. Left: Multiple cycles at C/5 rate. Right: Comparison of result at C/10, C/5 and 1C discharge rate 535

Figure V- 18: Voltage-area capacity results from HPPC test of 800 μm thick electrode 535

Figure V- 19: (left) Scheme for magnetic alignment of removable pore former followed by pyrolysis and sintering. Lower right image shows end-on view of aligned pores. (right) DST test protocol (top) and comparison of discharge capacity for homogeneous and aligned porosity electrodes of same density and thickness 536

Figure V- 20: (a) Schematics of the utilization of SLMP for the SiO electrode. SLMP particles are loaded on to the SiO anode. Rolling compression was used to crush the Li₂CO₃ shell of SLMP to release lithium metal and laminate it on the surface of SiO electrode. This process is called SLMP activation. (b) SLMP particles loaded on the SiO electrode before activation. The inset shows the SEM image of a single SLMP particle. (c) The SiO electrode surface after electrolytes are added onto the SiO electrode with activated SLMP after 12 hours. This shows the disappearance of SLMP and indicates the successful prelithiation of the SiO electrode. (d) SiO/NMC full cell performance with or without the SLMP capacity-enhancement additive, two cycles at C/20, two cycles at C/10, and then C/3. (e) The first cycle voltage curves of the two cells..... 539

Figure V- 21: (a) Chemical structure of PFM conductive polymer binder. (b) Particle size analysis via light scattering for the SiO pristine particles, embedded is the SEM image of the particles with a scale bar of 1 μm . (c) Cycling performance of the SiO/PFM electrode after calendared into different porosities. (d) Rate performance..... 540

Figure V- 22: (a) Structure of poly(1-pyrenemethyl methacrylate) (PPy) and poly(1-pyrenemethyl methacrylate-co-triethylene oxide methyl ether methacrylate) (PPyE). High-resolution TEM (HRTEM) images of (b) PPy and (c) PPyE 541

Figure V- 23: (a) Charge (delithiation) capacities of PPy and PPyE-based Si electrodes at C/10. (b) First-cycle voltage curves. (c) Rate performance. (d) Charge (delithiation) capacities of PPy and PPyE-based Si electrodes at 2C rate. The mass loadings of Si for each cell are labeled in the plot 541

Figure V- 24: (a) Chemical structure of PPyMAA conductive polymer binder. (b) A comparison of 0.3 g of high-tap-density nanoSi (left) and regular nanoSi produced by chemical vapor deposition (right). (c) Histograms of AFM rupture force distribution corresponding to pulling a single polymer chain from a glass surface. Averaged rupture forces for PPyMAA, PAA, PPy, and PVDF on glass substrate were 95 ± 58 , 99 ± 54 , 72 ± 40 and 68 ± 38 piconewton (pN), respectively, with mean rupture forces \pm standard deviations and N= # of observed unbinding events. The pulling velocity is 1000 nm/s and dwell time is 0.5 seconds. (d) Charge (delithiation) capacities of high tap density Si electrodes at C/10 with different binders 542

Figure V- 25: Capacity versus cycle number for NCM (left), LCO (center) and HVLCO (right) in half cells cycled between 2.8 and 4.1 V at C/10 charge and C/2 discharge.....	547
Figure V- 26: Nyquist plots of electrochemical impedance data taken of the full-cell (left), two anodes divided by 2 (center), and two cathodes divided by 2 (right)	547
Figure V- 27: Capacity versus cycle number for a Graphite/NCM cell cycled between 2.8 and 4.2 V at different rates.....	548
Figure V- 28: Average voltage on charge and discharge plotted versus cycle number	548
Figure V- 29: Left: SEM of an electrode that has been cross sectioned exposing the current collector, laminate, SEM tape, and Aluminum stage; right: EDS image of the distribution of fluorine in cross sectioned electrode.....	549
Figure V- 30: a. Cycling stability of a porous Si anode from thermite reaction with a high areal discharge capacity of ~ 2 mAh/cm ² . b. Cycling stability of a thick porous Si (thermite) anode after modification. c. Cycling stability of a thick porous Si (thermite) anode after modification at low rate of ~ 0.06 mA/cm ² . d. A full-cell of the NCA cathode and porous Si anode with an areal capacity of ~ 1.8 mAh/cm ²	552
Figure V- 31: A. Schematic view of graphite/Si/carbon shell product. B. (a) SEM images of blend graphite/nano-Si, (b) blend graphite/nano-Si/hard carbon, (c) the product after synthesis and (d) TEM image of the product. C. Cycle retention (full circle) with areal capacity (empty circle) at 0.2C (1C=600mA/g) blend graphite/nano-Si (black), blend graphite/nano-Si/hard carbon (blue), and the product (red) at various C-rate (0.2C fixed for charging test, 1C = 600mA/g)	553
Figure V- 32: XRD patterns of SiO-alloy with milling time, after treatment and etching	553
Figure V- 33: Specific charge/discharge capacity/Coulombic efficiency vs. cycles of <i>nc</i> -Si and <i>nc</i> -Si/carbon in Li/Li ⁺ system.....	554
Figure V- 34: (a)&(b) SEM images, (c) EDAX spectra, (d) TEM image of the final <i>nc</i> -Si product	554
Figure V- 35: Nanoflakes and nanorods obtained by LPCVD of Si on water soluble template.....	554
Figure V- 36: Long term cycling of a) Si flakes, b) Si nanorods; and c) voltage vs capacity plot of Si Nanorods showing 13% FIR Loss.....	555
Figure V- 37: Galvanostatic discharge-charge profiles measured from anodes of (a) porous Si/C without SLMP, (b) porous Si/C with 1.0 mg SLMP, (c) Si powder/CNT without SLPM, and (d) Si powder/CNT with 0.91 mg SLMP.....	556
Figure V- 38: a. Experimental results from a symmetrical supercapacitor. b. The energy density and power density as a function of the current densities for two pouch cells of LIC250 and LIC395. c. The specific discharge energy as a function of cycle number for the LIC pouch cells. d. Time resolved in situ ⁷ Li NMR spectra of the LIC	557
Figure V- 39: (a) Schematic diagram of the artificial-SEI coating formed by reducing 1-fluorodecane on the surface of Li _x Si NPs in cyclohexane. TEM images of Li _x Si NPs (b) before and (c) after coating	562
Figure V- 40: (a) XRD pattern of artificial-SEI coated Li _x Si NPs sealed in Kapton tape. (b) XPS of artificial-SEI coated Li _x Si NPs. Corresponding high-resolution XPS spectrum around F 1s peak region is shown in the inset. (c) High-resolution XPS spectra of C 1s. (d) Raman spectrum reveals the peak near 1762 cm ⁻¹ as the stretching vibration mode of C=O	562
Figure V- 41: (a) 1 st cycle galvanostatic discharge/charge profiles of artificial-SEI coated Li _x Si NPs. (b) 1 st cycle voltage profiles of Si NPs/coated Li _x Si composite (55:10 by weight) and Si NPs control cells (The capacity is based on the total mass of Si in the electrodes.). (c) 1 st cycle voltage profiles of graphite/coated Li _x Si composite (85:5 by weight) and graphite control cells. (d) Cycling performance of graphite/coated Li _x Si composite and	

graphite control cells at C/20 for the first three cycles and C/5 for the following cycles (1C = 0.372 A/g, the capacity is based on the mass of graphite and Si in coated Li_xSi NPs). The purple line is the Coulombic efficiency of graphite/coated Li_xSi composite 563

Figure V- 42: (a) The extraction capacity of artificial-SEI coated NPs exposed to dry air for varying periods of time. The inset shows the change of capacity as a function of exposure time. (b) The extraction capacity of artificial-SEI coated NPs exposed to air for 6 hrs at different humidity levels. (c) XRD patterns of uncoated (top) and coated (bottom) Li_xSi NPs in humid air for 2hrs with 10% RH 564

Figure V- 43: Density (orange profile) and percent thickness (blue profile) of the AIHQ films in relation to temperature. Results reveal the densification (thickness reduction) of the AIHQ films with increasing temperature treatments 568

Figure V- 44: XAS spectra of O K-edge (TEY modes) in AIHQ thin films treated at 25, 100, 200, 350, and 500 °C under Ar environment 569

Figure V- 45: (a) Cyclic capacity and CE of a Si anode coated with as-deposit AIHQ (blue symbols) compared to the cyclic capacity and CE of a Si anode coated with Ar-treated AIHQ (green symbols). (b) A rate test demonstrates that the Ar-treated electrode can achieve an average specific charge capacity of 1798 mAh g⁻¹ at a rate of 5C and specific charge capacities of about 1500 mAh g⁻¹ at a rate of 10C. All the capacities were normalized based on total Si-active material in each electrode 570

Figure V- 46: (Left) Analysis of EIS spectrum of LMR-NMC cathode at 4 V. (Right) Activation energies extracted from the temperature dependence of different contributions to the cathode impedance 574

Figure V- 47: (a) Charge transfer resistance and (b) double layer capacitance as a function of voltage for LMR-NMC cathodes at RT..... 575

Figure V- 48: (a) X-ray diffraction patterns of Li_2MnO_3 thin films and powder. (b) Raman spectra of Li_2MnO_3 thin films and powder. (c) Voltage profiles of Li_2MnO_3 electrodes cast from a slurry. (d) Voltage profiles of Li_2MnO_3 thin film electrodes..... 575

Figure V- 49: Raman spectra of electrodes as a function of the state of charge and history of electrochemical cycling. (a) Normalized spectra of thin films. (b) Photographs of thin films analyzed in panel a. (c) Normalized spectra of slurry electrodes. (d) Same spectra as shown in panel c except the raw (not normalized) intensities are plotted..... 576

Figure V- 50: (a) First and second principal components extracted from Raman maps of slurry and thin film electrodes cycled 10 times and charged to 4.8 V. (b) Raman map of the percent of the second component needed to reproduce the experimental spectra for the slurry sample. (c) Raman map of the percent of the second component needed to reproduce the experimental spectra for the thin film sample 577

Figure V- 51: (a) Cyclic voltammograms of $\text{Li}_2\text{Cu}_{0.5}\text{Ni}_{0.5}\text{O}_2$ (first three cycles) acquired with a scan rate of 0.1 mV/s over different voltage windows: (i) 4.3 – 1.5 V (ii) 4.3 – 2.25 V (iii) 3.9 – 1.5 V (iv.) 3.9 – 2.25 V (v.) 3.6 – 1.5 V (vi.) 2.8 – 1.5 V. (b) Voltage profiles for cells cycled galvanostatically (50 mA per gram of active material) between 4.3 - 1.5 V. (c) Voltage profiles for cells cycled galvanostatically (50 mA per gram of active material) between 4.3 - 2.25 V. Cycles 1, 2, 5, 10, and 20 are shown..... 578

Figure V- 52: XANES data collected at the Cu and Ni K-edges at different states of charge 579

Figure V- 53: (left) x-ray diffraction patterns of $\text{Cu}_{1-y}\text{Fe}_y\text{F}_2$ materials and (right) discharge of CuF_2 and $\text{Cu}_{0.8}\text{Fe}_{0.2}\text{F}_2$ 582

Figure V- 54: The powder x-ray diffraction patterns of different discharge states of CuF_2 and $\text{Cu}_{0.5}\text{Fe}_{0.5}\text{F}_2$. The tick marks are the standard patterns of the different phases. The top shows the discharge curves of the two compounds.....	583
Figure V- 55: Cycling behavior of (left) CuF_2 , (middle) $\text{CuF}_2/\text{MoO}_3$, and (right) $\text{CuF}_2/\text{VOPO}_4$	583
Figure V- 56: The initial cycling behavior of the solid solution $\text{Cu}_{1-y}\text{Fe}_y\text{F}_2$, (left) $y=0.2$, (right) $y=0.5$ cathode	584
Figure V- 57: The initial cycling behavior of the solid solution $\text{Cu}_{1-y}\text{Fe}_y\text{F}_2$ cathode, for $y= 0.5$	584
Figure V- 58: Cycling behavior of a Sn_2Fe composite electrode at 0.2 mA/cm^2 . The Sn/C/Ti atom ratio is $1/10/0.25$	584
Figure V- 59: Cycling capacity using LiPF_6 and FSI based electrolytes of (left) baseline carbon anode, and (right) advanced SnFeC anode	585
Figure V- 60: (a) Cycling performance at different C rates in the voltage range of $2.0 \sim 4.8 \text{ V}$ and (b) charge/discharge profile evolution of LMR cathode at different stages of cycling at C/10 rate	587
Figure V- 61: Crystal structure of the pristine and cycled LMR cathode. (a) High resolution Z-contrast image of pristine material. (b-d) High resolution STEM image of LMR particles after (b) 1 cycle, (c) 10 cycles and (d) 100 cycles at C/10. (e) Atomic models explaining the structural evolution pathway based on the close observation from the structural changes in cycled materials	587
Figure V- 62: (a) Ni 2p and (b) Mn 2p x-ray photoelectron spectroscopy spectra of $\text{Li}[\text{Li}_{0.2}\text{Ni}_{0.2}\text{Mn}_{0.6}]\text{O}_{2-\delta}$ materials	588
Figure V- 63: (a) Charge/discharge profiles at C/10; (b) rate performance; (c) electrochemical impedance spectra; and (d) cycling performance at C/3 after 3 formation cycles at C/10 of $\text{Li}[\text{Li}_{0.2}\text{Ni}_{0.2}\text{Mn}_{0.6}]\text{O}_{2-\delta}$ materials	588
Figure V- 64: (a) Voltage profiles vs. specific capacity, (b) voltage profiles vs. areal capacity, (c) cycling performance and (d) capacity retention of NMC electrodes with different areal capacity loadings.....	589
Figure V- 65: SEM images of Li anodes after 300 cycles in cells using (a, c) 2 mAh cm^{-2} NMC counter electrode and (b, d) 4 mAh cm^{-2} counter electrode in terms of (a, b) surface views and (c, d) cross-section views	590
Figure V- 66: Structure tracking of the intermediate and final products in preparing $\text{Li}_3\text{V}_2(\text{PO}_4)_3$ (LVP). (a) X-ray diffraction patterns of the precursor (black), intermediate phase (blue) and final product (red), (b) bright-field TEM image and selected area electron-diffraction pattern (inset; recorded from the areas labeled by the green circle) of the intermediate phase), (c-d) XANES spectra and Fourier transformation magnitude of the EXAFS of V K-edge from intermediate (blue), final LVP (red), precursor V_2O_5 (grey) , and reference compounds of VPO_4 (purple), and V_2O_3 (green).....	595
Figure V- 67: <i>Real time</i> tracking of the crystal growth of LVP during calcination by <i>in-situ</i> XRD. (a) Time-resolved XRD patterns of the intermediate during heating from RT to 730°C under an Ar atmosphere, (b) evolution of the crystal size (red square) and concentration of LVP (black circle) with time	596
Figure V- 68: Fast rate capability of LVP nanocrystals. (a) cycling performance and charge-discharge curve (inset) at 10 C in the window of $3.0 - 4.3 \text{ V}$, (b) evolution of the CV curves of LVP as a function of scan rates (from 0.1 to $10 \text{ mV}\cdot\text{s}^{-1}$)	596
Figure V- 69: Structural properties of the synthesized LVP nanocrystals. (a) Synchrotron XRD pattern and Rietveld refinement with observed data points (red points), calculated data (black line), Bragg positions (green bars) for as-obtained LVP, (b) high- resolution	

TEM image and corresponding Fourier Transform (inset) of LVP, indicating its single-crystallinity, (c) thermo-gravimetric analyzer (TGA) curve of LVP during heating in air 597

Figure V- 70: *In-situ* studies of ion exchange in $\text{Li}(\text{Na})\text{VPO}_5\text{F}_x$. (a) Time-resolved XRD patterns, (b) the integrated Bragg peak intensity of (311) of the Na-phase (phase I) and Li-phase (phase II) at fixed temperatures, 72°C and 120°C, (c) illustration of the configuration of Na^+ ions (golden) and Li^+ ions (green) in the *ab* plane determined by structure refinement 598

Figure V- 71: Structure and electrochemical properties of the $\text{Li}_x\text{Na}_{(1-x)}\text{VPO}_5\text{F}_{0.5}$ (LVPOF) electrode. (a) typical transmission electron microscopy (bright field) image (inset: electron diffraction recorded from the particle along the zone axis [001]), (b) voltage profiles (at C/10 rate) of the LVPOF electrode ($x=1.34$) for the 1st and 2nd cycles, (c) voltage profile (at C/10 rate) and cycling stability of the LVPOF electrode ($x=1.02$) 599

Figure V- 72: Structure and stability of novel ternary metal fluorides. (a) Synchrotron XRD patterns from $\text{Cu}_y\text{Fe}_{1-y}\text{F}_2$ along with CuF_2 (PDF#42-1244) and FeF_2 (PDF#45-1062), (b) high-resolution TEM image of as-synthesized $\text{Cu}_{0.5}\text{Fe}_{0.5}\text{F}_2$ nanocrystallites (inset: electron diffraction pattern from a large area), (c) XRD patterns from representative ternary fluorides of varying metal species, $\text{M}^1_{0.5}\text{M}^2_{0.5}\text{F}_2$ ($\text{M}^1, \text{M}^2 = \text{Cu, Fe, Ni, Co}$) 600

Figure V- 73: Electrochemical properties of $\text{Cu}_y\text{Fe}_{1-y}\text{F}_2$ solid solution. (a) Voltage profiles (first discharge at a current 5 mA g^{-1}) of the $\text{Cu}_y\text{Fe}_{1-y}\text{F}_2$ series along with a simple mixture of CuF_2 and FeF_2 (b) voltage profiles of $\text{Cu}_{0.5}\text{Fe}_{0.5}\text{F}_2$ for the first five cycles (9.2 mA g^{-1}), (c) cyclic voltammetry (CV) curves for the first (red) and second (black) cycles at a rate of C/40, in comparison to that of FeF_3 (adapted from Ref. 14), (d) quasi-equilibrium voltage profile from $\text{Cu}_{0.5}\text{Fe}_{0.5}\text{F}_2$ obtained from GITT measurements (inset; 150 mA g^{-1} for 3.5 hrs followed by a 15 hr rest). All the measurements were performed at room temperature 601

Figure V- 74: Design of micro-reactors for both *in-situ* and *ex-situ* combinatorial studies of synthesis reactions, enabling *high-throughput* synthesis of new cathode materials (an example of $\text{Cu}_x\text{V}_{1-x}\text{O}_y$ being used here) 602

Figure V- 75: (a) First cycle discharge capacity and efficiency as a function of *x* in a $\text{Li}_x\text{Mn}_{0.53}\text{Ni}_{0.28}\text{Co}_{0.19}\text{O}_8$ LLS electrode; (b) First-cycle charge and discharge profiles of cells with a $0.1\text{Li}_2\text{MnO}_3 \cdot 0.9\text{LiMn}_{0.4}\text{Ni}_{0.55}\text{Co}_{0.5}\text{O}_2$ cathode before (black) and after acid treatment and annealing at 450°C (red) and 750°C (blue); (c) First charge (black) and discharge (red) capacity and FCE (blue) of the cathodes in (b) 605

Figure V- 76: A comparison of the electrochemical cycling behavior of a LLS electrode with normalized formula $\text{Li}_{1.063}\text{Ni}_{0.265}\text{Mn}_{0.542}\text{Co}_{0.193}\text{O}_y$, (left) laboratory bench scale; and (right) scaled at Argonne’s processing facility, MERF 606

Figure V- 77: (a) Arrhenius plots, and (b) conductivity vs. composition plots of substituted $\text{Li}_{3-2x}\text{Ni}_x\text{PO}_4$ coating materials; (c) capacity vs. cycle number plots of $\text{Li}_{3-2x}\text{Ni}_x\text{PO}_4$ -coated LiCoO_2 electrodes at various current rates 607

Figure V- 78: SEM of (a) *Pnma*, (b) *Pn21a*, and (c) *Cmcm* polymorphs of LiCoPO_4 and corresponding XRD patterns 610

Figure V- 79: SEM of (a) *Pnma*, (b) *Pn21a*, and (c) *Cmcm* polymorphs of LiCoPO_4 and corresponding XRD patterns 611

Figure V- 80: Cyclic voltammetry of the three LiCoPO_4 polymorphs 611

Figure V- 81: XRD patterns of LiMPO_4 (*Cmcm*) with *M* = Mn, Fe, Co, and Ni 611

Figure V- 82: SEM images of (a) PMMA colloidal crystal, (b) 3-DOM carbon, (c) $\alpha\text{-LiVOPO}_4$, and (d) $\alpha\text{-LiVOPO}_4/\text{PEDOT}$ composite. The scale bars in (a, b) and (c) are 1 μm and 500

nm, respectively. The first discharge curves and cycling performances of three α -LiVOPO ₄ samples are also shown.....	612
Figure V- 83: (a) SEM image of the α -LiVOPO ₄ /graphene nanocomposite (~ 3 wt. % graphene) and (b) its first charge-discharge profiles at C/20 rate	613
Figure V- 84: Structural analysis of the as-prepared g-VO ₂ nanocomposite by microwave-assisted solvothermal method: (a) powder XRD pattern; (b, c) low- and high-magnification SEM images showing a secondary g-VO ₂ particle and the detailed VO ₂ nanorods and rGO nanosheets; (d) STEM image showing the encapsulation of an individual VO ₂ (B) rod by rGO layers; (e) elemental mapping of an individual g-VO ₂ nanorod showing the different distribution area of V and C; and (f, g) HR-TEM image and the SAED pattern of a small VO ₂ (B) nanorod with good crystallinity	613
Figure V- 85: Voltage-capacity profiles (a, c, e) and cycling performance (b, d, f) at different voltage windows: (a, b) 3.3 – 1.5 V; (c, d) 3.0 – 0.05 V; (e) 2.0 – 0.05 V; (f) 2.0 – 0.05 V and 2.3 – 0.05 V	614
Figure V- 86: Capacity fade and voltage hysteresis were evident in cycle testing of cobalt-, nickel-, and silver-bearing metaphosphate/vanadate glasses (CoMP-50V, NiMP-50V, and AgMP-50V, respectively).....	618
Figure V- 87: GITT testing of metaphosphate/vanadate glass cathodes showed persistent voltage hysteresis	618
Figure V- 88: TEM images of thin sections from (a) charged and (b) discharged nickel metaphosphate/vanadate glasses both showed intact glass particles. A small number of surface nanoparticles were found in the discharged cathodes (c).....	619
Figure V- 89: Molybdate substitution can be used as an environmentally friendlier alternative to vanadate substitution in certain mixed polyanion glass materials.....	619
Figure V- 90: Vanadate substitution increased the voltage, capacity, and cycleability of copper metaphosphate glass	620
Figure V- 91: Tailoring the polyanion composition was shown capable of reducing the 1 st cycle irreversible loss, improving the voltage hysteresis, and increasing the intercalation capacity in a lithium copper phosphate glass (P = phosphate, B=borate, V=vanadate)	620
Figure V- 92: Energies of O in NMCs as a function of distance from the surface. The shaded region represents the surface and shows that oxygen will be easily lost	624
Figure V- 93: Half-cell cycling results for Ti-substituted NMC (NMCT) between 2.0-4.7V or 2.0-4.55V and regular NMC between 2.0-4.7V. The initial extent of lithium extraction is the same for NMCT between 2.0-4.55V and NMC between 2.0-4.7V, but the capacity retention is better for NMCT, as predicted by theory	624
Figure V- 94: Cycling data for NMCs prepared different ways	625
Figure V- 95: Mn L-edge soft x-ray absorption spectra of NMC-442 electrodes cycled to 4.7V, in total electron yield (TEY) mode, which probes the top 5 nm of the surfaces. The low energy shoulder on the L3 edge is a marker for reduced Mn. The co-precipitated sample shows a greater degree of surface reconstruction compared to the spray pyrolyzed sample	625
Figure V- 96: Elemental mapping using x-ray transmission microscopy of a spray pyrolyzed NMC-442 particle from different views. Voxel sizes are 32.5nm x32.5 nm x 32.5 nm. See below for color key	626
Figure V- 97: Elemental association distributions for the particle shown in the prior figure	626
Figure V- 98: Elemental distribution as a function of the distance from microsphere surfaces calculated using the TXM data. The shaded region represents surfaces	627

Figure V- 99: a) EELS mapping across a grain boundary of two primary particles of an NMC-442 sample made by spray pyrolysis. b) shows the variation in Ni content across the grain boundary shown in the inset 627

Figure V- 100: Synthesis of cross-linked polymers via thiol-ene chemistry: Schematic representation of the thiol-ene reactions between a tetrathiol crosslinker and difunctional ene monomers to coat sulfur-loaded carbon paper electrodes 631

Figure V- 101: Structure of PETT-FC, PETT-EO, PETT-Ester, and PETT-Sulfone..... 632

Figure V- 102: Fabrication scheme for the composite separator membrane. A glass fiber membrane was coated with the crosslinked polymer made of tetrathiol crosslinker and divinylperfluorohexane. The monomer solution was originally mixed with Al₂O₃ particles, and they were filtered and mostly present on the surface of the glass fiber membrane in the final composite separator 632

Figure V- 103: Discharge voltage curves of a NaCrO₂ half cell at different current densities cycled between 2.0 and 3.6 V vs. Na/Na⁺. Charging current density was C/10 in each cycle 633

Figure V- 104: Electrochemical characterization of the polymer-coated sulfur electrodes. (a) Time-dependent electrolyte solvent (1:1 DME/DOL) uptake was measured and calculated according to the equation, $(W_{wet} - W_{dry})/W_{dry}$ where W_{dry} is the membrane weight before soaking and W_{wet} is the weight after liquid uptake. (b) Charge/discharge cycle performance and (c) voltage curves of PETT-FC, PETT-EO, PETT-Ester, and PETT-Sulfone electrodes measured between 1.5 and 3.0 V vs. Li/Li⁺ at 0.5C-rate..... 633

Figure V- 105: Chemical interactions between ester groups in the polymer backbone and lithium polysulfides. (a) Lithium 1s XPS and (b) ATR-FTIR spectra of the bare sulfur-loaded carbon, PETT-FC, PETT-EO, and PETT-Ester electrodes after discharging to 1.5 V. The electrodes were washed with DME and transferred to XPS chamber without any air exposure by using a transfer chamber. Schematic illustration proposes the lithium bond model between the ester group and lithium polysulfides 634

Figure V- 106: Processing scheme for PETT-Ester polymer coating on a porous PVDF membrane 635

Figure V- 107: Charge/discharge voltage curves of 6-bromohexyl ferrocene catholyte with the PETT-Ester-coated PVDF membrane as a separator 635

Figure V- 108: Initial 5 charge/discharge voltage curves of NaCrO₂ with bare stainless steel anode current collector coated with various polymers. (a) PETT-FC, (b) PETT-EO, (c) PETT-Sulfone and (d) PETT-Ester..... 636

Figure V- 109: (a) Synchrotron HR-XRD patterns and (b) initial voltage profiles of Li/LT-LiCo_{1-x}Ni_xO₂ (x = 0 and 0.1) cells cycled between 2.5 and 3.9 V at the rate of 15 mA/g. The selected 2θ ranges in (a), highlighted in separate panes, show the non-uniform distribution of lattice parameters in LT-LiCoO₂. Inset in (b) compares the cycling stability of LT-LiCoO₂ and LT-LiCo_{0.9}Ni_{0.1}O₂ 639

Figure V- 110: (a) XRD patterns and (b) initial discharge profiles of LiCo_{0.9}Ni_{0.1}O₂ samples synthesized at various temperatures (400 and 800 °C)..... 640

Figure V- 111: (a) XRD patterns of LT-LiCoO₂ and LT-LiCo_{0.9-y}Ni_{0.1}Mn_yO₂ samples (y = 0, 0.1, and 0.2). Initial voltage profiles of Li/ LT-LiCo_{0.9-y}Ni_{0.1}Mn_yO₂ (y = 0, 0.1, and 0.2) cells charged to upper cut-off voltages of (b) 3.9 V and (c) 4.2 V at a rate of 15 mA/g. Capacity vs. cycle number plots are provided as insets in (b) and (c) 641

Figure V- 112: Design principal for high voltage electrolytes 643

Figure V- 113: Synthesis of F-carbonate and ¹H-NMR and GC-MS spectra 645

Figure V- 114: Optimization of ternary fluorinated electrolytes 646

Figure V- 115: Diffusion coefficients of EMC and FEMC in a 1:1 molar ratio solution 647

Figure V- 116: Diffusion coefficients of EMC and FEMC in a 1:1 molar ratio solution with 0.5 M LiPF ₆	648
Figure V- 117: Leakage current measured at 55°C	649
Figure V- 118: Cycling data of LNMO/1.0 M LiPF ₆ in TFPC/F-EMC/F-EPE=3/5/2 v/v/v with 1% LiDFOB/Li cells.....	649
Figure V- 119: Capacity retention of LNMO/graphite cells with 1.0 M LiPF ₆ TFPC/F-EMC 3:7 V/V.....	649
Figure V- 120: Capacity retention of LNMO/graphite cells with 1.0 M LiPF ₆ FEC/F-EMC/F-EPE 3:5:2 V/V/V.....	649
Figure V- 121: Voltage profiles of graphite/Li half cells with (a) TFP-PC-E, (b) HFP-PC, (c) FEC and (d) TFPC	650
Figure V- 122: TEM image of the cycled graphite electrode with fluorinated electrolyte and Gen 2 electrolyte	650
Figure V- 123: SEM image of the cycled graphite electrode with fluorinated electrolyte and Gen 2 electrolyte	651
Figure V- 124: XPS profiles of C _{1s} , O _{1s} , and Mn _{2p} from cycled graphite anodes.....	652
Figure V- 125: (a) LNMO/graphite cell assembly with incorporated lithium metal; (b) lithium metal working mechanism at the formation cycles; (c) direct shorting of graphite anode using SLMP; (d) prelithiation of graphite anode using electrochemical method	653
Figure V- 126: (a) Capacity retention and (b) coulombic efficiency of LNMO/graphite cells cycled at C/3, 55 °C using HVE3 electrolyte with and without Li compensation (the 1 st method), compared with Gen 2 electrolyte without Li compensation, 3.5-4.9 V.....	654
Figure V- 127: SEM images of Li _{1.2} Ni _{0.13} Mn _{0.54} Co _{0.13} O ₂ crystals	657
Figure V- 128: HAADF STEM image of a) an entire needle-shaped Li _{1.2} Ni _{0.13} Mn _{0.54} Co _{0.13} O ₂ crystal, b) and c) zoomed in view of the crystal structure, d) color-coded HAADF image showing domains of the monoclinic variants, and e) models showing the monoclinic structure in [100], [1-10] and [110] directions	658
Figure V- 129: a) HAADF STEM image, b) EEL spectra collected from the surface (top) and the bulk (bottom) corresponding to the HAADF image, and c) L3/L2 ratio of Mn, Co and Ni determined from the EELS data	658
Figure V- 130: a) First charge-discharge voltage profiles of the Li _{1.2} Ni _{0.13} Mn _{0.54} Co _{0.13} O ₂ half cells, b) rate capability of the crystal samples, c) and d) long-term cycling and capacity retention of the cells at a current density of 20 mA/g	659
Figure V- 131: Soft XAS spectra of Co L- edge collected in AEY (a and d), TEY (b and e) and FY (c and f) modes on pristine (bottom) and cycled (top) Li _{1.2} Ni _{0.13} Mn _{0.54} Co _{0.13} O ₂ composite electrodes, and g) Co L3 peak ratio of the TEY spectra, with a higher ratio corresponding to a lower oxidation state.....	660
Figure V- 132: a) Average charge and discharge voltages of the Li _{1.2} Ni _{0.13} Mn _{0.54} Co _{0.13} O ₂ half cells and b) comparison of the charge and discharge voltage gaps at cycle 5 and 85	661
Figure V- 133: a) dQ/dV profiles, b) and c) percentage of the phases present during in situ discharge of x=0.5 and x=0.3, and d) rate capability of the crystal samples	661
Figure V- 134: Possible formation pathway of the metal complexes upon EC oxidation at the Li _x Ni _{0.5} Mn _{1.5} O ₄ surface by an electron transfer, propagation, proton transfer and a proton coupled electron transfer (PCET) mechanism	665
Figure V- 135: Impedance evolution of graphite symmetric cells filled with 1 M LiPF ₆ , EC/DEC (1:2) spiked with 500 ppm of Mn ^{II/III} compounds, measured at 50% of SOC.....	666

Figure V- 136: SEI layer forms after 50 cycles on 100 nm Si thin film (coated 8 nm Alucone/non coated) in 1M LiPF6 EC:DEC [1:2] and corresponding impedance spectra.....	666
Figure V- 137: (a) Near-field IR (top) spectrum of particle in Si surface film compared to ATR-FTIR spectrum of Li ₂ C ₂ O ₄ . Inset: AFM topography with particle marked	667
Figure V- 138: Near-field spectroscopic absorption of SiO ₂ substrate through grapheme membrane.....	667
Figure V- 139: Comparison of UV ultrafast LIBS emission from Si (a) in liquid and (b) in air	668
Figure V- 140: <i>In situ</i> X-ray diffraction (XRD) of Li ₂ MoO ₃ during the first charge. (a) The XRD pattern of the Li _{2-x} MoO ₃ electrode right after charging to 4.8 V. (b) Contour plot of diffraction peak evolution of (003), (101), (104), (107), (108) and (110) during delithiation. (c) The XRD pattern of the Li ₂ MoO ₃ electrode before charge. (d) Charge curve at a current density of 10 mA g ⁻¹ from open circuit voltage (OCV) to 4.8 V during XRD data collection	673
Figure V- 141: XAS spectra of Li ₂ MoO ₃ during the first charge. (a) <i>In situ</i> XANES spectra at Mo K-edge during charging to 4.8V. (b) <i>Ex situ</i> FT-EXAFS spectra of Li _{2-x} MoO ₃ at pristine (x=0), half charged (x=0.75) and fully charged (x=1.47) states. The lower panel shows the FT-EXAFS spectra of MoO ₂ and α-MoO ₃ references.....	674
Figure V- 142: (a) XRD patterns for LiNi _{0.5-x} Mn _{1.5-x} Fe _{2x} O ₄ (2x = 0, 0.2, 0.33, 0.5) with the inset graphs showing the emergence of impurity phase as 2x exceeds a certain limit. A pure phase can be indexed by the Fd $\bar{3}$ m space group. (b) Illustration of the crystal structure of LiNi _{0.5-x} Mn _{1.5-x} Fe _{2x} O ₄ . (c) Variation of the lattice parameter as a function of the concentration of Fe. The linear relationship indicates that solid solution is formed in the LiNi _{0.5-x} Mn _{1.5-x} Fe _{2x} O ₄ (2x = 0, 0.2, 0.33) series	675
Figure V- 143: Rendering of the 3D structure of a selected LiNi _{0.33} Mn _{1.34} Fe _{0.33} O ₄ particle is shown in panel (a) with the scale indicated in the axis and the color legend shown in the inset. Panels (c) through (g) are slices at different depth of the particle showing that it is a solid piece with no internal pores and the density distribution is relatively homogeneous. The elemental concentration over the line path indicated in panel (e) is plotted in panel (b) (the blue, green, and red curves represent the concentration of Mn, Ni, and Fe respectively), which is in good agreement with the elemental composition of the material. Panels (a) and (c) through (g) are reconstructed from nano-tomography data collected at 8380 eV (above the absorption k edges of all the three transition metal elements), while the data plotted in panel (b) is retrieved from the evaluation of the energy dependency of the absorption coefficient using a method known as Absorption Correlation Tomography.....	676
Figure V- 144: Electrochemical performance and XANES spectra. (a) Charge and discharge profiles together with capacity retention (inset graph) of LiNi _{0.5-x} Mn _{1.5-x} Fe _{2x} O ₄ (2x = 0, 0.33). Cells were cycled at C/5 which corresponds to current density of 0.11 mA/cm ² . (b) Rate capability of LiNi _{0.5-x} Mn _{1.5-x} Fe _{2x} O ₄ (2x = 0, 0.33). (c) dQ/dV plot of LiNi _{0.5-x} Mn _{1.5-x} Fe _{2x} O ₄ (2x = 0, 0.33). (d) Fe K-edge XANES spectra of pristine, charged and discharged samples of LiNi _{0.5-x} Mn _{1.5-x} Fe _{2x} O ₄ (2x = 0.33)	677
Figure V- 145: ⁷ Li MAS NMR spectra of Li _{1.08} Mn _{1.92} O ₄ electrodes at different state of charge (SOC). The spectra were acquired at 4.7 T with a MAS frequency of 40 kHz. The impurity Li ₂ MnO ₃ (marked on the spectra) is electrochemically inactive upon charging. The isotropic shift regions are marked with a red dashed square. The other spectral regions are dominated by spinning sidebands	680

Figure V- 146: ^7Li NMR T_2' measurements of $\text{Li}_{1.08}\text{Mn}_{1.92}\text{O}_4$ measured during battery cycling. (1 st charge 0 – 1; 1 st discharge, 1 – 2). The measurements were performed at 13, 25, 40, 60 and 70°C.....	681
Figure V- 147: ^1H , ^7Li and ^{19}F MAS NMR spectra of reduced protonated ($^{\text{H}}$ -FEC) and deuterated ($^{\text{D}}$ -FEC)	682
Figure V- 148: Two proposed reduction products of FEC/VC, LiVD (top) and the carbonate polymer (bottom).....	683
Figure V- 149: <i>In situ</i> ^{23}Na NMR spectra for continuous galvanostatic plating, and galvanostatically cycled samples, at currents of 0.5, 1 and 2 mA cm ⁻² (A-C, and A*-C*, respectively) with the superscript (*) denoting galvanostatically cycled samples. Stack plots vs. time (in min.) are shown. The resonance assigned to Na metal continues to grow until the cell fails (e.g., 3000 mins for B) due to extensive short circuits.....	683
Figure V- 150: Fraction of high surface area (F_{HSA}) Na during galvanostatic cycling at various current densities. A ratio of 1 indicates complete microstructure deposition while 0 indicates smooth deposition.....	684
Figure V- 151: Discharge-charge curves for Li-O ₂ cells using mesoporous SP and TiC, and macroporous rGO electrodes, with capacities limited to 500 mAh/g (based on the mass of carbon or TiC) and a 0.25 M LiTFSI/DME electrolyte. For SP and rGO electrodes, 0.05 M LiI was added to the LiTFSI/DME electrolyte in a second set of electrodes (purple and red curves). All cells in were cycled at 0.02 mA/cm ² . The horizontal dashed line represents the position (2.96 V) of the thermodynamic voltage of a Li-O ₂ cell	685
Figure V- 152: (a) cation ordering in transition metal layer: $0.5\text{Li}_{4/3}\text{Mn}_{2/3}\text{O}_2 \cdot 0.5\text{LiNi}_{1/2}\text{Mn}_{1/2}\text{O}_2$. (b) oxygen vacancy formation energy of $\text{Li}_{8/12}\text{Ni}_{3/12}\text{Mn}_{6/12}\text{M}_{1/12}\text{O}_2$ at different configurations. #1 is the model without substitution	689
Figure V- 153: (a) Voltage profiles of the pristine and surface modified $\text{Li}_{1.133}\text{Ni}_{0.3}\text{Mn}_{0.567}\text{O}_2$ at different cycle numbers (0.1 C, 2-4.8V), (b) 1 st and 2 nd charge-discharge voltage profiles of the pristine and surface modified $\text{Li}_{1.144}\text{Ni}_{0.136}\text{Co}_{0.136}\text{Mn}_{0.544}\text{O}_2$ at 0.05 C.....	689
Figure V- 154: Electrochemical charge/discharge profile with corresponding lithium occupancy at different states of delithiation/lithiation for a) HLR and b) LLR	690
Figure V- 155: (a) Specific capacity versus cycling for galvanostatic cycling of a-Si thin films at C/2 rate and (b) Coulombic efficiency comparison of cells cycled with traditional electrolyte, 1:1 EC:DEC (squares), and FEC-containing electrolyte, 45:45:10 EC:DEC:FEC (circles)	691
Figure V- 156: A relative composition of the 10nm outer SEI after: first lithiation; first delithiation; and 100 cycles	691
Figure V- 157: A relative composition of the 10nm outer SEI after 100 cycles. The layer is adjacent to and in contact with the electrolyte 1:1 EC:DEC and 45:45:10 EC:DEC:FEC when cycled	692
Figure V- 158: ADF-STEM image of (a) pristine Si, (b) lithiated Si after one cycle, (c) lithiated Si with FEC after one cycle, EELS spectra (d) O-K edge, and (e) Li-K edge.....	693
Figure V- 159: ADF-STEM images of the lithiated silicon nanoparticles cycled in EC/DEC at a) 1 cycle and b) 5 cycles.....	694
Figure V- 160: Relative composition of the SEI after (a, b) first lithiation, (c, d) first delithiation, and (e, f) 100 cycles in the delithiated state.....	694
Figure V- 161: CV of Si(100)-hydrogen terminated.....	698
Figure V- 162: Illustration of the <i>in situ</i> spectro-electrochemical apparatus.....	698

Figure V- 163: SFG profile of Si-OC₂H₅ (ethoxy) groups on Si(100) 698

Figure V- 164: We show the evolution of SFG signal under reaction conditions of crystalline silicon Si(100)-hydrogen terminated anode to that of Si(100)-OC₂H₅ 699

Figure V- 165: The SFG profiles of crystalline silicon oxide Si(100)-Ox anode after cycling 699

Figure V- 166: The SFG profiles of crystalline silicon oxide Si(100)-Ox anode after cycling 699

Figure V- 167: A) and B) Time-resolved TEM images show the development of lithiation profiles of the alucone and Al₂O₃ coated SiNWs and schematics of the Li diffusion paths through the SiNWs that dictate the lithiation behavior; C) Average lithiation thickness vs. time for the alucone (black square) and Al₂O₃ (red dot) coated SiNWs..... 702

Figure V- 168: (a-c) [010] zone STEM-HAADF images to show a 10-cycles Li₂MnO₃ particle and its outer surface lattice structure. (d) and (e) highlight the lattice difference between Mn₃O₄-spinel and I41 structure. Purple and green indicate Mn and Li, respectively. (f) [100] zone STEM-HAADF image of the surface layer after 10 cycles. STEM-HAADF images to show inner bulk lattice structure of pristine sample (g) and 10-cycles sample (h). The intensity profile along the blue lines in (g) and (h) are shown in each figure 703

Figure V- 169: Li_{1.2}Ni_{0.13}Co_{0.13}Mn_{0.54}O₂ (NC-LMR) sample. (a) [010] zone axis STEM-HAADF image showing the EDS mapping region. (b) Surface plot of Mn K map. (c) Surface plot of Co K map. (d) Surface plot of Ni K map. (e) Integrated line scan profile showing X-ray counts distribution across the layered structure. (f) Based on counts ratio that from TM-layer and Li-layer, 4% Co and 41% Ni were estimated to seat in Li-layer due to an interlayer mixing. (g) Optimized crystal model for NC-LMR based on EDS mapping results..... 704

Figure V- 170: a) Pure C2/m stacking in Li₂MnO₃. (b) Standard Reitveld refinement (red) of Li₂MnO₃ diffraction data (black) showing the misfit due to stacking faults. (c) Fit of the data in (b) using a stacking fault model derived from DIFFaX analysis..... 707

Figure V- 171: a) Raw X-ray powder diffraction data for Li_{1.2}Mn_{0.6}Ni_{0.2}O₂ with no coherent stacking. (b) Fit to the data in (a) using randomly faulted + coherent C2/m regions calculated from DIFFaX 708

Figure V- 172: (left) First- (solid) and second-cycle (dashed) charge/discharge voltage profiles for a series of layered-spinel Li_{2-x}MnO_y cathode powders. (right) Electron microscopy/diffraction data, acquired at NUANCE, for the x=1 sample 708

Figure V- 173: (a) DFT simulation of Ga-substituted LiCoO₂. (b) EXAFS fits of LiCo_{1-x}Ga_xO₂. (c) First-cycle voltage curves for Li_{1-x}Cr_xO₂ 709

Figure V- 174: Rate performance in first discharge of Li/S batteries..... 712

Figure V- 175: Specific capacity as a function of concentration for carbon paper and glassy carbon 713

Figure V- 176: Model vs. experimental data at different C-rates (C/2, C/4 and C/25)..... 714

Figure V- 177: Updated model (Updated) and Dilute model (Dilute) predictions of Li₂S deposition at 3.5 C discharge current throughout cathode at the end of discharge 714

Figure V- 178: C/12 discharge and charge of custom Li-S cell 715

Figure V- 179: Simulation domain showing (from left to right) positive current collector, porous electrode, separator, and lithium negative electrode. For clarity, porous matrix and separator are shown as transparent..... 715

Figure V- 180: Comparison of 3C discharge curves obtained by experiment, macroscale simulation, and microscale simulation 715

Figure V- 181: Illustration of Li_2MnO_3 indicating the 4g, 4h and 2b sites.....	718
Figure V- 182: Structure of layered Li-excess material of in the (100) direction and the Li-ion migration process between the transition metal layer and Li-layer.....	719
Figure V- 183: A schematic of a migrated Mn ion, impacting the Li site preference in the Li layer.....	720
Figure V- 184: Density of states (DOS) of LiCoO_2 as predicted by various electronic structure methods in comparison to experimental spectroscopic measurement.....	722
Figure V- 185: Computed voltage profiles of $\text{Li}_{1-x}\text{CoO}_2$ ($0 \leq x \leq 1$), as predicted by GGA, GGA+U, and HSE with different mixing parameters in comparison to the experimental reference.....	723
Figure V- 186: XRD shows a pure disordered rocksalt phase; EELS spectra confirm that Mn and O are both redox active.....	723
Figure V- 187: Cycling performances of $\text{Li}_{1.25}\text{Nb}_{0.25}\text{Mn}_{0.5}\text{O}_2$ at 55°C (a) and room temperature (b).....	724
Figure V- 188: First charge profile of $\text{Li}_{1.2}\text{Ni}_{1/3}\text{Ti}_{1/3}\text{Mo}_{2/15}\text{O}_2$. The redox processes for different charge states are indicated in the figure.....	724
Figure V- 189: Na-vacancy orderings occurring in the Na_xMO_2 systems with seven different choices of M.....	725
Figure V- 190: Structural evolution as a function of Li/Si content.....	728
Figure V- 191: Formation of Li_6O complex at Li/Si = 3.48.....	728
Figure V- 192: Cluster models of 3- and 4- coordinated Al complexes. A, 3-O coordination; B, 4-O coordination; C, 4-O coordination with a terminal OH group. Li^+ binding on cluster model A, B, and C. Li^+ ions are denoted as purple spheres. Listed distances are in Å. Light blue, pink, red, grey, and white spheres represent respectively Si, Al, O, C, and H atoms.....	730
Figure V- 193: Electron current determined for various values of applied voltage for the two model systems. A clear enhancement of the electron conductivity is found in the supersaturated film.....	731
Figure V- 194: Electrostatic potential map follows a reaction occurring at the solid/electrolyte interphase region of the $\text{Li}_{13}\text{Si}_4/\text{LiF}/\text{Li}_2\text{VDC}$ surface. The sequence illustrates the events preceding a 2-step decomposition of Li_2VDC yielding 2 CO_3 groups and C_2H_2 . One CO_3 anion separates first from the whole molecule (at approximately 3931 fs) and short after (at 4031 fs) the other CO_3 group breaks apart from the acetylene molecule.....	731
Figure V- 195: Surface models for Li_2EDC on top of a LiF covered surface showing a coverage of 1.7 oligomers/ nm^2 and Li_2EDC dimer formation.....	732
Figure V- 196: Effects of EC reduction rate (k_2) on SEI thickness (\bar{x}) growth.....	733
Figure V- 197: Film growth at open circuit. Electron transfer rate was set at various rates taken from the literature.....	733
Figure V- 198: Top: EDC film on Li(100) loses a CO_3^{2-} spontaneously. Bottom: Li_2CO_3 film on Li(100) loses a O^{2-} (1 eV barrier).....	734
Figure V- 199: Thin liquid EC film decompose on incrementally stretched Li(x)Si surface with increasing “x.”.....	734
Figure V- 200: Comparison of continuous thin film and patterned model structure allows Si enabled experimental correlation of the irreversible capacity loss with SEI failure.....	738
Figure V- 201: Shell failure mechanisms as a function of Si nanowire size and coating thickness. With thicker coatings and Li concentration gradient, the coating is mechanically stable until full lithation of Si.....	738

Figure V- 202: Continuum mechanical model identified the critical shell thickness of lithiation in Si-C yolk-shell structure 739

Figure V- 203: Engineered SEI with specified amounts of Li_2CO_3 and LiF co-existing on silicon thin film electrodes, showing Li diffusion is peaked with 50% LiF by TOF-SIMS results, due to space charging effect..... 739

Figure V- 204: Micro-four-line-probe with electrode film sample on top. Sampling area for ionic conductivity is $70 \times 500 \mu\text{m}$ 744

Figure V- 205: The DPP model uses superpositions of spheres to represent active material (blue) and carbon/ binder/solvent domains (green) 744

Figure V- 206: The effect of changing granular diameter (a force parameter) of CBD particles on simulated properties, while holding other parameters and box volume constant: (a) pressure, (b) elasticity, and (c) viscosity. Error bars (some smaller than symbol size) show 95% confidence intervals from multiple simulations. Lines are a guide to the eye..... 745

Figure V- 207: Viscosity at different shear rates for slurry containing carbon black and binder (green), and for slurry that additionally includes active material (blue), from experiment (line) and simulation (symbols). In some cases error bars are smaller than symbol sizes. Lines are used for experiments due to the close spacing of the data 745

Figure V- 208: Simulated cross section of cathode (left) compared to experimental results. The SEM/FIB image (center) is segmented (right) using computer tools developed at BYU 746

Figure V- 209: Photograph of new 6-line probe, showing dual sets of external connections on the edges of the probe, converging to a μm -scale sampling region in the center. The probe is mounted in a computer-controlled xyz stage..... 746

Figure V- 210: Modulus determined from many nanoindentations. Materials are from Ohara..... 751

Figure V- 211: Indentation of a $3\mu\text{m}$ thick Li film at strain rates of $1/\text{s}$ and $0.1/\text{s}$, blue and green respectively 752

Figure V- 212: Phase angle for 100Hz modulation corresponding to the indentation tests at left..... 752

Figure V- 213: Modulus determined from nanoindentation 752

Figure V- 214: Cumulative hardness for selected maps. Areas 7 and 8 had visible dark areas; areas 9 and 13 were still white 753

Figure V- 215: Correlation of the pulse echo wavespeed (black) with initiation of failure. The noise in the voltage precedes the eventual short where the voltage drops to zero. In this test, failure occurs at 0.1 and $0.2 \text{ mA}/\text{cm}^2$ 753

Figure V- 216: Secondary electron SEM images of LLZO fracture surfaces densified between 900 and 1100 C ($10,000 \text{ X}$) 755

Figure V- 217: Critical current density as a function of the Li-LLZO interfacial resistance, which was controlled by the surface contamination 756

Figure V- 218: EIS data for Li-LLZO-Li cells using the standard surface preparation (a) and the new surface treatment (b)..... 756

Figure V- 219: Composite membrane of 50vol.% Ohara glass ceramic powder and PEO+ LiTf salt (on blue background)..... 760

Figure V- 220: Relative conductance after overnight exposure to H_2O or DMC vapor. Concentration indicates the maximum available quantity of the solvent..... 760

Figure V- 221: Conductivity of two different composite membranes compared to the pure components 761

Figure V- 222: Electrochemical impedance of PEO+LiTf coated LLZO ceramic plate. Scans before and after exposure to DMC vapor at room temperature 761

Figure V- 223: DSC scans for designated samples normalized by the total mass.....	761
Figure V- 224: Time delayed increase in conductivity after exposure in standard or solvent-free gloveboxes	761
Figure V- 225: EIS of thick and thin LLCZN pellets at room temperature	765
Figure V- 226: EIS of thick and thin LFMO pellets at room temperature	765
Figure V- 227: EIS plot of LLCZN electrolyte/LFMO cathode system	765
Figure V- 228: Structured garnet surface, white shining areas are deposited garnet columns	766
Figure V- 229: Impedance of cathode on smooth and structured garnet electrolyte.....	766
Figure V- 230: Synthesis procedure of PFPE-DMC	766
Figure V- 231: Cyclic voltammetric results for LiTFSI/PFPE	767
Figure V- 232: Photograph, formula, and top and side SEM images of PVDF-HFP gel membrane	767
Figure V- 233: CV of Li/PVDF-HFP&IL/Ti system	767
Figure V- 234: EIS of garnet/cathode and garnet/gel/cathode	768
Figure V- 235: Li grand canonical phase diagram of Li-La-Zr-O system	768
Figure V- 236: Models for the interfaces between Li metal and garnet surface materials	768
Figure V- 237: Model for garnet-electrode interfaces, which take inputs from first principles calculations and experimental condition parameters	769
Figure V- 238: (a) Fabrication process for the hollow carbon nanosphere-modified Cu electrode. (b) and (c) SEM images of carbon-coated polystyrene nanoparticle array. (d) to (g) As fabricated hollow carbon nanosphere thin film after removal of template	772
Figure V- 239: (a) Cycling performance of hollow carbon nanosphere modified electrode and control Cu electrode. (b) Voltage profiles of the Li deposition/dissolution process. (c) Comparison of the hysteresis of Li deposition/dissolution for the modified electrode and control electrode	773
Figure V- 240: Chemical vapor deposition growth of h-BN. (a) Experiment setup for h-BN growth. (b), (c) and (d) SEM images of as grown h-BN sample at different stage	774
Figure V- 241: h-BN as interfacial layer for lithium metal. Morphologies of lithium metal surface without (a and c) and with (b and d) h-BN coating at first cycle (a and b) and tenth cycle (c and d). (e) and (f) Coulombic efficiency and average voltage hysteresis of lithium metal anode upon cycling, with and without h-BN coating at different current densities and areal capacities	775
Figure V- 242: Characterizations of graphene and its performance in cycling of Li metal anode. (a) Raman spectrum of graphene film. The wavelength of excitation laser is 632.8 nm. (b) HR-TEM image of mismatched two-layer graphene. Two sets of hexagonal spot patterns were shown in the FFT image inset. (c) Top view SEM image of the first Li metal deposition on graphene protected anode at 0.5 mA/cm ² . (d) Cycling performance and average voltage hysteresis of Li metal anode with and without graphene protection at different current rate	776
Figure V- 243: Schematics of the fabrication processes of the polymer nanofiber mat. (a) Precursor solution synthesis; (b) PAN/PVP hybrid nanofiber by co-electrospinning and its corresponding SEM image. The resulting nanofiber forms a core-shell structure with PAN as the core and PVP as the shell; (c) Proposed structural formula for oxidized PAN and its corresponding SEM image. PVP is removed from the hybrid fiber through thermal decomposition. Scale bars are 2 μm	777
Figure V- 244: Cycling performances of the control Cu electrode and modified Cu-OxPAN electrode at various current rates. (a) Comparison of the Coulombic efficiency of Li	

deposition on bare Cu and Cu-OxPAN electrode. (b) Comparison of the voltage profiles of the Li plating/stripping process with Li metal as the counter and reference electrode with current density of 3 mA/cm². (c) Comparison of voltage hysteresis of the Li plating/stripping process with Li metal as the counter and reference electrode with current density of 3 mA/cm²..... 777

Figure V- 245: Schematic of the fabrication of the Li-coated PI matrix. Electrospun PI was coated with a layer of ZnO via ALD to form core-shell PI-ZnO. The existence of ZnO coating renders the matrix “lithiophilic” such that molten Li can steadily infuse into the matrix. The final structure of the electrode is Li coated onto a porous, non-conducting polymeric matrix 778

Figure V- 246: SEM images and the corresponding schematics showing the well-confined stripping/plating behavior of the Li-coated PI matrix. Top view SEM images of (a) the exposed top fibers of the Li-coated PI electrode after stripping away 5 mAh/cm²Li, (b) exposed top fibers partially filled with Li when plating 3 mAh/cm²Li back and (c) completely filled PI matrix after plating an additional 2 mAh/cm²Li back 779

Figure V- 247: Electrochemical behaviors of the Li electrodes in EC/DEC electrolyte. (top) Cross-sectional SEM images of nanoporous lithium anode before and after complete lithium stripping. (bottom) Comparison of the cycling stability of the Li-coated PI matrix and the bare Li electrode at a current density of 1 mA/cm² with fixed capacity of 1mAh/cm² 780

Figure V- 248: Cycling performances of graphite | | NCA full cells containing the three electrolytes E1Cs, E1VC and E2 at (A) RT and (B) 60°C..... 783

Figure V- 249: Comparison of cell performance of graphite | | NCA full cells containing two electrolytes, E17Cs and E17. (A) Initial charge/discharge voltage profiles at C/20 rate at RT and (B) cycling stability at 60°C at C/2 rate after two 784

Figure V- 250: Comparison of low-temperature performance of graphite | | NCA full cells containing two electrolytes, E17Cs (A) and E2 (B). Cells were charged at a C/5 rate at RT, kept for 3 hours at selected low temperature, and then discharged at a C/5 rate at that low temperature 784

Figure V- 251: (A) Micro-XRD patterns of the graphite electrodes charged to 0.3 V in various electrolytes. SEM (B) and TEM (C) images show the graphite exfoliation in the E1 electrolyte 785

Figure V- 252: SEM images of graphite electrodes: (A) pristine graphite and (B-D) graphite electrodes discharged to 0.3 V in electrolytes of E1 (B), E1Cs (C) and E1FEC (D)..... 785

Figure V- 253: TEM images of graphite anodes discharged to 0.3 V from E1 (A), E1FEC (B) and E1Cs (C) 786

Figure V- 254: SEM images (a, b) and TEM images (c, d) of graphite anodes after 100 cycles at 60°C from graphite | | NCA cells with E1Cs (a, c) or E1FEC (b, d)..... 786

Figure V- 255: Electrochemical behavior of various LiPF₆-CsPF₆ electrolytes on graphite surfaces. (A) Lithiation/de-lithiation profiles of Li | | graphite half cells using electrolytes of E1, E1Cs, E1FEC, and conventional E2. (B and C) Comparison of differential capacity (dQ/dV) plots of Li | | graphite cells using E1, E1Cs, and E1FEC (B), and E2 and E2Cs for the 0.75 V peak (C)..... 787

Figure V- 256: Electrochemical behavior of various LiTFSI-CsTFSI electrolytes on graphite surfaces. (A) Initial lithiation profiles of graphite in different carbonate electrolytes. (B and C) Comparison of the 0.75 V reduction peaks via dQ/dV plots for EC-PC-EMC (5:2:3 by wt.) electrolytes at different Cs⁺ concentrations (B) and various electrolytes

containing 0.9 M LiTFSI and 0.1 M CsTFSI in different EC-PC-EMC mixtures (C). The current density for both lithiation and de-lithiation was 0.075 mA cm ⁻² (C/20 rate).....	787
Figure V- 257: Schematic mechanism of SEI film formation promoted by Cs ⁺ . (A) In a conventional electrolyte, Li ⁺ favors PC to form solvates. (B) In a Cs ⁺ -containing electrolyte, due to the preferential formation of Li ⁺ -(PC) _n solvates, Cs ⁺ coordinates with EC molecules and its solvates have priority to be electrochemically reduced.....	788
Figure V- 258: Lithiation voltage profiles of graphite electrodes in (a) control electrolyte, (b) E20PC-Cs electrolyte at different discharge current densities ranging from 0.2 to 2.0 mA cm ⁻² . SEM images showing the Li dendrite formation on the surface of graphite electrodes in control electrolyte E2 (c-f) and in E20PC-Cs electrolyte (g-k) at different current densities: (c, g) 0.2 mA cm ⁻² ; (d, h) 0.5 mA cm ⁻² ; (e, j) 1.0 mA cm ⁻² ; (f, k) 2.0 mA cm ⁻²	789
Figure V- 259: (a) Initial charge/discharge profiles at C/20 (1C = 1.5 mA cm ⁻²) and (b) long-term cycling performance of graphite NCA full cells using electrolytes containing different amounts of PC at RT. (c) Rate capability at RT. (d) Long-term cycling stability (C/2 rate for charge and discharge) of graphite NCA full cells using non-PC control and E20PC-Cs electrolytes at an elevated temperature of 60°C	790
Figure V- 260: Long-term cycling stability of Li NMC442 coin cells with 10 electrolytes at RT. (a, b) Specific capacity vs. cycle number; (c, d) Coulombic efficiency vs. cycle number	791
Figure V- 261: Cell Energies at elevated voltages normalized to 4.2 V for NMC111/graphite.....	795
Figure V- 262: Cell Energies at elevated voltages normalized to 4.2 V for LCO/graphite	796
Figure V- 263: Retention and recovery capacities and gassing volume for several solvent compositions.....	797
Figure V- 264: NMC111/graphite cells cycled at 1 C and 60 C. at three voltages (4.20, 4.35 and 4.50 V) for both the hydrocarbon control electrolyte (top panel) and Daikin fluorinated electrolyte (bottom panel).....	798
Figure V- 265: Photos of NMC111/graphite cells after the cycling reported in the prior figure. The photos show cells filled with hydrocarbon control electrolyte (top) and the Daikin fluorinated electrolyte (bottom). The post experiment gas volumes vs voltage are graphed in the right	798
Figure V- 266: Cycle life(1 C, 60 C, 3.0-4.5 V) of fluorinated electrolytes containing different additive packages. The hydrocarbon control electrolyte is shown in blue	799
Figure V- 267: Gas volume for NMC111/graphite cells with various additive combinations after 60 C storage at 4.5 V	800
Figure V- 268: Cycle life at 4.6 V Daikin fluorinated electrolyte (capacity - top, resistance – bottom)	801
Figure V- 269: Calendar life at 4.6 V Daikin fluorinated electrolyte (capacity - top, resistance – bottom)	802
Figure V- 270: RT 4.6 V calendar life fluorinated vs. conventional electrolyte.....	803
Figure V- 271: Three different electrolyte compositions heated to 60C (left) and 85 C(right)	803
Figure V- 272: ΔOCV and gas volume as a function of voltage for both the hydrocarbon control electrolyte (black) and Daikin fluorocarbon electrolyte (red)	804
Figure V- 273: DOCV vs. gas volume for various concentrations of electrolyte	805
Figure V- 274: Overcharge testing on NMC111/graphite cells filled with hydrocarbon (left) and Daikin fluorinated electrolyte (right)	805
Figure V- 275: Systematic approach to electrolyte development	807

Figure V- 276: Additives show synergies with differing solvent formulations 808

Figure V- 277: Best performing high dielectric constants were identified in EMC blends 809

Figure V- 278: Evaluation of best performing high dielectric constant solvents with a variety of low viscosity solvents..... 809

Figure V- 279: Carbonate-free formulations exceed performance of control electrolyte 810

Figure V- 280: Carbonate-free formulations achieve 300 cycles to 80% capacity retention 810

Figure V- 281: Early results on carbonate-free and EC-free formulations show promise at higher voltage..... 811

Figure V- 282: Scanning electron microscope images of a) Chemically derived nano sulfur; b) Commercially procured sulfur; c) Composite multilayer electrode architecture with a uniform coating of lithium orthosilicate on a sulfur-carbon mixture. The layer structure is clearly visible in the inset image. The top layer of orthosilicate is porous and consists of macroscopic particles fused as a result of the mechanical pressing. The soft sulfur-carbon inner layer consists of much finer particles of distinctly different morphology..... 816

Figure V- 283: a) Charge-discharge profiles (sulfur basis gravimetric capacity) of the various electrode architectures; b) Comparison of cycling behavior of the commercial sulfur, nano-sulfur prepared by slurry method, pellet method and the multilayer composite electrode; c) Comparison of cycling behavior (overall electrode areal capacity basis) of the various electrodes 817

Figure V- 284: Activation barriers for different migration paths of Li-ions in Li_4SiO_4 . Inset: pink 0 - Li-ion site; red (1)-(5) – Li vacancy sites for different migration pathways 818

Figure V- 285: Activation barriers E_a for different migration paths of Li-ions in pure and doped Li_4SiO_4 818

Figure V- 286: Image showing the yarn-like nature of the Flex – sulfur wires (Flex-SWs) 819

Figure V- 287: (a) SEM image (b) EDAX map of the flexible sulfur-polymer morphology shown in a prior figure 819

Figure V- 288: (a) Cycling behavior of various sulfur materials (b) Extended cycling and rate dependence of capacity in Flex-sulfur wires seen in a prior figure 820

Figure V- 289: Comparison of cycling behavior of various polymeric LIC electrolyte materials 820

Figure V- 290: (a) Transmission electron microscope (TEM) (left Figure) of oxide nanoparticles used as fillers in the GPE materials (b) Effect of oxide filler material on cycling behavior in polymer LIC materials (right Figure) 821

Figure V- 291: Morphology of sulfur-containing nanoporous CFMs 821

Figure V- 292: Improvement in cycling stability of sulfur cathodes by use of CFM materials..... 821

Figure V- 293: Effect of doping on electronic conductivity of sulfur 822

Figure V- 294: (a) Calculated S K-edge XAS of the radical S_3^- ion separated into contributions from the central S atom and the two terminal S atoms. (b) Electron density of the core-excited pi star and sigma star orbitals in the trisulfur radical molecule at 0 K 826

Figure V- 295: (a) Schematic of X-ray experiment, (b) Diagram of modified Li-S pouch cell, (c) Voltage profiles for the three discharged Li-S cells, (d) Sulfur K-edge XANES as a function of discharge for the three points indicated in (c) 827

Figure V- 296: First-principles XANES spectra of the trisulfur LiS_3 molecule dissolved in TEGDME, obtained from sampling ab initio molecular dynamics at 298 K. Each of the five major transitions that inform the spectra is indicated 827

Figure V- 297: Sulfur K-edge XAS during initial stage of discharge. We present a best fit of the experimental data (solid line) using independent spectra obtained from first-principles calculations (dashed line). The spectrum is broken into four regions according to the transitions occurring in each region	828
Figure V- 298: Sulfur K-edge XAS obtained for a discharging Li-S battery consisting of a solid polymer electrolytes (SEI) with LiClO ₄ , and a cathode of elemental sulfur, carbon black, SEI, and LiClO ₄ . Discharging was performed at C/60 to assure no significant change in speciation during spectrum collection	829
Figure V- 299: Speciation of sulfur K-edge spectra shown in the prior figure. Long chain dianions dominate early spectra, followed by mid-chain dianions, and ultimately, low chain dianions. Radical species attributing to the increase in intensity as shown in the inset of the prior figure.....	830
Figure V- 300: Photograph of GenII electrolyte solvent (EC/EMC) alone and with insoluble Se, Li ₂ Se, and a combination of the two	833
Figure V- 301: <i>In-situ</i> XANES measurement for Li-Se pouch cell in GenII electrolyte: (a) normalized XANES spectra of the cycling cell, (b) voltage profile, (c) derivative of normalized XANES spectra, and (d) linear combination fitting of residue values and corresponding phase compositions in different state of charge/discharge.....	834
Figure V- 302: Preparation of POP–sulfur composites with micropores as host materials for accommodation of nanosized sulfur particles.....	835
Figure V- 303: Performance of Li–S cells with POP–sulfur composite cathodes cycled between 1.5 and 3.0 V at a current density of 200 mA/g current. Voltage profiles (a) and capacity retention (b) of POP-A/S composite cell; 1st-cycle charge discharge profiles of POP-B/S and POP-C/S composite cells (c), and cycling performance of POP-B/S and POP-C/S composite cells (d). (Electrolyte: 1 M LiTFSI in 1,3-dioxolane (DOL) and CHF ₂ CF ₂ CH ₂ OCF ₂ CF ₂ H in a 1:2 volume ratio.).....	835
Figure V- 304: Raman spectra of typical Se _x S _y samples	837
Figure V- 305: High-resolution X-ray diffraction of typical Se _x S _y samples	837
Figure V- 306: <i>In situ</i> XANES of Li/Se ₂ S ₅ battery using a carbonate-based electrolyte	838
Figure V- 307: Capacity retention of Li/Se ₂ S ₅ cell using a carbonate-based electrolyte	838
Figure V- 308: Scanning electron microscopy images of (a) Ketjenblack carbon black, (b) multiwall carbon nanotube (CNT), and (c) ordered microporous carbon (OMC). The inset in (c) is a transmission electron microscopy image showing micron channels (about 5 nm in diameter) in OMC to host Se ₂ S ₅	839
Figure V- 309: (a) Weight loss of a Se ₂ S ₅ /Ketjenblack-CNT composite during TGA analysis, confirming the proper loading of the active material in carbon matrix, and (b) charge/discharge capacity of cell using the prepared electrode and a carbonate-based electrolyte	839
Figure V- 310: Charge/discharge capacity of cell with Se ₂ S ₅ /Ketjenblack-CNT electrode. The electrolyte was 1.0 M lithium bis-(trifluoromethanesulfonyl)imide (LiTFSI) in 1,3-dioxolane/1,1,2,2-tetrafluoroethyl-2,2,3,3-tetrafluoropropyl ether (1:1 by volume) with 0.1 M LiNO ₃	840
Figure V- 311: Additive effect on Li ₂ S cell activation	842
Figure V- 312: Li ₂ S cells cycling at C/10 after C/40 activation with LiI additive	842
Figure V- 313: S-cell discharge rate capability	843
Figure V- 314: Sulfur loading effect on 1 st discharge	843

Figure V- 315: Sulfur loading effect on coin cell cycling 843

Figure V- 316: CuS structure 843

Figure V- 317: (a) Voltage profile of CuS cycling between 3.0-1.8 V; (b) Voltage profile of CuS cycling between 3.0-1.0 V; (c) Capacity versus cycle number; (d) Capacity versus cycle number at different rates 844

Figure V- 318: Structures of pyrite (L), and marcasite (R) 844

Figure V- 319: Li/FeS₂ cells cycled between 2.5-1.1 V at C/10 (a) voltage profile; (b) Cycling capacity 845

Figure V- 320: TiS₂ structure 845

Figure V- 321: Li/TiS₂ cells cycled between 3.0-1.5 V at C/10 (a) Voltage profile; (b) Capacity versus cycle number 846

Figure V- 322: CoS₂ structure 846

Figure V- 323: Li/CoS₂ cells (a) Voltage profile cycled 3.0-1.0 V at C/30; (b) Capacity versus cycle number..... 846

Figure V- 324: Sulfur:MFCAs hybrid electrode C-rate discharge 847

Figure V- 325: S:CuS hybrid electrode cycling..... 847

Figure V- 326: S:CuS hybrid cell anode SEI morphology and chemical composition 848

Figure V- 327: S:Cu₂S interaction 848

Figure V- 328: S:Cu₂S cell cycling..... 848

Figure V- 329: FeS₂ activation w/ LiNO₃..... 848

Figure V- 330: FeS₂ activation w/o LiNO₃..... 848

Figure V- 331: ED of cycled S:FeS electrode..... 849

Figure V- 332: S:TiS₂ voltage profile..... 849

Figure V- 333: S:TiS₂ hybrid cell cycling 849

Figure V- 334: (a) Areal specific capacity dependence on the sulfur loading obtained at 0.1C, (b) electrode thickness as a function of calendaring pressure, (c) areal capacity dependence on pressure applied for calendaring the electrode, and (d) cycling stability of cells cycled at 0.1C (1C=1000 mAh/g)..... 853

Figure V- 335: a) Comparison of chemically synthesized Li₂S_x series products in DOL/DME solvent. Concentration of each sample is 0.2 M based on elemental sulfur. b) EPR spectra of Li₂S_x series products. Sulfur radicals were detected in Li₂S₈, Li₂S₆, Li₂S₄ and Li₂S₂, while there was no resonance signal from commercial Li₂S. c) The first discharge/charge curve of a Li-S battery tested in LITFSI-DOL/DME. d) The first discharge/charge curve of a Li-S battery tested in LiPF₆-EC/DMC..... 854

Figure V- 336: (a) Charge/discharge curves of graphite/sulfur full cell (LG/S) at different C rates in 5 M LiTFSI/DOL electrolyte without additive LiNO₃ and (b) its corresponding cycling stability and Coulombic efficiency. (c) Charge/discharge curves of LG/S full cell at 0.1 C in 1 M LiTFSI-DOL/DME with 0.1 M LiNO₃ and (d) its corresponding cycling performance. Areal capacity of sulfur cathodes: 2 mAh/cm². 1C = 1000 mA/g..... 855

Figure V- 337: (a) Areal specific capacity dependence on the sulfur loading obtained at 0.1C, (b) electrode thickness as a function of calendaring pressure, (c) areal capacity dependence on pressure applied for calendaring the electrode, and (d) cycling stability of cells cycled at 0.1C (1C=1000 mAh/g)..... 858

Figure V- 338: a) Comparison of chemically synthesized Li₂S_x series products in DOL/DME solvent. Concentration of each sample is 0.2 M based on elemental sulfur. b) EPR

spectra of Li_2S_x series products. Sulfur radicals were detected in Li_2S_8 , Li_2S_6 , Li_2S_4 and Li_2S_2 , while there was no resonance signal from commercial Li_2S . c) The first discharge/charge curve of a Li-S battery tested in LiTFSI-DOL/DME. d) The first discharge/charge curve of a Li-S battery tested in LiPF_6 -EC/DMC.....	859
Figure V- 339: (a) Charge/discharge curves of graphite/sulfur full cell (LG/S) at different C rates in 5 M LiTFSI/DOL electrolyte without additive LiNO_3 and (b) its corresponding cycling stability and Coulombic efficiency. (c) Charge/discharge curves of LG/S full cell at 0.1 C in 1 M LiTFSI-DOL/DME with 0.1 M LiNO_3 and (d) its corresponding cycling performance. Areal capacity of sulfur cathodes: 2 mAh/cm ² . 1C = 1000 mA/g.....	860
Figure V- 340: a) Synthesis procedure for carbon-sulfur composites, b) SEM of carbon micro-compartment as a substrate for nanosulfur loading, c) SEM of carbon micro-compartment after loading sulfur nanoparticles sonochemically.....	864
Figure V- 341: Schematic for ultrasonic synthesis of CCs-S composite. (a) Scanning electron micrographs of porous bare CCs. (b) Scanning electron micrograph of carbon-sulfur composite produced via the sonochemical sulfur deposition process. (c) Elemental mapping of the carbon-sulfur composite by X-ray dot-mapping. Sulfur is highlighted in green, while carbon is highlighted in red.....	864
Figure V- 342: a) Synthesis procedure for carbon-sulfur composites, b) SEM of carbon micro-compartment as a substrate for nanosulfur loading, c) SEM of carbon micro-compartment after loading sulfur nanoparticles sonochemically. Structural evolution as a function of Li/Si content	865
Figure V- 343: Schematic illustration of the mesoscale modeling approach, which includes Li_2S film formation, cathode microstructure evolution, performance prediction and poromechanics.....	865
Figure V- 344: (a) Li_2S film thickness and coverage variation versus time. (b) SEM image of Li_2S nanoislands formation on carbon substrate from F. Y. Fan et al., 2015, Advanced Materials, 27, pp. 5203-5209. (c) Snapshot of Li_2S nanoislands formation on carbon substrate from Coarse-Grained KMC simulation.....	866
Figure V- 345: Effect of Li_2S film thickness on active area of the cathode frameworks with different porosity	866
Figure V- 346: DFT calculated LiTFSI most favorable decomposition mechanisms from interaction of a Li atom from the surface with an specific location. Top: a Li..O attack is shown leading to C-S and N-S bond breaking. Bottom: a Li..N attack is found favorable through C-S and N-S bond breakings. Color code: Li: purple, O: red, F: light blue, N: blue, S: yellow, C: grey	867
Figure V- 347: Time evolution of S-S bond distances on one PS molecule illustrating PS decomposition at the model Li anode surface	868
Figure V- 348: Energy profile of Li_2S (111) layer formation on graphene calculated with DFT within the vdW-D3 approach. Color code: Green, violet and grey spheres represent S, Li and C atoms, respectively.....	868
Figure V- 349: Formation of Li_2S in the electrolyte phase. The snapshot depicts the LiS bond distances during formation of a Li_2S molecule from reduction of a S_8 ring. The LiS bond distances are followed in the graph as a function of time showing evidence of stable LiS bonds at ~ 400 and 600 fs, respectively. Color code: S: yellow, Li: purple, O: red, H: white, C: light blue	869
Figure V- 350: S_8 dissolution in the electrolyte phase near the opening of a 2nm carbon pore. Top: Snapshots illustrating the initial and final fragmentation of a S_8 ring. At 4500 fs S_3^{2-} is still intact. The other S dianions are paired with Li ions forming short-chain PS	

species. Bottom: Time evolution of the S-S and S-C distance of a S_2 radical anion (S atoms labelled S2 and S1). The snapshots depict Bader charges for the S atoms during the reduction process (Li ions are not shown). Formation of several radical anions (S^- , S_2^- , S_3^-) shortly becoming dianions is illustrated. Color code: S: yellow, Li: pink, C: blue, O: red, H: white..... 869

Figure V- 351: Adsorption energies of PS species inside carbon pores of the indicated diameters (1; 1.2; and 1.5 nm)..... 870

Figure V- 352: Adsorption of Li_2S_8 dissolved in DME over Mo-doped graphene layers. Color code: C: grey, S: yellow, Li: purple, Mo: blue, O: red..... 870

Figure V- 353: a) XRD pattern of ZCO/SWCNTs composite powders. b, c, f, g) SEM images of ZCO/SWCNTs composite powders from low to high magnifications. d) EDX spectrum from the selected area of SWCNTs in ZCO/SWCNTs composite. e) The corresponding weight and atomic percentage from the selected surface area of SWCNTs in ZCO/SWCNTs composite. h) EDX microanalysis on a selected area of a ZCO microsphere. i-l) Corresponding TEM image and EDX mapping images of the ZCO microsphere: selected TEM area i), Zn j), Co k), and O l)..... 873

Figure V- 354: a) Comparison of cycling performance of Li- O_2 cells with ZCO/SWCNTs composite, ZCO+SWCNT mixture, sole SWCNTs, and sole ZCO electrodes. b-d) The corresponding voltage profiles of ZCO/SWCNTs composite electrodes b), ZCO+SWCNT mixture electrodes c), and sole SWCNTs electrodes d), respectively, at a current density of 0.1 mA cm^{-2} and cycled under full discharge/charge protocol between 2.0 and 4.5 V for first 10 cycles..... 874

Figure V- 355: Voltage profiles of selected cycles for ZCO/SWCNTs composite a) and sole SWCNTs b) electrodes at a current density of 0.1 mA cm^{-2} under a capacity-limited cycling protocol with the controlled capacity of 800 mAh g^{-1} . c) Comparison of the first discharge/charge curves for ZCO/SWCNTs composite and SWCNTs. d) The corresponding cycling performance of ZCO/SWCNTs composite and SWCNTs for 50 cycles..... 875

Figure V- 356: SEM images of ZCO/SWCNT composite electrodes at different states: a) pristine, b) after the first discharge, c) after the first charge, d) after the 15th discharge, and e) after the 50th charge. f) The corresponding XRD patterns of these cycled ZCO/SWCNTs composite electrodes..... 875

Figure V- 357: (a) Voltage profiles of treated catalyst/carbon cloth air electrode in Li- O_2 coin cells at selected cycles. (b) Cycling stability of Li- O_2 coin cells with air electrodes of treated catalyst/CC, pristine catalyst/CC, and pure carbon cloth under full discharge/charge (2.0~4.5 V) cycling..... 876

Figure V- 358: Electrochemical performance of Li- O_2 cells using electrolyte with three salt concentrations cycled at a capacity (1000 mAh g^{-1}) limited protocol between 2.0 and 4.5 V at 0.1 mA cm^{-2} . Voltage profiles of the cells using LiTFSI-DME electrolytes with salt concentrations of 1 M a), 2 M b), and 3 M c). d) The cycling stability of these three cells 876

Figure V- 359: a-c) Voltage profiles of Li- O_2 coin-cells with the three concentration electrolytes cycled at a full discharge/charge protocol between 2.0 and 4.5 V at 0.1 mA cm^{-2} for 40 cycles, and d) comparison of their corresponding cycling stability 877

Figure V- 360: SEM images of plan-view air-electrodes in the charged state (a-c) and cross-sectional Li metal anodes (d-f) after 40 discharge/charge cycles from LiTFSI-DME electrolytes of 1 M (a, d), 2 M (b, e), and 3 M (c, f). The fibers on the surface of the

cycled Li metal anode in (f) are leftover glass fibers from the glass fiber paper used as separator in Li-O ₂ cells	878
Figure V- 361: Computational simulations of the Gibbs activation barriers for the C-H bond scission from CH ₂ groups a), and CH ₃ groups b) in DME, Li ⁺ -(DME) ₂ , and Li ⁺ ₂ -(DME) ₃ by the attack of O ₂ ^{•-}	878
Figure V- 362: Cycling stability of electrolytes, LiTFSI-3DMSO (a, c) and LiTFSI-4DMSO (b, d), in Li-O ₂ coin cells at two different capacity limitations at 1000 mAh g ⁻¹ (a, b) and 600 mAh g ⁻¹ (c, d).....	879
Figure V- 363: Cyclic voltammetry study of O ₂ reduction in a Li/O ₂ cell electrolyte: a,c) 0.1 M LiClO ₄ -DMSO at 30 °C and b,d) LiNO ₃ -KNO ₃ eutectic at 150 °C. Working electrode: Super P porous carbon (A= 0.785 cm ²), carbon loading ~5 mg/cm ² . Counter and reference electrodes: Li metal. Scan rate: 0.05 mV/s. Voltage window: 2.5-3.2 V vs Li/Li ⁺ . Current density expressed in mA per g of carbon	882
Figure V- 364: Li/O ₂ cell voltage and pressure profiles measured in a,c) 0.1 M LiClO ₄ -DMSO at 30 °C between 2.5 and 4.2 V and b,d) LiNO ₃ -KNO ₂ -CsNO ₃ molten salt electrolyte at 120 °C between 2.65 and 3 V. Positive electrode: Super P Carbon:PTFE 95:5 wt.%, current: 0.32 mA/cm ² (~80 mA/g carbon). Electrolyte loading: ~ 150 μL. Carbon loading: ~4 mg/cm ² . Pressure profiles depicted in c and d) are for the first cycle of the cell. Cell capacity expressed in mAh per g of carbon	882
Figure V- 365: Linear sweep voltammograms recorded at a Pt RDE (A= 0.196 cm ²) from a LiNO ₃ -KNO ₃ molten salt electrolyte containing Li ₂ O ₂ . v= 1 mV/s, from OCV to 3.3 V vs Li/Li ⁺ . T= 150 °C. Counter electrode: Pt wire, reference electrode: Li metal rod	883
Figure V- 366: SEM images of a discharge O ₂ electrode in LiNO ₃ -KNO ₃ electrolyte at 150 °C. Cell was discharged to 2.5 V cutoff at 80 mA/g _{carbon}	883
Figure V- 367: a) Li/O ₂ cell charging profile with in situ gas analysis. Cell employed a LiNO ₃ -KNO ₃ molten salt electrolyte, a Super P Carbon:PTFE cathode, and was charged at 150 °C, 80 mA/g _{carbon} to a 3 V cutoff. Capacity expressed in mAh per g of carbon. b) First cycle XRD patterns of a Super P Carbon cathode discharged/charged in a molten nitrate Li/O ₂ cell between 2.6 and 3 V, respectively	884
Figure V- 368: Li/O ₂ cell voltage profile. LiNO ₃ -KNO ₃ electrolyte. T= 150°C.....	884
Figure V- 369: XRD analysis of the carbon electrode following 50 cycles (cell death). XRD pattern references for Li ₂ O ₂ and Li ₂ CO ₃	885
Figure V- 370: SEM images of the carbon electrode following 50 cycles. Top image: Li ₂ O ₂ particles precipitated onto separator glass fiber. Right image: Li ₂ CO ₃ particles covering carbon surface	885
Figure V- 371: XRD pattern of the discharged AC cathode for 1000 mAh/g. The red histogram corresponds to the standard Li ₂ O ₂ patterns. The LiO ₂ pattern (black histogram) is from the structure calculated from density functional theory.....	889
Figure V- 372: Raman spectra of the toroids on the surface of the discharged activated carbon cathode for the six different conditions noted in the figure. The values of the peaks (in cm ⁻¹) are: 1123 (S1), 1505 (S2), 1340 (D), 1600 (G)	889
Figure V- 373: Voltage profiles showin the how the Pd nanoparticle based cathode material dramatically reduces the charge overpotential in a Li-O ₂ battery. (a) Porous carbon only, (b) porous carbon with Al ₂ O ₃ coating and Pd nanoparticles.....	890
Figure V- 374: a) The oxidized Mo ₂ C (101)-Mo surface with a MoO ₃ -like portion (the highlighted region shows a MoO ₃ -bulk unit-like configuration in the inset) on top surface layer	

after the adsorbed O ₂ molecules dissociate. b) The electronic density of states (e-DOS) around the Fermi-level (E _f)	891
Figure V- 375: The change of the natural logarithm of O ₂ ⁻ concentration with time	894
Figure V- 376: Cyclic voltammograms at various scan rates in 1 M TEABF ₄ DMSO electrolyte (A) and 1 M LiBF ₄ DMSO electrolyte (B) saturated with O ₂ on a glassy carbon-disc electrode	895
Figure V- 377: Cyclic voltammetry for the O ₂ redox reaction on the surface of pyrolytic graphite (PG) edge layer, PG basal layer and glassy carbon in 30% KOH aqueous electrolyte (A) 0.1 M TEABF ₄ acetonitrile electrolyte (B) saturated with O ₂	896
Figure V- 378: Comparison of cyclic voltammetry of O ₂ redox reaction on glass carbon and Pt electrodes in 0.1 M TEABF ₄ acetonitrile electrolyte saturated with O ₂ . The scan rate is 50mv/s	897
Figure V- 379: Comparison of linear voltammetry of the oxidation of soluble B-O ₂ ²⁻ in 0.1M LiClO ₄ acetonitrile electrolyte containing 20mM TPFPB and saturated with Li ₂ O ₂ . The experiments were done on rotating disk electrode. Rotating rate is 800 rpm, scan rate is 50mv/s	897
Figure V- 380: First 50 cycles for a Li-air flow cell with and without B additive	898
Figure V- 381: (a), (b) and (c) The SEM images and the crystallite size distribution of nano-size (r=44 nm, r=120nm) and sub micro-size (r=440 nm) Li ₄ Ti ₅ O ₁₂ ; (d) <i>in situ</i> XRD patterns collected during chemical sodiation of the nano-size 44nm (top), 120nm (middle) and sub micro-size (bottom) Li ₄ Ti ₅ O ₁₂ , the sodium insertion caused phase transition behavior is strongly related to the particle size of the material (e) Enlarge view of the (111) reflections for the pristine Li ₄ Ti ₅ O ₁₂ ; (f) XRD patterns of the sub micro-sized Li ₄ Ti ₅ O ₁₂ collected after chemical sodiation of 20 h, 40 h and 80 h respectively, new Na ₆ LiTi ₅ O ₁₂ phase emerged after long time reaction; Sodiation completed in 2h and 24h respectively for 44nm and 120nm Li ₄ Ti ₅ O ₁₂ ; (g) The charge-discharge curve (1st: dash line and 30th: solid line) of Na storage into Li ₄ Ti ₅ O ₁₂ (0.1C, 0.5 V-3 V)	901
Figure V- 382: Ex situ Fe K-edge XANES spectra of the NaFe(1.63) electrode collected at different charge and discharge states.....	901
Figure V- 383: <i>Ex situ</i> Fourier transformed magnitude of Fe K-edge EXAFS spectra of the NaFe(1.63) electrode collected at different charge and discharge states.....	902
Figure V- 384: Structure evolution upon Na extraction/insertion. (a) In situ XRD patterns collected during the first discharge/charge of the Na/Na _{0.44} [Mn _{0.44} Ti _{0.56}]O ₂ cell under a current rate of C/10 at a voltage range between 1.5 and 3.9 V. For easy comparison with results in the literature, the 2θ angle has been converted to values corresponding to the more common laboratory Cu Ka radiation (χ = 1.54 Å). (b) Evolution of the Lattice parameters during charge/discharge process.....	903
Figure V- 385: Charge transfer mechanism upon Na extraction/insertion in Na _{0.44} [Mn _{0.44} Ti _{0.56}]O ₂ . (a) In situ XANES spectra at Mn K-edge collected during initial charge and discharge at a current rate of C/8 between 1.5 and 3.9 V voltage range (Data are obtained in two different in situ cells for charge and discharge process separately); (b) Variation of Mn K-edge position during initial charge and discharge; (c) Ti and Mn K-edge XANES spectra ex situ collected at different charge/discharge states. Spectra of reference materials were represented for comparison. (d) Mn L-edge sXAS spectra collected on Na _x [Mn _{0.44} Ti _{0.56}]O ₂ samples in comparison with that of Na _x MnO ₂ (x = 0.22, 0.44 and 0.66). The spectra of chemically prepared samples are shown in thick solid lines, while those of electrochemically prepared ones are in thin dot lines. The calculated spectra (thick	

dash lines) using the linear combination of the Mn ²⁺ , Mn ³⁺ and Mn ⁴⁺ reference spectra agree well with experiments.....	904
---	-----

TABLES

Table I- 1: Major Li-ion technology technical challenges and potential pathways.....	3
Table I- 2: FY 2015 Vehicle Technologies Program Wide Funding Opportunity Announcement: List of Awardees.....	9
Table I- 3: FY 2015 Vehicle Technologies Incubator Funding Opportunity Announcement: List of Awardees	10
Table II- 1: Summary of USABC performance targets for EV batteries.....	12
Table II- 2: Summary of USABC performance targets for PHEV batteries	13
Table II- 3: Summary of USABC performance targets for 12V Start/Stop Vehicle Applications.....	14
Table II- 4: Discharge characterization capacities for Seeo modules. 80°C internal temperature, 30°C ambient environment.....	34
Table II- 5: Peak Power results for modules 1, 2 and 3 at BOL, taken at 80% DOD. Internal temperature was 80°C, external temperature was 30°C.....	36
Table II- 6: DST225 cycle life results for module 1, from initial measurements (RPT0) through cycle 150 (RPT4). Internal temperature was 80°C, external temperature was 30°C.....	37
Table II- 7: RPT results for Module 2 initially (RPT0) and after ten DST225 and fast charge cycles. All data was recorded and reported by ANL. Internal temperature was 80°C, external 30°C.....	38
Table II- 8: Aging effects study.....	54
Table II- 9: USABC targets	62
Table II- 10: Cell format study.....	64
Table II- 11: Positive blend, theoretical performance vs. measured	65
Table II- 12: Physical properties of samples selected from base sheet optimization trials.....	70
Table II- 13: Thermal and mechanical properties of samples selected from base sheet optimization trials	71
Table II- 14: Shutdown characteristics of selected samples	71
Table II- 15: USABC Gap Analysis chart of selected base and ceramic coated membranes.....	73
Table II- 16: Cell chemistries evaluated	76
Table II- 17: In plant - processable high loading electrode study for high energy cell design.....	87
Table II- 18: SiNANOde Cell Self discharge.....	90
Table II- 19: Brief CVD SiNANOde Production Cost.....	91
Table II- 20: State of the Art Graphite Battery – Cathode Fixed Brief CVD SiNANOde Production Cost	91
Table II- 21: 18650 cell design with advanced chemistry	101
Table II- 22: Thermal Systems List.....	113
Table II- 23: Component Cost Assumptions.....	117
Table II- 24: DC impedance of dry electrodes at beginning of life.....	119

Table II- 25: Different combinations and cell sizes for the cost model..... 126

Table II- 26: Summary of formation cycles for 3DCuSnFe-Si-Graphite/ NMC(532) final cells:
averaged values from 27 single layer pouch cells (SLP)..... 139

Table III- 1: Thermal and Electric Loads in the NMP Recovery Process (4.1M kg-NMP/year)..... 158

Table III- 2: Air Flow and Energy Loads in the Processing of Air for a Dry Room (4000-m², 4-m tall) 158

Table III- 3: Heat Loads in the NMC Production Process (4000 kg NMC per day) 160

Table III- 4: Energy and GHG Intensity of Cathode and Anode Materials for Lithium-Ion Batteries 165

Table III- 5: Incremental Cost of HEV Drive Systems and Incentives in the MD Market Segment 174

Table III- 6: Percentage Cost Savings or Cost Increase from each Standardization Strategy at
Different Annual Battery Pack Production Volumes..... 175

Table III- 7: List of battery deliverables tested 180

Table III- 8: Comparison of key attributes of the USABC and QC/T 743 protocols..... 180

Table III- 9: Testing activities under the USABC Program 185

Table III- 10: Testing activities under the Benchmark Program..... 185

Table III- 11: Testing activities under the FOA-2011 Program 185

Table III- 12: Testing activities under the FOA-ARRA Program 185

Table III- 13: Anticipated testing activities for FY16 186

Table III- 14: Testing activities under the ABR Program 186

Table III- 15: Suggested Test Matrix..... 208

Table III- 16: Sample list of parameters and variables exchanged across the different domains 259

Table IV- 1: Electrodes fabricated for the Electrode Library in order to perform silicon-based
electrode studies using varying amount of silicon content 271

Table IV- 2: Capacity values for varyings amount of silicon content in electrodes at different
lower cutoff voltages (LCV). Refer to the prior table for composition and material
information 272

Table IV- 3: Effect of Upper Cutoff Voltage for NCM523, NCA, and HE5050 286

Table IV- 4: Electrode parameters used in electrode curling study..... 290

Table IV- 5: Distribution of electrode sheets from the CAMP Facility’s Electrode Library 291

Table IV- 6: Electrolytes evaluated for performance and abuse tolerance 309

Table IV- 7: 2032-type coin cell components and sizes/volume 319

Table IV- 8: Area oversize percent for the anode and cathode pairs used in this study 321

Table IV- 9: Values of relevant parameters in estimating the electrolyte volume 323

Table IV- 10: Electrolyte volumes used, in multiples of total pore volume of relevant cell
components (cathode, anode, and separator) 323

Table IV- 11: The general procedures adopted for full cell, coin-cell testing 329

Table IV- 12: Lattice constants of NCM523 vs annealing time and temperature 333

Table IV- 13: NMC333 surface energies..... 338

Table IV- 14: Comparison of positive electrode interfacial and oxide active material parameters
for electrochemical model 362

Table IV- 15: Battery performance based on baseline chemistry determined by BatPAC model 371

Table IV- 16: Parameters varied in the formation of pouch cells. 374

Table IV- 17: Viscosity tuning of the prepared cathode dispersion	377
Table IV- 18: Capacity at different rate of 18650 cells shipped as final deliverable cells.....	378
Table IV- 19: Cell Specifications for ABR Target Goals	383
Table IV- 20: PPM of Mn measured from metal dissolution studies on HCMR™//Graphite cells	390
Table IV- 21: Go/No-Go of surface-coatings on HCMR™ materials	391
Table IV- 22: Two Iterations of Cell Designs Towards Planned Final Cell Build at the End of the Program.....	396
Table IV- 23: GAP Analysis of the HCMRTM-XE Baseline Cells From The HPPC Experiments	397
Table IV- 24: Summary of performance of full cells with different precycled Si anodes	403
Table IV- 25: Range of Si-based anode materials evaluated in the program	424
Table IV- 26: Process comparison between batch, CSTR and TVR.....	438
Table IV- 27: Summary IC analyses, K-F moisture titration results and pH of 1 M aqueous solution for various samples of LiFSI.....	449
Table IV- 28: Self Discharge Current Results.....	450
Table IV- 29: Formulated samples and procedures for preparation	450
Table IV- 30: Ion chromatography analyses for electrolyte	450
Table IV- 31: Effect of the treatment of electrolyte with lithium chloride on self-discharge current	451
Table IV- 32: Effect of added impurity on cell degradation.....	452
Table IV- 33: Electrode parameters for pouch cells.....	469
Table IV- 34: Formation cycle procedures	471
Table IV- 35: Sample conditions.....	471
Table IV- 36: Adhesion (combined dry and wet) and binder distribution results for anode (water based binder) and cathode (NMP based binder) electrodes.....	489
Table IV- 37: Anode properties and electrochemical characteristics for anodes dried using standard and ADP methods	490
Table IV- 38: Cathode properties and electrochemical characteristics for anodes dried using standard and ADP processes.....	491
Table IV- 39: Formation characteristics for pouch cells fabricated with Lambda anode and cathodes matched with Navitas electrodes.....	492
Table IV- 40: Comparison of anode performance by static and continuous ADP drying	495
Table IV- 41: High Pressure Gurley Values Have Dropped.....	498
Table IV- 42: UV ceramic coating details	499
Table IV- 43: Silicon anodes consume and trap significant amounts of lithium, reducing first cycle efficiency and cell-level energy. Current lab-scale prelithiation methods add extra lithium and address first cycle loss – but are no scalable.....	503
Table IV- 44: Summarized modeling results for the Nyquist plots	511
Table IV- 45: Performance characteristics sought	513
Table V- 1: Doctor blade heights and final thickness of laminates.....	548
Table V- 2: Nanoindentation results of AIHQ thin films treated at various temperatures in air revealing the highest H/E* for the AIHQ coating heat-treated at 150°C.....	568
Table V- 3: HOMO-LUMO energetics of electrolyte solvents and additives.....	644

Table V- 4: Li salt dissociation in fluorinated electrolyte by 2D-DOSY NMR.....	646
Table V- 5: Lithium cycling requirements to match Li-ion cathodes	758
Table V- 6: Molecular design approach for anode SEI additives	808
Table V- 7: Salt efficacy is very solvent dependent	810
Table V- 8: Cycling characteristics of various sulfur battery systems synthesized and evaluated in this work.....	822
Table V- 9: Exact spectral weightings used in linear combination fitting of spectra.....	828
Table V- 10: Composition of SexSy prepared for this study	836
Table V- 11: Hybrid Electrode Formulation for Power Test.....	847
Table V- 12: PS reactivity at the anode: Reactions with Li in eV.....	867
Table V- 13: Reaction rate constants (Initial concentration for O ₂ - 0.01 M)	894
Table V- 14: Relative molar ratio of different solvents in the Li ⁺ solvation adducts obtained from ESI-MS spectra of 5mM LiBF ₄ DMSO and other solvents (1:1) mixture. The voltages of Cone and Extractor are 20 and 0V for ESI-MS	895

I. Introduction

I.A Vehicle Technologies Office Overview

The Department of Energy's (DOE's) Vehicle Technologies Office (VTO) develops advanced transportation technologies that would reduce the nation's use of imported oil. Technologies supported by VTO include electric drive components such as advanced energy storage devices (batteries and ultracapacitors), power electronics and drive motors, advanced structural materials, advanced combustion engines, and fuels. VTO is focused on funding high-reward/high-risk research conducted by national laboratories, universities, and industry partners and promising improvements in critical components needed for more fuel efficient (as well as cleaner) vehicles.

VTO works with U.S. automakers through the United States Council for Automotive Research (USCAR)—an umbrella organization for collaborative research consisting of FiatChrysler LLC, the Ford Motor Company, and the General Motors Company. Collaboration with automakers through the US DRIVE (Driving Research and Innovation for Vehicle Efficiency and Energy Sustainability) Partnership enhances the relevance and the potential for success of such programs.

During the past year, the U.S. government continued its strong R&D support of plug-in electric vehicles (PEVs) such as plug-in hybrids, extended range electric vehicles and all-electric vehicles. In March 2012, President Obama announced the *EV Everywhere* Grand Challenge. One of the primary objectives of this Grand Challenge is to enable U.S. innovators to rapidly develop/commercialize the next generation of technologies which can achieve the cost, range, and charging infrastructure necessary for widespread adoption of PEVs. Significant penetration of PEVs into the transportation sector would reduce our dependence on foreign oil, greenhouse gas emissions and negative economic impacts associated with crude oil price fluctuations.

An important prerequisite for the electrification of the nation's light duty transportation sector is the development of more cost-effective, longer lasting, and more abuse-tolerant PEV batteries. In fiscal year 2015, the DOE VTO battery R&D funding was nearly \$80 million. The R&D focus continued to remain on the development of high-energy batteries for PEVs and very high power devices for hybrid vehicles. This document summarizes the progress of VTO battery R&D projects supported in FY 2015. The electronic version of this report is accessible at <http://energy.gov/eere/vehicles/downloads/vehicle-technologies-office-2015-energy-storage-rd-annual-report>.

I.B Vehicle Technologies Battery R&D Overview

I.B.1 DOE Battery R&D Goals and Technical Targets

The *EV Everywhere* Grand Challenge¹ established a vehicle-level framework in which the technological progress toward achieving the Grand Challenge objectives can be evaluated. To meet those objectives, batteries, power electronics, motors, lightweight materials and vehicle structures must see dramatic advances. Accordingly, performance and cost targets have been established for all the key technical areas associated with a PEV. Achieving those targets will meet the needs for a range of vehicle types – including plug-in hybrids as well as short and long range all-electric vehicles. Some of the technology targets, derived from computer modeling as well as from hardware-in-the-loop simulation of batteries operating in PEVs under multiple drive cycles, are shown in Figure I- 1.

¹ For more information, please see <http://energy.gov/eere/everywhere/about-ev-everywhere>.

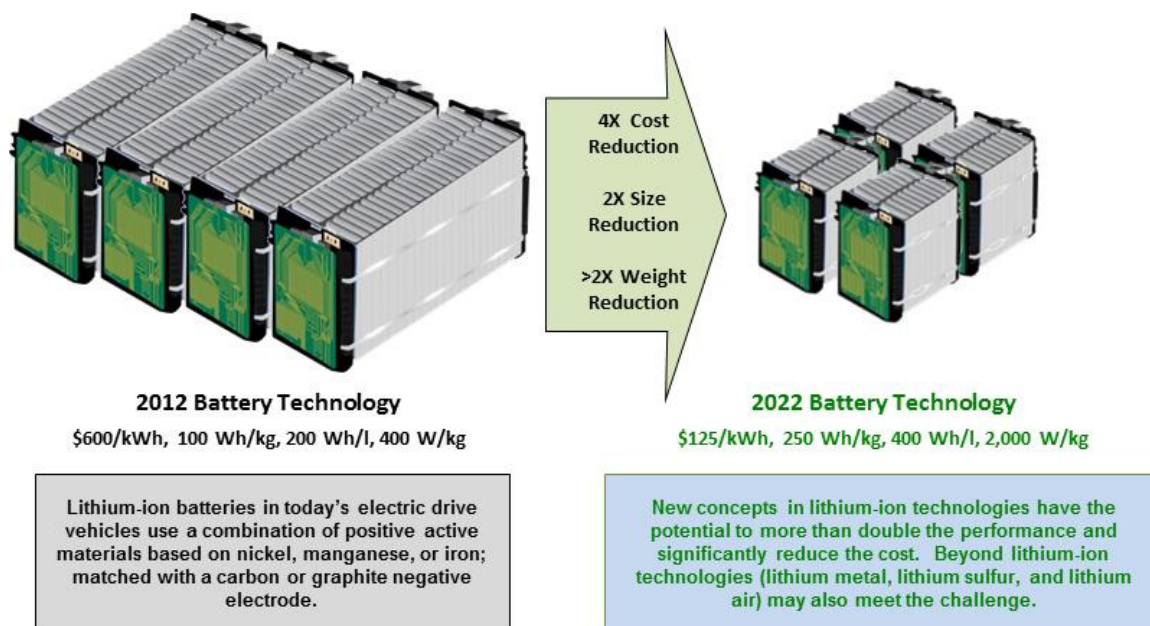


Figure I- 1: Battery advancements needed to enable a large market penetration of PEVs

I.B.2 DOE Battery R&D Plans

The objective of the VTO battery R&D effort is to advance the development of batteries to enable a large market penetration of electric vehicles. Program targets focus on overcoming technical barriers to enable market success. They include: (1) a significantly reduced battery cost, (2) increased battery performance (power, energy, and durability), (3) reduced battery weight & volume, and (4) increased battery tolerance to abusive conditions such as short circuit, overcharge, and crush.

Current battery technology performs far below its theoretical limits. For example, in the near-term, with existing lithium-ion technology, there is an opportunity to more than double the battery pack energy density (from 100 Wh/kg to 250 Wh/kg) by using new high-capacity cathode materials, higher voltage electrolytes, and high capacity silicon or tin-based intermetallic alloys to replace the graphite anodes. Despite recent promising advances, much more R&D is needed to achieve the performance and lifetime requirements for deploying those advanced technologies in PEVs.

In the longer term, battery chemistries “beyond Li-ion” – lithium-sulfur, magnesium-ion, lithium-air, and certain other advanced chemistries – offer the possibility of specific energy levels significantly greater than current lithium-ion batteries and potentially greatly reduced battery costs. However, major shortcomings in cycle life, power density, energy efficiency, and/or other critical performance parameters (as well as cost) currently hinder the commercial introduction of state-of-the-art “beyond Li-ion” battery systems. Innovative breakthroughs would be needed for those new battery technologies to enter the market.

The increases in energy density described above are critical to achieving the *EV Everywhere* cost and performance targets. Additional R&D efforts, including those related to pack design optimization and simplification, manufacturing improvements at cell/pack levels, reduced production cost for battery materials, and novel thermal management technologies will also help reduce battery cost. The associated technical challenges and potential solutions to those challenges are listed in Table I- 1.

Table I- 1: Major Li-ion technology technical challenges and potential pathways

Barrier/Challenge	Potential Solutions
<ul style="list-style-type: none"> Reduce the cost and improve the performance of lithium-ion battery technology. 	<ul style="list-style-type: none"> Improved material and cell durability. Improved energy density of active materials. Reduction of inactive material. Improved design tools/design optimization. Improved manufacturing processes.
<ul style="list-style-type: none"> Develop higher energy battery technology such as next generation lithium-ion, lithium-sulfur and lithium-air <ul style="list-style-type: none"> Issues with these materials include poor cycle life, low power, low efficiencies, and safety. 	<ul style="list-style-type: none"> Improved electrolyte/separator combinations to reduce dendrite growth for Li metal anodes. Advanced material coatings. New ceramic, polymer, and hybrid structures with high conductivity, low impedance, and structural stability.
<ul style="list-style-type: none"> Improve abuse tolerance performance of battery technology. 	<ul style="list-style-type: none"> Non-flammable electrolytes. High-temperature melt integrity separators. Advanced materials and coatings. Improved understanding of reactions. Battery cell and pack level innovations such as improved sensing, monitoring, and thermal management systems.

I.B.3 Energy Storage R&D Programmatic Structure

The energy storage effort includes multiple activities, ranging from focused fundamental materials research to battery cell and pack development and testing. The R&D activities can involve either short-term directed research by commercial developers and national laboratories or exploratory materials research generally spearheaded by the national laboratories and universities. These consist of five major program elements which are inter-related and complementary, namely:

- Advanced Battery Development.
- Battery Testing, Analysis, and Design.
- Applied Battery Research (ABR).
- Manufacturing and Process Development.
- Focused Fundamental Research, also called Exploratory Battery Materials Research (BMR)

The *Advanced Battery Development program*'s goal is to support the development of a domestic advanced battery industry whose products can meet electric drive vehicle performance targets. Such R&D activity focuses, for example, on the development of robust battery cells and modules to significantly reduce battery cost, increase life, and improve its performance. It takes place in close partnership with the automotive industry, through our cooperative agreement with the United States Advanced Battery Consortium (USABC). DOE works in close collaboration with USABC to develop battery and ultracapacitor requirements for various vehicle types² and test procedures.³ In FY 2015, the USABC supported 9 cost-shared contracts with developers to further the development of batteries for PEVs and HEVs. DOE often directly supports battery and material suppliers via contracts administered by the National Energy Technology Laboratory (NETL). In FY 2015, NETL managed 20 battery R&D contracts. Chapter II focuses on the battery development program.

² See uscar.org/guest/article_view.php?articles_id=85

³ See uscar.org/guest/article_view.php?articles_id=86

The Battery Testing, Analysis, and Design activity is complementary to the battery development program. High level projects pursued in this area include performance, life and abuse testing of contract deliverables, laboratory- and university-developed cells, and benchmark systems from industry; thermal analysis, thermal testing and modeling; development of new test procedures and maintenance of current test procedures; development of tools for the computer aided engineering of batteries; requirements analyses; cost modeling; other energy storage use and life studies; and recycling studies of core materials. Battery technologies are evaluated according to USABC Battery Test Procedures. The manuals for the relevant applications (PEV and HEV) are available online^{4, 5, 6}. Benchmark testing of an emerging technology is performed to remain abreast of the latest industry developments. In this report, Chapter III focuses on the *Battery Testing, Analysis, and Design* activity.

The *Applied Battery Research* (ABR) activity is focused on the optimization of next generation, high-energy lithium-ion electrochemistries that incorporate new battery materials. It emphasizes identifying, diagnosing, and mitigating issues that impact the performance and lifetime of cells constituted of advanced materials. It investigates the interaction between cell components (cathodes, anodes, electrolytes, binders, conductive additives, and separators) as they impact performance and life. Typical issues associated with incorporating new material developments into working PEV cells can include: (1) inadequate power capability needed to meet PEV requirements, (2) insufficient cycle life stability to achieve the 1,000 to 5,000 “charge-depleting” deep discharge cycles, and (3) poor performance at lower temperatures. ABR is conducted by a team that includes six national labs and several universities. Chapter IV lists all the projects under this activity.

The *Battery Manufacturing and Process Development* activity complements the ABR activity. It involves R&D at the national labs on systematic material engineering and customized scaled processes to accomplish kilogram-level high quality material production. It also involves in-line analysis methods of quality control to detect electrode flaws and contaminants and developing new atomic layer deposition techniques more amenable to high-throughput manufacturing. It also includes industry partnerships to develop novel electrode/cell manufacturing technologies utilizing proven and emerging battery chemistries, reducing the ratio of inactive to active material, higher process-yielding designs, cost-effective drying processes, novel separator coatings, commercially scalable prelithiation methods, and novel battery architectures. The projects in this activity are also listed in Chapter IV.

The *Advanced Battery Materials Research* activity addresses fundamental issues of materials and electrochemical interactions associated with lithium batteries. It develops new/promising materials and uses advanced material models to discover new materials, their failure modes, as well as scientific diagnostic tools/techniques to gain insight into why material and systems fail. Battery chemistries are monitored continuously with periodic substitution of more promising components based on advice from participants within this activity, from outside experts, and assessment of world-wide battery R&D. This work is carried out by a team of researchers located at several national labs, universities, and commercial entities. The program is also studying issues critical to the realization of beyond Li-ion technologies, such as solid-state technology, lithium metal systems, lithium sulfur, and lithium air. Some of the main areas of focus are to devise new methods to understand and stabilize lithium metal anodes; to contain Li polysulfides to enable the use of sulfur cathodes; and to develop electrolytes that support lithium air and Li/sulfur cells. Chapter V lists all the projects that are part of the Advanced Battery Materials Research (BMR) activity.

Several *Small Business Innovation Research* (SBIR) contracts are also supported by VTO, in addition to the R&D described above. SBIR projects have been the source of new ideas and concepts. These SBIR projects are focused on the development of new battery materials and components.

The Electrochemical Energy Storage Roadmap describes ongoing and planned efforts to develop electrochemical storage technologies for plug-in electric vehicles (PEVs) and can be found at the EERE Roadmap page <http://energy.gov/eere/vehicles/downloads/us-drive-electrochemical-energy-storage-technical-team-roadmap>.

⁴ United States Advanced Batteries Consortium, USABC Electric Vehicle Battery Test Procedure Manual, Rev. 2, U.S. Department of Energy, DOE/ID 10479, January 1996.

⁵ U.S. Department of Energy, PNGV Battery Test Procedures Manual, Rev. 2, August 1999, DOE/ID-10597.

⁶ United States Council for Automotive Research, RFP and Goals for Advanced Battery Development for Plug-in Electric Vehicles, uscar.org.

VTO has established extensive and comprehensive ongoing coordination efforts in energy storage R&D across all of the DOE complex and with other government agencies. Coordination within DOE and with other government agencies is a key attribute of the VTO energy storage R&D efforts. VTO coordinates efforts on energy storage R&D with the DOE Office of Science, the DOE Office of Electricity, and the Advanced Research Projects Agency – Energy (ARPA-E). Coordination and collaboration efforts also include membership and participation in the Chemical Working Group of the Interagency Advanced Power Group (IAPG), active participation in program reviews and technical meetings sponsored by other government agencies, and participation of representatives from other government agencies in the contract and program reviews of DOE-sponsored efforts. DOE also coordinates with the Department of Transportation/National Highway Traffic Safety Administration (DOT/NHTSA), the Environmental Protection Agency (EPA), and with the United Nations Working Group on Battery Shipment Requirements. Additional international collaboration occurs through a variety of programs and initiatives. These include: the International Energy Agency’s (IEA’s) Implementing Agreement on Hybrid Electric Vehicles (IA-HEV), the eight-nation Electric Vehicle Initiative (EVI), and the Clean Energy Research Center (CERC) bilateral agreement between the U.S. and China.

I.B.4 Recent *EV Everywhere* Highlights

- America is **the world’s leading market for electric vehicles** and is producing some of the most advanced PEVs available today. Consumer excitement and interest in PEVs is growing, despite the recent drop in gasoline prices. In 2012, PEV sales in the U.S. tripled, with more than 50,000 cars sold. In 2013, PEV sales increased by 85% with over 97,000 vehicles sold. In 2014, PEV sales increased by 20%, with annual sales of over 118,000 PEVs. In 2015, PEV sales remained steady with annual sales of 115,000 PEVs even though oil prices have been extremely low for the year.
- In **commercial applications of DOE-supported technologies**, several technologies that were developed under partially VTO-sponsored projects, have moved into commercial applications. Hybrid electric vehicles on the market from BMW and Mercedes are using lithium-ion technologies which were developed under DOE projects with Johnson Controls Inc(JCI). JCI will also supply Li-ion batteries to Land Rover for hybrid drive sport utility vehicles. Lithium-ion battery technology developed partially with DOE funding of a USABC project at LG Chem is being used in GM’s Chevrolet Volt extended-range electric vehicle (EREV), the Cadillac ELR EREV, the Chevy Bolt EV, and the Ford Focus EV battery. LG Chem will also supply Li-ion batteries to Eaton for hybrid drive heavy-duty vehicles.
- The 2015 DOE PEV **Battery Cost Reduction Milestone** of \$275/kWh was accomplished. DOE-funded research has helped reduce the current cost projection (from three DOE-funded battery developers) for a PHEV 40 battery to an average \$264 per kilowatt-hour (of useable energy). This cost projection is derived by using material costs and cell and pack designs, provided by those developers, which are then input into ANL’s peer-reviewed (and in public domain) Battery Production and Cost model (BatPaC). The cost projection is based on a production volume of at least 100,000 batteries per year. The battery cost is derived for batteries that meet DOE/USABC system performance targets. The battery development projects focus on high voltage and high capacity cathodes, advanced alloy anodes, and processing improvements. Details of the material and cell inputs and cost models are available in spreadsheet form and in quarterly reports. DOE’s goal is to continue to drive down battery cost to \$125/kWh by 2022.
- **24M** is developing a novel and inexpensive manufacturing process that requires fewer unit operations for a higher process yield, and results in electrode and stacked cell fabrication in one-fifth of the time (and footprint) for conventional stacked cell lines. Also, the semisolid electrodes require no drying activity and no organic solvents. Finally, the process is able to make thick electrodes (from 200-1,000 microns). This increases the energy density and has the potential to reduce the cost of stacked cells due to the lesser amount of “non-energy storing” materials in each cell, such as separators and current collectors. 24M’s electrodes show both excellent energy and power capability, Figure I- 2. The enhanced areal capacity of 24M’s electrodes (i.e., the amount of capacity/energy they store per unit area of the electrode) is two to four times that of conventional electrodes.

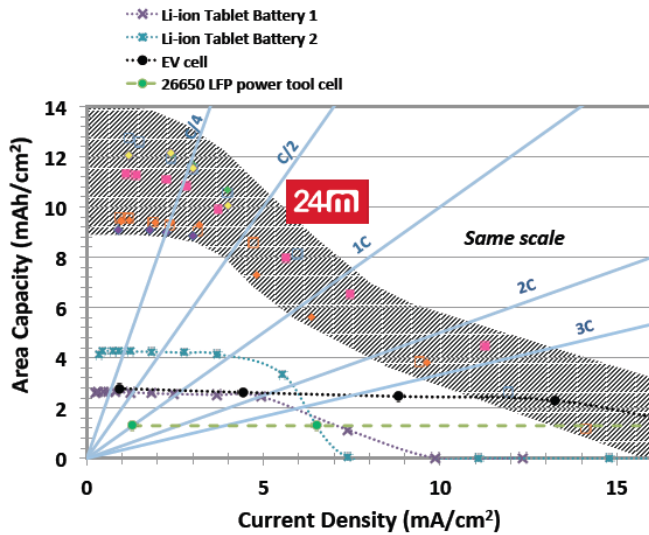


Figure I- 2: Comparative capacity per unit area of cells using 24M electrodes (shaded area) vs. traditional cells (curves shown near 2 and 4 mAh/cm², both plotted as a function of current density, or cell discharge power. The 24M cells range in capacity from .003Ah to 2Ah

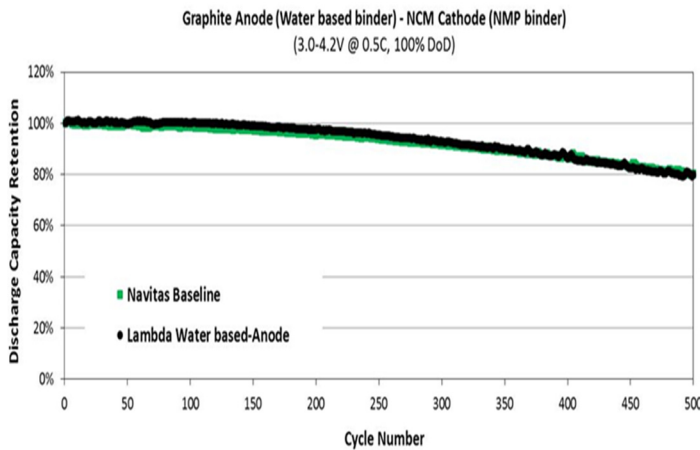


Figure I- 3: Cycle life testing for battery cells show identical performance of battery electrodes dried with VFM (Lambda) or dried with IR/Convection dryer (Navitas)

electrodes placed into graphite/NMC cells by its partner, Navitas Systems. Those cells have shown cycle life values that are indistinguishable from those for cells made by using traditional drying. In addition, this technique would potentially permit the drying of much thicker electrodes than occurring currently. (See Figure I- 3.)

- ANL has teamed with Strem Chemicals to provide industry and the battery research community with next-generation battery materials. Specifically, Strem, a manufacturer and distributor of specialty chemicals, has licensed 23 separate pieces of intellectual property from ANL and will distribute nine battery solvents and additives via its marketing and global distribution networks. The materials were all invented at Argonne’s Electrochemical Energy Storage Center and scaled at the laboratory’s Materials Engineering Research Facility (MERF). The agreement with Strem both funds and represents successful technology transfer across the research spectrum: from invention at the bench to scale-up, and ultimately into use by industry.

- Lambda Technologies** is developing variable frequency microwave (VFM) drying technology employing penetrating energy that selectively targets the solvent in the entire volume of the wet electrode, thereby simultaneously driving the solvent out. (In contrast, convection dryers heat only the electrode surface; thus solvent removal proceeds layer by layer as heat transfers inwards and hence takes much longer than VFM to finish the drying process.) VFM is estimated to result in a 30-50% reduction in the operating cost of the electrode drying procedure.

This process has been applied to NMC

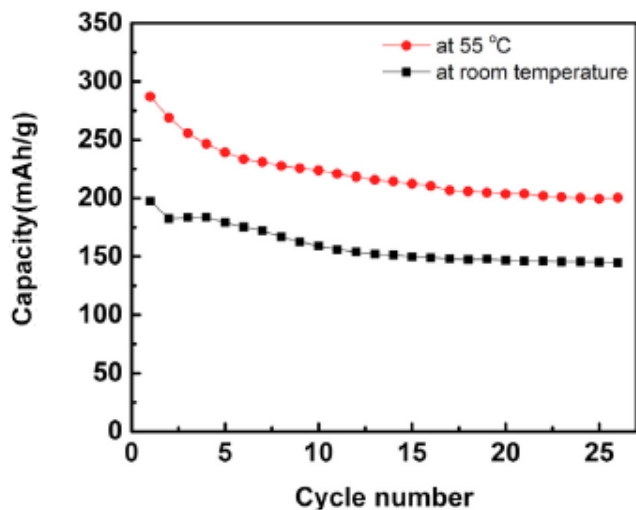


Figure I- 4: Discharge capacity of $\text{Li}_{1.25}\text{Nb}_{0.25}\text{Mn}_{0.5}\text{O}_2$. vs. Li metal half cells cycled at 55 °C and room temperature versus cycle number

- MIT has designed, prepared, and tested a new disordered rock-salt material with Li-excess, $\text{Li}_{1.25}\text{Nb}_{0.25}\text{Mn}_{0.5}\text{O}_2$. It shows a high capacity of 287 mAh/g and specific energy density of 909 Wh/kg (vs. 650Wh/kg for today’s best in class cathodes) in the first cycle at 55 °C. Combined *in situ* XRD and EELS measurements indicate that Mn and O both reversibly contribute to the charge transfer with oxygen providing almost half of that capacity. Together with previous work on understanding Li transport in Li-excess and disordered materials, this material is an important new direction to create high capacity cathode materials. (See Figure I-4.)

- NREL has developed (and patented) an Internal Short Circuit (ISC) device to emulate defects that cause ISCs in Li-ion

cells. The intent of the device is to enhance the design of Li-ion batteries by testing the effects of the ISC (which can lead to thermal runaway). The ISC device can be placed in any location within a cell

to produce four different types of shorts. The device is made from small discs of copper and aluminum, a copper puck, separator, and thin layer of wax. After its implantation in a cell, the cell is heated, melting the wax layer, which is then wicked away, allowing the metal components to come into contact and inducing an ISC. After several design iterations, NREL has delivered more than 300 ISC devices to NASA and several industry partners for use in evaluating the abuse tolerance of new cell designs and materials, as well as the cell-to-cell propagation of ISC in modules. Discussions to produce higher volumes of the ISC device via automation are currently underway with manufacturers. (See Figure I- 5.)

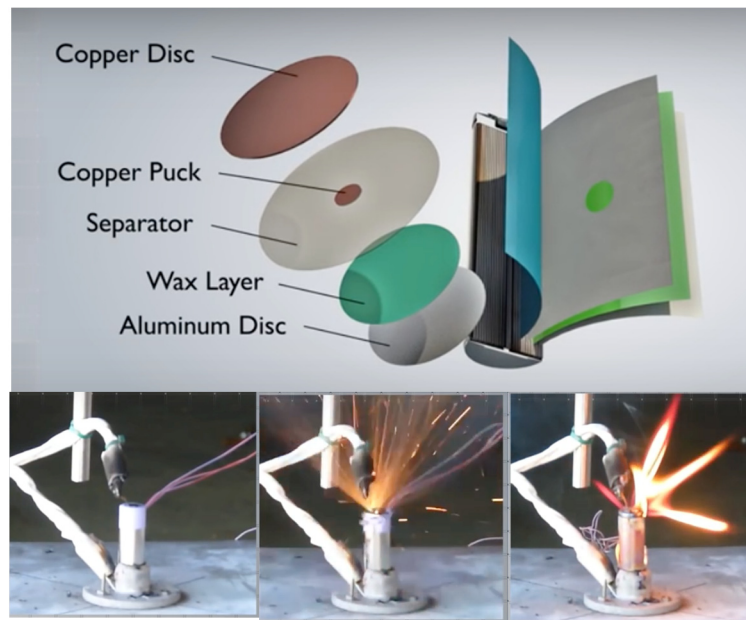


Figure I- 5: Top: Components of ISC device that can be placed anywhere in a cylindrical or prismatic cell. Bottom images left to right: a Li-ion cell with ISC device, a few minutes after melting the wax, and going into thermal runaway

- **Stanford University** has developed Li_xSi - Li_2O core-shell nanoparticles (NPs) as a high-capacity prelithiation reagent to compensate for the first cycle irreversible capacity loss of various anode materials, such as Si. Li_xSi NPs were synthesized by mechanical stirring of a mixture of Si NPs and Li metal at elevated temperatures inside an argon atmosphere. A dense passivation layer is formed on the Li_xSi NPs after exposure to trace amounts of oxygen, preventing the Li_xSi from further oxidation in dry air (Figure I- 6a). Scanning transmission electron microscopy (STEM) clearly shows (Figure I- 6b) a dense Li_2O passivation layer on the surface of the Li_xSi NPs. First cycle voltage profiles of Si

NPs/ Li_xSi - Li_2O composite and Si NPs show that the incorporation of this prelithiation reagent compensates for the capacity loss of Si NPs (Figure I- 6c). The composite (red curve) shows an initial loss of only 10%, whereas the Si NPs (blue curve) show an initial loss of 30%. In full cells, that initial loss of lithium must be compensated by excess cathode, which effectively reduces the cell energy.

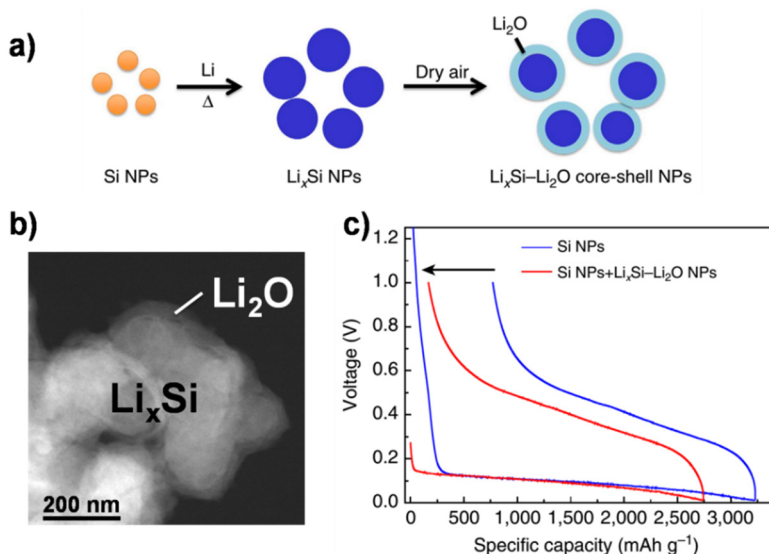


Figure I- 6: (a) Schematic representation of Li_xSi - Li_2O NPs synthesis method. (b) STEM image of Li_xSi - Li_2O NPs. (c) 1st cycle voltage profiles of Si NPs/ Li_xSi - Li_2O and Si NPs show that the incorporation of Li_xSi - Li_2O NPs compensates the 1st cycle capacity loss of Si NPs

- In January 2015, DOE released a Funding Opportunity Announcement (FOA) that solicited proposals in the areas of advanced light-weighting, advanced battery development, power electronics, advanced combustion technology, and natural gas utilization in transportation. These areas of interest applied to light, medium-, and heavy-duty on-road vehicles.⁷ In September 2015, DOE announced the selection of 24 new projects (worth nearly \$55 million) to develop and deploy cutting-edge vehicle technologies that will strengthen the U.S. clean energy economy. These technologies will play a key role in increasing vehicle fuel efficiency and

reducing petroleum consumption, while also supporting the DOE *EV Everywhere* Grand Challenge to have the U.S. become the first nation in the world to produce plug-in electric vehicles that are as affordable as 2012's gasoline-powered vehicles. (Through the Advanced Vehicle Power Technology Alliance with DOE, the Department of the Army is contributing an additional \$2.26 million in co-funding to projects focused on battery modeling technologies and computational fluid dynamics.) Specifically, in the area of advanced batteries, 10 projects totaling \$26.1 million were awarded in the areas of advances in existing and next-generation battery material manufacturing processes, advances in electrode and cell fabrication manufacturing, and electric drive vehicular battery modeling for commercially available software (see Table I- 2). These projects, which were initiated in FY 2016, will be described in more detail in the next year's annual report.

- In January 2015, VTO issued an "Incubator" FOA, which supports innovative technologies and solutions that could help meet existing goals that are not represented in a significant way in the EERE offices' existing Multi-Year Program Plans (MYPPs) or current R&D portfolios.⁸ In August 2015, 8 new "incubator" projects (worth \$10.4 million) were selected, of which 3 projects were in the advanced battery area (worth \$3.3 million) (See Table I- 3.) These include one project each from the areas of new advanced stable electrolytes for high voltage electrochemical energy storage, statically and dynamically stable lithium-sulfur batteries, and high-performance Li-ion battery anodes from electro-spun nanoparticle/conducting polymer nanofibers.

⁷ Fiscal Year 2015 Vehicle Technologies Office Program Wide Funding Opportunity Announcement, DE-FOA-0001201, Jan 22, 2015

⁸ Fiscal Year 2015 Vehicle Technologies Office Incubator Funding Opportunity Announcement, DE-FOA-0001213, Jan 22, 2015.

Table I- 2: FY 2015 Vehicle Technologies Program Wide Funding Opportunity Announcement: List of Awardees

Applicant	Location	Project Title/ Description	Federal Cost Share
Advances in Existing and Next-Generation Battery Material Manufacturing Processes (Area of Interest 4)			
Cabot Corporation	Billerica, MA	This project will develop and demonstrate low cost flexible aerosol manufacturing technology for the production of high performance lithium-ion battery cathodes with long cycle life.	\$2,977,876
The Curators of The University of Missouri	Columbia, MO	This project will develop an integrated flame spray process for low cost production of battery materials for lithium-ion batteries and beyond.	\$2,215,560
Boulder Ionics Corporation	Arvada, CO	This project will demonstrate advanced lithium salt and electrolyte production using continuous-flow process intensification techniques to enable higher performance and lower cost.	\$2,399,833
Navitas Advanced Solutions Group, LLC	Ann Arbor, MI	This project will demonstrate a commercially scalable process to fabricate nanocomposite silicon anodes.	\$1,125,430
Advances in Electrode and Cell Fabrication Manufacturing (Area of Interest 5)			
Miltec UV International, LLC	Stevensville, MD	This project will develop and demonstrate the use of ultraviolet curing technology to reduce manufacturing cost and improve the performance of lithium-ion battery electrodes.	\$2,054,560
Palo Alto Research Center, Incorporated	Palo Alto, CA	This project will utilize co-extrusion technology to fabricate and validate high-energy and high-power electrodes for electric vehicle applications.	\$2,999,115
PPG Industries, Incorporated	Allison Park, PA	The project will develop novel binders and active materials to enable a low-cost, water-based, electrodeposited lithium-ion battery (LIB) electrode coating system and manufacturing process.	\$2,999,275
Electric Drive Vehicular Battery Modeling for Commercially Available Software (Area of Interest 6)			
General Motors LLC	Warren, MI	This project will develop commercially available software that improves the computational processing time of battery pack performance modeling by a factor of 100.	\$2,955,360 (jointly funded)
Analysis and Design Application Company Ltd	Melville, NY	This project will develop a commercially available software tool that is capable of predicting battery performance at the electrode level in order to improve battery cycle life and computational efficiency at the cell and pack level.	\$2,880,000 (jointly funded)
Ford Motor Company	Dearborn, MI	This project will develop commercially available software that is capable of predicting battery safety performance under typical abuse test conditions.	\$3,500,000 (jointly funded)

Table I- 3: FY 2015 Vehicle Technologies Incubator Funding Opportunity Announcement: List of Awardees

Applicant	Location	Project Title/ Description	Federal Cost Share
Silatronix	Madison, WI	New Advanced Stable Electrolytes for High Voltage Electrochemical Energy Storage (Develop an innovative electrolyte providing stable performance at high voltage (>5V))	\$1,332,660
University of Texas Austin	Austin, TX	Statically and Dynamically Stable Lithium-sulfur Batteries (Develop an innovative polysulphide blocking layer to develop lithium-sulfur batteries for automotive applications)	\$891,000
Vanderbilt University	Nashville, TN	High-Performance Li-Ion Battery Anodes from Electrospun Nanoparticle/Conducting Polymer Nanofibers (Develop a novel electrospun anode material utilizing a conductive polymer binder)	\$1,040,030

I.B.5 Organization of this Report

This report covers all the FY15 projects that were ongoing (or starting up) as part of the energy storage R&D effort in VTO. Chapter II through V contain descriptions and progress of various R&D projects supported through VTO funding. A list of individuals who contributed to this annual progress report (or who collaborate with the energy storage R&D effort) appears in Appendix A. A list of acronyms is provided in Appendix B.

We are pleased with the progress made during the year and look forward to continued work with our industrial, government, and scientific partners to overcome the remaining challenges to delivering advanced energy storage systems for vehicle applications.



David Howell
Program Manager, Hybrid and Electric Systems
Vehicle Technologies Office



Tien Q. Duong
Manager, Advanced Battery Materials Research
Vehicle Technologies Office



Peter W. Faguy
Manager, Applied Battery Research
Vehicle Technologies Office



Brian Cunningham
Lead, Battery Testing, Analysis and Design
Vehicle Technologies Office

II. Advanced Battery Development

One of the primary objectives of the energy storage effort is the development of durable and affordable advanced batteries and ultracapacitors for use in advanced vehicles, from start/stop to full-power HEVs, PHEVs, and EVs. The battery technology development activity supports this objective through projects in several areas:

- Full-scale battery R&D under multiple battery development contracts—conducted through the United States Advanced Battery Consortium (USABC)
- Numerous advanced cell, materials and components contracts—administered through the National Energy and Technology Laboratory (NETL), and
- Small Business Innovative Research (SBIR)—to fund early-stage R&D for small businesses/entrepreneurs

All battery development projects are conducted with a set of technical goals in mind and in order to overcome specific technical barriers which prevent the large-scale commercialization of advanced automotive batteries.

Technical Goal

- By 2022, reduce PEV battery cost to \$125/kWh.

Technical Barriers

- **Cost** – The current cost of Li-based batteries is approximately a factor of up to four too high (on a \$/kWh) basis for PEVs. The main cost drivers being addressed are the high costs of raw materials and materials processing, cell and module packaging, and manufacturing.
- **Performance** – The performance advancements required include the need for much higher energy densities to meet the volume and weight requirements, especially for the 40 mile PHEV system and longer range EVs, and to reduce the number of cells in the battery (thus reducing system cost).
- **Abuse Tolerance** – Many Li batteries are not intrinsically tolerant to abusive conditions such as a short circuit (including an internal short circuit), overcharge, over-discharge, crush, or exposure to fire and/or other high temperature environments. The use of Li chemistry in the larger (PEV) batteries increases the urgency to address these issues.
- **Life** – A 15-year life with 5,000 HEV cycles or 1,000 EV cycles is unproven.

Technical Targets

- Focus on the small-scale manufacture of cells, batteries, and advanced materials for high-power applications (HEVs) and high-energy applications (e.g., PEVs).
- Attempt to meet the requirements for EVs, PHEVs, HEVs, and 12V start/stop batteries developed with industry – as shown in Table II- 1, Table II- 2, and Table II- 3.

Accomplishments

- The R&D activity remains fully underway with multiple battery development contracts being conducted through the USABC. A revised set of EV battery performance requirements was posted on the USABC site this year. Current USABC-funded projects with Envia Systems, JCI, Xerion, Maxwell Technologies, Saft, Leaden Energy, SKI, and ENTEK are covered in this report.
- Numerous advanced cell, materials, and components contracts are ongoing – administered through the National Energy and Technology Laboratory (NETL). These include projects by Amprius, XALT Energy, OneD Material, 3M, Seo, Pennsylvania State University, and Denso.

Table II- 1: Summary of USABC performance targets for EV batteries⁹

USABC Goals for Advanced Batteries for EVs – CY 2020 Commercialization			
End of Life Characteristics at 30°C	Units	System Level	Cell Level
Peak Discharge Power Density, 30 s Pulse	W/L	1,000	1,500
Peak Specific Discharge Power, 30 s Pulse	W/kg	470	700
Peak Specific Regen Power, 10 s Pulse	W/kg	200	300
Useable Energy Density @ C/3 Discharge Rate	Wh/L	500	750
Useable Specific Energy @ C/3 Discharge Rate	Wh/kg	235	350
Useable Energy @ C/3 Discharge Rate	kWh	45	N/A
Calendar Life	Years	15	15
DST Cycle Life	Cycles	1,000	1,000
Selling Price @ 100K units	\$/kWh	125	100
Operating Environment	°C	-30 to +52	-30 to +52
Normal Recharge Time	Hours	< 7 Hours, J1772	< 7 Hours, J1772
High Rate Charge	Minutes	80% ΔSOC in 15 min	80% ΔSOC in 15 min
Maximum Operating Voltage	V	420	N/A
Minimum Operating Voltage	V	220	N/A
Peak Current, 30 s	A	400	400
Unassisted Operating at Low Temperature	%	> 70% Useable Energy @ C/3 Discharge rate at -20°C	> 70% Useable Energy @ C/3 Discharge rate at -20°C
Survival Temperature Range, 24 Hr	°C	-40 to+ 66	-40 to+ 66
Maximum Self-discharge	%/month	< 1	< 1

⁹ For more details and for additional goals, see uscar.org/guest/article_view.php?articles_id=87.

Table II- 2: Summary of USABC performance targets for PHEV batteries

Characteristics at End of Life (EOL)		PHEV-20 Mile	PHEV-40 Mile	xEV-50 Mile
Commercialization Timeframe		2018	2018	2020
AER	Miles	20	40	50
Peak Pulse Discharge Power (10 sec)	kW	37	38	100
Peak Pulse Discharge Power (2 sec)	kW	45	46	110
Peak Regen Pulse Power (10 sec)	kW	25	25	60
Available Energy for CD (Charge Depleting) Mode	kWh	5.8	11.6	14.5
Available Energy for CS (Charge Sustaining) Mode	kWh	0.3	0.3	0.3
Minimum Round-trip Energy Efficiency	%	90	90	90
Cold cranking power at -30°C, 2 sec- 3 Pulses	kW	7	7	7
CD Life/Discharge Throughput	Cycles/MWh	5,000/29	5,000/58	5,000/72.5
CD HEV Cycle Life, 50 Wh Profile	Cycles	300,000	300,000	300,000
Calendar Life, 30°C	Year	15	15	15
Maximum System Weight	kg	70	120	150
Maximum System Volume	Liter	47	80	100
Maximum Operating Voltage	V _{dc}	420	420	420
Minimum Operating Voltage	V _{dc}	220	220	220
Maximum self-discharge	%/month	<1	<1	<1
System Recharge Rate at 30°C (240V/16A)	kW	3.3	3.3	6.6
Unassisted Operating and Charging Temp Range	°C	-30 to +52	-30 to +52	-30 to +52
-30°-52°	%	100	100	100
0°	%	50	50	50
-10°	%	30	30	30
-20°	%	15	15	15
-30°	%	10	10	10
Survival Temperature Range	°C	-46 to +66	-46 to +66	-46 – to +66
Max System Production Price @100,000 units/year	\$	\$2,200	\$3,400	\$4,250

Notes

1. Peak discharge pulse power and peak regen pulse power targets are applicable for the charge-sustaining mode.
2. HPPC-current rate used to approximate the required 10-kW rate during the HPPC test and the static capacity test.
3. With the battery manufacturer’s concurrence, an increase recharge rate can be used to accelerate life testing. Maximum system recharge rate refers to the maximum power expected from a standard garage outlet.
4. Values correspond to end-of-life (EOL).
5. The PHEV-20 and PHEV-40 targets correspond to commercialization in FY 2018; x-EV targets correspond to commercialization in FY 2020.
6. The x-EV cell is intended for architectures requiring power levels higher than those for PHEV-20 and PHEV-40.

Table II- 3: Summary of USABC performance targets for 12V Start/Stop Vehicle Applications

Characteristics	Units	Target	
		Under hood	Not under hood
Discharge Pulse, 1 sec	kW	6	
Max discharge current, 0.5 s	A	900	
Cold cranking power at -30°C (three 4.5-s pulses, 10s rests between pulses at min SOC)	kW	6 kW for 0.5s, followed by 4 kW for 4s	
Minimum voltage under cold crank	V _{dc}	8.0	
Available energy (750W accessory load power)	Wh	360	
Peak Recharge Rate, 10s	kW	2.2	
Sustained Recharge Rate	W	750	
Cycle life, every 10% life RPT with cold crank at min SOC	Engine starts/miles	450k/150k	
Calendar life at 30°C, 45°C if under hood	Years	15 at 45°C	15 at 30°C
Minimum round-trip energy efficiency	%	95	
Maximum allowable self-discharge rate	Wh/day	2	
Peak Operating Voltage, 10s	V _{dc}	15.0	
Sustained Operating Voltage - Max	V _{dc}	14.6	
Minimum Operating Voltage under Autostart	V _{dc}	10.5	
Operating Temperature Range (available energy to allow 6kW, 1s pulse)	°C	-30 to +75	-30 to +52
-30°C to -52°C	Wh	360 (to 75°C)	360
0°C	Wh	180	
-10°C	Wh	108	
-20°C	Wh	54	
-30°C	Wh	36	
Survival Temperature Range (24 hours)	°C	-46 to +100	-46 to +66
Maximum System Weight	kg	10	
Maximum System Volume	L	7	
Maximum System Selling Price (@250k units/year)	\$	\$220	\$180

II.A USABC Battery Development Projects

II.A.1 High Energy Lithium Batteries for Electric Vehicles (Envia Systems)

Objectives

- Develop high capacity silicon-based anode composites capable of supporting long cycle life by controlling electrode pulverization, lithium consumption and conductivity loss.
- Develop high capacity cathode composites capable of supporting cycle life, calendar life, power, safety, and low/high temperature cell requirements.
- Develop a manufacturable and cost effective pre-lithiation process capable of supporting large-format high-capacity pouch cells.
- Screen and optimize various electrolyte formulations and coated separators to support meeting the USABC performance, cost and safety cell targets.
- Design, build, test and deliver large capacity pouch cells integrating high capacity Si-based anode and cathode composites along with optimized electrolyte formulations, separators and pre-lithiation process that meet the USABC EV cell goals for the CY 2020.

Project Details

Oliver Gross (USABC Program Manager)
DE-EE0006250 Recipient: Envia Systems Inc.

Herman Lopez (Envia Systems - PI)
7979 Gateway Boulevard, Suite 101
Newark, CA 94560
Phone: 510-962-3687; Fax: 510-790-7012
Email: hlopez@enviasystems.com

Subcontractor:
A123 Systems
Waltham, MA

Nanoscale Components, Hudson, NH

Start Date: June 2014
Projected End Date: July 2017

Technical Barriers

- There are numerous technical barriers associated with materials, cell components, cell design and manufacturing that need to be addressed in order to develop cells that will meet the USABC EV energy, power, cycle life, calendar life, temperature, safety and cost cell targets for CY2020.
- High capacity silicon-based anodes are required to meet the high-energy cell targets. Unfortunately, silicon-based anodes introduce significant challenges in cycle life, especially at the required high electrode loading and density levels, due to pulverization and lithium consumption. Pulverization of silicon happens due to the volume expansion of silicon (over 300%) during the lithium insertion process resulting in loss of contact between the silicon and current collector. Lithium consumption is another issue that causes the battery capacity to fade. The volume expansion & contraction of silicon anodes create newly exposed surfaces, which react to form a new solid-electrolyte interface (SEI) layer that consumes lithium continuously as the battery cycles.
- High capacity silicon-based anodes are subject to a high irreversible capacity loss. In order to achieve mass adoption of this technology, a cost effective and scalable pre-lithiation process needs to be developed.
- High capacity lithium-rich cathodes will also be required to meet the cell performance, durability, and cost targets. Unfortunately, high specific capacity lithium-rich cathode materials suffer from a fundamental problem of high resistance, particularly at low states of charge; and transition metal-ion dissolution, which leads to reduced power, low usable energy, poor cycle life and poor calendar life; compromising it highly for automotive applications.
- Optimization of cell design and integration will be required to meet the USABC performance, cost and safety cell targets. Various design changes can improve certain cell performance metrics while adversely affecting others and potentially complicating the cell assembly.

Technical Targets

- Develop a silicon-based anode composition and formulation able to meet cycle life and power requirements suitable for EV applications.
- Develop a lithium-rich NMC composite cathode material with low DC-resistance, voltage fade and good cycling stability.
- Design, build and deliver cells that meet the USABC EV battery targets (350Wh/Kg & 750Wh/L available energy densities, 1000cycles, 15 years calendar life, \$100/kWh). Cells will be delivered to the Idaho National Laboratory (INL), the Sandia National Laboratory (SNL) and the National Renewable Energy Laboratory (NREL) for independent testing.

Accomplishments

- Down-selected a lithium-rich NCM cathode composition, dopant and surface coating based on capacity, average voltage, DC-resistance, usable energy and cycle life.
- Completed the first screening of various nano-silicon, Si-SiO_x and Si-alloy anodes based on capacity, cycle life, irreversible capacity loss, processability and manufacturability.
- Shown significant cycle life improvement from surface coated silicon-based anodes in small format cells with material scale-up and large capacity cell validation ongoing.
- Successfully built (1-20Ah) baseline and iteration #1 cells incorporating promising materials, cell components and cell design meeting year 1 cell targets.
- Nanoscale successfully pre-lithiated and delivered 50m of silicon-based anode rolls to support cell development.
- Build #1 cells have been built by A123, integrating promising pre-lithiated anode, cathode, electrolyte and cell design with cells currently under test.
- Continued to improve the cell cost modeling to reflect the current and final project cell goals.

Introduction

This project is developing a new battery system based on novel high capacity NMC cathode composites and high capacity silicon-based anode formulations that could meet the USABC EV cell performance requirements. At the conclusion of the program, Envia will demonstrate a lithium-ion battery (LIB) with usable specific energy greater than 350Wh/Kg and usable energy density greater than 750Wh/L while maintaining other performance requirements of EV cells, including power, calendar life, cycle life, safety and cost. This will be achieved through a collaborative effort across several organizations, where each organization provides expertise on specific components of the material, processing and/or cell. (See Figure II- 1.) Ultimately, large format cells meeting the USABC goals will be built and delivered to the National Laboratories for testing.

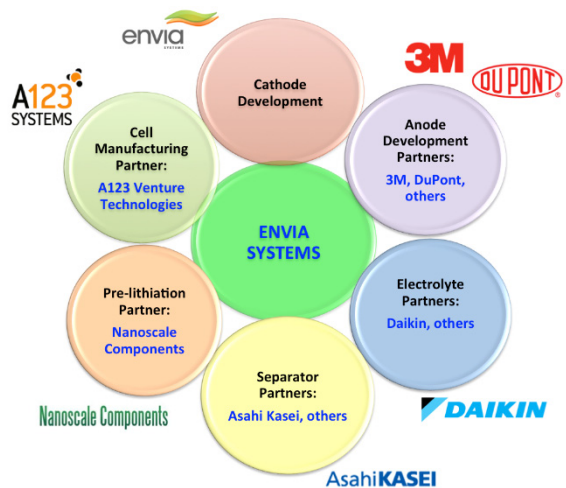


Figure II- 1: Development areas and partners

Approach

Envia is utilizing a system-level approach to screen, develop and optimize the critical cell components (cathode, anode, electrolyte and separator), cell design (N/P ratio, electrode design and pre-lithiation) and cell formation and testing protocols that will enable meeting the USABC EV cell level goals for the year 2020. The development will consist of integrating Envia's high capacity lithium-rich composite cathodes, pre-lithiated silicon-based high capacity anodes, high voltage electrolyte and ceramic coated separator into large capacity (20-50Ah) pouch cells. The developed cells will exhibit high energy density and power, good cycle life and calendar life and acceptable low temperature performance while meeting the cell level cost and safety targets.

Envia is leveraging its material, process and cell development expertise to develop, modify and engineer material and cell-level solutions to meet the cell specifications. During this project, Envia has partnered with leading companies like 3M, DuPont, Daikin America, Asahi Kasei, Nanoscale Components and A123 Venture Technologies to enable the development of the best anode, electrolyte, separator, pre-lithiation process and cell manufacturing, respectively. Proper partnerships will increase the probability of meeting the USABC project goals by leveraging the strength of each partner, with Envia mainly focusing on its core strengths of cathode and anode development, and cell design. Partnering with large chemical and cell partners also ensures that any developed technology will have a clear path to high volume production and commercialization.

The program has been structured in a way that as it progresses throughout the three years, the cell targets increase in difficulty with respect to specific energy, energy density and cycle life. (See Figure II- 2.)

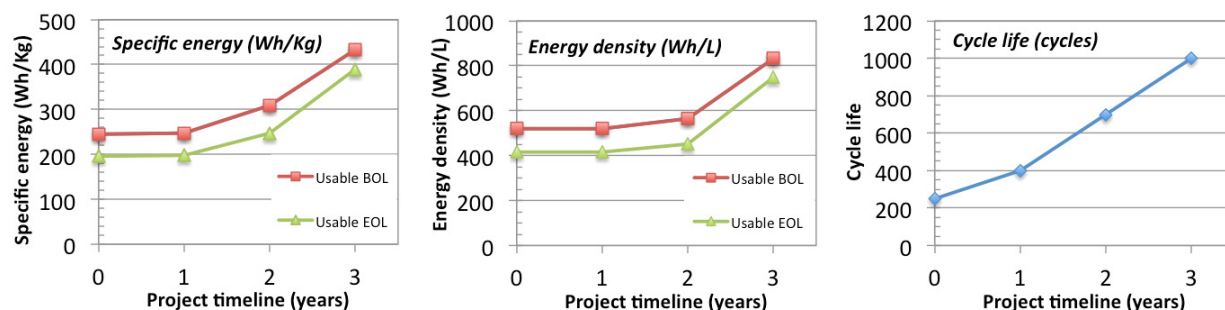


Figure II- 2: Projected cell development timeline

Results

Anode Development

Envia has screened multiple silicon anodes by integrating commercially available silicon based materials from 3M and DuPont as well as commercial silicon-based material vendors. Initial screening of various nano-silicon, Si-SiO_x-C and Si-alloy anodes based on capacity, cycle life, irreversible capacity loss, processability and manufacturability have taken place. During the material screening, Envia has tested the materials following vendor recommendations as well as by applying its electrode formulation, processing and coating know-how to further improve the performance of the silicon materials. At the completion of Year 1 in the Program, Envia has integrated a Si-SiO_x-based carbon composite anode into the baseline and iteration #1 cell builds, as the down-selection of the final anode material composition continues. The C/3 reversible capacity of the current Si-SiO_x-based carbon composite anode is ~1250mAh/g and is expected to increase as the program progresses (see Figure II- 3).

Anode material development has focused on optimizing the anode composition, electrode formulation and material coating. Engineering the precise amount of carbon, the type of carbon and processing to form the composite have taken place. Similarly, various electrode formulations have been explored by controlling the formulation ratios, binder type, conducting additive type and processing conditions. Various conducting coatings have also been explored with promising cycle life improvement observed in small format cells from two Si-SiO_x-C-coated composite anodes. Material scale-up and validation of cycle life in large capacity pouch cells is ongoing.

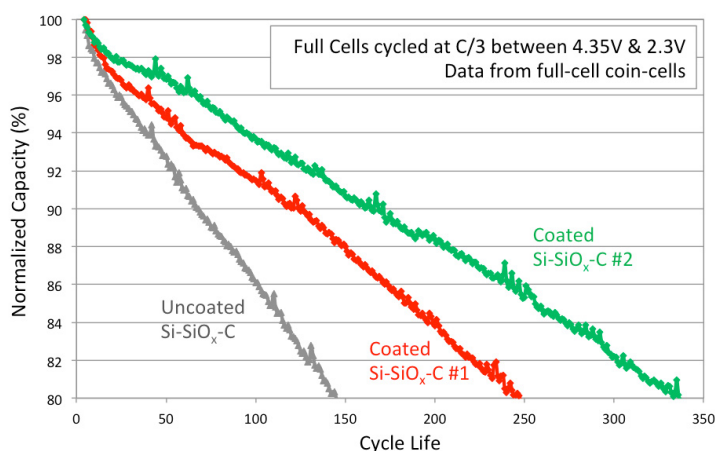


Figure II- 3: Cycle life improvement of coated Si-SiO_x-C anode

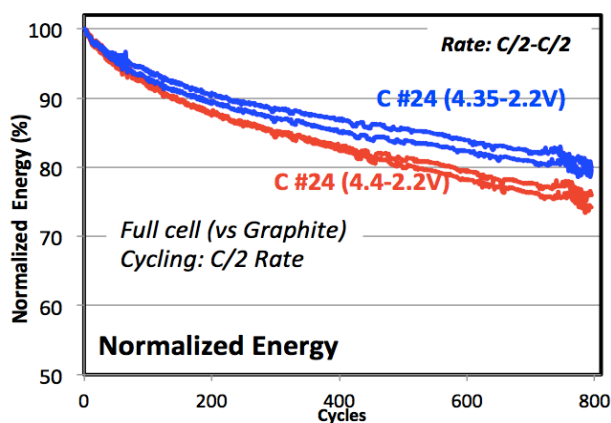


Figure II- 4: Cycle life from down-selected lithium-rich cathode (C#24)

anode capable of meeting the USABC EV cell targets.

Nanoscale continues its rapid progress building a new pilot scale prelithiation line able to support building large format pouch cells. The new pilot line has the following attributes: 1) 50x larger than the initial line; 2) 5x wider to support a 300mm anode width with 10x longer length for faster throughput; 3) designed for near production levels of automation. The new pilot scale line is nearly operational with initial trials on graphite and silicon rolls ongoing. The next cell build of the program (iteration #2) is expected to use the new pilot scale line to prelithiate the anode.

Cell Development

In order to meet the EV program cell targets, multiple cell builds are scheduled throughout the program. Currently, baseline 21Ah capacity cells and 1.2Ah capacity cells from iteration #1 have been successfully built and are going through testing and failure analysis. The cell builds incorporated promising materials, cell components and a cell design meeting year 1 cell targets. Cell build iteration #1 also served as the first time that cells were assembled, integrating materials and a cell design from Envia, prelithiation from Nanoscale and cell assembly from A123.

Parallel with the large cell builds, smaller cell builds consisting of a smaller number of cells have taken place and will continue to be built to evaluate and down-select the best electrolyte, separator, cathode, anode, cell design, and testing conditions that will feed the larger builds.

Cathode Development

Envia has down-selected a lithium-rich manganese-rich NMC cathode composition, dopant and surface coating based on capacity, average voltage, DC-resistance, usable energy and cycle life. The down-selected cathode material (C#24) has shown ~800 cycles and ~550 cycles to 80% energy retention in graphite cells when cycled at a C/2 rate at the voltage window of 4.35V-2.2V and 4.4V-2.2V, respectively (see Figure II- 4). Cathode material development will continue exploring various cathode blends incorporating manganese-rich, cobalt-rich and nickel-rich materials.

Prelithiation Development

A consequence of working with high capacity silicon-based anodes (especially with SiO_x-based materials) is an inherent high irreversible capacity loss. In order to mitigate this challenge, prelithiation is a requirement. Envia has partnered with Nanoscale Components to electrochemically prelithiate the anode materials via a scalable, manufacturable and cost effective roll-to-roll electrochemical process. Currently Nanoscale has successfully prelithiated and delivered 50m of silicon-based anode (A#7) to support cell development. Other anode formulations and compositions have been attempted and will continue to be optimized during the program to develop a prelithiated

In order to continue to improve the materials, an important aspect of cell development, cell design and cell assembly is to understand the failure mechanisms of the cell. Recently, the 21Ah baseline cells underwent postmortem analysis after cycling for 340 cycles (see Figure II- 5). Post mortem analysis methodologies and procedures continue to be developed as physical, chemical, structural and electrochemical information is extracted from the cycled cell in an effort to understand and mitigate the failure modes.

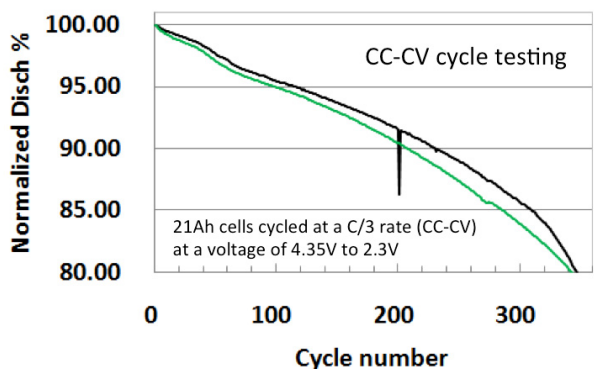


Figure II- 5: CC-CV cycling of baseline 21Ah pouch cells

development partners and a careful postmortem analysis will be central to the effort, and critical for the success of the project.

FY 2015 Publications/Presentations

1. “High Energy Lithium Batteries for Electric Vehicles”, ES247_Lopez_2015_p, US DOE Vehicle Technologies Program Annual Merit Review, AMR, 2015.

Conclusions and Future Directions

Envia will continue to use a system-level approach to screen, develop and optimize the critical material and cell components (cathode, anode, electrolyte, separator), prelithiation, cell design (N/P ratio, electrode design) and cell formation and testing protocols that will enable meeting USABC EV cell targets. Development has started on all fronts and will continue with the goal of down-selecting the best materials, components and processes to integrate in the upcoming cell build iteration #2 scheduled for Q1 in FY 2016. Close interaction with all the

II.A.2 Development of a High Energy Density Cell and Module for EV Applications (LG Chem Power, Inc.)

Objectives

- Development of a high energy density, low-cost cathode material to meet the requirements of the USABC targets for long-range EV battery.
- Development of a high capacity Si-based anode that is capable of long cycle-life.
- Understanding/optimization of high capacity electrode structures that will enable manufacturing low-cost, long-life EV batteries.
- Fabrication and testing of modules with high capacity cathodes and Si-based anodes using a suitable thermal management system. Since cells using Si anodes are expected to undergo considerable volume changes, the objective is to develop a mechanical structure effective in retaining the cells as well as thermally managing them to prolong life and abuse-tolerance.

Project Details

Chulheung Bae (USABC Program Manager)
DE-EE0006250 Recipient: LG-CPI

Mohamed Alamgir (LG Chem Power - PI)
LG Chem Power, Inc.
1857- Technology Drive
Troy, MI 48083
Phone: 248-29-2375
Email: alamgir@lgcpi.com

Subcontractor:
LG Chem
LG Chem Research Park
104-1, Moonji-dong, Yuseong-gu
Daejeon 305-380, South Korea

Start Date: February 2015

Projected End Date: January 2018

Technical Barriers

- Development of a high capacity cathode that has long cycle- and calendar-life, and is low cost and abuse-tolerant.
- Development of a Si-based anode that has high capacity and long cycle-life.
- Ability to produce high capacity electrodes which have sufficient power to support long-range EV.
- Meeting the USABC energy density goal of 1000 Wh/l and the cost target of \$100/kWh.

Technical Targets

- Usable energy density of 640 Wh/l.
- Cycle-life of 1,000.
- Cell cost target of \$100/kWh.

Accomplishments

- Studies to improve the durability of Mn-rich cathode materials using scaled-up ALD coating technologies.
- Synthesis and characterization of doped Mn-rich cathode to improve cycle-life and voltage fade.
- Studies to eliminate gassing in Mn-rich cathode materials especially when charged to high voltages.
- Comparative studies of Si-based anode materials such as SiO₂, Si alloy and Si-carbon composites.
- Studies with large capacity pouch cells and high loading of SiO₂.
- Studies to develop high loading electrodes.

Introduction

The development of a high energy-density, low-cost EV battery fulfilling USABC requirements necessitates the use of a very high capacity cathode material as well as a high energy density anode material. A survey of the current crop of cathode and anode materials having the potential to meet the performance, life and cost targets shows that high energy density cathodes such as Li-rich NCM and Si-based anodes are the most

attractive choices for this purpose. The current program is aimed at utilizing these electrode materials for achieving those objectives.

Approach

In order to achieve the program objectives, the following key approaches will be pursued.

- Use of high capacity NCM cathodes – this will entail both Mn-rich and high Ni content cathode materials.
- Use of a high capacity Si-based anode that has the best cycle-life.
- Development of a high loading electrode to realize a high energy density.

Results

The following is a summary of the progress we have made this year.

Cathode Development

We are pursuing two approaches to develop a long-life, high capacity cathode material.

- Use of Mn-rich NCM
- Use of Ni-rich NCM

Although the Mn-rich NCM has a very high capacity (~250 mAh/g), when charged to high voltages such as 4.6V, it also has several well-known drawbacks. These include poor life due to the dissolution of Mn^{2+} when charged to high voltages, gassing, voltage fade as well as low power at low SOC. The life issue has been considerably improved when certain coatings are used. The improvement is significant when the coatings are applied using ALD which ensures a controllable coating. In this project, we are trying to optimize the conditions for coatings of large amounts of powders. The data (on the next page) in Figure II- 6 show the potential of the ALD coating to improve the cycle-life of the Mn-rich cathode. The cell #4 showed higher capacity retention than the baseline cells. We are continuing this work using a larger batch of cathode powders to examine the impact of scaling-up of the ALD process on performance.

We are also studying the effect of the ALD coating on the capacity and durability of Ni-rich NCM cathodes. Initial data presented in Figure II- 7 show that the capacity and the rate capability of the cells are not significantly affected by the coating. The cells will next be subjected to durability studies.

We are also studying the effect of doping on the durability especially the voltage fade issue of the Mn-rich cathode. Current data seem to show some of this effect but further studies are necessary to confirm the results.

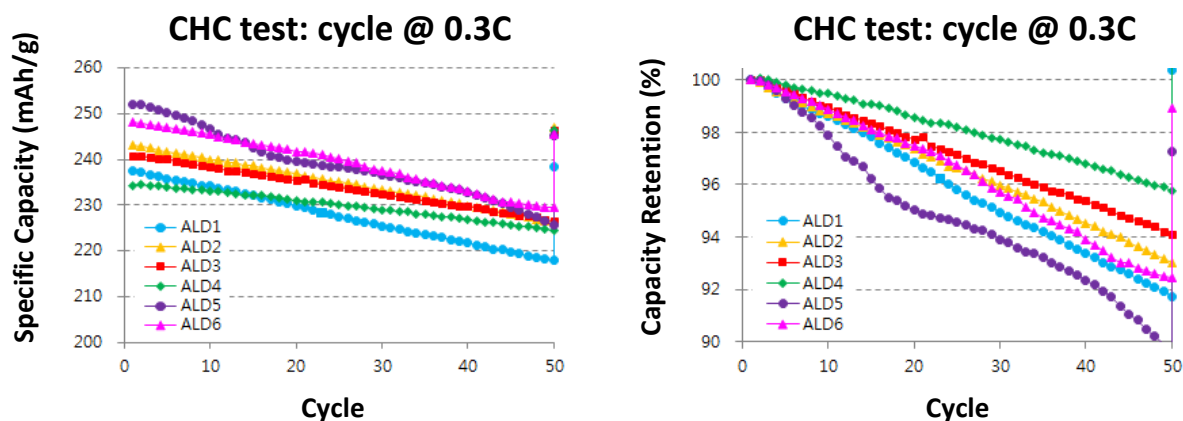


Figure II- 6: Effect of ALD coating on the cyclability of Mn-rich NCM. The numbers refer to different coating conditions

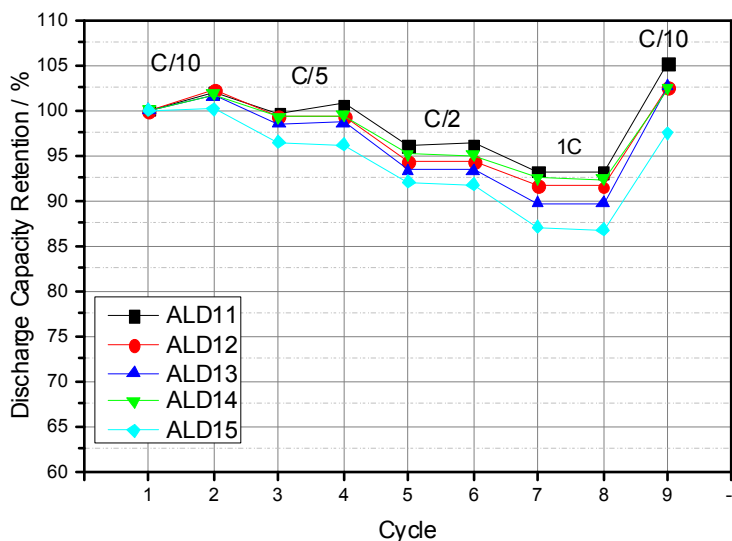


Figure II- 7: Effect of ALD coating Ni-rich NCM cathode. The numbers refer to different coating conditions

Si-anode Development

We are exploring various Si-anode options to develop an anode that has high energy density, undergoes less volumetric expansion and is also low-cost. Among the several candidates studied, SiO appears to show the lowest expansion, while Si-carbon composite shows the highest (Figure II- 8). We note here that our preliminary studies have been carried out with relatively low levels of Si-based anode materials so that the realized capacities are below ~600 mAh/g.

Managing the volume expansion of Si-based electrodes is a key requirement for ensuring the cycle-life and hence in order to

identify electrode characteristics optimum for durability, we have been investigating various properties of the Si electrodes. Figure II- 9 shows the effect of different electrode porosities on cycle-life. The data show that at a low electrode porosity (high calendaring pressure), the cell cycles quite poorly.

Despite the challenges, we do see good opportunities for optimizing various cell parameters to ensure good durability for the Si-based cells. We demonstrate this by using the example in Figure II- 10 which shows that depending on the type of Si anode used, one could obtain a reasonable cycle-life. While the Si-alloy based cell delivered fewer than 400 cycles with about a 60% rise in resistance, those using SiO delivered close to 1000 cycles with less than a 10% rise in resistance. Again, these data were obtained at low discharge rates and (as mentioned above) at low levels of SiO loadings.

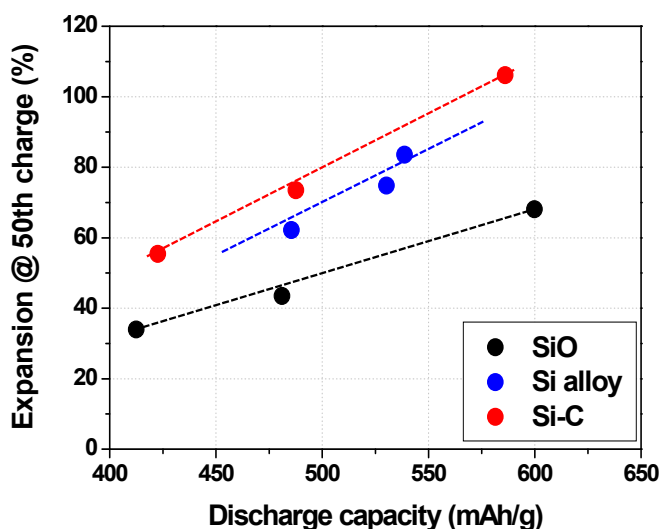


Figure II- 8: Comparison of the expansion of various Si-based electrodes. The data are for cells after the 50th charge

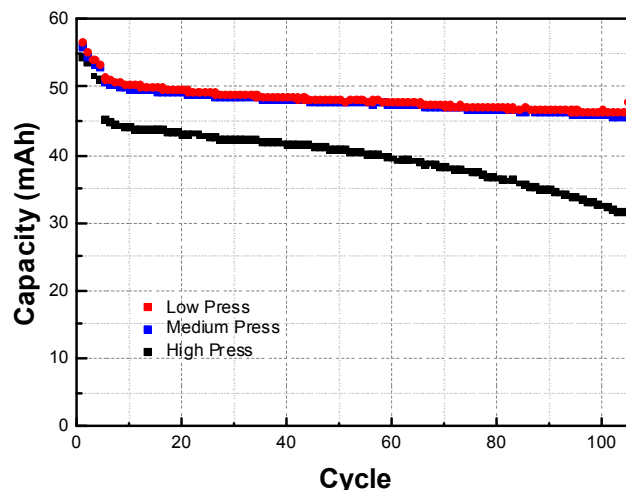


Figure II- 9: Effect of SiO electrode porosity on cycle-life

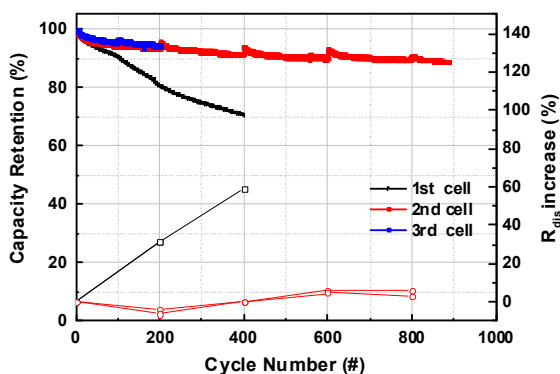


Figure II- 10: Comparison of the cycle-life of Si-alloy and SiO-based full cells at room temperature and 0.3C rate

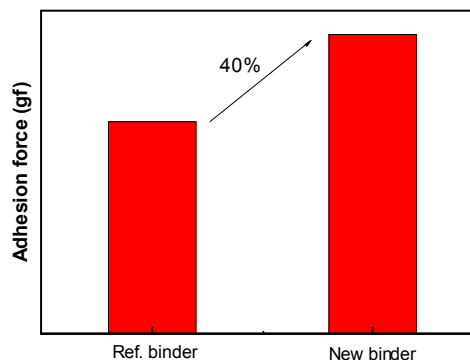


Figure II- 11: Comparison of the adhesion force of two cathode binders

Studies to Develop High Loading Electrodes

It is imperative that one develops electrodes having a high loading to increase the energy density and to reduce the cell cost. With that objective in mind, we have been examining various ways to develop high energy density electrodes. For example, to be able to fabricate a thick, high capacity electrode, an efficient binder system with enhanced adhesion properties is necessary. An example of such a binder is given in Figure II- 11 for the cathode. The data show that the new binder shows a ~40% higher adhesion force than the reference binder.

Conclusions and Future Directions

Future work will improve upon the cathode and anode life characteristics by using the approaches outlined above. In particular, coating/doping and use of suitable electrolyte will be continued to improve cell durability and gassing that plagues the Mn-rich cathode. Si-based anodes will be optimized with respect to loading level, durability and mechanical expansion.

Significant effort will also be devoted to fabricating high capacity electrode to increase the energy density. This will include extensive physico-chemical characterization of high loading electrodes.

Cells made by using the most optimized cathode/anode from the above studies will be built into modules to characterize their thermo-mechanical behavior in order develop an optimized mechanical and thermal management system that will be robust with respect to life and abuse-tolerance.

FY 2015 Publications/Presentations

No publication/presentation in 2015.

II.A.3 Advanced High-Performance Batteries for Electric Vehicle (EV) Applications (Amprius)

Objectives

- Amprius is working on a three-year, anode-focused USABC project to develop/deliver vehicle-size cells that meet the USABC's technical requirements. Throughout the project, Amprius will improve its silicon nanowire anode material and cell performance in a baseline cell and transfer learnings to larger cells. At the project's end, Amprius will deliver ~40 Ah cells with end of life specific energies of 350 Wh/kg and energy densities of 750 Wh/L.

Project Details

Al Masias (USABC Program Manager)
DE- EE0006250 Recipient: Amprius, Inc.

Ionel Stefan (Amprius, Inc. – PI)
225 Humbolt Court
Sunnyvale, CA 94089
Phone: 800-425-8803; Fax: 866-685-7420
Email: ionel@amprius.com

Start Date: January 2015
Projected End Date: January 2018

Technical Barriers

- The project addresses the key performance and production challenges to the commercialization of high-capacity cells and batteries with silicon nanowire anodes. The following barriers are addressed:
 - Energy: Low Wh/kg & Wh/L.
 - Cycle Life: < 1,000 Cycles.
 - Size: Small Anodes and Cells.
 - Cost: High \$/kWh.

Technical Targets

- Deliver cells that meet USABC EV battery goals. Amprius will deliver high-capacity pouch cells at the conclusion of the project's first, second and third years. Idaho National Laboratory will independently test the performance and safety of Amprius cells according to USABC's test protocols.
- Available Energy Density @ C/3 Discharge Rate: 750 Wh/L.
- Available Specific Energy @ C/3 Discharge Rate: 350 Wh/kg.
- DST Cycle Life: 1,000 Cycles.
- Peak Discharge Power Density, 30 s Pulse: 1500 W/L.
- Peak Specific Discharge Power, 30 s Pulse: 700 W/kg.
- Peak Specific Regen Power, 10 s Pulse: 300 W/kg.
- Calendar Life: 15 Years.
- Selling Price @ 100K units: \$100.
- Operating Environment: -30°C to +52°C.
- Normal Recharge Time: < 7 Hours.
- High Rate Charge: 80% ΔSOC in 15 min.
- Peak Current, 30 s: 400 A.
- Unassisted Operating at Low Temperature: > 70% Useable Energy @ C/3 Discharge Rate at -20°C.
- Survival Temperature Range, 24 Hr: -40°C to+ 66°C.
- Maximum Self-discharge: < 1%/month.

Accomplishments

- Designed the project's baseline, Year 1 cells, to achieve a target capacity of 2.4 – 3.2 Ah.
- Built Silicon-NCM cells with average capacities of 2.7 Ah, specific energies of 310 Wh/kg, and energy densities of 712 Wh/L.
- Built Silicon-LCO cells with average capacities of 2.8 Ah, specific energies of 329 Wh/kg, and energy densities of 808 Wh/L.

- Tested cycle life. The Silicon-NCM cells that Amprius tested continue to exhibit stable DST cycling; at the end of October 2015, the cells had achieved 400 cycles. The four Silicon-LCO cells tested also continue to exhibit stable cycling; at the end of October 2015, the cells had achieved 100 cycles.
- Exceeded numerous USABC performance goals. Amprius' ~2.7 Ah Silicon-NCM cells exceeded USABC's targets for peak discharge power density and peak specific discharge power. Amprius' ~2.8 Ah Silicon-LCO cells exceeded USABC's targets for available energy density, peak discharge power density, peak specific discharge power, peak specific regen power, and survival temperature range.
- Reduced the main gap in performance, cycle life, by tuning anode structure and identifying electrolyte additives that improve solid electrolyte interphase (SEI) stability and extend cycle life.
- Sourced and tested advanced cell components (e.g. separators) and cathode materials.
- Designed the project's interim, Year 2 cells, to achieve a target capacity of ≥ 10 Ah. Began to make hardware changes to prepare for building larger anodes and the project's interim, Year 2 cells.

Introduction

Current lithium-ion cells have only a limited room to improve specific energy or energy density; their active materials – a graphite anode paired with one of several commercially available cathodes – are used at energy capacities close to their theoretical limits and their packaging has already been optimized. New active materials are needed to boost performance and extend driving range.

Silicon has significant potential as a new anode material; silicon offers nearly 10 times the theoretical energy capacity of graphite. However, when charged with lithium ions, silicon swells up to four times its volume, causing capacity fade and mechanical failure. Because of the swelling, conventional approaches for silicon anodes have not produced cells with the long cycle life required for electric vehicle applications.

Approach

Innovative Approach: Amprius possesses an innovative silicon technology – an anode made of silicon nanowires – that is capable of addressing the silicon swelling and thus meeting USABC's commercialization criteria. Amprius' technology is unique in three respects: (1) material, (2) structure, and (3) results. First, Amprius' anode material is made of silicon rather than graphite or a graphite-silicon composite. Second, Amprius' anode structure is composed of nanowires rather than particles. Third, Amprius has demonstrated both a high energy and a long cycle life in full cells with silicon nanowire anodes.

Amprius' unique, patent-protected material and structure – nanowires that are “growth-rooted” (i.e. grown directly on the current collector, without binders) – address swelling by enabling silicon to successfully expand and contract internally. Because the nanowires are attached to the current collector, Amprius does not rely on particle-to-particle contact and is able to achieve not only a long cycle life, but also a high electrical conductivity and power.

Before the USABC project, Amprius achieved >700 Wh/L at start of life and >400 C/2 cycles at 100% depth of discharge (DOD). To meet USABC goals, Amprius will:

- Increase specific energy and energy density by tuning the anode structure and using advanced components (e.g. thinner substrates and separators). Amprius may also transition from LCO to a different commercially available cathode material (e.g. NCM or a higher-voltage LCO).
- Extend cycle life by optimizing anode structure and identifying and/or developing electrolyte formulations that improve Solid Electrolyte Interphase (SEI) stability and cell performance.
- Increase anode and cell size by developing methods for (1) handling larger anodes; (2) improving the uniformity of silicon growth and deposition technologies; (3) reducing defect density; and (4) utilizing manufacturing methods that inherently scale to larger dimensions

Results

Amprius has made the following progress:

Designed the Project’s Baseline, Year 1 Cells to Achieve a Target Capacity of 2.4 – 3.2 Ah

Amprius designed the baseline cell to include 16 layers of silicon nanowire anodes, a 10 μm ceramic coated separator, a 10 μm anode foil and a 12 μm cathode foil. Amprius’ design will enable production of cells with target capacities of 2.4 - 3.2 Ah (depending on the cathode’s voltage and reversible capacity loading).

Built Silicon-NCM Cells Averaging 2.7 Ah, 310 Wh/kg and 712 Wh/L

Amprius built 36 Silicon-NCM cells with average capacities of 2.7 Ah, specific energies of 310 Wh/kg, and energy densities of 712 Wh/L. The standard deviations of the cells’ capacities and energies was < ~4.0%.

Built Silicon-LCO Cells Averaging 2.8 Ah, 329 Wh/kg and 808 Wh/L

Amprius built 18 Silicon-LCO cells with average capacities of 2.8 Ah, specific energies of 329 Wh/kg, and energy densities of 808 Wh/L. The range of the cells’ capacities and energies was < ~2.5%. (See Figure II- 12, Figure II- 13, Figure II- 14, and Figure II- 15.)

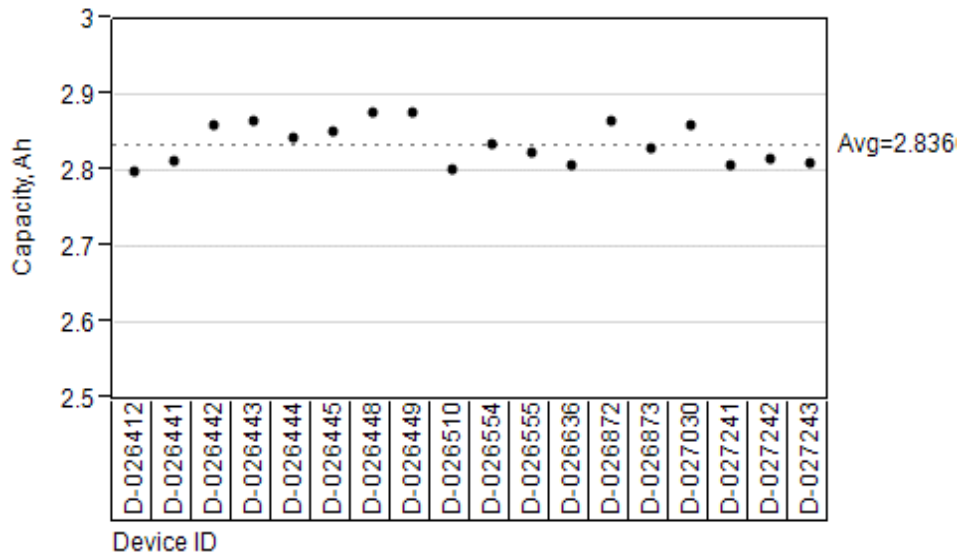


Figure II- 12: Capacities of Amprius’ 18 Silicon-LCO Cells

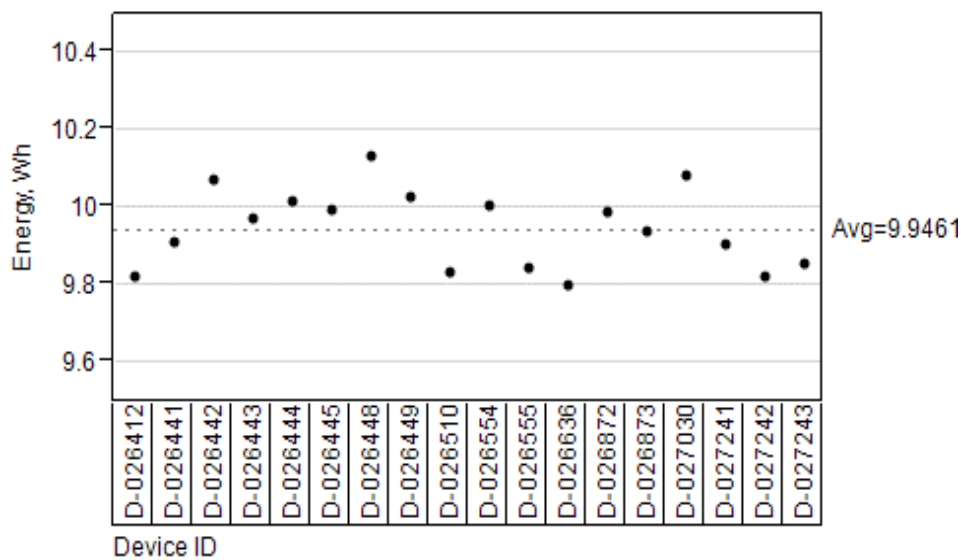


Figure II- 13: Energies of Amprius’ 18 Silicon-LCO Cells

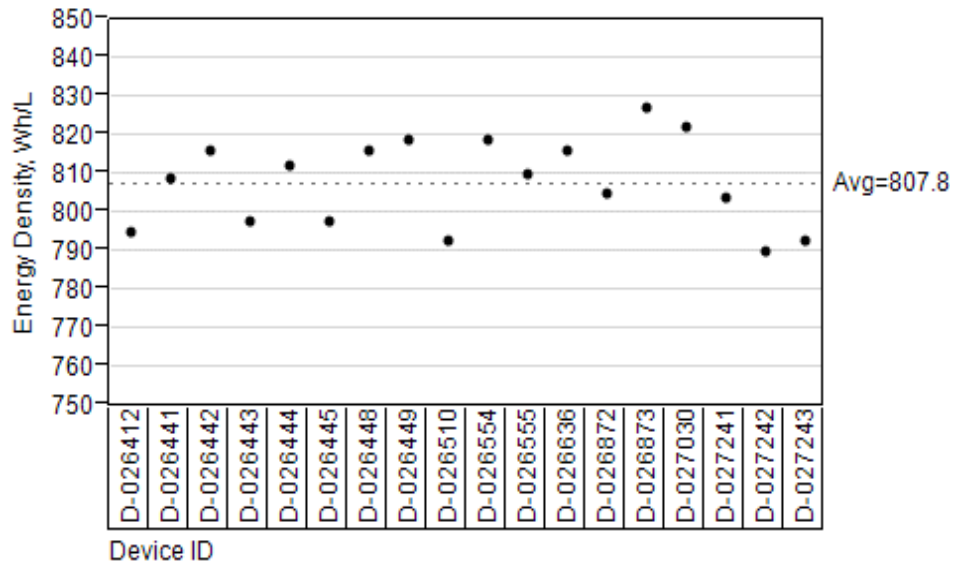


Figure II- 14: Energy Densities of Amprius' 18 Silicon-LCO Cells

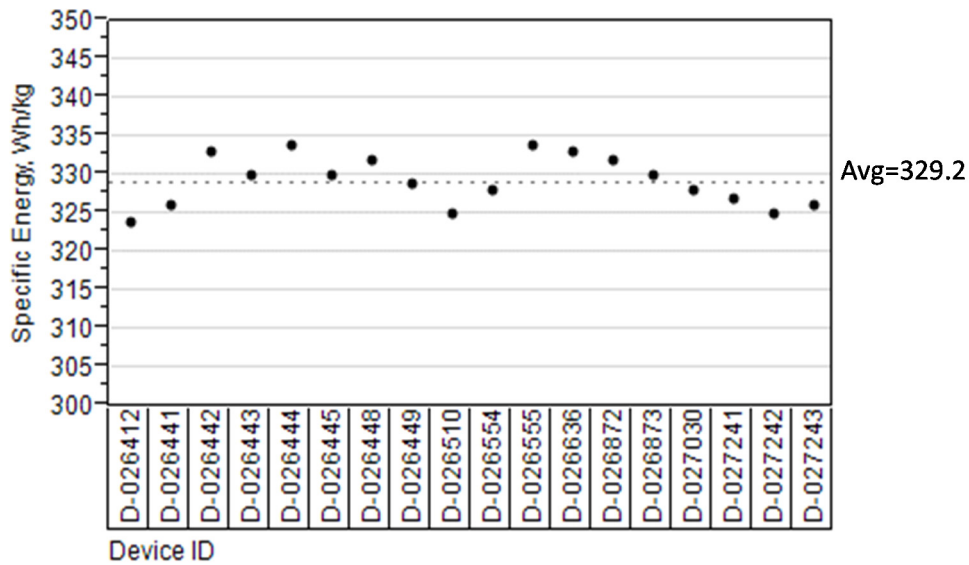


Figure II- 15: Specific Energies of Amprius' 18 Silicon-LCO Cells

Tested Cycle Life and Demonstrated Stable Cycling to 400 Cycles (and Counting)

The Silicon-NCM cells Amprius tested continue to exhibit stable cycling; at the end of October 2015, the cells had achieved 400 cycles. The Silicon-LCO cells tested also continue to exhibit stable cycling; at the end of October 2015, the cells had achieved 100 cycles. (See Figure II- 16.)

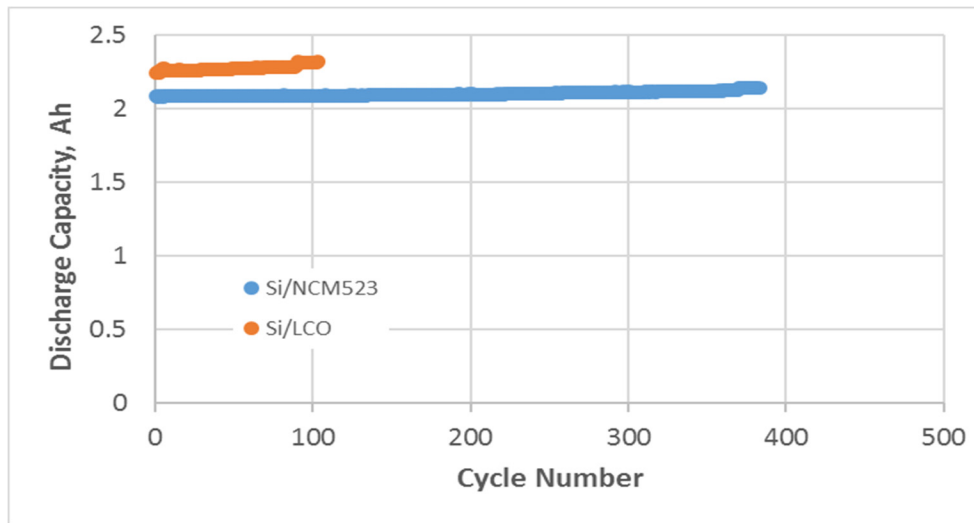


Figure II- 16: Amprius’ cells continue to cycle. Amprius’ Silicon-NCM cells continue to exhibit stable cycling past 400 cycles. Amprius’ Silicon-LCO cells also continue to exhibit stable cycling past 100 cycles

Exceeded Numerous USABC Performance Goals

Amprius’ ~2.7 Ah Silicon-NCM cells exceeded USABC’s targets for Peak Discharge Power Density and Peak Specific Discharge Power. Amprius’ ~2.8 Ah Silicon-LCO cells exceeded USABC’s targets for Available Energy Density, Peak Discharge Power Density, Peak Specific Discharge Power, Peak Specific Regen Power, and Survival Temperature Range. Amprius continues to evaluate whether the company’s Silicon-NCM and Silicon-LCO cells meet the USABC’s other performance and safety targets. (See Figure II- 17, Figure II- 18.)

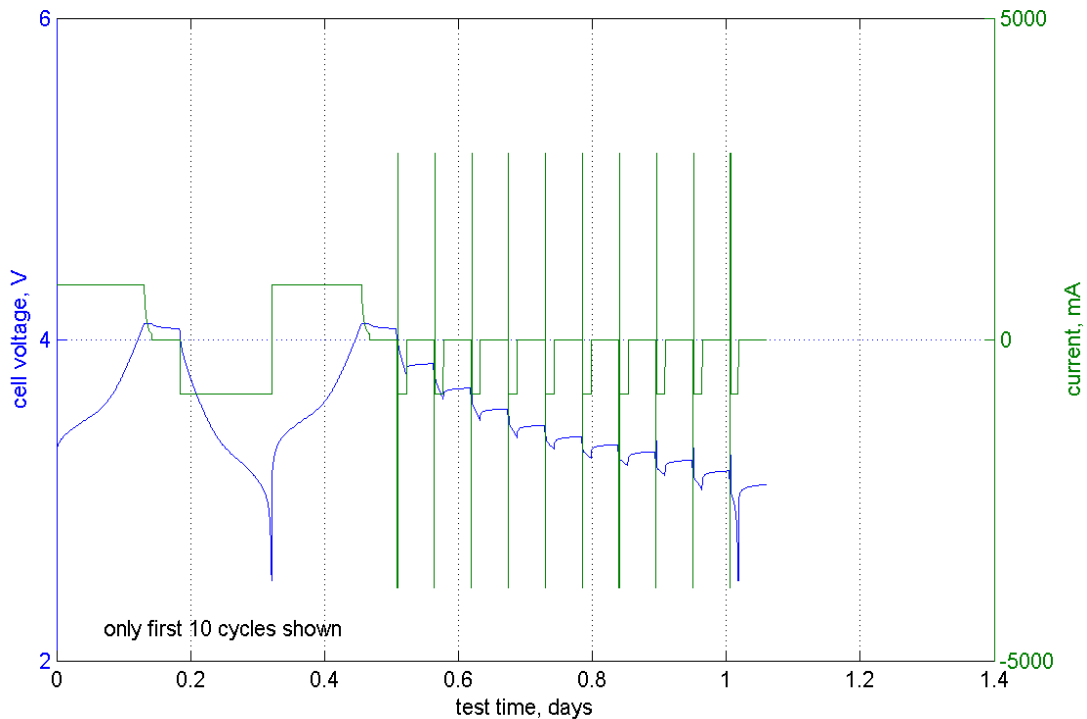


Figure II- 17: Voltage and Current Profiles from the HPPC Test, which Amprius’ Silicon-NCM Cells Passed

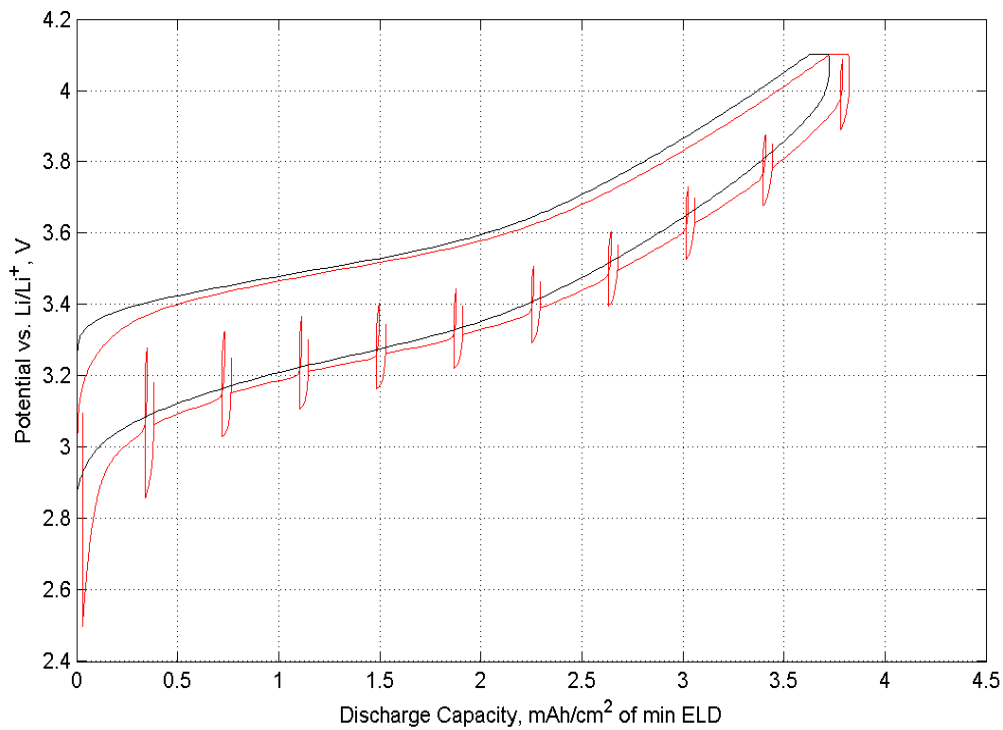


Figure II- 18: Potential-Capacity Curves from the HPPC Test, which Amprius' Silicon-NCM Cells Passed

Extended Cycle Life by Tuning Anode Structure and Identifying New Electrolyte Formulations

Amprius extended cell cycle life by optimizing anode structure, improving silicon surface chemistry, and identifying and/or developing new electrolyte formulations that improve Solid Electrolyte Interphase (SEI) stability and cell performance. (See Figure II- 19, Figure II- 20.)

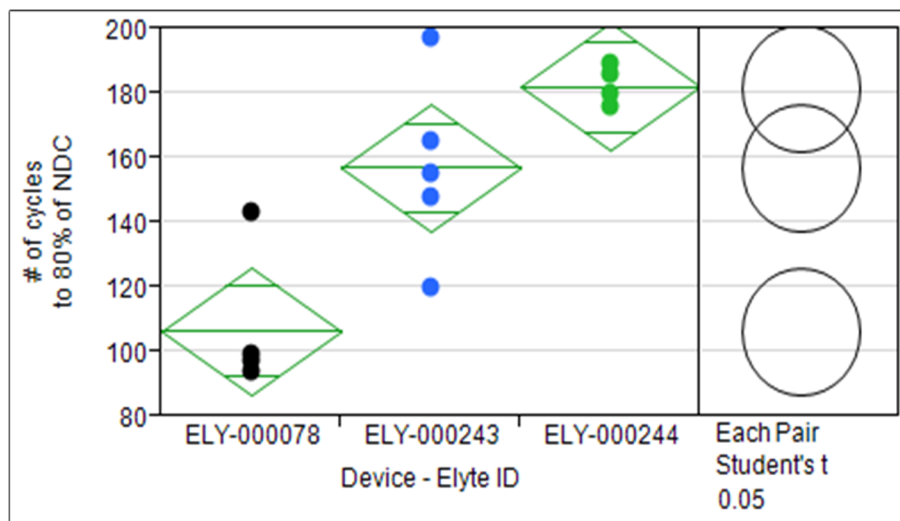


Figure II- 19: Amprius identified solvent compositions that extend the cycle lives of cells with silicon nanowire anodes

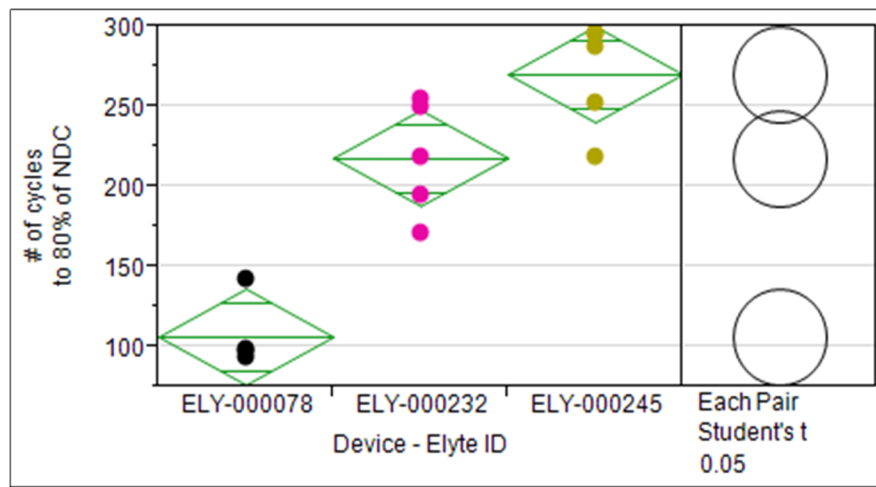


Figure II- 20: Amprius identified electrolyte additives that extend the cycle lives of cells with silicon nanowire anodes

Sourced and Tested Advanced Cell Components (e.g. Separators) and Cathodes

Amprius sourced and tested NCM powders from four vendors, LCO powders from two vendors, separators from three vendors, and electrolytes from two vendors. Amprius also evaluated other advanced cathodes. Amprius will select and use the best-performing components and materials to build the Year 1 cell deliverables that will be due to the Idaho National Laboratory.

Designed the Project's Interim, Year 2 Cells to Achieve a Target Capacity ≥ 10 Ah

Amprius designed the project's interim, Year 2 cells, to achieve a target capacity of ≥ 10 Ah. Amprius designed the interim cells to include 30 layers of larger silicon nanowire anodes. The anodes for the interim Year 2 cells will be of the same width, but twice the length, as the anodes for Amprius' baseline Year 1 cells. Amprius also began to make hardware changes to prepare for building the project's interim Year 2 cells. (See Figure II- 21.)

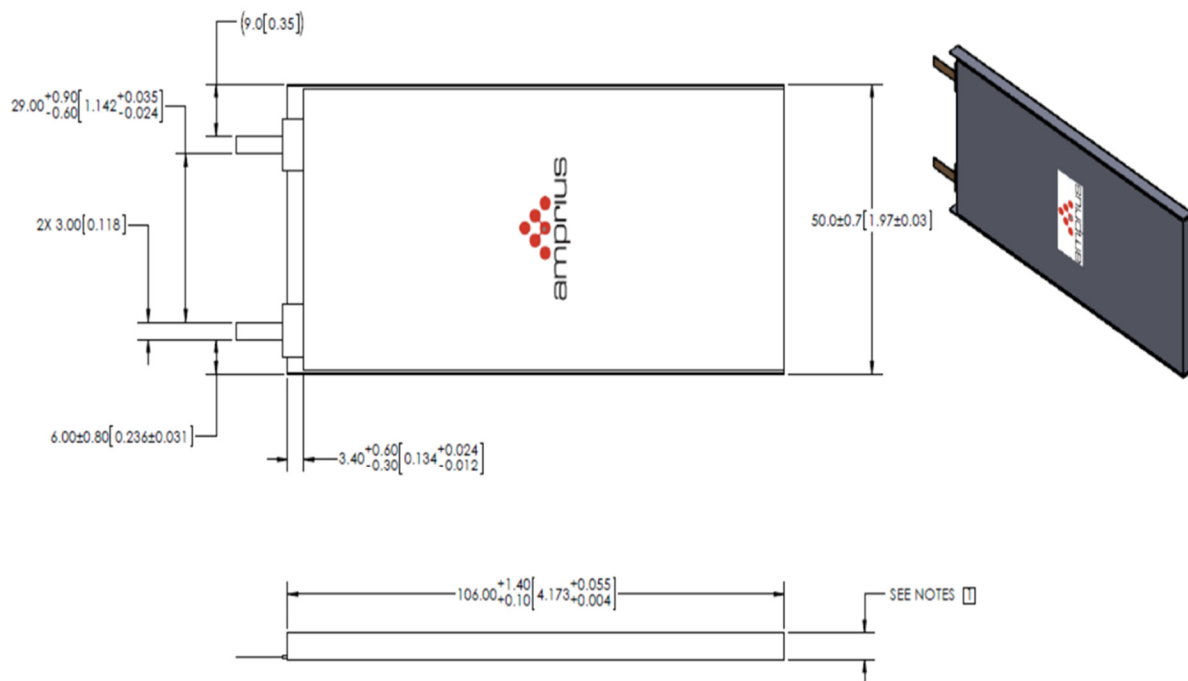


Figure II- 21: Amprius' design for the interim, Year 2 cells, with a target capacity of at least 10 Ah

Conclusions and Future Directions

During the project's first nine months, Amprius made significant progress increasing cell energy, extending cell cycle life and demonstrating that its silicon nanowire-based cells exceed USABC's power goals. During the project's next three months, Amprius will build and deliver > 2 Ah cells for independent testing at Idaho National Laboratory.

During Year 2, Amprius will continue to (1) increase cell energy by optimizing anode structure and exploring advanced components, (2) extend cell cycle life by tuning anode structure and testing new electrolyte formulations, and (3) finish making hardware changes and start building larger anodes and the project's interim cells with capacities ≥ 10 Ah.

FY 2015 Publications/Presentations

None

II.A.4 EV Technology Assessment Program (Seeo)

Objectives

- The goal of this USABC/DOE program is to gain a better understanding of Seeo's proprietary solid-state battery technology that operates cells at elevated temperatures between 70 and 90°C. Seeo has developed battery module and pack technology to control internal cell temperatures, while providing a standard interface for delivering power to an electric vehicle.

Project Details

Harshad Tataria (USABC Program Manager)

DE-EE0006250 Recipient: Seeo, Inc.

Scott Mullin (Seeo, Inc. – PI)

3906 Trust Way

Hayward, CA 94545

Phone: 510-244-5123; Fax: 510-782-7337

Email: smullin@seeo.com

Start Date: October 2014

Projected End Date: July 2015

Technical Barriers

- Demonstrate and evaluate performance of solid-state batteries with Li-metal anodes.
- Demonstrate capability of module technology to operate cells at warm temperatures (80°C internal) with ambient temperature of 30°C.

Technical Targets

- Module with >11 Ah and > 1800 Wh at C/3.
- Perform a series of defined USABC tests at Argonne National Laboratory (ANL), National Renewable Energy Laboratory (NREL) and Sandia National Laboratory (SNL).

Accomplishments

- Built a total of six 1.8 kWh modules and six Single-Module Thermal Chambers (SMTCs) and delivered three modules and three SMTCs to ANL.
- Completed characterization testing program at ANL. Results summarized here are all with 80°C internal, 30°C ambient.
- Accessed 11.4 Ah at C₃/3 (average from 6 modules).
- Module-level energy of 1807 Wh, and specific energy of 144 Wh/kg (actual module weights) or 141 Wh/kg (max rated weights) (averages from 6 modules). Equates to 154 Wh/L.
- Module-level specific peak-power discharge of 241 W/kg or 258 W/L (from actual module values).
- Completed 150 DST₂₂₅ (module-level) cycles, with peak-power results linearly extrapolating to end-of-life past 1600 cycles (80% of original capacity).
- Demonstrated that core technology is capable of completing US06 profiles at 438 W/kg or 479 W/L (module-level).
- Stand test results and calculations predict a 32.4 kWh pack in a 2S9P configuration could retain >50% of its internal energy after 30 days of self-heating with 1.2 to 1.8" of insulation paneling.
- Testing at the National Renewable Energy Laboratory (NREL) and the Sandia National Laboratory (SNL) are scheduled to be performed by the end of 2015.

Introduction

Solid-state batteries with lithium metal anodes are viewed as the next-generation battery technology. Seo has scaled this technology up to 11 Ah cells and integrated those cells into a module with the required battery management system and mechanical enclosure that manages the cells at an elevated temperature. This technology assessment program (TAP) was intended to demonstrate the performance and viability of this technology with testing at Argonne National Laboratory (ANL), National Renewable Energy Laboratory (NREL) and Sandia National Laboratory (SNL)

Approach

The TAP program was executed in two consecutive phases

- Phase 1: Module Build and Delivery – Build six modules and six single-module thermal chambers (SMTCS), and then deliver three modules and three SMTCs to USABC for testing.
- Phase 2: Module Testing – Perform at three national labs: Argonne National Lab (ANL), National Renewable Energy Laboratory (NREL) and Sandia National Laboratory (SNL), and perform parallel testing on modules at Seo. The test plans are summarized as follows:
 - ANL will perform characterization testing, including constant-current discharge rate tests ($C_3/3$, $C_3/2$, $C_3/1$), dynamic stress test (DST) discharges to 100% DOD, peak power determination from 0 to 90% DOD, 80% DOD DST cycle life (200 cycles with reference performance tests (RPTs) every 50 cycles), and fast charge testing.
 - NREL will perform thermal testing, including freeze/thaw (three cycles, from -40 to 80°C) and thermal imaging.
 - SNL will perform abuse testing, including thermal ramp to 150°C on one module, and overcharge to 200% SOC on one module.
 - Seo will perform characterization testing, as well as US06 drive cycle discharge characterization, and a stand test at 80°C internal (untethered).



Figure II- 22: (left) Seo 1.8 kWh module. (right) Seo Single-Module Thermal Chamber (SMTC)

The modules for this program contained 48 cells in series, and include internal heaters for temperature control and electronics for cell and module management (see Figure II- 22). In addition to the modules, Seo provided six single module thermal chambers (SMTCs). The SMTC is a test fixture that is designed to retain heat while the module is at elevated temperature. During some usage scenarios, internal heat generation causes the module to self-heat. In these scenarios, the

SMTC monitors the module temperature and provides active cooling as needed. To provide cooling, the SMTC retracts its mechanically-actuated side panels and turns on its internal fans to force air over the module. This air cooling strategy maintained the modules within operating bounds for all tests within this program.

Results

The results for each characterization test are described and discussed under each of the sub-headings below. Test preparations are still being made at NREL and SNL. Final results from both labs are expected in Q4 2015.

Discharge characterization – constant-current rate tests and DST_{225}

ANL received three modules and measured their weights. These modules are identified herein as numbers 1, 2 and 3. The three modules remaining at Seo are referenced as 4, 5 and 6. The module weights are specified as 12.8 kg max. ANL reported average and standard deviation as 12.54 ± 0.07 kg for modules 1, 2 and 3, while Seo reported 12.56 ± 0.08 kg for modules 4, 5 and 6 (the module specification is 12.8 kg max). The first test

sequence is a rate test referenced to the C/3 capacity (denoted C₃). Three rates were tested (sequenced in order of increasing rate: C₃/3, C₃/2, C₃/1), with three discharges performed at each rate. Example voltage profiles at each C-rate are shown in Figure II- 23 below. The C/3 and C/2 discharge curves have fairly flat voltage responses and achieve approximately the same capacity access. The 1C curve exhibits more pronounced polarization. DST₂₂₅ discharges (225 W/kg with respect to the 12.8 kg maximum module rated weight) were performed to 100% DOD. The capacities measured for all of these tests are given in Table II- 4. Module 4 was not fully characterized by Seo due to limited testing capability. The averages and standard deviations are also shown for each lab’s results at each C-rate. The results are all within overlapping statistical populations. ANL reported averages of 11.3 Ah for C₃/3, 11.2 Ah for C₃/2, 9.3 Ah for C₃/1, and 11.4 Ah for DST₂₂₅.

Table II- 4: Discharge characterization capacities for Seo modules. 80°C internal temperature, 30°C ambient environment

Module	C ₃ /3 capacity [Ah]			C ₃ /2 capacity [Ah]			C ₃ /1 capacity [Ah]			DST ₂₂₅ [Ah]
	1	2	3	1	2	3	1	2	3	
1	10.93	10.99		11.03	11.15	11.17	9.97	9.98	9.94	11.26
2	11.41	11.42		11.25	11.26	11.27	9.16	9.14	9.12	11.43
3	11.45	11.46		11.24	11.24	11.24	8.90	8.91	8.85	11.35
4	11.83									11.45
5	11.40	11.38		11.11	11.11	11.10				11.40
6	11.89	11.26		11.13	11.18	10.74				10.82
ANL	11.3 ± 0.3			11.2 ± 0.1			9.3 ± 0.5			11.4 ± 0.1
Seo	11.5 ± 0.3			11.1 ± 0.2			9.6 ± 0.4			11.2 ± 0.1
Combined	11.4 ± 0.3			11.2 ± 0.2			9.4 ± 0.4			11.3 ± 0.1

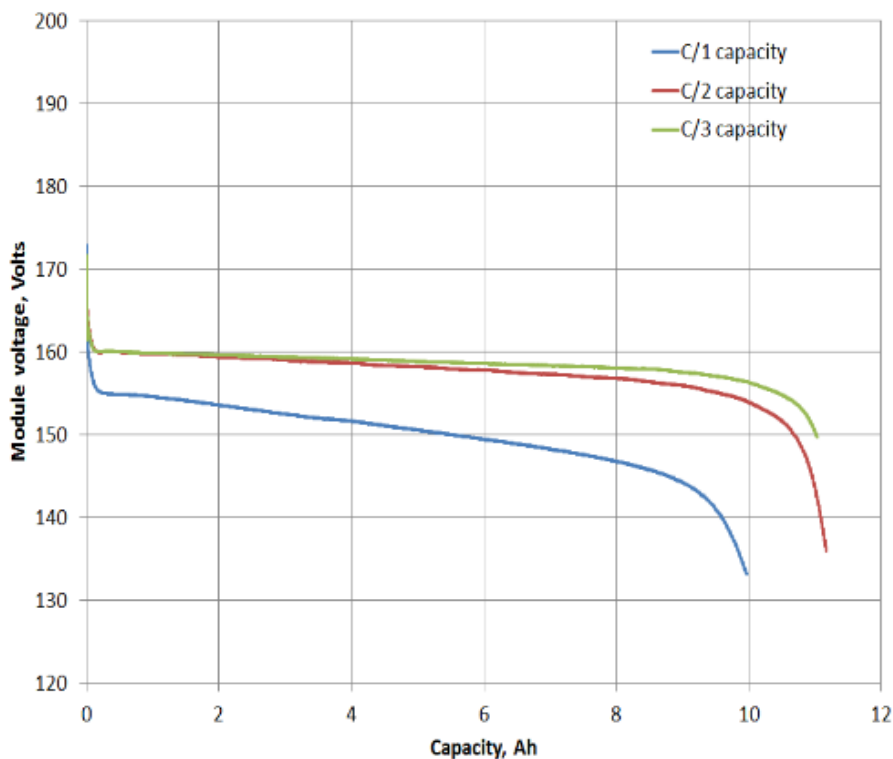


Figure II- 23: Constant-current rate test discharge curves for Seo modules. 80°C internal temperature, 30°C ambient environment

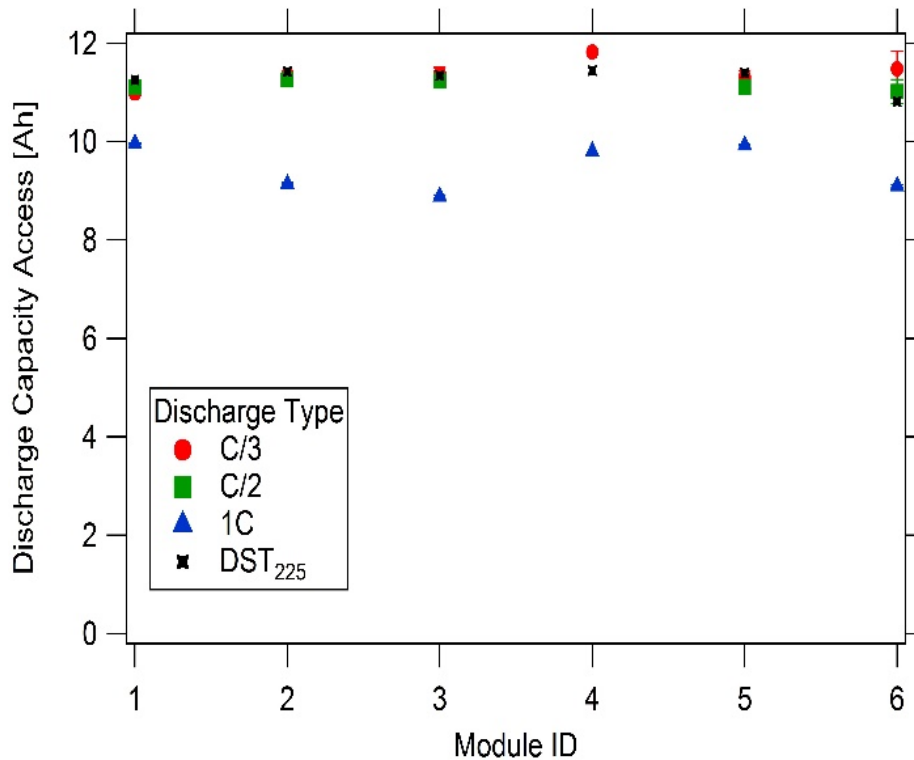


Figure II- 24: Discharge capacities for all characterization data reported by ANL (modules 1, 2 and 3) and Seo (modules 4, 5 and 6). Modules were tested with internal temperatures of 80°C, while in 30°C ambient environments

The C_{3/3}, C_{3/2}, and DST₂₂₅ results all exceed the module specification of 11 Ah. The discharge data for all six modules across all four characterization discharge tests is compared graphically in Figure II- 24. In this figure, each data point is plotted as average ± 1 standard deviation, as given in Table II- 4. For all modules, the C_{3/3} and C_{3/2} capacities were similar, but the C_{3/2} capacities were systematically lower as expected. The DST₂₂₅ capacities were also similar to the C_{3/3} capacities, and varied around the mean (above or below) for each module.

The module energy and energy density are rated at C_{3/3}. ANL reported 1747 Wh for module 1 at RPT0 (the initial RPT test), and subsequent ratings of 1833, 1820 and 1820 Wh at RPT1, RPT2, and RPT3, respectively (each after 50 80% DST₂₂₅ cycles). These values correspond to 136 Wh/kg initially (using the maximum rated weight of 12.8kg), to 143 Wh/kg at RPT1. The increase in energy from RPT0 to RPT1 is most likely due to the module balancing improving during the initial cycle period. ANL measured 1818 Wh and 1799 Wh average for modules 2 and 3, respectively. Seo measured modules 4, 5 and 6 to have 1891, 1820 and 1893 Wh, respectively. For all measurements combined, ANL measured 1790 ± 30 Wh and Seo measured 1828 ± 45 Wh. Combined, all measurements averaged across the six modules gave 1807 ± 45 Wh. This equates to module-level energy densities of 144 ± 3.8 Wh/kg using measured module weights.

Peak Power Characterization

Peak Power characterization results are discussed next. The test was run with a 3.143A baseline current and 22A pulses. The USABC test manual specifies (procedure 3, page 9 for detailed calculations) that three calculations should be performed on the Peak Power test data. These are denoted “(2/9)”, “Vlimit” and “Imax”. The weight used to calculate the specific power (W/kg) was the specified module weight (12.8 kg). The reported peak power value is determined as the minimum value of these three calculations. In all cases, the “Imax” calculation computes as the minimum. Imax is the maximum power specification provided by the manufacturer (Seo), which suggests that the technology is, in principle, capable of higher power output than the manufacturer specifies. Figure II- 25 shows all three calculated values as a function of DOD, as measured by ANL for module 1. The power capability is consistent across the full DOD range (0% to 90% DOD): the (2/9) and Vlimit outputs decrease about 35% as the cell is discharged, while the Imax output varies by about 5%. The reported or rated value of the Peak Power test is taken at 80% DOD. These results for modules 1, 2

and 3 are summarized in Table II- 5. The average rated peak pulse power was 240.9 ± 0.9 W/kg. The peak power test was part of the RPT sequence, along with C₃/3 discharge and DST₂₂₅ discharge.

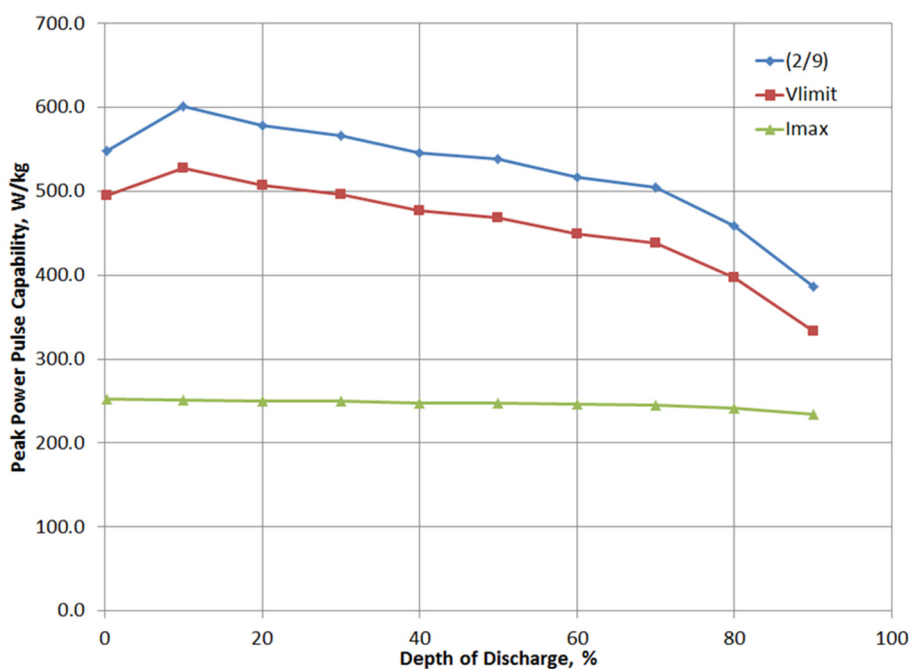


Figure II- 25: Peak Power results for module 1 at beginning of life (BOL), from 0% DOD to 90% DOD in 10% increments. Internal temperature was 80°C, external temperature was 30°C

DST₂₂₅ Cycle Life

After characterization testing, ANL performed DST₂₂₅ (2880 W peaks) cycle life testing on module 1. Note that the weight used is the Seo-specified weight of 12.8 kg (actual weights were slightly lower, as reported above). For the DST₂₂₅ cycle life testing, reference performance tests (RPTs) were conducted at the beginning of life, and also at 50 cycle intervals (approximately 20 days). The RPT included two C/3 discharges (100% DOD), one DST₂₂₅ discharge (100% DOD) and one Peak Power test. The bulk cycling included DST₂₂₅ discharges to 80% DOD based on the DST Ah rating. End-of-life (EOL) is defined as measuring capacity < 80% of the rated capacity as measured for the C/3 rate for the DST₂₂₅ profile (8.8 Ah), or measuring Peak Power < 2304 W (180 W/kg) at 80% DOD (80% of rated Peak Power). The RPT periods are numbered, starting at 0 for the initial (i.e. RPT0). As of September 30, 2015, RPT3 has been completed (after 150 DST₂₂₅ cycles), and the module is scheduled to complete 200 cycles and RPT4 in October 2015. The RPT results are summarized in Table II- 6.

Table II- 5: Peak Power results for modules 1, 2 and 3 at BOL, taken at 80% DOD. Internal temperature was 80°C, external temperature was 30°C

Pack	80% DOD peak pulse power - BOL						Reported (W/kg)
	(2/9) (W/kg)	V _{limit} (W/kg)	I _{max} (W/kg)	Measured (W/kg)	Res. (W/kg)	V _{irt} (V)	
1	439.3	384.2	240.5	240.1	1051.4	163.1	240.5
2	458.8	397.2	241.1	240.7	995.3	162.2	241.1
3	473.9	412.4	242.9	241.8	969.0	162.6	242.9

The C₃/3 and DST₂₂₅ capacity and energy results are shown graphically in Figure II- 26 and the peak power results are shown in Figure II- 27. The module capacity and energy both increase from RPT0 to RPT1, and then subsequently decrease slightly. The Peak Specific Discharge Power is initially 240.5 W/kg at RPT0, and fades to 236.3 W/kg at RPT3 (1.7% fade after 150 cycles). The Peak Discharge Power Density is initially 263.2 W/L at RPT0 and fades to 258.5 W/L at RPT3 (1.8% fade after 150 cycles). The data to-date suggests that the module is aging in a consistent manner.

Table II- 6: DST225 cycle life results for module 1, from initial measurements (RPT0) through cycle 150 (RPT4). Internal temperature was 80°C, external temperature was 30°C

Cycle	RPT	C/3 Capacity Ah	C/3 Energy Wh	DST Capacity Ah	DST Energy Wh	80% DOD 2/9 Power, W/kg	80% DOD Vlimit Power, W/kg	80% DOD Imax Power, W/kg	80% DOD measured Power, W/kg	80% DOD res milliohms	80% DOD Virfree V	Min Power, W/kg
0	0	11.031	1747.464	11.258	1744.635	439.3	384.2	240.5	240.1	1051.4	163.08	240.5
50	1	11.551	1833.789	11.414	1766.234	424.5	371.3	239.2	238.1	1088.0	163.08	239.2
100	2	11.488	1819.947	11.355	1750.195	408.4	356.7	237.4	236.6	1128.8	162.93	237.4
150	3	11.488	1819.67	11.271	1736.2	399.0	348.2	236.3	235.7	1154.4	162.87	236.3

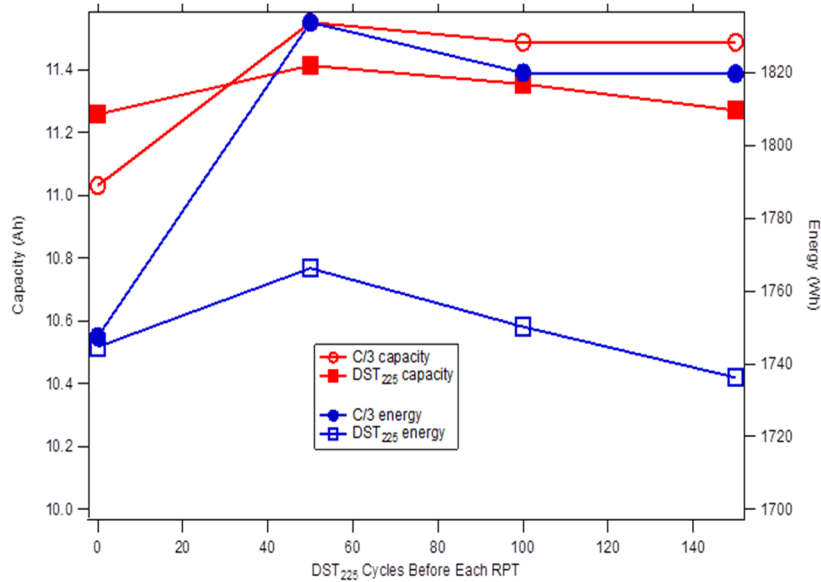


Figure II- 26: DST₂₂₅ cycle life RPT results – C₃/3 and DST₂₂₅ capacity and energy

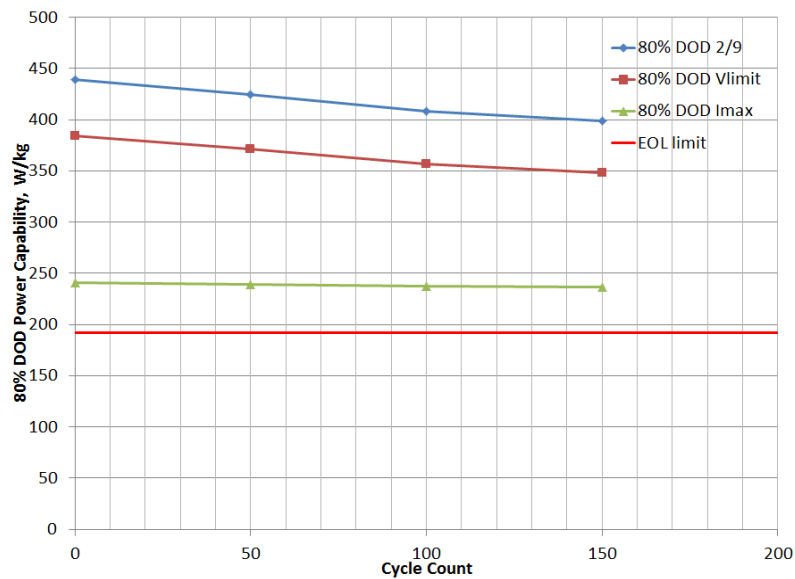


Figure II- 27: DST₂₂₅ cycle life RPT results – peak power at 80% DOD

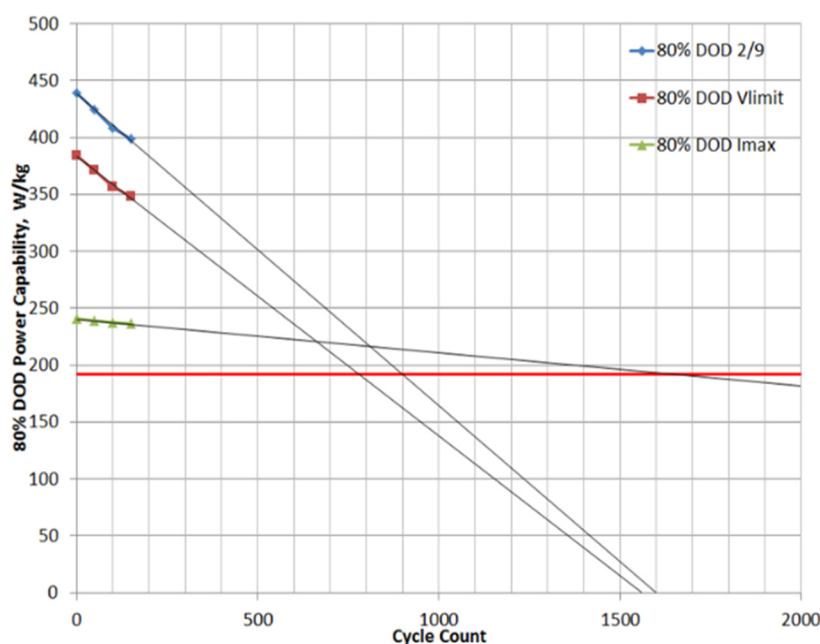


Figure II- 28: Peak power capability showing extrapolation towards the EOL limit (red line). Internal temperature was 80°C, external temperature was 30°C

The Peak Power results can be extrapolated to provide a predictive measure of the module life. Linear fits to the data between RPT0 and RPT3 and extrapolation to the EOL limit are shown in Figure II- 28. The EOL limit is based on the rated Peak Power (determined by the I_{max} calculation), such that the I_{max} linear prediction is the most consistent. The I_{max} EOL prediction is approximately 1600 cycles based on this data. For comparison purposes, the 2/9 and V_{limit} calculations extrapolate to the I_{max} EOL condition at approximately 900 and 775 cycles, respectively. It should be noted that the trends in the Peak Power data may not follow a linear fade trend, particularly at higher cycle numbers. It should also be noted that the Peak Power data up through RPT3 follow slightly curved trends (there is less fade between cycles 100 through 150 than between cycles 50 through 100).

Fast Charge

After completing characterization testing, Module 2 underwent ten DST₂₂₅ cycles, fast charge testing, and a follow-up RPT test. The DST₂₂₅ cycles were to 80% DOD, same as the cycle life module. The fast charge test was performed following procedure 12 of the USABC manual, as follows:

- Charge module to 100% SOC
- Discharge to 60% DOD at C/3 rate
- Immediately charge at fastest rate defined by the developer (5.5 A) until 40% of rated capacity (in Ah) is returned.
- Immediately discharge battery at C/3 rate to determine the amount of recharge available for use

Table II- 7: RPT results for Module 2 initially (RPT0) and after ten DST225 and fast charge cycles. All data was recorded and reported by ANL. Internal temperature was 80°C, external 30°C

RPT	C/3 Capacity Ah	C/3 Energy Wh	DST Capacity Ah	DST Energy Wh	80% DOD 2/9 Power, W/kg	80% DOD Vlimit Power, W/kg	80% DOD I _{max} Power, W/kg	80% DOD measured Power, W/kg	80% DOD res milliohms	80% DOD Virfree V	Min Power W/kg
0	11.466	1800.9	11.35	1765.6	473.9	412.4	242.9	241.8	969.0	162.6	242.9
1	11.460	1811.9	11.396	1762.2	463.5	400.3	241.2	239.4	982.7	161.9	241.2

The fast charge test was run at 5.5 A (C/2) and also at C/3 for comparison. Results from these tests are summarized in Table II- 7. Both the C/2 and C/3 charges were completed successfully without hitting the

upper voltage cutoff (3.6 V, cell-level). The fast charge efficiency in terms of usable capacity recovery was 99.4% for the C/2 rate, and 99.5% for the C/3 rate. The fast charge efficiency in terms of usable energy recovery was 97.3% for the C/2 rate and 97.8% for the C/3 rate.

US06 Testing

The test plan called for testing a US06 profile scaled to 5600 W (437.5 W/kg) to 80% DOD for ten cycles, following that similarly done for the DST₂₂₅ cycles. The profile for this US06 test was named “USABC Seo Vehicle US06 Profile” and it was provided by the Program Manager. The power profile is shown in Figure II-29. This test was originally scheduled for modules 2 and 3 at ANL. Seo determined via internal testing that the module were experiencing failures after running the US06 profile at this power. Specifically, the module power electronics contain power MOSFETs that gate the module high-voltage and act as a solid-state on/off switch for the module. The MOSFETs were observed to fail in a shorted state, such that the module external terminals were always in a high-voltage state.

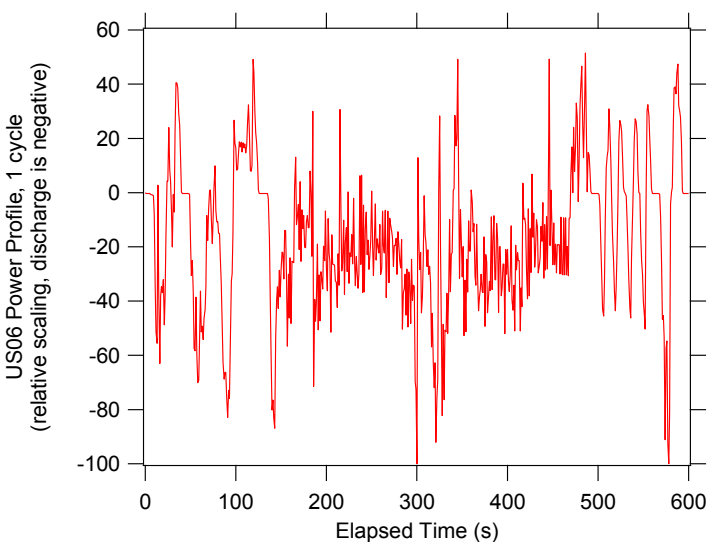


Figure II- 29: USABC Seo vehicle US06 drive cycle profile.. The reference power is scaled by the value on the y-axis. For instance, at 5600 W, the max discharge is 5600 W and the max regeneration power is 2883 W

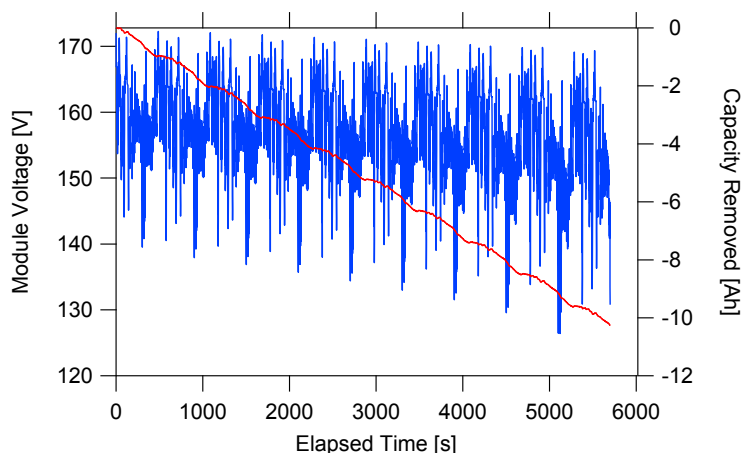


Figure II- 30: US06 full discharge at 438 W/kg (module). Internal temperature was 80°C, external temperature was 30°C

The current Seo module design does not accommodate for this failure scenario, such that there could be potential safety issues (safe handling of high voltage terminals) and module control issues (a standard cold-start procedure requires the cells to be isolated from the heaters – with shorted MOSFETs, powering the heaters causes the cells to go into a fault state). Modules experiencing this failure require a controller board replacement. Seo observed this failure mode 3 out of the 4 times the US06 profile was run in-house, and temperature recordings indicated that the MOSFETs were routinely exceeding their temperature specification by at least 25°C. Seo was unable to find drop-in replacement MOSFETs with higher power ratings, and other identified fixes would either incur safety issues (such as bypassing the MOSFETs manually) or were outside of the TAP program scope or timing (such as redesigning the controller board). Seo determined that decreasing the US06 power rating to 70% of the original (to 306 W/kg) would keep the MOSFETs within their operating temperature. These results and options were discussed with the TAP working group on July 15, 2015, wherein the USABC advised Seo as follows: 1) Seo should provide data that had already been taken for the full-scale (437.5 W/kg) US06 profile

rather than reduce the power level for the test. 2) ANL should run ten US06 cycles at the cell level (116.7 W, or 1/48th of the module power scaling factor) and report the results using Seo cells that are being separately

tested in direct collaboration with the DOE. The 70%-scaled US06 profile stays well within the operating specification limits. This scaled-down profile will be used for the module thermal imaging test at NREL.

Figure II- 30 shows the 438 W/kg US06 profile measured by Seo for module 4. The data shown was captured using the voltage and current recordings by an Aerovironment ABC-150. In this case, the module was fully discharged until one the lower voltage cutoff (2.5 V, cell). The net capacity and energy recovered from this discharge cycle were 9.97 Ah and 1486 Wh (over 90% of the rated capacity). This shows a successful completion of this profile at the module-level and demonstrates that the current-generation Seo cell is capable of handling higher currents than the DST₂₂₅ profile.

Stand Test

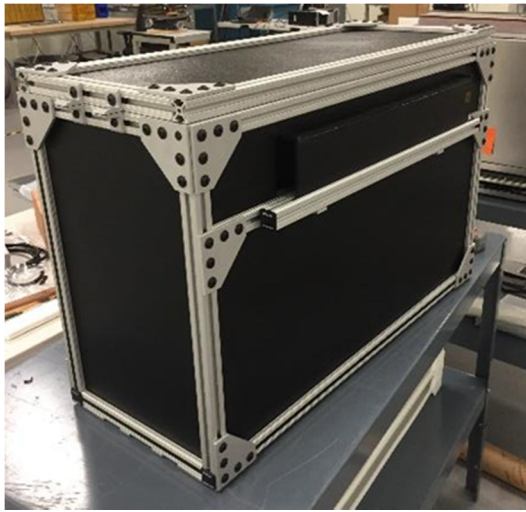


Figure II- 31: Stand test fixture (STF) for a single module

The test plan called for a 30-day stand test with the module remaining at 80°C under its own power. The stand test procedure calls for maintaining the cells at their rated operating temperature. USABC desired to capture all losses, which due to the nature of Seo's warm module technology, includes cell self-discharge, parasitic losses to power the controller board electronics, and parasitic losses to power heaters to maintain the operating temperature. Seo determined that heat losses would account for the vast majority of all losses (cell self-discharge is minimal over 1 month, and electronics load is about 2 Wh/day). Heat losses depend crucially on the enclosure design and pack configuration, such that the stand test results would not represent the results for a full pack design. For example, heat loss scales with the surface to volume ratio of a pack - a single module is substantially disadvantaged relative to two modules, four modules, etc. by having a much larger surface area relative to the active volume (and battery energy).

Furthermore, the single-module thermal chamber (SMTC)

used generally in this program is not representative of a fully-engineered pack design. The SMTC was designed as a test fixture that performs some basic insulation, cooling and control functions for short-timescale tests. The SMTC was not designed with long-term heat retention in mind, and it has several design choices that are not representative of a full pack environment, including air gaps between the insulation, vacuum panel insulation on only some surfaces, and it contains only one module. Seo performed a 48-hour stand test on the SMTC and determined that the heat loss would consume 50% of the module's energy in only three days (13.1 W total heat loss for 80°C setpoint in a 30°C thermal chamber). Seo designed and built a new test fixture (called the Stand Test Fixture, or STF) which was specifically designed for heat retention and to serve as a tool for evaluating vacuum panel technology as well as for evaluating engineering design effects on warm-battery thermal management. The STF is shown in Figure II- 31.

The STF design changes relative to the SMTC includes using thicker vacuum panels, using vacuum panels on all sides, and minimizing air gaps between insulation. For expediency, a single module was used in this design. One of USABC's primary goals for this TAP program is to gain a better understanding of Seo's existing technology. These results and designs were discussed with the TAP working group on July 15, 2015, wherein the USABC advised Seo as follows: 1) Seo will run a stand test using the STF and report the results to USABC. 2) Seo will provide detailed heat transfer calculations for the SMTC and STF and report those to USABC for evaluation. Seo completed the stand test and provided a detailed report to USABC on September 17, 2015, that included stand test results and detailed heat transfer calculations for both the SMTC and STF. Some key results from that report are summarized here.

The stand test in the STF was run for 15 days with an internal setpoint of 80°C with the whole apparatus contained within a 30°C environment. The module was fully charged and equilibrated at 80°C, at which point the external power was removed and the module was maintained in self-heating mode. After 15 days (within 5 minutes), the external connections were re-made and the module was fully discharged at a C/3 rate. Figure II- 32 shows a C/3 discharge before the stand test and a C/3 discharge performed at the end of the stand test.

The C/3 discharge at the end of the stand test recovered 1.87 Ah and 295 Wh, compared to a baseline of 11.57 Ah and 1835 Wh recovered from the initial C/3 discharge. The difference is 9.7 Ah or 1540 Wh used over 15 days (360 hours). The average loss over that period is 4.3 W at an average current of 0.027 A. This loss can be reasonably assumed to be entirely due to heat required to maintain the module operating temperature. The module and STF used in this test retained > 50% of the internal energy for 8.9 days with this particular design combination.

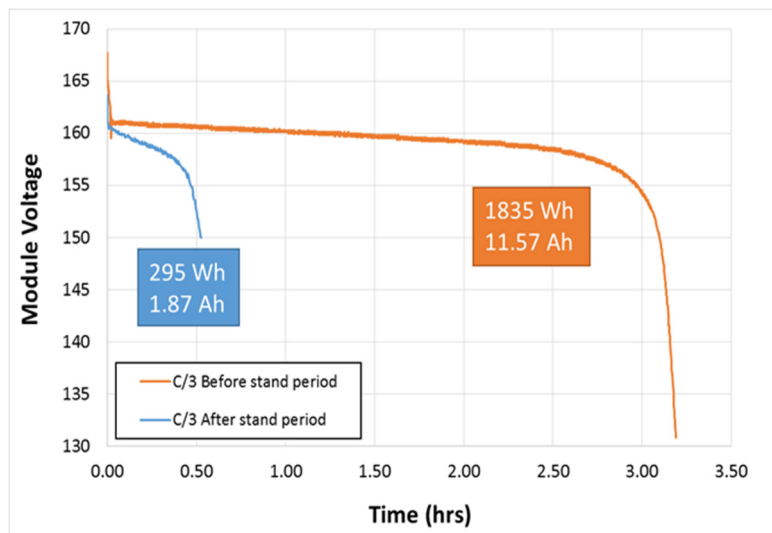


Figure II- 32: C/3 discharges before (orange, baseline) and after (blue) a 15-day stand test using the module’s internal power for heating. Internal temperature was 80°C, external temperature was 30°C

Detailed thermal models were created for both the SMTC and STF and compared to the stand test results. These models were quasi 1-dimensional, accounting for series resistances in the insulation, and accounting for air gaps, cable pass-throughs, and skin-conduction along the vacuum insulation panels as parallel-paths for heat transfer. This modeling methodology has been submitted to NREL for review. The modeled heat loss for the SMTC was 17.8 W, compared to a measured 13.1 W heat loss. The modeled heat loss for the STF was 5.6 W, compared to a measured 4.3 W heat loss. Using the same methodology, Seo modeled heat loss for a conceptual 32.4 kWh pack design with 18 modules in a 2S9P configuration, as shown in Figure II-33.

Conclusions and Future Directions

All module and SMTC hardware deliverables were met by Seeo. ANL has completed the agreed-upon test plan, and under an agreed-upon extension will continue DST₂₂₅ cycle life testing until 200 cycles have been achieved. NREL has received a module and developed a detailed test plan. NREL is making testing preparations and is scheduled to complete module testing in Q4 2015. The NREL test plan includes three freeze/thaw tests (the module will be thermally cycled between -40°C and 80°C) and a US06 discharge profile

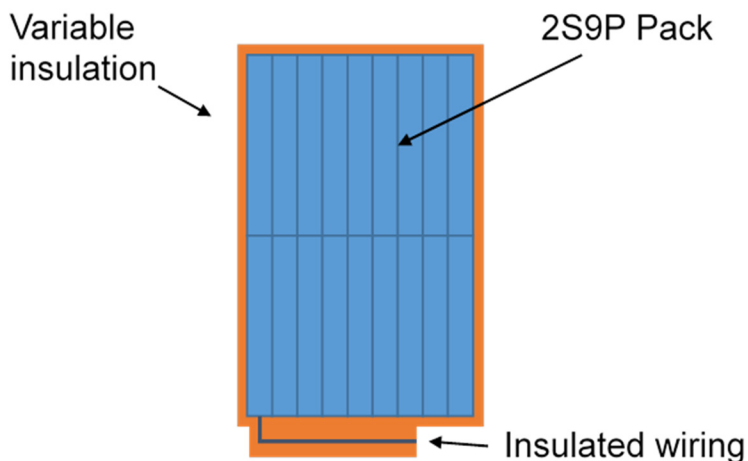


Figure II- 33: Conceptual 32.4 kWh pack design with 18 modules in a 2S9P configuration that would retain 50% of the pack energy after 30 days at 80°C using internal power

(at 306 W/kg) in a thermal chamber, during which the module will be imaged with a thermal camera. SNL is also making test preparations and is scheduled to complete testing in Q4 2015. The SNL test plan has been developed, and includes two abuse tests: thermal ramp to 150°C with a 15 minute hold (5°C/minute) on one module, and overcharge (at 1C, to 200% SOC) on one module.

At 80°C internal and 30°C ambient, the average results from all 6 modules were 11.4 Ah C₃/3 discharge capacities, and rated energies of 144 Wh/kg or 154

Wh/L. Peak power discharges averaged 241 W/kg or 258 W/L using the I_{max} calculation, which is based on the rated current from the developer (Seeo). Higher powers were demonstrated with the US06 profile (438 W/kg), but module power electronics limitations prevented long-term cycling of the module at this level. This limitation will be addressed in the next revision of the module design. The DST cycle life (150 cycles) shows no appreciable capacity or energy fade, and only a 1.8% fade in the rated power (using the I_{max} calculation). Extrapolations in the power fade predict end-of life (at 80% of original rating) at 1,600 cycles, assuming a linear trend in power fade in the reported Peak Power (determined by the I_{max} calculation).

US06 and stand tests were performed at Seeo at the direction of USABC. Seeo demonstrated the US06 profile on a module at 438 W/kg (module-level), recovering 9.97 Ah (over 90% of the rated capacity). Seeo performed a 15-day stand test and found that self-heating could maintain an internal setpoint of 80°C for 8.9 days before 50% of the module energy was depleted. Using detailed thermal modeling, Seeo estimates a 32.4 kWh pack could pass this test at 30 days with 1.2” to 1.8”-thick insulation. These results and analyses have been submitted to NREL for review.

Seeo’s development efforts going forward are focused on increasing the energy density of the cell technology towards a doubling of the present level, improving the rate capability, and achieving the aggressive performance and cost targets for the technology as outlined in the USABC goals for 2020.

Seeo was acquired by Robert Bosch in August 2015. The acquisition brings the added resources of Bosch and further drives the focus of the development to achieve the goals mentioned above with the ultimate target to commercialize the technology.

II.A.5 PHEV Battery Development (Xerion ABC)

Objectives

- Implement StructurePore™ technology to produce low-cost, high-power and high-energy batteries for next generation Plug-in Hybrid Electric Vehicle (PHEV).
- Design and produce cells with maximized energy density at the USABC power density goal by optimizing electrode structural parameters.
- Deliver 36 prototypes (18 Xerion StructurePore™ cathodes with traditional anodes, and 18 optimized cells with Xerion cathodes and Xerion anodes) to USABC for their own testing purposes.

Project Details

Renata Arsenault (USABC Program Manager)
DE-EE0006250 Recipient: Xerion Advanced Battery Corp

John Busbee (Xerion Advanced Battery Corp – PI)
60 Hazelwood Drive
Champaign, IL 61820
Phone: 720-377-6888; Fax: 866-242-1069
Email: j.busbee@xerionbattery.com

Subcontractor:
Polaris Labs
8114 SW Nimbus Avenue, Bldg 4-C
Beaverton, OR

Start Date: July 2014
Projected End Date: May 2016

Technical Barriers

- The StructurePore™ electrode is composed of a thin layer of active material conformally grown on a 3D nanostructured current collector. The key to the realization of large-format, commercially viable batteries is the capability of producing highly scalable, consistent and manufacturable 3D conductive porous scaffold as current collectors. In addition, because the active material is synthesized using a non-conventional, low-temperature method, and significant development efforts are needed to ensure that their electrochemical performance (specific capacity, cycle life, etc.) can match conventional process battery technology.
- It must be demonstrated that the material and processing costs for the novel architecture platform do not exceed those of conventional, mature battery technology on a normalized per kWh basis.

Technical Targets

- Develop scalable and manufacturable processes to produce StructurePore™ electrodes.
- Develop, produce and deliver 18 full cells that consist of Xerion StructurePore™ cathodes and Xerion StructurePore™ anodes. Each cell will have a total capacity of > 920 mAh, gravimetric energy density of > 197 Wh/kg, and volumetric energy density of > 350 Wh/L.
- Develop, produce and deliver 18 full cells that consist of Xerion StructurePore™ cathodes and traditional graphite anodes. Each cell has a total capacity of > 920 mAh, gravimetric energy density of > 197 Wh/kg, and volumetric energy density of > 350 Wh/L.

Accomplishments

- Demonstrated large-scale 3D nanostructured current collectors.
- Demonstrated spinel LMO active material by electrodeposition in non-aqueous bath.
- Fabricated initial pouch cells with spinel LMO and graphite.

Introduction

Xerion proposes a 3D electrode technology called StructurePore™, which is composed of a thin layer of active material directly electroplated on a 3D nanoporous current collector. The 3D current collector provides an efficient electron pathway and a large surface area for high material loading. The pores in the structure enable ions to shuttle quickly in the electrolyte between electrodes, and the thin active material coating significantly reduces the solid-state ion diffusion length compared with the micro-scaled active material particles in

conventional batteries. Thus, the StructurePore™ electrode greatly improves power while maintaining energy. Xerion has initially demonstrated cells with 96 Wh/kg and 161 Wh/L at 1C and exceptional power performances, for example, achieving 90% state of charge in five minutes and delivering 30,000 W/kg at a 290C discharge. According to theoretical calculations, a geometrically optimized StructurePore™ can achieve much higher energy densities (>197 Wh/kg and >350 Wh/L).

Since the StructurePore™ electrode utilizes 3D nanostructure templating and low-costs electrodeposition instead of active material powder processing (high-temperature), it can potentially reduce raw material cost by 30%. In addition, the reduced internal resistance and porous nature have the potential to deliver improved cycle life and enhanced safety for a given commercial battery material. Because of the materials-agnostic nature of this technology, it can also be applied to future, high-energy chemistries, allowing a continued technology development pipeline to ensure high performance as new materials technologies mature.

Approach

Innovative Approach: Xerion has experience in developing large-scale 3D conductive scaffold and in electrodeposition of high-quality, dense active materials on the scaffold. Laboratory scale prototypes have been continuously assembled in a sustained effort to optimize these materials and processes. Moving beyond the laboratory scale, Xerion is working with Polaris Battery Labs on the development of larger-scale, pouch cell prototypes. Polaris specializes in solving problems related to scale-up and the fabrication of pouch cells.

Results

We have achieved the following progress:

3D Nanostructured Current Collectors

Because of its lightweight and chemically inert nature, XABC is utilizing a nanostructured carbon foam as the cathode collector. Efforts in FY2015 in this area focused on scaling up the template inversion process to produce an optimized foam that has demonstrated all processes necessary for scaling to commercial scales. Optimization efforts have produced a mechanically robust, 3D carbon foam that has approximately a 10% carbon filling-fraction and 1 micron pore size and sufficient electrical conductivity to produce abundant electrical power for PHEV applications. The resultant carbon foams, as seen in Figure II- 34, can be produced with thicknesses greater than 200 microns with good microstructural uniformity, and large enough cast dimensions for multiple electrodes.

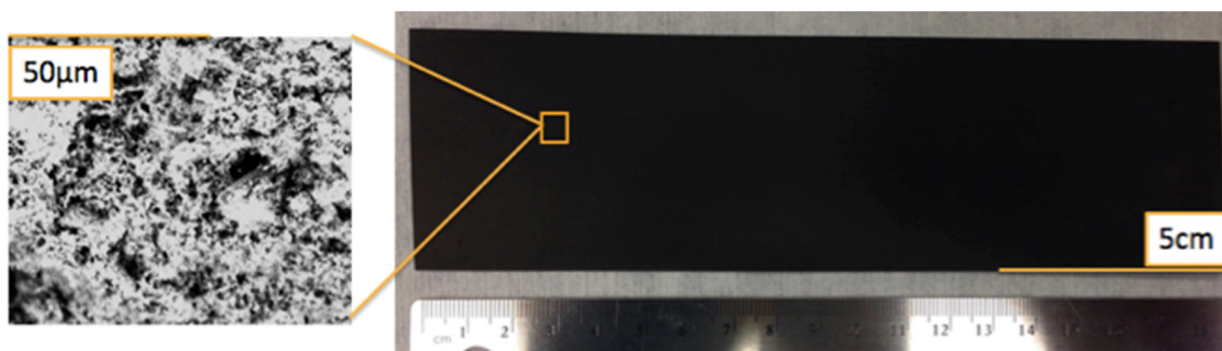
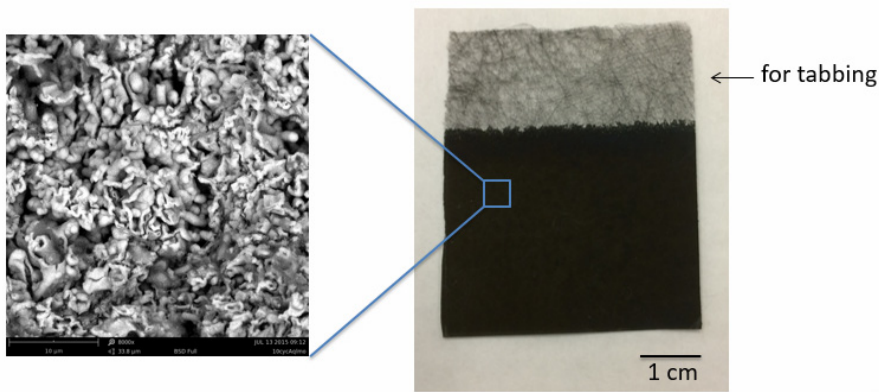


Figure II- 34: Large format StructurePore™ carbon scaffold

Active Material Development

While several active material systems have shown promising results when applied to the StructurePore™ architecture, the decision was made to focus on development of material systems that have been previously fielded in automotive battery systems. This both reduces adoption risk and allows a better basis of comparison for prototype cells using the StructurePore™ architecture. For this reason, the focus of the development efforts was shifted to a spinel-phased LiMn_2O_4 (spinel LMO). To continue to reduce development risk, XABC has developed electroplating methodologies to produce spinel LMO in both an aqueous and non-aqueous plating solution.



Leveraging earlier aqueous electroplating work for the LMO system, XABC has created a process to produce high quality spinel LMO from an aqueous solution, as shown Figure II- 35. As can be seen in the inset, the LMO forms a dense, conformal coating that is uniform across the cross-section

Figure II- 35: LMO from aqueous bath

of the electrode. This improved uniformity can be attributed to optimization of bath constituents and temperature, as well as conductivity improvements realized during the optimization of the carbon scaffold. Figure II- 35 illustrates that the LMO coating is visually uniform across the cathode and is free of pin-hole defects.

Figure II- 36 (a) shows a charge/discharge curve from a spinel LMO cathode half-cell versus lithium. The specific capacity of ~ 120 mAh/g (when charged to 4.3 V) and the distinct voltage plateaus at 4.1V and 3.9 V are indicative of a well-formed, single phase spinel LMO system. Figure II- 36 (b) shows good capacity retention at higher C-rate discharge (up to 30C) for the same half-cell system. The aqueous plating process has several advantages in that it occurs at room temperature and is rapid and cost-effective, but more optimization and scale-up work remains to be completed to produce a consistently high yield of good films with expected cycle life.

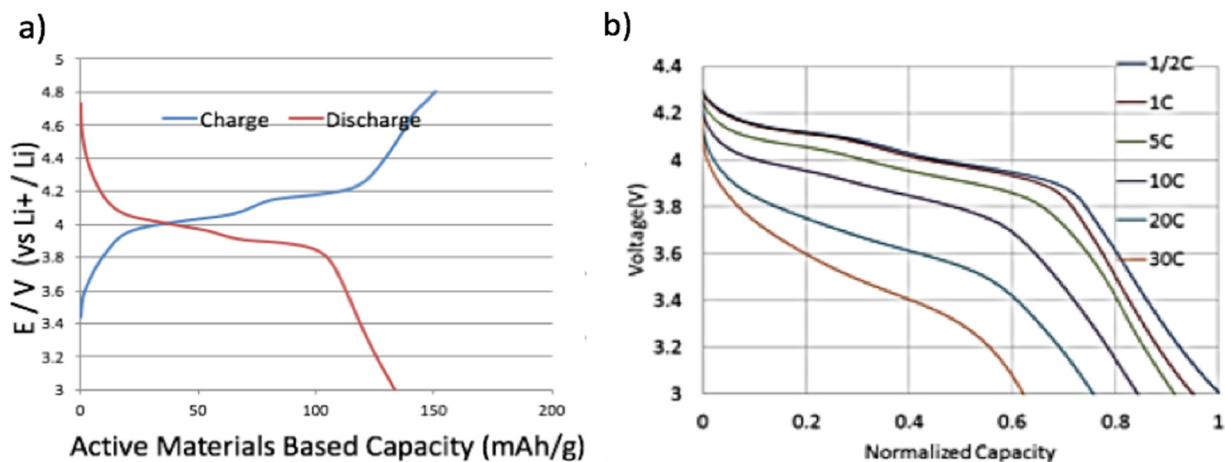


Figure II- 36: a) Charge/discharge curve, and b) power curve data for aqueous LMO

XABC has additionally developed an electroplating methodology to produce high quality spinel LMO from a non-aqueous plating bath. This procedure has been optimized to produce a highly uniform film across the cross-section, but unlike the aqueous LMO system, the morphology of the resultant coating is nodular, resembling a sintered powder, as can be seen in the inset of Figure II- 37. Figure II- 37 shows that a cathode produce using this system if visually smooth and uniform across the surface of the electrode.

Figure II- 38 a) displays x-ray diffraction data for a spinel LMO cathode produced with the non-aqueous electroplating process. The red traces are experimental data from the cathode while the blue lines indicate the expected peak positions from high quality spinel-phased LiMn_2O_4 .

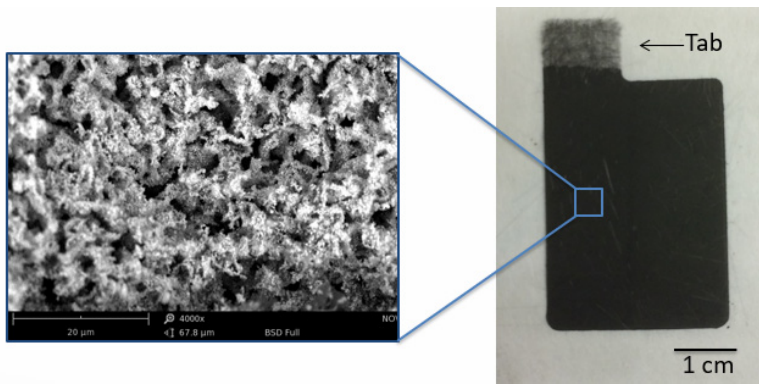


Figure II- 37: Non-aqueous spinel LMO on StructurePore™ Cathode

The close alignment to the expected values provides an initial indication that the deposited material is a single phase, spinel LMO. Figure II- 38 b) further demonstrates this result in that the charge/discharge performance shows distinctive voltage plateaus that are indicative of the spinel phase. To date, the non-aqueous system has shown higher yield and better cycle—as such, follow-on pouch cell development has

been conducted using the non-aqueous spinel LMO, as can be seen in the following sections.

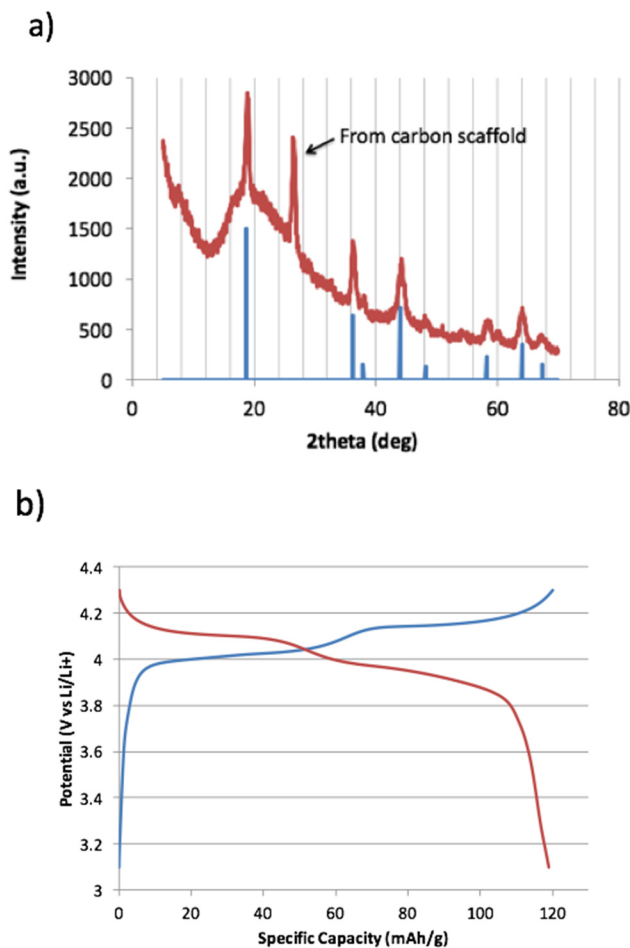


Figure II- 38: a) XRD of LiMn_2O_4 deposited by electroplating in a non-aqueous bath. The red curve is experimental data and the blue lines are the expected peak locations of a single phase spinel. b) Voltage curve for non-aqueous LMO

High Rate Carbon Anode

StructurePore™ cathodes, when matched with commercial graphite anodes, were not able to demonstrate high power performance in full cell tests. Cells produced with a reference electrode indicated that the anode power performance was insufficient to match the cathode power performance.

For this reason, in FY2015, XABC developed a high power, composite graphite anode system, which is based upon commercial graphite powder. The system shows good specific capacity $\sim 320 \text{ mAh/g}$ and cycle life comparable to traditional graphite anode, while demonstrating much better power performance than a traditional graphite slurry on copper system. Utilizing this composite anode, StructurePore cells with a 10% overmatch in energy were able to demonstrate high power performance and good overall energy density.

Figure II- 39 (a) shows half-cell performance of the composite anode at several c-rates. The overpotentials shown in the figure indicate much better power performance at high discharge rates than is typical in a commercial graphite anode. Figure II- 39 (b) illustrates that under half-cell cycling, the anode maintains good cycle performance. Based upon these positive results, XABC undertook additional scaleup activities to be able to produce the anode in sufficient scales to complete production of the program prototypes.

Pouch Cell Development

XABC completed all major tasks required to scale its negative electrode, and is completing the fixtures necessary to fully scale the non-aqueous cathode production. While the USABC deliverable prototypes will be assembled via a subcontract, XABC is completing all tasks and equipment acquisitions necessary to produce lab scale prototype pouch cells in-house. During the evolving development process, XABC has continued cell design discussions with USABC personnel. The resultant cell design will affect many critical production aspects, including the amount of electrodes required per cell, and will thus drive lead times for prototype delivery. XABC will continue to communicate with USABC regarding cell requirements as development draws to an end and lab-scale production begins.

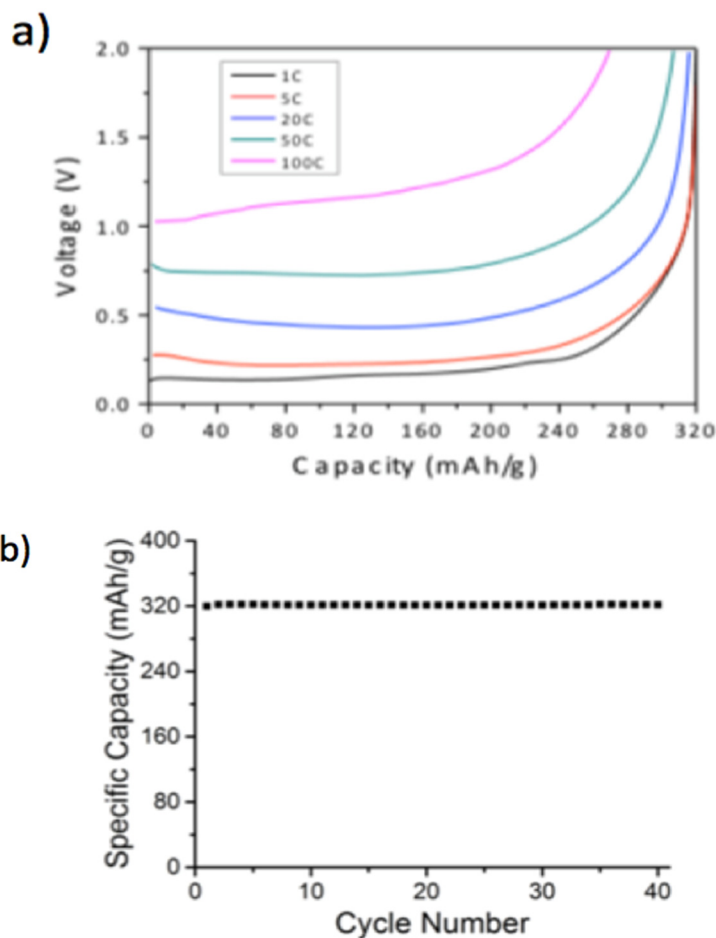


Figure II- 39: Porous carbon composite anode (a) power and (b) cycle life data. Electrode areal charge density is 1 mAh/cm²

outs. Figure II- 40 (a) shows an ultrasonic weld with 20 layers of nickel-coated carbon foam used as a surrogate demonstration system during anode development. As for the cathode, aluminum-coated carbon foam is used for tabbing.

In addition, XABC has been developing more in-depth relationships with potential material suppliers. This is both to secure supply of sufficient raw materials to ensure available at larger scales, and also to refine the raw material costs for production scales.

In preparation for pouch cell fabrication, XABC has begun exploring two tab welding methodologies. The first technique, Focused Melt Resistance (FMR) welding is a specialized method that uses resistance heating to melt metal into a porous structure—like StructurePore™ electrodes. This work has been accomplished at a vendor, Innovative Welding in Dayton, OH. The second technique, ultrasonic welding, is a traditional approach widely used in the battery industry. Initial efforts in this area have been accomplished by Polaris Battery Labs in Beaverton, OR.

Both techniques have shown promise for welding metal tabs to 3D StructurePore™ electrode cut

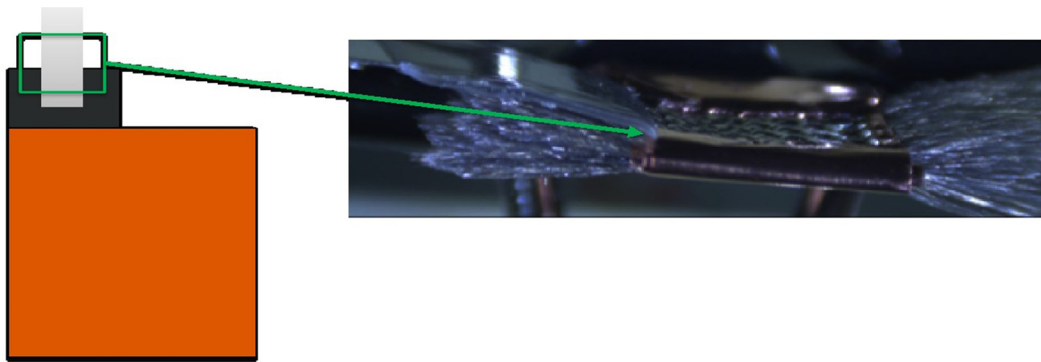


Figure II- 40: Twenty layer ultrasonic electrode weld

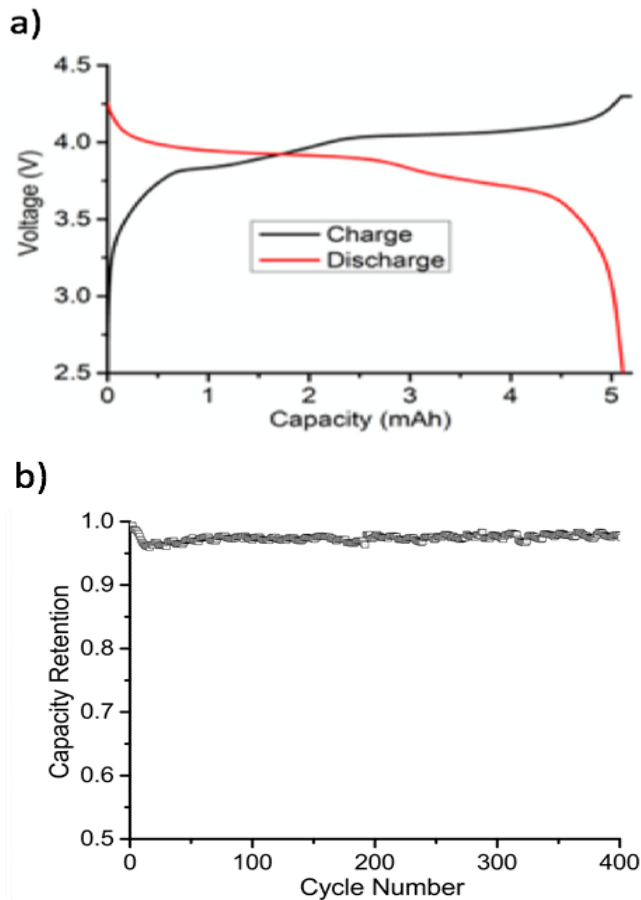


Figure II- 41: a) Characteristic voltage curves for initial LMO pouch cells from non-aqueous bath. b) Cycle life for same pouch cell. Electrode areal charge density is 2mAh/cm²

Initial Pouch Cell Fabrication and Data

To test pouch cell assembly techniques, and to further improve design feasibility during scale-up, small single pairs of cathode and anode were produced and tested utilizing the non-aqueous LMO StructurePore™ cathode and the XABC composite high power graphite anode. Subsequent testing on these cells has shown promising performance, with the characteristic charge/discharge curves shown in Figure II- 41 (a) and 95% capacity retention over 400 cycle displayed in Figure II- 41 (b).

The energy density of this cell, neglecting the packaging is 250 Wh/L. Previous coin cell prototypes using this system have exceeded the program goal of 350 Wh/L. The power performance at this loading is presented in Figure II- 42, and an image of the pouch cell is presented in Figure II- 43.

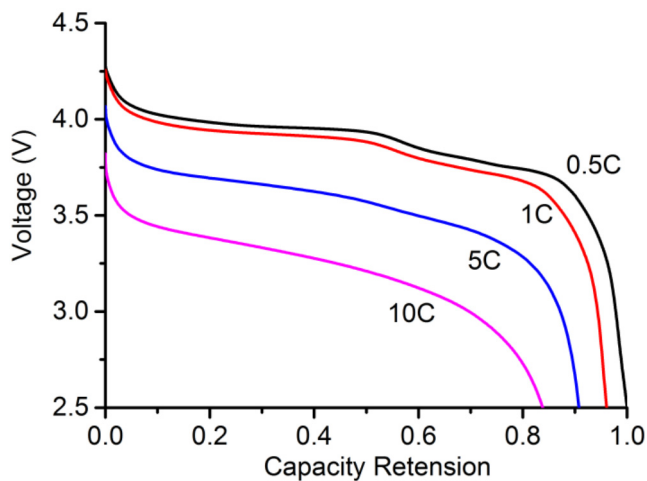


Figure II- 42: Power curves for LMO pouch cell. Electrode areal charge density is 2mAh/cm²

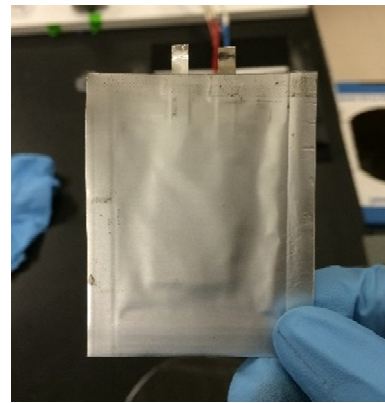


Figure II- 43: Initial LMO pouch cell from non-aqueous bath (left) and charged high power graphite negative electrode (right). Cathode dimension: 16 mm X 23 mm X 0.12 mm. Anode dimension: 18 mm X 25 mm X 0.08 mm. Separator thickness: 0.02 mm

Conclusions and Future Direction

XABC has produced and demonstrated spinel-phased LMO StructurePore™ cathodes. These active materials show good crystallinity and uniformity across the electrode. They have demonstrated electrochemical performance with the distinctive voltage plateaus expected from high quality LMO, as well as an excellent preliminary cycle life. XABC has additionally developed and demonstrated a high power composite graphite anode that enables high power performance at the same specific capacity as commercial electrodes. Full cells in a coin cell package have demonstrated high capacity retention at specific energies above 350 Wh/L, which is the program goal. When full cells of the StructurePore cathodes and composite anodes were assembled in an initial small pouch cell, energy density of 250 Wh/L was achieved, with a capacity retention of 95% after 400 cycles. Final prototype cells are expected to exceed the 350 Wh/L program goal.

As the program continues, XABC will continue to refine and scale its prototype production process to accommodate electrode fabrication for all 36 prototypes for USABC. Various aspects of the non-aqueous deposition technique will be modified to accommodate the larger electrodes shown in Figure II- 43. XABC will also install some additional capital equipment that will be necessary for bulk production.

XABC will assemble prototype pouch cells in conjunction with an assembly partner. These prototypes will be tested at Argonne National Laboratory and a USABC gap chart will be generated with the data.

FY 2015 Publications/Presentations

None.

II.A.6 Development of Advanced High-Performance Batteries for 12V Start-Stop Vehicle Applications (Maxwell Technologies)

Objectives

- The objective of this program is to develop a hybrid lithium-ion/ultracapacitor energy storage system that meets or exceeds all USABC technical and economic goals for 12V Start-Stop vehicles applications.

Technical Barriers

- In order for 12V stop start systems to achieve mass adoption they must be affordable, have excellent performance, and be easy to integrate into vehicles.

Barriers addressed:

- Performance: Cold cranking.
- Integration: Mass and volume.
- Cost: \$/pack

Technical Targets

- Cold Cranking: Withdrawal of 360Wh followed by cold soak to -30°C, and then perform 3 successive crank cycles of 0.5 seconds at 6kW, 4 seconds at 4kW, and 10 seconds at rest.
- Mass: 10kg.
- Volume: 7L.
- Cost: USABC ultimate goal \$180 (not-under hood application), contracted project goal \$230.

Accomplishments

- Delivered 3 Generation 1 Proof of Concept (POC) modules to Argonne National Labs (ANL) for testing.
- Delivered 6 Generation 1 pouch ultracapacitor cells to ANL for testing.
- HPPC and Cold Crank testing performed on POC modules.
- Modeled optimizations based on POC test results.
- Built 2 additional POC modules with low temp A123 cells (both 20Ah and 14Ah) as selected by model.
- Demonstrated three successful cold cranks with both high power and low temperature A123 cell POCs.
- Final electrolyte, solvent, and separator selections made.
- Pouch cell design, process development, and drying process optimizations completed.
- Gas getter investigations concluded with no suitable selection moving forward.

Project Details

Scott Jorgensen (USABC Program Manager)
DE-EE0006250 Recipient: Maxwell Technologies

Jeffrey Kim (Maxwell Technologies, Inc. - PI)

3912 Calle Fortunada

San Diego, CA 92123

Phone: 858-503-3246

Email: jkim@maxwell.com

Subcontractor:

None

Start Date: October 2014

Projected End Date: April 2016

Introduction

There is a very strong technical and economic case developing in the energy storage industry for the hybrid combination of ultracapacitors and batteries in a variety of applications. It is a natural fit for applications that share a healthy requirement for both energy and power and for those applications that are required to function at very low temperatures. The emerging hybrid electric vehicle market is such an application.

The growing proliferation of start-stop or micro hybrid technology in mainstream passenger vehicles demonstrates the value, benefit and ease of adoption of that type of electrical hybrid configuration. As the costs

of battery cells and ultracapacitors continue to fall, the value proposition of that combination in the micro hybrid market becomes even more compelling.

This 19 month program will determine the technological and economic feasibility of adopting a hybrid energy storage system consisting of lithium-ion batteries and Maxwell ultracapacitors to an automotive start-stop application as specified by USABC and DOE. The proposed Maxwell 12V Start-Stop system consists of a single pack containing lithium-ion battery cells and the “to be developed” optimized Maxwell UCAP cells controlled by a single electronic management system.

Ultimately, the results of this program will provide insight into how to best hybridize different forms of energy storage technologies for compact, high performance, and cost effective solutions to a variety of vehicle applications.

Approach

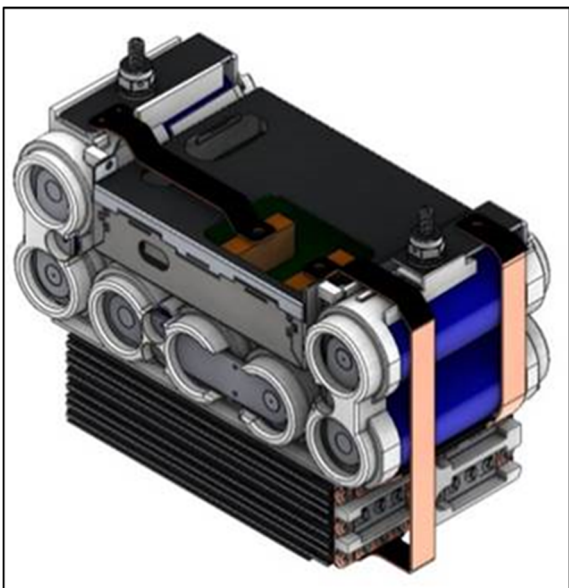


Figure II- 44: The baseline POC module design



Figure II- 45: The baseline POC module deliverable

The goal of the program will be achieved through the execution of three parallel development tracks. The first track (Task 1) will be the use of a proof-of-concept module to study the electrical, life cycle and control/communication performance of the hybrid pack. The second (Task 2) will be the development of the optimized configuration of the Maxwell ultracapacitor that is needed for weight, volume and cost conformance. The third (Task 3) will be the detailed CAD design of the envisioned prototype module to validate the system weight, volume, and cost and determine critical thermal and vibration characteristics of the proposed 12V Start-Stop system. When combined, the results of each of these development tracks will provide a complete, verified comparison of the proposed system’s performance and cost against the USABC 12V Start-Stop Gap Chart.

Results

Task 1: Design and build of the POC modules

The first task was to design and build a working ultracapacitor and LFP module to evaluate a direct parallel hybrid system against the USABC goals. These POC modules consisted of off-the-shelf components including Maxwell 3000F ultracapacitors and A123 20Ah LFP batteries. As shown in Figure II- 44, the design utilized separate LFP and ultracapacitor packs connected together via bus bars in a Group 31 form factor. In addition, a combined battery and capacitor monitoring board was included to maintain balance in each of the cell strings and report health status. The baseline POC design was finished in the first half of the year, and then built and tested to USABC 12V start-stop requirements. Figure II- 45 shows the baseline POC module as packaged prior to shipping to ANL for testing.

Task 1: Testing and model optimizations of the POC modules

A Matlab Simulink model of the hybrid system was built using parameters measured from HPPC testing of individual UCAP and LFP cells. This model, shown in Figure II- 46, was able to replicate HPPC results over temperature as well as permitting prediction of cold crank performance at both beginning and end of life.

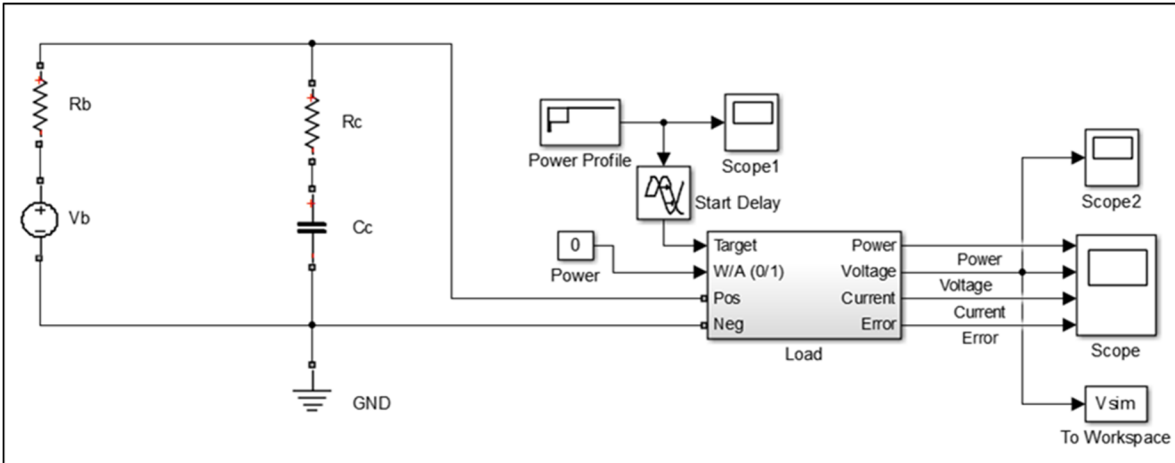


Figure II- 46: The Simulink model of the hybrid system

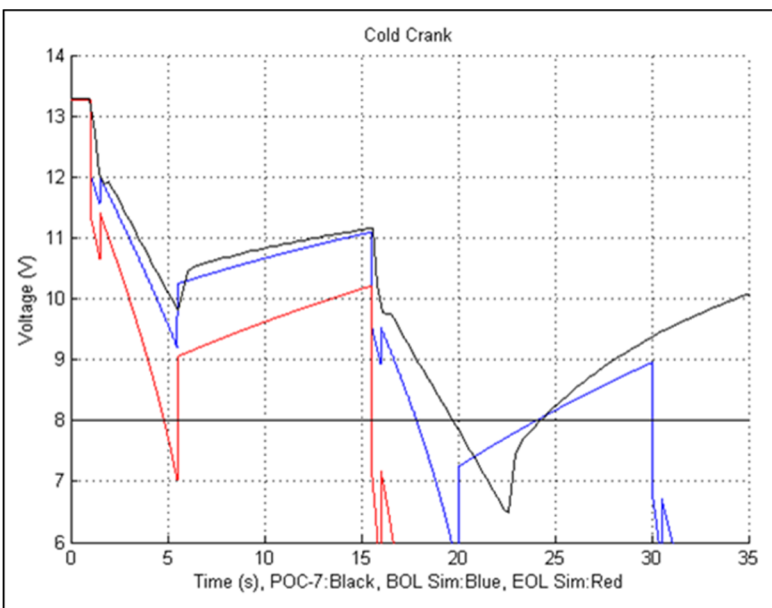


Figure II- 47: The Simulink model predictions of cold crank performance

As shown in Figure II- 47, the model’s predictions for the beginning of life cold crank performance, shown in blue, closely fit with the measured performance, shown in black, for the first 15 to 20 seconds of crank, prior to the system going under voltage. This model showed that for the hybrid system to fully pass the USABC cold crank profile, a battery with pulse resistance of less than 15mΩ at -30C would be needed.

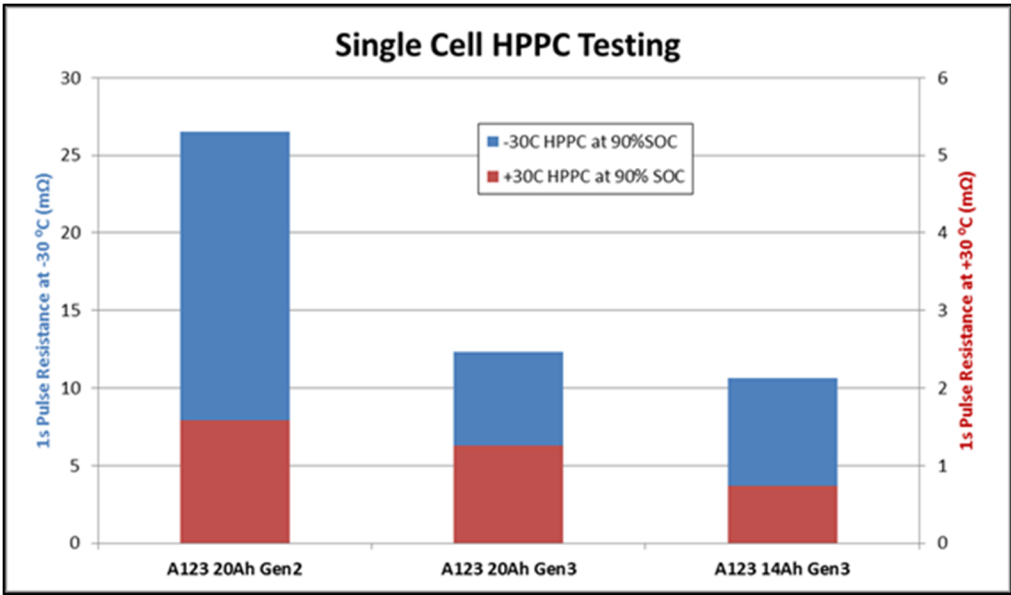


Figure II- 48: Warm and cold discharge resistances for three A123 cells performance

Task 1: Build and test of optimized POC modules

Working with A123, Maxwell tested several next generation cells with new electrolyte formulations for better cold performance. Figure II- 48 shows the results of HPPC testing of these single cells at +30C and -30C. Based on these results, the A123 20Ah Gen3 cells were selected for the next POC deliverable as they had adequately low cold temperature discharge performance while still maintaining high energy density. A POC module was then built with these cells, as shown in Figure II- 49, and tested to the cold crank profile, with the results shown in Figure II- 50. The minimum cold crank voltage was above 9.5V, passing the test with significant margin.



Figure II- 49: POC 9 built with the 20Ah Gen3 A123 cells

Task 2: Baseline Cells

A baseline configuration of the ultracapacitor pouch cell was constructed using the same internal components as the current commercial Maxwell ultracapacitor can cell including the electrode formulation, electrolyte, current collectors, and separators. The cells were verified with good cycle and aging performance as seen in Figure II- 51 and Table II- 8. The baseline cells are currently undergoing testing at ANL.

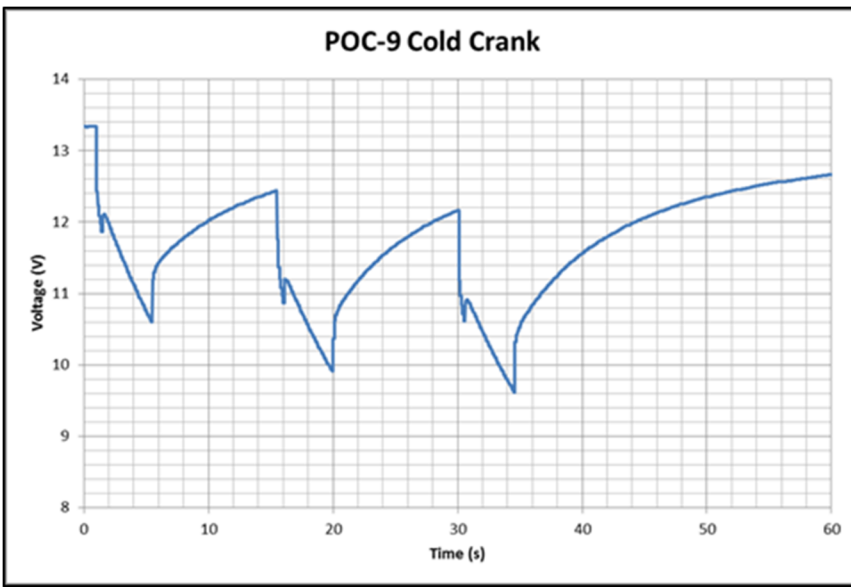


Figure II- 50: The voltage trace during cold crank on POC 9

Task 2: Electrolyte Development

Successful development of an electrolyte that significantly reduces the gas generation at high temperature is essential to a viable ultracapacitor pouch design.

Studies of the salt used in the current Maxwell ultracapacitor shows that it is not stable when water is present. During the search for an alternate salt with higher conductivity and better stability, Maxwell's team has analyzed several

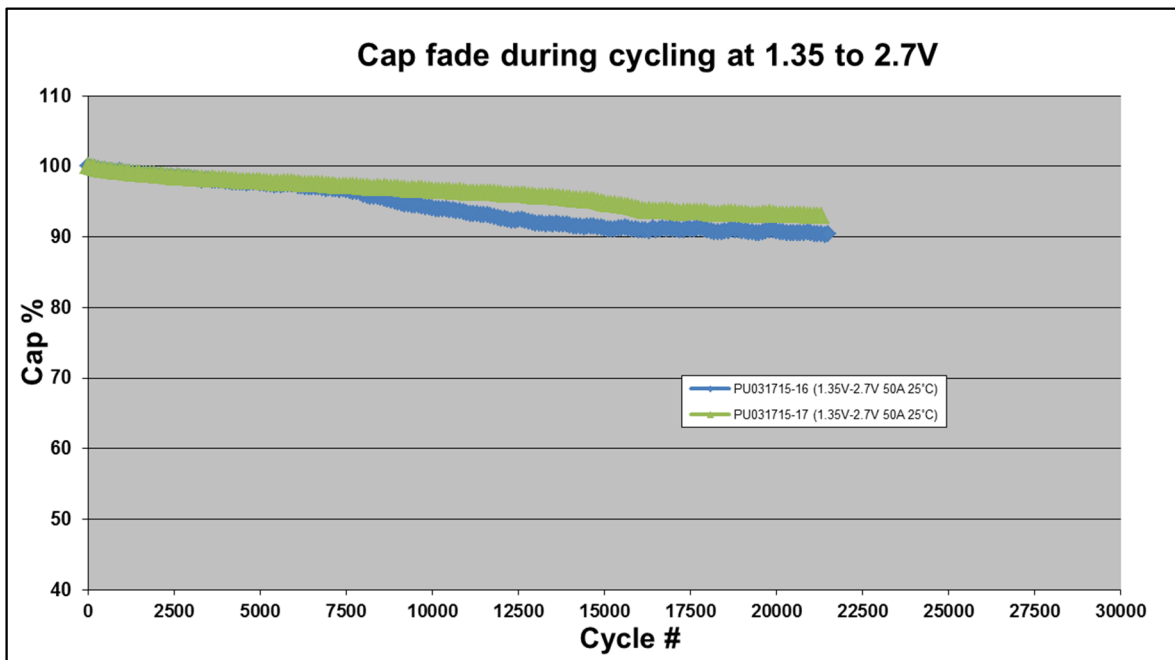


Figure II- 51: Cap fade testing of Baseline cells

Table II- 8: Aging effects study

Baseline cell name	Tested on 12/15/2014			Tested on 5/22/2015		
	C (F)	R (Ω)	RC	C (F)	R (Ω)	RC
PU121214-1	1214	0.00063	0.77	1212	0.00062	0.75
PU121214-2	1221	0.00061	0.75	1218	0.00061	0.74
PU121214-5	1224	0.00060	0.74	1228	0.00061	0.75
PU121214-8	1217	0.00061	0.75	1222	0.00064	0.79

combinations of salts and solutions. They concluded the investigation with the best candidate that shows similar capacitance performance, 4% improvement in ESR, similar life performance, and 50% better gassing performance than the control.

Various electrolytes were evaluated for conductivity,

viscosity, voltage windows, boiling points, cold temperature performance, and cost including several acetonitrile based electrolytes, carbonate based electrolytes, and ionic liquids. Both commercially available and in-house formulations were evaluated. Several carbonate based electrolytes with good conductivity and lower

costs were pursued as gassing performance was better than acetonitrile. However, these electrolytes increased internal resistance; the ESR was generally three to four times higher than acetonitrile based electrolytes. Ionic liquids had good life and excellent gassing performance, but the high ESR, high costs, and relatively high melting points did not fit the needs for this program. Thus, the final conclusion was acetonitrile with the selected salt.

Additives were the next logical step in mitigating gassing in ultracapacitor pouch cells. Several gas suppression candidates were evaluated. So far, two candidates show promising results. One very promising additive had reduced gassing by 50% as shown in Figure II- 52, though it did cause a slight ESR rise of 7.5%. Investigations continue as additional additives are planned for evaluation.

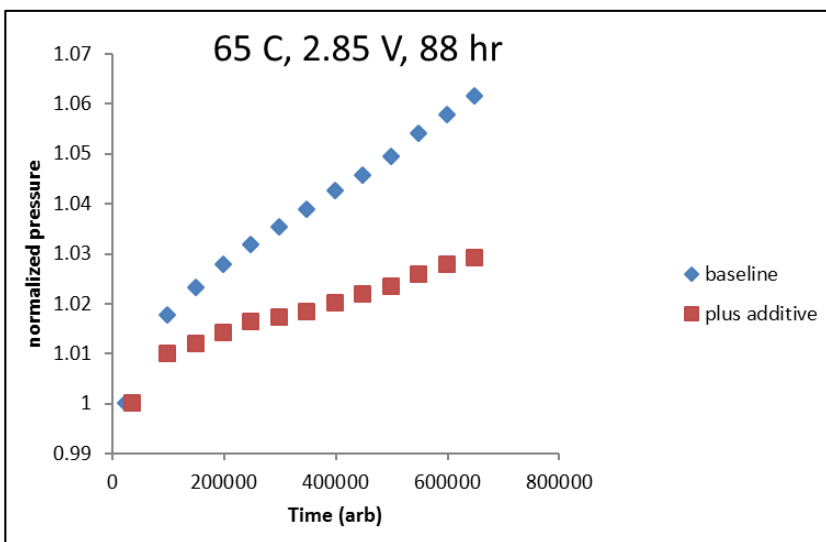


Figure II- 52: Gassing reduction with additive

Task 2: Ultracapacitor pouch Gas Management

Understanding the mechanisms by which gas is generated is crucial in attempting to preempt gas formation. In addition to moisture being a known cause for gassing, it was also observed that minimizing functional groups and impurities will mitigate gas generation. Additionally, the possibility of utilizing a gas getter was investigated, as well as a pressure relief valve should there be no viable mitigation options.

Maxwell’s engineers have

worked with suppliers to improve carbon impurities. They have ordered samples with fewer functional groups and testing is ongoing. Maxwell also worked with suppliers to identify a separator that improved cell life.

The team also evaluated several commercially available in-house gas getter materials that combine with gas molecules either chemically or by absorption. Two candidates were selected for further investigation. The first candidate had excellent performance, but was prohibitive in cost. The second candidate had much more reasonable costs, but was not effective enough. The team worked with the vendor to improve the performance of the second candidate, but to no success. The gas getter investigations were concluded with no suitable selections.

The team also evaluated several pressure relief valves for a pouch cell application. Although a valve was considered and sample pouch cells were made, in consultation with the USABC project work group, a decision was made to abandon this strategy as the design brings about serious ventilation and exposure concerns for occupants, as well as other design challenges and complexities in system integration.

Task 2: Cell Packaging Development

Efforts have been made to improve the vacuum sealing process by changing the orientation of the sealer and improving the design of the impregnation process. In addition, the drying process has been further improved to minimize the moisture in the system. The result of these changes show a better gassing time than the control.

Pouch tab welding improvements have also been made, with the key change being implementation of a wider (50mm) welder. Doing so averted the potential quality and efficiency issues seen using a narrower weld. Additionally, there was an approximately 6% ESR improvement in the initial testing as a result of the tab welding change.

Task 3: Design of Prototype modules with ultracapacitor pouch cells

Based on the model and the test results of the POC with Gen3 A123 cells, a prototype CAD model has been created, as seen in Figure II- 53, showing that USABC volume and mass targets can be achieved for a start-

stop hybrid system using ultracapacitor pouch cells that are being developed in the parallel task of this program.

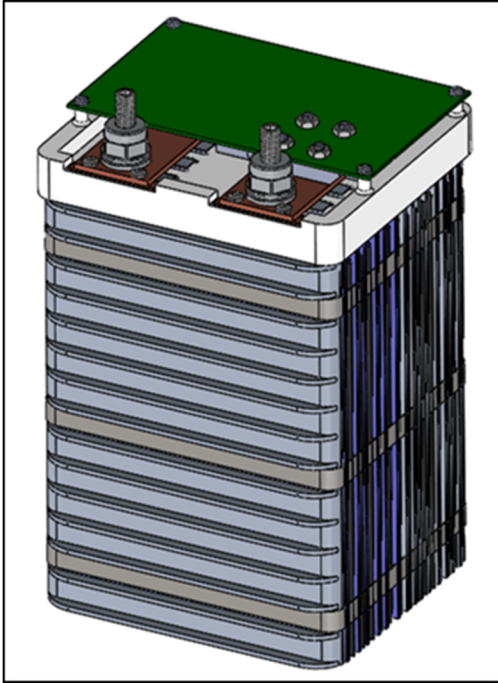


Figure II- 53: The prototype CAD model

Conclusions and Future Directions

Development of the ultracapacitor pouch cell has progressed notably in the past year with finalizations made in the electrolyte formulation, separator, pouch cell design, and several processing steps and optimizations all to mitigate gassing. Further investigations in additives, higher purity carbon to mitigate gassing, and improved fabrication steps in tab welding to improve ESR will continue as final selections are targeted by the end of the program.

This program has already shown that an ultracapacitor and LFP hybrid system can meet the USABC cold crank requirements with less mass and volume than either an ultracapacitor or LFP solution alone. In addition, the extended cycle and stand testing of the final delivery POC units intend to validate that a hybrid system will maintain its impressive cold crank properties over the vehicles lifetime.

Maxwell is convinced that the combination of batteries and capacitors is critical to the advancement of automotive energy storage technology and as such is very enthusiastic about the ultimate prospects of this program.

FY 2015 Publications/Presentations

1. 2015 DOE Annual Peer Review Meeting Presentation.

II.A.7 A 12V Start-Stop Li Polymer Battery Pack (LG Chem Power, Inc.)

Objectives

- The goal of this program is to develop a low-cost, abuse-tolerant 12V Start-Stop battery that will be capable of meeting the life, cold-cranking and cost targets of USABC.

Technical Barriers

In order for 12V stop start systems to achieve mass adoption they must be affordable, have excellent performance, and easy to integrate into vehicles.

Barriers addressed:

- Performance: Cold cranking.
- Integration: Mass and volume.
- Cost: \$/kWh.

Technical Targets

- Cold Cranking: Withdrawl of 360 Wh followed by cold soak to -30°C, then perform 3 successive crank cycles of 0.5 seconds at 6kW, 4 seconds at 4kW, and 10 seconds at rest.
- Mass: 10kg
- Volume: 7L
- Cost: USABC goal: \$220 (underhood application) project goal: \$240.

Accomplishments

- A number of LMO based cathode materials with different compositions and morphologies have been examined with respect to power and durability. Data show that the higher the surface area, the higher is the power.
- Several LTO based anode active materials having different morphologies and surface properties were evaluated for power, manufacturability and durability.
- Cathodes and anodes having different porosities were studied with respect to cell performance and durability.
- The effect of various conductive carbons has also been evaluated.
- Considerable focus has been put on work to minimize gassing at high temperatures.
- Data obtained thus far show excellent abuse-tolerance characteristics for the program cells.
- A battery pack with a simple mechanical and thermal design has been developed and is being evaluated for robustness, efficiency and cost.
- Concepts to develop a simplified BMS have been developed and are currently being studied.

Introduction

12V Start-Stop batteries are gaining increasing attention as cost-efficient approach to reduce carbon emission on a global scale. To achieve this objective, Li ion batteries offer promising alternative to PbA batteries because of their much higher specific energy and longer life. Key challenges for realization of this objective are life, cold-cranking power and cost. The objective of this proposal is to address these key issues.

Project Details

Scott Jorgensen (USABC Program Manager)
DE-EE0006250 Recipient: LG-CPI

Mohamed Alamgir (LG Chem Power - PI)
LG Chem Power, Inc.
1857- Technology Drive
Troy, MI 48083
Phone: 248-291-2375
Email: alamgir@lgchem.com

Subcontractor:
LG Chem
LG Chem Research Park
104-1, Moonji-dong, Yuseong-gu
Daejeon 305-380, South Korea

Start Date: January 2015
Projected End Date: December 2016

Approach

To achieve the above objectives, the following approaches are being pursued:

- Develop a long-life, abuse-tolerant cell using LTO/LMO active materials.
- Manipulate cathode and anode properties such as their morphologies/surface area to increase their power.
- Optimize cathode and anode compositions to enhance power.
- Optimize cathode and anode porosities, as well as optimize electrolyte compositions with respect to life and power.
- Develop a battery pack design including BMS that is simple and cost-effective.

Results

The following summarizes the progress LG/LGCPI has made so far in this program.

Optimization of Cathode

LGCPPI evaluated three different types of cathode active materials which varied in their surface areas. The data show that as the particle size decreases, the surface area increases and there is a corresponding decrease in discharge and charge resistance (Figure II- 54). LMO3, with 80% higher surface area than the baseline cathode LMO1 showed the most decrease in resistance of close to 30%.

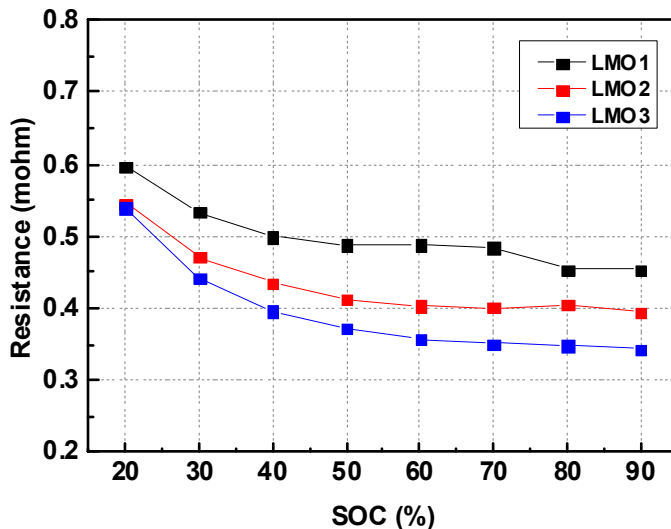


Figure II- 54: Effect of cathode materials surface area on the discharge resistance. Cathode 1) Baseline; Cathode 2) surface area: 30% more than baseline; Cathode 3) Surface area: 80% more than baseline

Cathodes having different porosities were also fabricated and tested. The cathode porosities varied by up to 25%. The data below (Figure II- 55) show that the lower the porosity, the lower is the electrode resistance. The cathode with the lowest porosity (25% relative to the baseline) showed the lowest electrode resistance. This reduction in resistance can be attributed to improved particle-to-particle contact in the denser electrode. Additionally, and as shown in Figure II- 56, the lower the porosity of the cathode, the better is the adhesion of the electrode to the current collector.

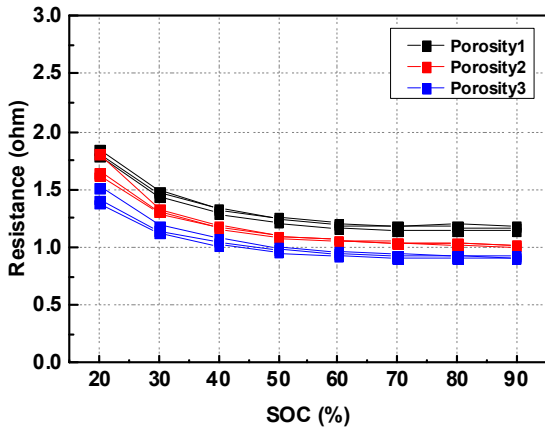


Figure II- 55: Effect of cathode porosity on cell resistance. Cathode 1) Baseline; Cathode 2) 13% lower porosity than baseline; Cathode 3) 25% lower porosity than baseline

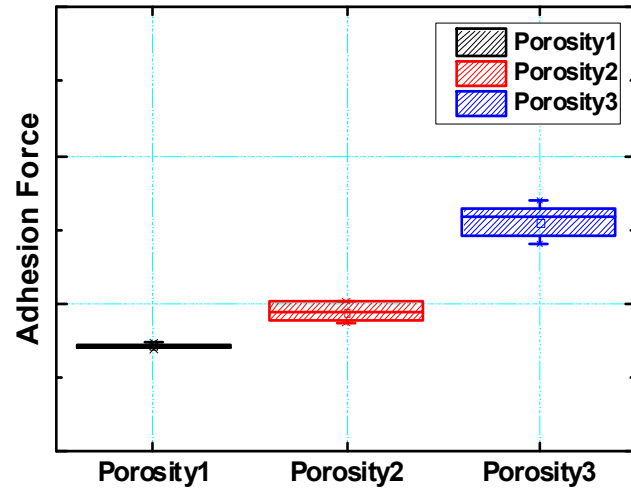


Figure II- 56: Effect of porosity on electrode adhesion

The lower porosity electrodes resulted in improved cold cranking power. This is illustrated by the initial test data available with the cells in Figure II- 57. The cathode having the lowest porosity showed the highest cold-cranking power. Further optimization work is currently underway to improve these data.

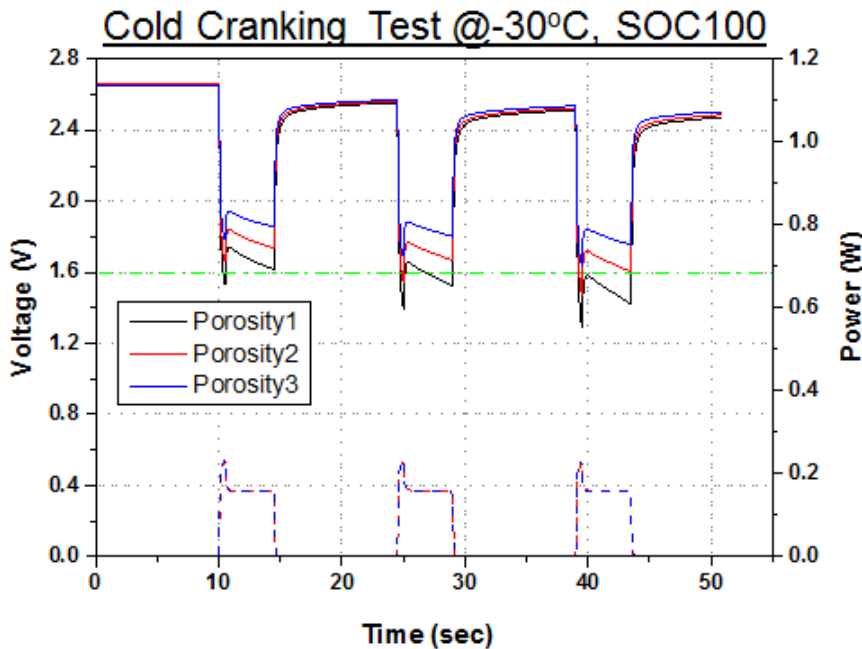


Figure II- 57: Effect of cathode porosity on cold-cranking power. Cathode 1) Baseline; Cathode 2) 13% lower porosity than baseline; Cathode 3) 25% lower porosity than baseline

Development of 12V Battery Pack

Preliminary designs to efficiently package and thermally manage the 12V battery packs have now been developed. A number of novel options to hold the cells in a mechanically robust and cost-effective manner were evaluated and are currently in the process of being down-selected. Several approaches that can efficiently shield the cells from exterior heat while being able to shed heat from the cells during operation are also being studied. Simulation data for one such approach are given in Figure II- 58. The data show that the thermal system is quite robust in that the inside of the pack remains below 50°C even after storage at 75°C for 4 hours.

LGCPPI has also been developing a simplified BMS system in order to meet one of the key design and program objectives of a low-cost 12V Start-Stop battery pack.

Conclusions and Future Directions

LG/LGCPPI have identified their baseline cathode and anode active materials with compositions and morphologies, as well as electrode formulations that have the potential for meeting the cold-cranking power and durability targets of our program. Innovative concepts to develop a simplified pack and BMS have also been developed. Key tasks for future cell work will be the development of additional material and design improvements that will lead to further improvements in the cold-cranking power and durability of the battery. The resulting 12V battery packs will be subjected to extensive characterization, life and abuse-tolerance tests.

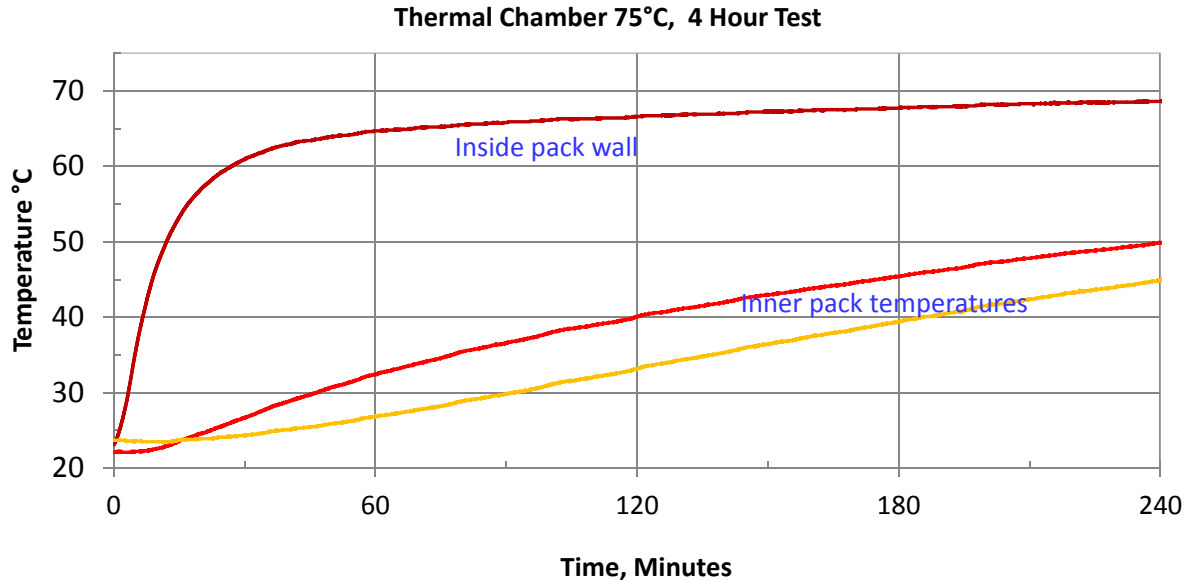


Figure II- 58: Simulation data for the pack temperatures when stored at a 75°C ambient for 4 hours

FY 2015 Publications/Presentations

1. “A 12V Start-Stop Li Polymer Battery Pack”, ES249_Alamgir_2015_p, US DOE Vehicle Technologies AMR, 2015.

II.A.8 Development of 12V Start-stop Microhybrid Batteries (Saft)

Objectives

Saft proposes to develop an advanced, high-performance battery module for 12V Start-Stop (12VSS) vehicle applications. This technology is based on Saft's proprietary LTO lithium-ion battery technology and will advance the work undertaken in the first Phase development project with USABC.

Technical Barriers

A number of key technical barriers will need to be overcome to achieve both a commercial product and its widespread adoption. The cost of a Li-ion battery product is generally the most challenging requirement for deployment in the automotive industry. With this in mind, Saft has proposed to undertake a novel design to eliminate numerous factors that raise the overall cost of a battery whilst retaining the performance and lifetime characteristics that are necessary for an automotive application.

Barriers addressed:

- Reduction in the use of high cost materials and manufacturing.
- Extending the lifetime performance of the technology through alternative chemistries and mechanical construction.
- Optimization of system control for communication and cell balancing.

Technical Targets

- Qualify the polymer to ensure it can be sealed hermetically preventing external moisture penetration or permeation of electrolyte to the atmosphere.
- Minimize gas generation by electrochemical methods and accommodate or safely evacuate gases generated over the lifetime of the product.
- Reduce impedance growth at high temperature to meet cycle life requirements, whilst retaining low temperature (-30°C) performance characteristics.
- The overall performance targets outlined by the USABC for the final battery are shown in Table II- 9 below.

Accomplishments

- Identification of two electrolyte blend systems giving promising results for low temperature conductivity.
- Further analysis of electrolyte blends to investigate gas evolution, with identification of potential methods of significant gas reduction.
- Design of experiments and testing to determine impact of LMO/NMC positive electrode blend on cell performance.
- Optimization studies of cell formats indicating the potential for performance targets to be met by both cylindrical and prismatic formats.

Project Details

Harshad Tataria (USABC Program Manager)
DE-EE0006250 Recipient: Saft America, Inc.

Ian O'Connor (Saft America, Inc. – PD/PI)
2625 Hanover Street
Palo Alto, CA 32204
Phone: 904-861-2320; Fax: 650-331-2199
Email: ian.o'connor@saftamerica.com

Start Date: June 2015

Projected End Date: December 2017

Table II- 9: USABC targets

End of Life Characteristics	Units	Target		End of program Targets
		Under hood	Not under hood	
Diascharge Pulse, 1s	kW	6		10.2
Max discharge current, 0.5s	A	900		900
Cold cranking power at -30°C (three 4.5-s pulses, 10s rests between pulses at min SOC)	kW	6kW for 0.5s, followed by 4kW for 4s		100%
Minimum voltage under cold crank	V _{dc}	8		8
Available energy (750W accessory load power)	Wh	360		432
Peak Recharge Rate, 10s	kW	2.2		7
Sustained Recharge Rate	W	750		750
Cycle life, every 10% life RPT with cold crank at min SOC	Engine starts/miles	450k/150k		450k/150k
Calendar life at 30°C, 45°C if under hood	Years	15 at 45°C	15 at 30°C	15 at 15°C
Minimum round-trip energy efficiency	%	95%		95%
Maximum allowable self-discharge rate	Wh/day	2		2
Peak Operating Voltage, 10s	V _{dc}	15		15
Sustained Operating Voltage -- Max	V _{dc}	14.6		14.6
Minimum Operating Voltage under Autostart	V _{dc}	10.5		10.5
Operating Temperature Range (Available energy to allow 6kW, 1s pulse)	°C	-30 to +75	-30 to +52	-30 to +75
-30°C to -52°C	Wh	360 (to 75°C)	360	360
0°C	Wh	180		180
-10°C	Wh	108		108
-20°C	Wh	54		54
-30°C	Wh	36		36
Survival Temperature Range (24 hours)	°C	-46 to +100	-46 to +66	-46 to +100
Maximum System Weight	kg	10		10
Maximum System Volume	L	7		7
Maximum System Selling Price (@250k units/year)	\$	\$220	\$180	\$220

Introduction

This project will result in the development and delivery to USABC of fully functional prototype monoblock assemblies with cells in either a cylindrical or prismatic format as part of a 12 V start-stop battery system. The cells will be placed in an injection molded thermoplastic monoblock container which also incorporates battery management electronics with individual compartments to house the cells.

The objective is to eliminate separate cell and module containers and integrate them into one. The electrodes will be placed directly into their respective compartments, connected, and sealed. Furthermore a battery management system will be developed according to the needs of the proposed monoblock battery. An analysis of functions required to adequately manage a LMO/LTO system will be conducted. The battery management hardware will utilize a microprocessor for data measurement and communication and will be enclosed within the monoblock housing for a robust & cost-effective design.

Approach

Innovative Approach: This project is primarily focused on developing a low cost lithium-ion product for the automotive industry. A key innovative approach to achieve this is combining the cell and module packaging in a single injection-molded thermoplastic polymer monoblock assembly (see Figure II- 59). This eliminates the need for individual isolated cell packaging and also mitigates the impact of packaging materials on the overall cost of the final product. Under the Phase I program with USABC, Saft identified a promising design of the overall monoblock. For the Phase II program Saft aims to continue this development incorporating low-cost, high performance cell chemistry and robust, yet simplified system design including busbars and electronics. Ultimately, we aim to provide to USABC deliverable modules in the form of multiple, fully functional

prototypes. In addition, Saft proposes to include other innovative design, development, and process improvement ideas which will reduce cost, reduce formation time several-fold, and provide simple, robust battery monitoring electronics.

- Design and manufacture a single monoblock whilst matching the mechanical limitations set by USABC. In particular the focus will be on achieving the performance characteristics within the 7 liter volume provided for the final module.
- Achieve cold crank performance at a temperature of -30°C as defined in the USABC test manual. This will be achieved by coupling an LTO negative electrode with a LMO-based positive electrode, either pure LMO or a blend of LMO/NMC, which will be defined through design of experiments and testing. The electrolyte selection is also key to achieving good conductivity at low temperatures.
- Achieve increased high cycle-life/calendar life of up to 450k cycles by limiting the impedance growth over time and preventing/accommodating significant gassing.
- Achieve a cost target of $< \$220/\text{monoblock}$ incorporating a system control unit capable of preventing overcharge for the battery and communicating with the vehicle for voltage/temperature monitoring.

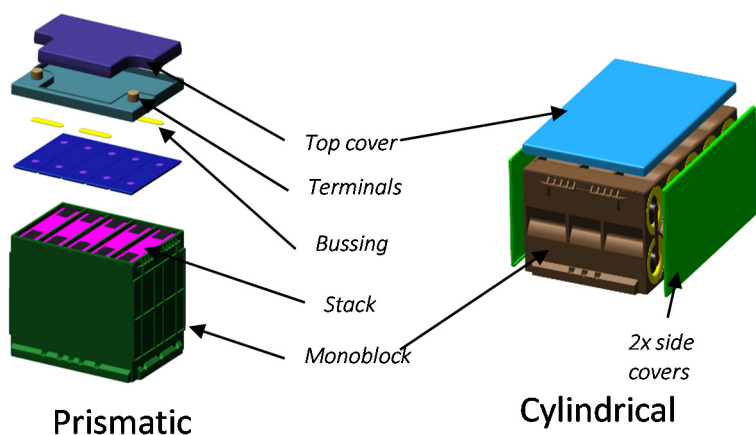
Results

The project efforts were initiated in July 2015 and we have achieved the following progress:

Mechanical design

From the Phase I program, Saft identified that the desired monoblock configuration, and goals for high-volume manufacturing and reduced cost would require the development of novel assembly methods. This development involved studies of the internal bussing of electrode stacks, their feed-through from within the battery to the circuit board, and eventually to the terminals on the outside of the start-stop battery.

For the Phase II program, Saft will continue to expand on these efforts and the initial focus of the development project has been to identify the different performance characteristics and design constraints related to a prismatic or cylindrical monoblock design.



Saft has worked toward optimizing the overall design to achieve the performance targets set out by USABC whilst still targeting low cost and keeping within the volume and mass requirements. For the prismatic design, modifying the dimensions of the module, whilst retaining the same volume, does not impart any significant benefits to the performance. With the cylindrical design however, modifying the length and width of individual cells can have a significant impact on the performance. With this in mind Saft has worked towards optimizing the

Figure II- 59: Cylindrical vs Prismatic module design

cell design to achieve the best expected performance. In both the prismatic and cylindrical cell design we were able to generate designs that offer the best opportunity to achieve the key performance requirements. A model of each of the formats can be seen in Figure II- 59.

In both cases, the electronics will be located at the top of the module. A number of alternative formats were considered, in particular for the cylindrical cells. Cell orientation, size and number can all have an impact on the capacity and cranking capability of the final monoblock. The characteristics of the numerous alternative designs investigated can be seen in Table II- 10. In the majority of orientations, the cylindrical cells could not achieve the capacity that Saft has identified as a requirement to meet the cold cranking. Doubling the number of cells from 5 to 10 for the cylindrical format enabled us to reduce the loading of the overall cells. Lower

loading also ensures better low temperature performance and generally Saft has identified that a loading of no higher than 9 mg/cm²/side is required to meet the USABC requirements.

Table II- 10: Cell format study

	Cylindrical Cell Format							Prismatic Cell Format
	5 cells - Vertical		5 cells – horizontal - Y	5 cells – horizontal - X	10 cells 3 rows	10 cells 2 rows		5 cells
(+) Electrode Loading (mg/cm ² /side)	5.0	10.48	5.00	5.00	5.00	5.00	8.09	5.00
Capacity (Ah)	34.53	45.99	32.69	33.75	33.44	37.72	46.02	46.01
Energy (Wh)	431.6	574.85	408.65	421.85	418.00	471.50	575.20	575.00
IEC External Dimensions	Yes	Yes	Yes	Yes	No	No	No	Yes
Volume – 7L	Yes	Yes	Yes	Yes	Yes	Yes	Yes	Yes

Moving forward, Saft will put together a range of selection criteria aimed at identifying the best overall format choice to achieve the requirements of the USABC.

With respect to the polymer casing, the Phase I program identified the best candidate for development of a polymer monoblock as glass-filled polyphenylene sulfide (PPS). Saft will initiate polymer permeation testing to confirm the capabilities of the polymer to achieve the required lifetime characteristics.

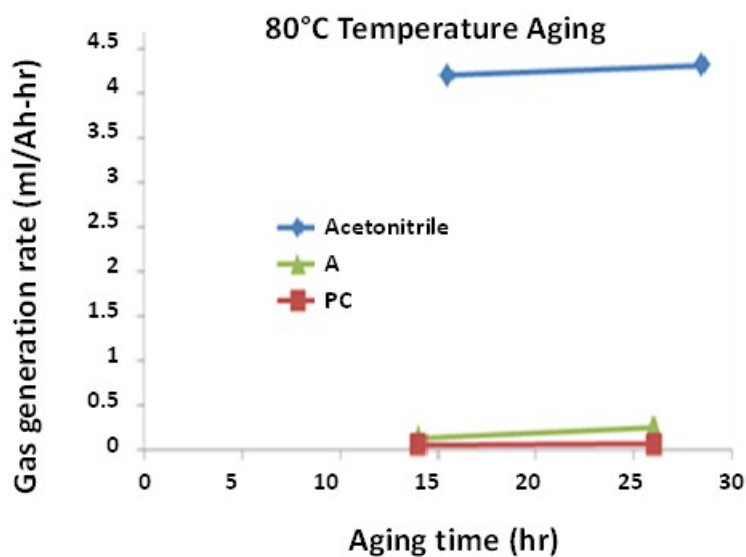


Figure II- 60: Gassing rates of different electrolytes

Chemistry Development Electrolyte

The motivation behind the initial electrolyte studies has been to identify electrolytes with good low temperature conductivities, to ensure cold cranking performance. Furthermore, measuring the gassing rates of these electrolytes at higher temperatures will ensure a good understanding of the potential to minimize and accommodate gassing in the final module.

We began by screening electrolytes for ionic conductivity at -30°C and we have so far identified two electrolyte systems that are promising. One is an acetonitrile-based electrolyte with a very high

ionic conductivity (~12 mS/cm), and therefore excellent cold cranking performance, however this is at the expense of a high gas generation rate.

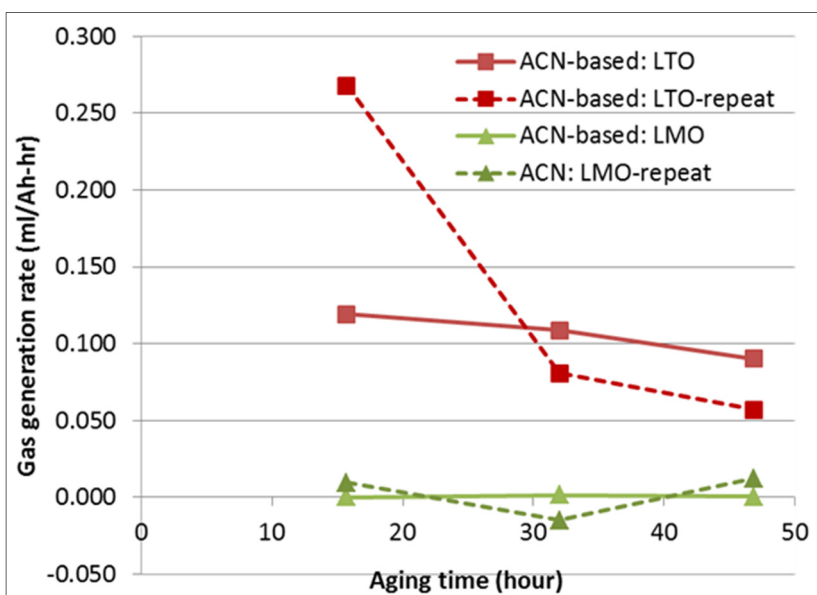


Figure II- 61: Comparison of gassing between LTO and LMO electrodes

The second electrolyte is based on an alternative solvent, which will hereafter be called solvent A. This has decent ionic conductivity, comparable to that of pure acetonitrile (~5 mS/cm) and therefore decent cold cranking performance, however not as good as that of the acetonitrile blend. It does however have a significantly better gas generation rate than the acetonitrile based electrolyte. In Figure II- 60 we can see a comparison between pure acetonitrile, pure propylene carbonate and solvent A. The measurements were taken using the same cell set-up and test conditions. Full cells were

charged to 100% SOC, wet lithiated LTO and de-lithiated LMO were soaked in the electrolytes.

Through further analysis, we were able to identify that the largest contribution to the overall gassing came from the LTO electrode as can be seen in Figure II- 61. Approaches can be taken in the future to minimize the impact of the LTO electrode on gassing whether through modifying the raw materials (for example, through ALD coating) or modifying the cell design. Modification and further investigation of solvent blends may further reduce the level of gassing. Additionally, the introduction of additives into the solvent blends has not yet been investigated and can frequently have a very positive effect on reducing the overall gassing rates of electrolytes.

Cell Development

The initial focus on the cell chemistry is identifying a positive blend that will enable cold crank capabilities that are superior to those studied in the Phase I program. In that case the performance of the LTO negative and NMC positive electrode based cells could not achieve the cold crank requirements according to the USABC test parameters. NMC was identified as the biggest contributor to poor performance.

Table II- 11: Positive blend, theoretical performance vs. measured

Blend	Theoretical Discharge Capacity (mAh/g)	Formation DCH2 capacity (mAh/g)-C/10
100%LMO	103	101.03
10%NMC	108	101.94
30%NMC	119	114.58
70%NMC	141	134.20
100%NMC	157	151.63

Saft undertook efforts to set up a design of experiments (DOE) utilizing the same LTO negative with a varying blend of LMO/NMC positive electrode.

Table II- 11 details the different blends investigated as well as the theoretical capacities and the different performances measured. LMO is generally a lower energy system at room temperature;

however it can provide significantly better cold crank performance at low temperature. With the LMO addition to the positive electrode it was hoped that any reduction in overall energy would be more than compensated at cold temperature by the better cranking performance capabilities. With this in mind, Saft set up a design of experiments to investigate the performance of different polymer blends of LMO/NMC.

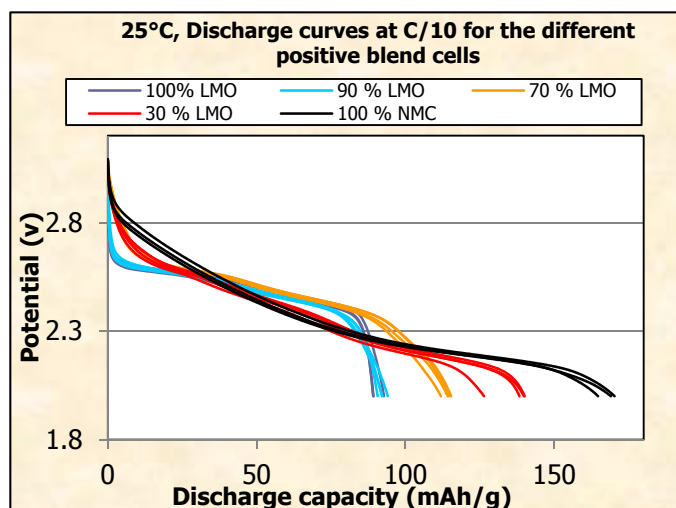


Figure II- 62: Discharge curves of positive electrode blends

In Figure II- 62, we can see the discharge curves for each electrode blend at room temperature. The testing was carried out using single-layer electrodes and acetonitrile-based electrolyte. It demonstrates the performance of the blend compositions against the overall discharge capacity. Note the longer curve and therefore higher discharge capacity of the NMC, which corresponds quite well with that predicted by the theory, however we can also see the steeper discharge curve indicating that LMO will in fact have a higher voltage at low SOC. The overall performance trend also corresponds quite well to that which would be expected as we vary the composition from 100% LMO to 100% NMC. This effect is exacerbated at low temperatures.

Indeed, when we carried out further testing at low temperature we found a significant performance difference as we increased the concentration of LMO in the positive electrode blend. An experiment was set up at -30°C to investigate the cold cranking performance of the electrode blends defined in the DOE. The electrolyte used was again an acetonitrile based solvent blend along with a LTO negative electrode. The results of this testing can be seen in Figure II- 63. The tests in this particular graph were carried out at 100% SOC but further testing is required to confirm the performance difference extends across the full range of SOC's. We find the best cold crank performance to be the electrode fabricated with 100% LMO as was predicted through the room temperature testing. The tests were again carried out using single layer electrodes and confirmation testing will be carried out with multi-layer electrodes. The line at 1.6 volts indicates the minimum voltage requirement to achieve the cold cranking. The performance will progressively decrease as the SOC is reduced but the pure LMO electrode still has a significant potential above the minimum threshold, at least at 100% SOC. Ultimately, after further testing, with acetonitrile based electrolyte and low loading of electrodes Saft was able to pass the cold crank requirement at below 25% SOC. Further testing on larger cells will be required to get a true reflection of what would occur in a real-world application.

System Development

The final monoblock assembly will include an integrated, cost-effective battery monitoring system. The areas of responsibilities between the systems development team and mechanical development team have been identified. An analysis of the functions required to adequately manage the electrochemical system has been initiated. This includes a high level architecture spec of the requirements and a statement of work which will be generated and provided to Jabil.

Conclusions and Future Directions

Polymer Development

Saft will continue to optimize the different cell formats to achieve a more precise understanding of potential module performance and cost. We will identify the best decision criteria to distinguish between the cylindrical and prismatic designs. For the polymer study, we will finalize a matrix comparison for and confirm the selection of polymers to be investigated. The polymer test plan will need to be finalized also and include test duration, temperature, design set-up, quantities etc. Ultimately we will also purchase the materials required for immersion and permeation testing.

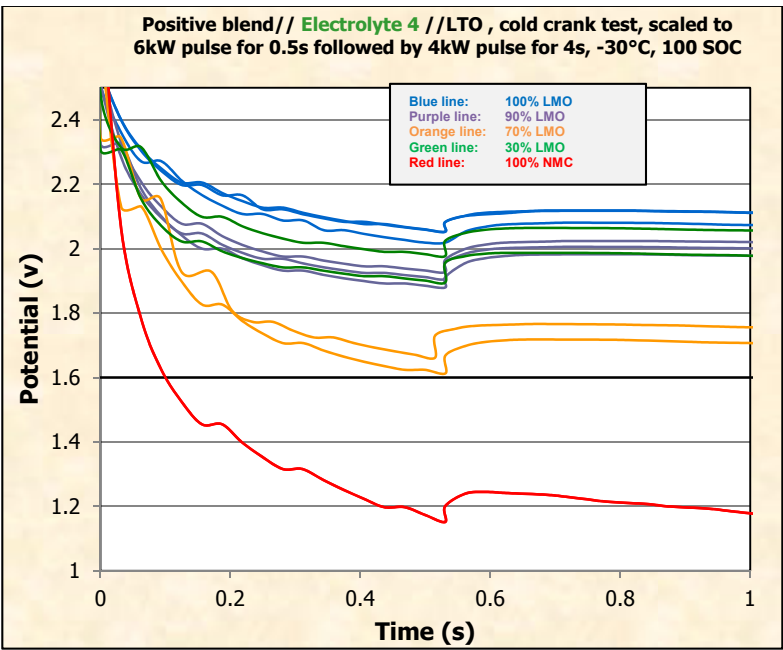


Figure II- 63: Cold crank curves of positive electrode blends

Chemistry development

For the electrolyte studies, we will continue to investigate gassing and electrolyte conductivity and the impact on cold crank performance. Additional electrolytes and blends will be studied which combine good conductivity and reduced gas generation. Additives and coatings will also be investigated to reduce gassing. C-size full cell studies will be carried out with multi-layer electrodes with cold crank performance testing. Additionally electrode optimization studies will be initiated with work on optimizing positive and negative electrode formulation (binder, percolating network etc.)

System Development

Saft will identify the PCB

Specifications and determine appropriate industry standards to follow for circuit design, with a focus on the target cost. Saft will subcontract to Jabil and work with them to select the most cost-effective microcontroller solution for the subsystem. Additionally we will focus on the interconnection design and determine the optimal solution for packaging, reliability, and cost for connections between the cells/busbars and the PCB.

FY 2015 Publications/Presentations

1. None.

II.A.9 Advanced Polyolefin Separators for Li-Ion Batteries Used in Vehicle Applications (AMTEK Research)

Objectives

To develop advanced separators with improved high voltage oxidation resistance, safety features (high temperature dimensional stability, lower shutdown temperature), and lower cost for lithium-ion batteries in electric vehicle applications.

Technical Barriers

One of the main technical challenges in this project is the development of lithium-ion batteries with voltage stability up to 5V. This technical barrier applies to the whole system in which the proper electrodes, electrolyte with additives, advanced separator and case material must be properly selected so that the integrated system meets the high voltage requirements. The other main challenge is finding a solution to the proposed USABC targets that is both technically feasible *and* cost effective. The proposed work suggests adding value to the separator in terms of cell performance, voltage oxidation resistance, safety (low shrinkage, shutdown), while simultaneously reducing cost.

Technical Targets

- Voltage tolerance: 4.5 - 5.0 V.
- Air permeability: Gurley less than 250s/100cc.
- Electrical resistance: MacMullin Number < 9.
- High temperature dimensional stability: shrinkage less than 5% at 180°C.
- Shutdown Temperature: 105°C (stretch goal)
- Wetting rate: >20% improvement compared to baseline.
- Cost: <\$1/m²

Accomplishments

- Demonstrated a reduced shutdown temperature lower by 6-10°C lower than the baseline separator.
- Achieved >20% improved wetting compared to baseline control.
- Demonstrated high temperature dimensional stability (<5% shrinkage in MD, TD at 180°C, 30 minutes) with ceramic coated separator.

Project Details

Robert Waterhouse (AMTEK Research LLC)
DE-EE0006250 Recipient: AMTEK Research LLC

Weston Wood (AMTEK Research LLC)
250 N. Hansard Avenue
Lebanon, OR 97355
Phone: 541-259-3901; Fax: 650-331-2199
Email: wwood@entek.com

Subcontractor:
Farasis Energy, Inc.
21363 Cabot Boulevard
Hayward, CA 94545

Start Date: June 2015
Projected End Date: June 2017

Introduction

ENTEK has proposed to develop an advanced separator with high voltage oxidation resistance, improved safety features, and reduced cost to meet the EV requirements given by the USABC Program. The Program consists of three phases: Phase I will develop and incorporate the desired features into the separator; Phase II will develop approaches for reducing cost; and Phase III will prove out the technology in large format, high voltage cells built by or partner, Farasis Energy.

Approach

Phase I will be based on our existing process technologies (extrusion-extraction of base films together with coatings on these base films), to incorporate value-added features (such as improved wettability, lower temperature shutdown, reduced thermal shrinkage, and improved oxidation resistance) into the separator.

In Phase II, we will investigate incorporation of these same features into separators by using lower cost, in-line technologies compatible with our existing manufacturing process. In-line process capability, as opposed to an off-line secondary process, will be critical for achieving the lowest possible cost structure.

In both Phase I and phase II, the developmental separator materials will be thoroughly characterized for their mechanical, chemical, and electrical properties, including cycling in coin cells and 18650 cells built by Farasis. The 18650 cells will be tested for electrochemical performance (cycle life, power, and calendar life) and thermal abuse.

In Phase III, the best candidate separator films from Phase II will be delivered to Farasis Energy for incorporation into larger format (25 Ah) Li-ion batteries with high voltage spinel positives and graphite negatives. These cells will be delivered to USABC/DOE for testing. Prior to building the 25 Ah deliverable cells, there will be a prototype build of 2 Ah pouch cells, to confirm the performance of the high voltage chemistry in a pouch cell design and to provide the data for a Go/No Go decision with USABC, on whether to proceed with the final deliverables.

Results

The main tasks for June, 2015 through October, 2015 were:

- Base sheet optimization to reduce shutdown temperature, while maintaining or improving other key properties of the separator
- Investigation of corona treatment to evaluate its effectiveness in improving wetting of the separator

Base sheet optimization for improved shutdown, sheet quality

Three production trials were conducted in efforts to improve properties of the base sheet:

Trial #1: In this trial, we investigated the effects of different proportions of high molecular weight and low molecular weight low viscosity polyolefins. The primary purpose of this trial was to determine the effect of low molecular weight polyolefin loading level on the shutdown temperature, physical properties, and sheet quality. Up to 75 parts low molecular weight polymer was added to the formulation.

Trial #2: The primary purpose of this trial was to optimize process conditions, including screw speed, slurry content, temperature, and pressure, in order to improve uniformity in the base sheet of formulations selected from Trial #1. Process modifications included screw speed, temperature profile, and die pressure. Data from samples targeting a porosity of 48% and thickness of 20 μm are presented in this report.

Trial #3: After the process optimization trial (Trial #2), an additional formulation trial was conducted to improve sheet quality while maintaining low shutdown temperature characteristics. A compatibilizer was incorporated, to accommodate differences in viscosity between the high and low molecular weight polyolefins. Additionally, a lower melt viscosity polyolefin (compared to Trials #1 and #2) was added to further reduce the shutdown temperature. Up to 15wt% low viscosity, low melting temperature polyolefin was added to the formulation.

A summary of the physical properties of selected samples from each trial is shown in Table II- 12. ENTEK 20 EPH (20um nominal thickness, ~48% porosity) was used as a control sample for comparison.

Table II- 12: Physical properties of samples selected from base sheet optimization trials

Sample Description	Porosity	Calculated Thickness	EMVECO Thickness	Basis weight	Gurley	Puncture
	%	μm	μm	g/m ²	s/100cc	gf
20 EPH Control	48.9	20.2	21.0	9.9	148	463
Trial #1: Formulation	46.3	15.2	21.5	7.8	94	318
Trial #2: Process Optimization	47.9	19.6	28.0	9.8	135	403
Trial #3: Formulation Optimization	48.6	21.2	21.7	10.5	157	490

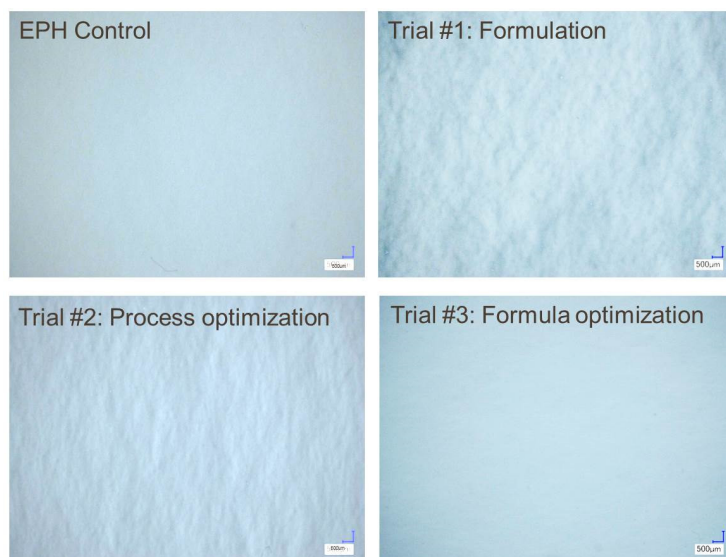


Figure II- 64: Optical images of selected samples from base sheet optimization trials

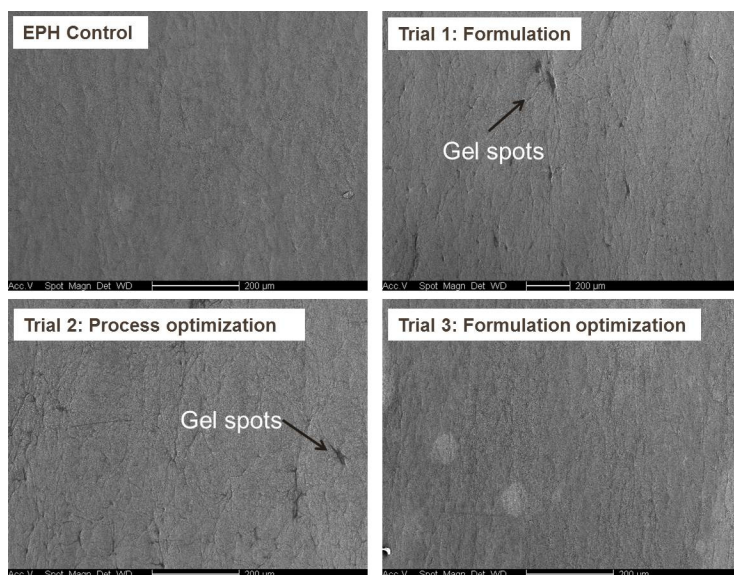


Figure II- 65: SEM images of samples from optimization trials

Table II- 12 shows physical properties of the trial samples. Selected samples from Trials #1 and #2 show large differences in calculated thickness based on roll length and diameter, compared to micrometer measured thickness, indicating that these membranes have a rough surface. Optical images of these samples prepared from Trials 1 and 2 (Figure II- 64) show that these samples have a grainy appearance with lighter and darker portions in the separator. Furthermore, SEM images show gel spots in the separator (Figure II- 65). The poor sheet quality may be a result of differences in melt viscosity between grades having differing molecular weights, leading to incomplete gelation of the polymers with high molecular weight. In order to adjust for differences in viscosity between the high and low molecular weights, a compatibilizer was incorporated to compensate for the differences in viscosity between the high and low molecular weight polyolefins. A lower melt viscosity polyolefin was added, to further enhance shutdown temperature characteristics. Further formulation optimization in Trial #3 resulted in excellent sheet quality (Figure II- 64, Figure II- 65, and Figure II- 66).

Thermal and mechanical properties of the control and trial samples are shown in Table II- 13. For Trials 1 and 2, mechanical properties tend to decrease in comparison to the control samples. There is a slight decrease in both puncture strength (Table II- 12) and tensile strength (Table II- 13) from incorporating larger portions of low viscosity polymer. We

attribute these results to less physical entanglement of the polymer chains (lower molecular weight polymer) or lower biaxial polymer chain alignment during processing. In contrast, samples prepared in Trial #3 showed excellent mechanical properties, similar to the 20 EPH control sample.

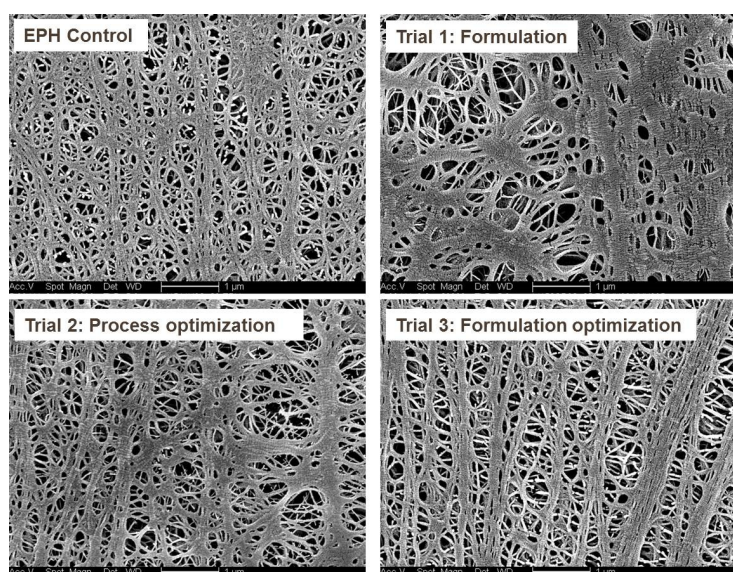


Figure II- 66: SEM images (20k magnification) of selected samples from the base sheet optimization trials

Shutdown testing was conducted on control and trial samples under constant heating rate and pressure. The electrolyte used for shutdown testing was 1M LiTFSI in 1:1 v:v ratio of polyethylene carbonate: triethylene glycol dimethylether. This electrolyte was chosen because it is non-flammable and has a high boiling temperature. The separator was wetted in electrolyte, sandwiched between graphite sheets, and heated at a rate of 60°C/min under a pressure of 450 psi. The electrical ac impedance of the separator was measured as a function of temperature. “Shutdown temperature” was defined as the temperature at which the impedance increased to 1000x the impedance at 100°C.

Table II- 13: Thermal and mechanical properties of samples selected from base sheet optimization trials

Sample Description	120°C shrinks 30 min	120°C shrinks 30 min	MD Tensile	XMD Tensile	MD Elongation	XMD Elongation
	MD%	XMD%	kg/cm ²	kg/cm ²	(%)	(%)
20 EPH Control	10.4	3.9	1081	585	134	248
Trial #1: Formulation	7.0	1.0	937	589	82	241
Trial #2: Process Optimization	5.7	-0.3	715	412	114	282
Trial #3: Formulation Optimization	11.4	6.1	1211	661	103	394

Table II- 14: Shutdown characteristics of selected samples

Sample Description	Shutdown Temperature	Impedance at 100°C
	°C	Ohms
20 EPH Control	160.0	5.8
Trial #1: Formulation	155.3	5.9
Trial #2: Process Optimization	152.1	7.0
Trial #3: Formula Optimization	154.0	6.7

Shutdown results are shown in Table II- 14. Samples prepared from all three trials show improved shutdown characteristics compared to the 20 EPH control. For these trial membranes, the polymer flows more readily due to lower melt viscosity compared to conventional UHMWPE, allowing pores to collapse more quickly at temperatures above melting point.

Corona treatment for improved wetting

Improved separator wetting may enhance electrode utilization, and therefore improve the capacity and cycle life of lithium-ion batteries. Additionally, improved separator wetting may decrease the time required for electrolyte filling, and therefore reduce the cost of cell manufacturing.

The first method explored for improving wetting was to apply a corona treatment to the surface of the separator. A two factorial design was implemented to study the effect of corona treatment level on the base material properties:

Corona power output (kW): 0.3, 0.6, 0.9

Web speed (m/min): 10, 20, 30

The 20 EPX separator (Enhanced Performance, highly porous, 53%) was used as a base membrane.

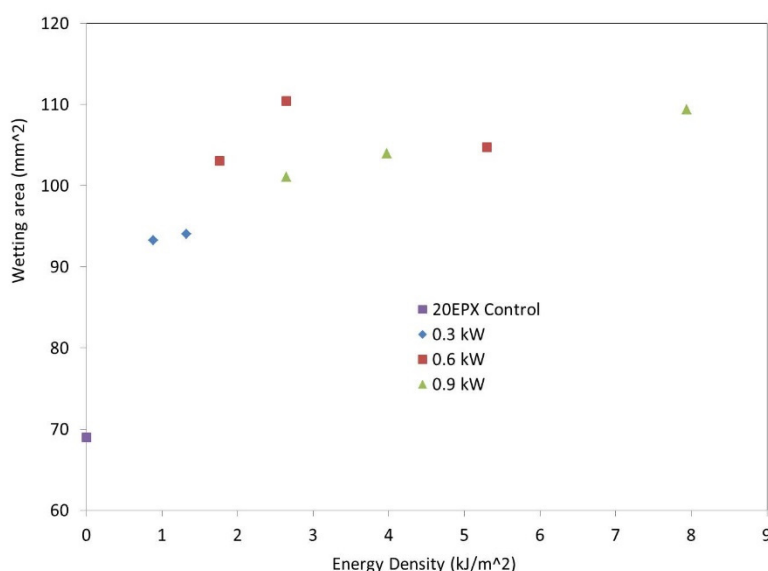


Figure II- 67: Effect of corona treatment intensity level on wetting. Wetting data collected 5 minutes after applying solvent

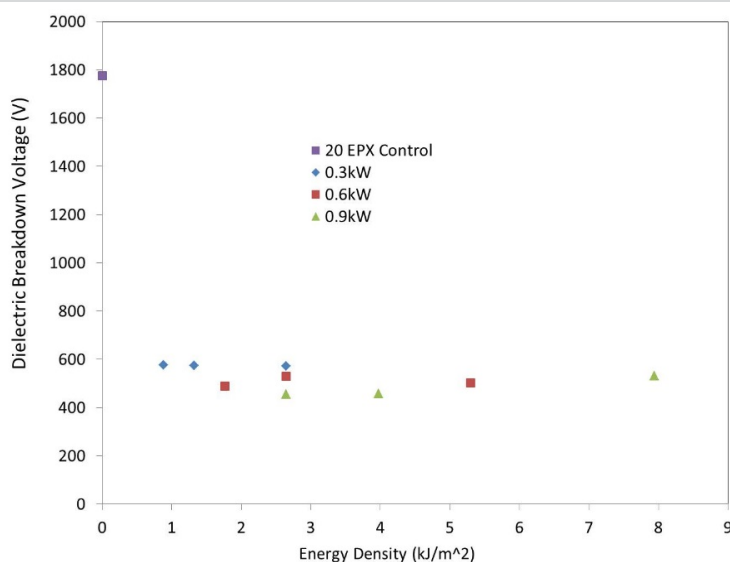


Figure II- 68: Effect of corona treatment on dielectric breakdown voltage

The wetting characteristics of the 20 EPX control and corona treated samples were determined using a “droplet wetting” test, in which the spreading area of a droplet (5ul) was measured on a piece of separator suspended horizontally in air. Propylene carbonate/tri(ethylene glycol) dimethyl ether in proportions of 1:1 by volume was used as the liquid for the wetting experiment. The wetting area was measured after 5 minutes for each sample. Results showed that, in general, wetting improved with increasing corona treatment level (Figure II- 67).

However, dielectric breakdown voltage decreased significantly after corona treatment, even at the lowest energy density tested (Figure II- 68). Figure II- 69 shows optical microscopy images at 100x magnification under transmitted light. Pinholes formed even at the lowest corona treatment intensity tested (0.3 kW, 30 m/min, 0.88 kJ/m²), as shown by the bright spots in the images. Pinhole formation is likely due to localized arc discharge during the corona treatment. We attribute the reduction in both Gurley numbers and dielectric breakdown voltage subsequent to corona treatment to pinhole formation. Because of the risk

for pinhole formation, associated with corona treatment, further corona development will be suspended at this time. Other methods for improved wetting, including ceramic filler addition, will be investigated in the coming months.

Conclusions and Future Directions

- Initial formula and process optimization trials indicated poor sheet quality when incorporating high concentrations of low viscosity polyolefin into the formulation. Further formulation optimization with

a “viscosity compatibilizer” resulted in membranes having excellent sheet quality, mechanical properties, and improved shutdown features. (See “Trial 3: Formula” in Table II- 15 with the USABC gap analysis).

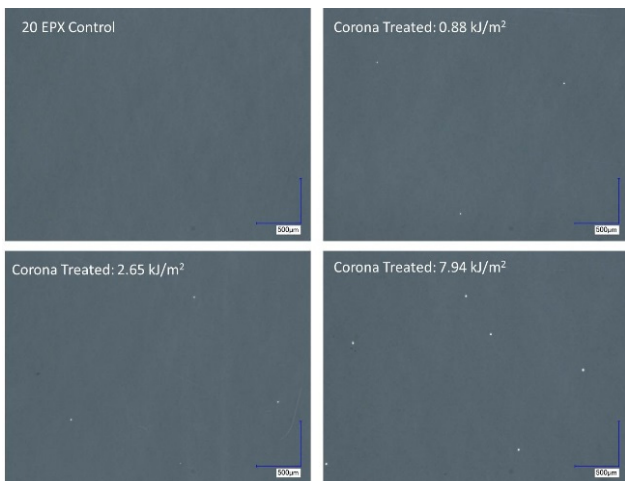


Figure II- 69: Optical images (transmitted light) of corona treated samples at varying intensity levels

- Corona treatment was effective in significantly improving the wettability of the base membranes. However, pinholes were formed due to corona arcing during treatment.
- Thus, corona treatment work will be suspended at this time.
- Future work will include incorporating inorganic filler into the base membrane, to enhance rate performance and wetting. Additionally, coatings will be applied to the membranes to enhance voltage oxidation resistance, wetting, and shutdown features in the coming months.

FY 2015 Publications/Presentations

- None at this time.

Table II- 15: USABC Gap Analysis chart of selected base and ceramic coated membranes

Parameter	Units	20 EPH	Trial 2: Process	Trial 3: Formula	16 EPH + 4µm ceramic coating	Advanced Separator Goal	USABC Goal
Nominal Thickness	µm	20	20	20	20	<25	<25+/-1
Permeability	s/10cm ³	14.8	13.5	15.7	23.5	<25	<25 (Energy) <11 (Power)
MacMullin	None	7.9	8.8	9.2	7.6	<9	<8 (Energy) < 4 (Power)
Wettability	None	Wets in electrolyte	Wets in electrolyte	Wets in electrolyte	Wets in electrolyte	>20% improvement	Wets in electrolyte
Average Pore size	µm	<0.2	<0.2	<0.2	<0.2	<0.2	<0.2
Puncture	gf/25.4µm film	588	375	572	509	>300	300
Thermal Stability	MD% shrink, 90°C (1 h)	2.4	1.2	2.9	<1	<3	<5
Thermal Stability	MD% shrink, 180°C (30 min)	>60	>60	>60	2.6	<5	-
Tensile Strength	PSI at 2% offset	7040	4700	6891	5632	>3000	1000 psi at 2% offset
Cost	\$/m ²	-	-	-	-	1.00	0.60
Shutdown Temperature	°C	160.0	152.3	154.0	153.3	10°C Less than baseline*	105
High Voltage Resistance	V	-	-	-	-	4.5-5	5

**Shutdown” defined as the temperature at which the impedance reaches 1000x the impedance at 100°C under 60°C/min heating rate.

II.B Advanced Lithium Battery Cell Technology

II.B.1 Development of Large Format Lithium-ion Cells with Higher Energy Density (XALT Energy)

Objectives

- The objective of this project is to research, develop, and demonstrate Li-ion battery cells that are capable of achieving an energy density of at least 500 Watt-hours per liter while maintaining comparable performance standards in terms of cycle life, calendar life, and durable cell construction and design capable of being affordably mass-produced.

Technical Barriers

- The energy density needed to both effectively and efficiently power electric vehicles (EV) is not available with current lithium-ion cell technology. Today's solution falls significantly short of meeting the general consumer's cost and life expectations. In order for the EV industry to be successful, battery cell with twice the energy density must be developed.

Technical Targets

- Develop and optimize new materials and design of lithium-ion cells which will double the energy density of commercially available cells from 260 – 340 Wh/L to 500 – 750 Wh/L.
- Implement these improvements to mass production system exceeding 500 Wh/L, superior overall performance and cost compared to currently available PHEV and EV cells, and safety comparable to today's commercial Li-ion cells.
- Improve EV battery affordability by reducing cell cost to \$0.20 – 0.25/Wh.

Accomplishments

- The selected high capacity cathode (HCC) materials tested by XALT Energy have demonstrated approximately 215 mAh/g (0.05C) and 180 mAh/g (1C). Applying Atomic Layer Deposition (ALD) coatings at Pneumaticoat Technologies, satisfactory performance has been obtained. XALT Energy is testing full cells with ALD coated HCC and graphite anode materials.
- Using the HCC materials we were able to manufacture full 2Ah cells and to design, by means of our computer models, large format cells 255mm x 255mm with a projected capacity of 95Ah.
- First ever deposited proprietary solid state electrolytes were used to coat the HCC powders.
- Using HCC materials with ALD coatings we were able to exceed 1,000 cycles of charge and discharge in 2Ah cell format at C/3-C/3 rate and to exceed 750 cycles at 1C-1C.
- Based on the 2Ah cells performance, the large format 95Ah cells are expected to achieve an energy density of approximately 530 Wh/L.

Project Details

Christopher Johnson (NETL Program Manager)
DE-EE0005384 Recipient: XALT Energy

Fabio Albano, Ph.D. (XALT Energy)
2700 S. Saginaw Road
Midland, MI 48640
Phone: (989) 486-8501
Email: fabano@xaltenergy.com

Subcontractors:
Argonne National Laboratory
National Renewable Energy Laboratory
Oak Ridge National Laboratory

Start Date: October 2011
Projected End Date: February 2016

Introduction

XALT Energy is developing a large format battery cell design that could double the energy density of current lithium-ion cells.

According to our preliminary data from 2Ah cells, the highest energy density has been achieved by increasing the capacity of the active materials. Lithium manganese-rich-based high capacity cathode (HCC) and high capacity anode (HCA) materials are currently under investigation. The anode materials could be either silicon-based or high-capacity-carbon based. Two-Amp-hour (2Ah) format development cells have been produced for the evaluation of the materials. Ninety-five-Amp-hour (95Ah) production size cells will be produced and delivered to ANL for testing during the months of November-December 2015 to demonstrate that the materials can be scaled up cost effectively to a production scale manufacturing environment. Preliminary discussions with prospective costumers have been initiated to develop a cell assessment program for the large format cells to be deployed in a variety of EVs.

Approach

The following approach will be taken to achieve the goals:

- Simulate performance of large format cells using computer models and simulations based on the material properties and inform the construction and design of future cells based on the models performance projections.
- Use coin cell measurements and high precision coulometry (HPC) techniques to determine early stage design flaws and failure modes.
- Collaborate with Pneumaticoat Technologies to develop the ALD coatings for cathode and anode materials and with Oak Ridge National Laboratory (ORNL) to characterize these materials.
- Design and fabricate sample cells in 2-Ah format, using HCC and HCA or graphite anode materials. The cell design is a direct scale down version of the large format 255mm x 255mm production cell manufactured by XALT Energy.
- Design and fabricate a full size, 95-Ah cell, that can be produced in XALT Energy's cell manufacturing facility.

Results

Down-selection Process

The following cell chemistries were evaluated and their respective performance is summarized in Table II- 16:

1. FCG-NMC / Si – Hi%
2. FCG-NMC / Si – Lo%
3. NCA / Graphite
4. ALD Coated – NCA / Graphite
5. FCG-NMC / Graphite
6. ALD Coated – FCG-NCA / Graphite

Neither of the NMC / Si – Hi% nor the NMC / Si-Lo% chemistries could meet the cycle life or rate capability requirements. Neither the NCA / Graphite nor the ALD coated NCA / Graphite chemistries could meet the cycle life target. The FCG-NMC / Graphite chemistry met both the specific capacity and rate capability requirements, but fell just short of the cycle life target. The FCG-NMC was then ALD-coated with Al_2O_3 and this enabled the chemistry to meet the cycle life target with little or no detrimental effects on the specific capacity or rate capability requirements. The results of the FCG-NMC / Graphite and ALD Coated FCG-NMC/Graphite chemistries are discussed in detail below.

Table II- 16: Cell chemistries evaluated

Metrics	Target	Si - Hi%	Si - Lo%	NCA	NCA + ALD	FCG-NMC	FCG-NMC + ALD
Cycle Life (C/3, 25°C)	>1000	<100	<500	<200	<250	<800	<1100
Specific Capacity, mAh/g	A:>400 C:>180	>600	400-600	160-180	160-180	170-190	170-190
Capacity Ratio % 0.05C/1C	80%	35%	60%	90%	90%	95%	95%

ALD-coated FCG-NMC / Graphite Cells

XALT Energy has performed extensive testing on different materials and cell chemistries. ALD-coated FCG-NMC and Graphite is the cell chemistry downselected for proceeding to large format builds and potential commercialization. The ALD-coated FCG-NMC and graphite chemistry has shown the best balance of energy density, power density, and cycle life in 95x64mm prototype cells.

XALT Energy tested 15 cells with several iterations of ALD-coated FCG-NMC/Graphite cells in the 95x64mm configuration. The cell iterations are as follows:

- 3 Cells - Controls
- 5 Cells – 4 layer, Al₂O₃coated cathode
- 5 Cells – 8 layer, Al₂O₃coated cathode
- 5 Cells – 4 layer, TiO₂ coated cathode
- 5 Cells – 8 layer, TiO₂ coated cathode

Pre-test analysis methods

- TEM
- EIS

The following tests were performed on these cells:

- Rate Capability Testing
- HPPC
- 1C Cycle Life Testing
- C/3 Cycle Life Testing

Post-test analysis methods

- TEM
- EIS

Pre-test analysis

TEM

Cathodes were analyzed with TEM at ORNL prior to assembly. TEM images indicate the presence of conformal ALD coatings on both the TiO₂ and Al₂O₃ coated cathodes (see Figure II- 70).

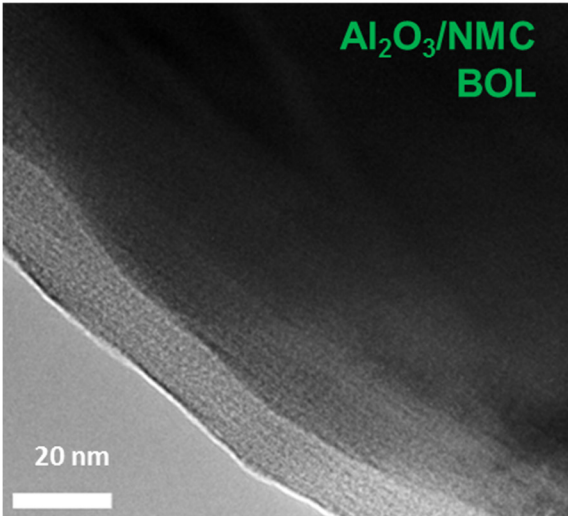
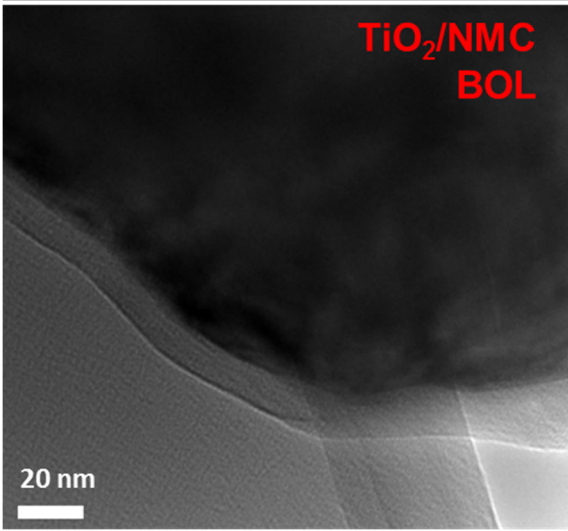
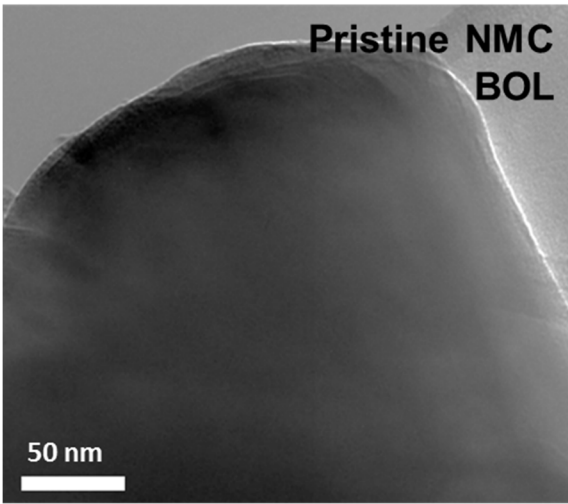


Figure II- 70: TEM images of uncoated, TiO₂ coated, and Al₂O₃ coated electrodes prior to cycling

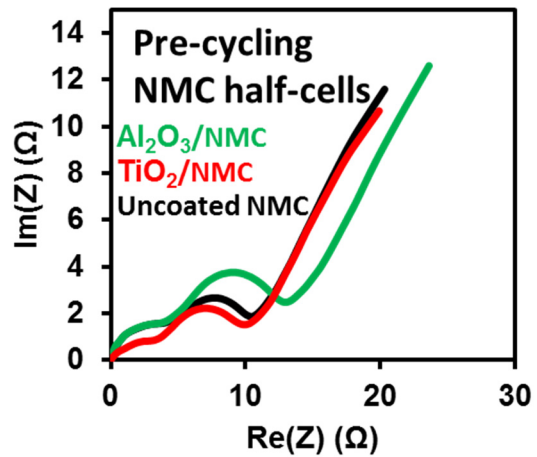


Figure II- 71: EIS analysis of uncoated, TiO₂ coated (red), and Al₂O₃ coated (green) cathode electrodes shows similar impedance profiles prior to cycling

Cathodes were analyzed with EIS at ORNL prior to assembly. The ALD coated cathodes showed impedances similar to the uncoated cathode (see Figure II- 71).

Rate Capability

The ALD coatings reduced rate capability of the cells from the un-coated controls by 5-10% depending on the coating type and thickness (see Figure II- 72).

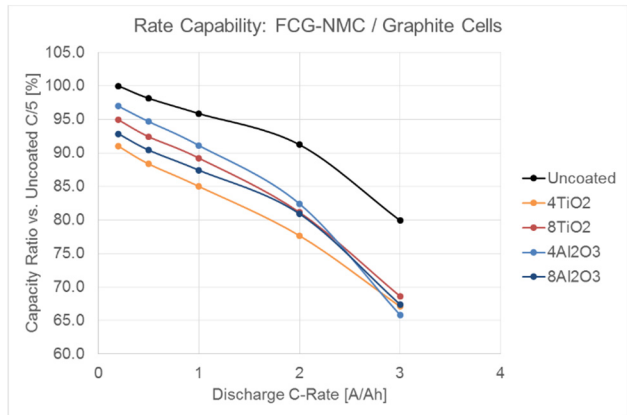


Figure II- 72: Rate capability testing of uncoated, 4 layer TiO₂, 8 layer TiO₂, 4 layer Al₂O₃, and 8 layer Al₂O₃ coatings

HPPC Testing

The ALD coatings had little effect on the power of the cells. The 30s peak power for the cells ranged from 200-1400W/kg. (See Figure II- 73.)

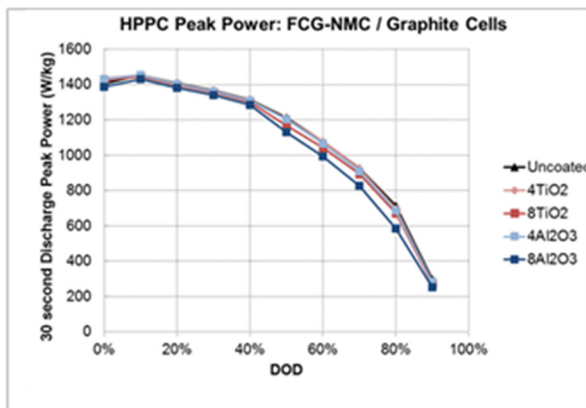


Figure II- 73: Peak power discharge testing of uncoated, 4 layer TiO₂, 8 layer TiO₂, 4 layer Al₂O₃, and 8 layer Al₂O₃ coatings

1C Cycle Life Testing

The ALD coatings influenced the rate of capacity fade in the cells. The Al₂O₃ coatings reduced the rate of capacity fade; whereas the TiO₂ coatings increased the rate of capacity fade. The Al₂O₃ coatings also reduced the initial capacity of the cell. (see Figure II- 74)

C/3 Cycle Life Testing

The ALD coatings influenced the rate of capacity fade in the cells. The Al₂O₃ coating reduced the rate of capacity fade; whereas the TiO₂ coating increased the rate of capacity fade. The Al₂O₃ coating also reduced the initial capacity of the cell. (See Figure II- 75)

Post-test analysis

TEM

Cathode electrodes from the cycled cells were removed after cycling and analyzed with TEM at ORNL.

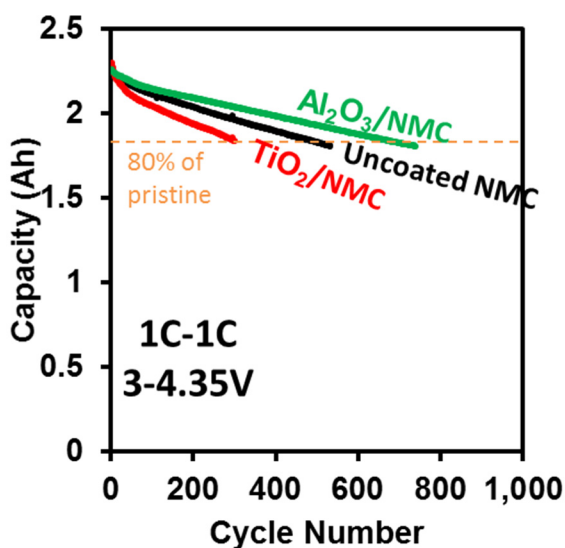


Figure II- 74: Cycle life testing at 1C-1C from 3.0-4.3V of uncoated, 4 layer TiO₂, 8 layer TiO₂, 4 layer Al₂O₃, and 8 layer Al₂O₃ coatings

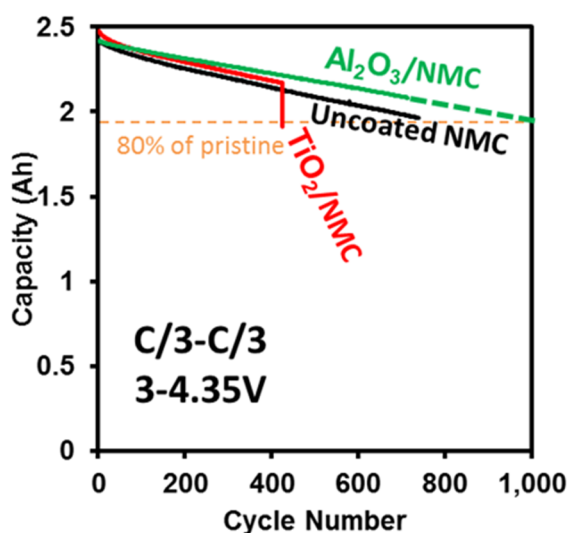


Figure II- 75: Cycle life testing at C/3-C/3 from 3.0-4.3V of uncoated, 4 layer TiO₂, 8 layer TiO₂, 4 layer Al₂O₃, and 8 layer Al₂O₃ coatings

TEM images indicate the presence of spinel phases post-cycling in the uncoated and TiO₂ coated cathodes. The TiO₂ coating was not conformal after cycling. Spinel phase formation is a known mechanism of capacity fade in the cells. However, the Al₂O₃ coated cathodes showed no presence of spinel phases post-cycling. The Al₂O₃ coating was still intact and was conformal during the post-test analysis. The reduced rate of capacity fade compared to the control is attributed to the mitigation of spinel phase formation (see Figure II- 76).

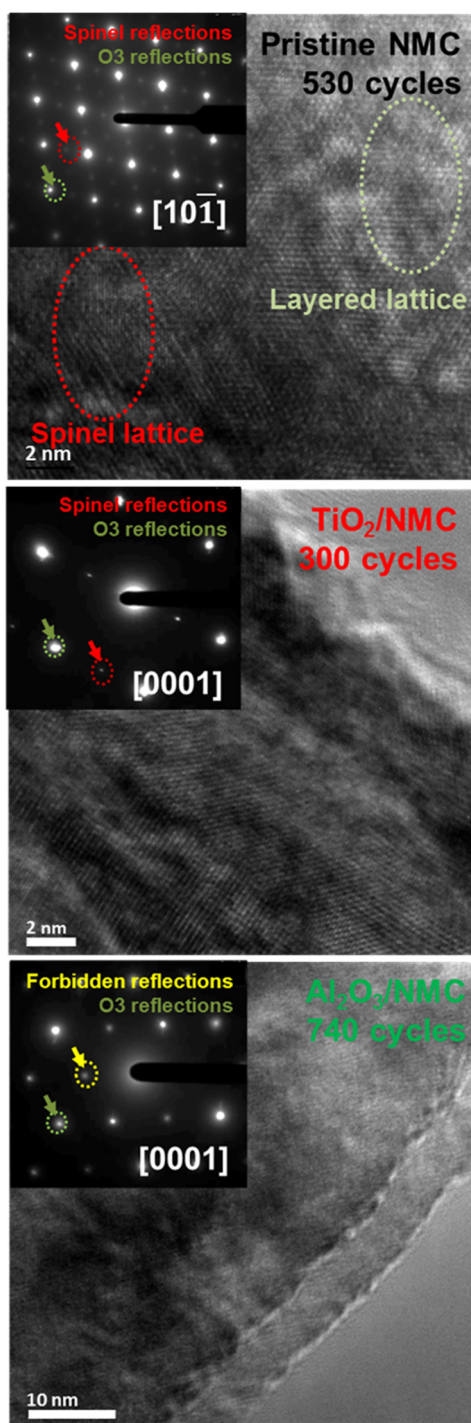


Figure II- 76: TEM images of uncoated, TiO₂ coated, and Al₂O₃ coated electrodes post 1C-1C cycling. Images on the left are brightfield images while images on the right are high resolution images

EIS

Cathode electrodes from the cycled cells were removed after cycling and analyzed with EIS at ORNL. The Al₂O₃ coated cathode showed less impedance growth as compared to the TiO₂ coated and uncoated cathodes (see Figure II- 77).

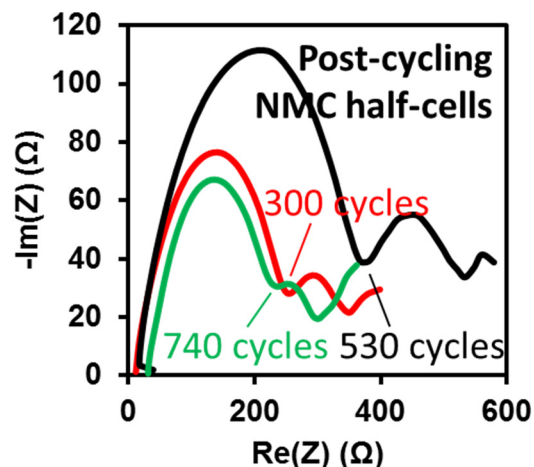


Figure II- 77: EIS analysis of uncoated, TiO₂ coated (red), and Al₂O₃ coated (green) cathode electrodes post 1C-1C cycling. The Al₂O₃ coated cathode shows less impedance growth with cycling

95UHE Cell Design

A high energy commercial cell design was created with a designed capacity of 99Ah and a nameplate capacity of 95Ah. The cell uses an already commercialized graphite material for the anode and an ALD coated FCG-NMC material for the cathode active materials. The cell uses XALT's standard 255mm × 255mm format with a 16μm separator to provide maximum energy density while maintaining low cost and manufacturability. The anode and cathode electrode thicknesses and porosities were optimized to provide maximum energy density while still meeting manufacturing constraints as shown in Figure II- 78.

The energy density of the cell is expected to be 530Wh/L with a minimum cycle life of 1,000 cycles at a C/3 rate and 100% DOD, meeting our targets for energy and durability. The cell is also expected to meet the targets for rate capability and have >80% of its name plate discharge capacity at the 1C rate based on tested prototype cells and preliminary modeling.

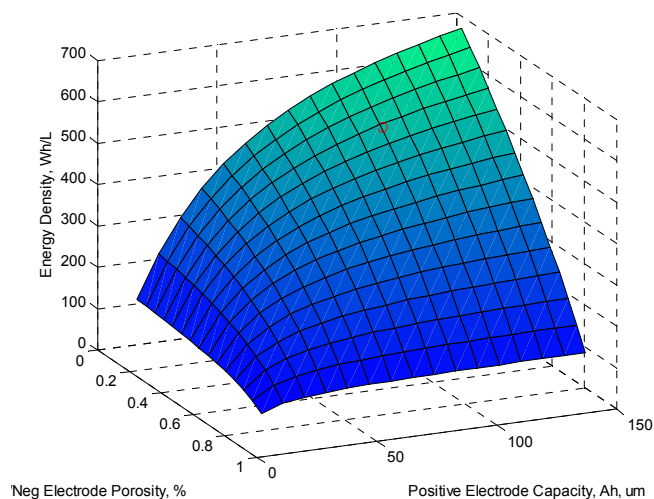


Figure II- 78: Plot of optimized cell energy density based on adjustable design parameters and manufacturing constraints

Conclusions and Future Directions

- Baseline 2Ah cell test results show that the design and fabrication are suitable to produce large format 95Ah cells in MBP.
- XALT Energy evaluated the cell performance of HCA materials and demonstrated >600 mAh/g of specific capacity. However, due to poor cycle life and rate capability Xalt chose to focus on Graphite/FCG-NMC active materials.
- XALT Energy is expecting to achieve the goal of >500 Wh/L in energy density using a FCG-NMC cathode material with ALD coating for improved cycle life.
- XALT Energy believes, from the results obtained so far, it is moving in the right direction and will continue with the development of cells with HCC and HCA improved via ALD coatings.
- Preliminary data from 2Ah HCC/HCA cells with ALD has been provided and is now available to DOE.
- NREL will develop models with XALT Energy that can be used to study and further optimize high energy cells using HCA and HCC materials.
- 95Ah UHE Cell to be built Q4 of 2015 24 large format (95Ah) cells will be delivered to Argonne National Lab for testing in the first quarter of 2016.
- Market analysis and commercialization reports will be provided to DOE at the end of 2015 to support deployment of the large format cells in EVs.

FY 2015 Publications/Presentations

1. 2015 Beyond Lithium Ion VII, Oak Ridge, TN.
2. 2015 Materials Research Society Meeting, Boston, MA.
3. 2015 Electrochemical Society Presentation, Phoenix, AZ.

II.B.2 Innovative Cell Materials and Designs for 300 Mile Range EVs (OneD Material)

Objectives

- We propose to develop a 700~1000 mAh/g Si nano-composite anode (SiNANode™) with a target life of 800 cycles, and an eventual goal of achieving an energy density of 1,600 mAh/g at the end of the program, when eventually combined with a well-performed cathode in unique large format pouch cell to achieve high energy density. An ideal target will be a cell with 800 Wh/L and 350 Wh/kg, which is capable of driving 300 miles on a single charge and achieving a cell level cost target of <150 \$/kWh.

Technical Barriers

- In order for EVs to achieve mass adoption and make a significant dent in U.S and global CO₂ production, the key problems of driving range per charge & cost per kWh must be addressed.

Barriers addressed:

- Performance: Low Wh/kg & Wh/L.
- Life: Poor deep discharge cycles.
- Cost: High \$/kWh.

Technical Targets

- Anode Targets: 700-1000 mAh/g and > 800 cycle; 1,600 mAh/g as needed at end of the project.
- Cathode Targets: 255 mAh/g and >800 cycles or other well-performed cathode and 800 cycles.
- Cell Targets: 350 Wh/kg, 800 Wh/L, <\$150/kWh at end of the project.

Accomplishments

- SiNANode can be controlled in 500 ~ 1800mAh/g with an ICE of > 92%, which met the targets.
- SiNANode development has been extensively explored on various graphite/carbon powder substrates using low cost precursors, which significantly reduced its production cost and met the projected cell level cost target of <150 \$/kWh or <15 \$/kWh if using 10% anode cost in a cell cost structure. Our separate cost analysis report indicates that the SiNANode can meet DOE's 2020 battery goal of \$125/kWh, i.e. \$9/kWh for SiNANode material.
- 700~1000 mAh/g SiNANode has been cycled 800 cycles at ~80% retention, which met the target.
- 600mAh/g SiNANode/NCA cell has shown 1000 cycles at 80% retention. The improved 1100mAh/g SiNANode/NCA cell has a slower capacity fading than 600mAh/g SiNANode/NCA cell, indicating that it can be well-cycled under the managed silicon expansion and the tailored SEI.
- 1500mAh/g SiNANode/LCO pouch cells achieved 310~350Wh/kg and >850Wh/L, which met the energy density targets. The pouch cells with those electrodes have achieved ~300 cycles at 80% retention though LCO cathode is not as stable as NCA cathode. We have developed a new electrolyte C1.1 that enables higher coulombic efficiency and hence cycling performance for SiNANode cell with electrolyte C1.1 is better than that with previous electrolyte C1. Further electrolyte additive development will enable much stable cycling performance.

Project Details

John Tabacchi (NETL Program Manager)
DE-EE0005443 Recipient: OneD Material, LLC

Yimin Zhu (OneD Material, LLC – PD/PI)
2625 Hanover Street
Palo Alto, CA 94304
Phone: 650-331-2232; Fax: 650-331-2199
Email: yimin.zhu@onedmaterial.com

Subcontractor:
A123 Systems
200 West Street
Waltham, MA

Start Date: October 2011

Projected End Date: September 2015

- EaglePicher licensed the SiNANode technology for use in high performance lithium-ion batteries with energy density in the range of 300 Wh/kg for niche markets, enabling the world's first Si nanowire anode production by a leading US battery maker.
- LMR-NMC cathode achieves a reversible specific capacity of 275 mAh/g, which results in pouch cells of 300~400Wh/kg coupled with 1200mAh/g SiNANode. However the LMR-NMC cathode has voltage fading and requires high voltage electrolyte. Therefore, it cannot be used as a reliable cathode for the SiNANode cell's cycling performance evaluation.
- Delivered the high energy density cells with >850Wh/L and 300~350Wh/kg significantly advance the current state-of-the-art in Li ion technologies.

Introduction

Based on the ability to generate solar and wind power locally and to distribute this power, more and more people believe that batteries based on Li-ion technologies are the optimal solution to electrify transportation. The cell that we propose with a novel SiNANode™ and composite cathode, will significantly advance the current state-of-the-art for Li-ion technologies.

Approach

Innovative Approach: The objectives outlined above will be accomplished by combining a high energy cathode technology with SiNANode™, a Si graphite composite. Cathode materials currently being used in PHEVs and EVs have a maximum capacity of ~150 mAh/g or less. We will use the well-performed cathode or the composite cathode containing a layered component with high specific capacity. The major technology innovations will be undertaken to accomplish the objectives of this effort:

1. Improve SiNANode™ capacity from 650 mAh/g to 700~1000 mAh/g in Phase I and to 1,600 mAh/g later. Graphite particle size and morphology will be further optimized to achieve this goal.
2. Achieve increased endurance of cycle-life from 220 to >800. To achieve this, innovative surface modification of the Si nanowire anode is required for improved stability and SEI formation. The electrolyte and binder chemistry will be optimized.
3. Achieve cell energy density of 350 Wh/kg and volumetric density of 800 Wh/L by combining the above high energy anode and cathode materials. The baseline performance of the full cell at the onset of the effort is 210 Wh/kg and 400 Wh/L
4. Achieve cost reduction resulting in <\$150/kWh (cell level). This will be achieved by moving from synthetic graphite (\$35/kg) to natural graphite which is projected to be \$5-\$10/kg. Cost reduction will also be supported through increased efficiency in manufacturing processes and scale-ups of both the anode and the cathode.

Results

We have achieved the following progress:

Cycle Life Enhancement for 700~1000 mAh/g Anode

We have been continuously working on producing pilot-scale manufacturing quantities of SiNANode. The specific capacity of ~650mAh/g has been achieved and the SiNANode half cells can be cycled more than 1200 times with a capacity retention of > 85%. Using a baseline cathode (LCO) the SiNANode was integrated in the full cells and exhibited ~350 cycles at ~76% capacity retention, which still showed much higher anode-specific capacity over graphite anode. After 200 cycles SiNANode full cell showed a capacity fading rate comparable to graphite full cell. (See Figure II- 79.)

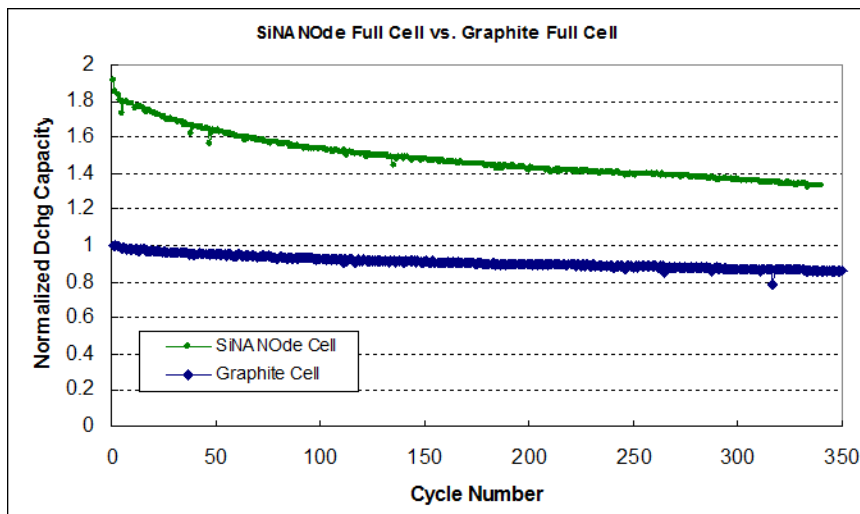


Figure II- 79: Baseline SiNANode/LCO full cell

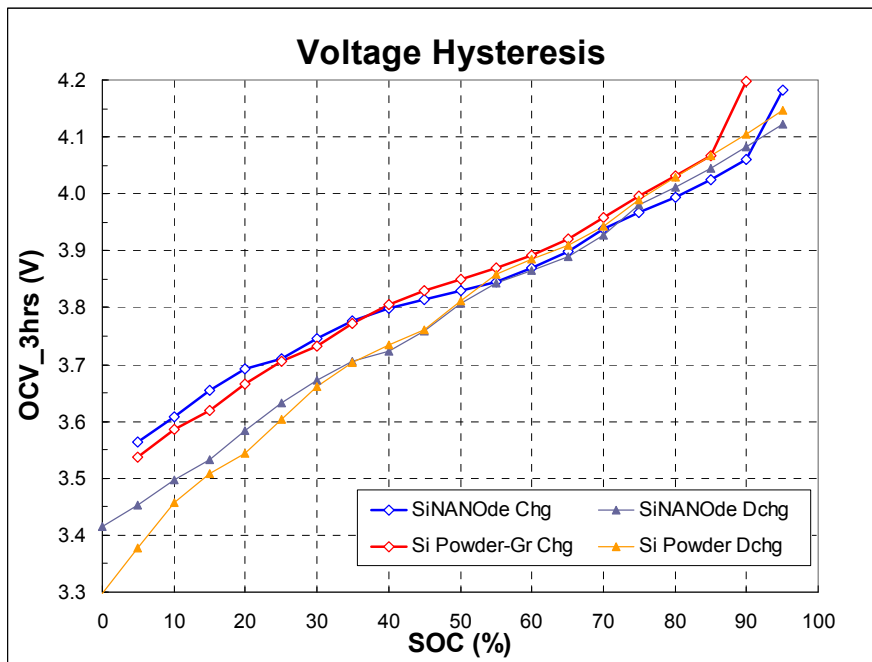


Figure II- 80: Voltage hysteresis of SiNANode and Si powder-graphite full cells

A problem peculiar to HEV battery is the voltage hysteresis phenomenon, in which measured OCV after charge (discharge) is higher (lower) than estimated OCV as per the Nernst equation. This voltage hysteresis has been modeled by adding a simple voltage modification term to Nernst equation, by using a SOC-dependent voltage source including hysteresis. This method needs historical information, as to whether battery has been charged or discharged, and the SOC and OCV are then no longer in a one-to-one relationship. Minimizing the voltage hysteresis is certainly critical. With the full cell of SiNANode/LCO, this cell voltage hysteresis has been evaluated. In our SiNANode cell, the voltage hysteresis effect is much less pronounced (<0.1V). The hysteresis effect is less pronounced for 8%SiNANode/LCO full cell in comparison with 8%Si powder-graphite/LCO full cell. (See Figure II- 80.)

It is well known that OCV and SOC are related to one another by the Nernst equation. SOC is predicted or estimated by using Nernst equation at the time when OCV can be measured or estimated.

We have made improvement in the specific capacity of SiNANode of up to 850mAh/g of reversible capacity. We further improved the conductivity of SiNANode to optimize the SiNANode material, which has showed longer cycling life of ~800 cycles at 79% capacity retention at 0.3C cycling in the half cells. It should be noted that at beginning the cell has been used for various C-rate testing. (See Figure II- 81.)

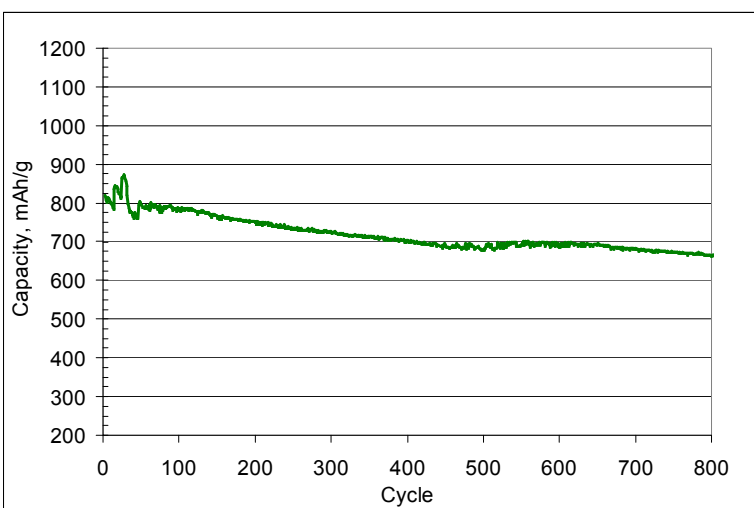


Figure II- 81: SiNANOde half cell with 700~1000mAh/g

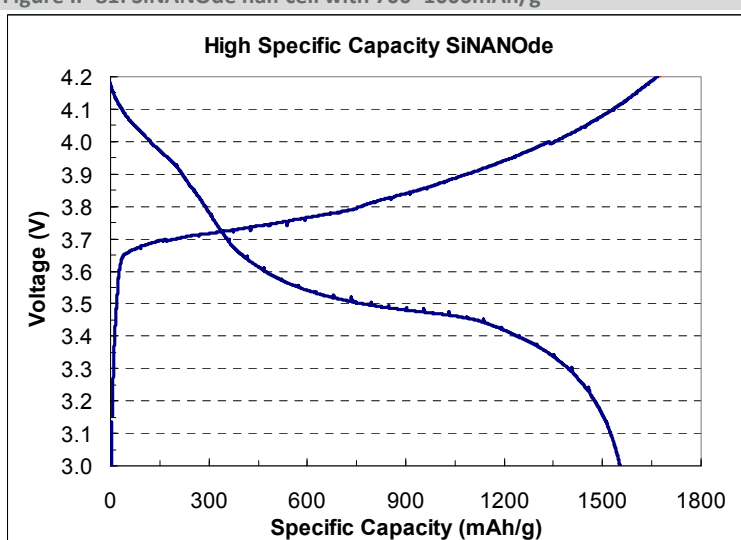


Figure II- 82: >1600mAh/g SiNANOde's voltage profile

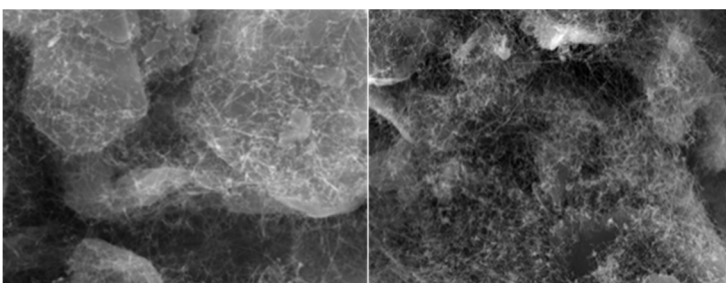


Figure II- 83: Uniform Si Nanowire distribution on graphite powders for 700mAh/g (Left) and >1600mAh/g (Right)

Enhanced Si Capacity 1,600 mAh/g Anode

We are improving the high specific capacity of SiNANOde and obtained 1678mAh/g. The first coulombic efficiency is still greater than 92%, Figure II- 82. Various binders have been used to achieve better cycling performance. Even though the specific capacity has been increased up to >1600mAh/g the Si nanowires can also be uniformly distributed on the graphite powders, shown in Figure II- 83. This proves that the SiNANOde production approach allows tuning Si-content over a wide range.

Optimization of Cathode Composition

We have tested Mn-rich cathode materials in coin half cells to confirm their electrochemical performance, so that the optimal cathode will be combined with Si anode, SiNANOde. To improve the cathode materials, its surface has been modified in various ways in Figure II- 84(Top). The ICE of the cathode electrode can be improved by optimizing its electrode composition in Figure II- 84 (Middle). Those improvements result in enhancement of its C-rate performance (Figure II- 84, Bottom).

It is critical to identify an appropriate high voltage electrolyte to enhance the cathode cyclability. In Figure II- 85, cell #2 uses an electrolyte tailored to have high voltage stability, which shows much better cycling performance over the cell#1 using the regular electrolyte.

Feasibility Test of High Energy Cells with Mn-rich Cathode and SiNANOde

In order to demonstrate very high energy density in the cells using Mn-rich cathode and ~1200 mAh/g SiNANOde, various cells were designed to achieve 250, 300, 350, and 400 Wh/kg. One key finding from this work is that the rate capability needs to be improved.

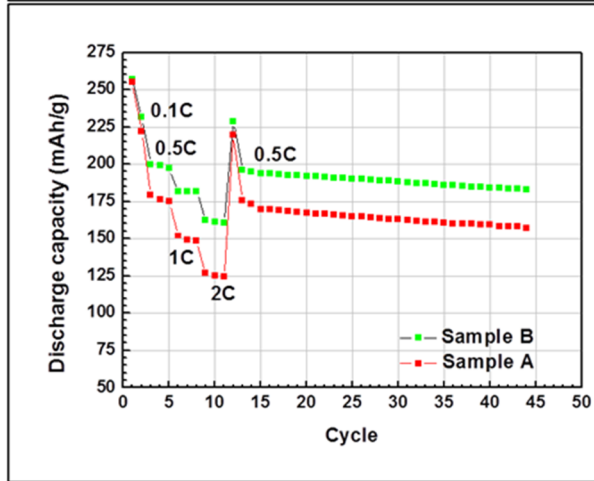
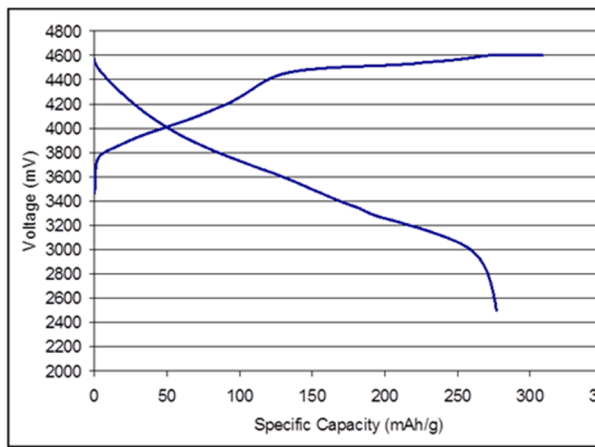
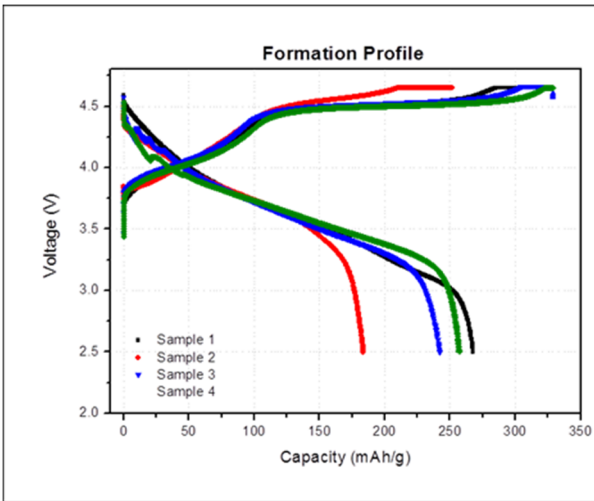


Figure II- 84: Voltage profiles and rate capabilities of cathode candidates

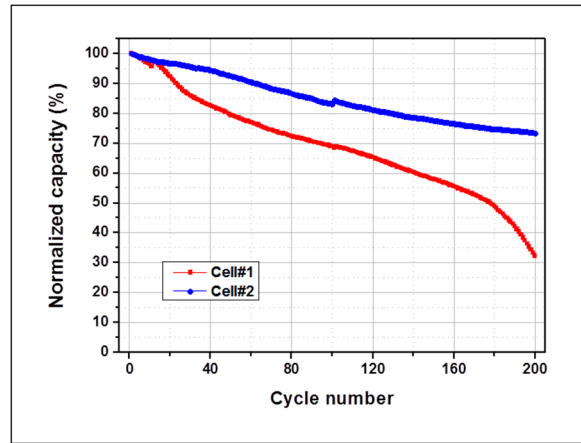


Figure II- 85: Cathode cyclability vs. different electrolyte

The cycle life test of each cell is carried out at 0.3C under 80% DOD. In the case of 400 Wh/kg cell, its initial capacity decreases, compared with other cells. The 400Wh/kg cell showed ~55% capacity retention at 150th cycle (Figure II- 86).

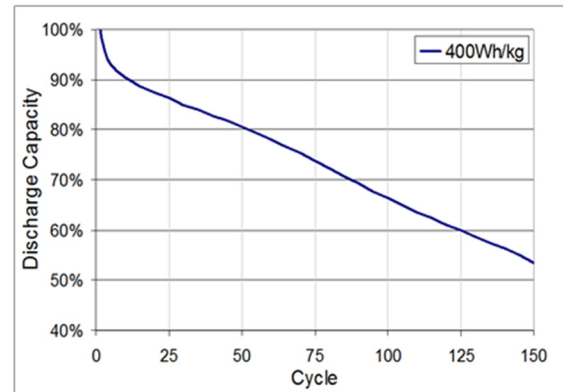


Figure II- 86: Cycle life at 0.3C rate (80% DOD)

The anode used in Figure II- 86 has a specific capacity of 1000~1200mAh/g, as shown in Figure II- 87a, which showed stable cycling performance. At beginning, the cell formation has been done at 0.05C. The high capacity SiNANode material shows better cycle life at 0.5C. This implies that the high capacity cathode also has negative impact on the cycle life of the full cell (Figure II- 86), which suggests that in order to evaluate SiNANode cyclability we should select other cathodes (e.g. NCA or LCO or NCM). In addition, the reversible specific capacity of SiNANode has been further increased up to 1200~1400mAh/g by controlling Si nanowire content in our recently improved SiNANode, shown in Figure II- 87b.

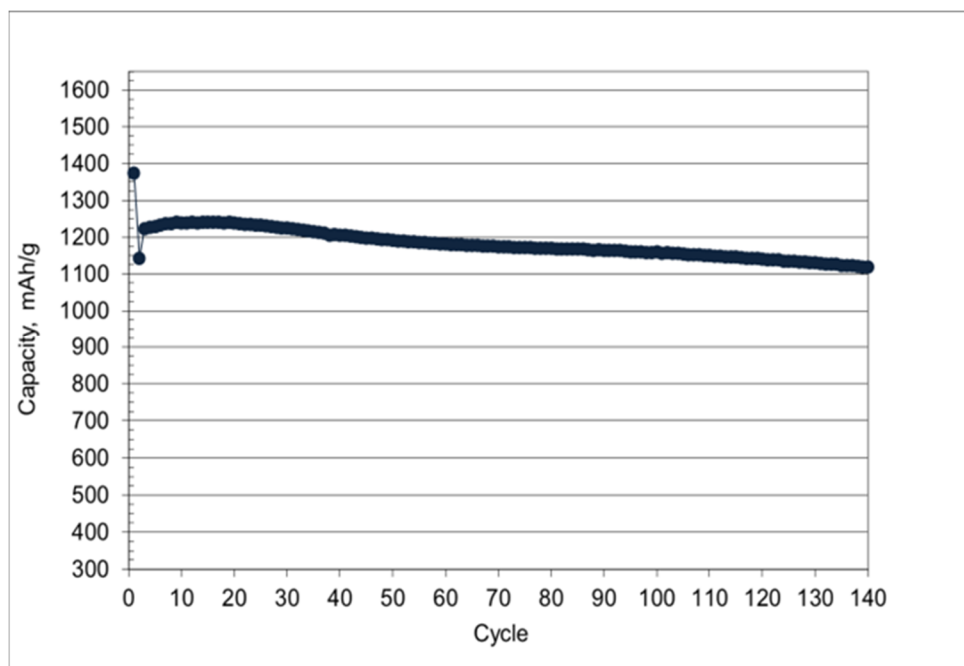
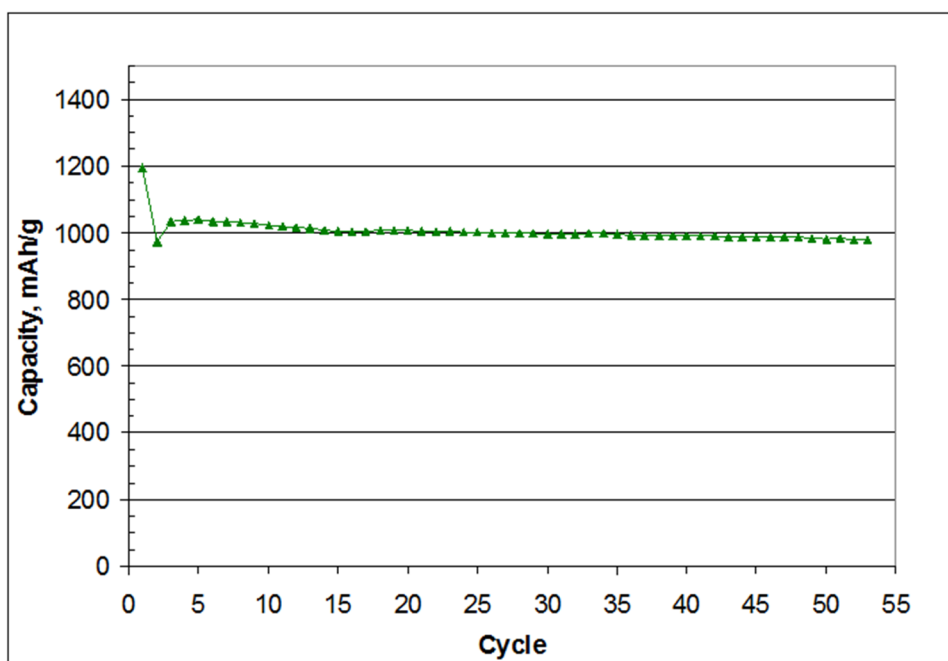


Figure II- 87: (a) 1200mAh/g SiNANode cyclability in half cell; (b) 1400mAh/g SiNANode cyclability in half cell

LMR-NMC indeed has a specific capacity of $>270 \text{ mAh g}^{-1}$ in 4.6~2.5V but it requests high voltage electrolyte for its cycling otherwise its specific capacity will not be as high as NCA, NCM and LCO in 4.4~3V.

Well-established LCO, NCA or NCM has a specific capacity of 160~200mAh/g, which only uses a conventional electrolyte (Figure II- 88).

Further reducing inactive material content in the cathode electrode may increase the cell energy density. We have demonstrated good performance for NCA and LCO cathode electrode with only 2% total inactive material.

Cell Design Study for High Energy Cells with Well-established Cathode and SiNANode

It is found that the electrode loading is a dominant factor in demonstrating a high energy cell with various cathodes and SiNANode anode. The electrodes with the desired high loadings may be difficult to coat on larger coater and can result in a substantial increase in the resistance. Thus, we have prepared the electrode with higher loading through formulation work so that the pouch cells can be made using production equipment.

In addition, cell design study has been carried out using three different grades of Si anodes with specific capacity of 600, 800 and 1200 mAh/g, respectively. The cell operation voltage is up to 4.4 V (Table II- 17).

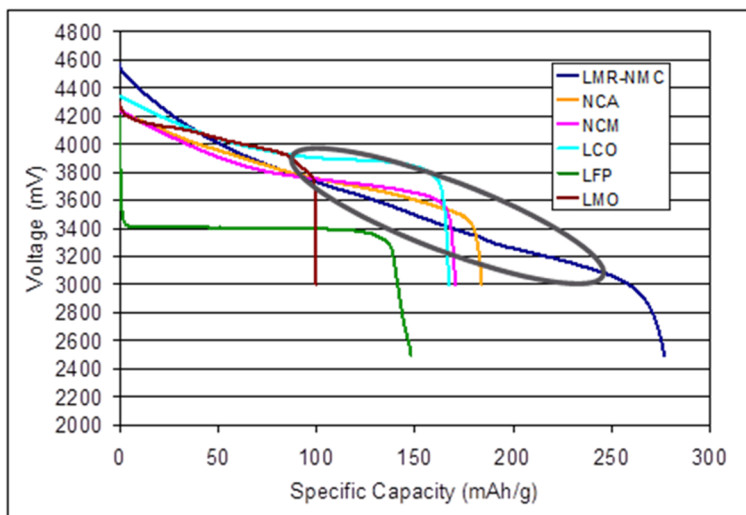


Figure II- 88: Discharge voltage profiles of various cathode materials

Table II- 17: In plant - processable high loading electrode study for high energy cell design

Loading	600 mAh/g	800 mAh/g	1200 mAh/g
Processable high loading (in plant), 4.4 V	290 Wh/kg	320 Wh/kg	330 Wh/kg
Not processable → processable high loading (in plant), 4.4 V	300 Wh/kg	330 Wh/kg	350 Wh/kg

graphite anode, as shown in Figure II- 91. As a reference, commercial graphite cell can be cycled 1000 times at 81% capacity retention. This demonstrates that the SiNANode can be very stable and that it can be further improved by forming more stable SEI in the first 100 cycles.

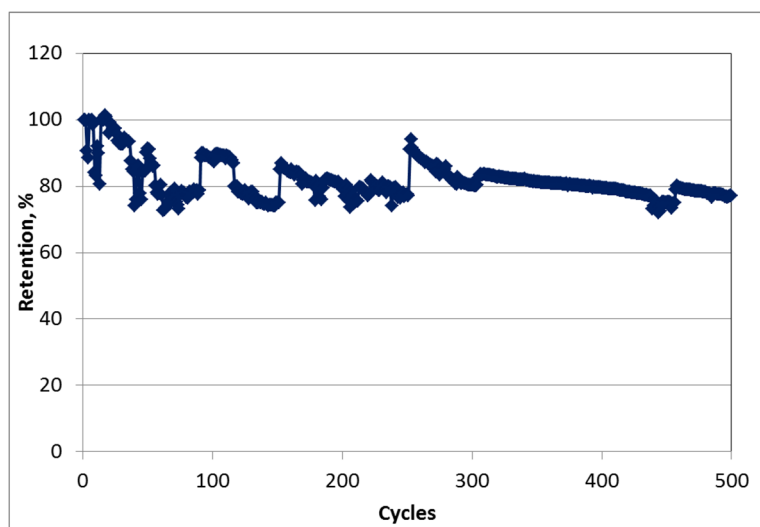


Figure II- 89: Cycle life of the pouch cell using 600 mAh/g SiNANode at 0.5C rate (DOD 100)

Cycle Life Improvement of Pouch Cell with 600~1000 mAh/g Anode

Pouch cells have been built using the 600 mAh/g SiNANode and NCA cathode (Figure II- 89). As the electrode has been heavily calendered the capacity retention is about 80% over 500 cycles. An energy density of 250~290 Wh/kg can be achieved for SiNANode NCA pouch cells.

The pouch cells have showed acceptable cell thickness change of < 12% cell swelling over 500 cycles (Figure II- 90).

Combining with the well-performed NCA cathode the SiNANode cylindrical cell shows >1000 cycle 80% retention at +0.3C/-0.5C cycling. A relatively faster capacity reduction is observed in the first 100 cycles. In subsequent cycles, the cell approaches a more stable zone and stabilizes for 1000 cycles around 82% retention, which also shows higher anode-specific capacity over

In addition, the SiNANode/NCA combination has also demonstrated good cycle life of ~1000 cycles at 70% retention in the third party pouch cells under confidential agreement.

In addition, the SiNANode/NCA combination has also demonstrated good cycle life of ~1000 cycles at 70% retention in the third party pouch cells under confidential agreement.

High capacity SiNANode/NCA pouch cell has recently achieved a reversible capacity of ~ 1100mAh/g with a stable cycling performance of 250 cycles at 80% retention and 430 cycles at 70% retention at +0.3C/-0.5C, as shown in Figure II- 92.

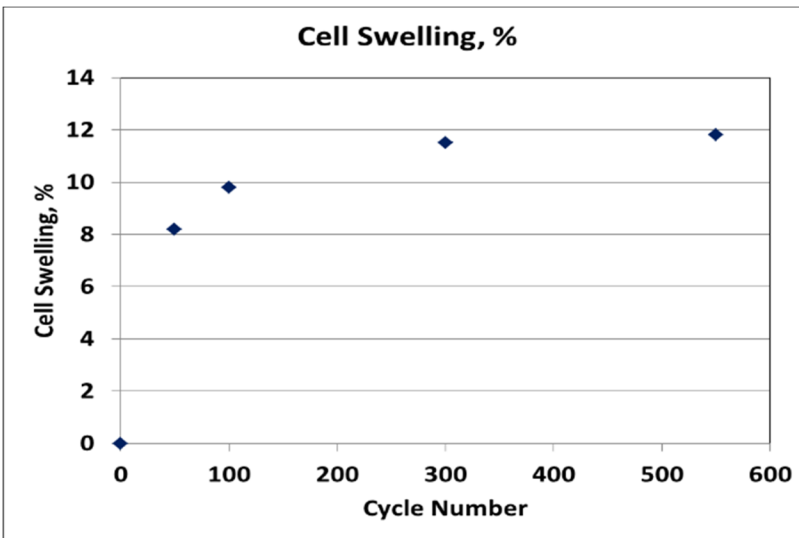


Figure II- 90: Thickness change of High Energy Density Pouch Cells: SiNANode/NCA

Low Temperature Performance for SiNANode Pouch Cells at C/2

At 25°C ~ -20°C, SiNANode pouch cell shows a typical temperature-dependent performance similar to graphite pouch cell in Figure II- 93. Even at -30°C, SiNANode cell can be charged at C/2 for 5% prior to 4.2V while graphite cell cannot be charge at C/2 as the cell voltage instantly jumps to 4.2V and starts CV charge. SiNANode cell exhibits two discharging steps at -30 ~ -40°C, indicating that it has potential to be discharged at higher voltage if extending the first step.

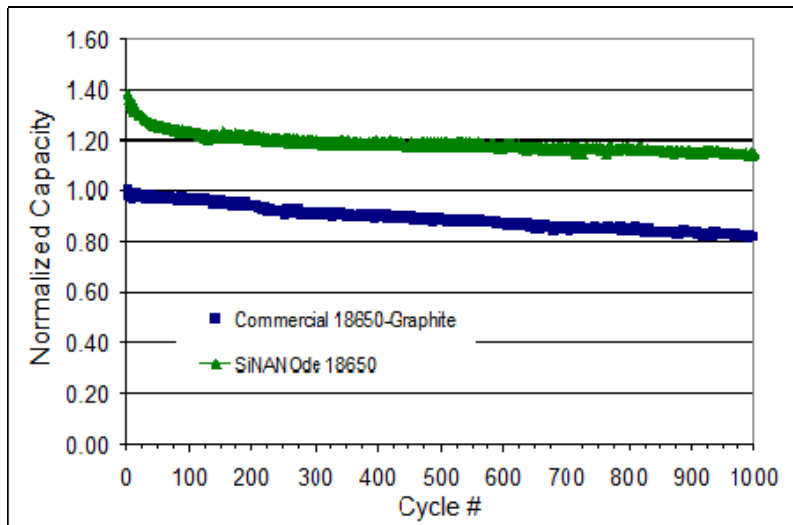


Figure II- 91: 600mAh/g SiNANode/NCA full cell cyclability

Specific Power of High Energy SiNANode Pouch Cells

At 0.1C ~ 1C, SiNANode pouch cell (Top) has a specific power similar to graphite pouch cell (Bottom). At 4.5C, superior power performance can be achieved in the high energy density SiNANode pouch cell in Figure II- 94.

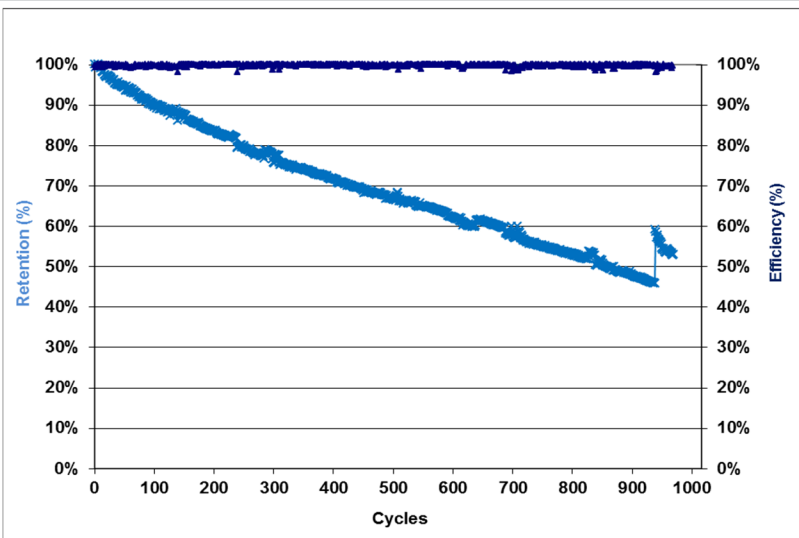


Figure II- 92: 1100mAh/g SiNANode/NCA pouch cell performance

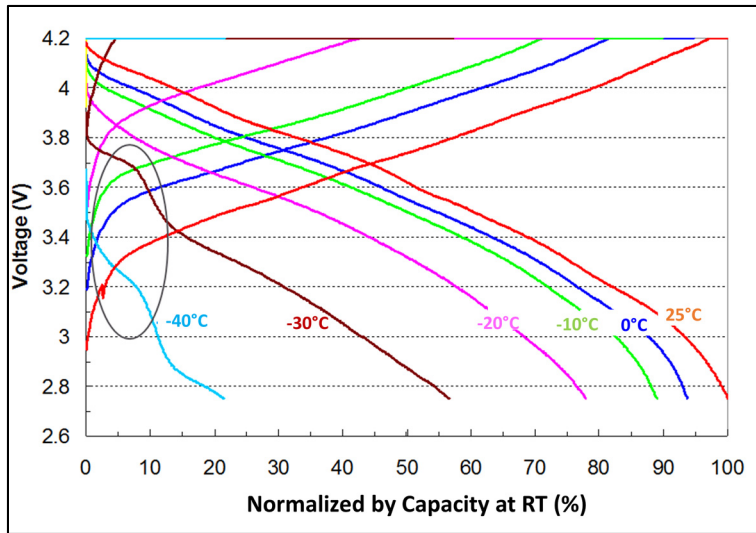


Figure II- 93: Low temperature performance of SiNANode/NCA cell

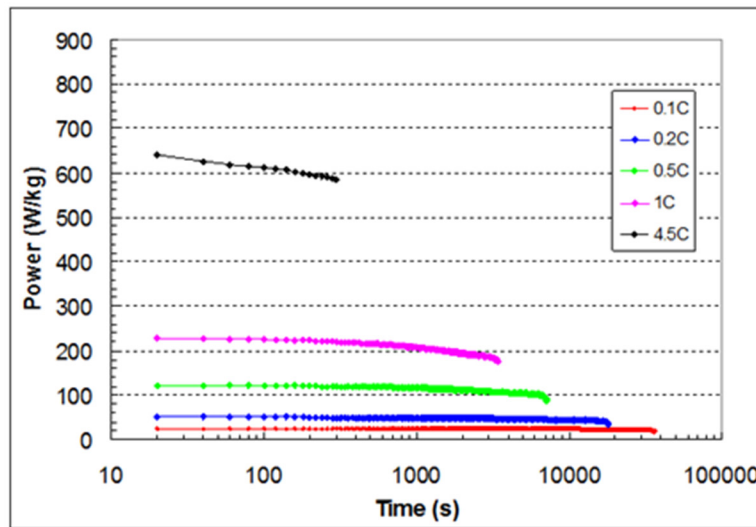
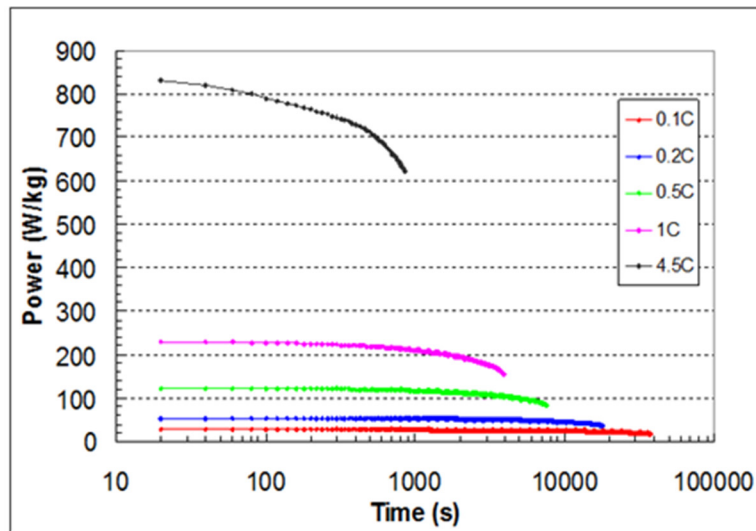


Figure II- 94: Pouch Cell Specific Power of SiNANode vs. Graphite

Self discharge of High Energy SiNANode Pouch Cells

SiNANode cells’ self-discharge properties have been investigated at 20°C for one month or at 60°C for one week. SiNANode cell’s self discharge and subsequent recharge is comparable to that of commercial graphite cells (Table II- 18).

Table II- 18: SiNANode Cell Self discharge

Condition	8% SiNANode/LCO Normalized to Graphite/LCO Control
Retention % @20°C at end of 1 month	99.6%
Realized capacity upon recharge after discharging at 20°C for 1 month	98.7%
Retention % @60°C at end of 1 week	98.7%
Realized capacity upon recharge after discharging at 60°C for 1 week	99.3%

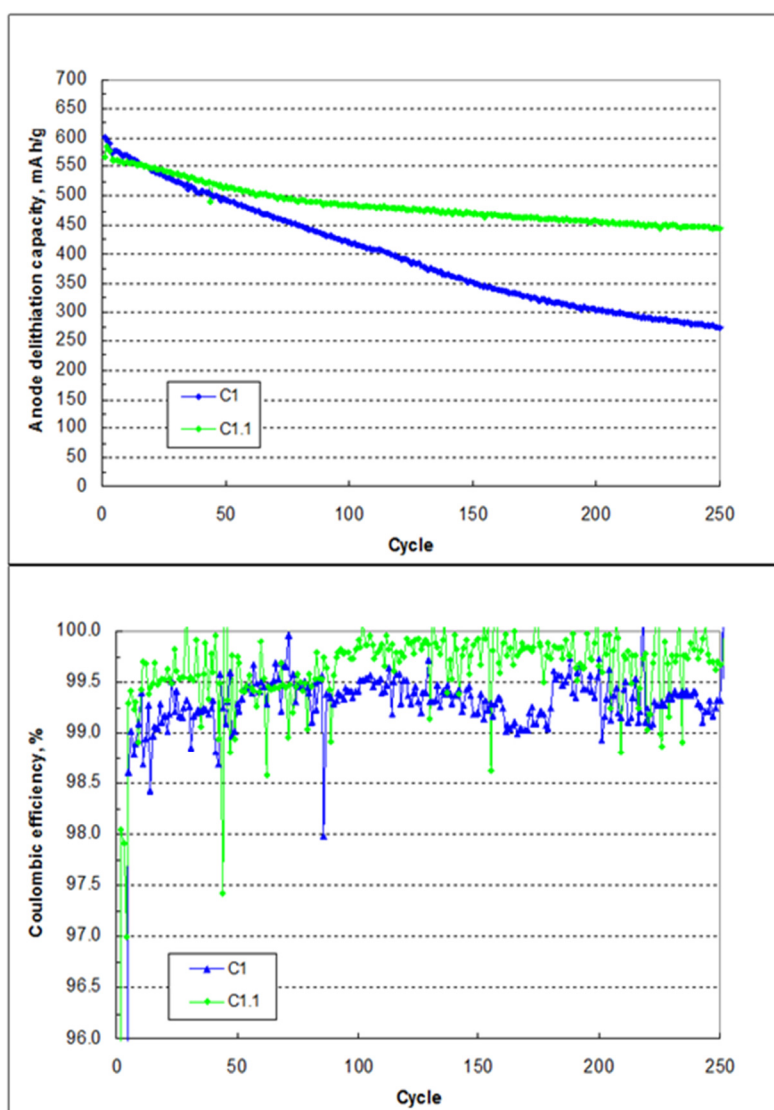


Figure II- 95: New electrolyte enables better cycling performance

Other Development

We have developed a new electrolyte C1.1 that enables higher coulombic efficiency and hence cycling performance for SiNANode cell with electrolyte C1.1 is better than that with electrolyte C1 over 250 cycles (Figure II- 95).

SiNANode made by growing Si nanowires on different graphite substrate has been extensively explored, which led to a wide range of tunable Si nanowire density on the various graphite substrates (Figure II- 96). Smaller graphite powders have higher surface area that can host more Si nanowires. This has allowed the growth of Si nanowires with >50% Si/C (by weight) in the SiNANode composite.

The 500~700mAh/g -SiNANode pouch cells have already showed the volumetric energy density >620Wh/L in conventional 4.2 ~3.0V range. The SiNANode electrode density can be as high as 1.5g/cm³ (Figure II- 97) without destroying Si nanowires.

There is no crack during winding SiNANode electrode around 0.9 mm-diameter pin (see Figure II- 98).

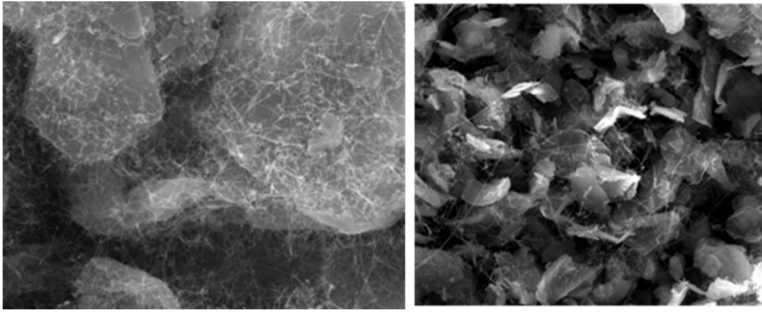


Figure II- 96: Si Nanowire grown on larger graphite powders (Left) and smaller graphite powders (Right) for >800mAh/g

CVD Si Nano-material Cost

To analyze SiNANOde cost we are using REC’s FBR polysilicon production cost as a baseline, which is \$12.5/kg pure silicon. For 8%SiNANOde its production introduce 8%Silicon into the SiNANOde composite, i.e. \$1 is added to graphite cost in a 8%SiNANOde. Accordingly, \$2, \$4 and \$5 will be added to graphite costs in a 16%, 32% and

40%SiNANOde composite, respectively (without including IP royalties cost).

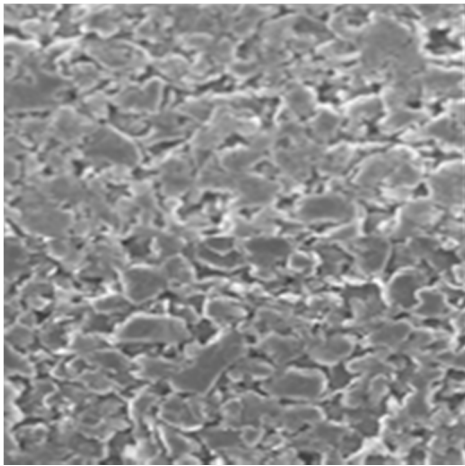


Figure II- 97: Calendered SiNANOde Anode (Left) and Graphite Anode (Right) with 1.5g/cm³

We provide a brief cost analysis at large scale production (see Table II- 19). SiNANOde development has been extensively explored on various graphite/carbon powder substrates using low cost precursors, which significantly reduces its production cost and meet the projected cell level cost target of <150 \$/kWh or <15 \$/kWh if using 10% anode cost in a cell cost structure. Our separate cost analysis report indicates that the SiNANOde material will enable DOE’s 2020 battery goal of \$125/kWh. More detailed analysis is separately submitted to DOE.

To analyze SiNANOde cell energy density, we have reverse-engineered a certain state of the art graphite/LCO cell, to produce the data shown in Table II- 20. This indicates that the cathode is much thinner than the anode (the anode specific capacity is ~2x higher than the cathode specific capacity).

Table II- 19: Brief CVD SiNANOde Production Cost

Materials	\$/kg
Silane-based REC FBR Granular p-Si production cost*	12.5
8% Si precursor cost in SiNANOde	1
16% Si precursor cost in SiNANOde	2
32% Si precursor cost in SiNANOde	4
40% Si precursor cost in SiNANOde	5

*Note: REC Silicon CEO, Tore Torvund, Granular Polysilicon Technology in SNEC, Shangjai, 2012

Table II- 20: State of the Art Graphite Battery – Cathode Fixed Brief CVD SiNANOde Production Cost

Components	Spec
Electrode Loading	3.7 mAh/cm²
Al Foil Thickness	12~15 µm
Cathode Thcikness (Double Sided, w/ Al Foil)	137 µm
Cu Foil Thickness	6~8 µm
Anode Thickness (Double Sided, w/ Cu Foil)	178

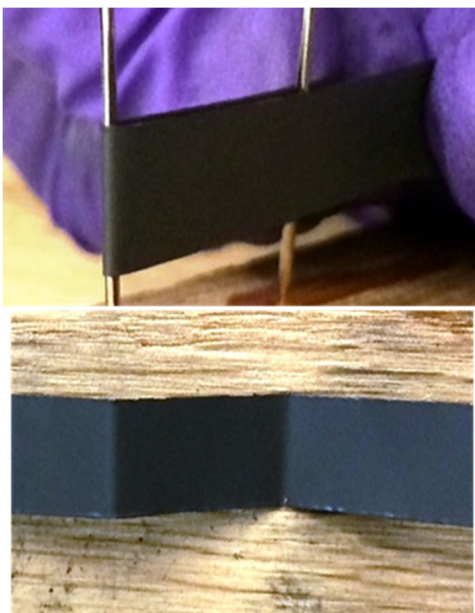


Figure II- 98: Winding on 0.9 mm diameter pin

Using a commercially available LCO cathode, a 32%SiNANode pouch cell with a capacity of 4.39 Ah achieved a very high volumetric energy density of 876 Wh/L at C/10 discharge for the cell using 9 μm Cu and 15 μm Al foils, shown in Figure II- 100, thanks to the anode thickness reduction. The volumetric energy density can be readily improved to 1000 Wh/L by improving the electrode density and using 7μm Cu foil and 12μm Al foil. The corresponding specific energy density of ~310 Wh/kg at C/10 discharge from the same cells (Figure II- 101). The specific energy density can be further improved by reducing weight from tab terraces, Cu foils, Al foils, electrolyte and cathode, to enable cells with the energy density of 350 Wh/kg, as demonstrated by one of our licensees.

Conclusions and Future Directions

We have made dramatic progress in Si composite anode (SiNANode™). In December 2014, EaglePicher licensed

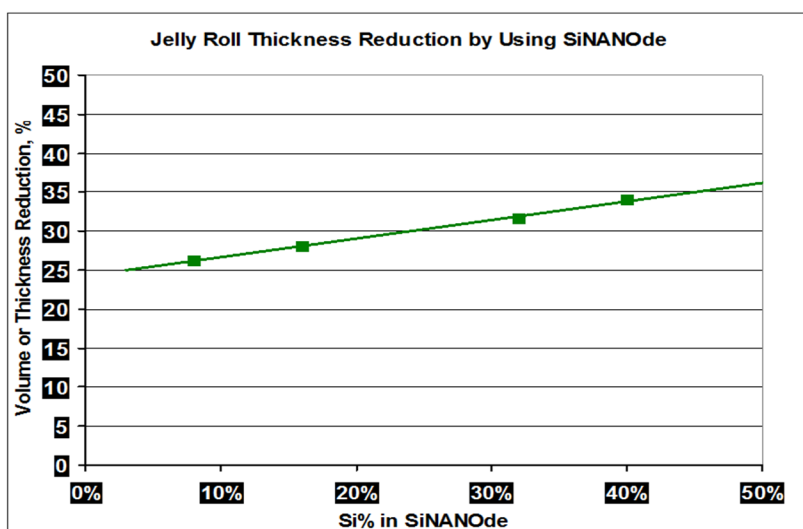


Figure II- 99: Cell thickness reduction vs. Si% in the anode diameter pin

the SiNANode technology for use in high performance Lithium-ion Batteries for specialized Markets, to build a new factory and enable the world's first Si nanowire anode production by leading US battery maker. Our recent work has enabled the cell energy densities of >800 Wh/L, 300~350 Wh/kg, which has been cycled (100% DOD) for 1000 times. Further improvement on the cycle life and cost will result in adoption of SiNANode for transportation applications.

The specific capacity of SiNANode can be controlled

in a range of 500 to 1800 mAh/g by tuning amounts of engineered silicon nanowires on the appropriate low cost graphite powders and using lower cost precursors, resulting in significantly lowered production costs while maintaining high energy density and adequate cyclability. Initial coulombic efficiency has been improved up to more than 92% for all the SiNANode products. Almost 100% utilization of Si capacity has been realized in the cells. By optimizing Si nanowire coverage and distribution on the desired graphite surface and by optimizing electrolyte and binder chemistry as well as by improving pouch cell formation protocol, cycle life has been greatly improved. We have demonstrated a cycle life of more than 800 cycles at a capacity retention of 79% for the SiNANode with 700~1000 mAh/g in half cell. We have also demonstrated good cycling performance of >1000 cycles in the full cells combining with well-performed NCA cathodes. The improved 1100mAh/g SiNANode/NCA cell has a slower capacity fading than 600mAh/g SiNANode/NCA cell.

Further cathode development has achieved a reversible specific capacity of >275 mAh/g and has improved its C-rate performance from 0.2C to >0.5C even at high loading. Therefore, we are able to make full cells with

high energy densities of 300~400Wh/kg using the SiNANode of 1200mAh/g and the LMR-NCM cathode materials.

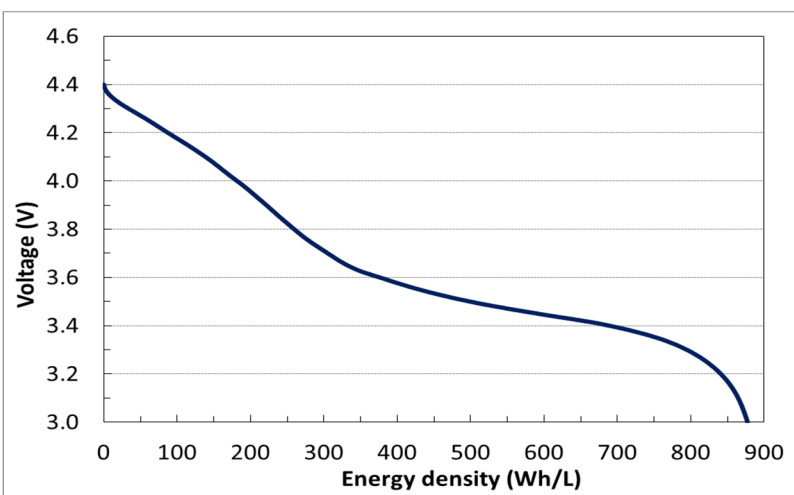


Figure II- 100: 32%SiNANode/LCO pouch cell: discharged at C/10

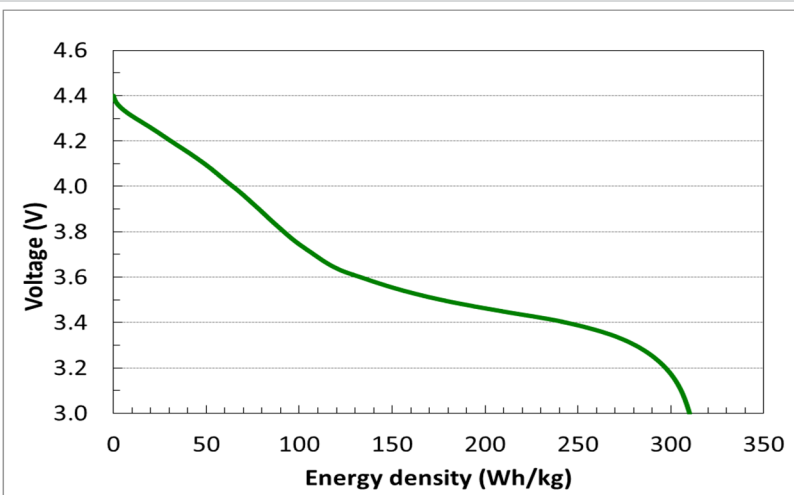


Figure II- 101: 32%SiNANode/LCO pouch cell: discharged at C/10

The energy density of the commercial cathode has been improved by reducing inactive material content and by increasing the electrode density.

We are determining the optimal Si%, electrode density and thickness so that we are able to achieve high energy density in the cells with good C-rate performance and cycling performance. For the well-established cathodes of LCO, NCA and NCM, anode thickness in cells has become dominant factor to further increase cell energy densities.

The pouch cell has showed an energy density of 883Wh/L using 1500mAh/g SiNANode and LCO cathode. Pouch cells with those electrodes have achieved ~300 cycles at 80% retention. We have been working on further improving the cycle life of the 1500mAh/g SiNANode towards at least 1000 "C/3" cycles, just like what the SiNANode material has already demonstrated >1000 cycles for the anode 600+mAh/g in the 18650 cell of typical

SiNANode/NCA. The pouch cells have showed acceptable cell thickness increase of < 12% over 550 cycles. We are currently working with several battery vendors on further improving the cycling performance by designing cell conditioning protocols, matching electrodes and optimizing SEI formation.

We have developed a new electrolyte C1.1 that enables higher coulombic efficiency and hence cycling performance for SiNANode cell with electrolyte C1.1 better than that with previous electrolyte C1. The stable SEI formation using proprietary electrolyte can minimize the pouch cell thickness increase. SiNANode development has been extensively explored on various graphite/carbon powder substrates using low cost precursors, which significantly reduces its production cost and meet the projected cell level cost target of <150 \$/kWh or <15 \$/kWh if using 10% anode cost in a cell cost structure. Our separate cost analysis report indicates that the SiNANode material can meet DOE's 2020 battery goal of \$125/kWh, i.e. we can deliver our SiNANode material with \$9/kWh.

The SiNANode cell's self-discharge and subsequent recharge is comparable to commercial graphite cells. The hysteresis effect is less pronounced for 8%SiNANode full cell in comparison with 8%Si powder-graphite full cell.

We delivered the high energy density cells with >800Wh/L and 300~350Wh/kg, as well PHEV cells using SiNANode and commercial cathode materials to U.S. DOE.

These achievements have proved that the proposed technical approach is practical to make high energy density cells for transportation applications.

FY 2015 Publications/Presentations

1. “Next Generation Batteries with High Energy Density and Better Control”, Yimin Zhu, 2015 32nd International Battery Seminar & Exhibition, March 9~11, 2015; Fort Lauderdale, Florida.

II.B.3 Advanced High Energy Li-ion Cell for PHEV and EV (3M Company)

Objectives

Leverage a cross-functional team to develop and demonstrate an Advanced High Energy Li-Ion Cell with superior performance envelope. The specific deliverables include:

- Baseline cell, based on the advanced materials developed in 3M's current contract number DE-EE0005499 titled, "High Energy Novel Cathode/Alloy Automotive Cell".
- Advanced cell > 2Ah with, achieved by cell level integration of high capacity Si anode with $\geq 15\%$ improvement in lithiated volumetric capacity, high voltage cathode with 10% increase in Cathode Energy Factor (CEF), advanced electrolyte and advanced stable Si anode composite with novel conductive polymer binder.

Project Details

John Tabacchi (NETL Program Manager)

DE-EE0006448 Recipient: 3M Company

Jagat D. Singh (Program Manager)

3M Center, Building 209-2C-26

St. Paul, MN 55144

Phone: (651) 575-1230; Fax: (651) 736-7478

E-mail: jdsingh@mmm.com

Subcontractor:

General Motors, Umicore, Iontensity, Army Research Laboratory, Lawrence Berkeley National Laboratory

Start Date: October 2013

Projected End Date: March 2016

Technical Barriers

LIB shows a remarkable robustness as witnessed through its application in today's world of portable consumer electronics, despite being a quasi-stable chemistry. The operation at high voltages helps provide increase in energy along with significant challenges in life performance. The development of advanced materials (anode, cathode and electrolyte) is important to address this challenge. The key technical barriers are:

- Short term cycle life and low rate capability
- High voltage electrolyte stability
- Si alloy volume expansion over life

Technical Targets

The technical targets are:

- Develop a >2Ah Advanced High Energy Li-Ion cell for EV and PHEV applications.
- Develop a high voltage NMC based cathode.
- Develop electrolyte for high voltage NMC and Si alloy anode.
- Develop a high capacity Si alloy anode.
- Develop advanced stable Si anode composite with novel conductive polymer binder.

Accomplishments

The key accomplishments are:

- Baseline cell delivered by 3M for testing at Argonne National Laboratory.
- Scaled up (100+ kg) of baseline high voltage NMC based cathode material by Umicore.
- Scaled up (100+kg) of baseline Si alloy anode material by 3M.
- Development of advanced high energy and high voltage (>4.5V) NMC based cathode material.
- Screening electrolyte additives which synergistically work with high voltage cathode and Si alloy anodes.
- Gap analysis of baseline cells by GM.
- Demonstration by Leyden Energy of excellent cycle life and low cell expansion after 600 cycles in 100% DOD window in pouch cells with Si alloy anode.
- First iteration of stack pouch cells assembly by Iontensity.

- Down selected advanced chemistry, i.e., Silicon alloy anode and high voltage NMC based cathode.
- Assembled 18650 cells with advanced chemistry and sampled to GM for evaluating the effect of full cell UCV to cycle life.
- Umicore identified the processing technique to determine the feasibility of the scale up of advanced cathode.
- Army Research Laboratory investigating electrolyte formulations and additives to enable the long term performance of advanced chemistry in full cells such as 18650 and pouch cells.

Introduction

Lithium-ion Battery (LIB) technology's potential to enable a commercially viable high energy density is the key to a lower \$/Wh, i.e., a low-cost battery. The design of a High Energy LIB (HE-LIB) with high power, safety and long life is a challenge that requires cell design from the ground up and synergy between all components. 3M Company (3M), the Recipient, strongly believes that this challenge can be addressed by 'teaming' key commercial businesses [General Motors (GM), Umicore and Leyden Energy (Leyden)] as well as select labs [Army Research Laboratory (ARL) and Lawrence Berkley National Laboratory (LBNL)]. The technology from each team member will be complimentary and a close working relationship spanning the value chain will drive productivity. This HE-LIB would provide more energy efficient and environmentally friendly vehicles, meeting or exceeding performance expectations and goals, thus making America less dependent on imported oil.

Approach

This project takes a team approach to address the project challenges. Each team member brings strong technical expertise to the table. The team consists of

- 3M: Development of advanced cathode, anode and electrolyte. Sample 18650 cells.
- Iontensity: Design, test, diagnose and sample pouch cells.
- Army Research Laboratory: Development of advanced electrolytes.
- Lawrence Berkeley National Laboratory: Development of advanced conductive binder for Si alloy anode.
- General Motors: Evaluate cells and perform gap analysis vs. vehicle requirements.
- Umicore: Develop cathode synthesis and demonstrate pilot scale manufacturing.

The proposed work will be performed in two distinct phases. Phase I will focus on advanced materials development and baseline validation. Phase II will focus on iterative integration of advanced materials and testing in 18650/Pouch cells.

Results

Advanced Anode Development

3M Anode team made progress in improving the performance of Si alloy anode with improvement in the alloy microstructure. The change was achieved by improving the alloy manufacturing process and changes to the composition. (See Figure II- 102, Figure II- 103)

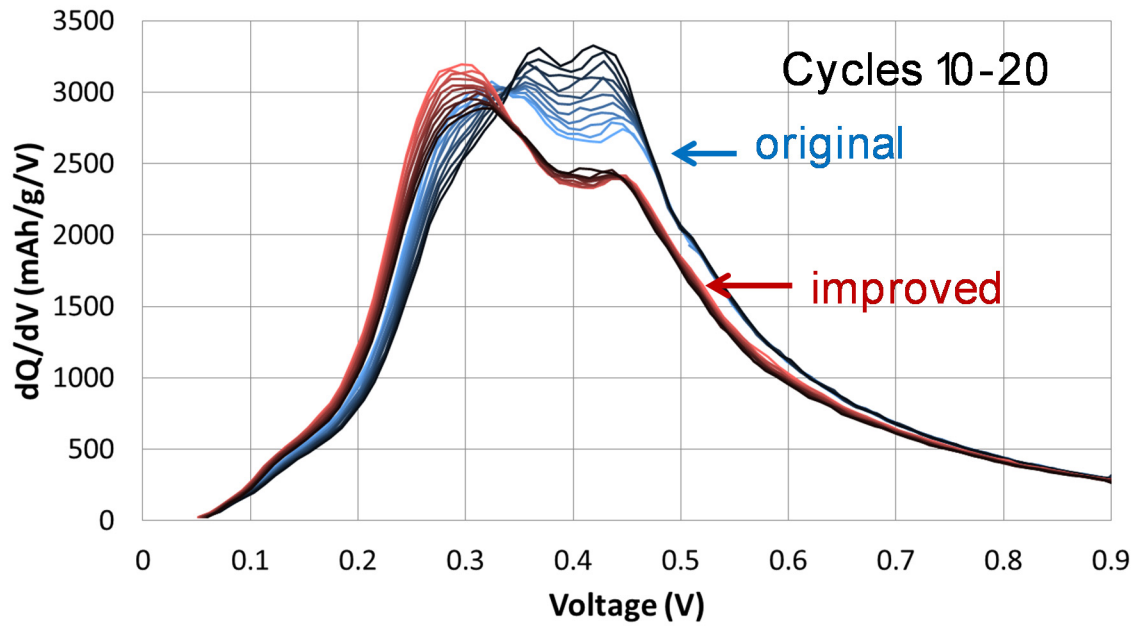


Figure II- 102: dQ/dV comparison of original Si alloy and the new version of Si alloy with improved microstructure

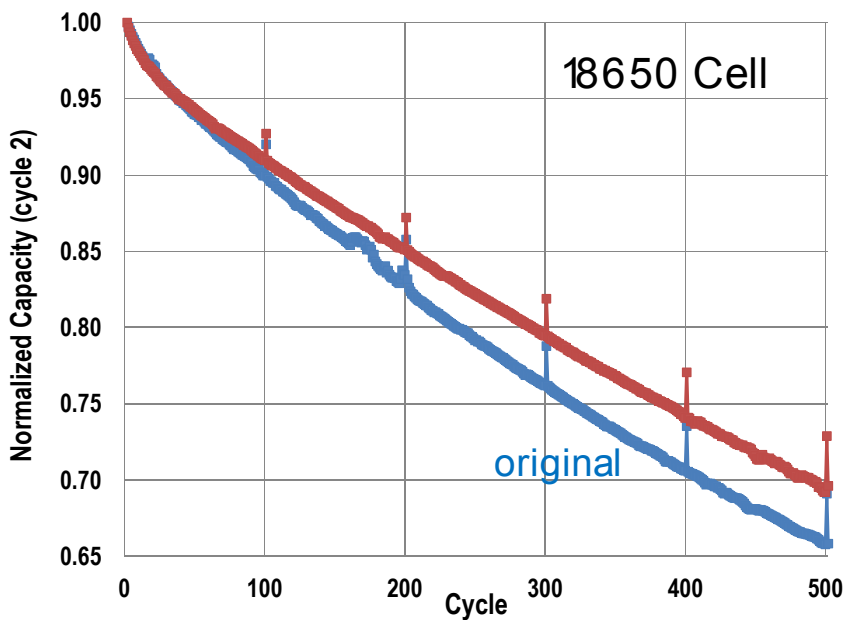


Figure II- 103: Cycle life comparison of original Si alloy and the new version of Si alloy with improved microstructure. 18650 cells with improved microstructure show lower fade than the 18650 cells with the original Si alloy

Various techniques to study particle coating were also studied. The figure below (Figure II- 104) shows the effect of pitch coating on the Si alloy anode particle.

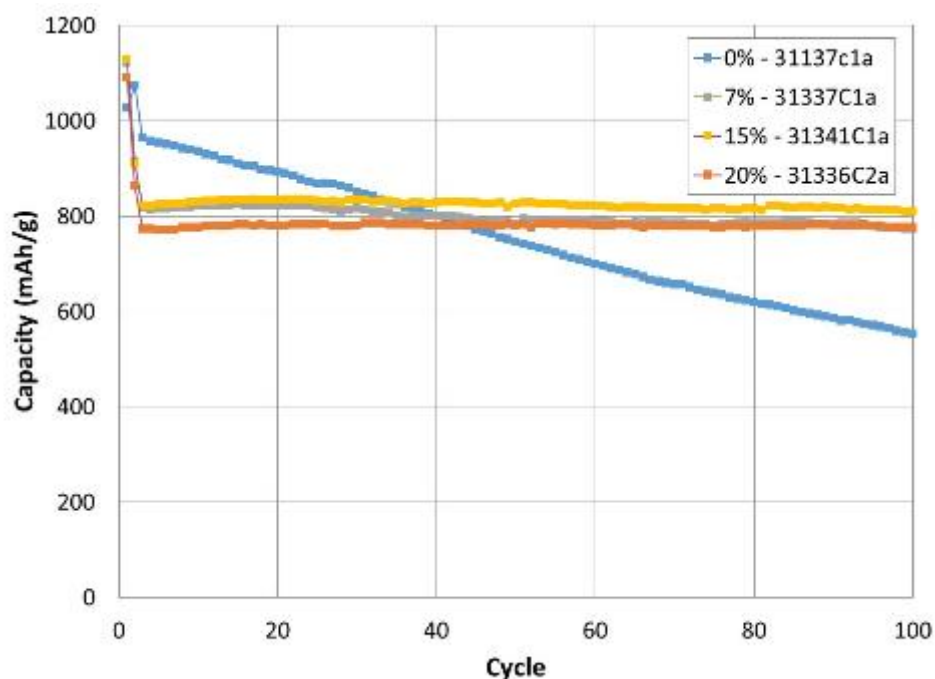


Figure II- 104: Half cell cycling of pitch coated V11 annealed at 500°C, pitch amounts are listed in the legend

Advanced Anode Binder Development

Inspired by the mussel holdfast foot protein, combined with the established side-chain conductive polymer, a DOPA-containing conductive polymer was developed and characterized as an effective binder for a Si-alloy anode in lithium-ion batteries. The facile synthetic route of the side-chain conductive polymer relaxes the requirement for synthesis and allows easy incorporation of the functional adhesion moieties such as DOPA. A quantitative analysis of the adhesion between polymer and silica confirms the strong adhesion force, which contributes significantly to improving the capacities and cycle lives of the Si alloy anode. The commercial Si-alloy anodes reaches a high specific capacity of 800 mAh/g, a much higher value compared to the state-of-the-art graphite anode. Combined with a prelithiation method, the lithium-ion full cell based on this novel binder-enabled high capacity anode delivers a high 1st cycle efficiency (84%) and a stable cycling at high material loadings. The mussel-inspired functional conductive polymer binder solves the volume expansion and low first-cycle coulombic efficiency problems, leading to a high-energy lithium-ion chemistry.

Advanced Cathode Development

Based on 3M coating recipe for La-coated NMC materials preparation, Umicore developed scalable process by solution based wet-coating. Up to 5.0 wt% of LaPO₄ coating on NMC622 clearly showed homogeneous coating without agglomeration of LaPO₄. Based on this results, Umicore optimized LaPO₄ coating wt% and finally selected 0.5 mol% LaPO₄ at 500°C heat treatment temperature which showed good coating morphologies. (Figure II- 105)

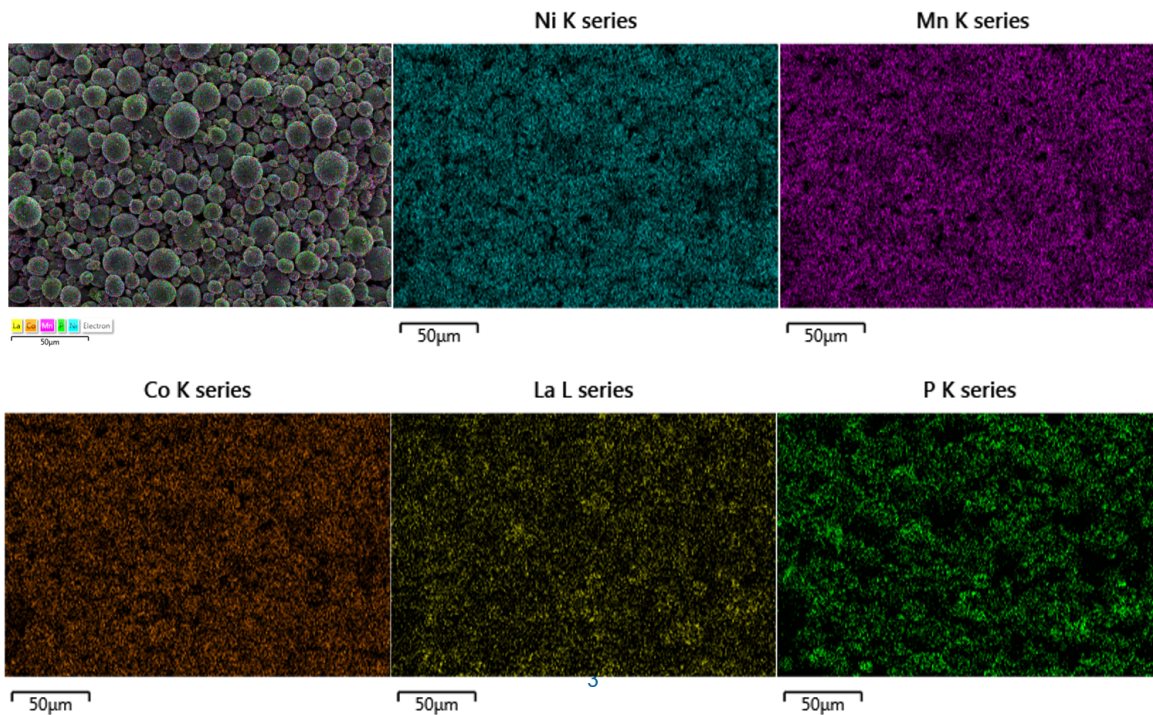


Figure II- 105: SEM and EDS mapping results of 0.5 mol% LaPO₄ coated NMC622 materials (T2696)

Compared to reference sample (P0357, 3M designed process, Lab-scale), electrochemical properties of Umicore coating materials (T2696) showed higher performances such as capacity, rate capability and cycle stability than 3M one.(Figure II- 106)

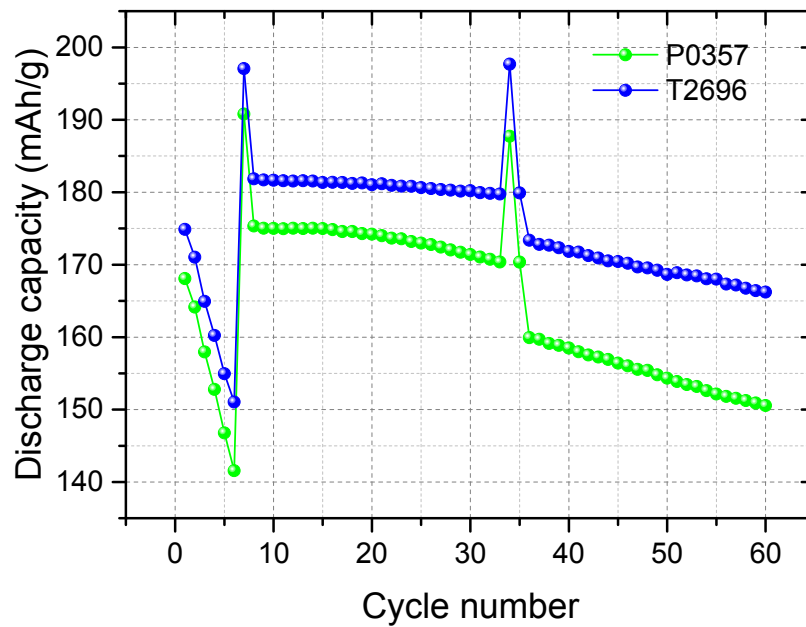


Figure II- 106: Coin-cell comparison results for 3M (P0357) and Umicore materials (T2696)

Advanced Electrolyte Development

Raising the lower cutoff voltage has a much more dramatic effect on the cell performance than lowering the upper cutoff voltage. We have determined that a voltage range of 3.0-4.45V is ideal for this system for improved cycle life while maintaining a high capacity. The capacity versus cycle life for the coin cells tested in the baseline electrolyte under different upper and lower cutoff voltages are summarized in the figure below (Figure II- 107).

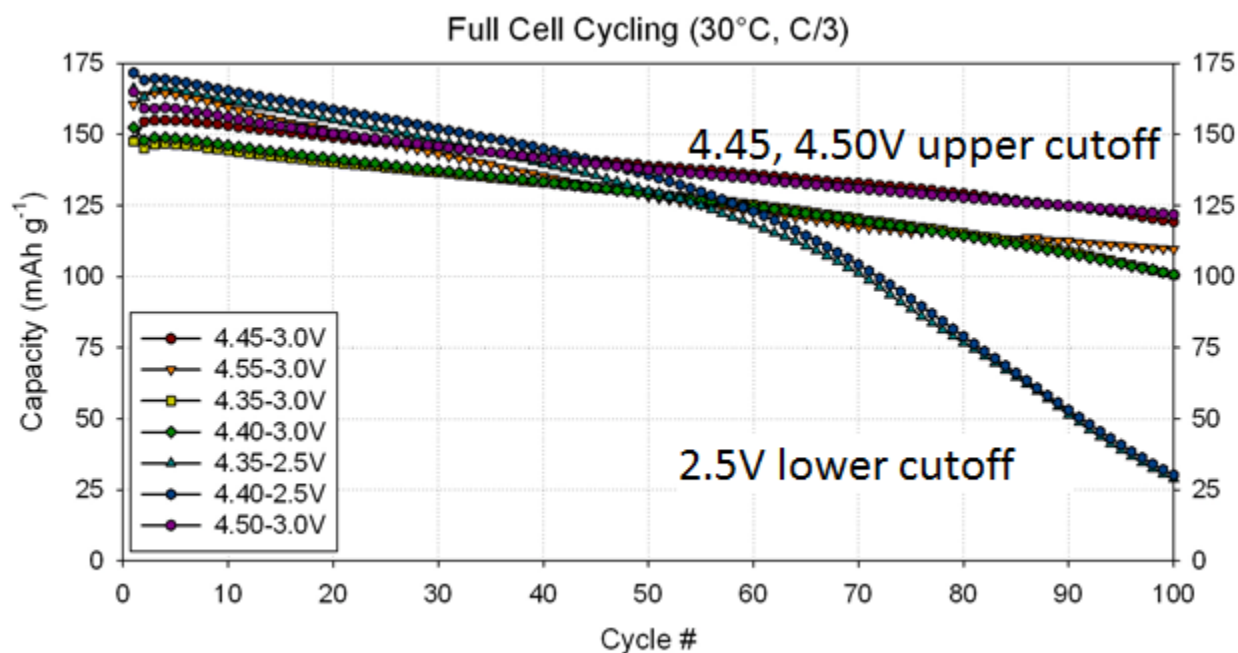


Figure II- 107: Effect of voltage window on the cycle life performance

Cycling of full cells in coin cell format with various different electrolytes produced viable options for testing in pouch cell format. Although electrolyte containing 10% fluoroethylene carbonate (FEC) has better cycle life than the baseline (no FEC) electrolyte, FEC-containing electrolytes have produced large volumes of gas in pouch cells. For coin cells cycling between 4.5 and 3.0 V as shown in the figure below (Figure II- 108), the use of some additives other than FEC have similar performance, but with less gas production.

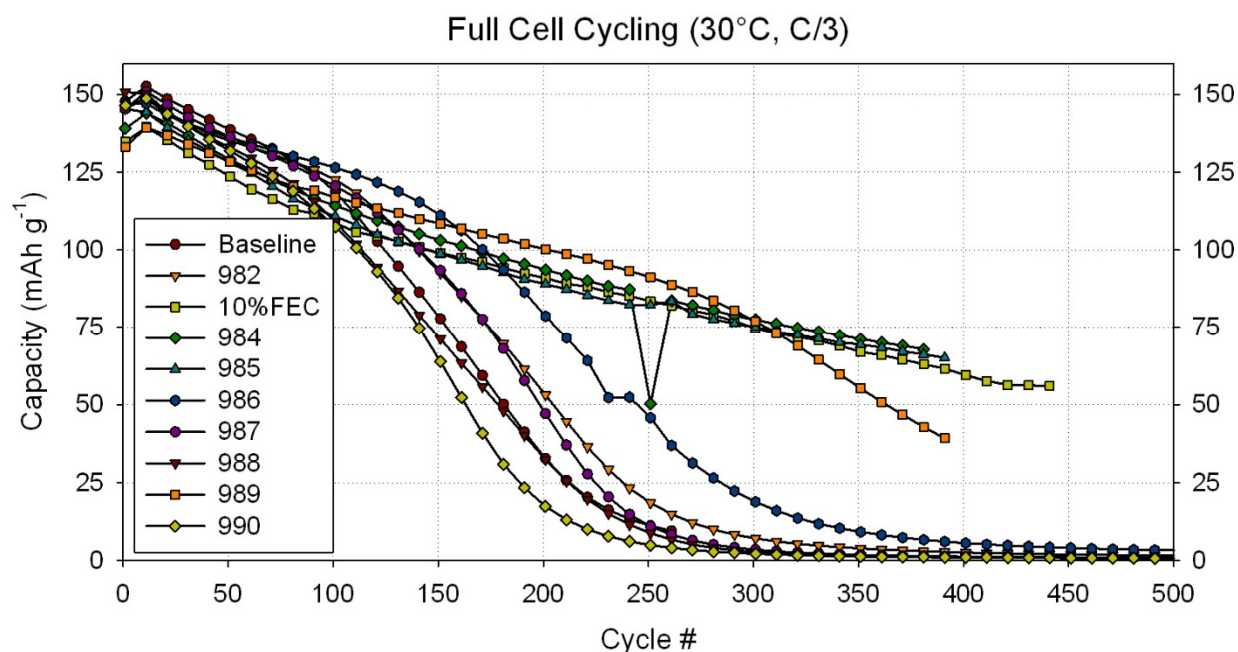


Figure II- 108: Effect of different electrolyte on cycle life performance

Large Cell Evaluation

18650 cells were assembled at 3M and sampled to GM for evaluation. The table below (Table II- 21) shows the key properties of the 18650 cell design. Three full cell design with UCV of 4.4V, 4.5V and 4.6V were shipped to GM. The team wants to study the effect of UCV to the cell energy at EOL.

Table II- 21: 18650 cell design with advanced chemistry

Cell Design UCV		4.4V	4.5V	4.6V
Cathode	Material	Coated NMC 622		
	Specific Capacity	190.7 mAh/g	202 mAh/g	212.8 mAh/g
	Loading	25.0 mg/cm ²		
	Composition	C622/SP/KS6/PVDF-94/1.25/1.25/3.5		
Anode	Material	Si Alloy (CV7) + Graphite		
	Specific Capacity	811.2 mAh/g		
	Loading	5.8 mg/cm ²	6.17 mg/cm ²	6.5 mg/cm ²
	Composition	CV7/BTR/KS6/SP/LiPAA-60/20/13/1/6		
	N/P ratio	1.1	1.1	1.1
Separator		Celgard 2325		
Electrolyte		Standard		

Advanced Chemistry Evaluation at GM

During this year, 18650 cells with advanced chemistry are being evaluated by GM. The evaluation includes cycle life, rate capability, HPPC (Hybrid Pulse Power Characterization) at various temperatures. The test results will be compared with those of the baseline cells to demonstrate cell chemistry and processing progress. Since the testing is still ongoing, only representative results are reported here.

Two cells were tested in parallel for each test protocol, and good consistency between the two cells was observed. All tests were run on a Maccor 4000 cycler; the cells being contained in temperature controlled thermal chambers. All tests were carried out at two different potential windows: 4.4-2.5 and 4.5-2.5 V, defined as 100% SOC. Currently, no difference in performance or durability has been observed between these potential windows. The testing conditions related to the results are shown in Figure II- 109 and Figure II- 110 and are described below.

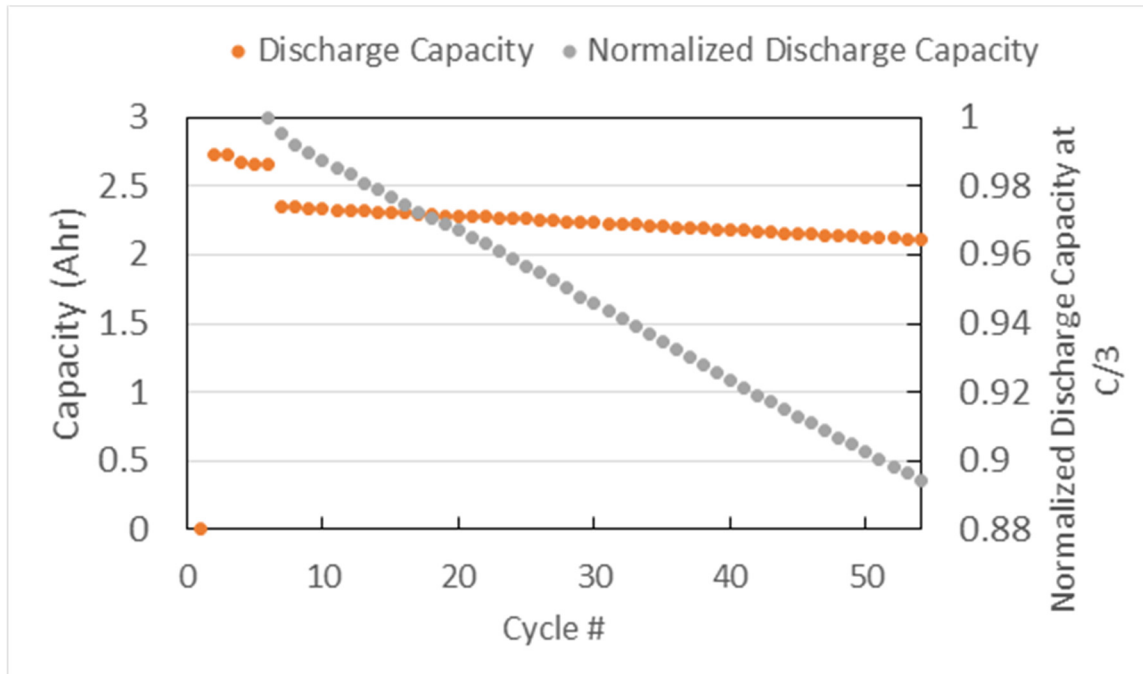


Figure II- 109: Cycle life at 30 °C at C/3 between 2.81 V and 4.29 V corresponding to 5-95% of SOC, and defining 4.4-2.5 V as the 100% SOC

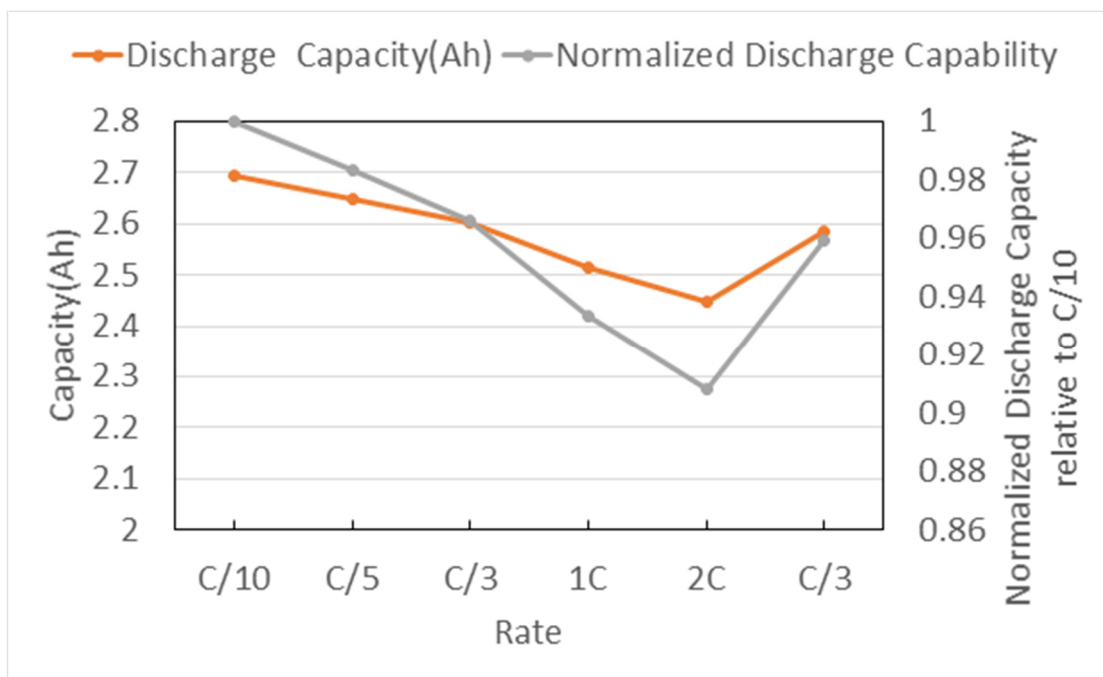


Figure II- 110: Rate Capability testing at 25 °C between 4.4-2.5 V

Cycle life was carried out at 30 °C, between 5 and 95% of SOC, and at C/3 rate. Rate capability was carried out at 25°C and comprised two cycles each at C/10, C/5, C/3, 1C and 2C rates. The reported capacity at each rate is the average of the two cycles. At the end, C/3 was repeated to check the capacity recovery after the high rate testing. Key findings

1. Figure II- 109 shows the cycle life testing results between 5 and 95% of SOC using 4.4-2.5 V as the 100% SOC window. Because the test is still ongoing, only 50 cycles are reported here. The 1st discharge capacity at C/3 is 2.36 Ah. It dropped to 2.11 Ah, 90% capacity retention, over the 50 cycles. If no other degradation mechanisms emerge in the following cycles, the predicted cycle life for this cell is about 100 cycles; i.e., where capacity retention will drop below 80%. Although the cycle life performance is much improved compared with the baseline cells (200 vs. 45 cycles), it is still far below the Project target of 1000 cycles.
2. Figure II- 110 shows the rate capability of the cells at 25 °C at 4.4-2.5 V. At C/10, the discharge capacity is 2.7 Ah, 96.6% of capacity is maintained at C/3, and 93.3% and 91% of capacity were obtained at 1C and 2C. At the end of the test sequence, a capacity check was performed at C/3, which was close to the initial C/3 capacity and indicates that the cells were not damaged by the higher C-rate tests. For the baseline cell, the initial discharge capacity at C/3 was about 91% of value at C/10. At 1C and 2C, only 83% and 73% of capacity remained respectively. Comparing these two sets of data, there is a significant improvement for the rate capability.

Advanced Chemistry Evaluation at Iontensity

Iontensity has developed formulations for the supplied active cathode materials based on its experience with similar chemistries. The cathodes are formulated with high active material content, typically between 94 and 96.5%, for high energy density. 3M's NMC 622C was formulated with 96.5% active material as was the very first control cell build of NCM 523. Umicore's CS-MHL (T2400) was formulated with 94% active material. Prior to this program, Iontensity had also used LCO where a 98% active material formulation was possible. The cathodes in this study provided three major benefits over industry standard LCO: (1) higher charge voltage, (2) higher gravimetric energy density, and (3) the irreversible capacity loss of the Umicore core shell and 3M NCM materials were higher than LCO and better matched the higher irreversible loss of the Si alloy, leading to a better, more symmetrical cell design. A range of CV-7 formulations from 20% to 60% were also tested. Two types of graphite were used in addition to a PAA based binder. Three current collectors were tested: (1) 10 μm Cu foil, (2) 18 μm Cu foil, and (3) 15 μm Ni foil. The high loadings of the Si alloy anode formulations made it difficult to process the 10 μm Cu foil. The 15 μm Nickel foil is lighter than the 18 μm Copper foil providing higher gravimetric energy density in addition to higher volumetric energy density based on thickness. The Ni foil also has a higher tensile strength than either Cu foil.

A major observation from this study was the occurrence of "rippling" seen on the surface of some of the pouch cells. Obviously this rippling is not observed on the surface of 18650 cells and can go undetected. Autopsies revealed that the rippling originated at the anode current collector. Three factors were identified: (1) use of a stiff PAA binder, (2) the % Si alloy in the formulation, and (3) the tensile strength of the current collector. The cells with the 10 μm Cu foil rippled at the low 20% Si alloy formulation. The cells with the 18 μm Cu foil showed rippling with 40% Si alloy and higher. Excessive rippling seen in the higher Si alloy formulations resulted in lower volumetric energy densities even though the capacities were higher. Maximum energy density in the 18 μm Cu foil cells was seen at 30% to 40% Si alloy. The cells with the Ni foil did not ripple and their energy densities were not as affected.

Cycle life of the lithium-ion pouch cells was higher for (1) lower % Si alloy content and (2) lower charge voltage of 4.35V versus 4.5V. A greater amount of Si expansion and particle isolation in the higher % Si alloy is believed to lower the cycle life. Higher charge voltage is believed to have resulted in increased electrolyte degradation also leading to lower cycle life. Note that optimizing the electrolyte formulation for high voltages was not part of this program. Our measurements for the increase in thickness from a fresh (as assembled) cell, to a fully charged cell during the formation process are shown in Figure II- 111. It is clear that the percentage in cell thickness increase is a function of the percentage of Si alloy in the formulation for the 18 μm Cu foil to a greater extent than the higher tensile strength 15 μm Ni foil.

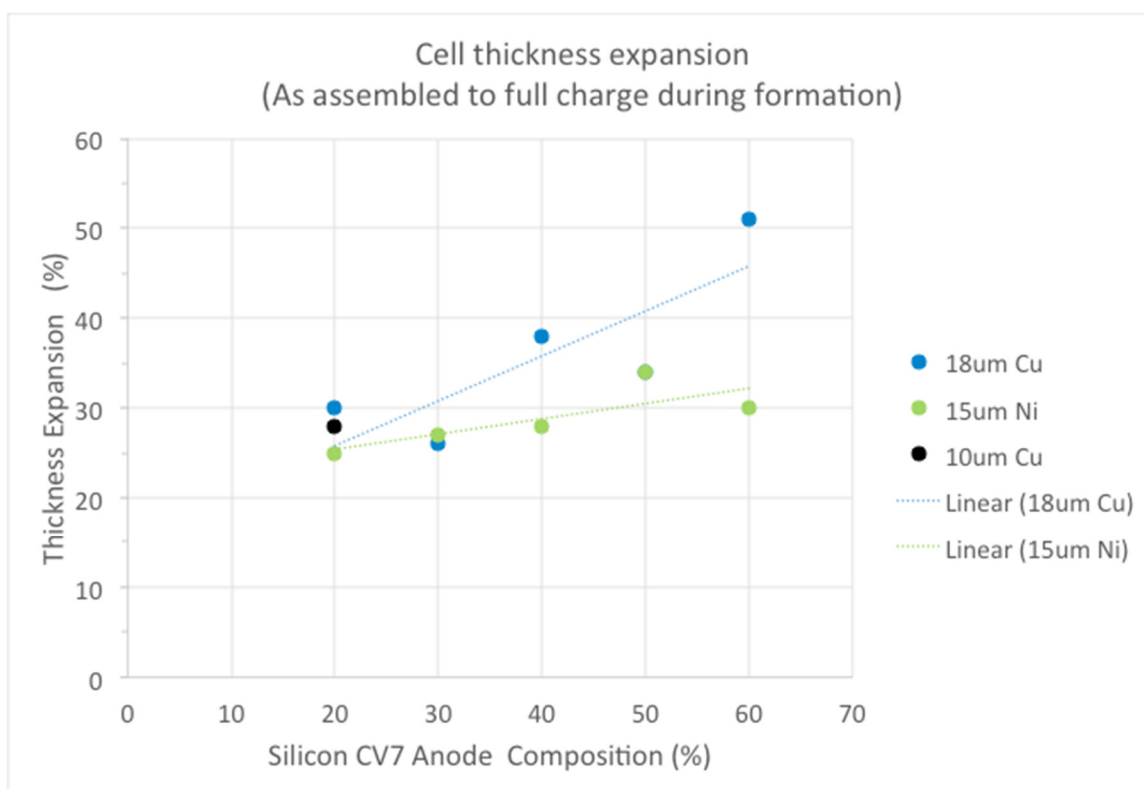


Figure II- 111: Cell Thickness Expansion versus % CV7 Silicon Alloy in Anode

Conclusions and Future Directions

The team has made significant progress in the last year. We have down selected the advanced chemistry and started the scale up of these materials. The team is in the no cost extension phase of the project. In the remaining months, the work will be directed towards

- Evaluation of full cells with scaled up advanced chemistry, i.e., advanced Si anode and advanced NMC cathode
- Assembly and sampling of 18650 cells with advanced chemistry to ANL.

FY 2015 Publications/Presentations

1. "Silicon Alloy Anode: Sudden Fade Challenge", ES256_Singh_2015_p, US DOE Vehicle Technologies AMR, 2015.
2. "Advanced high energy Li-Ion Cell for PHEV and EV", ES210_Singh_2015_p, US DOE Vehicle Technologies AMR, 2015.

II.B.4 Development of High-Energy Lithium-Sulfur Battery Cells (PSU)

Objectives

- Develop a novel nanocomposite sulfur cathode for lithium-sulfur batteries with high energy density, efficiency, and cycle life.
- Develop a novel Li-rich composite anode for Li-S batteries to improve cell cycle life.
- Develop novel electrolyte and electrolyte additives for Li-S batteries to improve cell efficiency, stability, and safety.
- Design, fabricate, test, and optimize the design of Li-S batteries using the above new technologies to maximize energy, power, abuse tolerance, and other favorable traits.
- Perform thermal testing of the developed Li-S cells and materials.

Project Details

Christopher Johnson (NETL Program Manager)
DE-EE0005475 Recipient: Pennsylvania State University

Donghai Wang (Project Manager)
328 Reber Building
University Park, PA 16802
Phone: (814) 863-1287; Fax: (814) 863-4848
E-mail: dwang@psu.edu

Subcontractor:
EC Power, Argonne National Laboratory

Start Date: September 30, 2011
Projected End Date: September 15, 2015

Technical Barriers

- Polysulfide dissolution and shuttling, combined with degradation of the lithium metal anode and formation of an unstable SEI layer, can severely limit cell lifespan.
- High sulfur loading in the cathode is required for achieving a high energy density; however, high loading often leads to parts of the electrode becoming inaccessible to electrolyte, thereby decreasing energy density and cycle life.
- Cathodes must have high active material loading – however, the low density of sulfur and common composite materials (porous carbon, etc) make thin, crack-free, high-loading electrodes difficult to achieve.
- Electrolyte modifications that decrease polysulfide solubility or improve SEI layer stability often come at the cost of increased impedance and other issues.

Technical Targets

- Deliver baseline cells with energy density 280 Wh/L and 80% capacity retention after 500 cycles at 1C rate.
- Develop carbon-sulfur cathode material composed of at least 85 wt% sulfur with capacity of at least 1300 mAh/g, coulombic efficiency > 95%, and 90% capacity retention in 100 cycles at C/3 charge and discharge rate.
- Develop anode with capacity of 1500 mAh/g and capacity retention of 90% after 100 cycles at C/3.
- Full cell tests with cell irreversible capacity < 15%, coulombic efficiency > 95%, and self-discharge < 0.3% per day.
- Thermal stability characterization of the lithiated electrode via DSC.
- Scale up active material production to the 1 kg level.
- Design pouch cells with energy density > 500 Wh/l, 80% capacity retention after 300 cycles at C/2.
- Nail penetration testing at USABC EUCAR Level 3.

Accomplishments

- Prepared 100 pieces of LiP coating sheets (4.4 cm × 5.6 cm each) to fabricate 1 Ah LiP / S pouch cells.
- Studied the cycling efficiency of LiP electrode to understand LiP electrode behavior during charge and discharge and its degradation mechanisms.

- Fabricated pouch cells with PSU-7 cathodes, LiP anodes, and ANL's electrolyte that achieved a 1.35 Ah capacity.

Introduction

DOE goals require the development of a high-energy, high-power, high-efficiency, long-lasting, low-cost, and safe battery. This project aims to meet these goals by using the extremely promising lithium-sulfur battery chemistry. The Li-S cathode has a theoretical capacity of 1672 mAh/g with a nominal voltage of 2V. In addition, sulfur does not experience any significant size change during lithium insertion/extraction, making it very stable in principle.

The price of lithium-sulfur's great promise is the set of major challenges with which it is replete. Lithium polysulfides – intermediate charge/discharge states of the cathode – are highly soluble in traditional electrolytes and can move throughout the battery, experiencing redox reactions and thus causing poor efficiency and loss of active material. Additionally, lithium metal commonly used as the anode is vulnerable to mossy lithium and dendrite growth and cannot generally form a stable SEI layer, causing further capacity loss and safety concerns. These factors, combined with optimization and thermal safety considerations, still necessitate a significant body of work to bring the Li-S to the commercialization stage.

Approach

To design a superior lithium-sulfur battery, we will focus on several aspects of cathode, anode, electrolyte, and whole-cell study and design.

Our sulfur cathode study will hit four main points. To improve volumetric energy density, we will test new methods of generating well-structured carbon frameworks. To improve sulfur loading, we will optimize the pore geometry of our carbon framework and investigate new framework materials and structures. Since mitigating polysulfide dissolution is critical to improving battery stability, we will investigate additives and novel materials that promise to adsorb polysulfides and find an optimal composition and synthesis method. Additionally, with an eye to commercialization, we will optimize our production methods and conditions, particularly in regards to designing cathode materials that can be easily made into electrodes with realistic active material loading and which can be produced in large batches.

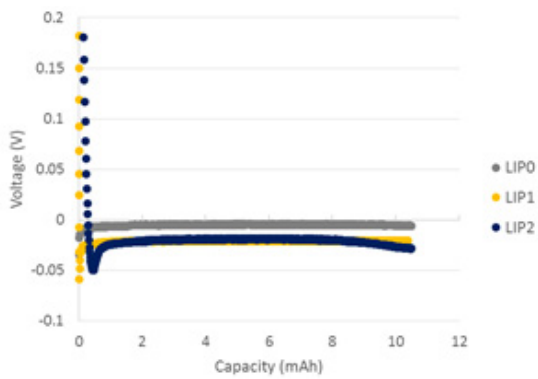
On the anode side, we will investigate promising options for generating lithium powder-based and silicon-based anodes, that we may promote stable SEI formation and prevent dendrite growth. Anode coating methods will also be investigated to this end, and anode-electrolyte compatibility will be studied to ensure excellent whole-cell performance.

Our study of electrolyte options for our sulfur battery will aim to improve SEI stability, decrease active material loss, increase active material utilization, and ensure battery safety. To this end, we will develop new electrolyte systems and additives and test the effects of existing additives on our full battery system, with particular focus on silane/siloxane-based systems and ionic liquid additives.

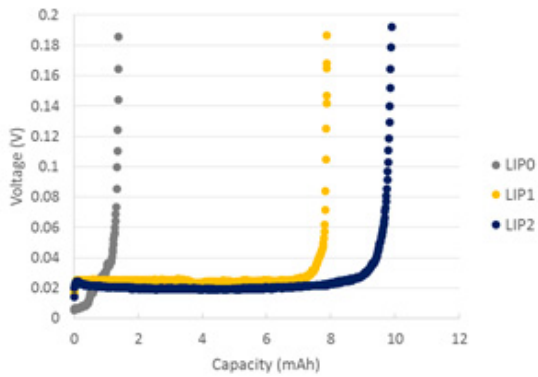
Additionally, we will optimize cell fabrication and design parameters, such as electrode size and N/P ratio, number of electrodes per stack, etc, to get the most out of our cutting-edge materials. In particular, we will take on the challenge of making electrodes with commercially-viable loadings by optimizing electrode composition and fabrication techniques. Cell modeling and experimental testing will be combined to inform these efforts. The thermal stability and abuse tolerance of our cell components and full cells will also be tested, ensuring safe batteries. Finally, the self-discharge and other half-cell and full-cell properties of the battery system will be fully characterized and optimized.

Results

We studied the cycling efficiency of LiP electrodes. Three different formulations of LiP electrode were tested in LiP / Li foil coin cells: LiP0 (90 wt% Li Powder + 10 wt% binder), LiP1 (80 wt% Li Powder + 10 wt% additive + 10 wt% binder), and LiP2 (60 wt% Li Powder + 20 wt% additive + 20 wt% binder). The electrolyte used was 1.0 M LiTFSI in DME/DOL (1:1 in vol.) with 0.4 M LiNO₃.



(a)



(b)

Figure II- 112: Voltage changing with (a) Li deposition amount (mAh) to LiP electrode and (b) Li dissolution amount (mAh) from LiP electrode at the 36th cycle in LiP / Li foil coin cells

The lithium in LiP electrode was initially dissolved at 0.50 mA/cm² until cut-off voltage at 1.0 V. Subsequently, Li deposition to LiP electrode at 0.50 mA/cm² for 10.5 mAh (constant for all cycles) and Li full dissolution from LiP electrode at 0.50 mA/cm² until 1.0 V were repeated. Accordingly, cycling efficiency is the Li full dissolution amount each cycle divided by the 10.5 mAh of Li deposition amount. As a result, we can obtain lithium loss on LiP electrode during cycling in terms of cycling efficiency and study how content of additive affects cycling efficiency.

As shown in Figure II- 112(a) for the 36th cycle, when Li deposits to LiP electrode at a constant current (i.e., 0.50 mA/cm²), the voltage of LiP electrode versus Li foil decreases to a negative value and shortly rebounds to a stable voltage (around -20 mV for LiP1 and LiP2 but only about -4 mV for LiP0). Such small voltage (-4 mV) on LiP0 suggests that micro internal short occur due to lithium dendrite growth. Figure II- 112 (b) exhibits the voltage profile during Li dissolution from LiP electrode at a constant current (i.e., 0.50 mA/cm²). When the voltage of LiP electrode increases to 1.0 V, Li full dissolution amount is determined: 1.5 mAh for LiP0, 8.0 mAh for LiP1 and 10.2 mAh for LiP2. Thus, there is a huge Li loss on LiP0 electrode (i.e., 10.5 mAh – 1.5

mAh = 9.0 mAh loss) and the cycling efficiency is only 14%. The lost Li is wasted for lithium dendrite growth and “dead” Li formation. On the other hand, LiP1 and LiP2 have cycling efficiency of 76% and 97%, respectively. Figure II- 113 illustrates their cycling efficiency varying with cycle number. The cycling efficiency of LiP2 keeps above 85% for 66 cycles and decreases to 61% at the 67th cycle. LiP1 shows fluctuating cycling efficiency above 76% before decreasing to 63% at the 48th cycle. The cycling efficiency of LiP0 stays above 90% for 27 cycles and

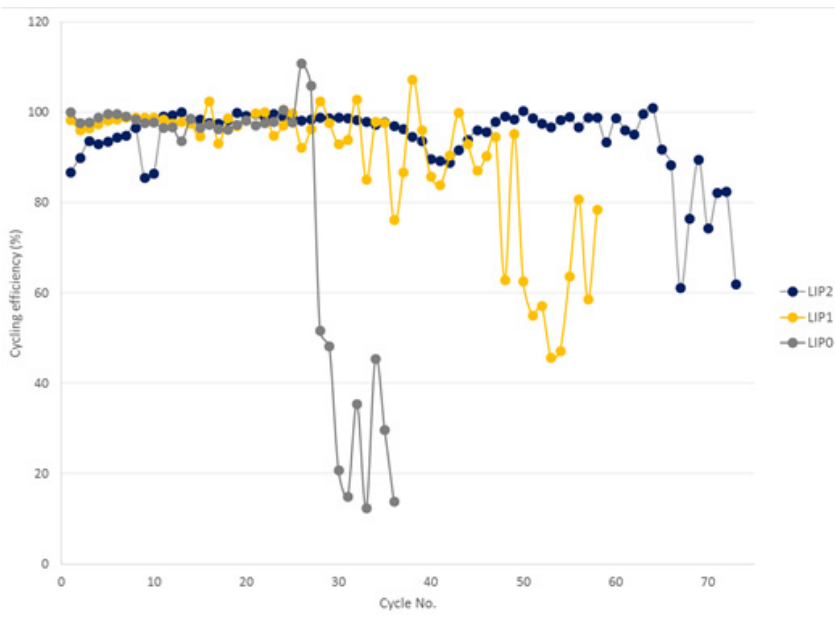


Figure II- 113: Cycling efficiency of LiP electrode in LiP / Li foil coin cells, varying with cycle number

falls to 52% after 28 cycles. The sharp decrease of cycling efficiency is at the 67th cycle on LiP2, at the 48th cycle on LiP1 and at the 28th cycle on LiP0, and hence it indicates the additive in LiP1 or LiP2 electrode is beneficial to inhibiting lithium dendrite growth to delay micro internal short.

Nyquist plots of electrochemical impedance spectra (EIS) at cycle 2 are shown in Figure II- 114. When the Li deposition amount is 0% in Figure II- 114(a), the semi-circular arc on LiP0 electrode (110 ohm wide) is much greater than that on LiP2 (only 16 ohm wide), which suggests that the interfacial resistance on LiP0 (i.e., Cu foil with 0% Li deposition on LiP0) is much higher than that on LiP2 with 20% additive. In Figure II- 114(b) at 50% Li deposition amount, the semi-circular arcs on LiP0 and LiP2 become smaller than 0% Li deposition amount but LiP0 still has higher interfacial resistance than LiP2 (6.6 ohm vs. 4.2 ohm). Figure II- 115 shows the ohmic resistance (high frequency intercept at real axis) and the interfacial resistance (mid-frequency semi-circular arc width) obtained from the EIS Nyquist plots, varying with Li deposition amount to LiP electrode at cycle 2. LiP0 has a slightly higher ohmic resistance than LiP2. Accordingly, the 20 wt% additive in LiP2 electrode helps to improve electronic conductivity and reduce the ohmic resistance. Also, the interfacial resistance on LiP2 is lower than LiP0 at all different Li deposition amounts, as shown in Figure II- 115(b).

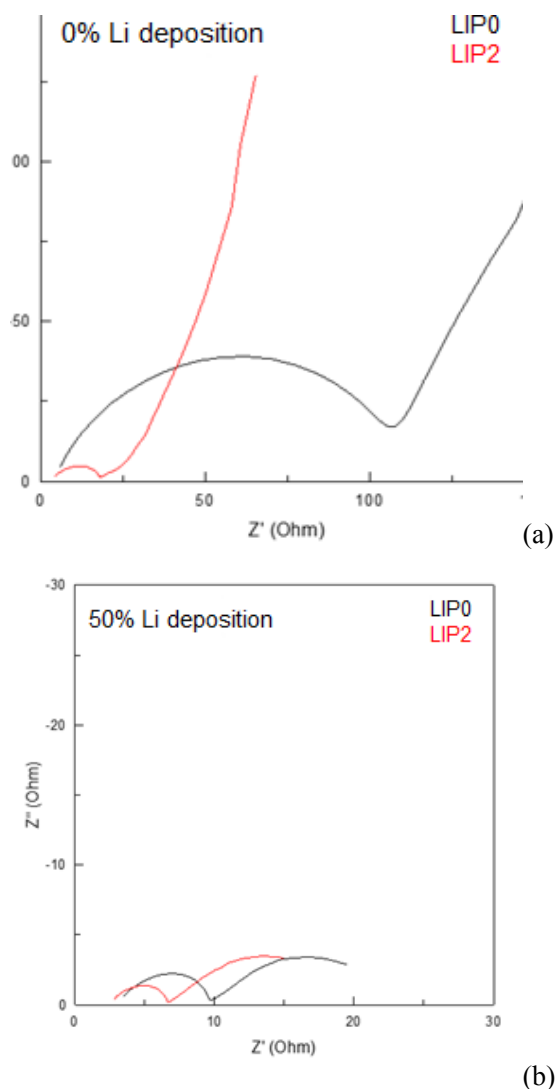


Figure II- 114: Nyquist plots of electrochemical impedance spectra measured at (a) 0% Li deposition (b) 50% Li deposition to LiP electrode at cycle 2 in LiP / Li foil coin cells

Pouch cells were fabricated with PSU-7 as the cathode material, LiP as the anode material, and ANL's electrolyte. Carbon nanofibers were added into PSU-7 to improve the conductivity. The total cell weight was 26g. Figure II- 116 illustrates the voltage profile for a pouch cell cycled with these materials. The discharge profile consists of two plateaus that are typical for Li-S cells, representing the formation of higher-order and lower-order polysulfides. Polarization is observed upon charging, but disappears during cycling and does not seem to significantly affect the coulombic efficiency or capacity retention.

Figure II- 117(a) and (b) illustrate the cycling performance of a pouch cell. The pouch cell was activated at C/20 in the first two cycles. The current rate was then increased to C/10 in subsequent cycles. A 1.35 Ah

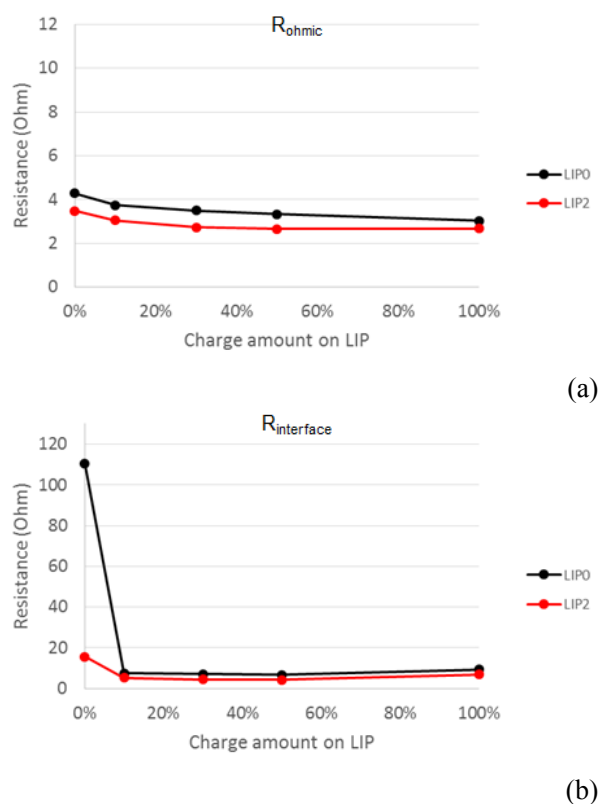


Figure II- 115: (a) R_{ohmic} and (b) $R_{interface}$ obtained from Nyquist plots varying with Li deposition amount to LiP electrode at cycle 2 in LiP / Li foil coin cells

capacity and a greater than 90% coulombic efficiency were achieved in the first cycle. Additionally, a discharge specific energy density of 120 Wh kg⁻¹ was achieved, taking into account all of the cells components. The capacity retention over the first six cycles is nearly 100%.

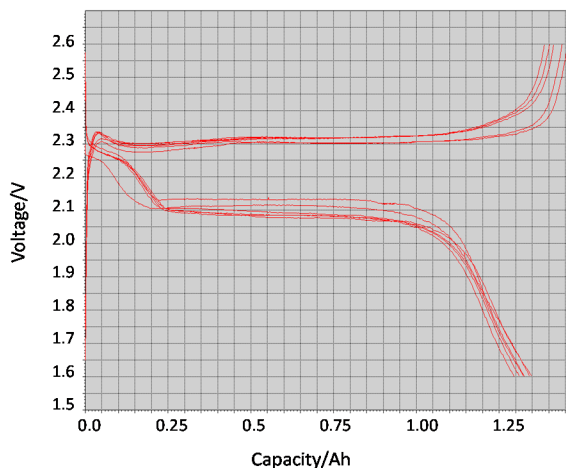


Figure II- 116: Voltage profile for a pouch cell made with PSU-7 cathode, LiP anode, and ANL's electrolyte

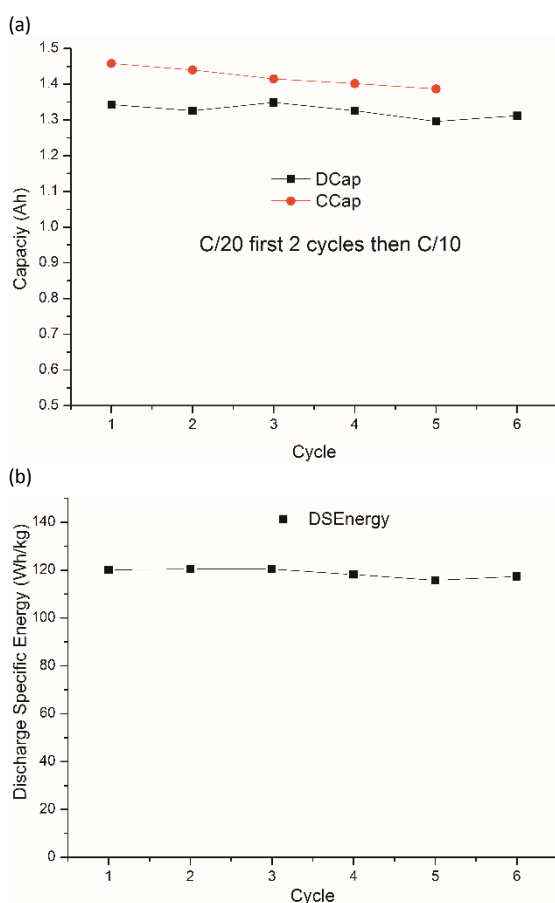


Figure II- 117: The (a) capacity and (b) discharge specific energy for a pouch cell with PSU-7 cathode, LiP anode, and ANL's electrolyte. The cells were cycled at C/20 in the first 2 cycles, then at C/10 in subsequent cycles

Opportunities for Training and Professional Development

More than 15 graduate students have been trained to gain knowledge and skills on materials development by working on the project with advisors and postdoc researchers.

3 postdoc researchers have attended professional conference to present their study.

Conclusions and Future Directions

In order to complete this project, work will focus most heavily on pouch cell development, optimization, and fabrication. We will incorporate other high-performance materials designed in this project into the 2 Ah pouch cells being developed, including scaling up nitrogen-doped cathode material production and further developing electrolytes and electrolyte additives to mitigate polysulfide shuttling and irreversible loss. We will also continue to optimize design parameters of pouch cells and pouch cell components, such as N/P ratio and electrolyte choice, and will investigate the source of the differences seen to date between coin cell and pouch cell performance. Safety evaluations, such as nail penetration and oven tests, will also be conducted.

Participants & Other Collaborating Organizations

Name: Donghai Wang (Penn State)

Project Role: Principal Investigator

Nearest person month worked: 1

Contribution to Project: Dr. Wang has managed the project as a whole and worked on the development of sulfur cathode.

Name: Chao-Yang Wang (EC Power)

Project Role: Co-principal Investigator

Nearest person month worked: 0.3 month/year

Contribution to Project: Dr. CY Wang has managed the subcontract to EC Power and has worked with the EC Power team to develop Li powder-based anode technology and pouch cell fabrication technology.

Name: Zhengcheng Zhang (ANL)

Project Role: Co-principal Investigator

Nearest person month worked: 0 month

Contribution to Project: Dr. Zhang has managed the subcontract to ANL and has worked with ANL to develop novel electrolytes for Li-S pouch cells.

FY 2015 Publications/Presentations

1. Song, J. X., Gordin, M. L., Xu, T., Chen, S. R., Yu, Z. X., Sohn, H.S., Lu, J., Ren, Y., Duan, Y. H., Wang, D. H. Strong Lithium Polysulfide Chemisorption on Electroactive Sites of Nitrogen-Doped Carbon Enables High-Performance Lithium-Sulfur Battery Cathodes. *Angewandte Chemie International Edition* 2015, 54, 4325.
2. Azimi, N., Xue, Z., Rago, N. D., Takoudis, C., Gordin, M. L., Song, J. X., Zhang, Z. Z., Wang, D. H. Fluorinated Electrolytes for Li-S Battery: Suppressing the Self-Discharge with an Electrolyte Containing Fluoroether Solvent. *Journal of Electrochemical Society* 2015, 162, A64.

II.B.5 Stand Alone Battery Thermal System (DENSO)

Objectives

- Reduce the vehicle battery pack size by 20% (or increase driving range by 30%) through an optimized battery thermal management system.

Technical Barriers

- In order for EVs to achieve mass adoption and make a significant dent in U.S and global CO₂ production, the key problems of driving range per charge & cost per kWh must be addressed.
- Barriers addressed:
- Life: Reduced life due to high temperature.
- Cost: High \$/kWh.

Technical Targets

- Develop a simulation program that will duplicate the battery thermal behavior in the vehicle.
- Develop a detailed thermal system design based on the information from the simulation program.
- Produce a prototype thermal system and bench testing to prove the system is able to achieve the goals of the project.

Accomplishments

- Established a set of test conditions to which the battery pack will be evaluated.
- Basic cell characteristics have been identified and used for the simulation model.
- A battery simulation model was created in AMESim software which can duplicate battery behavior found in actual vehicle tests.
- The battery model was evaluated at various temperatures and driving conditions with a variety of thermal system technologies to find the best solution.
- Prototype components were built and installed in a test bench to validate the results of the simulation models.
- Bench testing was completed to validate simulation results.
- Calculation was done to estimate cost of thermal system compared to the cost savings by downsizing the battery pack.

Project Details

Bruce Mixer (NETL Program Manager)

DE-EE0005410 Recipient: DENSO International America, Inc.

Bradley Brodie (DENSO International America, Inc – PM/PI)

24777 Denso Drive
Southfield, MI 48086

Phone: 248-372-8851; Fax: 248-350-7774

Email: bradley_brodie@denso-diam.com

Subcontractor:

National Renewable Energy Laboratory
15013 Denver West Parkway
Golden, CO 80401

Start Date: October 2011

Projected End Date: September 2015

Introduction

The objective of this project is to design a thermal system that will enable a PHEV/EV Battery Pack Size Reduction by 20%. To accomplish this, DENSO proposed a dedicated stand-alone thermal system to manage the battery pack temperature efficiently. The National Renewable Energy Laboratory (NREL) would support the project through cell characterization, creating the battery simulation model and the life model used to calculate the life of the battery pack. FCA provided actual vehicle data as a baseline, test conditions, and battery pack to be used for the bench testing.

Approach

The intent of the project is to demonstrate that a thermal system could enable the reduction of the battery pack size through optimal thermal management. The key points are considering performance at cold temperatures and battery life when exposed to high temperatures.

Phase I: A battery pack model was created in AMESim to simulate the battery pack. It uses equivalent circuit models (empirical), as a physics based model is too complicated for the purpose of this study. The type of equivalent circuit model is DC resistance-capacitor (RC) circuits.

Phase II: After the battery model was created in Phase I, Phase II involved incorporating the battery model with a thermal system model. This is needed to include a battery management system simulation and influence of temperature from the vehicle cabin and the ambient to the battery pack. The conditions (temperatures, drive profiles) used for the evaluation were provided by FCA based on their experience with specifying the battery packs for electric vehicles. Four different thermal systems were evaluated in five different climates, and for each climate, five driving habits were evaluated which resulted in 25 scenarios to be evaluated for each thermal system concept.

Phase III: Based on the optimal system found from Phase II simulation, actual prototype components were created and testing on a test bench to validate the simulation results.

Results

Below are the results for Phase I through Phase III of the project.

Phase I: Battery simulation model creation

For Phase I, the creation of a battery simulation model was the required task. The model was based on the Fiat 500EV battery pack. Actual vehicle data was provided to DENSO from FCA to compare our results. Cell-level characteristics data and simulation guidance were as provided by the National Renewable Energy Laboratory. Figure II- 118 shows the pack voltage and pack current during a drive cycle compared to actual vehicle data using the same drive cycle.

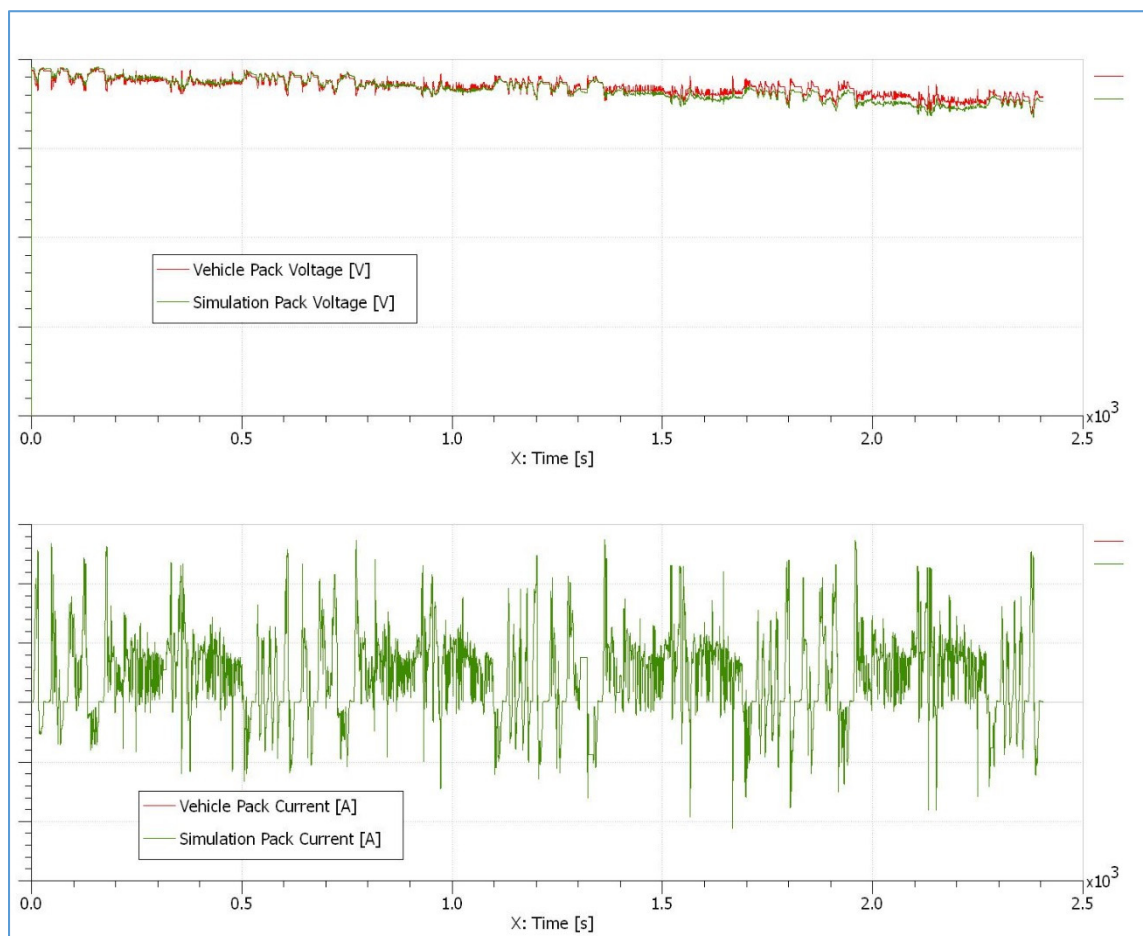


Figure II- 118: Battery Simulation Compared to Actual Vehicle Results

Phase II: System Simulation to Find the Optimal System

During phase II, the goal was to find the best thermal system from the point of performance and energy savings. Four different thermal systems were evaluated, each using different technologies, as listed in Table II- 22.

Table II- 22: Thermal Systems List

	Cooling Method	Heating Method	Comment
1 (PTC)	R-134a Refrigeration	PTC (electric heating)	Base System
2 (HP)	R-134a Refrigeration	R-134a Heat Pump	Improve Efficiency
3 (GIHP)	R-134a Refrigeration	R-134a Gas Injection Heat Pump	Improve low temperature performance
4 HP+PCM	R-134a Refrigeration + 10 kg PCM	R-134a Heat Pump	Add passive heat adsorption

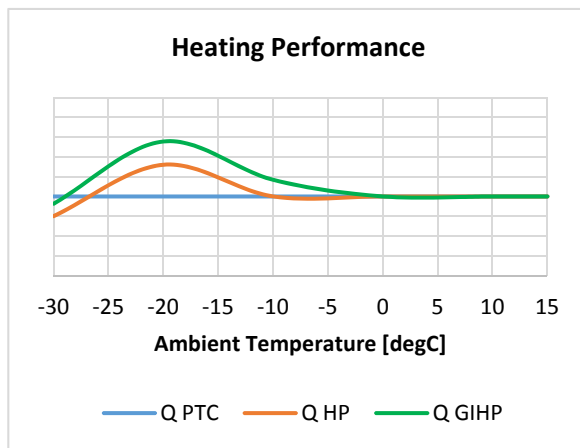


Figure II- 119: PTC and Heat Pump Heating Performance Compared

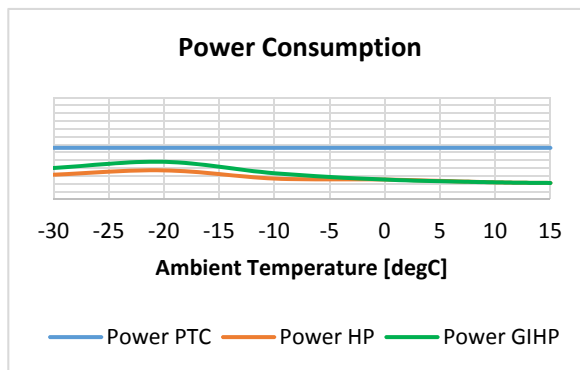


Figure II- 120: Comparing Heating System Power Consumption

Referring to Table II- 22, system 1 is considered our base system found in PHEV and EV vehicles currently in the market. Cooling is done using R-134a refrigeration system, and heating is provided using a high voltage PTC (Positive Thermal Coefficient) heater. The only difference is typically the R-134a system is linked to the vehicle cabin cooling system. In this study, we made it a dedicated system for only the battery. System 2 is same as system 1 for cooling, but we removed the high voltage heater and are now using the R-134a refrigeration system as a heat pump to provide heat. In this case, hot refrigerant exiting the compressor is used to heat coolant fluid flowing into the battery pack. System 3 is similar to System 2, except that it is using gas injection heat pump. This is similar to a two stage compressor system that allows for more performance at lower temperatures. Finally, System 4 is same as System 2, but PCM (phase change material) is added to provide passive cooling. This helps to smooth out peaks in temperature.

The main difference in all the systems involved the heating of the battery. In recent years, it has become clear that actively heating the cabin or battery of an electric or plug in vehicle is a large contributor to reduced driving range. In this study, we compare heating using PTC heat, heat pump, and gas injection heat pump. The heating performance of each technology is shown in Figure II- 119. The PTC heater has a constant

performance compared to ambient; however the heat pump system's performance will increase as ambient temperature increases. Therefore, control logic was implemented in the simulation model to limit the heat pump system to have similar performance as the PTC heater. This means that the compressor RPM is reduced

in the heat pump to reduce the performance. Note that HP performance is same or higher than PTC from -25°C and warmer.

In Figure II- 120, we look at the power consumption of each system at various ambient temperatures. It is clear that the heat pump is using less power than the PTC heater, however as shown in Figure II- 119, it still provides the same heating performance. The relationship between heating performance and power consumption is referred to as the coefficient of performance (COP). In Figure II- 121, the COPs for each heating method are compared.

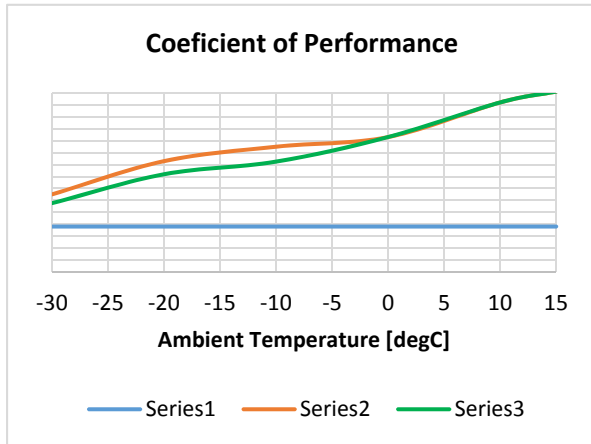


Figure II- 121: COP Comparison of PTC and Heat Pumps

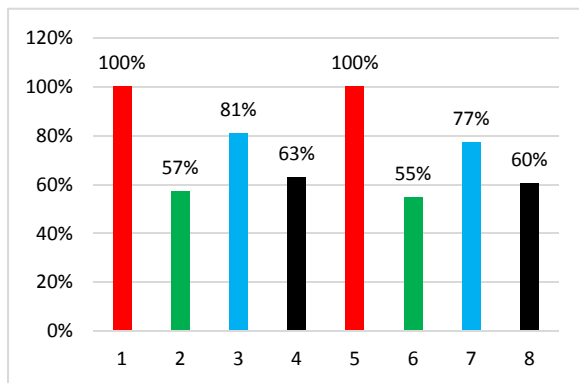


Figure II- 122: Thermal System Energy Usage at -20C Driving Conditions

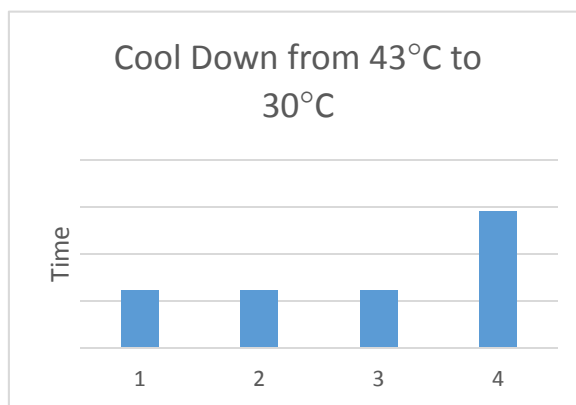


Figure II- 123: Time to Cool the Battery Pack from Hot Soak

After understanding the basic performance of each system, it was time to simulate each one in driving conditions at cold ambient. Figure II- 122 shows each thermal system at -20°C using UDDS and HFET driving patterns. In each case, the PTC heater was considered the baseline and its power consumption was leveled to 100%. The power consumption of the other systems is then shown as a percentage compared to the base system. Figure II- 122 shows that a heat pump systems offer a significant reduction in energy usage compared to PTC electric heating. Gas injection heat pump consumes more power than the regular heat pump, but as shown in Figure II- 122, at -20°C it also is producing more heating performance and thus heats the battery faster. Notice that the HP system with PCM requires 6% more energy than the HP system without PCM at -20C UDDS. This is because the PCM at these temperatures acts as a thermal mass. As a result for the studies in cooling mode, the system used does not have PCM and is the only R-134a A/C system.

Figure II- 119 - Figure II- 122 showed results of the system in heating mode; which is heating the battery in cold ambient. Figure II- 123 shows basic results of cooling the battery using the different systems.

In studying Figure II- 123, one can see the comparative time (and energy) it takes to cool the battery pack from 43°C to 30°C is the same for PTC, HP and GIHP systems. This is because in cooling mode, the vapor compression R-134a system is basically the same for all three systems. However, the Heat Pump + PCM show an increase in time to cool down, and more energy is used. The reason is at this temperature, the PCM is only single phase and there is simply more heat mass that needs to be cooled down. In this high ambient cool-down condition, the PCM actually hurts performance.

The phase change material does have an advantage in areas such as Seattle (see Figure II- 124). The purpose of studying PCM or pack insulation is to keep the battery packs as close to optimal temperature as possible without using any energy, for example, when the vehicle is parked but not plugged in. But in extreme temperatures like those occurring during Miami summers or Minneapolis winters, these temperatures are beyond the PCM melting point so there is actually only

negative effect as shown in Figure II- 120 and Figure II- 121, due to the added thermal mass. Because it was difficult to decide if adding PCM or battery pack insulation was worth the added mass, cost, and packaging

space in the system. For this study, it was decided to leave them out and only focus on the active cooling and heating systems. However, if used correctly, PCM and insulation can have the positive effect of reducing peak temperatures in the battery cells and improving life (hot peaks) or driving range (cold peaks).

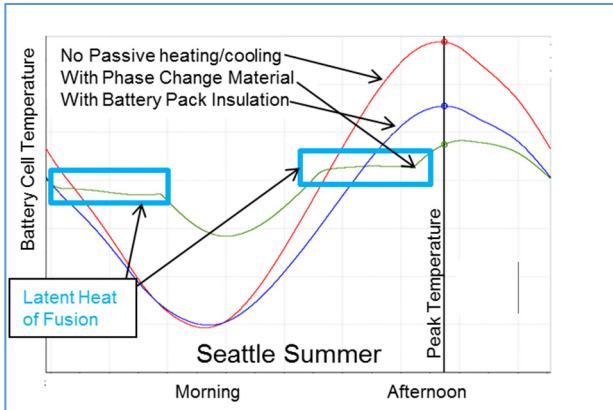


Figure II- 124: Study of passive heating and cooling; most benefit is found in mild ambient like Seattle

The final step in the simulation is to consider the effect on battery life. One approach for this is to measure the relative capacity of the battery pack throughout the life cycle of a battery. Figure II-125 shows the relative capacity for minimal thermal management, aggressive thermal management, assuming the battery pack were always at a constant temperature for its entire life which, while it is not actually possible in a vehicle, is shown here for comparison purposes. In Figure II- 125, for this study, the goal is to keep the relative capacity greater than 75% for 8 years. This is achieved using minimal thermal management, which is considered the base case for this project. But, using aggressive thermal management (keeping the battery pack cooler) as

shown on the green line, takes longer to achieve a 75% battery life. If we know our target is 75% battery capacity after 8 years, the capacity of the battery in the beginning could be reduced so as to end at the same capacity as the base system. In Figure II- 126, the capacity of the battery pack was reduced at the beginning, to have 75% capacity at the end of 8 years. The battery pack size could be reduced by 5%. This is 15% less than the objective which was 20% battery pack size reduction. However, due to the natural aging of the battery pack, as seen from calculations; if the battery pack were at a constant temperature during its entire life, the pack size could be reduced ~10-15% from base size. Therefore, even if the cell is kept at the optimal temperature for its entire life, the natural aging (resistance growth) of the battery cells itself would make achieving a 20% reduction very difficult!

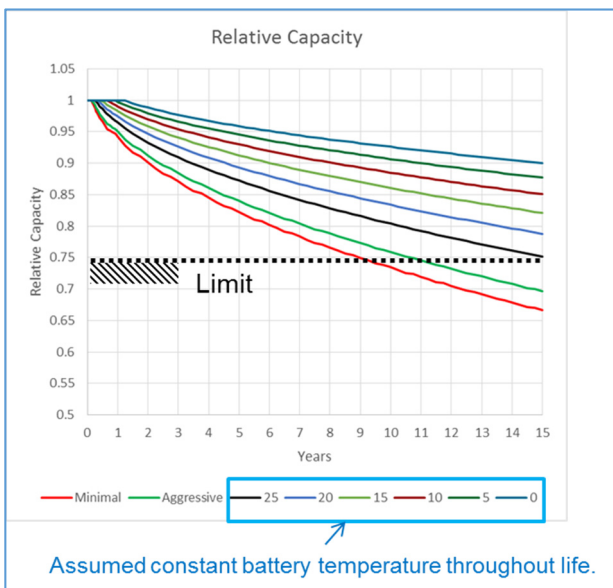


Figure II- 125: Relative Capacity of Battery Pack during Battery Life

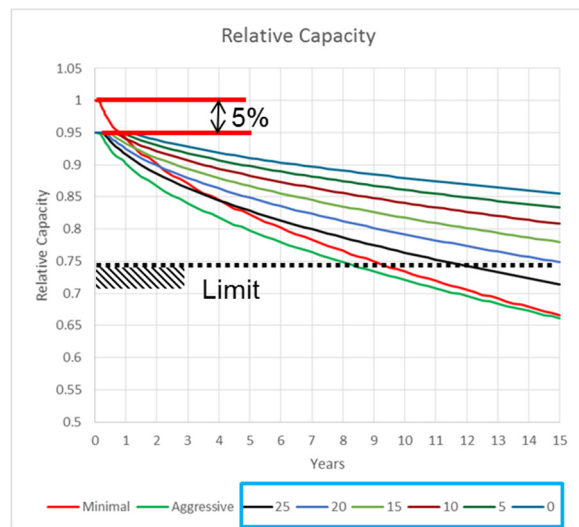


Figure II- 126: Battery Pack Capacity Can Be Reduced 5% and Achieve Life Requirements

Phase III: Prototype Making and Bench Testing

The following is a list of prototype components created for these experiments. (All parts manufactured by DENSO, unless noted otherwise.)

- Electronic expansion valves
- Coolant chiller (for cooling the battery using cold refrigerant)
- Water cooled condenser (for heating the battery using hot refrigerant)
- Outside heat exchanger (used as a condenser in cooling mode, and evaporator in heating mode)
- Electirc compressor (300V model because it was easily available, but for a target of 2 kw, lower power compressor could be used)
- Clear accumulator bottle (to make sure liquid does not enter the compressor, and clear to monitor the refrigerant and oil level)
- Coolant pump (made by Peirberg)

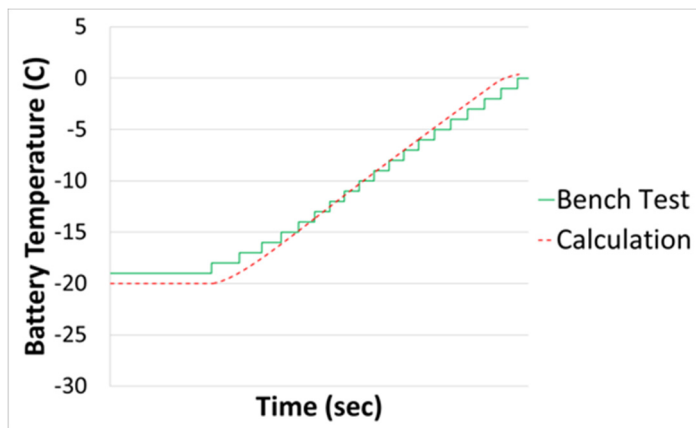


Figure II- 127: -20°C to 0°C Warm Up Test

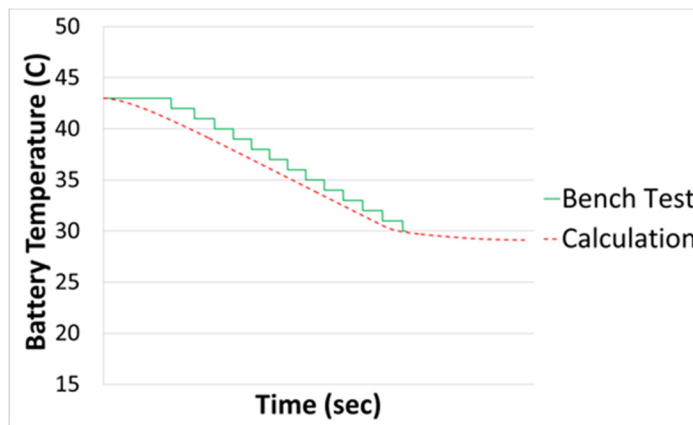


Figure II- 128: 43°C to 30°C Cooling Test Comparison

Figure II- 127 - Figure II- 130 compare the bench test results to simulation results.

Figure II- 127 is testing the system to warm up the battery from -20°C soak to 0°C. The internal battery temperature was monitored by the battery CAN data. During that testing, both simulation and bench were limited to 2kW compressor power.

Figure II- 128 shows results of cooling the battery pack soaked at 43°C to 30°C. It is noted that there is a small difference at the beginning, due in likelihood to losses in the coolant lines that were not fully accounted for in the simulation model.

Also, Figure II- 129 and Figure II- 130 show results for drive cycles; i.e., when the battery is charged and discharged at a known rate based on actual vehicle testing. The bench testing also demonstrates that the calculation results are very similar to that measured on the bench. It should also be noted that, as shown in the Davis Dam test, the accuracy of the battery temperature measured from the battery pack CAN data is $\pm 1^\circ\text{C}$.

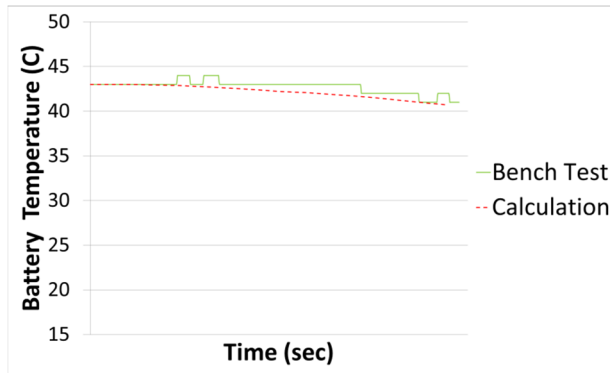


Figure II- 129: US06 Drive Cycle starting at 43°C soak

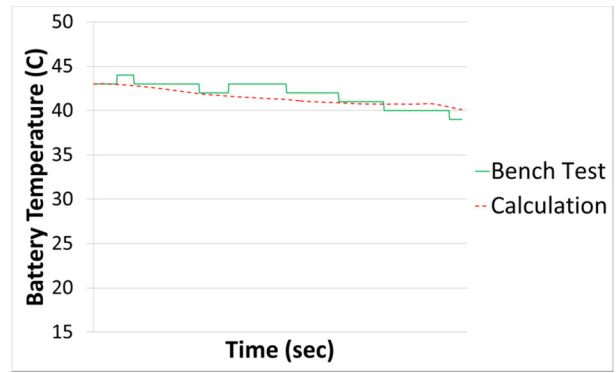


Figure II- 130: Davis Dam Test starting at 43°C soak

Conclusions and Future Directions

During this project, a battery simulation model was created in AMESim to accurately predict the battery pack characteristics of a Fiat 500EV battery pack. The simulation model predicts voltage, current, heat transfer and battery life. A thermal system was also found that works well to save energy when heating the battery, compared to PTC heater, and can reduce the battery pack size by 5% when used with effective controls.

Table II- 23: Component Cost Assumptions

Assumptions	
Baseline Battery Pack Size	24 kWh
New Battery Pack Size (5% Downsize)	22.8 kWh
Battery Pack Cost (based on industry data)	\$250/kWh
Base Thermal System Cost (chiller + PTC Heater)*	\$450
Stand Alone System Cost*	\$800
System Cost Integrated into Vehicle A/C*	\$450

Based on the above information, the final conclusion should be based on the overall cost savings. The purpose of the project is to find a system that can reduce the battery pack cost, and thus enable an overall vehicle cost reduction. Table II- 23 lists the cost assumptions for major system components, and Figure II- 131

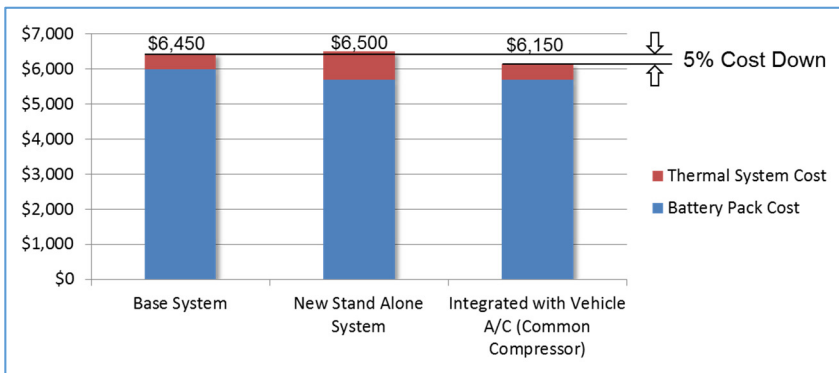


Figure II- 131: Cost Down Is Achieved If AC Compressor Is Common With Cabin Cooling

shows results of the cost analysis. Because the stand alone system adds another compressor, its cost mostly offsets cost savings from the reduced battery size. The only way to reduce overall cost is to use a common electric compressor with the cabin cooling and battery cooling (i.e., not a “stand alone” system).

The final conclusion of this project is that NREL should do system bench testing to validate the results found at DENSO. This work is

ongoing and will be completed by November, 2015.

II.C Low-cost Processing Research

II.C.1 Cells or Battery Packs with Significant Cost Improvement (JCI)

Objectives

- The objective of this contract was to develop a portfolio of advanced technologies to reduce the manufacturing cost of large format Li-ion cells by 50%. There are four key goals:
 - Fast cell formation process.
 - Non-NMP electrode.
 - Direct separator coating.
 - Integration of these three advanced manufacturing technologies to achieve cost savings through the elimination of material, lower capital equipment expenditures, and reduced energy and manufacturing costs.

Technical Barriers

- In order for EVs to achieve significant penetration rates in the U.S. new vehicle market, the manufacturing cost per kWh must be reduced. Specific barriers are:
 - Electrode and cell assembly manufacturing cost
 - Formation time(cost)
 - Electrode material, specifically solvent costs

Technical Targets

- Bundled, 50% reduction in the manufacturing cost of large format Li-ion cells

Accomplishments

- The final deliverables to Argonne National Laboratory are summarized in Table II- 24.
- The performance of the dry electrode was substantially improved at end of contract demonstrating significantly improved rate capability
- The cycle life of new formation processed cells shows similar capacity retention compared to baseline cells within 300 cycles
- Dry electrode: Cells built with final dry electrode demonstrated 91% performance of the baseline cells with a 53% cost reduction vs. the wet coating process.
- Aqueous cathode: These cells demonstrated 98% of the baseline design and a 3.5% cost reduction compared to the NMP based electrode process. The cells with the newly developed mixing process delivered promising performance and quality as well.
- Direct coated separator: These cells demonstrate equivalent performance to the baseline and a 56% cost reduction in the assembly process compared to the conventional PE separator.
- Fast Formation: Reduced formation lead time from 24 to 7 days with excellent performance and detectability

Project Details

Renata Arsenault (USABC Program Manager)
Recipient: Johnson Controls Inc. (JCI)

Michael G. Andrew (JCI)
5757 N. Green Bay Road
Glendale, WI 53209
Phone: 414-524-6173
Email: Michael.G.Andrew@jci.com

Team Members:
Maxwell Technologies Inc.
Entek Membranes, LLC
University of Wisconsin-Milwaukee

Start Date: April 1, 2012

Projected End Date: March 31, 2014

Results

The final deliverables to Argonne National Laboratory are summarized in Table II- 24. Figure II- 132 shows the DC impedance of dry electrodes at beginning of life. The rate capability of the dry electrode/laminated separator design is favorable.

As shown in Figure II- 133, the final integrated cells show a significant improvement at the 5C rate, it shows a similar performance compared to baseline cells and 20% better compared to interim integrated cells. The profiles of 5C continuous discharges are summarized in Figure II- 134. Significant improvements were achieved in the charge transfer, ohmic, and concentration polarizations.

Table II- 24: DC impedance of dry electrodes at beginning of life

Deliverable	Technology			Capacity	Quantity	
	Cathode	Anode	Separator		Date Delivered	
Design #1	Aqueous	Base	Base	15 Ah	18	2/3/2015
Design #2	Aqueous	Dry	Lamination	15 Ah	4	2/17/2015
Design #3	Dry	Dry	Lamination	3 Ah	24	3/2/2015

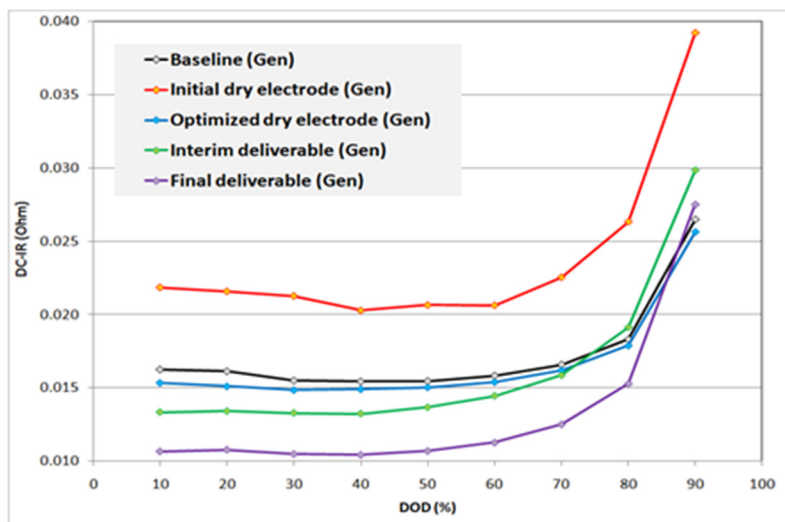


Figure II- 132: Comparison of DC impedance of dry processed electrodes

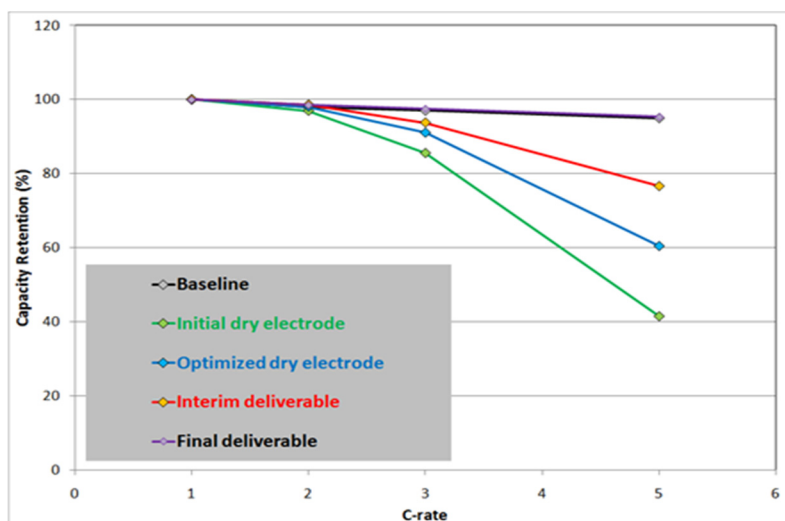


Figure II- 133: Rate capability – dry process electrodes

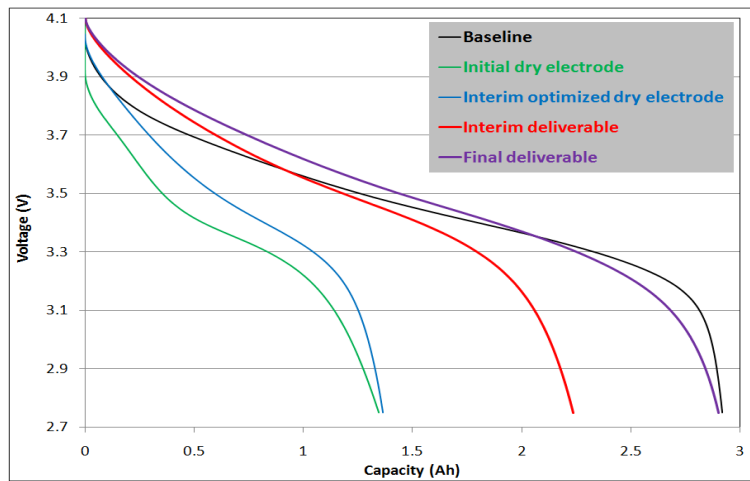


Figure II- 134: Profiles of 5C continuous discharges with the dry process electrodes

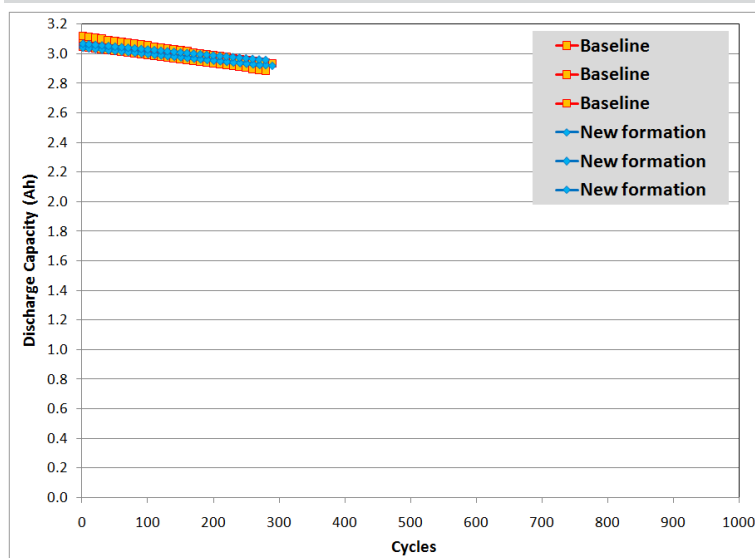


Figure II- 135: 1C/1C 100% DOD cycle life (3~4.2V) at 45°C

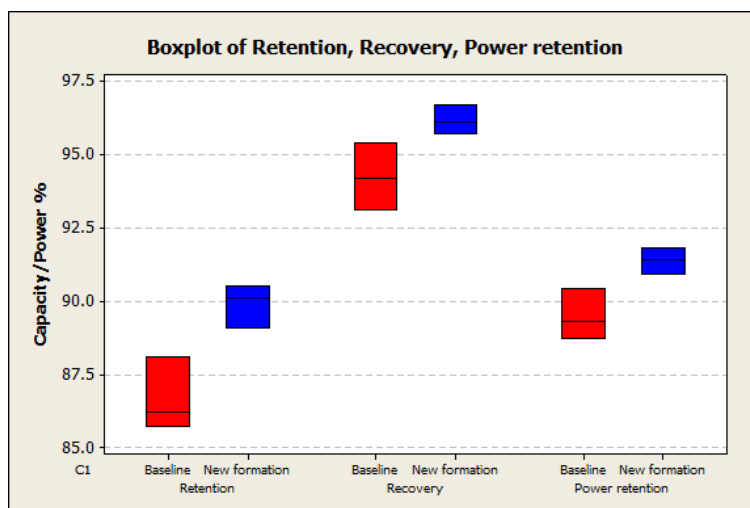


Figure II- 136: Calendar life test at 60°C for 1 month

New Formation Process

Performance results from the new formation process were encouraging. The cycle life of new formation processed cells shows similar capacity retention compared to baseline cells within 300 cycles (see Figure II- 135).

The results of calendar life testing are summarized in Figure II- 136. The new formation cells show higher capacity retention and recovery as well as improved power compared to baseline formation cells. Also, variation was significantly reduced.

Wettability of Battery Materials by Electrolyte, Improved Filling Performance

The wetting properties of the battery materials were investigated to help reduce the manufacturing time needed to accomplish the electrolyte filling stage in the production process. A dynamic wetting balance test was developed to provide critical testing ability used to:

- 1) Address manufacturing issues related to wetting and;
- 2) Characterize current and novel materials used as individual battery components.

The wetting balance test was used to measure the properties of the final anode and cathode materials. The wetting balance test is a reliable method to quantify the wetting kinetics of individual materials used in the battery. It has also shown to be applicable to better understanding the impact of manufacturing processing conditions such as extent of calendaring on the wetting of internal components.

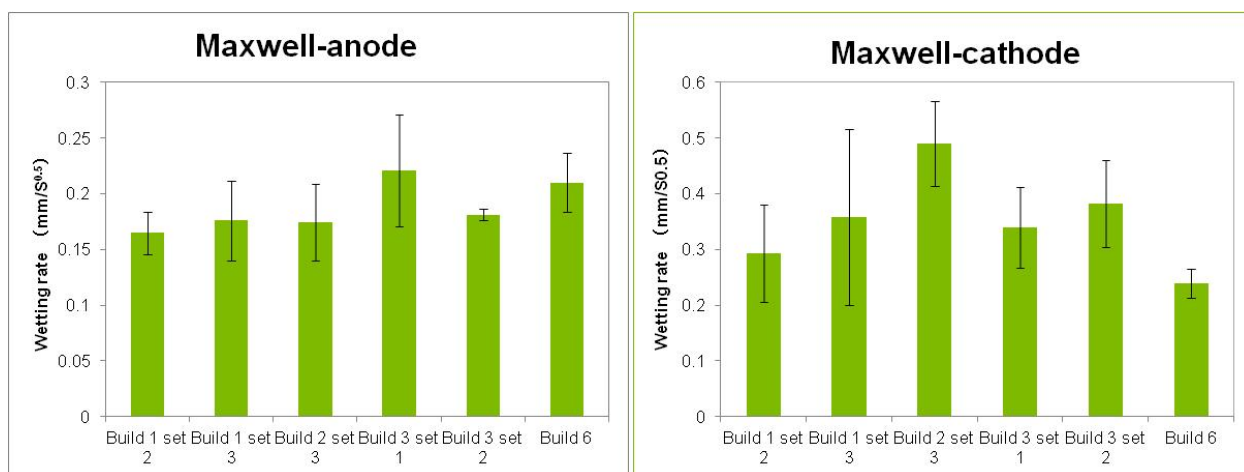


Figure II- 137: Wetting balance test results for the Maxwell dry-coated electrodes. Wetting rates are shown for all past samples and the final Build 6. Anode kinetics were similar to the highest wetting rates observed. Cathode kinetics were somewhat below historical values though the absolute values of the wetting rates for Build 6 cathode are higher than the anode. Testing was done in a baseline 3:7 EC:EMC solution with 1.2M LiPF₆ for all samples

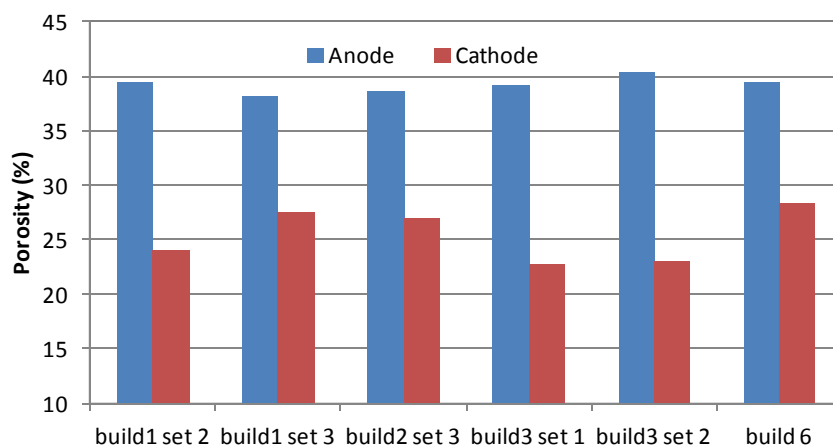


Figure II- 138: Porosity of Maxwell dry-coated samples as determined by Hg porosimetry. Cathode porosity was improved for Build 6 relative to Build 3 samples

Separator Technologies

Efforts focused on direct separator-electrode integration to increase the electrode stacking speed during cell assembly and thus reduce overall manufacturing costs.

Four approaches were investigated for applying a porous separator layer to both sides of negative electrode roll stock:

- “Wet” coating of a PVDF/solvent mixture onto the electrode
- “Wet” coating of a PE/solvent mixture onto the electrode
- “Dry” coating of a PE powder on the electrode
- Direct lamination of inorganic filled PE separator to the electrode

The direct lamination method showed the best cell performance and the highest probability of success in scaling up. This direct lamination approach was used for interim and final cell deliverables. Final deliverables were divided into 3Ah and 15Ah formats.

Substantial improvements in laminate quality were seen over time throughout the project. Further work should include modifying the separator to improve the mechanical integrity and filler uniformity.

ENTEK demonstrated feasibility of directly integrating separator to the electrode prior to cell stacking, and thus potentially reducing manufacturing costs associated with cell assembly.

Because of the good capacity retention and exceptional rate capability seen in the integrated cells, this approach was used for interim and final cell deliverables. The final deliverables included both 3Ah and 15Ah format cells, in which “dry” processed negative electrodes were supplied by Maxwell. For the 3Ah format cell deliverables, the anode material was supplied as discrete pieces rather than roll-to-roll stock. For the 15Ah format deliverables, laminates were prepared in a continuous, roll-to-roll process.

Though the yield for the 15Ah format laminates for final 15Ah format cell assembly was less than planned, the possibility of integrating the separator to the electrode by continuous lamination was clearly demonstrated. Further improvements in separator, electrode, and calender equipment tolerances are required to improve yield during continuous lamination.

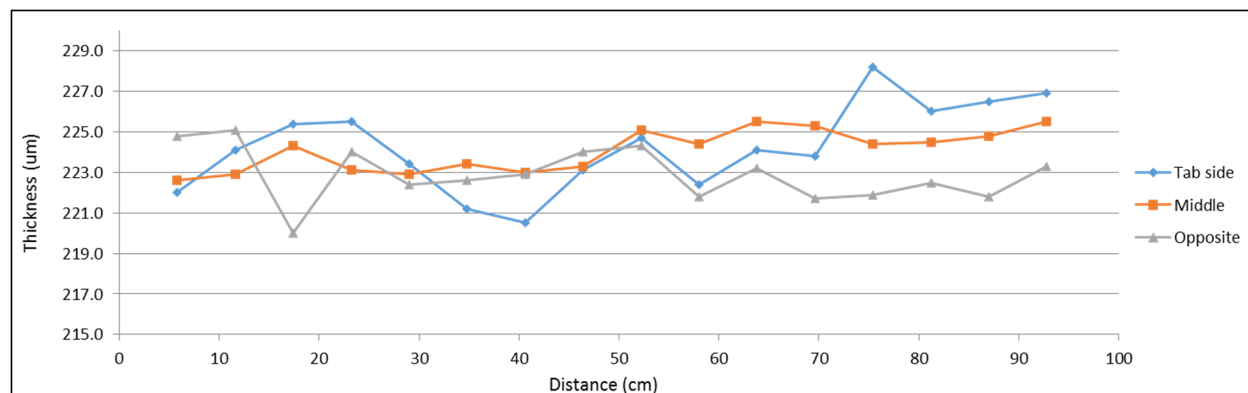


Figure II- 139: Thickness of laminates as a function of machine direction thickness using ENTEK calendaring equipment for 15Ah final deliverables

Non- NMP Coated Electrodes

Maxwell Technologies developed a dry electrode coating technology that brings both cost economy and improved performance to traditional energy storage electrode fabrication methods, techniques and configurations with the added capability to create structures that have been previously impossible to construct. Maxwell made significant advances in the application of the dry coating process to lithium-ion electrodes including the development of successful anode and cathode powder formulations, proof-of-concept demonstrations of powder mixing and free standing film production for both anode and cathode, and proof-of-concept demonstrations of powder-to-electrode roll stock production. There was also significant learning and lessons gleaned with most focused around process and equipment requirements necessary for controlled production of continuous roll film.

Maxwell was unable to attempt to demonstrate the final 15Ah format roll stock cathode deliverable of the program due to the unavailability of capable processing equipment. Despite the logistic difficulty encountered with the 15Ah format cathode, the final cumulative results of the program indicate that large-scale dry process roll stock electrodes are technically feasible and economically attractive.

The following figures show the final performance characteristics with earlier results shown for comparison. Significant improvements in cell rate performance (Figure II- 140) throughout the program culminating in the matching of the baseline target. The internal resistance of the cell also showed steady improvement as the formulations and processes improved dropping below the baseline target (Figure II- 141).

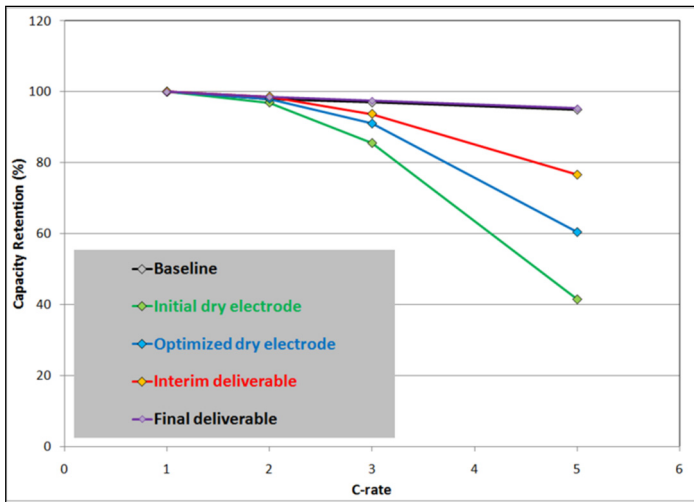


Figure II- 140: 3Ah Pouch Cell Rate Performance

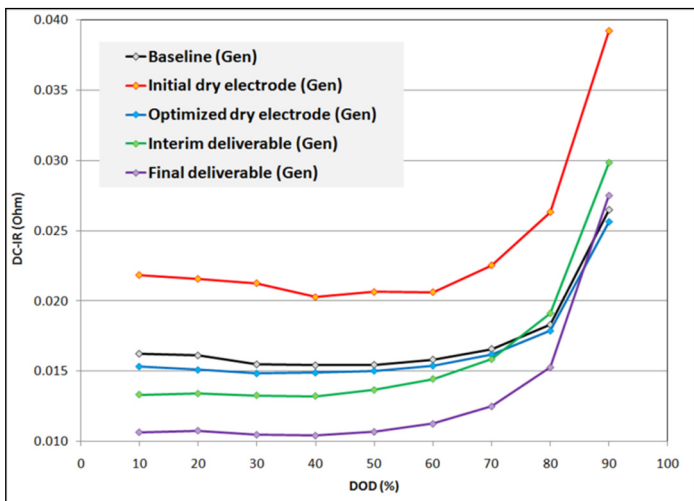


Figure II- 141: 3Ah Pouch Cell HPPC Performance (5C Gen, 10 sec)

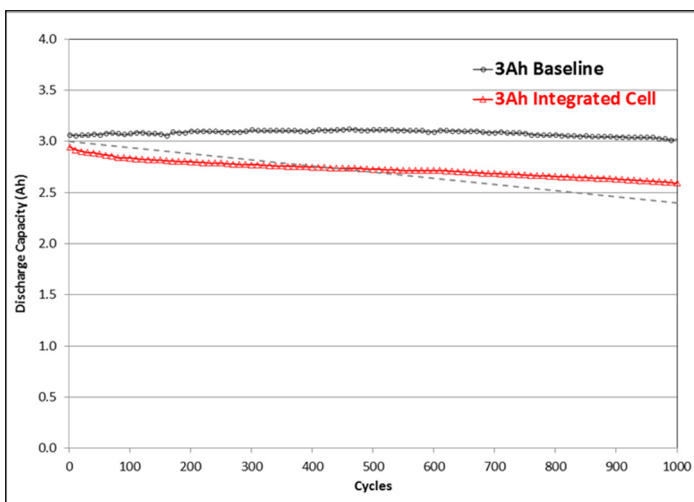


Figure II- 142: 3Ah Pouch Cell Cycle Life Performance (1C/1C Full Swing)

Cell cycle life performance of the 3Ah Final Deliverable Integrated Cell (Maxwell electrodes with Entek separator) is shown in Figure II- 142.

Roll stock process development included the equipment and processes for powder mixing, free-film calendaring and electrode laminating at pilot-scale production rates and scale.

Unlike wet coating methods, dry coating of electrodes consists of a two-step process, calendaring the powder into a free-standing film without the current collector backing as a first step. The free-standing film is then laminated to the current collector as a second step.

The roll stock development was hampered in this program by the very restricted availability of the pilot-scale calender originally intended to be modified and dedicated to this work. Limited experiments on the unmodified pilot-scale calender within this program were successful to the degree that they proved the capability of calendaring roll stock production, verified the type of equipment modifications required for further development and produced anode stock suited for use in Entek's process development.

Dry Electrode Technology Development

The objective was to incorporate lithium-ion battery active material powder into Maxwell's dry electrode process technology, baseline initial dry battery electrode performance, and improve dry electrode configuration and performance to match wet coated electrode. The battery active materials used in this program were NMC and graphite. Initially, at a 5C discharge rate tested to 100% DOD, the dry electrodes provided capacity retention of about 40% compared to about 95% for wet coated electrodes. Subsequent improvements in formulation and process ultimately produced dry electrodes with high rate discharge capability that is comparable to wet coated electrodes at 5C discharge rate and better HPPC results.

Controlled in dry electrode build consistency and uniformity also

contributed to good cycle life results in initial evaluation at 1C/1C charge/discharge.

3Ah Format Electrode Roll Stock Development

Work concluded on the formulation of both anode and cathode powders in conjunction with the development of powder mixing, free-standing film calendaring and electrode lamination techniques. Existing, in-house powder mixers proved inadequate for the necessary final condition of the powders and alternative commercial mixers were investigated and tested. Ultimately, a suitable mixing platform was identified that was able to supply the specified powder formulation in quantities that enabled the production builds.

Limited availability of the pilot-scale calender precluded adequate quantities of electrode roll stock. Instead the necessary quantity of individual electrodes (finished size) were produced to enable the JCI cell build and DOE shipment deliverable. The free standing film for the electrodes was calendered on Maxwell's lab-scale, manually fed calenders and the electrodes were laminated individually. With a frozen powder formulation and film-to-electrode process configuration (using the lab-scale equipment described), the electrodes were fabricated to support the JCI 3Ah cell deliverable to DOE.

15Ah Electrode Roll Stock Development

The objective was to further develop the powder formulations and optimize the roll stock processes for 15Ah format electrodes.

Further work was completed on the powder formulations with significant improvement on the electrochemical performance and processing capability.

Due to restricted availability of the pilot-scale calender only a small number of runs of either electrode were possible. Finally, the calender was damaged (the cause unrelated to the process validity) during a trial cathode roll stock run and remained unavailable for the duration of the program. The result of the 15Ah format roll stock calendaring was:

- Three rolls totally 170m of 15Ah format anode roll stock shipped to Entek. The 70m roll being fully within the loading and thickness specifications and the remaining two being suitable for Entek pre-run trials.

Conclusions on the Dry Coating Process

Maxwell's dry coating process can be applied to current commercial lithium-ion electrode production.

- Powder formulations and lab-scale processes have been successfully developed that produce dry coated cathodes with NMC and dry coated anodes with graphite that have demonstrated benchmark electrochemical performance in fully integrated 3Ah pouch cells.
- A commercially available pilot-scale powder mixing platform candidate has been identified and tested.
- Despite limited access to the pilot-scale calender, the roll stock runs completed demonstrated that, with identified equipment modification, both anode and cathode 15Ah format roll stock are possible.
- The extensive cost model for dry coated lithium-ion electrode manufacturing developed within this program shows results which support the overall cost reduction objective of this program.

Aqueous Cathode

The focus of the aqueous cathode work was to develop the formulation for a power cell design which decreases loading weight and increases carbon content. The quality of aqueous cathode has been improved significantly with optimized mixing process. Figure II- 143 shows the surface of aqueous cathodes relating to mixing processes, the new optimized mix processed aqueous cathode has better dispersion maintain porous structure well.

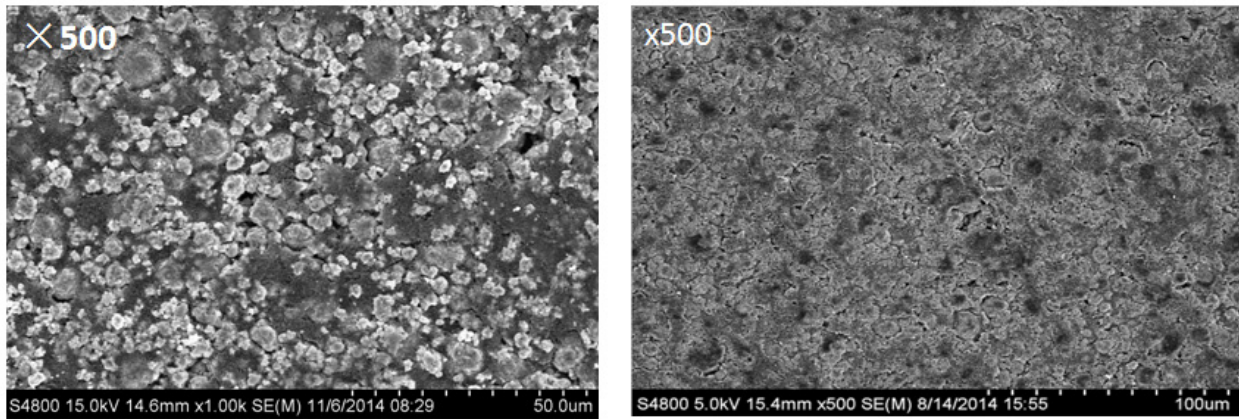


Figure II- 143: The surface SEM images of aqueous cathode: (a) New mix processed aqueous cathode, (b) Old mix processed aqueous cathode

The ASI results of new processed aqueous cathode are summarized in Figure II- 144. It shows much lower ASI compared to the old process for both generation and regeneration.

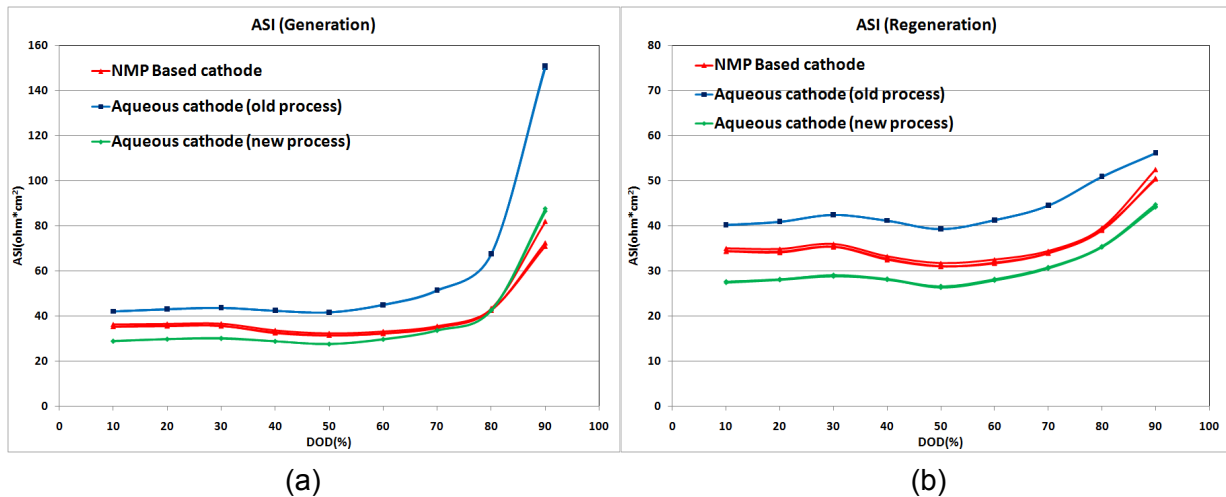


Figure II- 144: The ASI thru HPPC test (5C/3.75C, 10sec pulse)

Figure II- 145 and Figure II- 146 show the cycle and calendar life performance of new processed aqueous cathode compared to NMP cathode and old processed aqueous cathode. It has exceptional cycle performance and a minimal impedance increment.

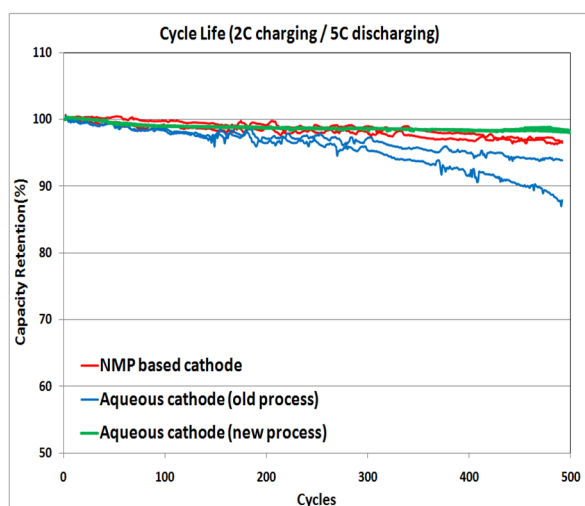


Figure II- 145: Cycle life results (2C charging / 5C discharging, 100% DOD from 3 to 4.2V)

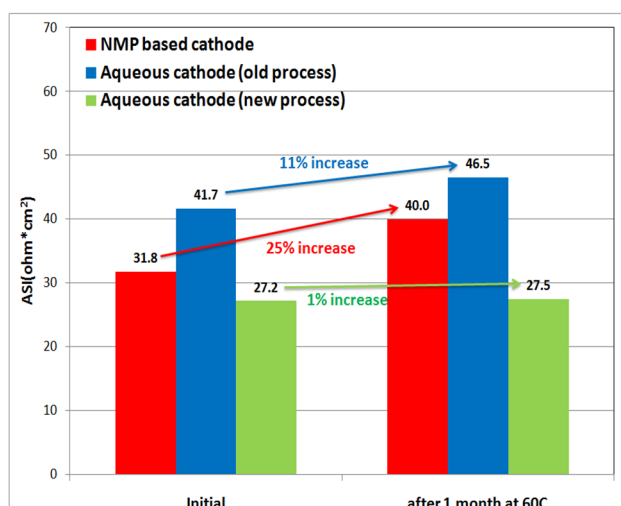


Figure II- 146: Calendar life results at SOC100% and 60°C

Cost Model

A modular cost model was finalized to support multiple technologies. The high level process for cost model calculation is described below. Table II- 25 illustrates different combinations and cell sizes for the cost model. The key cost model parameters are:

Table II- 25: Different combinations and cell sizes for the cost model

	Baseline	Aqueous and Laminated Separator	Dry Coating and Laminated Separator
15Ah	X	X	X
27Ah	X	X	X
41Ah	X	X	X

- Annual plant capacity
- Annual work weeks
- Weekly work hours
- Capital depreciation
- Fixed rate
- Variable rate
- Number of machines required
- Hourly fixed rate
- Fixed rate per cycle hour

At model completion we were able to estimate the cost impact for:

- Technology-agnostic process
 - Cell assembly
 - Formation
- Technology-dependent process – Aqueous, Dry Coating and laminated separator (see Figure II- 147)
 - Coating and mixing
 - Slitting and calendaring



Figure II- 147: Technology-dependent processes impacting cost estimates – aqueous, dry coating and laminated separator

Some of the results obtained from the cost model are summarized in the five figures on the following page (see Figure II- 148 - Figure II- 152). Figure II- 148 shows the cycle life results under a particular scenario (2C charging / 5C discharging, 100% DOD from 3 to 4.2V). Figure II- 149 shows the separator cost reduction estimate for laminated separator. Figure II- 150 shows an estimate of the formation cost reduction. Figure II- 151 shows the cost comparison upon an integration of all the proposed solutions, while excluding the formation effect. Including the formation effect increases the total savings to almost double that value as shown in the Figure II- 152.

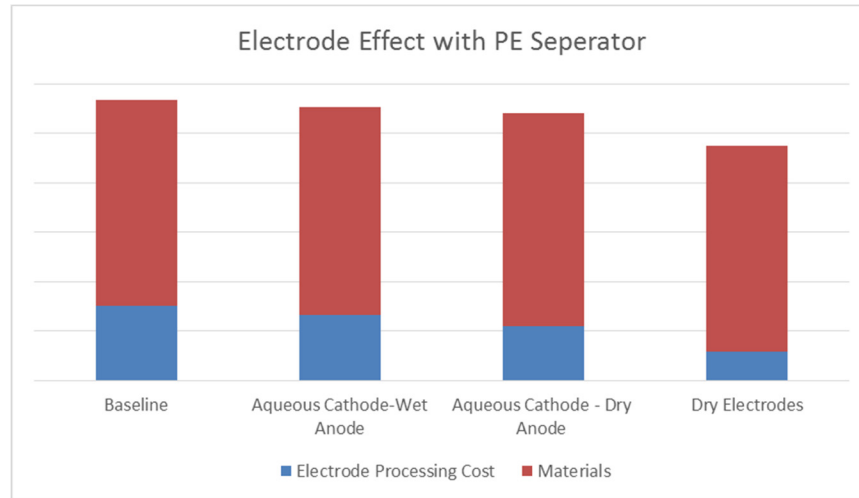


Figure II- 148: Cycle life results (2C charging / 5C discharging, 100% DOD from 3 to 4.2V)

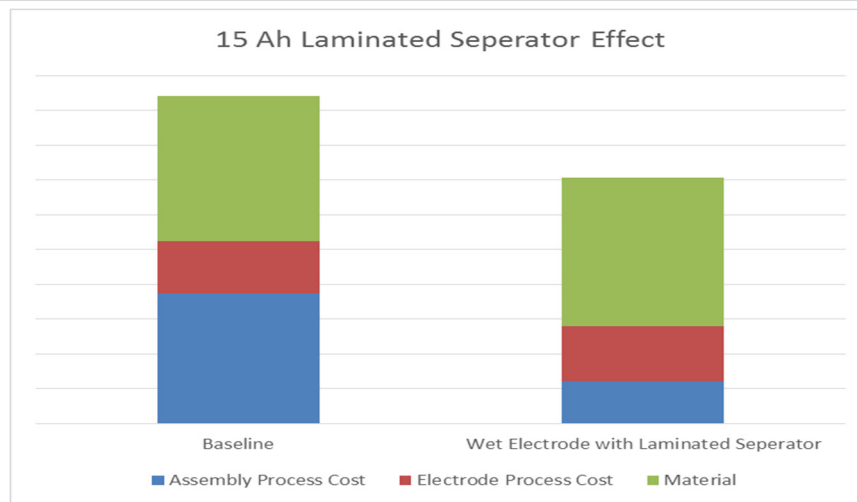


Figure II- 149: Separator cost reduction estimate for the laminated separator

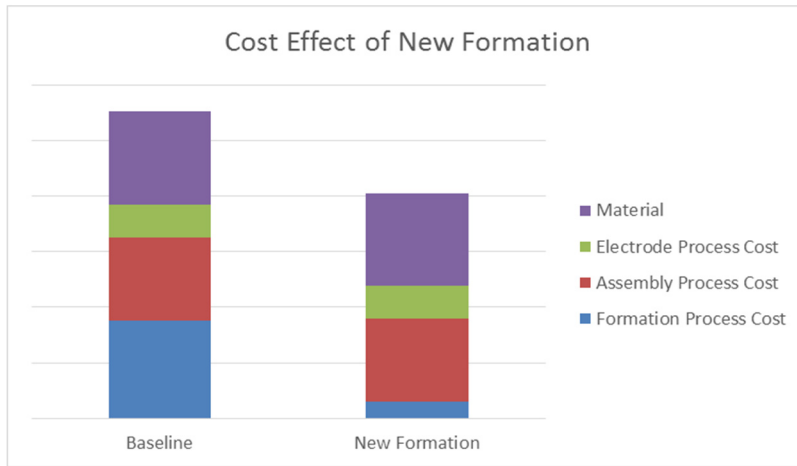


Figure II- 150: Formation cost reduction

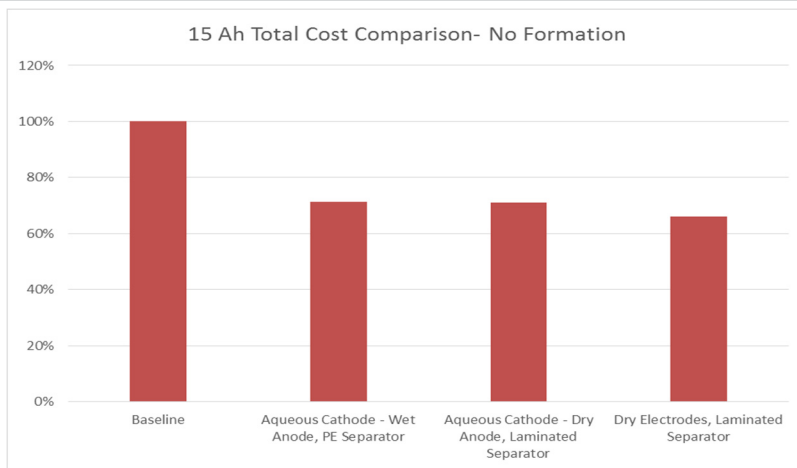


Figure II- 151: Cost comparison for the integration of proposed solutions (excluding formation effect)

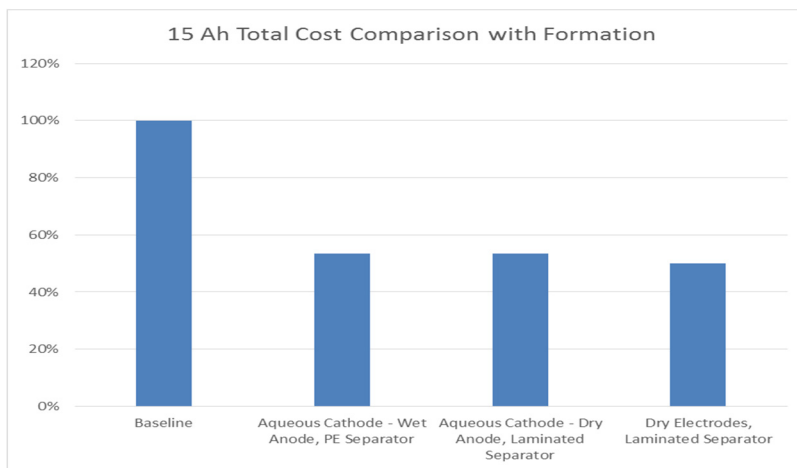


Figure II- 152: Cost comparison for the integration of proposed solutions (including the formation effect)

II.C.2 Utilization of UV Curing Technology to Significantly Reduce the Manufacturing Cost of LIB Electrodes (Miltec UV International)

Objectives

- Reduce lithium-ion battery electrode manufacturing costs by 50% by replacing solvent-based binder with UV curable binder.
- Demonstrate that battery cells made from UV cured binder electrode coatings perform equal to or greater than equivalent cells made using solvent based binders.

Technical Barriers

The technical barriers to realizing the full cost saving potential of UV curable binder technology in these applications are:

- Development of mixing techniques applicable to solvent-free slurries that ensure homogenous mixing and viscosities compatible with electrode coating techniques.
- Confirmation that the UV cured binder materials retain chemical inertness and adhesion after long term electrochemical exposure.
- Development and demonstration of high speed coating and UV curing techniques that ensure complete curing of the electrode coating.

Technical Targets

- Cathode Targets: 90/5/5% NMC/Carbon/UV Curable Binder (originally 87/5/8%)
- Manufacturing cost reduction > 50% over conventional PVDF cathode binder
- Pouch cell performance \geq conventional PVDF
- Process speeds >50 meters/minute

Accomplishments

- Demonstrated cathode with 90/7/3% NMC/Carbon/UV curable binder with excellent adhesion, calendaring and performance half cell performance essentially equal to conventional PVDF cathode.
- Demonstrated a 90/5/5 UV cathode coating could be cured at 100 meters/minute.
- Project began year with 8% UV binder and now all work is in 3-5% UV binder range. Reactive impedance and IV impedance were significantly reduced (>200%) so that Miltec produced a single layer pouch cell that was nearly equal to reference PVDF cathode. This improvement was accomplished by continuous improvement of binder ingredients, cure conditions, mixing, and application techniques.
- Delivered final pouch cells to DOE with 90/5/5 NMC/carbon/binder for independent testing.
- Completed cost model showing the UV process reduces manufacturing costs by approximately 90% over PVDF process. Total electrode cost decrease 25% for two-side coated electrodes and 50% for single-side coated electrodes, including materials over that of the conventional solvent process.
- As the contract comes to a close, Miltec continues to make very good progress toward producing UV cathodes with the performance required for commercial Lithium-ion batteries.

Project Details

John Tabacchi (NETL Program Manager)
DE-EE0005421 Recipient: Miltec UV International

Gary Voelker PD
Dr. John Arnold PI
146 Log Canoe Circle
Stevensville, MD 21666
Phone: 410-604-2900; Fax: 410-604-2906
Email: gvoelker@miltec.com, jarnold@miltec.com

Subcontractors:
Argonne National Laboratory
Oak Ridge National Laboratory

Start Date: October 2011
Projected End Date: November 2015

Introduction

Previously identified UV curable binders and associated curing technology have been shown to reduce the time required to cure electrode coatings from tens of minutes to less than a second. This revolutionary approach can result in dramatic increases in process speeds, significantly-reduced capital (by a factor of 10 to 20) and operating costs, reduced energy requirements, and reduced environmental concerns and costs due to the virtual elimination of harmful volatile organic solvents and associated solvent dryers and recovery systems. The accumulated advantages of higher speed, lower capital and operating costs, reduced footprint, lack of VOC recovery, and reduced energy cost can result in a reduction of 90% in the manufacturing cost of cathodes. When commercialized, the resulting cost reduction in lithium batteries will allow storage device manufacturers to expand their sales in the market and thereby accrue the energy savings of broader utilization of HEVs, PHEVs and EVs in the U.S., and a broad technology export market is also envisioned.

Approach

The objectives outlined have been accomplished by an iterative research and development process. Multiple lithium-ion battery cells were fabricated using various approaches to UV curing technology; performance of the cells evaluated; and analytical testing used to further improve the performance of the cells. Final pouch cells made with UV curable binders were submitted to the DOE for independent testing and performance verification. Our goals for 2015 were to complete the iterative development to improve cathode sample preparation and coin cell testing using UV curable binder technology. It was learned in the first year of the effort that the use of UV curable binder technology to conventional carbon anode material was problematic because of the extreme absorptive qualities of the anode carbon. The project has therefore focused on cathode preparation and the results have exceeded the goals. NMC pouch and coin cells using UV curable binder have been prepared with performance at the baseline goal. Miltec began operation of a slot die coater installed on an existing UV lamp system designed for lithium-ion battery electrodes. The slot die coater is capable of coating on a 10" current collector at a width of 8" and operating at coating speeds up to 200 fpm. Initial problems with operation of the reel to reel subsystem have been corrected and extensive testing on the slot die/UV curing system is underway. Because of the success of UV curing hand drawn samples at 100 meters/minute, a modified printing technology is being added to the Miltec laboratory UV system for evaluation. It is believed that the printing technology will be able to coat at the higher speeds (100 meters/minute) and will be more operable than slot die at the higher viscosities of UV curable binder mixtures.

Results

Miltec has achieved the following progress:

Developed and demonstrated performance of the cathode with 5% UV binder, 5% of carbon and 90% NMC.

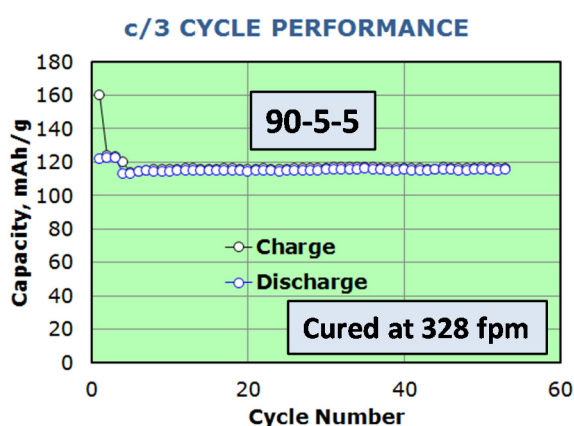
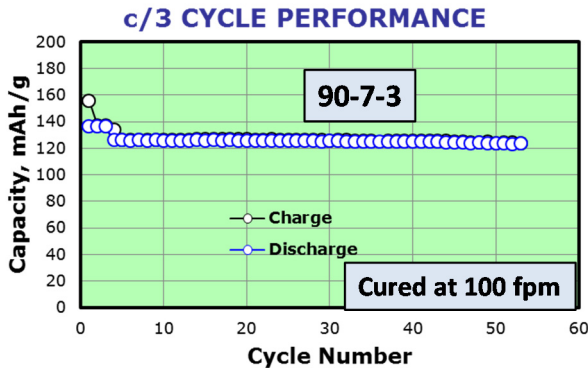


Figure II- 153: Capacity over 50 cycles of the 90-5-5 sample (NMC:carbon:binder) cured at 328 fpm (100 meter per minute) under 3 lamps

At the beginning of this fiscal year Miltec started actively pursuing the development of 90-5-5 formulations (NMC-carbon-binder). These developments overcame issues with poor adhesion, excessive shrinkage and depth of cure. Miltec developed coatings with excellent adhesion that at the same time could be cured at 100 meter per minute (328 fpm) and have good battery performance. (See Figure II- 153.)

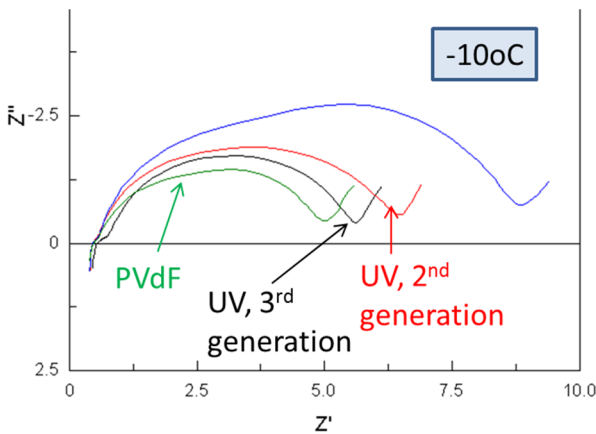
Developed and demonstrated performance of the cathode with 3% UV binder, 7% carbon and 90% NMC.



At the end of the current year, all developments from the coatings with 5% UV binder allowed us to advance and demonstrate a successful coating with good cure with only 3% UV binder which had excellent adhesion and calendered well. Samples showed good electrochemical performance. (See Figure II- 154.)

Figure II- 154: Capacity over 50 cycles of the 90-7-3 sample (NMC:carbon:binder) cured at 100 fpm (~ 30 meters per minute) under 3 UV lamps

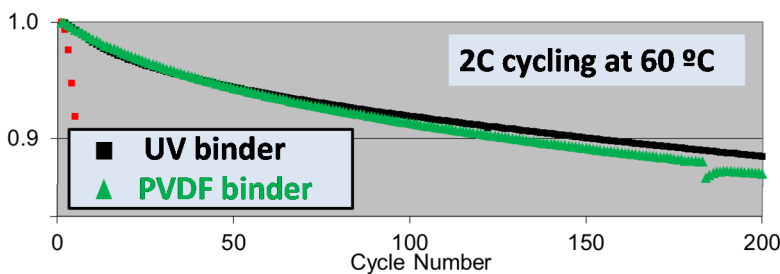
Developed cathode with 5% UV binder that surpassed the PVDF reference in pouch cell capacity retention after 200 elevated temperature cycles.



In FY 2015, we significantly decreased AC impedance and IV resistance through the iterative research of binder combinations, cure conditions as well as mixing and application techniques: by the end of the year AC impedance and IV resistance were reduced by 200% and 50%, respectively, comparing to the end of last year. (See Figure II- 155.)

Figure II- 155: AC impedance comparison of cathode with 5% PVDF and UV binder taken at -10°C

Current cathode with 5% UV binder Developed 90-5-5 (NMC:carbon: UV binder) cathode with better (by ~7%) capacity retention over 200 cycles



Significantly lower impedance and resistance allowed Miltec to produce a single-layer pouch cell that superseded PVDF reference by ~7%. (See Figure II- 156.)

Figure II- 156: Cathode with 5% UV binder demonstrated better capacity retention (by ~7%) than cathode with 5% PVDF binder

Conclusions and Future Directions

Miltec UV with the support of Argonne National Laboratory and Oak Ridge National Laboratory made dramatic progress in demonstrating the potential cost savings attributable to the use of UV curable binder to replace conventional binders in the manufacture of LIB cathodes. Pouch cells with performance equal to a conventional reference cell have been made at binder content comparable to commercial products and UV curing at 100 meters/minute has been demonstrated. Miltec UV has been selected for the negotiation of a new cooperative agreement to continue the development efforts required leading to commercialization of this revolutionary technology. These efforts include the testing of 100 meter/minute coating and UV curing while staying focused on long term cycling with low reactive impedance and overall performance equal to conventional solvent based cathode coatings. A cost model indicates the manufacturing cost for a 2-sided coated cathode can be reduced by 90% and the overall cost of the cathode reduced 25% including materials.

FY 2015 Publications/Presentations

1. “Utilization of UV or EB Curing Technology to Significantly Reduce Costs and VOCs in the Manufacture of Lithium-ion Electrodes”, ES132_Voelker_2015, US DOE Vehicle Technologies AMR, 2015.

II.C.3 High Capacity Alloy Anodes (Applied Materials)

Objectives

- Applied Materials is working on a new class of Li battery anodes with high capacity based on an innovative micro-cell porous 3DCu-Li alloy structure.
Objectives include:
- Develop and demonstrate the feasibility of depositing alloy anode materials at high deposition rates.
- Characterize, evaluate, and optimize the resulting electrodes using pouch cells and demonstrate the low cost potential of the new manufacturing methodology.

Technical Barriers

- In order for EVs to achieve mass adoption and make a significant dent in U.S. and global CO₂ production, the key problems of driving range per charge & cost per kWh must be addressed.
- Barriers addressed:
- Performance: Low Wh/L and prismatic cell.
- Life: Cycle life of alloy based anodes is one the main issues that limit its viability. We are working closely with our partners (subcontractors) to understand the underlying issues leading to the low cycle life of these anodes and then make necessary process changes to meet requirements.
- Cost: High cost of manufacturing and \$/kWh. The equipment manufactured by Applied Materials will reduce the manufacturing cost of anodes.

Technical Targets

- Anode Targets: Demonstrate high capacity Li-ion battery cell anodes that are capable of achieving an energy density of at least 500 Watthours per liter (Wh/L) and a power density of at least 500 Watts per liter (W/L).
- Cathode Targets: LiNi_{1/3}Mn_{1/3}Co_{1/3}O₂ (NMC111) and LiNi_{0.5}Mn_{0.3}Co_{0.2}O₂ (NMC532) cathode materials.
- Cell Targets: Demonstrate cycle life (300-1000 cycles at 80% depth of discharge), calendar life (5-10 years), and durable cell construction and design capable of being affordably mass produced.

Accomplishments

- 3DCu current collector achieves capacity retention advantages up to 25-27% at 2C and 3C rates at high Graphite loading.
- 3DCuSnFe active anode achieves a high capacity of >500 mAh/g with improved C-rate performance, which results in significant capacity retention advantages up to 2-2.5x at 5C rate.
- We delivered the 3DCu-Graphite/NMC(111) and 3DCuSnFe-Graphite/NMC(532) cells to U.S. DOE for evaluation.
- 3 mAh/cm² 3DCu-Graphite/NMC cells have 1000 cycles at 88% retention by third-party verification.
- The interim 3DCuSnFe-Graphite/NMC(532) cells have a 30% thinner anode vs. standard Graphite/NMC cells.
- 3DCuSnFe alloy anode has been extensively evaluated with various Si-graphite/carbon powders and shows high energy density and unique cyclability with SiSnFe alloy.

Project Details

John Tabacchi (NETL Program Manager)
DE-EE0005455 Recipient: Applied Materials, Inc

Sergey Lopatin (Applied Materials, Inc – PD/PI)
3100 Bowers Avenue
Sanat Clara, CA 95052
Phone: 408-235-47422; Fax: 408-986-2840
Email: sergey_lopatin@amat.com

Subcontractors:
Lawrence Berkeley National Laboratory
Oak Ridge National Laboratory
FMC Lithium Division
Navitas Systems
Nissan Technical Center North America

Start Date: October 2011

Projected End Date: June 2016

- We have developed a modified electrolyte with additive that enables higher Coulombic efficiency and hence cycling performance for 3DCuSnFe-Si-Graphite cell.
- 3 mAh/cm² 3DCuSnFe-Si-Graphite/NMC(532) cells have been cycled 200 cycles at >80% retention in coin cell assemblies.
- The 3D electrode energy density has been improved by selecting Si alloy material content at total 9% from tested at 3%, 6%, 9% and 12%.
- We have optimized pouch cell formation protocol to achieve better cycling performance.
- 3 mAh/cm² 3DCuSnFe-Si-Graphite/NMC(532) pouch cells have showed acceptable cell performance after formation. Our observations indicated that stable interface formation is needed by using proprietary electrolyte.

Introduction

Based on the ability to distributively generate power locally through solar and wind, more and more people believe that batteries based on Li-ion technologies are the optimal solution to electrify transportation. The cell that Applied Materials and project partners develop with 3DCu current collector architecture, 3DCuSnFe alloy anode, will significantly advance the current state-of-the-art in Li-ion technologies.

Approach

Innovative Approach: The objectives outlined above will be accomplished by using electro-deposition technology, module, which allows for 3D-porous current collector and 3DCuSnFe nano-structure alloy. We will use modular technological steps for forming 3-3.5 mAh/cm² cells including process methodology for Si-Graphite coating by water soluble process to achieve adhesion to the 3D-porous structures. The major technology innovations that will be undertaken to accomplish the objectives of this effort are as follows:

1. Achieve cycling life from 300 to >1000 cycles for 3 mAh/cm² 3DCu-Graphite/NMC baseline cells with 3DCu current collector structure that has a very large surface to volume ratio to contact with Li-ion electrolyte. Graphite particle sizes, pore fill, adhesion and morphology will be further optimized to achieve this goal.
2. Extend 3D electrode concept to the high loading 3DCuSnFe-Graphite alloy electrodes. Improve 3D electrode volumetric capacity by reducing active material thickness from 100 to 70µm in interim cells. The alloy electrodes should allow a) low resistivity at the interface electrode/current collector, b) fast charge transfer at the interface electrode/electrolyte, and c) alloy expansion and contraction mitigated by reduced alloy grain size with Fe addition. This development allows the benefits of the 3DCuSnFe alloy and Si-Graphite to be utilized in a final cell with higher energy density.

Results

Micro-cell 3DCu-Li alloy architecture of controlled thickness forms continuous highly conductive Cu pathways for electrons through the full electrode. The technology holds great potential for electric vehicle Li-ion batteries.

The electrode structure also has a very large surface-to-volume ratio to contact with Li-ion electrolyte. Porous 3DCu current collectors and 3DCuSnFe nano-structure alloys can accommodate the volumetric expansion during electrochemical cycling and contribute to long cycle life. These electrodes are assembled into prismatic battery cells and tested to demonstrate the feasibility of producing Li-ion batteries with the target energy density (See Figure II- 157 and Figure II- 158). We have achieved the following progress:

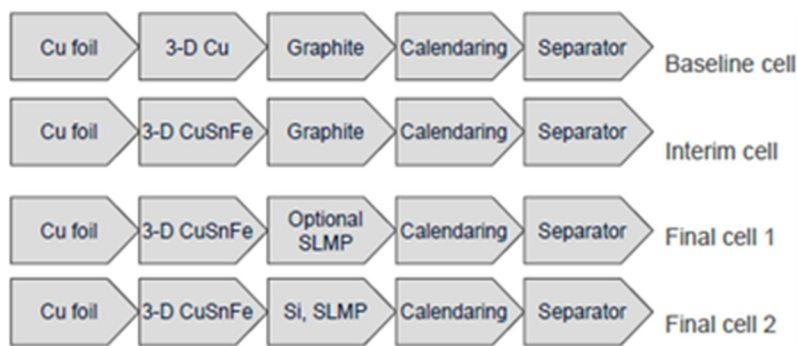


Figure II- 157: Schematic diagram of process flows for manufacturing baseline cells, interim cells and final cells with 3D current collector and alloy anodes (introducing Stabilized Lithium Metal Powder (SLMP) is optional)

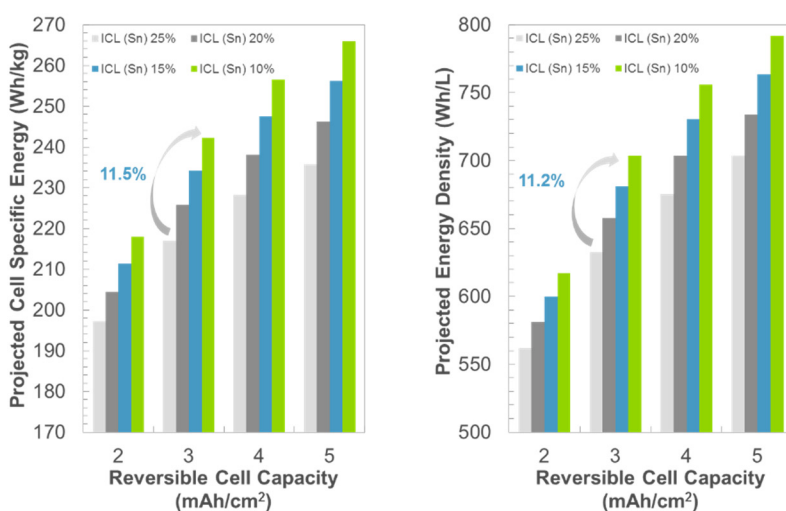


Figure II- 158: Effect of decreasing irreversible capacity loss (ICL) from 25 to 10% with increasing cell capacity (current loading from 2 to 5 mAh/cm²) on the interim cell energy parameters (3DCuSnFe / NMC design model)

Cycle Life of 3D Current Collector and Alloy Anodes

Equipment design concept and laboratory scale chamber prototype were developed. Plating module concept incorporated capability to form 3D structure on both sides of the Cu foil. The electro-deposition module allowed for 3D-porous structure formation in a single prototype tool for both 3DCu collector and 3DCuSnFe alloy anode. Baseline processes have been developed for (a) 3DCu current collector and (b) for Graphite coating using a water soluble process. Scanning Electron Microscopy (SEM) images of 3DCu Graphite structures showed pore fill and crack-free coating. 3DCu/Graphite baseline cell material was studied before and after calendaring. 3DCu remained unchanged with no mechanical damage as result of calendaring. Testing rate performance in half-cell assembly vs. Li demonstrated capacity retention advantages up to 25-27% at 2C and 3C-rates. Full cells 3DCu-Graphite vs. NMC, 30-38 mAh single layer baseline pouch cells, have been assembled and shipped to U.S. DOE for testing according to the

EV manual. These 3 mAh/cm² 3DCu-Graphite/NMC cells have shown 1000 cycles at 88% retention by third-party verification (Figure II- 170, cells 4 and 5).

Interim cell processes have been developed for 3DCuSnFe active material current collector. Coulombic efficiency (CE) of the alloy electrodes has been improved by following techniques: grain size reduction, pre-lithiation, and mitigation with combining alloy with Graphite.

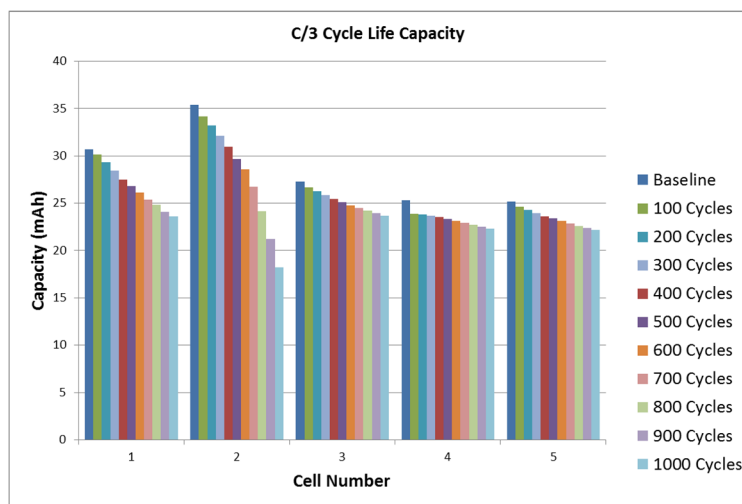


Figure II- 159: 3D Current collector baseline cells 3, 4 and 5 with 1000 cycles at 86-88% capacity retention

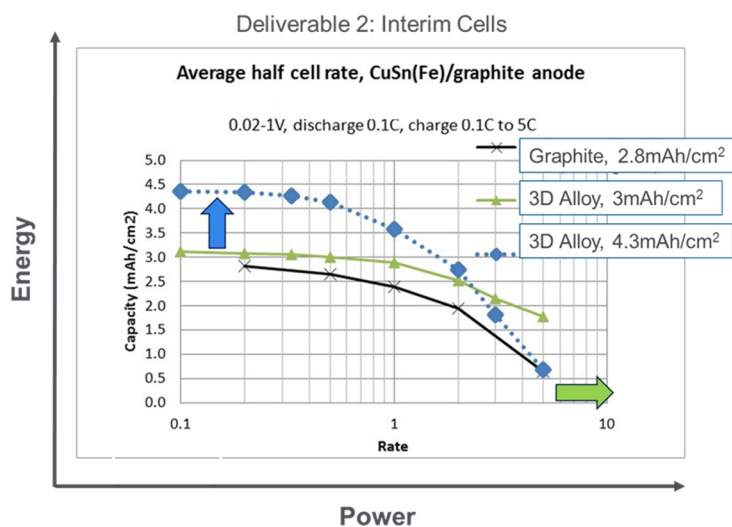
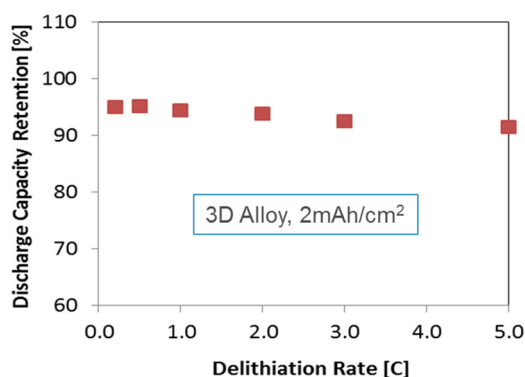


Figure II- 160: 3DCuSnFe/Graphite alloy anode capacity retention at high C-rates allows charging time improvement vs. Graphite anode

High Rate Capability 3DCuSnFe Anode

Electro-chemical deposition has been developed for forming ~50 nm grain sizes of alloy anode with Cu₆Sn₅(Fe) structure. Connected nano-size grains formed a conductive network of porous active material on Cu foil. Dense and porous versions of CuSnFe alloy depositions with thickness range between 12-50 microns were developed. The mass loading, chemical composition, porosity, thickness were controlled to obtain the required loading. Testing rate performance in half-cell assembly vs. Li demonstrated capacity retention advantages up to 2-2.5x at 5C-rate (Figure II- 159). Development of 3DCuSnFe nano-structure alloy anode resulted in 30% electrode thickness reduction.

Optimization of 3DCuSnFe Anode Composition

Various binders have been evaluated to achieve better adhesion and cycling performance.

Optimizing 3DCuSnFe-binder electrode with various bending tests (Figure II- 160) resulted in enhancement of its adhesion. We have tested 3DCuSnFe-binder materials in coin half cells to confirm their electrochemical performance, so that the final design anode will be combined with Si-Graphite coating.

Feasibility Test of High Capacity Cells with 3DCuSnFe and Si-Graphite Coating

In order to demonstrate high capacity cells using 3DCuSnFe-Si-Graphite/NMC(532) various cells were designed (see Figure II- 161). The key finding is that the anode/cathode matching and Irreversible Capacity Loss (ICL) need to be improved.

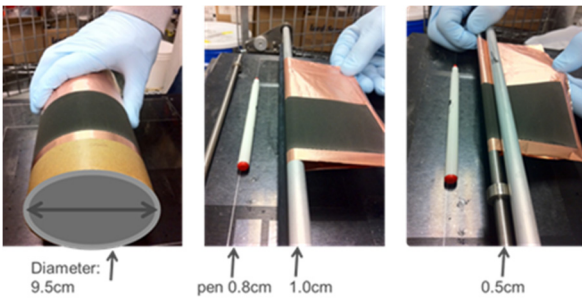


Figure II- 161: 3DCuSnFe-binder electrode bending test over various diameter rolls

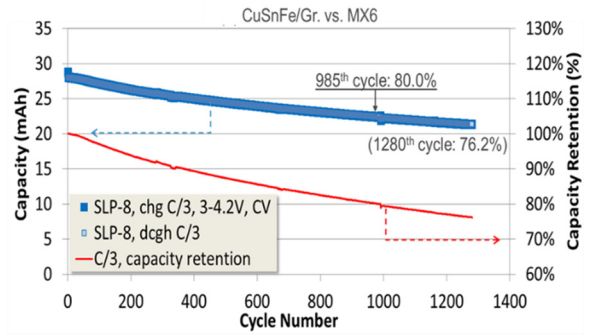


Figure II- 162: 3DCuSnFe-Graphite/NMC(111) interim cell with 985 cycles at 80% capacity retention

The cycle life test of each interim cell is carried out at C/3, 3-4.2 V. Figure II- 162 shows that the interim cell is capable of 985 cycles at 80% capacity retention. The 3DCuSnFe-Graphite anode used in interim cell has a capacity of 3 mAh/cm², tested for rate performance in Figure II- 160, which showed capacity retention and stable cycling performance. Current results show that more optimizations for the cell formation protocol, ratio of alloy anode to Si-Graphite and for alloy pre-lithiation are necessary. Experimental cells including coatings of 3DCuSnFe with Si-Graphite were assembled and are being tested. 3D electrode energy density has been improved by selecting Si alloy material content at total 9% (Figure II- 163) from tested at 3%, 6%, 9%, and 12%. 3 mAh/cm² 3DCuSnFe-Si-Graphite/NMC(532) cells have been cycled 200 cycles at 80% retention in coin cell assemblies (Figure II- 163).

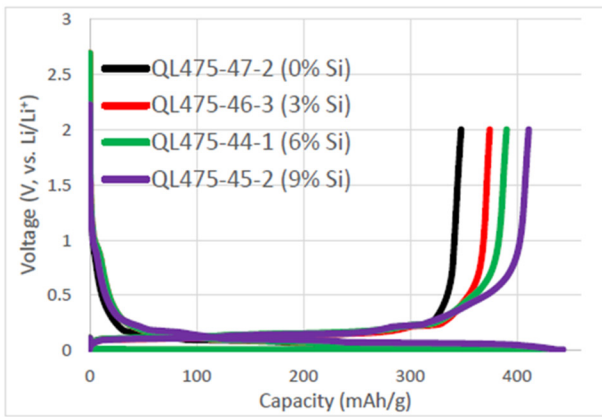
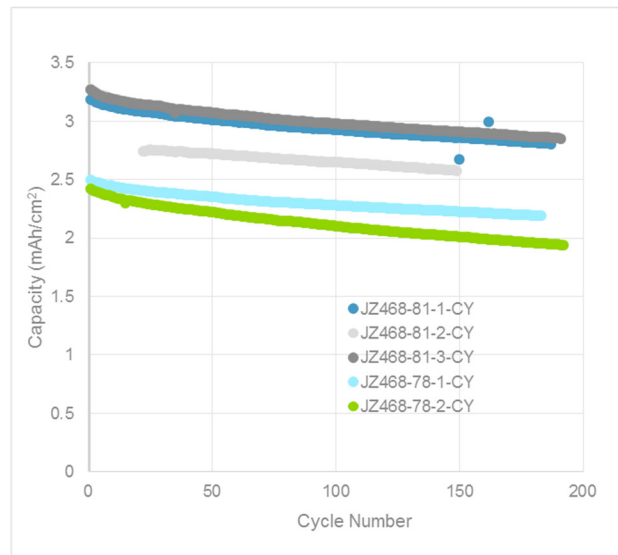


Figure II- 163: 3D electrode energy density with different Si alloy material content at 3%, 6%, 9%; and 2-3 mAh/cm² 3DCuSnFe-Si-Graphite/NMC(532) cells cycled 200 cycles at >80% retention in coin cell assemblies



To study the effect of different porous versions of 3DCuSnFe on the electrochemical performance, one batch of slurry was prepared and casted onto different substrates. In this study, baseline bare Cu foil and two porous 3DCuSnFe versions were used as substrates. One is the non-calendered porous 3DCuSnFe foil, and the other is calendered porous foil with reduced 3DCuSnFe thickness by 2x. To reach the target capacity >400 mAh/g, the dried electrode composition was 82 wt.% graphite, 9 wt.% Si, 7.5 wt.% binder, and 1.5 wt.% carbon black. Further reducing inactive material content in the anode electrode may increase the cell energy density. The loading of electrode materials for various substrates was adjusted as needed to attain 3.5 mAh/cm².

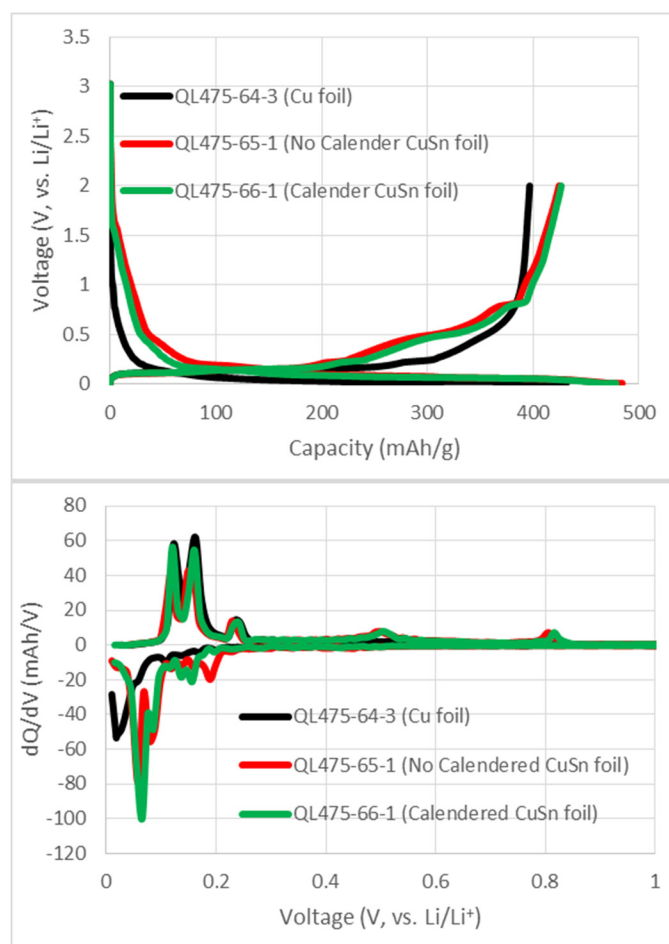


Figure II- 164: The voltage profiles and differential capacity curves of final half cells with different 3DCuSnFe versions during formation cycle

After drying at 80°C in vacuum oven overnight, three 0.5 inch disks were punched from each electrode coupon, and the weight of each disk was measured. The standard deviation (STDEV) of weight observed on the calendered porous foil (0.2) is much lower than that of the non-calendered foil (0.7), indicative of more uniform Si-graphite coated throughout the whole calendered porous foil. Therefore, the calendering process is beneficial to achieve the electrodes with uniform coating when we use the 3D porous 3DCuSnFe foil as substrates.

For each electrode, half coin cells were assembled with Li metal as counter electrodes. After cell formation, rate and cycling tests were carried out. The formation protocol is as follows: 2 cycles at C/25; followed by 3 cycles at C/10. The first cycles during formation are shown in Figure II- 164. Formation results show that porous 3D CuSnFe foils enable low electrode resistance and high specific capacity. Compared with Cu foil as substrate, the voltage profiles of cells with porous 3DCuSnFe alloy as substrates are higher (Figure II- 164), indicative of lower resistance in porous 3DCuSnFe foils. Voltage profiles of calendered porous 3DCuSnFe foil are slightly lower than those of non-calendered porous foil. This implies that, after alloy calender, the resistance of porous

3DCuSnFe-Si-Graphite electrode increases slightly. It is more apparent from the differential capacity curves.

For calendered 3DCuSnFe alloy, the first discharge peak appears at ~0.156 V, which is slightly lower than that of non-calendered alloy (at ~0.189 V). The reversible capacity of electrodes with Cu foil is ~395 mAh/g, while it is >425 mAh/g for both porous 3DCuSnFe alloy foils. The electrodes with calendered porous alloy have an irreversible capacity loss (ICL) of 11.48%, which is higher than that of Cu foil (8.5%), but lower than that of non-calendered porous alloy (12.45%). Based on the data obtained from half cells, full coin cells were assembled and characterized using electrodes prepared for half cells as anodes and using electrodes containing NMC as cathodes (93 wt.% NMC, 4 wt.% binder and 3 wt.% carbon black). After formation, the rate test was applied to full cells within the voltage window of 3-4.3 V. The rate test protocol was: charge to 4.3 V with a constant current density of C/10, and keep voltage at 4.3 V until current equals to C/50; discharge to 3 V with incremental constant current density from C/10 to 5C. The rate capabilities of cells are shown in Figure II- 165. Full cell rate test results show that porous 3DCuSnFe alloys have promising rate capability, especially at high rate. Figure II- 165 exhibits that cells containing porous alloys demonstrate almost identical capacity retention at low rate (<0.5 C), which is slightly higher than that with Cu foil. Above 0.5C, the capacity retention of Cu foil electrode dramatically decreases from ~89% at 0.5C to ~65% at 1C, ~37% at 2C, and finally to ~8% at 5C. However, the capacity retention of non-calendered porous 3DCuSnFe alloy remains relatively high at ~ 88% at 1C, 77% at 2C, and finally ~22% at 5C. The capacity retention of calendered porous alloy electrode is slightly lower than that of non-calendered one. These observations are consistent with what is observed from half cells. Data obtained from final half and full cells with various 3DCuSnFe alloys as substrates showed increased capacity, rate capability and durability vs. bare Cu foil.

Table II- 26: Summary of formation cycles for 3DCuSnFe-Si-Graphite/ NMC(532) final cells: averaged values from 27 single layer pouch cells (SLP)

Cycle #	Charge (mAh)	Charge (mAh/cm ²)	Discharge (mAh)	Discharge (mAh/cm ²)	ICL (%)
1 st	60.27	4.27	44.35	3.14	26.42
2 nd	44.63	3.16	43.67	3.09	2.17
3 rd	43.72	3.09	42.85	3.03	2.01
4 th	42.97	3.04	42.57	3.01	0.92
5 th	42.68	3.02	42.35	3.00	0.77

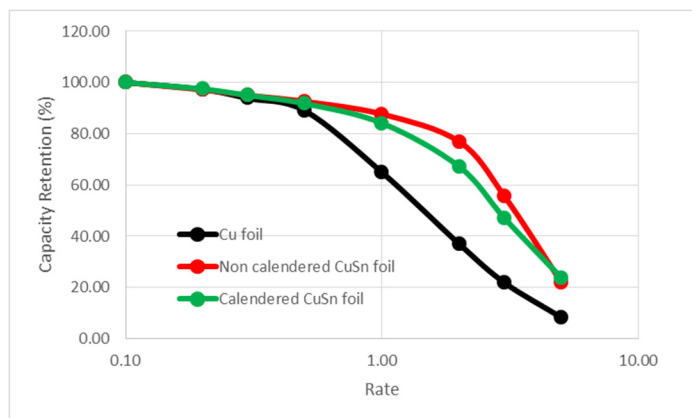


Figure II- 165: Rate capability of final full cells with different 3DCuSnFe porous versions of substrates

Si alloy % and 3DCuSnFe electrode density and thickness so that we are able to achieve high energy density in the cells with good C-rate and cycling performance. 3 mAh/cm² 3DCuSnFe-Si-Graphite/NMC(532) cells have been cycled 200 cycles at >80% retention in coin cell assemblies. The achievements have proved that the proposed technical approach is viable.

We have delivered 3D electrode pouch cells to U.S. DOE as 18 baseline cells and 18 interim cells, which have good cycling performance. Initial Coulombic efficiency has been improved to more than 99.96% for all the 3DCu-Graphite and 3DCuSnFe-Graphite electrodes. Coulombic efficiency was improved by grain size reduction, pre-lithiation, and mitigation with combining alloy with Graphite. The 3mAh/cm² 3DCu-Graphite/NMC pouch cells have 1000 cycles at 88% retention by third-party verification. Development of 3DCuSnFe nano-structure alloy anode resulted in half-cell and full cell electrode thickness reduction. Testing rate performance in half-cell assembly vs. Li demonstrated capacity retention advantages up to 2-2.5x at 5C-rate.

Equipment design concept and laboratory scale chamber prototypes were developed. Plating module concept incorporated capability to form 3D structure on both sides of the Cu foil. The individual module designs as well as module integration concepts continue to be fine-tuned. This allows producing the final sets of cell deliverables for the program. These cells incorporate the most optimal alloy anode composition. Stanford Linear Accelerator Center (SLAC) granted beam-time for better understanding and controlling the stability of this material.

Li-ion cells incorporating 3D-CuSnFe alloy anodes have shown significant C-rate advantages while maintaining high available capacity (>90% and >70% capacity retention, respectively, at 5C for 2 and 3mAh/cm² loading). Such performance, if sustained over the target cycle life of a Li-ion battery could yield >60% charging time reduction and significantly improved power performance for EV batteries. Toward this goal, the project team has jointly identified several technical issues and areas of cell design needing further improvement. Applied Materials and project partners continue development of the alloy anode to reduce

Both anodes and cathodes without visible cracks and delamination were paired, and assembled into single layer pouch cells with the anode /cathode ratio of 1.1. Summary of formation cycles is listed in Table II- 26.

Formation cycles data exhibits the high reproducibility of these 27 pouch cells with the expected loading. Table II- 26 indicates that the averaged initial capacity loss (ICL) of SLP cells is 26.42%, which is almost the same as that observed on full coin cells. The averaged reversible capacity of SLP cells is ~3.09 mAh/cm² (2nd cycle) with the current of C/25, and it decreased slightly to ~3 mAh/cm² (5th cycle) with current density of C/10, which is exactly our targeted loading of an individual cell.

Conclusions and Future Directions

We have made progress in electro-deposition of 3DCuSnFe alloy anode, Si-Graphite composite coating and cell performance improvement. By optimizing electrolyte and binder chemistry as well as by improving pouch cell formation protocol, cycle life has been greatly increased. We have determined the optimal

irreversible capacity loss, further improve the cycling performance and to complete comparative capacity retention analysis at $C/3$ - $5C$ rate for 3D alloy electrodes with different loadings of 3D alloy material.

FY 2015 Publications/Presentations

1. “High Capacity Alloy Anodes”, ES128 Lopatin, U.S. DOE Vehicle Technologies Annual Merit Review, June 2014, Arlington, VA.

II.C.4 Innovative Manufacturing and Materials for Low Cost Lithium-ion Batteries (Optodot Corporation)

Objectives

- Demonstrate technology that reduces the cell or battery inactive component weight, volume, and/or cost by at least 20% (goal of at least 40%), while maintaining overall cell or battery performance.
- Design, develop, optimize and improve the separator, current collectors, electrolyte, termination materials, and cell casing used for manufacturing lithium-ion batteries.
- Develop a simpler and faster battery coating and assembly process.

Technical Barriers

- At least a two-fold reduction in the cost of manufacturing lithium-ion batteries is needed for widespread adoption of electric vehicles. Even though improvements in the battery anode and cathode materials will provide significant cost reduction, it is difficult to achieve this overall two-fold level of cost reduction from incremental improvements of the current generation of battery inactive components and of battery coating and assembly processes.

Barriers addressed:

- Cost: Reduce to \$125/kWh by 2022.
- Performance: Increase energy density to 250 Wh/kg and 400 Wh/l by 2022 while increasing deep discharge cycle lifetime.

Technical Targets

- Develop a high performance cell that reduces the combined cost of the battery inactive components of separator, current collectors, electrolyte, termination materials, and casing by at least 20%.
- Demonstrate a manufacturing process based on new inactive components that provides high performance cells while reducing the coating and assembly cost by at least 20%.

Accomplishments

- Demonstrated slot die coating of the ceramic separator layer on re-usable release film on a 72" wide production coater at line speeds up to 35 m/min and projected as able to run at line speeds of at least 60 m/min.
- A proprietary re-usable release film was developed to eliminate any coating defects from premature release of the ceramic separator layer when it is overcoated with the electrode layer and to provide subsequent easy delamination of the electrode coated separator stack.
- Using the Argonne National Lab (ANL) battery cost model, cost savings from the 8 micron ceramic separator component including the reduced usage of electrolyte were estimated to be greater than 20% cost savings for the inactive components of the cell. This estimated saving meets the cost reduction objectives of this project from the thinner ceramic separator alone. Other benefits of a thinner ceramic separator layer include a 5% smaller battery volume and greater safety and longer cycle life and high temperature and high voltage operation of ceramic separator with very high dimensional stability at 220°C.

Project Details

John Tabacchi (NETL Program Manager)
DE-EE0005433 Recipient: Optodot Corporation

Steven A. Carlson (Optodot Corp – PD/PI)
100 TradeCenter, Suite G-700
Woburn, MA 01801
Phone: 781-569-5059; Fax: 781-569-5201
Email: scarlson@optodot.com

Subcontractors:

Madico, Inc., Woburn, MA
XALT Energy, Lee's Summit, MO
University of Rhode Island, Kingston, RI
Ashland Inc., Wilmington, DE

Start Date: October 2011

End Date: September 2015

- Built 2 Ah cells using anode separator coated stacks laminated on the anode side to both sides of a copper foil, along with a conventional two-side-coated cathode. A thin conductive adhesive coating was developed to provide excellent anode-to-copper foil adhesion. This laminated electrode stack process was expanded into a first full cell manufacturing process for use with the ANL cost model.
- The excellent dimensional stability of the ceramic separator layer with less than 1% shrinkage at 220°C was found to enable vacuum drying of the electrode separator stacks at 130°C. This high temperature vacuum drying of the dry cells before electrolyte filling resulted in increased cycle lifetimes. Under the ANL cost model, this has the potential to eliminate cell assembly operations in the dry room by about 50% for capital and operational savings.
- The very high temperature stability of the ceramic separator layer was shown to withstand the very high heats of the manufacturing option of high intensity photon (xenon flash) sintering to produce copper metal layers on the anode separator coated stack. A second full cell manufacturing process was developed for this option of a sintered copper metal layer pattern on the anode separator followed by a second anode lane coating.
- For both cell manufacturing processes, high pressure calendaring of the electrode separator stacks is needed. It was found that the ceramic separator had no degradation in cell performance and less than 10% compression when calendared.

Introduction

Optodot has proposed to develop a new set of battery inactive components and a new battery coating and assembly process. These innovative materials and manufacturing process are based on the use of a thinner, safer, and lower cost ceramic separator. The proposed work comprises development of advanced ceramic separator, current collector, and electrolyte materials and of advanced battery stack coating and current collection methods. A new system of edge connection and termination will be developed for use with these coated anode and cathode stacks. The boehmite all-ceramic separator layer enhances the cycle and storage life and high voltage and temperature stability of the cells. This enables the continued use of standard LiPF₆ electrolytes. Wider, two side simultaneous coating and higher speed industrial coaters will be utilized to make the coated battery electrode stacks to obtain the cost benefits of at least a five-fold increase in separator coating output. The new battery manufacturing process eliminates expensive conventional assembly equipment to precisely interleave the electrodes with free standing separators.

Approach

Optodot will characterize the performance and cost of the inactive components and assembly process of current baseline cells. Starting with a thinner ceramic separator layer for this project, Optodot and its subcontractors will overcoat this separator with conventional anode and cathode layers. In a first cell manufacturing approach, Optodot will laminate a copper foil on both sides to the anode side of the anode separator coated stacks. A thin conductive adhesive coating will be used to provide excellent adhesion of the laminated anode stack. A conventional cathode will be used in the cell builds. A conventional tabbing and termination process is suitable for this approach. In a second cell manufacturing approach, Optodot will design and develop thinner and lower cost current collector layers for the anode and cathode electrodes before coating a second anode or cathode layer. Optodot is also developing a cell termination and tabbing system for use in this second approach of making and demonstrating high performance 2 Ah cells of both energy and power types. With its subcontractors, Optodot is investigating the mechanism of the improved cycle life with boehmite ceramic separator layers and ways to optimize this property with the much thinner ceramic separator and coated battery stacks of this project. Optodot and its subcontractors will demonstrate and document the acceptable performance and overall cost reduction of these improved inactive components for lithium-ion batteries and of the simpler and faster coating and assembly processes. A cost analysis report will document the cell cost reduction achieved compared to the cost of current baseline cells.

Results

We have achieved the following progress:

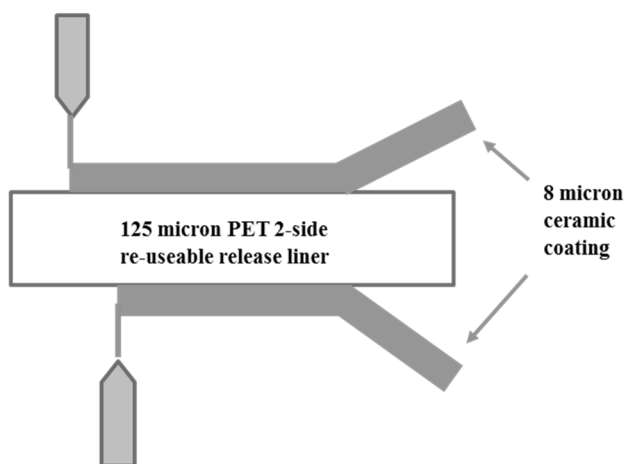


Figure II- 166: Dual side simultaneous separator slot die coating

The slot die coating of the 8 micron thick nanoporous ceramic separator on re-usable release film on a 72” wide production coater was demonstrated multiple times during FY2015. Production line speeds up to 35m/min were achieved with a projected line speed of at least 60 m/min on that coater. The estimated line speed on a new production coater using the latest advances in oven drying efficiency for battery electrodes and other similar coatings is at least 125 m/min. For providing an even lower cost for the thin separator, the feasibility of doing the slot die coating simultaneously on both sides of the re-usable release film with a single pass

through a flotation type of drying oven was demonstrated. This approach is similar to the dual side coating used to make some battery electrodes. As illustrated in Figure II- 166, this dual side simultaneous coating of the ceramic layer effectively doubles the product throughput compared to single side coating.

Assuming a 1.5 meter wide production coater with dual side slot die coating of the separator layer at a line speed of 125 m/min and considering that the separator is manufactured as a master roll that goes directly to overcoating with lanes of an electrode coating and subsequent calendaring, delamination, and slitting before cell assembly, the cost of the 8 micron boehmite ceramic separator, with profit included, is estimated at \$0.39/m².

The use of an 8 micron nanoporous ceramic separator as the layer on which the electrodes are coated to form anode and cathode coated stacks provides significant cell cost savings of at least 20% of the cost of inactive components of the cell, using the Argonne battery cost model, even without factoring in any cost savings from a simpler cell assembly process and from the multiple cell performance benefits of a nanoporous boehmite ceramic separator. The materials cost savings are derived from the use of the much thinner separator, a reduction in the usage of the electrolyte due to the thinner separator, and cell cost reduction in \$/kWh from the much thinner separator that allows about 5% by volume of additional active material to be used in the cell. This materials cost savings is independent of whether the approach of a laminated anode stack or of a coated anode stack and/or coated cathode stack is used to manufacture the cells.

In FY 2015, it was found that the release film being used was not providing a satisfactory ease of delamination of the electrode separator stacks from the release film after the stacks went through the electrode drying and calendaring steps. Thus, a new proprietary release film was developed which had a balanced release force for no premature delamination with coating defects when the electrodes were overcoated onto the all-nanoporous separator layer but provided an easy and efficient release of the coated and calendared electrode separator stacks from the re-usable release film. Figure II- 167 shows the experimental matrix of release forces evaluated to select the necessary balanced release force, which was a lower release force than used previously.

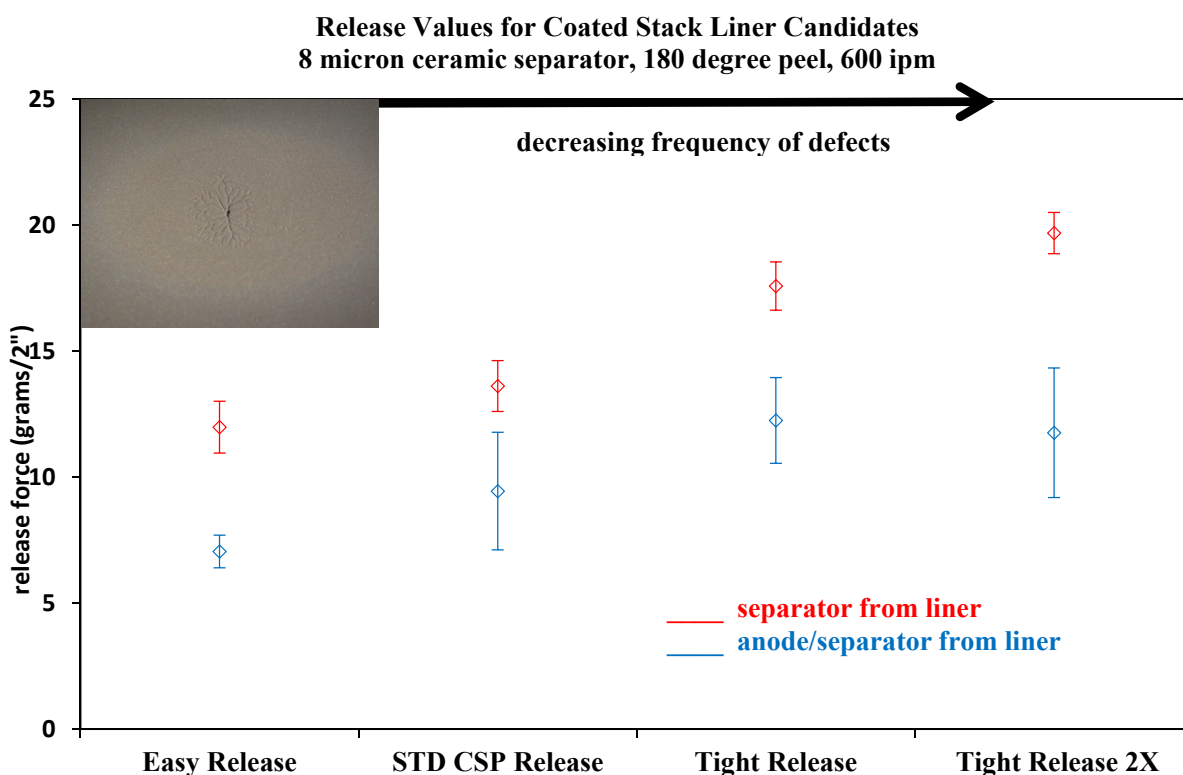


Figure II- 167: Experimental matrix for selection of the appropriate release liner

Besides the advantage of a proprietary release film that can be manufactured in-house for lower cost reasons and more quality control than with commercial release films, one major advantage of the new proprietary release film is that it was found to be more durable than commercial release films so the number of possible reuses for casting the ceramic coating and delaminating it, increased from about 5 to about 15, which provides large cost savings. The eventual degradation of the quality of the release film can be seen in the increase in the release force to above the acceptable range as indicated in the above figure. The second advantage of having a proprietary in-house release coating is that this provides a cost effective approach to “refreshing” the release film by coating a fresh new release coating over the old release coating.

The heat stable boehmite ceramic separator layers with only nanopores and with very high compression strength and the release films of this project have excellent stability to the heat and stress of the electrode coating process, as demonstrated during the machine-coating of the electrodes and the subsequent calendaring of the electrode/separator stacks. Safety and cell performance related features of the ceramic separator layer include dimensional stability of less than 0.5% shrinkage at 220°C, much greater compression strength than plastic separators, excellent thermal conductivity and heat dissipation, excellent cycling rate capability from the much thinner ceramic separator, high voltage and cycle life stability from the boehmite ceramic pigments, and non-flammability.

2 Ah pouch cells were built using anode separator coated stacks laminated on the anode side to both sides of a copper foil, along with a conventional two side-coated cathode. A thin conductive carbon adhesive coating was developed to provide excellent anode-to-copper foil adhesion. Figure II- 168 shows how this lamination would be done to make the anode laminated stacks.

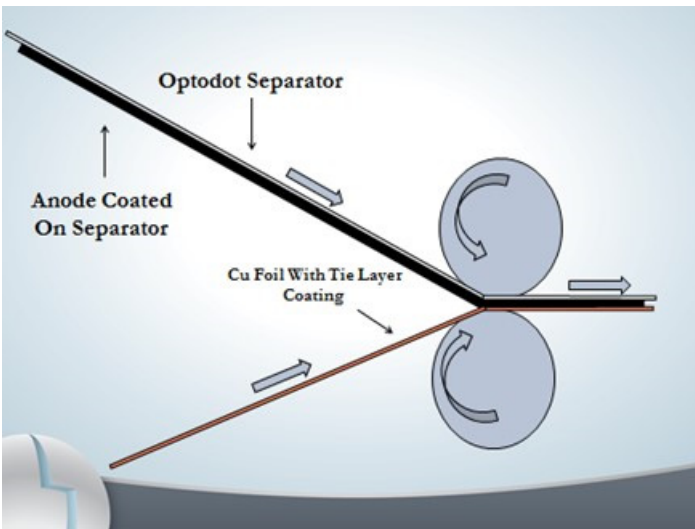


Figure II- 168: Schematic of lamination process for making the anode laminated stacks

A conductive coating on the copper foil for the anode is a recent industry trend with some major lithium-ion battery manufacturers.

The anode separator laminated stacks on the copper foil were punched after the lamination to provide an electrode-free copper foil tab for further conventional tabbing and termination. Figure II- 169 shows the formation cycling of one of these cells.

This laminated anode stack process was expanded into a first full cell manufacturing process for use with the ANL cost model. For estimating the cost, the cost of the coated copper foil is estimated to be about 20% above that of uncoated copper foil. Even with this higher

cost of the coated copper foil for the laminated anode stack approach, the cost benefits of the thin ceramic separator still represent at least a 20% cost savings in the overall cost of the inactive components of the cell. A possible lower cost alternative to the conductive coated copper foil is a conductive coated copper deposited layer on two sides of a thin plastic film substrate, such as PET and PEN film. It is known that these types of conductive films on plastic can be ultrasonically welded to each other to provide an excellent tab area for terminating the cell. Besides lower cost and perhaps being less thick, this alternative would weigh significantly less than the copper foil.

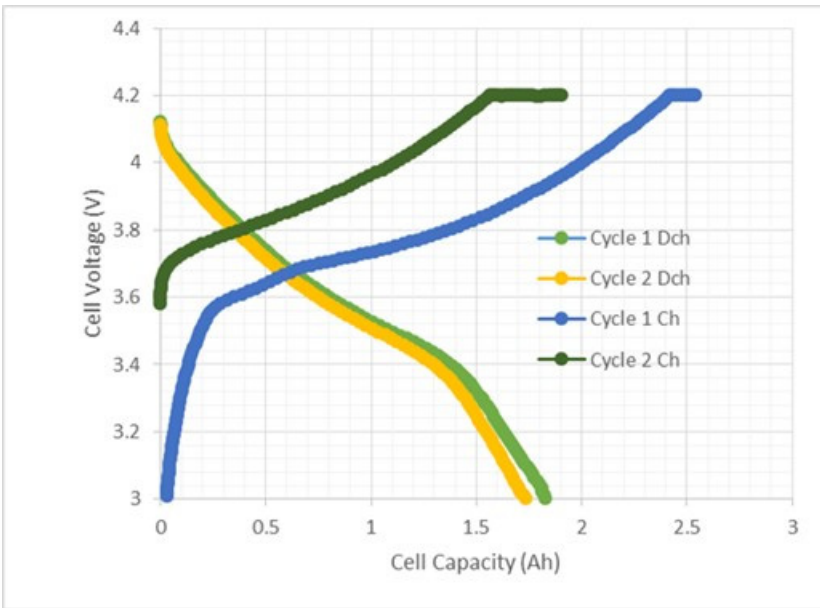


Figure II- 169: Formation cycling for 2 Ah cell with the anode laminated stack

In connection with this anode laminated stack process, the unique and excellent dimensional stability of the ceramic separator layer at 220°C was found to enable the vacuum drying of the electrode separator stacks at 130°C. This high temperature vacuum drying of the dry cells just before electrolyte filling resulted in increased cycle lifetimes. Under the ANL cost model, this offers the potential to eliminate cell assembly operations in the dry room by about 50% for capital and operational savings. The reduced dry room expenses are being quantified under the ANL

cost model to determine the cell assembly process and operational cost savings. Although this laminated anode stack process adds a delaminating and a laminating step along with a different arrangement for slitting, it appears that there should be additional process cost savings over the reduced inactive materials savings. This analysis will be detailed in the final report for this project.

A second approach to manufacture the electrode separator coated stacks of this project is to coat a conductive metal layer on the electrode coated in lanes onto the separator and then coat a second electrode layer in lanes onto the metal current collector layer. Further progress was made in FY2015 in developing a low cost proprietary process involving a pigmented copper or copper oxide nanoparticle ink for coating and then using

xenon flash lamp sintering to form about 3 micron copper metal layers as the anode current collector layer with an electrical conductivity of about 0.5 ohms/square. The estimated cost savings for this sintered copper current collector layer is about 40% with a large weight and volume reduction compared to the existing copper foils used as the substrate for coating the anodes. This full coated electrode stack approach cannot use conventional tabbing for edge connection and termination so a custom process was developed to do the tabbing. This includes coating the metal precursor ink before xenon flash lamp sintering in a pattern that includes some coating onto an electrode-free ceramic separator layer adjacent to the coated lanes of electrode and then adhering an intermediate short metal tab to this coated area, after sintering, for subsequent welding in a conventional tabbing and termination process. The adhesion of the intermediate short metal tab to the anode separator coated stack is greatly facilitated by the ability to adhere the ceramic separator layer to a metal surface with the assistance of some solvent and heat. The very high heat stability of the ceramic separator layer was shown to withstand the very high heats of this manufacturing option of using high intensity photon (xenon flash lamp) sintering to produce copper current collector metal layers on the anode separator coated stack.

A second full cell manufacturing process was developed for this option of a sintered copper metal layer pattern on the anode separator followed by a second anode lane coating and the custom tabbing and termination process described above. Although this second manufacturing option was not selected for the cell build deliverables of this project, a cost reduction analysis of this second option will be included in the final report on this project.

For both of these cell manufacturing processes, high pressure calendering of the electrode separator stacks is needed. Further work in FY 2015 showed that the ceramic separator suffered no degradation in cell performance and less than 10%, typically only about 5%, compression when calendered.

The new thin boehmite ceramic separator and electrode overcoating on the separator layer and cell manufacturing processes of this project are generic and compatible for use with various anode, cathode, and electrolyte materials as improved cell materials become available.

Conclusions and Future Directions

- Meeting the >20% improved cost, as well as the performance requirements, for the key inactive components of Li-ion cells and developing a low cost next generation manufacturing process will help meet the DOE goal of cost reduction to \$125/kWh by 2022 for EVs.
- Use of the 8 micron thick ceramic separator alone meets the project's >20% cost improvement objective for the inactive components, while providing the safety, cycle lifetime, and high voltage stability benefits of a boehmite ceramic separator with very high dimensional stability at 220°C with its ability to enable high temperature vacuum drying just prior to electrolyte filling. The unique cell manufacturing process options available by coating the electrodes onto the ceramic separator, rather than on a metal current collector foil, provide additional cost savings.

FY 2015 Publications/Presentations

1. "Ceramic Separators for Lower Cost, Safer, and Lighter Lithium Ion Batteries," Steven A. Carlson, 2014 Lithium Battery Power, November 11, 2014, Capital Hilton, Washington, DC.
2. "Innovative Manufacturing and Materials for Low Cost Lithium Ion Batteries", ES136_Carlson_2015_p, US DOE Vehicle Technologies AMR, June 2015.
3. U.S. Patent No. 8,962,182, "Batteries Utilizing Anode Coatings Directly on Nanoporous Separators," Steven A. Carlson. (Assigned to Optodot Corporation), February 24, 2015.

II.C.5 Dry Process Electrode Fabrication (Navitas Advanced Solutions Group, LLC)

Objectives

The goal of this program is to develop and demonstrate a solvent-free electrode fabrication process capability that will significantly reduce the cost of lithium-ion batteries. This should enable the cell manufacturers to reduce the cost of large format lithium-ion batteries. Navitas Systems has adapted a dry electrode process used in high volume production of ultracapacitor electrodes for use with lithium-ion battery electrodes.

Technical Barriers

Conventional lithium-ion battery electrodes are fabricated by casting slurries composed of active electrode powders with polymer binders and electronic conductivity additives. This approach imposes several fundamental limitations on cost and performance.

Manufacturing throughput and electrode thickness are limited by the slurry drying process. Solvent removal must be precisely controlled to attain highly uniform thickness and porosity of the coated electrode, free of any blistering, delamination, skin formation or particle segregation. The slurry casting and subsequent calendaring (compression) steps result in a highly tortuous pore structure that limits ion transport, and hence the rate (power) and thickness of the electrode. These barriers to increasing coating thickness ultimately limit the active material content in the cell.

Technical Targets

- Produce a dry-process cathode that can meet EV rate and cycle life criteria.
- Produce a low-cost anode that matches the cathode.
- Validate cost model by running pilot coating line at intended production speed.
- Demonstrate a prototype cell performance with the cathode and anode that meets EV rate and cycle life criteria.
- Deliver 24 cells in EV cell format.

Accomplishments

- Intensified cathode powder blending by 77% higher throughput.
- Reduced roll milled cathode thickness to meet EV electrode loading and porosity target.
- Eliminated key defect and improved electrode yield from <50% to >90% at EV cell dimension.
- Demonstrated high solid loading natural graphite anode process that meets cost reduction target.
- Down-selected anode formulation for EV cell final deliverable, matching capacity and rate of dry process cathode.

Project Details

John Tabacchi (NETL Program Manager)

DE-EE0005835 Recipient: Navitas Advanced Solutions Group, LLC

Mike Wixom (Navitas Advanced Solutions Group, LLC – PI)

4880 Venture Drive
Ann Arbor, MI 48108
Phone: (734) 205-1432
E-mail: mwixom@navitassys.com

Start Date: 10/01/2011

Projected End Date: 03/31/2016

Introduction

Conventional lithium-ion battery electrodes are fabricated by casting slurries composed electrode active materials, conductive additives, and polymer binders. This coating process is limiting the electrode manufacturing cost and the performance.

Manufacturing throughput and electrode thickness are limited by the slurry drying process. Solvent removal must be precisely controlled to attain uniformity of the coated electrode, free of any blistering, delamination, skin formation or particle segregation. The slurry casting and subsequent calendaring steps result in a highly

tortuous pore structure that limits ion transport, and hence the rate (power) and thickness of the electrode. These barriers to increasing coating thickness ultimately limit the active material content in the cell.

The slurry casting process thus drives higher battery cost through at least three mechanisms:

- Solvent drying and solvent recovery steps require capital equipment and reduce throughput.
- Energy is consumed both to dry the electrode films and to recover the casting solvent.
- Electrode thickness limitations increase the cell-level costs of excess non-active materials such as current collector, separator and packaging.

In this program, Navitas proposes to develop and demonstrate a solvent-free electrode fabrication process capability that will significantly reduce the cost of lithium-ion batteries. Combined with the selected high energy, long life and safe electrode materials, the results of this program will enable Navitas to offer low cost, high energy, and safe EV battery.

Dry electrode processing has been commercialized for high volume manufacturing of ultracapacitors. The first goal of this program is to modify and transfer the dry process for the production of lithium battery cathodes. The baseline cathode binder is not stable at the anode. Therefore the second goal is to create a competent dry processed anode. To meet these goals, we have laid out a program that will meet the following specific objectives:

1. A 20-50% reduction in cost of materials through increasing electrode coating thickness to reduce separator and current collectors.
2. Up to 80% reduction in capital equipment cost associated with electrode coating.
3. Up to 91% in energy saving by eliminating drying and solvent recovery.
4. Nearly 100% reduction in solvent emission and electrode scrap.
5. Define a low-cost anode fabrication that is stable over 500+ cycles to full charge.
6. Demonstrate the dry process electrodes in an EV battery.

Approach

Phase I extended the dry electrode process to the high energy and safe cathode material using established PTFE binder system. The cathode development determined the thickness limit at which EV rate and cycle life criteria can be met. The phase I program also yielded an anode formulation based on high solid loading low-cost natural graphite and advanced drying process that can pair with the dry process cathode to meet cell-level cost goals.

In Phase II, the electrode processes will be optimized and scaled up. The dry process electrode production will be demonstrated and modeled to validate cost savings assumptions. The low-cost electrodes will be assembled into a large format cell for EV applications.

Results

Cathode

Navitas has developed solvent-free dry process cathode containing blended lithium metal phosphate and oxide. The active materials, process additives, and polymer binders were selected on basis of electrochemical performance and process robustness. A cathode sheet can be prepared by being calendered to the desired thickness and porosity for EV battery. The free standing films are pressed and laminated onto an aluminum current collector. Over the past year, the cathode fabrication process has been scaled up to EV cell electrode footprint.

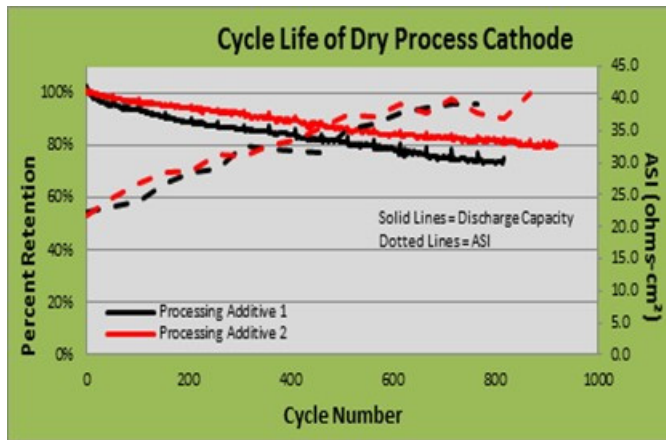


Figure II- 170: Cycle life study of dry process cathodes in full DLP cells; loading of 3.3mAh/cm²; cut off voltage 4.2-2.7V; charged and discharged at 0.5C

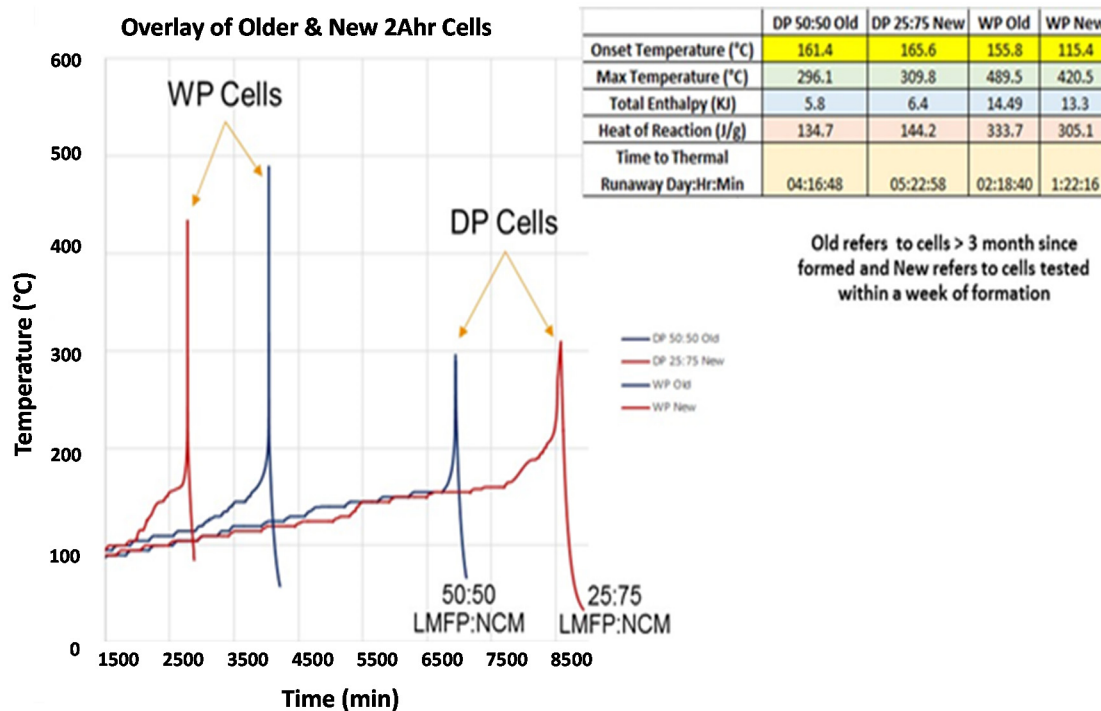


Figure II- 171: ARC data overlay of heat-wait-seek tests of pure NCM wet processed 2Ahr cells with that of dry processed 50:50 & 25:75 LMFP:NCM 2Ahr Cells

Navitas continued cycle life testing of double layer pouch (DLP) cells similar to the interim deliverable format which used Processing Additive 1 vs new electrode formed using Processing Additive 2. Updated results are shown below (Figure II- 170) including the change in area specific impedance (ASI). Percent retention is based on the 4th discharge. Processing Additive 1 retained at least 80% of its capacity up to cycle 572. Processing Additive 2 has retained at least 80% of its capacity up to cycle 918. Processing Additive 2 provides results in better conductivity and much lower residual moisture content.

Thermal Stability of Cathode: Accelerating Rate Calorimetry (ARC) testing of abuse tolerance was performed on dry process (DP) 2Ah cells. Prior work has shown significantly improved abuse tolerance of cells with DP cathodes compared to conventional slurry cast or ‘wet process’ (WP) cathodes at 50:50 LMFP:NMC 532 active material blends. ARC testing was then extended to higher LMC content cathodes to see if the benefit is retained in higher energy electrode formulation.

The extended test results did confirm that the abuse tolerance benefit is retained at the higher NMC content. Figure II- 171 shows that the thermal runaway event for the DP cells was delayed more than two days compared to the baseline wet-processed pure NCM 2Ah cell. The Figure shows an overlay of the original ARC test with 50:50 LMFP:NCM and pure NCM 2Ah cells that aged > three months with that of newer cells of wet processed pure NCM and DP 25:75 LMFP:NCM.

Even with large variations typically observed in pouch cell construction (reported by ARC Manufacturer), the ARC data clearly show that the DP cells are more thermally stable than the pure NCM wet process cells even at lower (25%) LMFP concentrations.

Anode

Over the past year Navitas struggled with scaling up the dry process anode to EV cell dimensions. Ultimately the mechanical properties of the DP anode presented in the FY 2014 Annual report resulted in an insurmountable scrap rate with scale-up. Navitas thus turned focus to a high-loading engineered pore (EP) anode, which is produced with an aqueous process and low water content. Interest in the EP anode was sparked by the benefits of a proprietary advanced drying process being developed in a complementary program, with the engineered pore structure facilitating mass transport of water from the electrode during the drying operation.

This hypothesis was confirmed by high rate bench scale batch drying of EP anode vs conventional cast electrodes. A further benefit of the EP anode design is to enable higher electrode loading for both the anode and cathode.

In addition to improving EV cell energy density, higher loading would enhance the mechanical properties of a capacity-matched free-standing DP cathode.

Lab-scale EP anode was produced and evaluated for concept demonstration. Single-layer-pouch (SLP) Li ion cells were assembled and tested for cycle life. The cells also contain the dry-processed cathode. A cycle life of 325 at 86% capacity retention is demonstrated in Figure II- 172. This is comparable to a baseline cell and projects to have a cycle life of >500 at 80% capacity retention.

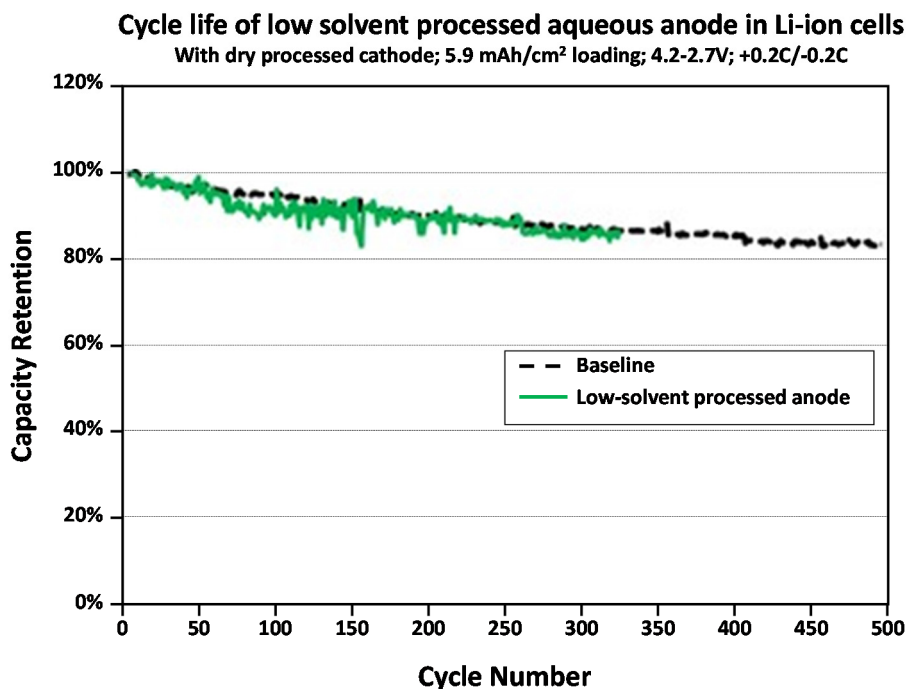


Figure II- 172: Cycle life of low-solvent processed anode in full Li ion cells with dry-processed cathode



Figure II- 173: Slot-die coated low solvent anode with loading of 4 mAh/cm²

The EP anode fabrication process was scaled up and demonstrated on a pilot scale slot-die coater. A double-sided EP graphite anode with a loading of 4 mAh/cm² was successfully coated (Figure II- 173). The electrode is being evaluated towards EV battery relevant performance.

Cell Prototype Assembly and Validation

Fourteen (14) 4 Ah prismatic cells containing dry process cathodes and slurry-cast anodes have been delivered to DOE as interim deliverables. A series of tests such as peak powder, 48 hr stand, and Dynamic Stress Test (DST) have been performed towards EV battery validation. DST data is presented in Figure II- 174.

4 Ah Cell Periodic Testing

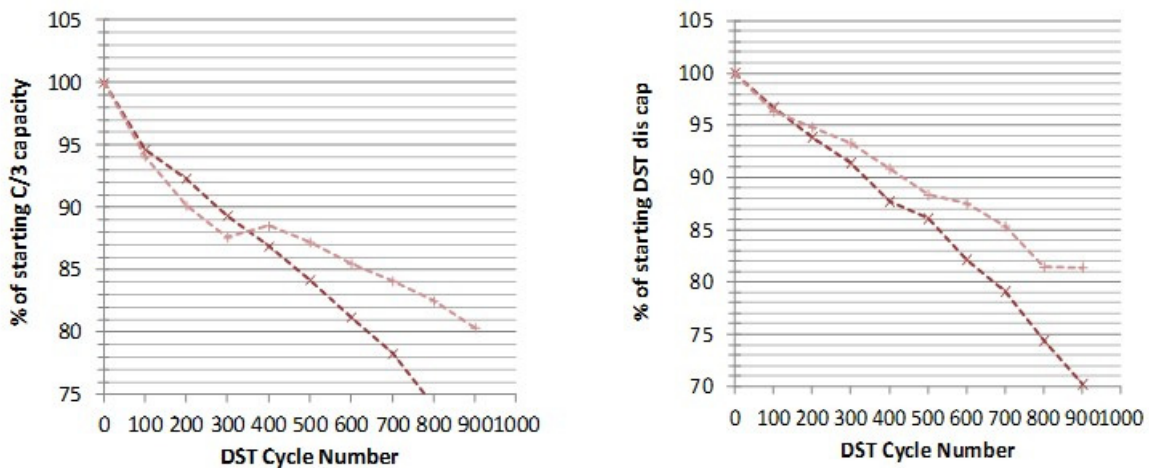


Figure II- 174: 4Ah cells are DST cycled 100 times to 80% DoD. Each 100 cycles, they are checked for C/3 discharge capacity to 100% DoD and DST discharge capacity to 100% DoD. They are also tested for peak power capability, and then they begin another 100 DST cycles to 80% DoD.

Conclusions and Future Directions

The dry process electrodes have been validated in a Li ion cell that meets EV battery footprint, rate and cycle life criteria. Potential abuse tolerance advantages of the dry process cathode formulation have been demonstrated. Several low-cost anode options have been evaluated. Future work will address process intensification, roll-to-roll fabrication, and assembly of 24 14Ah EV prototype cells.

FY 2015 Publications/Presentations

1. 2015 DOE Annual Merit Review Meeting Presentation

II.D Small Business Innovative Research (SBIR) Projects

Objectives

- Use the resources available through the Small Business Innovation Research (SBIR) and Small Business Technology Transfer (STTR) programs to conduct research and development of benefit to the Energy Storage effort within the Vehicle Technologies Program Office.

Project Details

Brian Cunningham (SBIR Projects Manager)

U.S. Department of Energy
1000 Independence Avenue, SW
Washington, DC 20585
Phone: 202-287-5686

E-mail: Brian.Cunningham@ee.doe.gov

Introduction/Approach

The Energy Storage effort of the Vehicle Technologies Office supports small businesses through two focused programs: Small Business Innovation Research (SBIR) and Small Business Technology Transfer (STTR). Both of these programs are established by law and administered by the Small Business Administration. Grants under these programs are funded by set aside resources from all Extramural R&D budgets; 2.9% of these budgets are allocated for SBIR programs while 0.4% for STTR grants. These programs are administered for all of DOE by the SBIR Office within the Office of Science. Grants under these programs are awarded in two phases: a 6-9 month Phase I with a maximum award of \$150K and a 2 year Phase II with a maximum award of \$1M. Both Phase I and Phase II awards are made through a competitive solicitation and review process.

The Energy Storage team participates in this process by writing a topic which is released as part of the general DOE solicitation. In FY12, the Energy Storage team decided to broaden its applicant pool by removing specific subtopics and allowing businesses to apply if their technology could help advance the state of the art by improving specific electric drive vehicle platform goals developed by the DOE with close collaboration with the United States Advanced Battery Consortium.

Phase II Awards Made in FY 2015

Under the SBIR/STTR process, companies with Phase I awards that were made in FY 2014 are eligible to apply for a Phase II award in FY 2015.

One Phase II grant was awarded in FY 2015 from four Phase I grants that were conducted in FY 2014.

Physical Sciences Inc. (Andover, MA 01810-1077). Higher energy density batteries are required in order to increase vehicle range and lower cost batteries are needed to make the technology affordable. This project will develop a new cell construction technique that will be demonstrated to enable the construction of cells with ~30% increase in energy density over the state of the art.

Phase I Awards Made in FY 2015

Eight Phase I grants were awarded in the Summer of FY 2015.

American Lithium Energy Corporation (Vista, CA, 92081). A next generation of a low cost and high energy density advanced solid state rechargeable lithium battery will be developed through the proposed project for use in the next generation of PHEV and EV rechargeable batteries.

Ballast Energy, Inc. (Berkeley, CA, 94710-2227). Developing the next generation of lithium-ion batteries for electric vehicles with a unique cost cutting innovation. Successful commercialization of its technology will contribute to more affordable electric vehicles.

Bettergy Corp. (Peekskill, NY, 10566-5330). Successful completion of the current program will make significant contribution toward development of the key energy storage system that can be used in the long range EVs to improve the vehicles energy efficiency and running range, reducing our reliance on foreign imported petroleum.

HICO Tech (State College, PA, 16801-2460). Supercapacitors and lithium-ion batteries are two major energy storage systems in the market. However, a performance gap exists between them. Novel lithium-ion hybrid

batteries based on Si-C composites anodes and porous carbon cathodes will be developed to bridge the gap with both high energy and power densities for hybrid vehicles.

Novarials Corporation (Nashua, NH, 03062-1441). The proposed ultrahigh safety battery separator technology is a critical technology for manufacturing high safety and long term stability lithium-ion batteries desired by electric vehicles, hybrid electric vehicles, and plug-in hybrid electric vehicles.

PH Matter, LLC (Columbus, OH, 43212-1155). In this project, pH Matter, LLC and the University of Akron will develop low-cost components to improve the energy capacity and durability of lithium-ion batteries. The technology will be used for automotive energy storage applications, such as electric vehicles.

SiLion, LLC (Boulder, CO, 80301-5465). Despite the slow rate of improvement in Li-ion technology, demand for a battery double the specific energy of current state-of-the-art (400 Wh/kg) is growing. To address this issue, this venture proposes to enable a safe, ~400 Wh/kg Si/Li-Mn-rich full-cell, compatible with the existing battery-manufacturing infrastructure, by utilizing a room temperature ionic liquid electrolyte.

Tiax, LLC (Lexington, MA, 02421-3102). Vehicles equipped with start-stop technology can enable significant improvements in fuel economy of vehicles. TIAX's novel battery technology can enable the widespread deployment of start-stop technology by enabling small, lightweight, and inexpensive start-stop systems for vehicle integration.

III. Battery Testing, Analysis, and Design

The Battery Testing, Analysis, and Design activity supports several complementary but crucial aspects of the battery development program. The activity's goal is to support the development of a U.S. domestic advanced battery industry whose products can meet electric drive vehicle performance targets. Within this activity, battery technologies are also evaluated according to USABC Battery Test Procedures. The manuals for the relevant PEV and HEV applications are available online. A benchmark testing of an emerging technology can be performed to remain abreast of the latest industry developments. High-level projects pursued in this area include the following topics:

- Cost Assessments and Requirements Analysis.
 - Cost modeling.
 - Secondary and other energy storage use and life studies.
 - Analysis of the recycling of core materials.
 - Requirements analysis for PEVs and HEVs.
- Battery Testing Activities.
 - Performance, life and abuse testing of contract deliverables.
 - Performance, life and abuse testing of laboratory and university developed cells.
 - Performance, life and abuse testing of benchmark systems from industry.
 - Thermal analysis, thermal testing and modeling.
 - Development of new test procedures.
 - Maintenance of current test procedures.
- Computer Aided Engineering of Batteries.
 - Development of tools for computer aided engineering of batteries.

The rest of this section lists the projects which were active for the above three key areas during FY 2015.

III.A Cost Assessments and Requirements Analysis

III.A.1 BatPaC Model Development (ANL)

Objectives

- To develop and utilize efficient simulation and design tools for lithium-ion batteries to enable the prediction of
 - Overall and component mass and dimensions
 - Cost and performance characteristics
 - Project the cost of battery pack values from bench-scale data

Project Details

Shabbir Ahmed, Kevin G. Gallagher, Paul A. Nelson, Dennis W. Dees (Argonne National Laboratory)
97000 Cass Avenue
Argonne IL 60439
Phone: 630-252-4553; Fax: 630-972-4553
Email: ahmeds@anl.gov

Start Date: October 2012

Projected End Date: September 2016

Technical Barriers

- Development of PHEV and EV batteries that meet or exceed DOE/USABC goals for
 - Cost
 - Performance

Technical Targets

- EV System Level (2020 Commercialization)
- Useable Energy Density @ C/3 Discharge Rate 500 Wh/L
- Useable Specific Energy @ C/3 Discharge Rate 235 Wh/kg
- Useable Energy @ C/3 Discharge Rate 45 kWh
- PHEV-40 mile (2018-2020 Commercialization)
- Peak Pulse Discharge Power for 10 sec and 2 sec: 38 and 46 kW
- Available Energy for Charge Depleting Mode and Charge Sustaining Mode: 11.6, 0.3 kWh

Accomplishments

- A new version of BatPaC has been released. It includes
 - A table of results that correspond to USABC suggested format with breakdown of mass, volume, and cost at the cell level.
 - Updated costs of lithium iron phosphate (LFP) cathode, current collectors, separator, and electrolyte
 - Updated thermal management calculations.
- A study of a flex plant, where different types of automotive batteries are manufactured, has been conducted and published. The results show significant cost reductions are possible because of economies of scale.
- A process model of a dry room has been set up to estimate the energy demand and costs of a dry room.
- A process model has been set up for the recovery of the cathode solvent n-methyl pyrrolidone (NMP) to estimate the energy demand and cost of the process.
- The production process for cathode materials such as NMC (Li_xNi_aMn_bCo_cO_y) has been modeled to estimate the energy demand and cost of production.
- The limitations of high areal capacity electrodes have been determined and implemented in a physics-based fashion in BatPaC.

Introduction

The penetration of lithium-ion (Li-ion) batteries into the vehicle market has prompted interest in projecting and understanding the costs of this family of chemistries being used to electrify the automotive powertrain. Additionally, research laboratories throughout the DOE complex and various academic institutions are developing new materials for Li-ion batteries every day. The performance of the materials within the battery directly affects the energy density and cost of the integrated battery pack. To estimate the manufacturing cost of Li-ion batteries, Argonne developed a performance and cost (BatPaC) model which was peer reviewed and is available on the web. It captures the interplay between design and cost of Li-ion batteries for transportation applications. Moreover, BatPaC is the basis for the quantification of battery costs in U.S. EPA and NHTSA 2017-2025 Light-Duty Vehicle Technical Assessment. This assessment is then used to determine what mileage (i.e. CAFE) and CO₂ emission standards are optimal from a cost-benefit analysis.

Approach

BatPaC is the product of long-term research and development at Argonne through sponsorship by the U.S. Department of Energy. Over a decade, Argonne has developed methods to design Li-ion batteries for electric-drive vehicles based on modeling with Microsoft® Office Excel spreadsheets. These design models provided all the data needed to estimate the annual materials requirements for manufacturing the batteries being designed. This facilitated the next step, which was to extend the effort to include modeling of the manufacturing costs of the batteries. The battery pack design and cost calculated in BatPaC represent projections of a 2020 production year and a specified level of annual battery production, 10,000-500,000. As the goal is to predict the future cost of manufacturing batteries, a mature manufacturing process is assumed. The model designs a manufacturing plant with the sole purpose of producing the battery being modeled. The assumed battery design and manufacturing facility are based on common practice today but also assume some problems have been solved to result in a more efficient production process and a more energy dense battery. Our proposed solutions do not have to be the same methods used in the future by industry. We assume the leading battery manufacturers, those having successful operations in the year 2020, will reach these ends by some means.

BatPaC solves the governing equations to determine the size of each layer, cell, and modules that make up the battery pack that can meet the desired requirements for power and energy. This allows the calculation of the mass of each material, the volume of the components, and the heat removal needed during discharge. The cost of the pack is then estimated based on a predefined manufacturing process. Current effort is directed at:

- improving the design capability by considering additional relevant design constraints, e.g., coating thicknesses to reflect charge/discharge rates, etc.,
- reducing the uncertainty of model predictions by setting up independent models of the manufacturing process that include energy and cost breakdowns,
- updating the cost of the materials,
- validating results with OEMs, manufacturers, and component developers.

Table III- 1: Thermal and Electric Loads in the NMP Recovery Process (4.1M kg-NMP/year)

Parameter	Value
Heat Load in Air Heater	3,800 kW
Heat Removal Load in Condenser	3,550 kW
Heat Transfer Load in Air-to-Air Heat Exchanger	2,750 kW
Heat Load in Distillation	400 kW
Heat Load in Electrode Dryer	130 kW
Total Thermal Energy Required	4,450 kW
Electric Power Required	1,500 kW
Total Energy Demand	5,900 kW

Preliminary estimates indicate that the cost of NMP recovery is less than \$1.5 per kg of NMP recovered. The recovery and recycle process is more economical since it is cheaper than the replacement cost of over \$3 per kg and the cost of disposing of it as a waste stream. This recovery process contributes ~\$40 to the cost of each battery pack costing approximately \$3,100.

Process Model for the Dry Room

Operations: The dry room is a key part of the manufacturing process where cell assembly and electrolyte filling is carried out. The walls, floor and ceiling are designed to prevent leakage and maintain the very low humidity environment. The air quality (humidity and temperature) is maintained by flowing in an air stream that can remove the humidity and heat generated within the room or the moisture infiltration resulting from materials

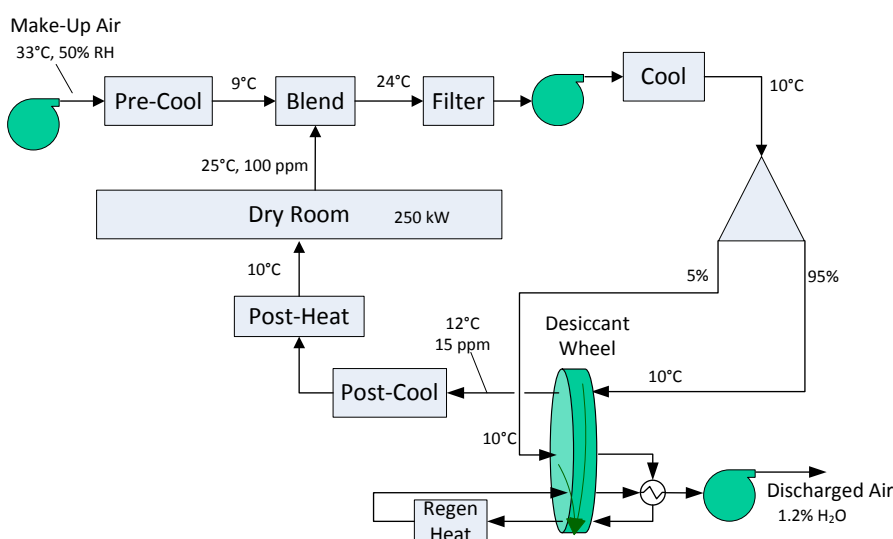


Figure III- 2: Schematic of the Air Processing for a Dry Room

Table III- 2: Air Flow and Energy Loads in the Processing of Air for a Dry Room (4000-m², 4-m tall)

Parameter	Value
Air Flow Rate through Dry Room	22 m ³ /s
Cooling Load at “Cool”	483 kW
Heating Load at “Regen	34 kW
Total Thermal Energy Required	34 kW
Electric Power Required	358 kW
Total Energy Demand	392 kW

transfer to/from the room. The air lock doors are flushed during the personnel transit through the door and are very effective.

Figure III- 2 shows a schematic of the processing of the air to and from the dry room. Make-up ambient air is cooled to ~9°C to remove the bulk of the moisture and then blended with the air exiting the dry room. The combined stream is filtered and cooled to 10°C and then split into the main stream (going to the dry room) and the purge stream. The main stream is passed through a desiccant wheel where the moisture content is reduced to ~15 ppm. The cooled gas is then fed into the dry room at a feed rate such that the exit gas is maintained at/below a

certain temperature (~25°C) and humidity (~100 ppm). For this study the feed rate into the dry room was controlled by varying the amount of make-up/purge flows, while the ratio of the main/purge flows was held constant (19). The desiccant wheel is regenerated by passing the purge stream, heated to 146°C, to remove the moisture that was trapped from the main stream. A heat exchanger is used to recover part of the energy used in the regeneration process. Table III- 2 lists some of the key results from the simulation of a dry room in a battery plant producing 100,000 packs per year of a 10 kWh PHEV batteries.

Preliminary cost estimates indicate the dry room contributes \$35 to the cost of the battery pack costing approximately \$3,100.

The process diagram and the base case scenario shown in Figure III- 2 and Table III- 2 assume that the heat exchanger in the desiccant regeneration loop is designed with an approach temperature of 20°C. The impact of this heat exchanger was studied by increasing the approach temperature to the limit where the heat exchanger is eliminated. The results are shown in Figure III- 3, which shows that with increasing approach temperature, the size (heat transfer area) of the heat exchanger drops exponentially, while the energy needed for the regeneration and therefore the total energy demand increases linearly. Based on a natural gas price of 2 cents/kWh, the figure shows that the cost of dry room operations decreases quite sharply if the approach temperature is relaxed from 20°C. These results suggest that the heat exchanger may be sized to balance the need for reduced cost versus lower energy consumption (CO₂ emissions).

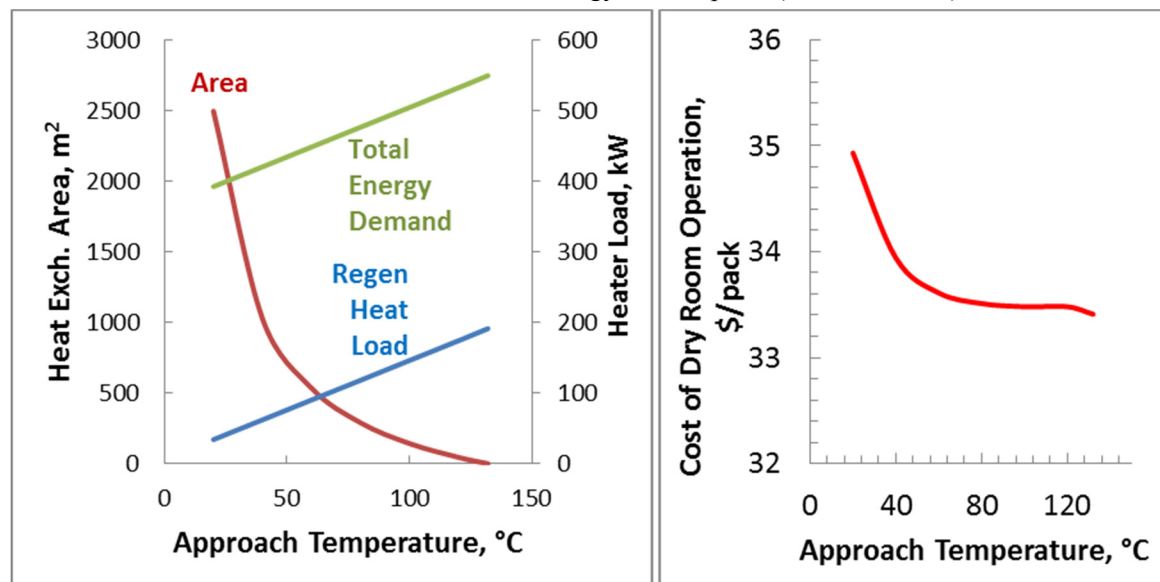


Figure III- 3: Effect of the Size of the Heat Exchanger on the Energy Demand and Cost of Dry Room Operations

Production of Cathode Materials – NMC333: The materials in a battery pack contribute over 30% of the cost and thus is an important cost driver. A study was conducted to understand the production process, particularly for the expensive cathode active materials, starting with NMC. Figure III- 4 shows a schematic of the production process where the metal sulfate is reacted with a carbonate $(\text{Ni/Mn/Co})\text{SO}_4 + \text{Na}_2\text{CO}_3 = (\text{Ni/Mn/Co})\text{CO}_3\downarrow + \text{Na}_2\text{SO}_4$ to produce the corresponding carbonate, in a continuous stirred tank reactor (CSTR). The carbonate is precipitated out and is separated from the slurry through repeated filtration and washing. The final filter cake is then dried and mixed with lithium carbonate and fired in an oven at 900°C to produce the lithiated NMC oxide ($\text{Li}_x\text{Ni}_a\text{Mn}_b\text{Co}_c\text{O}_y$). A similar process was also studied, where the sulfate material was reacted with a hydroxide to produce the corresponding hydroxide, according to the reaction: $(\text{Ni/Mn/Co})\text{SO}_4 + 2\text{NaOH} = (\text{Ni/Mn/Co})(\text{OH})_2\downarrow + \text{Na}_2\text{SO}_4$. The processes were simulated for a production capacity of 4000 kg/day of the NMC. Table III- 3 lists the energy loads of the processes. The largest heat demand is at the sintering furnace, representing nearly 50% of the total energy demand, as shown in Table III- 3. Preliminary estimates indicate that the cost of the NMC333 materials to be approximately \$20 (carbonate) and \$22 (hydroxide) per kg. The cost of the raw materials represent over 50% of the cost of production, with the price of cobalt representing the bulk of the sulfate cost.

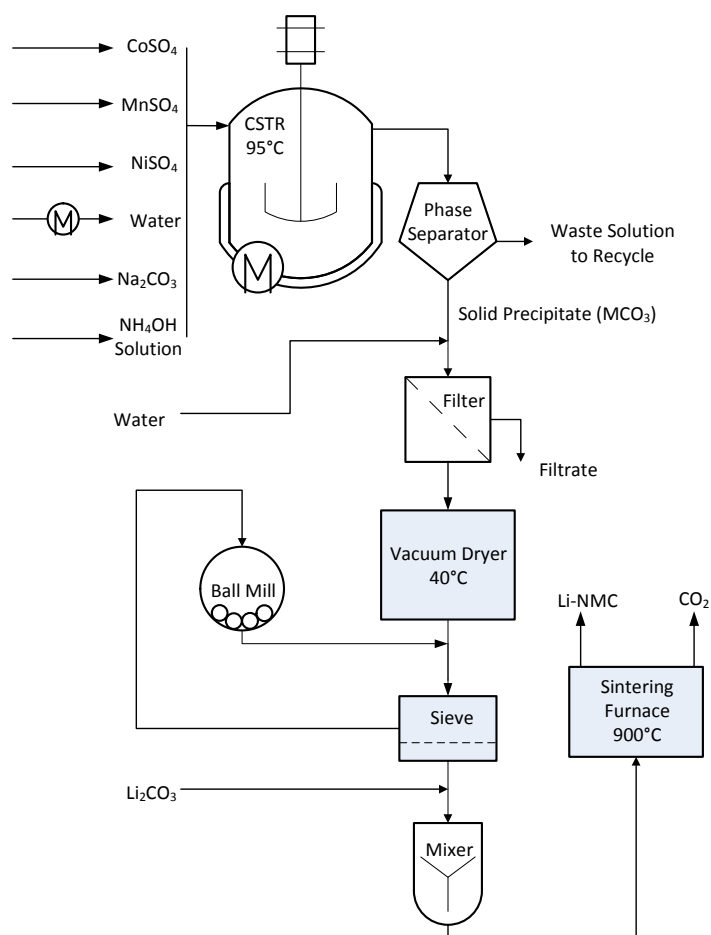


Figure III- 4: Schematic of the Production Process for NMC Cathode Material

Table III- 3: Heat Loads in the NMC Production Process (4000 kg NMC per day)

Parameter	Carbonate	Hydroxide
CSTR Temperature	90°C	60°C
Heat Load to Preheat Reactants	128 kW	52 kW
Heat Removal Required from CSTR	40 kW	89 kW
Heat Load in Dryer	55 kW	80 kW
Heat Load in Furnace	148 kW	158 kW
Total Energy Demand (Thermal and Electric)	354 kW	307 kW

cycled at increasing charge rates while maintaining a C/3 discharge rate. The drop-off in electrode capacity on increasing discharge rates are attributed to concentration gradients in the positive electrode that limit the utilization of available capacity, Figure III- 5. Higher electrode areal capacities must be operated at lower rates if the same intrinsic physical properties of electrolyte and electrode materials are maintained. This is captured by Eq. 1, which is now implemented into the BatPaC design algorithm. Here, the areal capacity is Q_A , the volumetric electrode capacity is Q_V , the time of discharge is t_d , γ is the utilization parameter and the remaining variables are properties of the electrode and electrolyte.

Electrode Thickness: BatPaC currently has a maximum 100 micron electrode thickness limitation as a design setting for all batteries. Based upon limited information this is considered a practical limit to achieve long-lived, high-performing cells. While there appears to be no universal understanding of this limitation, possible reasons include lithium plating on the graphite negative electrode, other effects from concentration gradients within the electrodes, issues with repeated volume changes during cycling, and/or manufacturing challenges. For most lithium-ion technologies, the electrode thickness limitation is reached for EV and larger PHEV battery applications where the battery power to energy ratio needed for the vehicle is lower. In these cases, increasing the electrode thickness limitation would significantly reduce battery cost. Based on the potential impact of thicker electrodes on cost, being able to accurately predict the effect of thicker electrodes on performance within the BatPaC framework is an important direction for the future.

Experiments and modeling are both required to determine the physical limitations during discharge and charge. This study is part of an integrated effort with the CAMP Facility (see section IV.B.1) to examine varying electrode thicknesses in lithium-ion battery technologies. Pouch cells 14.1 cm² in area were constructed with synthetic graphite and NMC622 of increasing areal capacity from 2.2 to 6.6 mAh/cm². The electrolyte used was 1.0 M LiPF₆ in a 3:7 by weight ethylene carbonate, ethylmethyl carbonate mixture with an additional 2 wt% vinylene carbonate (BASF). Cells of varying loading were discharged at increasing rates while maintaining a C/3 charge rate. Complementarily, the same cells were later

$$Q_A = \sqrt{\gamma Q_v t_d \frac{\varepsilon \widehat{D} \widehat{c} F}{\tau (1 - t_+^0)}} \quad (1)$$

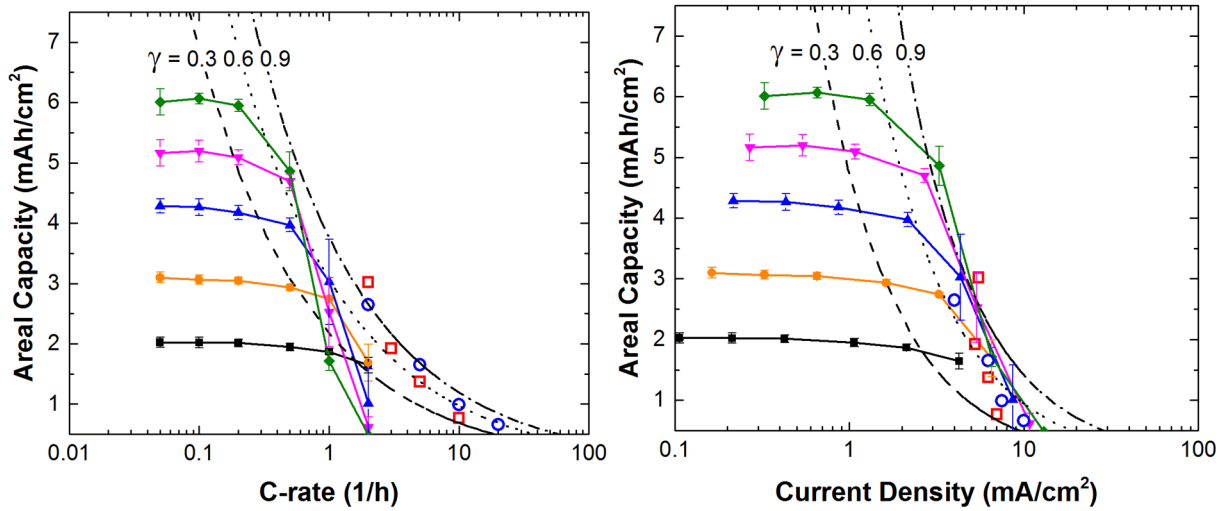


Figure III- 5: Rate capability study on NMC622/Gr pouch cells of increasing areal capacities shown as a function of C-rate (a) and current density (b). Dashed lines represent differing values of $\gamma = 0.3, 0.6,$ and 0.9 . Open symbols of blue (LFP/Gr) and red (NMC333/Gr) transformed from Zheng et al. [ENREF 9](#) *Electrochim Acta* 71 258 (2012)

For higher charging rates, both lower capacity and irreversible side reactions may occur. Our experiments suggest that graphite based cells should avoid current densities near or above 4 mA/cm^2 to prevent lithium plating and irreversible capacity loss. The onset of side reactions at this current density is a combination of concentration and interfacial polarization in the graphite electrode. The singular current density regardless of electrode areal capacity reflects a more complex interplay between mass and charge transport that results in similar electrode impedance values from 2.2 to 6.6 mAh/cm^2 . This is now implemented in the BatPaC model to calculate fast charging limitations.

Advanced Electrodes: Higher capacity electrode materials are sought to increase battery energy density while simultaneously lowering battery price. Silicon-alloy/graphite composite anodes are seen as an important step to achieving this objective. We used the BatPaC model to determine target performance and cost levels that should be achieved to meet the DOE/USABC EV Battery targets. The cathode in the simulation was a metal-oxide (e.g. NMC441) that achieves 200 mAh/g . The anode properties are varied assuming a delithiated density of 2.2 g/cm^3 . The electrode volumetric capacity is the key independent variable that decreases battery price and increases battery energy density. In Figure III- 6, we find diminishing returns for negative electrode volumetric capacities greater than 1000 mAh/cm^3 and for active material prices less than $\$25/\text{kg}$. We also find that engineering approaches to mitigate volume expansion may have a significant impact on the hoped increase in pack level energy density.

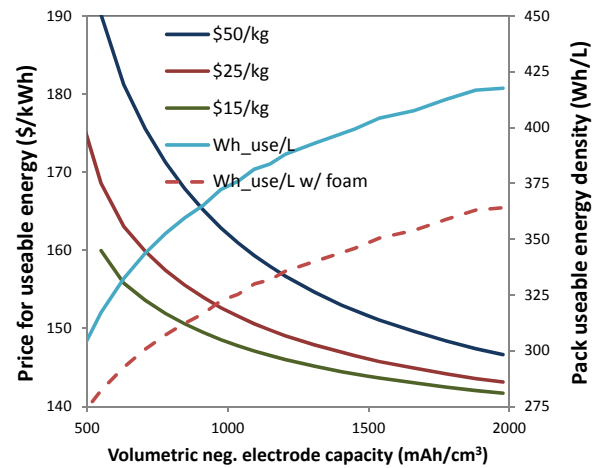


Figure III- 6: Battery price for a 45 kWh use and $90 \text{ kW}_{\text{net}}$ 360 V as a function of volumetric capacity of the advanced Li-ion negative electrode

Conclusions and Future Directions

In addition to updating BatPaC with time and technology sensitivity default data, this project has carried out several independent studies that are aimed to provide greater fidelity in BatPaC calculations and analytical insight.

- The study of the NMP recovery process has shown that the recovery and recycle of NMP is favored on both economic and environmental grounds, costing about a third of the cost of replacing the used NMP with a new purchase. The study further showed that the energy demand of the process is very high due to the constraint of maintaining a large differential between the NMP concentration in the dryer gas and the flammability limit.
- The Dry Room is an essential part of the cell assembly process in the battery plant. The cost of managing the air quality depends on the heat and humidity released in the dry room. Simulation of a base case system showed that approximately 400 kW of energy is needed and contributes more than \$34 to the cost of a PHEV battery pack.
- Modeling of the NMC cathode material production process shows that the cost of raw materials is key to determining the cost of the NMC product. For the processes studied and the set of assumptions used in the study, the cost is estimated to be between \$20-25 per kg. The energy demand of the processes are in the range of 300-400 kW for a plant producing 4000 kg of NMC per day.
- Electrolyte transport limits the utilization of the positive electrode at critical C-rates during discharge; whereas, a combination of electrolyte transport and polarization lead to lithium plating in the graphite electrode during charge. We have derived and included in BatPaC an analytical expression to provide design criteria for long lived operation based on the physical properties of the electrode and electrolyte.
- Advanced silicon-graphite anodes should target >1000 mAh/cm³ electrode volumetric capacity and less than \$25/kg purchase price to provide a path to reach DOE/USABC EV targets.

This project will incorporate the findings from these studies into the BatPaC model, while continuing to investigate the details of the other steps in the battery manufacturing process. The BatPaC model itself will be updated to reflect new developments in materials and technology, and improve the efficiency and accuracy of this design tool.

FY 2015 Publications/Presentations

1. “BatPaC Model Development,” S. Ahmed, K.G. Gallagher, P.A. Nelson, D.W. Dees, presented at the 2015 U.S. DOE Vehicle Technologies Office Annual Merit Review and Peer Evaluation Meeting, Arlington VA, June 9, 2015.
2. “PHEV and EV Battery Performance and Cost Assessment,” K.G. Gallagher, S. Ahmed, P.A. Nelson, D.W. Dees, presented at the 2015 U.S. DOE Vehicle Technologies Office Annual Merit Review and Peer Evaluation Meeting, Arlington VA, June 9, 2015.
3. “Cost savings for manufacturing lithium batteries in a flexible plant,” P.A. Nelson, S. Ahmed, K.G. Gallagher, D.W. Dees, *Journal of Power Sources*, Volume 283, 1 June 2015, Pages 506–516, <http://dx.doi.org/10.1016/j.jpowsour.2015.02.142>
4. K. G. Gallagher, S. E. Trask, C. Bauer, T. Woehrle, S. F. Lux, M. Tschech, B. J. Polzin, S. Ha, B. Long, Q. Wu, W. Lu, D. W. Dees, and A. N. Jansen “Optimizing areal capacities through understanding the limitations of lithium-ion electrodes” *Journal of the Electrochemical Society*, submitted (2015)

III.A.2 Battery Production and Recycling Materials Issues (ANL)

Objectives

- **Examine material scarcity** issues that may influence viability of automotive lithium-ion batteries
- Characterize drivers of cradle-to-gate energy and emissions intensity of lithium-ion batteries and identify means for their reduction
- **Characterize lithium-ion battery recycling** in the United States and abroad to identify the most promising recycling technologies as they evolve, barriers to recycling and influence of recycling on material scarcity
- **Engage with the international battery analysis community** to exchange information, improve analysis, and formulate EV LCA results communication
- **Develop improved recycling** process to maximize material recovery
- **Determine impact of battery reuse** on recycling processes and economics
- **Formulate actions** to address developing technical and institutional issues concerning used batteries

Project Details

**Linda Gaines and Jennifer Dunn
(Argonne National Laboratory)**

Center for Transportation Research
9700 S. Cass Avenue
Argonne, IL 60439
Phone: 630-252-4919; Fax: 630-252-3443
E-mail: lgaines@anl.gov

Start Date: Spring 2008
Projected End Date: Ongoing

Technical Barriers

- Future battery chemistry is not determined.
 - New cathode materials and battery compositions require expansion of GREET battery module to address evolving technology.
 - Battery recycling technology must handle uncertainty in battery chemistry developments.
- Automotive lithium-ion battery performance, safety, and environmental metrics must be co-optimized.
- Data access can be limited given emerging and evolving technology status, proprietary data concerns.
- Analysis has focused on GHG and energy impacts; other media should be examined for show-stoppers.
- Recycling economics in doubt because of low prices for lithium and other materials.
- Material recovered after use may be obsolete.
- Producers may be reluctant to use recovered materials.
- Mixed streams may be difficult to recycle.

Technical Goals

- Estimate energy use/emissions for current material production and battery assembly processes.
- Screen new battery materials for potential negative impacts from production or problems in recycling.
- Characterize and evaluate current battery recycling processes.
- Evaluate alternative strategies for additional material recovery and develop improved recycling processes.

Accomplishments

- Compared critical material demand to supply out to 2050 for maximum penetration of EVs.
- Compiled information on local environmental burdens of metal production.
- Analyzed cradle-to-gate impacts of producing four new cathode materials and two new anode materials (Si, Li).
- Determined and characterized current production and recycling methods for lithium-ion batteries.

- Performed battery production and recycling lifecycle analysis to compare impacts and identify ideal recycling processes.
- Determined roles battery chemistry plays in both environmental and economic benefits of recycling.
- Identified institutional factors that can enable or hinder battery recycling.
- Presented and published analyses and recycling process comparison.
- Released update to GREET battery module, incorporating new active materials. In FY15, also updated nickel and graphite data in GREET.
- Participated in IEA HEV Task 19, SAE, and USCAR working groups.

Introduction

Examination of the production of batteries from raw material acquisition to assembly illuminates the stages of this supply chain that incur the greatest energy and environmental burdens. Recycling of material from spent batteries will be a key factor in alleviating potential environmental and material supply problems. We examine battery material production, battery assembly, and battery recycling processes that are available commercially now or have been proposed. Battery materials, assembly and recycling processes are compared on the basis of energy consumed and emissions, suitability for different types of feedstock, and potential advantages relating to economics and scale. We compare the potential of recycling processes to displace virgin materials at different process stages, thereby reducing energy and scarce resource use, as well as potentially harmful emissions from battery production. Although few automotive batteries have been produced to date, viable processes will be required to recycle them when they are no longer usable. Secondary use of the batteries could delay return of material for recycling.

Approach

In our initial work, we developed cradle-to-gate energy consumption and air emissions for electric vehicle batteries with a LiMn_2O_4 cathode. These data were incorporated into Argonne's Greenhouse gases, Regulated Emissions, and Energy use in Transportation (GREET) model and released in GREET1_2014. We also estimated the maximum reasonable demand for battery materials, based on extremely aggressive scenarios for penetration of electric-drive vehicles. We combined vehicle demand growth with detailed battery designs and looked at how lithium demand might grow world-wide. We also estimated how much material could be recovered by recycling, thus reducing demand for virgin materials. We determined that cumulative world demand for lithium to 2050 would not strain known reserves. Although cobalt supplies, and possibly those of nickel as well, could be significant constraints by 2050, the envisioned move away from chemistries containing these elements would obviate potential problems.

Now, life cycle analysis (LCA) of batteries with other cathode materials based on detailed process data is being used to further identify potential environmental roadblocks to battery production, and to compare energy savings and emissions reductions enabled by different types of recycling processes. Analysis of recycling processes revealed cathode recovery as a key to process economic viability for low-Co cathodes. The cathode materials that are the focus of current work are lithium cobalt oxide (LiCoO_2), lithium iron phosphate (LiFePO_4), nickel manganese cobalt ($\text{LiNi}_{0.4}\text{Co}_{0.2}\text{Mn}_{0.4}\text{O}_2$), and an advanced cathode that has been the subject of research at Argonne, $0.5\text{Li}_2\text{MnO} \cdot 0.5\text{LiNi}_{0.44}\text{Co}_{0.25}\text{Mn}_{0.31}\text{O}_2$ (LMR-NMC). The anode paired with each of these cathode materials is typically graphite, although we have also developed an analysis for silicon and pure lithium anodes. In FY15, we updated material and energy flows for the production of graphite and nickel, an important cathode material component, in GREET. Table III- 4 contains the energy and GHG intensity of the different cathode and anode materials in GREET.

Results

Battery Production: Roughly half of battery mass consists of materials (Cu, steel, plastics, Al) that have been extensively documented in previous analyses. Therefore, our focus was on the active battery materials that are not as well-characterized, and their fabrication into finished cells. Our earliest work emphasized production of the raw materials and their conversion to active materials. Our focus then shifted to component manufacture and battery assembly, which must be repeated even if recycled materials are used. Previous work on Ni-MH batteries had suggested that these steps could be energy intensive.

Table III- 4: Energy and GHG Intensity of Cathode and Anode Materials for Lithium-Ion Batteries

Cathode or Anode Material	Cradle-to-Gate Energy Intensity (MJ/kg)	Cradle-to-Gate GHG Intensity (kg/kg)
LCO prepared hydrothermally (LiCoO ₂)	320	23
LCO prepared with a solid state method	180	13
NMC (LiNi _{0.4} Co _{0.2} Mn _{0.4} O ₂)	140	9.9
LMR-NMC (0.5Li ₂ MnO ₃ ·0.5LiNi _{0.4} Co _{0.25} Mn _{0.31} O ₂)	140	10
LFP prepared hydrothermally (LiFePO ₄)	60	4.0
LMO (LiMn ₂ O ₄)	40	3.6
LFP prepared with a solid state method	40	2.6
Silicon	1000	55
Lithium	160	12
Graphite	90	5.3

Argonne’s LCA of lithium-ion batteries is based upon a model of lithium-ion battery assembly that Nelson et al. (2011) developed. This peer-reviewed model provides an inventory of battery components and describes the equipment and steps involved in assembling these components into a battery at a manufacturing facility. Total energy for the manufacturing stage of overall battery production from cradle-to-gate is estimated to be only 2.2 MJ/kg, compared to over 130 MJ/kg for the material production (all steps that precede manufacturing) for a battery with a LiMn₂O₄ cathode. Therefore, recycling has the potential to save a very large fraction of the total battery production energy. Energy intensity of assembly is strongly dependent upon throughput because the dry room, which is energy-intensive to operate, likely consumes a relatively even amount of energy regardless of throughput. A low throughput yields a high energy intensity. In a mature industry, we expect that a battery assembly facility would operate closer to capacity, reducing the energy intensity of battery assembly.

Based on our analysis, recycling does provide energy conservation benefits and reduces the local impacts of metal recovery and purification. Recycling is even more beneficial when cathode

materials contain nickel or cobalt. Cathode materials with these metals have higher cradle-to-gate energy consumption and greenhouse gas (GHG) emissions than LiMn₂O₄ (30 MJ/kg LiMn₂O₄). The greater energy intensity of cobalt and nickel-containing cathode materials is evident when the cradle-to-gate energy consumption for different cathode materials are compared side-by-side as in Table III- 4. In the case of LiCoO₂, the recovery and purification of the metal dominates the overall energy consumption of producing this cathode material.

Figure III- 7 compares cradle-to-gate energy of producing batteries with different cathode types. Batteries with cobalt- and nickel-containing cathode materials have the greatest energy consumption on a per battery mass basis. On a per battery basis, the battery containing a LMR-NMC cathode and graphite anode has approximately the same cradle-to-gate energy consumption as a battery with an LMO cathode. LMR-NMC is about three times as energy intensive to produce as LMO but about 41% less of it is needed in the battery (when both batteries use graphite as the anode material) because its capacity is 250 mAh/g, 2.5 times greater than that of LMO.

Recycling Processes: Recycling can recover materials at different production stages, from elements to battery-grade materials. Figure III- 8 shows how some battery production processes can be avoided by the use of materials recovered by different recycling processes.

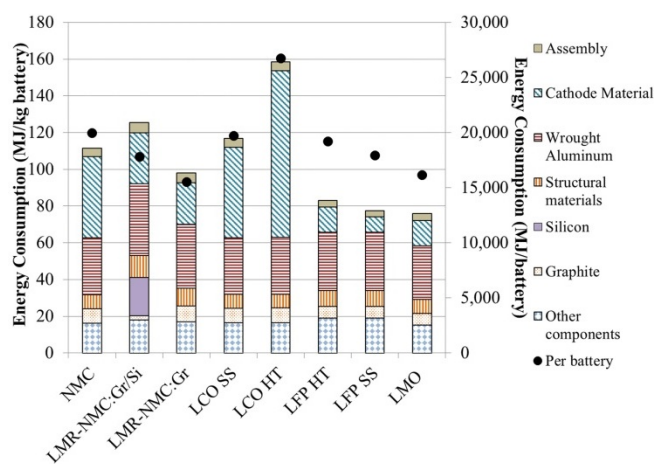


Figure III- 7: Cradle-to-gate energy consumption for batteries with different cathode materials (NMC= LiNi_{0.4}Co_{0.2}Mn_{0.4}O₂, LMR-NMC=0.5Li₂MnO₃·0.5LiNi_{0.44}Co_{0.25}Mn_{0.31}O₂, LCO=LiCoO₂, LFP=LiFePO₄, HT=hydrothermal preparation, SS=solid state)

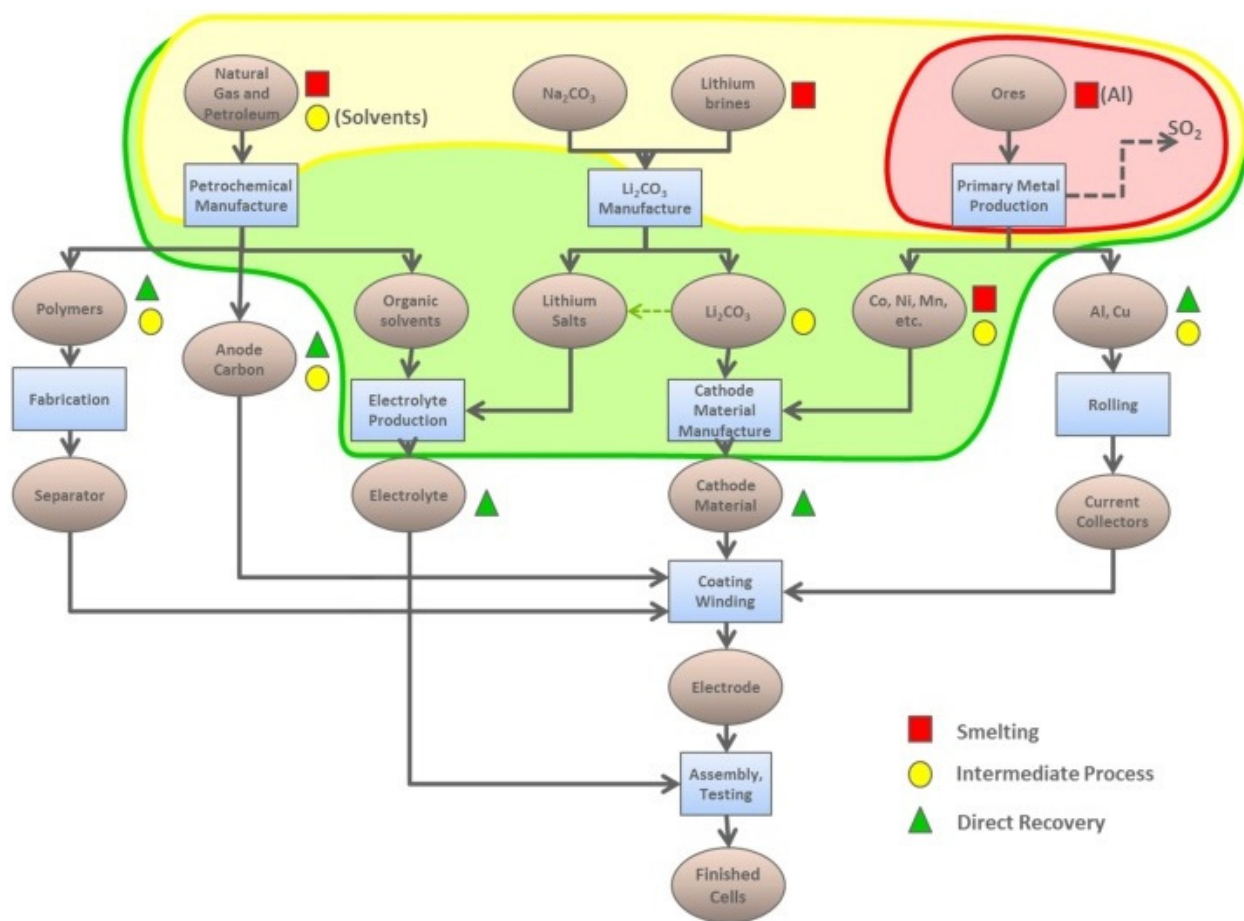


Figure III- 8: Schematic of Processes Avoided by Recycling

At one extreme are pyrometallurgical (smelting) processes that recover basic elements or salts. Smelting is operational now on a large scale in Europe, processing both Li-ion and Ni-MH batteries. At high temperatures, all organics, including the electrolyte and carbon anodes, are burned as fuel or reductant. The valuable metals (Co and Ni) are recovered and sent to refining so that the product is suitable for any use. If these are not contained in the batteries, the economic driver for smelting disappears. The other materials, including aluminum and lithium are lost. Smelting chemistry could possibly be changed to keep the lithium out of the slag or make the slag easier to handle.

At the other extreme, direct recovery of battery-grade material by a physical process has been demonstrated. This process requires as uniform a feed as possible, because impurities jeopardize product quality. The valuable active materials and metals can be recovered. If cathode material can be recovered, a high-value product can be produced, even if the elemental value of the constituent elements is low. This is a big potential economic advantage for direct recycling (see Figure III- 9). This is a low-temperature process with minimal energy requirement. Almost all of the original energy and processing required to produce battery-grade material from raw materials is saved. The quality of the recovered material must be demonstrated, and there must be a market for it in 10 or more years, when cathode materials may be different.

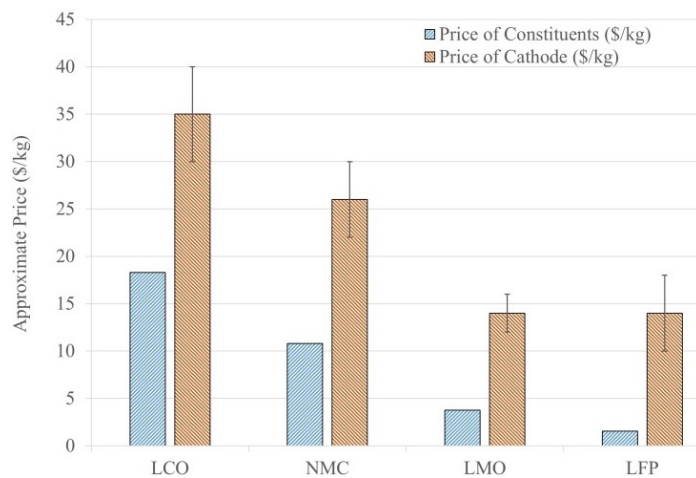


Figure III- 9: Comparison of element values to cathode price

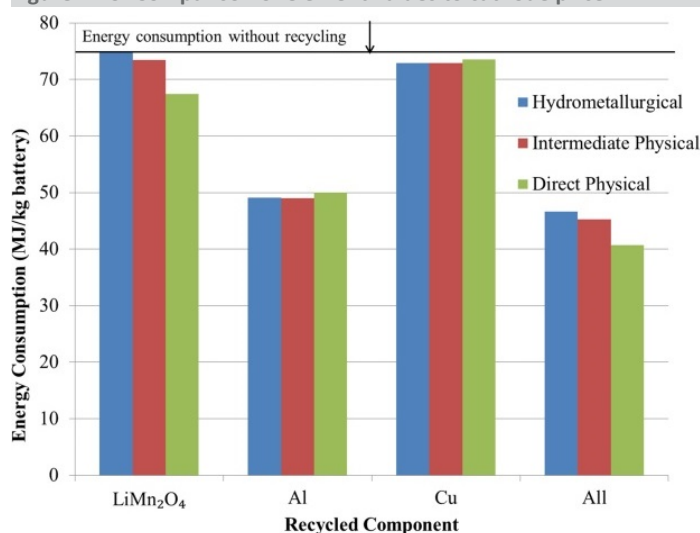


Figure III- 10: Energy required to produce battery

recyclers to sort before recycling. Argonne staff contributed heavily to the labeling standards recommended by the SAE. They also participate in several U.S. and international working groups to help enable recycling. Standardization of cell design, at least in size and shape, would foster design of automated recycling equipment. Standardization would also be beneficial to reuse schemes, where cells from various sources would be tested and repackaged in compatible groups for use by utilities or remote locations. It and proper labeling also help mitigate the emerging problem of Li-ion batteries implicated in fires and explosions disrupting secondary lead smelter operation, also being addressed by staff on SAE committees.

Relative Life-Cycle Energy Consumption and GHG of EVs Compared to ICEVs

Figure III- 13 compares life-cycle energy consumption on a per-km basis among BEV, PHEV50, and internal combustion engine vehicles (ICV) and breaks out the energy consumption in the fuel and vehicle cycles. The pioneer plant energy consumption for battery assembly is based on Ellingsen et al. (2014) while the nth plant energy consumption is based on Dunn et al. (2012). The latter is more reflective of a mature industry with assembly facilities operating at or near capacity. In all cases, even with the pioneer plant assembly energy intensity, EVs have lower life-cycle energy consumption than ICVs. The same is true for life-cycle GHG emissions. As Figure III- 11 shows, however, life-cycle SO_x emissions are higher in the case of EVs. The low sulfur content of gasoline is one reason why life-cycle SO_x emissions are lower for ICVs. Additionally, SO_x emissions from cathode material production contribute significantly to EV life-cycle SO_x emissions, but this impact can be reduced through integrating recycled materials into cathode material production (Figure III- 12). It is important to note that in the case of nickel, the location, ore type, and process characteristics will strongly

Intermediate or hydrometallurgical processes, such as the one funded by DOE under the Recovery Act (Toxco, now Retrieve Technologies), are between the two extremes. These do not require as uniform a feed as direct recovery, but recover materials further along the process chain than does smelting. Although the lithium can be recovered (as the carbonate), the high value of the cathode material is not preserved.

Figure III- 10 illustrates how, in the case of batteries with an LMO cathode, production energy for the entire battery can be minimized by the use of recycled metals as well as recycled cathode material.

Sulfur Emission Reductions by Recycling:

Several of the metals used in batteries are smelted from sulfide ores, leading to significant emissions of SO_x. These constitute a significant fraction of the vehicle's life-cycle emissions (see Figure III- 11). Recycling produces no such emissions, and thus cathode materials made from recycled materials would have lower production emissions, as can be seen in Figure III- 12.

Enablers of Recycling and Reuse: Material separation is often a stumbling block for recovery of high-value materials. Therefore, design for disassembly or recycling would be beneficial. Similarly, standardization of materials would reduce the need for separation. In the absence of material standardization, labeling of cells would enable

influence energy consumption and Sox emissions (Benavides et al. 2015). More information is needed to characterize nickel and cobalt production to better understand energy, air, and water quality implications of producing these metals. One key approach to reducing EV life-cycle GHG emissions is to use less carbon-intensive sources of electricity as Figure III- 14 illustrates. These results show that when EVs charge up with purely coal-derived electricity and have batteries that are produced in pioneer plants, their life-cycle GHG emissions are higher than those of ICVs. As the carbon intensity of the grid decreases, the relative GHG emissions grow smaller compared to those of an ICV.

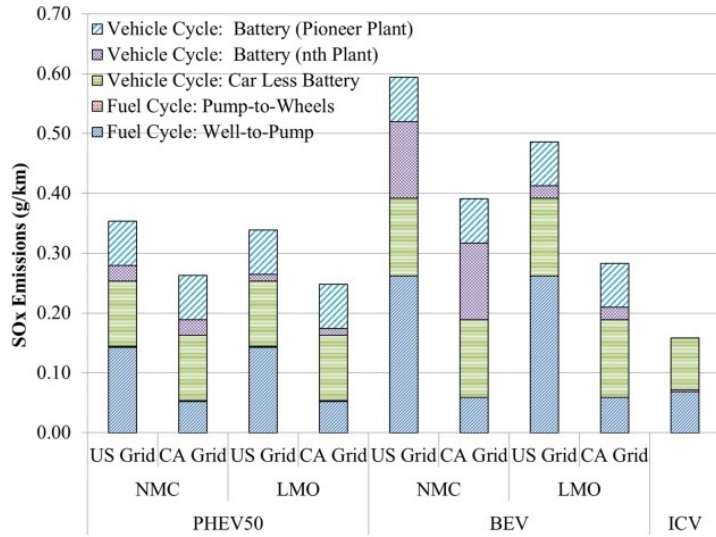


Figure III- 11: Batteries contribute a significant fraction of life-cycle sulfur emissions. Pioneer plant energy intensity based on Ellingsen et al. Nth plant assembly energy intensity based on Dunn et al. (2012) and reflects mature, high-throughput battery assembly facilities

Recycling Process Advancement

Direct recycling of lithium-ion batteries aims to recover the electrode material *per se*, rather than the elemental constituents. Several proposed methods to separate battery materials involve concentrated, strong acids or bases, which can dissolve cathode material. It is thus key to develop a fundamental knowledge of the behavior of cathodes under mild conditions. Water is an attractive process media for this, but it can react with cathode materials leaving them unusable for manufacturing new batteries. The nature of the reactivity between water and various cathode materials is not well-described in literature, especially with regard to impact on surfaces, ion solubility, and as applied to a recycling setting.

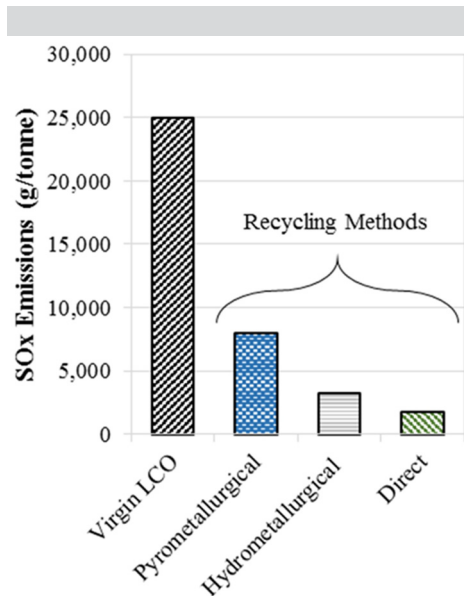


Figure III- 12: Cathodes made from recycled materials minimize sulfur emissions

We therefore examined aqueous reactivity of several commercially electrode materials: lithium cobalt oxide (LCO), lithium nickel cobalt manganese oxide (NMC), lithium nickel cobalt aluminum oxide (NCA), lithium iron phosphate (LFP), and lithium manganese dioxide (spinel). The variables include solution pH and temperature. These mild process conditions are representative of direct recycling. The observables were metal dissolution, morphology/surface changes, and electrochemical activity. The preliminary work compared relative reactivity of the cathode materials in dilute acid and base.

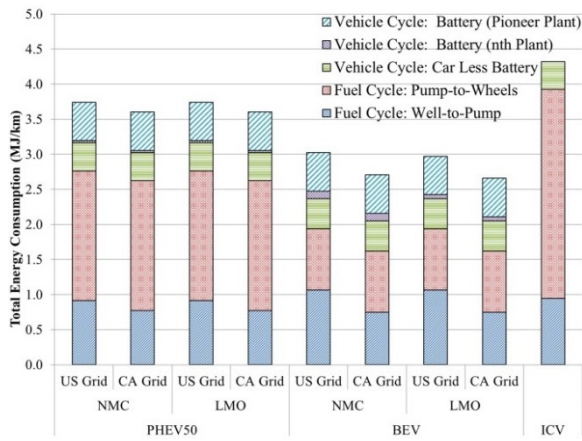


Figure III- 13: Fuel cycle and vehicle cycle total energy consumption for BEVs, PHEV50s, and ICVs. The PHEV50 (km) is modelled as being in charge-depleting (CD) and charge-sustaining (CS) modes during 47.5% and 52.5% of operation, respectively. The PHEV50 is assumed to have a fuel economy of 3.2 and 8.5 gasoline equivalent L/100 km in CD and CS modes, respectively. The BEV is assumed to have a fuel economy of 2.9 gasoline equivalent L/100 km mpgge while the ICV operates at 23 mpg. The liquid fuel used by the ICV and the PHEV30 during CS mode is conventional gasoline, 4% of which derives from oil sands recovered via in-situ production

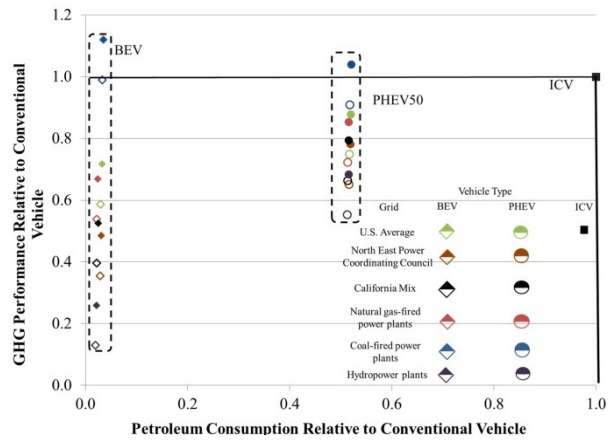


Figure III- 14: Relative performance of BEV (NMC cathode) and PHEV50 (LMO cathode) as compared to ICV. Green, orange, black, red, blue, and purple points represent results for vehicles powered with the average U.S. grid, North East Power Coordinating Council regional grid, the California grid, exclusively natural gas-fired power plants, exclusively coal-fired power plants, and hydropower plants, respectively. Hollow and full points represent results generated with the at capacity and low-throughput battery assembly energies, respectively

Figure III- 15 shows the degree to which Li was removed from the various cathode materials as a function of temperature and pH. Although NCA experienced the highest Li loss, the quality of the material is the suspected cause. This type of information will be critical in recycling process design.

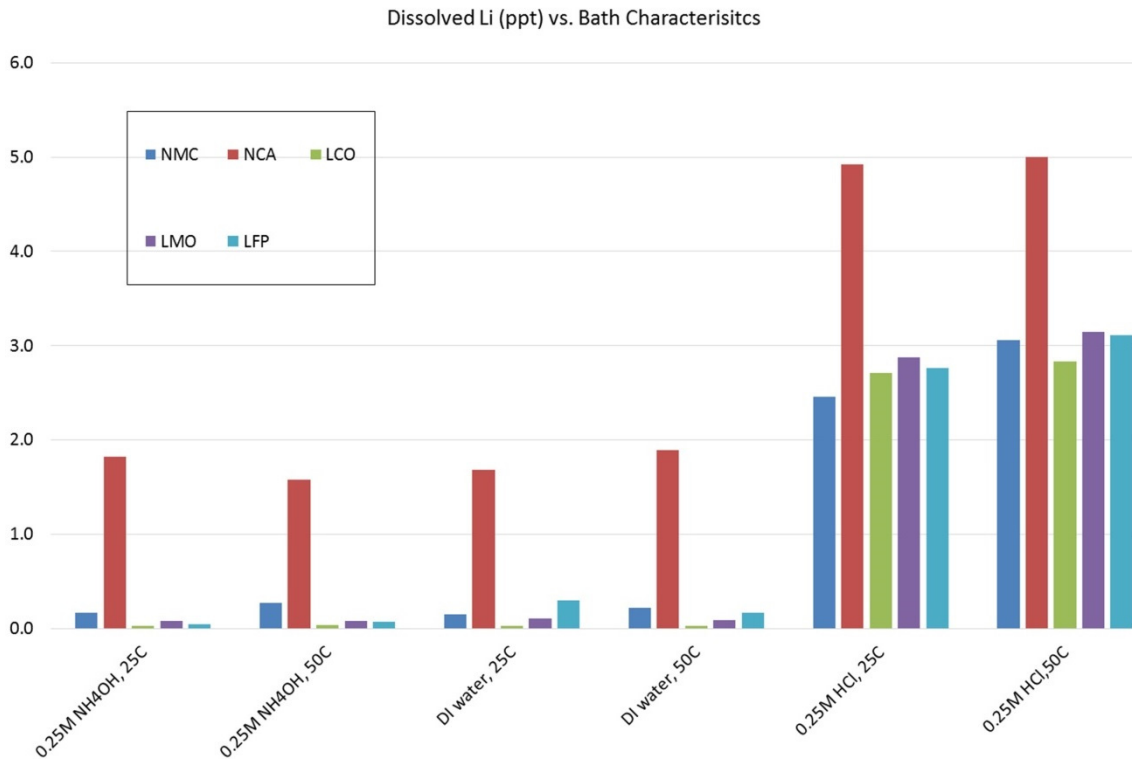


Figure III- 15: Lithium loss from cathodes under varied conditions

Future Work

- Determine and analyze viable recycling processes for all chemistries Collaboration with JCESR and BatPaC model developers at Argonne to identify emerging chemistries that merit analysis
- Refine GREET module as new data become available
- Examine local impacts of battery material production (e.g., emissions to air and water)
- Refine analysis of recycling processes to better estimate benefits and enable optimum process development
- Examine alternative sources of cathode metals, such as recycled batteries from electronic devices
- Submit manuscript on life-cycle GHG emissions, energy consumption, air emissions as a function of location (international)

FY2015 Publications/Presentations

Publications

1. Gaines, L. (2014), The Future Of Automotive Lithium-Ion Battery Recycling: Charting A Sustainable Course, *Sustainable Materials and Technologies* <http://dx.doi.org/10.1016/j.susmat.2014.10.001>
2. Dunn, J.B., James C., Gaines, L., Gallagher, K. "Material and Energy Flows in the Production of Cathode and Anode Materials for Lithium Ion Batteries," *Argonne National Laboratory, report no. ANL/ESD-14/10 Rev (2015)*.
3. Dunn, J.B., Gaines, L., Kelly, J. C., James, C., Gallagher, K.G. (2015) "The significance of Li-ion batteries in electric vehicle life-cycle energy and emissions and recycling's role in its reduction." *Energy and Environmental Science*, doi: 10.1039/C4EE03029J
4. "The Future of Automotive Lithium-Ion Battery Recycling: Charting a Sustainable Course," poster for TRB 2015 Annual Meeting (January 2015).
5. Benavides, P. B., Dai, Q., Sullivan, J., Kelly, J. C., Dunn, J. B. "Material and Energy Flows Associated with Select Metals in GREET2: Molybdenum, Platinum, Zinc, Nickel, Silicon." Argonne National Laboratory, report No. ANL/ESD-15/11 (2015).
6. "Life Cycle Analysis Summary for Automotive Lithium-Ion Battery Production and Recycling," paper accepted for 2016 TMS Annual Meeting (to be held February 2016).
7. *Lithium-Ion Battery Environmental Impacts*, in *Lithium-Ion Batteries: Advances and Applications*, Elsevier (2014) (book chapter).
8. *Life Cycle Assessment of Electric Vehicles – Key Issues of Task 19 of the International Energy Agency (IEA) on Hybrid and Electric Vehicles (HEV)*, G. Jungmeier, J.B. Dunn, A. Elgowainy, L. Gaines, S. Ehrenberger, E.D. Özdemir, H.J. Althaus, R. Widmer, Transport Research Arena 2014, Paris (paper).

Presentations

1. *Recycling Li-Ion Batteries: Questions and Issues*, The Battery Show, Novi, MI, (September 15-17, 2015)
2. *Enabling Future Li-Ion Battery Recycling*, International Meeting of Science for Recycling, Porto, Portugal (January 22-23, 2015)
3. *How Can We Enable EV Battery Recycling?*, International Battery Seminar, Ft. Lauderdale, FL (March 9-12, 2015)
4. *Impacts of Plug-In Hybrid Electric Vehicle Charging Choices in 2030*. IEA Task 19 Workshop (October 15–16, 2014)
5. *Enabling Future Li-Ion Battery Recycling*, Battery Council International, Savannah, GA (May 2015)

References

1. Benavides, P. B., Dai, Q., Sullivan, J., Kelly, J. C., Dunn, J. B. "Material and Energy Flows Associated with Select Metals in GREET2: Molybdenum, Platinum, Zinc, Nickel, Silicon." Argonne National Laboratory, report No. ANL/ESD-15/11 (2015).
2. Dunn, J.B., Gaines, L., Sullivan, J., Wang, M. (2012). "Impact of recycling on cradle-to-gate energy consumption and greenhouse gas emissions of automotive lithium-ion batteries." *Environmental Science and Technology*, 46: 12704-12710.

3. Dunn, J.B., Gaines, L., Kelly, J.C., James, C., Gallagher, K.G. (2015) “The significance of Li-ion batteries in electric vehicle life-cycle energy and emissions and recycling’s role in its reduction.” *Energy and Environmental Science*, doi: 10.1039/C4EE03029J
4. Ellingsen, L.A., Majeau-Bettez, G., Singh, B., Srivastava, A.K., Valøen, L.O., Strømman, A.H. (2014) “Life Cycle Assessment of a Lithium-Ion Battery Vehicle Pack.” *Journal of Industrial Ecology*, 18:113-12.
5. Nelson, P., Gallagher, K., & Bloom, I. (2011). *Modeling the performance and cost of lithium-ion batteries for electric-drive vehicles*. Argonne National Laboratory.

III.A.3 Battery Leasing & Standardization for Medium-Duty Hybrid Electric Vehicle (NREL)

Objectives

- Identify battery standardization and leasing strategies that will increase the adoption rate of fuel efficient hybrid electric vehicles (HEVs) in Class 6 commercial medium-duty (MD) fleets for parcel delivery trucks by reducing the payback period for the HEV relative to a conventional MD vehicle.

Technical Barriers

- Long payback periods (> 3 years) of current MD HEVs limit their mass adoption in commercial vehicle fleets.
- Annual sales and production volumes are low for MD Class 3-6 vehicles.
- Demanding duty cycles with annual mileages up to 30,000 miles per year impacts the life of batteries.

Technical Targets

- Identify battery leasing strategies that achieve the payback period and evaluate the business case for a battery leasing company
- Identify battery standardization strategies that further reduce battery cost and thereby the incremental cost of the HEV powertrain.

Accomplishments

- Collected information from stakeholders (MD vehicle OEMs, fleet operators, battery manufacturers and integrators) and performed market assessment of MD fleet vehicles.
- Performed economic analysis and determined that, under certain assumptions, leasing a MD HEV battery can reduce the payback period of the vehicle to less than 3 years for the vehicle fleet owner, albeit at higher total cost of ownership to the fleet.
- Identified drive cycle characteristics from Class 6 MD HEV parcel delivery truck drive cycles in the National Renewable Energy Laboratory's (NREL's) FleetDNA database and used them to derive battery requirements.
- Simulated performance and life of Class 6 MD HEV parcel delivery truck using NREL's FastSim and BLAST models, in order to identify an ideal battery size for fuel economy, 10-year life, and 12,000 to 22,000 mile/yr typical operation.
- Identified battery standardization strategies and quantified the cost/benefit of each strategy for annual battery pack sales ranging from 1,000 to 50,000 per year, using Argonne National Laboratory's BatPaC model.

Project Details

Brian Cunningham (DOE Program Manager)

DOE Agreement # 28883 Recipient:
National Renewable Energy Laboratory

Kenneth Kelly (NREL - PI)

15013 Denver West Parkway
Golden, CO 80401

Phone: 303-275-4465

Email: kenneth.kelly@nrel.gov

Subcontractor

James C. Paul (Ricardo)

P.O. Box 22637

Carmel, CA 93922

Phone: 831-624-8700

Email: james.paul@ricardo.com

Start Date: October 2014

Projected End Date: December 2015

Introduction

Medium-duty HEVs used by commercial vehicle fleets are selling in limited numbers due to (i) present low fuel prices and (ii) high incremental cost of the HEV technology, particularly the battery system, relative to a conventional powertrain. These two factors contribute to long payback times for the HEV technology. In the summer of 2014, MD HEV industry representatives contacted DOE VTO and NREL to investigate strategies that could make MD HEVs for delivery truck applications competitive with conventional MD vehicles.

Data from NREL's FleetDNA project indicate that a conventional delivery truck achieves around 7 miles per gallon (mpg) on average, while the same vehicle with an HEV powertrain achieves 8.2 mpg on average [4]. This has the following implications for an HEV with a \$15,000 net incremental cost (extra cost minus government incentives) to achieve simple payback compared to a conventional vehicle:

- At \$2.50/gallon diesel fuel prices, an HEV delivery truck would need to drive $\geq 30,000$ miles/year or more to pay for itself over its 10-year lifetime
- At \$3.50/gallon diesel, the average forecast for 2018-2020 [5], the HEV delivery truck would need to
 - Drive $\geq 22,000$ miles/year to pay for itself in 10 years, or
 - Achieve fuel efficiency ≥ 15 mpg and drive 22,000 miles/year or more to pay for itself in 3 years.

In these scenarios, the payback period can be cut in half if the HEV incremental cost is reduced from \$15,000 to \$7,500, which may be possible with future cost reductions for batteries and other HEV technologies. HEV payback period can also be strongly influenced by the business model of battery direct ownership versus battery leasing.

In order to shorten the payback period and increase HEV adoption rates in fleets, two focus areas for this analysis are to (i) evaluate the economics of a battery leasing business model for fleets and (ii) reduce battery costs through standardization.

Approach

The team leveraged multiple toolsets including NREL's FleetDNA database, FastSim vehicle simulator, and Battery Lifetime Analysis and Simulation Tool (BLAST) suite; Argonne National Laboratory's Battery Performance and Cost (BatPaC) model; and Ricardo's Total Cost of Ownership (TCO) model. Major elements of the project included:

1. Assessment of MD HEV delivery truck market
2. Interviews with stakeholders including industry experts from MD vehicle OEMs, fleet operators, battery manufacturers and integrators
3. Analysis of battery requirements
4. Evaluation of economics of battery leasing versus direct ownership
5. Identification of standardization strategies that show most promise to reduce battery upfront cost and thus reduce the incremental cost of HEV technology in the MD commercial delivery truck space.

Results

We have achieved the following progress:

MD HEV Market Assessment and Battery Requirements Analysis

Market analysis indicates production volumes of MD HEVs will remain relatively low through 2020. This study focuses on Class 6 trucks. The projected number of 2015 U.S. full-year new registrations of Class 6 trucks (all vocations) was 51,900 [6]. Based on several years of sales data from 2007 to 2013, HEVs represent a small portion of overall Class 6 truck annual sales—only around 900 vehicles per year [7-10]. With present market conditions, we forecast MD HEV annual production over the 2015 to 2020 timeframe will range from 1,000 to 4,400 vehicles per year [3].

The incremental cost of MD HEVs is still quite expensive due to low production/sales numbers and the need to cover non-recurring engineering (NRE) design costs. The typical incremental cost of a Class 6 HEV is around \$27,000, however this is partly offset by federal, state, and local incentives totaling about \$19,000 (Table III-5). The incremental cost of the technology is expected to come down in the future, but so would the incentives. Based on this, net incremental costs are forecast to range from \$15,000 at present to \$7,500 in the future.

To determine battery design requirements, the team performed analysis of vehicle drive cycles from the NREL FleetDNA database and selected a representative cycle for vehicle simulation. FastSim vehicle simulations were run for some 60+ hypothetical HEV designs. The simulations indicated a 45 kW battery yields optimal fuel economy for the Class 6 truck. The BLAST simulation tool showed Li-ion battery lifetime to be a strong function of total energy, which impacts the depth of discharge experienced by the battery during the HEV drive cycles. To achieve a 10-year, 200,000-mile total lifetime requires a battery with total energy of 1.8 to 2.5 kWh.

Table III- 5: Incremental Cost of HEV Drive Systems and Incentives in the MD Market Segment

Application	Incremental Cost	Battery Type	Typical Incentive Funding/ Voucher	References
Class 6 package delivery truck	\$35k	Li-ion	\$15k	8
Class 6 package delivery truck	\$21k	Li-ion	\$15k	9
Class 5 package delivery truck	\$12k	Nickel metal hydride	\$18k	4,10
Class 6 HEV	\$12k-\$40k	Li-ion	\$15k-\$30k	4

Preliminary Analysis of Battery Leasing Versus Direct Ownership

A spreadsheet model was created to perform a preliminary analysis of battery leasing versus direct ownership from both the lessee and lessor perspectives [2]. The analysis found that a battery leasing company (lessor) could achieve a 10% return on equity (ROE) with a lease price of \$177/month. A 10% ROE implies that the net worth of the lease at year 10 is equal to the compounded value of the initial capital outlay at year 0. Other assumptions included \$5,100 battery cost, 1.33 markup, 10-year battery life with linear depreciation, 39.3% taxes on net revenues and \$100/year/battery general and administrative costs. The lease price is sensitive to these baseline assumptions:

- Eliminating the corporate income tax reduces the lease price from \$177/month to \$132/month.
- Reducing the battery cost by 15% reduces the lease from \$177/month to \$151/month.
- Reducing the battery markup from 1.33 to 1.1 reduces the lease from \$177/month to \$166/month.

The analysis further found that 15% ROE for the lessor is not viable, as it raises the battery lease price too high, from \$177/month at 10% ROE to \$260/month at 15% ROE.

For the fleet owner (lessee), monthly fuel savings of operating an HEV compared to a conventional vehicle range from \$50/month at 12,000 miles/yr and \$2.50/gal fuel to \$175/month at 30,000 miles/yr and \$3.50/gal fuel. Under the battery leasing arrangement, the lessee also no longer has to pay upfront the \$5,100 x 1.33 markup cost of the battery, but still may bear other HEV incremental costs for the electric motor and inverter. As an example, avoiding the upfront battery cost generates an additional \$189/month savings over the 3-year period in simple terms. (Other HEV incremental costs, heavily dependent on future HEV production volumes, NRE costs, and government incentives can reduce this savings by 10% to 100%.)

To summarize, the business model for the battery leasing company allows them to achieve a reasonable 10% ROE over 10 years. The fleet owner benefits over the initial 3 years to the tune of \$40/month to \$170/month. The downside is that the fleet owner does not own the battery after 3 years.

Evaluation of Battery Standardization Strategies

Building off the recent analysis of battery standardization for commercial plug-in HEV and electric vehicle designs [13], Ricardo performed an analysis of battery standardization strategies for commercial Class 6 HEV batteries using the BatPac model from Argonne National Laboratory. Eight categories of strategies were considered:

1. Module housings, bus bar, attachments
2. Module voltages
3. Electrode dimensions
4. Communications
5. Current collectors
6. Safety systems
7. Module stack interface, heating/cooling, heat conductors
8. Interface for power transfer.

Within each category, a relative cost curve was derived to estimate impact of production volume on cost. In some categories, such as metal stampings for module housings, the cost versus production volume falls steeply due to high tooling costs. In other categories, such as printed circuit boards, the cost versus production volume

falls only slightly, indicating cost is less sensitive to production volume due to highly automated production processes that can efficiently produce the device even at low numbers.

At low production volumes of 1,000 battery packs per year (Figure III- 16), all but one of the strategies (standardized communications interface) results in a battery cost increase. At around 10,000 battery packs produced per year, five of the strategies become viable (i.e., cost of implementing strategy approximately equal to savings), the most advantageous being standardizing module housings, bus bars, and attachments. This strategy is estimated to reduce battery pack cost by 17%. At 50,000 battery packs produced per year, the standardized module housing, bus bar, and attachment strategy may reduce battery pack cost by 36%. The results are further summarized in Table III- 6.

It is apparent from this analysis that significant battery pack cost reductions are not achieved until annual production volumes reach 10,000 to 50,000 battery packs per year. But the annual production rate of all commercial MD delivery trucks—hybrids and non-hybrids—is presently only around 50,000 vehicles per year. This suggests two methods to achieve cost reductions:

1. Hybridize a significant portion, >20% of commercial MD vehicles, which may require significant government incentives, or
2. Identify and use battery cells and modules that are already produced in significant volumes, >50,000 packs per year, in some other application such as light-duty HEVs.

Table III- 6: Percentage Cost Savings or Cost Increase from each Standardization Strategy at Different Annual Battery Pack Production Volumes

Standardization Approach	Cost Savings or Penalty (% of delivered cost of battery to vehicle OEM) for indicated Production Volumes (Batteries/Year)				
	1,000	5,000	10,000	50,000	100,000
Module Housings, Bus Bar, Attachments	-89.80	-0.20	16.84	35.75	39.34
Module Voltages	-24.12	-0.19	4.40	9.90	11.60
Electrode Dimensions	-5.10	-0.43	1.41	5.29	6.81
Communications	2.22	2.30	2.41	3.42	5.05
Current Collectors	-0.26	-0.23	-0.20	0.24	1.17
Safety Systems	-0.39	-0.04	0.03	0.12	0.17
Module Stack Interface, Heating/Cooling Heat Conductors	-111.42	-41.60	-25.80	-4.75	1.16
Interface for Power Transfer	-32.46	-17.78	-14.89	-10.73	-6.10

 Standardization strategies that produce a cost saving at indicated production volume.

 Standardization strategies that produce a cost increase at indicated production volume.

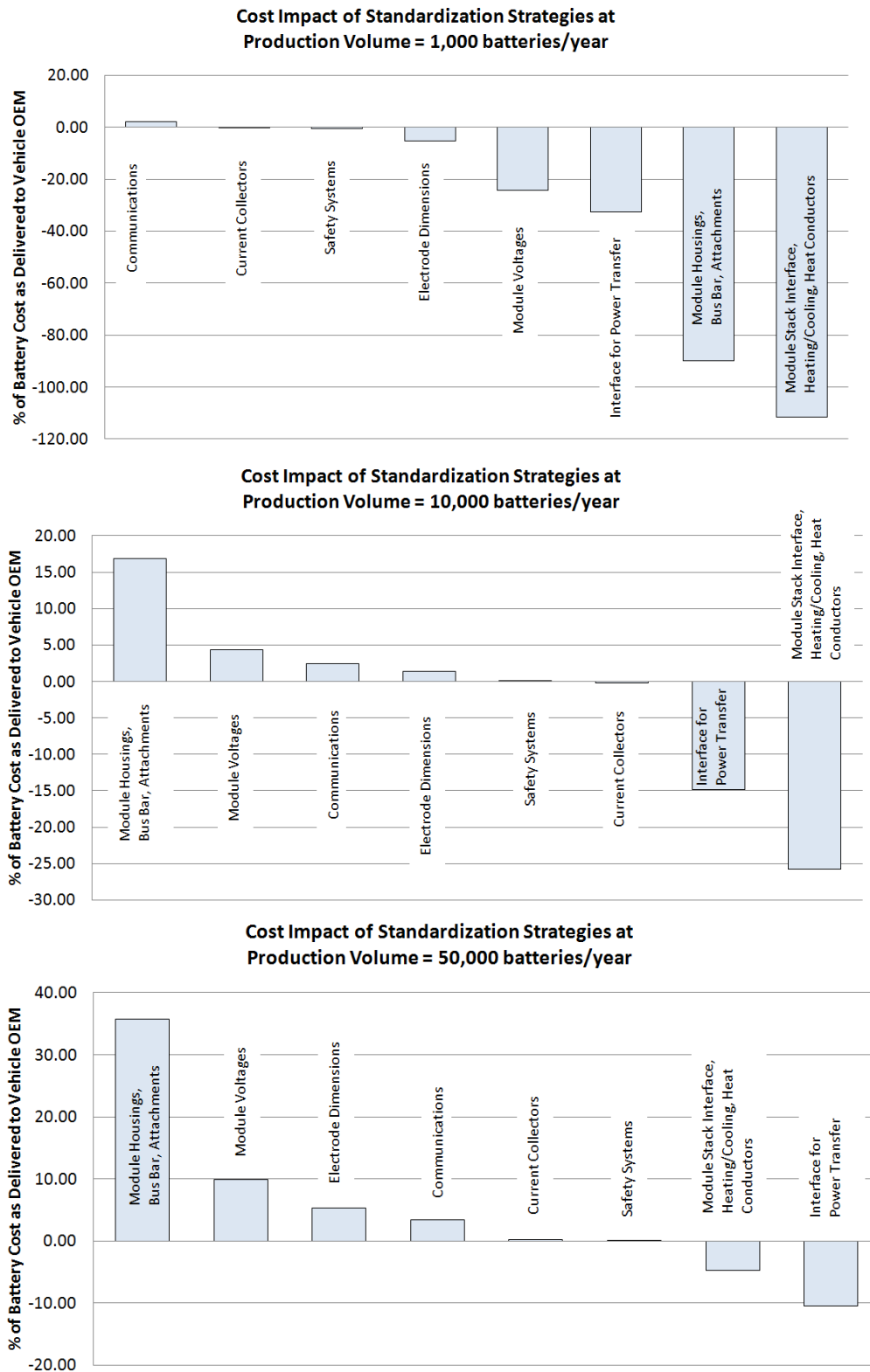


Figure III- 16: Impact of individual standardization strategies on battery cost (positive is cost reduction)

Conclusions and Future Directions

Commercial MD Class 6 trucks are presently produced and sold at rates of around 50,000 vehicles per year. With present market conditions, HEVs are only expected to account for 2-9% of this segment. But in order for battery costs to come down, battery packs must be produced at numbers of 10,000 to 50,000 per year or greater. Without significant government incentives to push hybridization, a possible path forward for MD vehicle original equipment manufacturers (OEMs) to bring down battery costs is to build business arrangements with light-duty vehicle OEMs to purchase battery modules similar to those used in their light-duty HEVs, which are already produced at high volumes.

Presently, commercial MD HEVs achieve about 17% greater fuel economy compared to conventional MD vehicles. With further optimization, this could be improved to 25-40%, which is similar to light-duty HEVs. This improved fuel economy, if it can be achieved with low HEV incremental cost, would shorten the payback period for MD HEVs.

A preliminary analysis of the battery leasing business model indicates that it can indeed shorten the payback period for MD HEVs. A battery leasing company could achieve a reasonable 10% return on equity. Whether the battery leasing strategy can shorten the payback period to less than 3 years greatly depends on the incremental cost of the HEV technology and government incentives.

An analysis methodology has been developed to evaluate the impact of a range of battery standardization strategies. The analysis models have been populated with vehicle duty cycles, battery requirements, and cost data, and preliminary analysis has been conducted on a range of strategies. In the remaining 3 months of the study, the team will review results with industry to obtain feedback on the analysis, refine the analysis, and establish best paths forward. A final technical report will be published in FY 2016.

Potential follow-on activities include:

- Link ANL's BatPaC battery cost model to NREL's BLAST battery operation model to evaluate the relation between battery component chemistries, life and cost for different vehicle types (HEVs, PHEVs, and EVs);
- Evaluate strategies for reducing the cost, volume, and mass of the balance of system (beyond electrochemical components);
- Extend the library of battery life models in BOM and BLAST to NMC and mixed oxide LMO for cathodes and titanate for anodes;
- Use BLAST to perform battery technical target and requirement analysis for various heavy-duty electrified vehicles (similar to work for USABC for 21st Century Truck);
- Evaluate the value of various **standardization** strategies of batteries for light duty plug-in electric vehicles.

FY 2015 Publications/Presentations

1. Interviews with vehicle OEMs (step vans), battery manufacturers (lithium-ion), governmental vehicle purchase incentive program administrators, and hybrid-electric drive system component manufacturers and suppliers, September 2-28, 2015.
2. J. Neubauer, A. Pesaran, "FY15 Milestone: Medium-Duty Hybrid Electric Vehicle Battery Leasing Scoping Analysis," December 2014 NREL-DOE Milestone Report, DOE-NREL AOP WBS 1.1.2.409.
3. K. Kelly, K. Smith, J. Cosgrove, B. Prohaska, A. Pesaran, J. Paul, M. Wiseman, "Battery Ownership Model: Medium-Duty HEV Battery Leasing & Standardization," September 2015 NREL-DOE Milestone Report, DOE-NREL AOP WBS 1.1.2.409.

References

1. Burton, J., Walkowicz, K., Sindler, P., and Duran, A., "In-Use and Vehicle Dynamometer Evaluation and Comparison of Class 7 Hybrid Electric and Conventional Diesel Delivery Trucks," SAE Int. J. Commer. Veh. 6(2):545-554, 2013, doi:10.4271/2013-01-2468. SAE Paper No. 2013-01-2468.
2. Annual Energy Outlook 2014, U.S. Energy Information Administration.
3. Clinton, P., Commercial Truck Registrations, Work Truck Magazine, September 3, 2015.

4. Lyden, S., The Latest Developments in Hybrid-Electric Medium-Duty Trucks, TruckingInfo, March 2014.
5. Cornils, H., Hybrid Solutions for MD Commercial Vehicles, ERC Symposium, University of Wisconsin, June 10, 2009.
6. Busdiecker, M., Technology Potential of Commercial Vehicle Transmissions, Heavy-Duty Vehicle Efficiency Technical Workshop, San Francisco, October 22, 2013.
7. Parish, R., et. al., Demand Assessment of First-Mover Hybrid and Electric Truck Fleets, CALSTART High Efficiency Truck Forum (HTUF), October 2012.
8. California Air Resources Board, Hybrid Truck & Bus Voucher Incentive Project (HVIP), Making the Case for Hybrid and Electric Trucks and Buses, <https://www.californiahvip.org/making-the-case>, Accessed September 12, 2015.
9. California Air Resources Board, Hybrid Truck & Bus Voucher Incentive Project (HVIP), Hino Motors Model 195h Delivery Truck with Parallel Hybrid System, Package Delivery, California HVIP Voucher Amount, https://www.californiahvip.org/docs/HVIP_Year4_EligibleVehicles.pdf, accessed September 17, 2015.
10. Paul, J., Bogen, M, Liss, J, Holmes, J, Sohnen. 2014. The Market Impact of Standardized Design in PEV Commercial Battery Pack Purchase and Disposal. California Energy Commission (CEC). Public Interest Energy Research (PIER) Project Number CEC-PIR-12-005. CEC document number not yet assigned, expected publication date: January 2016.

III.B Battery Testing

III.B.1 Battery Performance and Life Testing (ANL)

Objectives

- Provide DOE, USABC, and battery developers with reliable, independent and unbiased performance and life evaluations of cells, module and battery packs.
- Benchmark battery technologies which were developed with DOE/USABC funding to ascertain their level of maturity.

Technical Barriers

- This project addresses the following technical barriers as described in the USABC goals [1,2, and 3]:
- Performance at ambient and sub-ambient temperatures
- Calendar and cycle life

Technical Targets

- PHEV Technical Targets
- 15-y calendar life
- 5,000 CD cycles
- Other technical targets exist for EV, HEV, LEES, and 12 V SS applications.

Accomplishments

- Tested battery deliverables from many developers. (see Table III- 7)
 - Determined the effect of the Fast-Charge Test, which is in the USABC EV Test Manual [3], on battery performance
 - Compared EV battery test protocols used in the US and in China (Argonne lead; in progress).

Introduction

Batteries are evaluated using standard tests and protocols which are transparent to technology. Two protocol sets are used: one that was developed by the USABC [1, 2], and another which provides a rapid screening of the technology. The discussion below focuses on results obtained using the standard protocols.

Project Details

Brian Cunningham (DOE Program Manager)

Ira Bloom (PI), John Basco, Panos Prezas, David Robertson, Lee Walker

Argonne National Laboratory
9700 South Cass Avenue
Argonne, IL 60439

Phone: 630-252-4516; Fax: 630-972-4516

Email: ira.bloom@anl.gov

Start Date: September 2006

Projected End Date: Open

Table III- 7: List of battery deliverables tested

Developer	Application	Status
JohnsonControls, Inc.	PHEV20	On-going
	PHEV20	Complete
	PHEV20	On-going
	PHEV20	On-going
	PHEV20	On-going
XALT	EV	On-going
Optodot	EV	On-going
Daikin	EV-like	On-going
ANL/CAMP	EV-like	On-going
3M	EV	On-going
	Based on EV+PHEV	On-going
Seeo	EV-cell	On-going
	EV-module	On-going
Tiax	Based on EV+PHEV	On-going
Leyden Energy	12V SS	On-going
Navitas	EV	On-going
24-M	Based on EV+PHEV	On-going
Wildcat	EV-like	On-going
Maxwell	12V SS	On-going
Leyden	12V SS	On-going
Xerion	PHEV-20	On-going

Approach

The batteries are evaluated using standardized and unbiased protocols, allowing a direct comparison of performance within a technology and across technologies. For those tested using the USABC methods, the performance of small cells can be compared to that of larger cells and full-sized pack by means of a battery scaling factor [1, 2].

Results

Organizations in the US and China have developed independent battery testing protocols based on the same understand of the underlying electrochemical processes. These protocols are designed to characterize the performance of a battery and how the performance changes with time. However, each organization imbues the test protocol with its test philosophy. For example, one organization may test a battery to absolute failure (i.e. it no longer meets performance targets), while another may test the battery just long enough to obtain sufficient data to allow an estimation of when it is not able to meet performance goals.

Three organizations, ANL, INL and CATARC, collaborated to experimentally compare the test protocols used by the USABC and those used in China. The tests from the United States came from the U.S. Advanced Battery Consortium Electric Vehicle Battery Test Procedures Manual [3]. Those from China came from Automobile Standard QC/T 743-2006 [4].

The protocols were compared using cells based on commercially-available, LiFePO_4 /graphite chemistry. The key test parameters are shown in Table III- 8. It shows that there are many similarities between the two sets of test protocols, such as energy window and temperature. However, there are differences, such as the metric location (%DOD), magnitude and duration of the power pulse, which may impact the data produced. Additionally, cells were also tested using the QC/T 743 protocol, but without the large power pulse in reference performance test.

Table III- 8: Comparison of key attributes of the USABC and QC/T 743 protocols

Attribute	USABC	QC/T 743
DOD (energy) window	0–80% DOD	0–80% DOD
Temperature, °C	25	25
Capacity measurement rate	C/3	C/3
End-of-test criterion	20% degradation	20% degradation
Metric point	80% DOD	50% DOD
Power pulse duration, s	30	10
Power pulse current, A	75	225
Cycle life profile time	5 h	5 h, 45 min
RPT frequency, cycles (days)	50 (10.5)	24 (6)
RMS power of life cycle, W	50–51	12–13
RMS current of life cycle, A	15–16	3.5–4
Average voltage of life cycle, V	3.17, fading with time	3.27, without fading
Energy throughput of life cycle, Wh	27	19.5

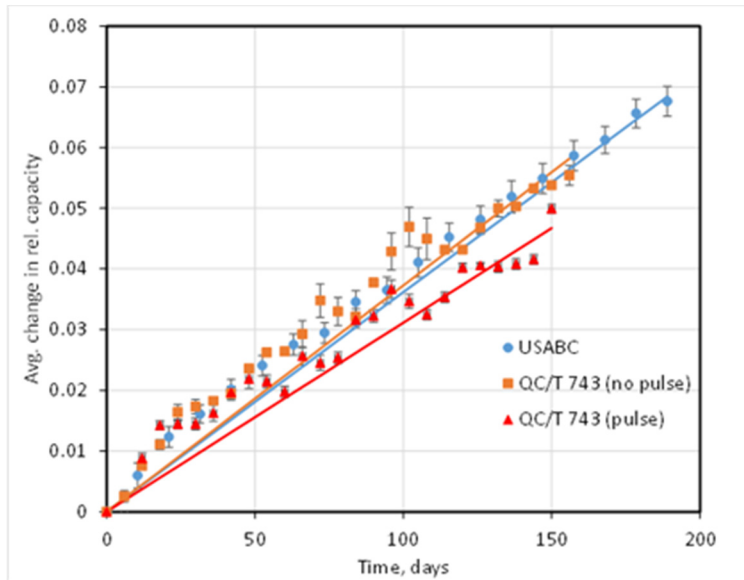


Figure III- 17: Average change in relative capacity vs. time for the three cycling protocols used in the experiments. The markers represent the data, and the solid curves, the least squares fit. The values of r^2 for these fits was 0.99. The error bars represent the standard deviation at that point ($\pm 1\sigma$). If $1\sigma \leq \sim 5\%$ of the reported value, the error bar will not be visible

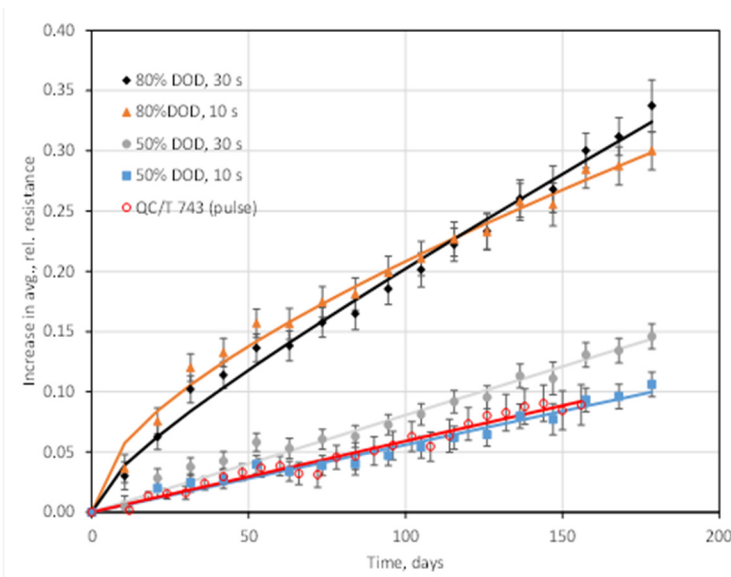


Figure III- 18: Increase in average, relative change in resistance vs. time for the cells tested using the USABC and QC/T 743 (pulse) protocols. The values from the former method were calculated at two values of %DOD and using two pulse widths to facilitate comparison with the values from QC/T 743 (pulse). The values of r^2 were typically 0.99. The error bars represent the standard deviation at that point ($\pm 1\sigma$). If $1\sigma \leq \sim 5\%$ of the reported value, the error bar will not be visible

- Continue testing PHEV contract deliverables
- Continue testing EV contract deliverables
- Begin testing LEES contract deliverables
- Continue acquiring and benchmarking batteries from non-DOE sources

Figure III- 17 shows the effect of cycling protocol on the average relative capacity fade for the cells tested. The results showed that the average, relative capacity fade followed linear-with-time kinetic rate laws. Statistically ($\pm 2\sigma$), the rates were the same.

As expected, cell resistance depended on %DOD and pulse width time. Figure III- 18 shows how the average, relative resistance changes with time based on results from both sets of protocols. Least-squares curve fitting shows that the data followed either linear-with-time, $\Delta R = at$, or mixed linear and parabolic, $\Delta R = at + bt^{1/2}$, rate laws. Based on the high values of r^2 , the fits were very good.

From the results in Figure III- 18, show that the %DOD and width of the pulse affected the apparent rate of resistance increase and the apparent mechanism of the increase. The rate law changed from linear-with-time to a mixed, linear-parabolic mechanism when the measuring point was changed from 50% to 80% DOD. Needless to say, the life estimates were also affected. The life estimate decreased from 537 to 189 days upon changing from 50% to 80% DOD.

Based on these results, differences in the protocols directly affected the data and the performance decline mechanisms deduced from the data. The testing protocols produced very similar data when the testing conditions and metrics used to define performance were similar.

Conclusions and Future Directions

Testing has been shown to be a useful way to gauge the state of a developer's technology and to estimate the life of a battery.

For the future, we plan to:

- Continue testing HEV contract deliverables

- Aid in refining standardized test protocols
- Upgrade and expand test capabilities to handle increase in deliverables
- Complete the fast-charge experiment
- Explore other possibilities for test protocol comparison and, perhaps, standardization with Europe, Japan and China

List of Abbreviations

HEV: hybrid electric vehicle

PHEV: plug-in hybrid electric vehicle

EV: electric vehicle

LEESS: Low-Energy Energy Storage System

12 V SS: 12-V start-stop vehicle

USABC: United States Advanced Battery Consortium (DOE, GM, Chrysler and Ford)

SOC: state of charge

ANL: Argonne National Laboratory

INL: Idaho National Laboratory

CATARC: China Automotive Technology and Research Center

FY 2015 Publications/Presentations

1. 2015 AMR Presentation
2. “Effect of Fast Charging on Lithium-Ion Cells: Performance and Post-test Results,” L. Somerville, P. Prezas, J. K. Basco, T. Duong and I. Bloom, International Battery Association-Pacific Power Sources Symposium, January 5-9, 2015, Kona, HI.
3. “Effect of Fast Charging on Lithium-Ion Cells: Performance and Post-test Results,” I. Bloom, L. Somerville, P. Prezas, J. K. Basco, and T. Duong, Department seminar, Illinois Institute of Technology, January 14, 2015.
4. “Effects of Fast Charging on Lithium-Ion Cells,” I. Bloom, P. Prezas, J. K. Basco, L. Somerville and T. Duong, 249th ACS National Meeting & Exposition, March 22-26, 2015, Denver, CO.
5. “A Comparison of US and Chinese EV Battery Testing: An Interpretation,” I. Bloom, D. Robertson, J. Christophersen, T. Bennett, F. Wang and S. Liu, 10th US-China EV and Battery Technology Workshop, Beijing, China, March 28-30, 2015.
6. “Battery Testing and Life Estimation at Argonne National Laboratory,” Lee Walker, David Robertson, Panos Prezas, John Basco and Ira Bloom, Tech-to-Market Workshop, Idaho Falls, ID, May 18-20, 2015.
7. “Effects of Fast Charging On Lithium-Ion Cell, L. Somerville,” P. Jennings, A. McGordon, C. Lyness, P. Prezas, J. K. Basco, J. Baren, T. Duong and I. Bloom, 227th ECS Meeting, Chicago, IL, May 24-28, 2015.

References

1. FreedomCAR Battery Test Manual for Power-Assist Hybrid Electric Vehicles, DOE/ID-11069, October 2003.
2. FreedomCAR Battery Test Manual for Plug-In Hybrid Electric Vehicles, June 2010.
3. Electric Vehicle Battery Test Procedures Manual, Revision 2, January 1996.
4. National Development and Reform Committee of the People’s Republic of China, 2006, Lithium-Ion Batteries for Electric Vehicles, Auto Industry Standard QC/T 743-2006, China Plan Publishing Company, March, http://www.d1ev.com/uploadfile/newsfile/20130819022042_547.pdf (in Chinese).

III.B.2 Electrochemical Performance Testing (INL)

Objectives

- Provide high fidelity science-based performance and life testing, analysis, modeling, reporting, and other support related to electrochemical energy storage devices under development by the Department of Energy's Vehicle Technologies Program.
- Develop test methodologies and analysis procedures for various alternative vehicle applications in conjunction with the U.S. Advanced Battery Consortium (USABC).

Technical Barriers

The successful adoption of cost-effective, safe, reliable and environmentally sustainable alternative electrified powertrain vehicles remains a challenge. Performance and life testing of electrochemical energy storage devices such as Li-ion batteries for transportation applications in a controlled, laboratory environment is a critical component of DOE's mission to support the development of electric drive vehicle and component technology. Battery testing at the Idaho National Laboratory (INL) addresses all of the primary technical barriers: performance, life, cost, abuse tolerance and reliability. Accumulated test data are useful to gauge battery capability relative to the established USABC targets as a function of aging as well as for developing battery life and cell-to-cell error models for advanced life and health prognostic tools. Performance and life testing are also useful for battery manufacturers as they develop lower-cost systems that can still meet the established targets. Finally, fresh and aged test articles are useful for abuse testing and thermal analysis in collaboration with other national laboratory efforts.

Technical Targets

- Battery performance and life testing in FY15 at INL focused on evaluating performance for multiple programs out of the DOE-EERE Vehicle Technologies Office. These include programs associated with USABC, FOA-2011, FOA-ARRA and the Applied Battery Research (ABR) program. Performance evaluation centered on the ability of programs to meet USABC technical targets for Plug-in Hybrid Electric Vehicles (PHEV), Electric Vehicles (EV), Low-Energy Energy Storage Systems (LEESS), 12 V Start/Stop (12V S/S), and power-assist Hybrid Electric Vehicles (HEVs). Additionally, work focused on providing support for other electrochemical energy storage programs which fell under the ABR umbrella.
- Technical targets for each of these automotive applications are available in the published manuals located on the USABC website (http://www.uscar.org/guest/article_view.php?articles_id=8).

Accomplishments

- Performance and life testing for USABC Programs:
 - 166 cells
 - 3 packs
- Performance and life testing for Benchmark Programs:
 - 46 cells
 - 12 modules

Project Details

Matthew G. Shirk

Idaho National Laboratory
P.O. Box 1625
Idaho Falls, ID 83415
Phone: 208-526-2132 Fax: 208-526-3150
E-mail: eric.dufek@inl.gov

Eric J. Dufek
Jon P. Christophersen
Christopher J. Michelbacher
Sergiy V. Sazhin
Lee K. Walker

INL Contract Numberf: DE-AC07-051D14517

Start Date: September 2006
Projected End Date: Open Contract

- Performance and life testing for FOA-2011 Programs:
 - 69 cells
- Performance and life testing for FOA-ARRA (American Recovery and Reinvestment Act) Programs:
 - 18 cells
- Performance and life testing for Applied Battery Research Programs:
 - 48 cells
- Published Revision 3 of the Battery Test Manual for Electric Vehicles (June 2015).
- Published Revision 1 of the 12V Start/Stop Vehicle Manual (May 2015).

Introduction

Advancing alternative electrified powertrain transportation, such as of EVs, HEVs and PHEVs, is a top priority within the Department of Energy (DOE) given its potential to reduce US dependency on oil. The INL Battery Test Center (BTC) is a world leader in science-based performance testing and assessment of advanced electrochemical energy storage technologies, primarily for automotive applications. It has been designated by DOE as a core capability and the lead test facility for USABC activities. The development of batteries and other energy storage devices requires validation testing from an independent source to accurately characterize the performance and life capability against the established USABC technical targets for EVs, HEVs, PHEVs, and other electric drive system applications.

Approach

High quality testing, validation, and analysis of electrochemical energy storage systems are critical for the successful adoption of alternative vehicles. The INL BTC has over 20,000 square feet of laboratory space and is equipped with over 700 test channels for advanced energy storage testing at the cell-level (e.g., up to 7V, 300A), module-level (e.g., up to 65V, 250A), and pack-level (e.g., 500-1000V, 500A). The test equipment can be programmed to perform any test profile while simultaneously monitoring constraints such as voltage, current and temperature limits. Batteries and other energy storage devices are typically subjected to a test sequence while housed inside thermal chambers to ensure consistent and repeatable results. To enhance testing and modeling capabilities the thermal chambers have a broad temperature range (e.g., -70 to 200°C).

Successful performance testing and accurate life modeling are highly dependent on the accuracy of the acquired test data. The INL BTC has developed advanced calibration verification and uncertainty analysis methodologies to ensure that the voltage, current, and temperature measurements are within the tolerance specified by the manufacturer (e.g., 0.02% of the full scale). These measured test parameters are subsequently used in various mathematical formulations to determine performance capability (e.g., resistance, energy, power, etc.). INL has also quantified the error associated with these derived parameters using the accuracy and precision of the relevant measured parameter (e.g., voltage) to ensure high-quality and repeatable results.

The INL BTC capability has also been enhanced with additional equipment for advanced characterization of battery technologies. For example, a Ling Dynamic Systems V8-640 SPA56k shaker table (installed in FY 13) is ready to provide select USABC Programs with non-destructive reliability and system robustness testing. Unconventional and untested cell designs are key drivers behind the interest in using a vibration system to perform mild abuse testing at INL. The shaker table is equipped with both safety shielding and thermal control chambers and is co-located with battery test equipment to allow performance testing immediately before and after vibrational assessment has occurred.

Results

INL Testing Activities. The INL BTC continues to test articles of various sizes and configurations using standardized test protocols. Table III- 9 and Table III- 10 summarize the testing activities under the USABC and Benchmarking Programs, respectively, for FY 15. The purpose of the USABC testing activities is to evaluate a candidate technology against specified targets (EV, HEV, PHEV, etc.) and, where applicable, previous generations of test articles from the same manufacturer. The purpose of the Benchmark Program is to evaluate devices that do not have existing contracts in place, but have technologies that are of interest to the

DOE VTO. At times, a Benchmark Program is also used to validate newly developed test procedures and analysis methodologies.

Table III- 9: Testing activities under the USABC Program

Manufacturer	Type	# of Articles	Application
LG/CPI	Cells	5	HEV
	Cells	36	PHEV
	Packs	3	PHEV
Envia	Cells	20	EV
K2	Cells	8	EV
Saft	Cells	13	HEV
	Cells	27	12V S/S
Maxwell	Cells	8	LEESS
Entek	Cells	36	PHEV
Leyden	Cells	13	EV

Table III- 10: Testing activities under the Benchmark Program

Manufacturer	Type	# of Articles	Application
Shandong WINA	Cells	3	EV
Axion	Modules	12	HEV
Hydroquebec	Cells	13	HEV
Sanyo	Cells	10	PHEV
EIG	Cells	20	12V S/S

Table III- 11 and Table III- 12 summarize the INL testing activities under the FOA-2011 and FOA-ARRA Programs, respectively, for FY 15. The FOA-2011 (i.e., 2011 Advanced Cells and Design Technology for Electric Drive Batteries awards) focuses on developing high performance cells for electric drive vehicles that significantly exceed existing technology, in regards to both cost and performance. Technologies addressed include EV, PHEV, and HEV applications; the INL focus in FY 15 was on PHEV cells (75 cells with advance materials were evaluated). The FOA-ARRA (i.e., 2009 Electric Drive Vehicle Battery and Component Manufacturing Initiative) focuses on battery and battery material manufacturing plants and equipment for advanced vehicle batteries.

Table III- 11: Testing activities under the FOA-2011 Program

Manufacturer	Type	# of Articles	Application
Miltec ANL	Cells	9	PHEV
Nanosys	Cells	8	PHEV
PSU	Cells	16	PHEV
Applied Materials	Cells	20	PHEV
Ampruis	Cells	16	PHEV

Table III- 12: Testing activities under the FOA-ARRA Program

Manufacturer	Type	# of Articles	Application
LG Chem	Cells	5	PHEV
Enerdel	Cells	5	PHEV
Saft	Cells	4	EV/HEV
	Cells	4	EV/HEV

The INL BTC tested a total of 362 devices in FY 15, including 347 cells, 12 modules, and 3 packs. Table III-13 summarizes the anticipated INL testing activities for FY 16, including cells from the Applied Battery Research (ABR) Program (Table III- 14). USABC and Benchmark Program testing on existing deliverables are expected to continue and new USABC deliverables will be added as well, including LG/CPI 12V S/S, LG/CPI EV, Envia EV, Amprius EV, and possibly Saft 12V S/S. For the FOA-2011 Program, INL expects to test three generations of deliverables from each awardee. For each program it is anticipated that test procedures, as defined in INL authored test manuals, will be used including the use of reference performance tests (RPTs) which typically include static capacity tests and cycle life testing, along with high and low temperature capacity testing.

Table III- 13: Anticipated testing activities for FY16

Program	Type	Manufacturer
USABC	Cells	LG/CPI, Envia, Leyden, Entek, Saft, Amprius, Dreamweaver, NOHMs, CoorsTek
Benchmark	Cells	Hydroquebec, Sanyo, EIG, Toshiba
ABR	Cells	ANL, Envia, Farasis, PSU
FOA-2011	Cells	Miltec ANL, Amprius, Applied Materials, Nanosys, PSU

Applied Battery Research Program. The purpose of ABR is to assess core performance, cycle life and accelerated calendar life of advanced lithium-ion cell chemistries. Table III- 14 summarizes the INL ABR testing activities in FY 15. Testing is underway on the baseline cell chemistries with interim deliverables scheduled to be shipped to INL in early FY 16. The testing will benchmark the performance capability of the cells relative to the established PHEV-40 or EV targets. A total of 12 cells will be subjected to life testing, with 3 cells undergoing cycle-life aging at 30oC and nine cells undergoing calendar-life aging (3 each at 30, 40, and 50°C). All cells are initially characterized with constant current discharges at the C1/1, C1/2 and C1/3 rates, an HPPC test, a 48-hr stand test, and impedance spectroscopy measurements. During life testing, the cells are periodically interrupted by RPTs at 30°C to track degradation rates compared to the targets.

Table III- 14: Testing activities under the ABR Program

Manufacturer	Type	# of Articles	Application
Envia	Cells	12	PHEV
Farasis	Cells	12	EV
PSU	Cells	12	EV
ANL	Cells	12	EV

Life Estimation

Understanding how testing and life estimation change over extended evaluation of batteries is important as it allows developing better judgement on how long is necessary to test specific battery types. To better understand the relationship between length of test and life estimation, INL performed analysis on a set of NMC/graphite cells which have been testing for a significant amount of time (over 7 years). As part of the testing protocol for this set of HEV cells, RPTs were performed on a set interval. As part of each RPT multiple metrics including capacity fade, resistance growth and power fade were monitored. As an example, Figure III- 19 contains the data associated with the capacity fade following the 67th RPT for cells tested at 30, 40, 50 and 60°C. The trend for each of these temperatures is expected with the most significant decay happening for the higher temperatures and with more modest declines in performance at 30 and 40°C.

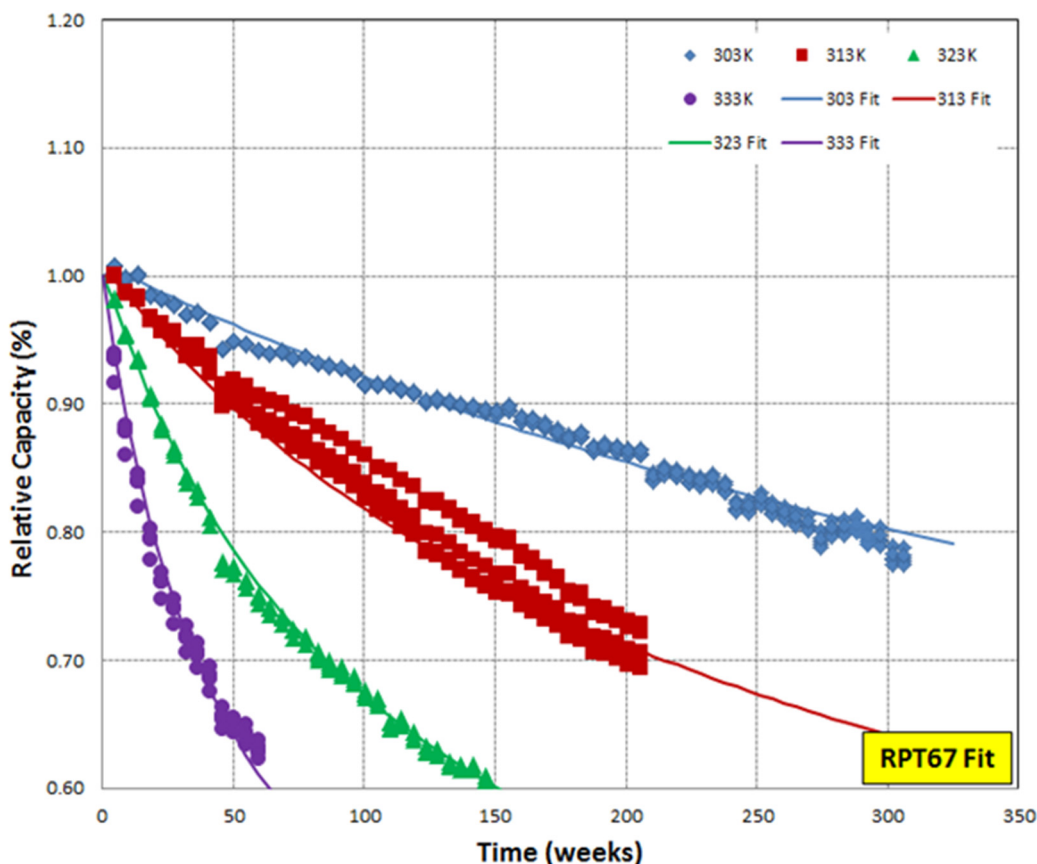


Figure III- 19: Capacity fade as a function of testing length. The solid line represents the BLE fit based on data from RPT 67

In addition to following the performance change as a function of length of cell evaluation, for each RPT a life estimate was calculated using the Battery Life Estimator (BLE). Figure III- 19 also contains the data (solid lines) corresponding to the fit associated with the BLE analysis for the 67th RPT. Plotting life estimates as a function of testing time provides the opportunity to see how life estimates change during performance testing. As seen in Figure III- 20, there is change for all three metrics of interest. The variability in the early testing period quickly diminished for all three metrics with very little change observed after the 15th RPT. This number of tests corresponds with roughly 1.5 years of testing for this specific chemistry. While little change in the estimated life for each of the three metrics is observed following the first 15 RPTs, there is a gradual increase in the confidence of the calculations as indicated by the dashed lines which show the upper and lower bounds of estimated life for a 95% confidence window. Other significant items associated with the BLE analysis include the fact that for this set of cells there is little difference between the life estimates determined using power fade and resistance increase, this is expected due to the close link between the two performance indicators. The data for this chemistry suggest that for effective analysis of anticipated life it is necessary to test sets of batteries a minimum of 15 RPTs to be able to estimate life with any significant level of confidence. The results of this analysis were presented at the Advanced Automotive Battery Conference in June as part of the presentation “Battery Life Modeling-Prediction vs. Results” (INL/CON-15-35145).

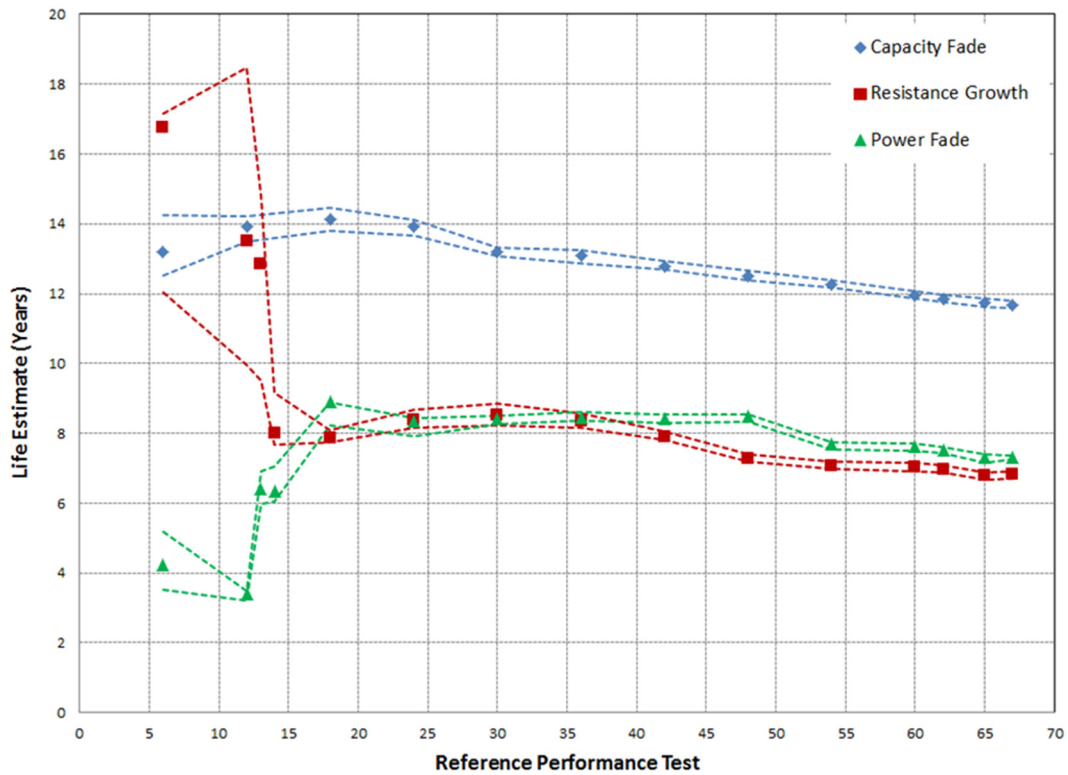


Figure III- 20: Life estimation determined using capacity fade, resistance growth and power fade as a function of aging

Battery Test Manuals

Two separate battery test manuals were published during FY 15. The first, the Battery Test Manual for 12V Start/Stop Vehicles, Revision 1 (INL/EXT-12-26503), was published in May 2015 while the Battery Test Manual for Electric Vehicles (Revision 3, INL/EXT-15-34184) was published in June 2015. The 12V Start/Stop manual underwent minor revisions which were focused on increasing its overall clarity and in maintaining terminology with other manuals including the recently released PHEV manual (released during 2014). The Battery Test Manual for Electric Vehicles, Revision 3 (EV Manual) underwent significant changes, as highlighted below. First and foremost the manual was updated to maintain consistency with other manuals such as the 12V Start/Stop and the PHEV manual. One of the most significant changes which occurred was in how different voltages are defined (Figure III- 21). The change in voltage definitions also changed key tests including the capacity measurement of the Self Discharge test which previously had been performed for the full state-of-charge window. In the new revision of the EV Manual the test only occurs within the operating range defined in Figure III- 21.

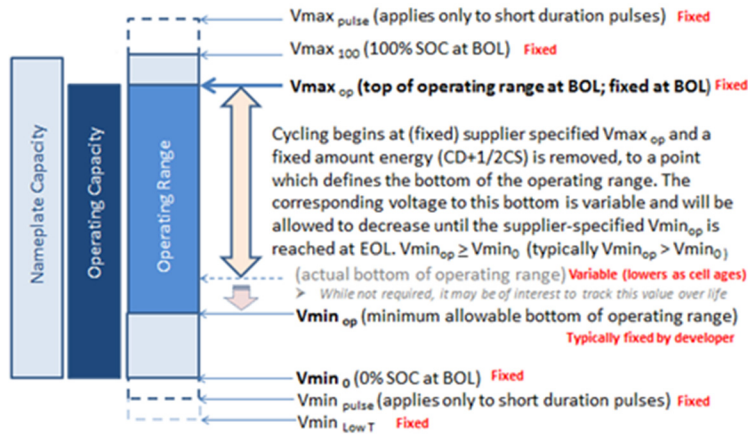


Figure III- 21: New EV Voltage Definitions and Key Concepts

The 3rd revision of the EV Manual also included the addition of a Hybrid Pulse Power Characterization (HPPC) test which includes both a low current and high current option. The low current HPPC is at a C/1 discharge pulse while the high current HPPC is at 75% of the maximum current (I_{max}). In addition to changes in the operating voltages and the addition of the HPPC there were other changes associated with how some of the tests are performed. A few specifics include changing the thermal performance test which saw a change in reference temperature from

25 to 30°C and adjustment of the maximum temperature test from 65°C to 52°C to account for changes in USABC goals. Other changes include the rate at which charge and discharge steps occur for the High Rate Charge test and the cycle life test. While Revision 2 of the EV Manual included RPTs there were changes included in the new Revision 3 which include the removal of the Variable Power Test and the addition of the low-current HPPC test and an HPPC verification test. The new adjustments to the EV Manual bring it into line with other recently published test manuals allowing for an easier transition and comparison across manuals.

Conclusions and Future Directions

Battery performance and life testing is critical for the successful adoption and implementation of advanced alternative vehicles. The INL BTC is a DOE core capability that is well equipped to conduct accelerated aging protocols on battery technologies of various sizes and shapes while ensuring high quality, repeatable results as an independent source of science-based performance assessment for DOE, the automotive industry, and the battery manufacturers. As such, testing on key programs funded through the Vehicle Technologies Office of DOE were conducted. A total of 362 devices were tested in FY 15. In FY 16, INL plans to continue this level of support for multiple programs with broad support for USABC, Benchmarking and the ABR programs in particular. In addition to testing and life modeling, INL will also continue developing and refining standard test protocols and analysis procedures in collaboration with USABC. In particular, a test manual for 48V mild hybrid EVs will be prepared and published during FY16. Additional activities which will be expanded in FY 16 will be in mild abuse testing of key deliverables from USABC programs including the vibrational assessment of new chemistries and cell formats currently being developed.

FY 2015 Publications/Presentations

1. Battery Test Manual for 12V Start/Stop Vehicles, Revision 1(May 2015) INL/EXT-12-26503, INL/EXT-14-32849, May 2015.
2. Revision 3 of the Battery Test Manual for Electric Vehicles (June 2015) INL/EXT-15-34184.
3. “Battery Life Modeling-Prediction vs. Results” Jon P. Christophersen, Eric J. Dufek and Chinh D. Ho, presented at the 2015 Advanced Automotive Battery Conference, Detroit, MI, June 17, 2015 (INL/CON-15-35145).

III.B.3 Battery Safety Testing (SNL)

Objectives

- Serve as an independent abuse test laboratory for DOE and USABC.
- Abuse testing in accordance with the USABC abuse testing manual.
- Successful testing of all deliverables from developers under USABC contracts.
- Revise the USABC abuse testing manual.
- Test the propensity towards propagation of cell failure through multiple cell batteries.
- Provide mechanical testing support to develop and validate mechanical models for EV batteries.
- Evaluate the effect of cell age on abuse response.

Project Details

Christopher J. Orendorff, Joshua Lamb, and Leigh Anna M. Steele

Sandia National Laboratories
P. O. Box 5800, Mail Stop 0613
Albuquerque, NM 87185-0613
Phone: 505-844-5879; Fax: 505-844-6972
E-mail: corendo@sandia.gov

Collaborators:
USABC Contractors/TAC
Ahmad Pesearan, NREL
Eric Dufek, INL
Ira Bloom, ANL

Start Date: October 2014

Projected End Date: September 2015

Technical Barriers

- Abuse tolerance of energy storage devices is identified as a barrier in USABC and DOE battery development programs.
- The failure modes for lithium-ion batteries are complex and need to be evaluated for all types of chemistry, design, packaging and systems for PHEV/EV applications.
- Lack of understanding of how single cell or cell group failures propagate and what the primary drivers are for different battery designs.
- Limited knowledge on how cell level abuse tolerance changes over the age of a cell or battery.

Technical Targets

- Perform abuse testing and evaluation of cells and modules delivered from contractors to USABC.
- Perform failure propagation testing and evaluation.
- Static mechanical testing of cells and batteries and tie to coupled mechanical/thermoelectrochemical models.
- Characterization and analysis of aged cells.
- Report results to DOE, the USABC TAC, and contractors to USABC.

Accomplishments

- Successful testing of cell and module deliverables through USABC contracts including
 - Envia, Entek, Farasis, Cobasys, LG Chem, JCI, Seo, and SKI
- Performed multi-cell pack propagation testing with varying electrical configurations and worked with NREL to model this response.
- Characterized cells aged to >40% capacity fade.
- Delivered a draft revision of the USABC abuse testing manual.

Introduction

Abuse tests are designed to determine the safe operating limits of HEV/PHEV energy storage devices. The tests are performed to yield quantitative data on cell/module/pack response to allow determination of failure modes and help guide developers toward improved materials and designs. Standard abuse tests are performed on all devices to allow comparison of different cell chemistries and designs. New tests and protocols are developed and evaluated to more closely simulate real-world failure conditions.

In scaling from the cell to the battery level, it is important that understanding safety performance includes a detailed understanding of cell-to-cell interactions. Single point failures from a single cell or group of cells can be initiated by a number of triggers including an internal short circuit, misuse or abuse, or a component failure at the battery or system level. Propagation of that single failure event (regardless of the initiation trigger) through an entire battery, system or vehicle is an unacceptable outcome to ensure EV battery safety. Our work focuses on evaluating the propagation of a single cell thermal runaway event through a battery using a variety of cell chemistries and design considerations.

While robust mechanical models for vehicles and vehicle components exists, there is a gap for mechanical modeling of EV batteries. The challenge with developing a mechanical model for a battery is the heterogeneous nature of the materials and components (polymers, metals, metal oxides, liquids). Our work will provide some empirical data on the mechanical behavior of batteries under compressive load to understand how a battery may behave in a vehicle crash scenario. This work is performed in collaboration with the U.S. Council for Automotive Research (USCAR).

Many development efforts directed toward improving safety performance are designed and evaluated using fresh cells. However, it is important to understand how reliable a material or design improvement will be over time or if there is a “tipping point” somewhere along the age of a battery where the intended or expected behavior changes. Our work is directed toward understanding the effects of cell age on the safety performance, thermal stability and abuse tolerance.

Approach

Abuse tolerance tests are performed to evaluate the response to potential abuse conditions.

- Test to failure of energy storage device
- Document conditions that cause failure
- Evaluate failure modes and abuse conditions using destructive physical analysis (DPA)
- Provide quantitative measurements of cell/module response
- Document improvements in abuse tolerance
- Develop new abuse test procedures that more accurately determine cell performance under most likely abuse conditions

Possible tests that can be performed cover three main categories of abuse conditions:

- Mechanical Abuse - Controlled crush, penetration, blunt rod, drop, water immersion, mechanical shock and vibration
- Thermal Abuse - Thermal stability, simulated fuel fire, elevated temperature storage, rapid charge/discharge, thermal shock cycling
- Electrical Abuse - Overcharge/overvoltage, short circuit, overdischarge/voltage reversal, partial short circuit

Batteries for failure propagation evaluation are based on cylindrical 2.2 Ah LiCoO₂ cells and 2.6 Ah LiFePO₄ cells in 1S10P configurations. Cell failure and thermal runaway are initiated by a mechanical nail penetration into a single cell. Batteries for mechanical testing are based on 5Ah LiCoO₂ pouch cells in a 1S12P configuration.

Results

Battery Abuse Testing

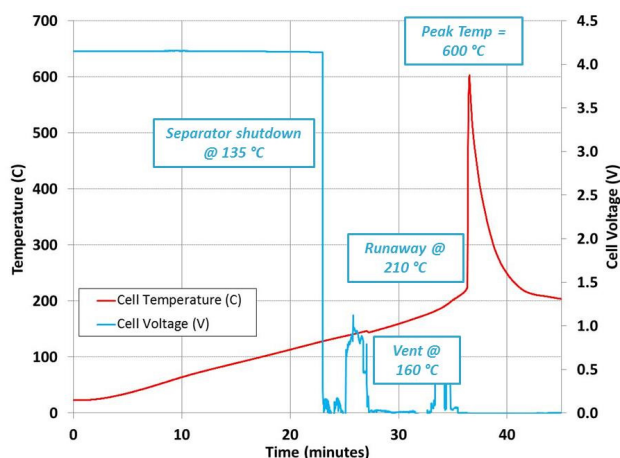


Figure III- 22: Cell temperature and voltage during a thermal ramp test of a COTS 18650 cell

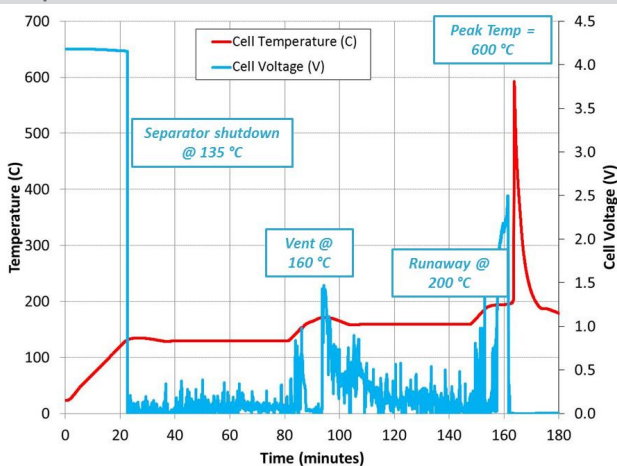


Figure III- 23: Cell temperature and voltage during a modified hotbox test of a COTS 18650 cell

cells to field and abusive failures have been conducted at Sandia, however less attention has been paid to how a battery system responds to the energetic failure of a constituent cell. A single cell failure may be a relatively rare occurrence, but the consequence of that failure can be significant if it propagates through the entire battery. To study this further, we have tested a series of small batteries constructed with COTS cells.

In FY14, we studied the effect of serial and parallel electrical configurations on failure propagation for 2.2 Ah LiCoO₂ cell batteries. In all cases, the failures were initiated by a nail penetration in the axial direction through the cell. We found that single cell failures in parallel configurations were more likely to propagate because in addition to the heat transfer contribution between cells, there is a short circuit current path to the failed cell which dominates the battery response. That short circuit path does not exist in the series configuration. An example of this failure propagation in a 1S10P LiCoO₂ battery is shown Figure III- 24. In this example, the center cell is shorted by a nail penetration which leads to a thermal runaway of that cell. In FY15, we focused on failure propagation through LiFePO₄ batteries using cylindrical 2.6 Ah cells (to closely match the capacity of the 2.2 Ah LiCoO₂ cell experiments).

One important difference between the LiCoO₂ and LiFePO₄ cell behavior is that an axial nail penetration of a single LiCoO₂ cell does result in thermal runaway, but does not do so for the LiFePO₄ cell. This is generally attributed to the more benign reactivity of LiFePO₄, relative to LiCoO₂. In the 1S10P battery configuration (connected with 125 μm thick x 5 mm wide nickel tab), there is sufficient discharge current from the adjacent

The actual USABC testing results are Protected Information and public release is prohibited. However, representative data is shown below for thermal abuse tests of commercial-off-the-shelf (COTS) cells purchased on the open market.

The thermal ramp test described in the current revision of the USABC manual is one where the test article is heated at a constant 5°C/min heating rate. This thermal ramp test of a COTS 18650 cell is shown in Figure III- 22. However, some in the industry favor a modified hotbox test, where the cell is heated and then held as prescribed temperatures. One version of this modified hotbox test performed on a COTS 18650 cell is shown Figure III- 23, where the cell is held at 130, 160, and 190°C intervals.

It is interesting to note that in both data sets, for the same cell, the metrics of abuse response are nearly identical. Both cells show voltage loss at 135°C, venting at 160°C, the onset of thermal runaway between 200-210°C, and a peak temperature of 600°C. While there may be some value in these long temperature soak periods for certain cells or cell components during a modified hotbox test, there does not appear to be any added value for this specific cell. In fact, the USABC thermal ramp test may be a more practical test procedure because it provides the same data in ~1/3 of the test time for this specific cell.

Failure Propagation

A number of studies on the response of single

cells to initiate thermal runaway in the effected LiFePO₄ cell, shown in Figure III- 25. However, failure propagation to surrounding cells does not occur because the short circuit current is limited by the melting of the nickel tab material during the experiment (Figure III- 25, inset). A separate external short circuit test of the 1S10P battery results in a ~1000 A peak discharge current. Melting the nickel tab, interrupts the short circuit current from the adjacent cells and the heat transfer from the initiated cell runaway alone is insufficient to propagate.

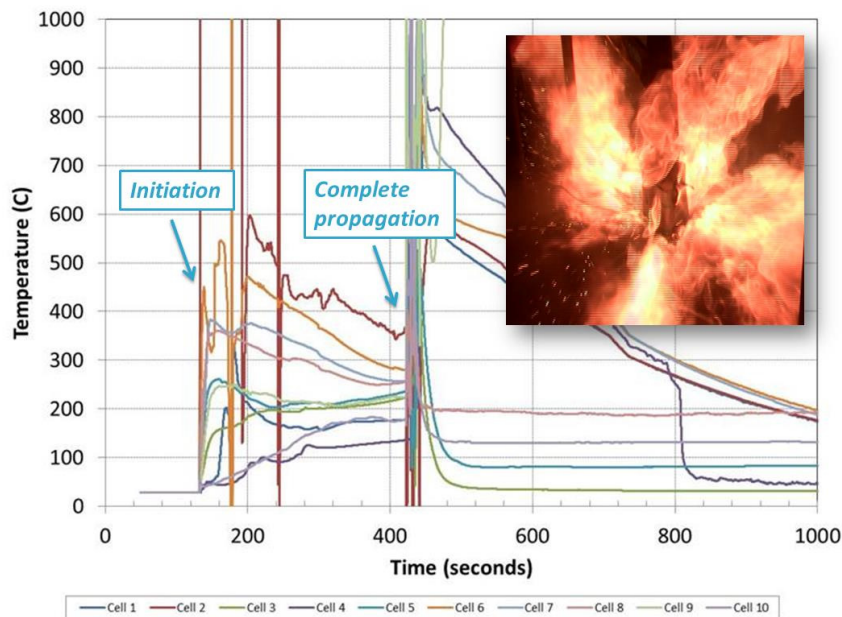


Figure III- 24: Cell temperatures during a propagation test of a 1S10P LiCoO₂ battery

for ~45 minutes. After 45 minutes, the center cell goes into thermal runaway and that failure propagates directly through the entire LiFePO₄ battery.

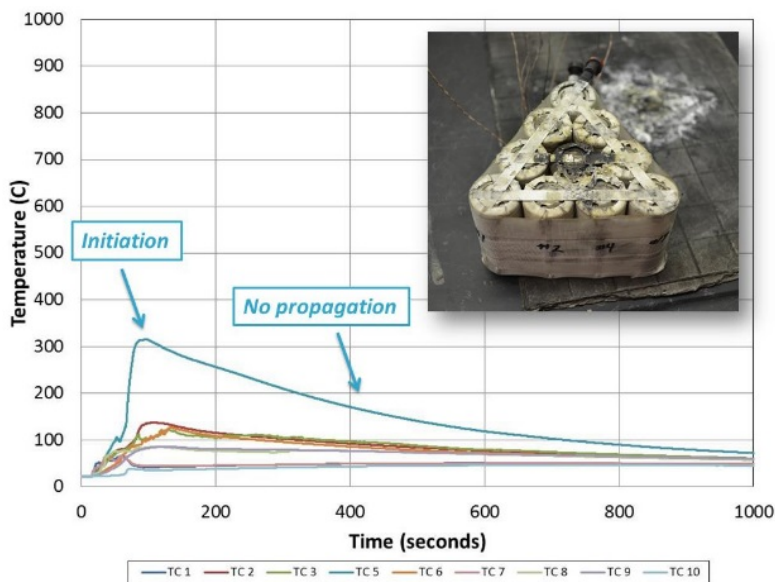


Figure III- 25: Cell temperatures during a propagation test of a 1S10P LiFePO₄ battery with cells connected with Ni tab

especially for chemistries considered to be more benign in their response to abuse conditions and heat transfer alone is not sufficient to propagation a failure event.

LiFePO₄ cells are connected with a more robust copper bus bar, as they might be in a battery configuration, to evaluate whether the sustained short circuit discharge current is sufficient to propagate the single cell failure. Figure III- 26 shows battery voltage and cell temperatures for the propagation test of the 1S10P LiFePO₄ battery where cells are bussed together with a copper bus bar. Nail penetration causes the center cell temperature to increase to ~95°C and is sustained

Failure propagation in LiFePO₄ batteries is more dependent on the short circuit current path than on heat transfer in this example, because the heat release and heat release rate from LiFePO₄ cells during runaway are considerably less than for other lithium-ion cell chemistries. Results suggest the even within the same series/parallel electrical configuration, construction of the battery package to sustain high discharge currents will impact the propagation behavior. This is an important consideration,

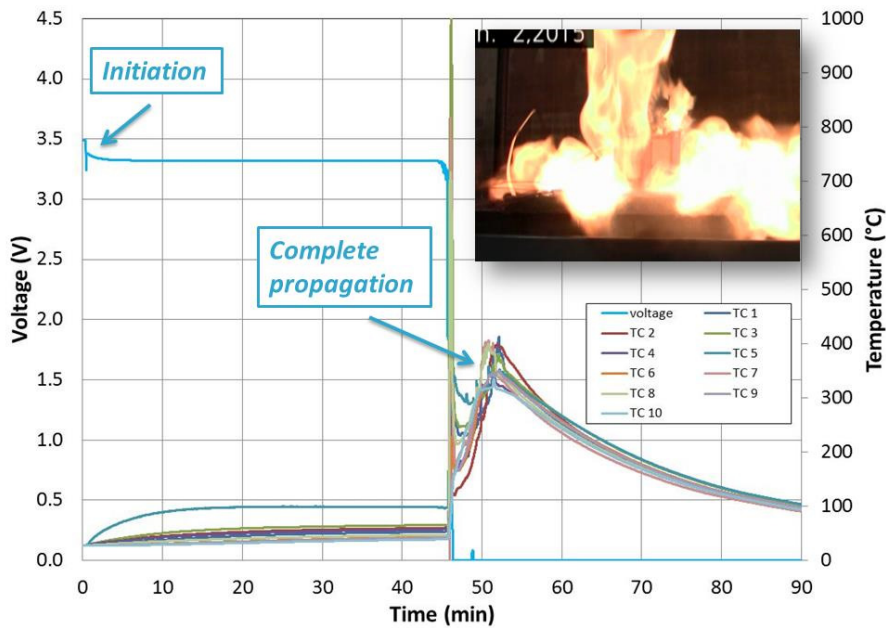


Figure III- 26: Cell temperatures during a propagation test of a 1S10P LiFePO₄ battery with cells connected with a copper bus bar

Mechanical Testing

This project is focused on providing mechanical testing support to the USCAR Crash Safety Work Group (CSWG) to set boundary parameters for mechanical models and to validate predictions made by the numerical models. The testing focus in FY14 was on fully constrained batteries to provide the most well defined experimental data set for the mechanical model. FY15 has focused on working with NREL to support building and validating the mechanical piece of the model. Figure III- 27 shows force and displacement for two replicates of a fully constrained crush experiment of a 12S1P battery (red and blue traces) with a flat plate impactor.

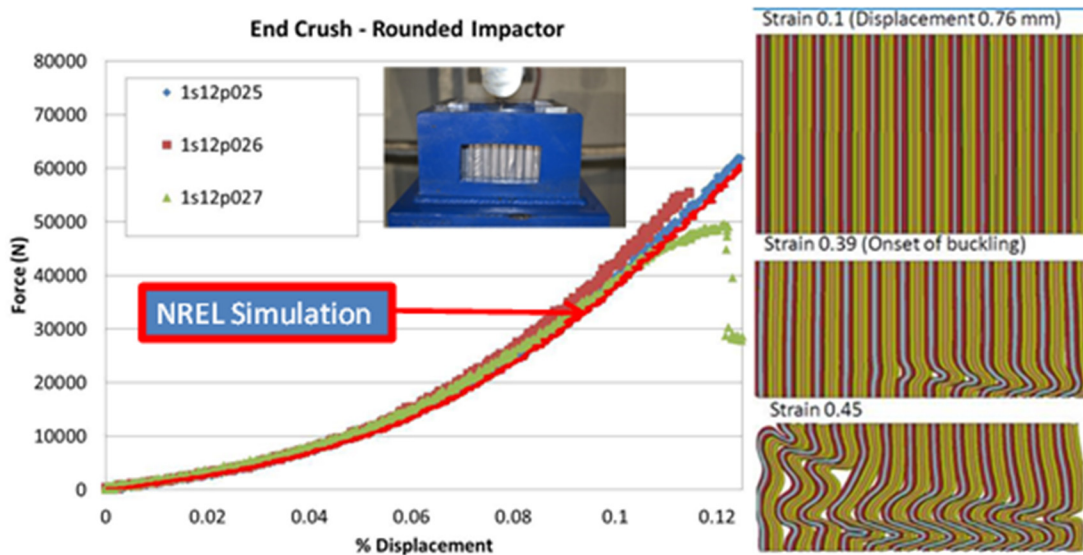


Figure III- 27: (Right) force and displacement during crush tests (red and blue traces) and a crush simulation (orange trace) of a 1S12P battery. (Left) Images from the simulation showing the buckling of the electrode layers in a sandwich model

Also plotted in Figure III- 27 is the first simulation result of this experiment based on a sandwich model (orange trace). While there is some deviation between the experiment and the model, the simulation does capture the electrolyte layer buckling failure mode at the observed peak applied force. Work will continue to use additional cell characterization data to refine the sandwich model followed by validation testing.

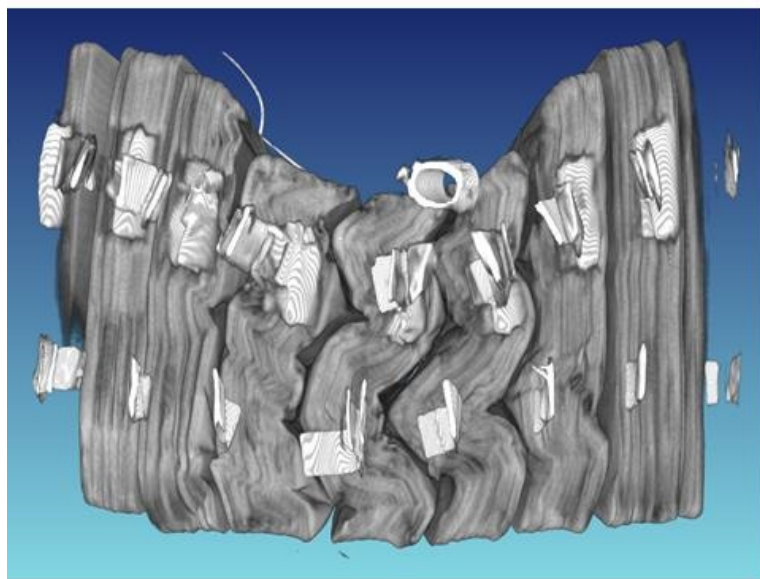


Figure III- 28: Computed tomography image of a 1S12P battery after a crush test using a cylindrical impactor

We have also studied battery crush behavior using cylindrical impactor shapes to emulate a vehicle level side impact pole test (FMVSS 214). Under these different loading conditions, there are more significant deviations between these preliminary simulations and experiments, shown in Figure III- 28 and Figure III- 29. The simulations do not capture the electrode buckling failure observed in the experiments. Refinement of the model and perhaps some additional generic constitutive models are needed to better predict these loading conditions.

Characterization of Aged Cells

While significant attention has been paid to cell performance over time (capacity fade, available power, etc.) there is very little known about how a cell failure, in particular thermal

runaway profiles, may change over time. Moreover, while measurable progress has been made in cell safety and advanced materials, there is surprisingly very little data on whether or not these materials improvements observed at the beginning of life (BOL) will continue to have the same positive benefit as these cells age. This is important not only in understanding cell behavior, but also in designing thermal management controls for battery systems. Since these are designed for new or fresh cells in a battery, we must understand how the runaway response may change over cell lifetime and how cell-to-cell variations in thermal response may change over time and also impact the system response.

Previous calorimetry and abuse testing results on 20% faded cells show only slight differences with the control cells at 100% SOC and significantly greater cell-to-cell variability. In FY15, we studied the abuse response of cells aged to 50% capacity fade. Accelerating rate calorimetry (ARC) measurements were made on aged cells and fresh cells and various depths-of-discharge (%DOD) to determine total energy released (kJ) and maximum heating rate (W). Figure III- 30 shows the total energy released as a function of % capacity fade for aged cells (20 and 50% capacity fade) and %DOD for fresh cells (20 and 50% DOD). Figure III- 31 shows the peak heating rate as a function of % capacity fade for aged cells and %DOD for fresh cells. Results show a linear relationship



Figure III- 29: Sandwich model of a 12S1P battery crush test using a cylindrical impactor

between energy release and both capacity fade and DOD. While the energy released from the 20% faded aged cell and the fresh cell at 20% DOD are relatively close (~20 kJ), the energy released values diverge more significantly at 50% fade and fresh cells at 50% DOD. A similar trend is observed for the peak heating rate with aged and fresh cells at different DODs, however, the relationship is non-linear. It is interesting to note that the reaction kinetics for the fresh cell at 50% DOD are on the order of <10 W which is considerably less than the aged cell to 50% capacity fade (~175 W).

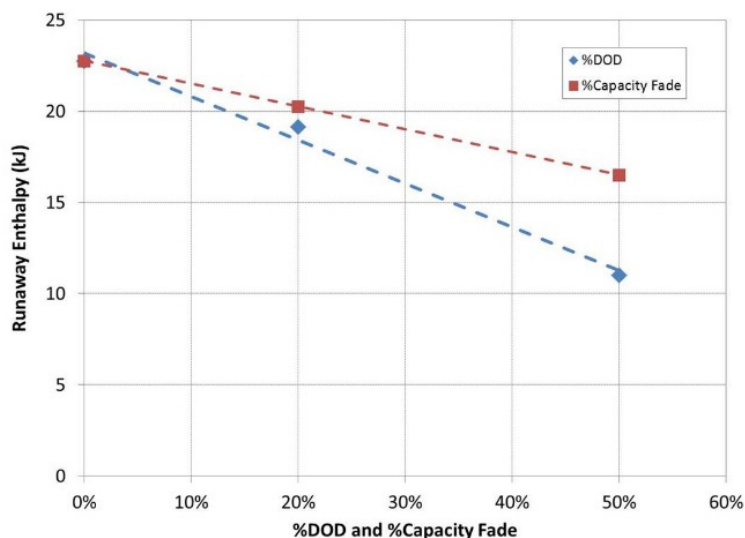


Figure III- 30: Heat released (kJ) as a function of % capacity fade and %DOD for aged and fresh COTS cells

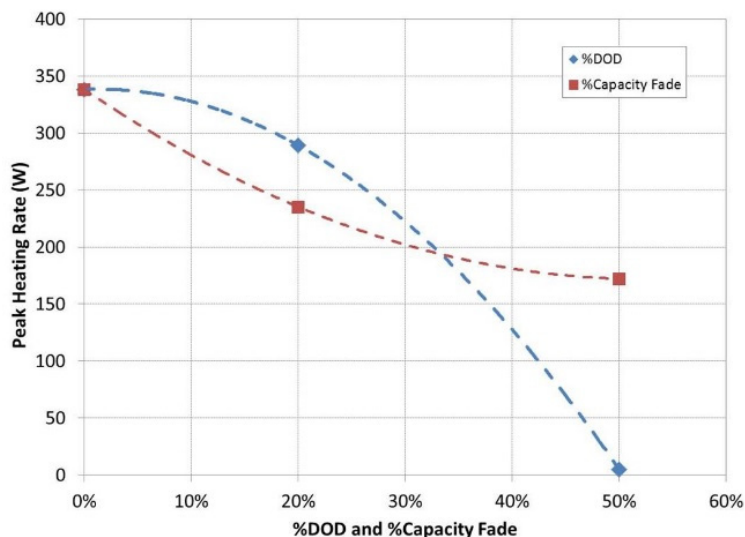


Figure III- 31: Peak heating rate (W) as a function of % capacity fade and %DOD for aged and fresh COTS cells

While the aged cells to 50% fade (at 100% SOC) and fresh cells at 50% DOD (50% SOC) have the same effective capacity, the chemical structure of the active materials and the interfaces are likely to be very different. For example, aged cells to 50% capacity fade at 100% SOC are measured at 4.2 V, which is a much higher potential than the fresh cells at 50% SOC measured at ~3.6 V. It is also likely that there is more electrochemically inaccessible lithium intercalated in the anode or in the anode SEI of the aged cell that does not contribute to capacity, but does contribute to a higher energy released and peak heating rate during runaway.

Conclusions and Future Directions

Testing continues on larger format, higher energy density cells and modules for USABC cell developers. This work requires careful control and monitoring of tests with the potential for significant energy release. Testing results have provided critical information to cell developers to aid in the development of increasingly abuse tolerant cell chemistries and module designs. This independent testing is also necessary to attain objective evaluations of these various designs and chemistries by the DOE and US automobile manufacturers. Testing will continue in FY16 on new module and cell designs from USABC contractors.

Work on failure propagation highlights the contributions of battery configuration and the effect of cell chemistry to the ability of a single point failure to propagate through a battery. Moreover, this work also emphasizes the fact that cell-level abuse testing may not be representative of the behavior at higher order levels of assembly (module or pack). Abuse testing at the module or pack level is important to get an accurate representation of the energy storage system response to an abuse condition. Our initial effort at modeling the propagation behavior shows good agreement with experimental results. Future work on this project will focus on passive design changes, active temperature management, and the development of refined simulations (in collaboration with NREL). The intent is that the modeling work will lead a predictive capability.

Mechanical testing of batteries under well-controlled experimental conditions provides baseline input parameters to for existing sandwich and generic constitutive mechanical models for batteries. Future work will focus on dynamic (high impact rate) testing and experiments to validate mechanical models.

Cells aged to 50% capacity fade show a measureable reduction in the thermal runaway reactivity, relative to fresh cells at 0% DOD (100% SOC). However, the thermal runaway behavior of fresh cells at 50% DOD is significantly different than aged cells to 50% capacity fade (at 0% DOD) because of the fundamental differences in the structure, chemical potential and interfacial chemistry of the two types of cells. Future directions for the aged cell abuse response work includes characterization of the aged cell materials to deconvolute active material contributions to the abuse response and numerical analysis of the aged cell data to better understand the observed cell-level trends.

FY 2015 Publications/Presentations

1. C. J. Orendorff et al. “Failure Propagation in Multi-Cell Batteries” SAND2014-17053, October 2014.
2. C. J. Orendorff et al. “Abuse Testing Update” USABC TAC, Southfield, MI, November 2014.
3. C. J. Orendorff et al., “Quantifying Thermal Runaway by Battery Calorimetry and Opportunities for Improvement” IAPG Safety Panel, San Diego, CA, February 2015.
4. J. Lamb et al. “Failure Propagation in Multi-Cell Lithium Ion Batteries” J. Power Sources 283 (2015), 517-523.
5. C. J. Orendorff et al. “Abuse Testing Update” USABC TAC, Southfield, MI, February 2015.
6. C. J. Orendorff et al., “Advancing Battery Safety through Materials Development and Testing” Next Generation Batteries 2015, San Diego, CA, April 2015.
7. J. Lamb et al. “Safety Testing Challenges for Grid-Scale Energy Storage Systems” Next Generation Batteries 2015, San Diego, CA, April 2015.
8. C. J. Orendorff et al. “Abuse Testing Update” USABC TAC, Southfield, MI, May 2015.
9. C. J. Orendorff et al. “Battery Safety Testing” DOE VTO Energy Storage Annual Merit Review, Washington D. C., June 2015.

III.B.4 Battery Thermal Analysis and Characterization Activities (NREL)

Objectives

- Thermally characterize battery cells and evaluate thermal performance of battery packs delivered by USABC developers.
- Provide technical assistance and modeling support to US Drive /USABC and developers to improve thermal design and performance of energy storage systems.
- Quantify the impact of temperature and duty-cycle on energy storage system life and cost.

Technical Barriers

- Decreased battery life at high temperatures.
- High cost due to an oversized thermal management system.
- Cost, size, complexity, and energy consumption of thermal management system.
- Decreased performance at low temperatures.
- Insufficient cycle life stability to achieve the 3,000 to 5,000 “charge-depleting” deep discharge cycles.

Technical Targets

- Quantify that battery operate from -30°C to 52°C without degradation in performance or life.
- Develop a high-power battery technology exceeding 300,000 cycles.
- Minimizing cost of battery thermal management system.
- Achieve 15-year calendar life at 30°C.

Accomplishments

- Obtained cells from various USABC battery partners including Johnson Controls Incorporated (JCI), LGCPi, SK Innovation, Leyden, Saft, and Seeo
- Obtained infrared thermal images of cells provided by USABC battery developers and identified any areas of thermal concern
- Used NREL’s unique calorimeters to measure heat generation from cells and modules under various charge/discharge profiles in order to design the appropriate thermal management system
- Obtained thermal and electrical performance data of cells under HEV, PHEV, and EV power profiles
- Determined that the energy efficiency of most titanate lithium-ion cells is above 96%
- Presented results of cell thermal characterization and pack thermal evaluation at USABC/battery developers review meetings.

Project Details

Brian Cunningham (DOE Program Manager)
DOE Agreement # 28883 Recipient: National Renewable Energy Laboratory

Matthew Keyser (NREL)
15013 Denver West Parkway
Golden, CO 80401
Phone: 303-275-3876; Fax: 303-275-4415
Email: matthew.keyser@nrel.gov

Partners: USABC, JCI, LG CPI, SK Innovations, Saft, Envia, Seeo, and Leyden

Start Date: October 2009

Projected End Date: September 2018

Introduction

The operating temperature is critical to achieving the right balance between performance, cost, and life for both Li-ion batteries and ultracapacitors. NREL has developed unique capabilities to measure the thermal properties of cells and evaluate thermal performance of battery packs (air- or liquid-cooled). NREL also uses its electrothermal finite element models to analyze the thermal performance of battery systems in order to aid battery developers with improved thermal designs.

Approach

NREL's calorimeters and infrared thermal imaging equipment were used to obtain thermal characteristics (heat generation, heat capacity, and thermal images) of batteries and ultracapacitors developed by USABC battery developers and other industry partners. NREL supports the Energy Storage Technical Team by participating in various work groups such as the JCI, LGCPI, SK Innovations, Leyden, Saft, and Seo USABC Working Groups.

Results

Calorimeter Testing

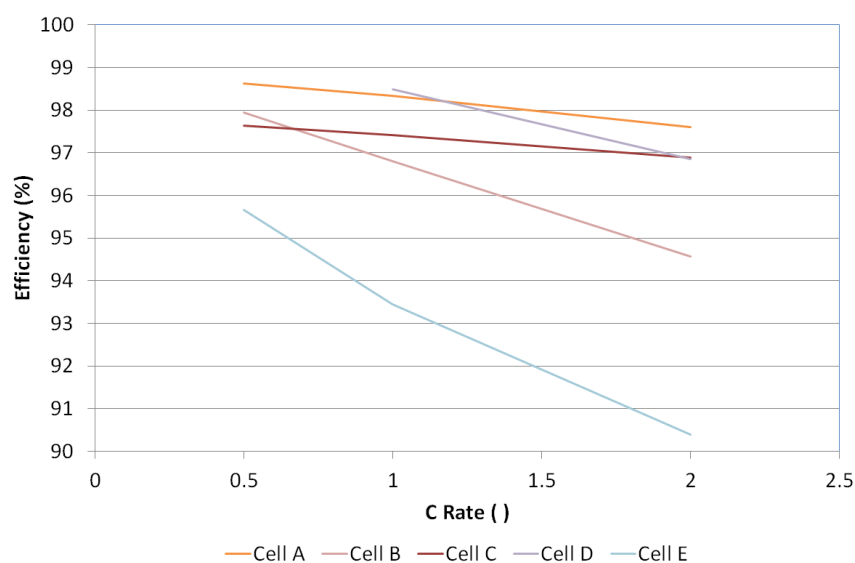


Figure III- 32 shows the efficiency of cells tested in FY15 at NREL at a calorimeter temperature of 30°C. The lithium-ion cells were fully discharged from 100% SOC to 0% SOC under C/2, C/1, and 2C currents. It should be noted that the cells in the figure represent both power and energy cells and have been developed for the HEV, PHEV, EV, and/or the 12 Volt Start/Stop programs within USABC. The figure shows that most of the lithium-ion cells, A- D, are very efficient over this cycling regime – typically greater than 94% for a 2C

Figure III- 32: Efficiency of cells tested at 30°C in NREL's calorimeter during FY15

discharge. The range of efficiencies at a 2C discharge rate is between 90% and 98%. An 8% difference in efficiency may not appear to be of serious concern; however, if a 50-kW pulse comes from the battery in an electrified advanced vehicle, then a 1% difference in efficiency results in an additional 500 W of power for the pulse duration. Taking the example further, an 8% difference results in 4,000 W of additional power. The efficiency differences between the cells will require the thermal management system to be tailored to the cell thermal characteristics so as not to affect the cycle life of the cells. Finally, Cell E shows a fairly low efficiency as compared to many of the other cells tested in FY15 and is an experimental chemistry. DOE and USABC are developing these new chemistries to realize energy density, power density, cycle life, and/or cost benefits. NREL's calorimeter is used to identify these outliers, but can also help determine if the inefficiency is due to chemistry or cell design.

During FY15, NREL tested a number of lithium titanate oxide (LTO) anode cells in its calorimeter. The efficiencies of these cells were typically the highest of the cells tested over the past three years for DOE/USABC. Figure III- 33 shows the charge and discharge efficiency of an LTO cell under a full charge/discharge from 100% ↔ 0% SOC. Of note, the charge efficiency of the cell is greater than the discharge efficiency—different from the typical graphite systems. The LTO anode has a very ordered structure with high surface area, which leads to the high efficiency under charge.

Figure III- 34 shows the charge efficiency of an LTO cell under a full charge from 0% to 100% SOC and also a partial charge from 20% to approximately 100% SOC. As can be seen from the graph, the full charge efficiency is slightly better than the partial charge efficiency—once again, an atypical result when compared to graphite systems. The reported efficiency numbers represent an average over the entire test range and the LTO cells are very efficient in accepting lithium ions at low SOC—thus, the charge efficiency over the full range is better than the partial range.

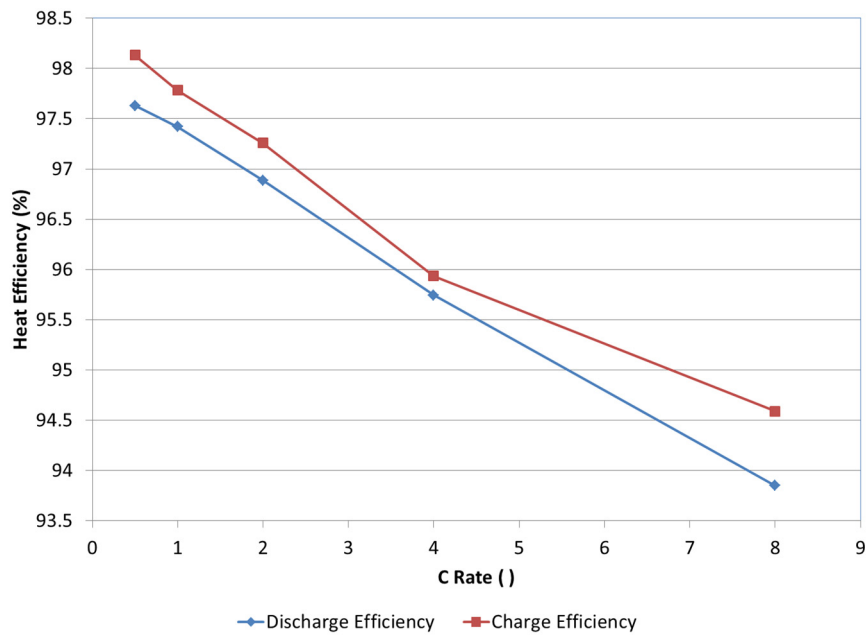


Figure III- 33: Efficiency of LTO cell tested at 30°C under a full charge/discharge

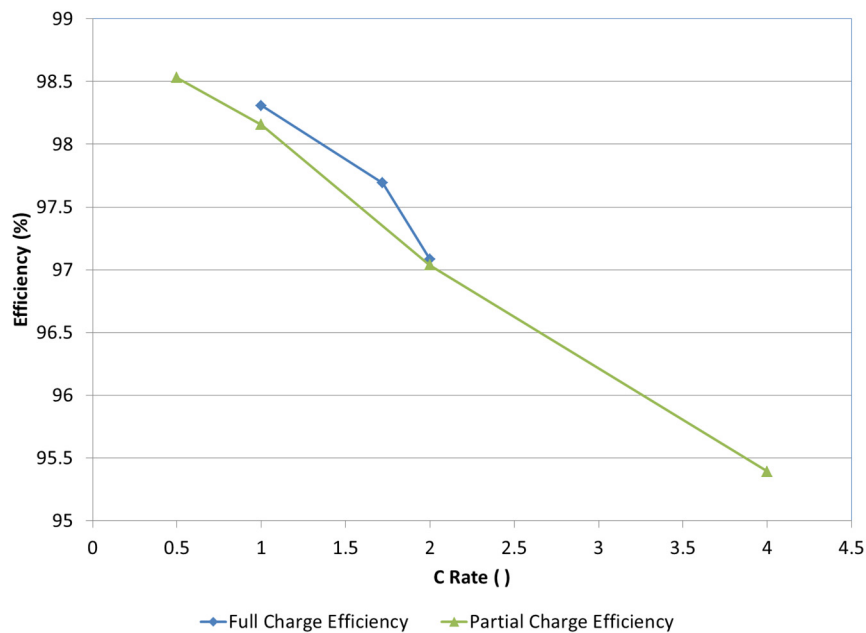


Figure III- 34: Efficiency of LTO cell tested at 30°C under a full and partial charge

Figure III- 35 shows the efficiency of an LTO cell under a constant current discharge from approximately 100% to 20% SOC. As noted above, the efficiency of LTO cells are quite high when tested at 30°C—for the cell in Figure III- 35, above 97% at a 2C rate. However, the cell decreases in efficiency as the temperature is lowered. The efficiency drops about 1.5% for a given discharge rate when the temperature is lowered from 30°C to 0°C. In contrast, the efficiency drops precipitously to 87% at a 2C rate when the cell is tested at -15°C.

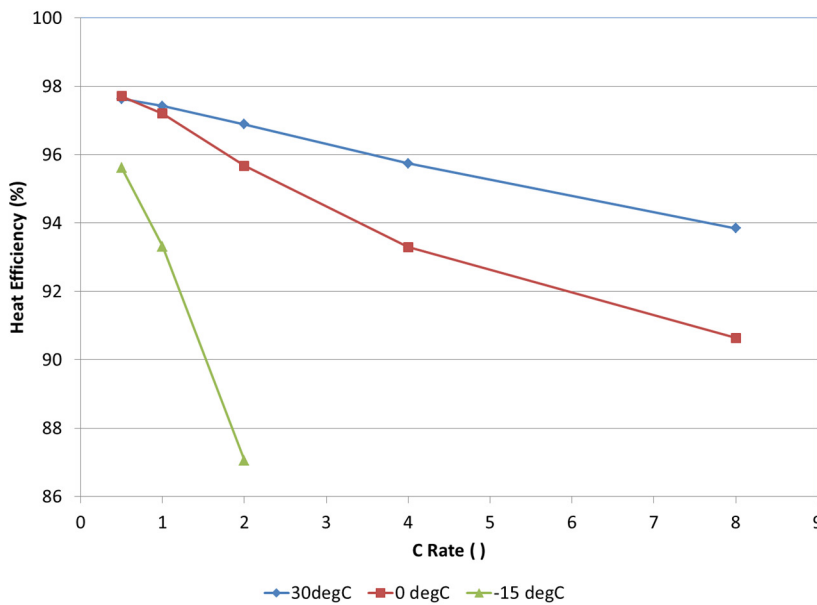


Figure III- 35: Efficiency of LTO cell at different temperatures under a partial discharge

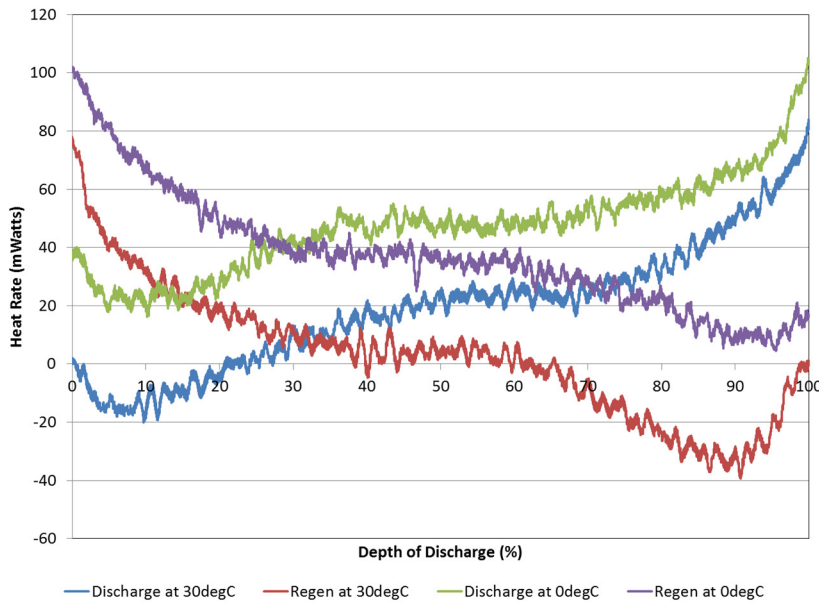


Figure III- 36: Entropic heating of LTO cell at 30°C and 0°C

NREL’s calorimeters are designed to be accurate enough to measure the electrochemical response from batteries under test. As car manufacturers progress from HEVs to PHEVs and EVs, the design of the battery pack will also change. For instance, an HEV battery pack is cycled within a very narrow band—typically within a window encompassing 10% of the overall energy window of the pack. In contrast, a PHEV and EV battery is typically cycled over a much wider range—80 to 90% of the battery’s capacity. Figure III-36 shows the heat rates of an LTO cell tested at 30°C and 0°C. The battery in this figure was cycled from 100% SOC to 0% SOC at a very low current—minimizing the current decreases joule heating of the cell and allows for the entropic heat signature to be assessed. As shown in the figure, the battery undergoes endothermic and exothermic heat generation over the cycling range. The primary differences in the heat signatures from 30°C to 0°C are primarily due to the resistance changes within the cell. The LTO cells do not have as many phase transitions as their graphite counterparts, which should positively affect the life of the cell.

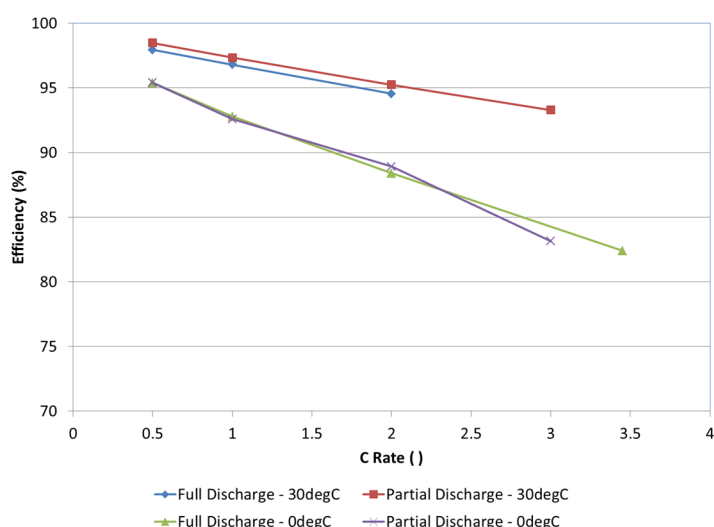


Figure III- 37: Efficiency comparison of PHEV/EV cell under full and partial discharge

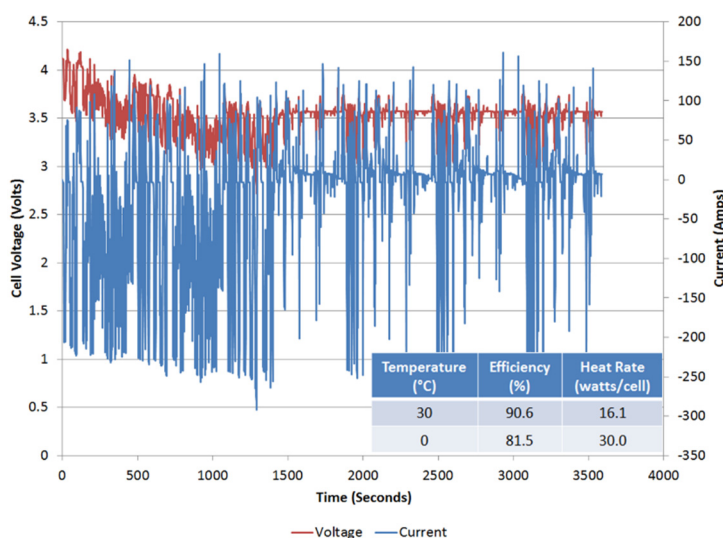


Figure III- 38: PHEV cell heat generation under US06 drive cycle

sustaining cycle. The average efficiency over this usage profile is approximately 90.6% at 30°C. However, the efficiency drops to 81.5% for the same profile as the temperature is lowered to 0°C. The data provided by the calorimeter will allow the battery manufacturer and OEM to size the active thermal management system so as to limit the maximum operational cell temperature while ensuring that the battery pack meets their cycle life specifications.

Infrared Imaging of Cells

NREL performs infrared (IR) thermal imaging of battery manufacturers’ cells to determine areas of thermal concern. It conducts IR thermal imaging under a set of prescribed procedures and environments to minimize the error from different sources such as reflective cell surfaces, radiation from surrounding surfaces, and cooling from the power cables attached to the cell. NREL combines the IR imaging equipment with a battery cycler to place the cells under various drive cycles, such as a US06 charge depleting cycle for a PHEV, to understand the temperature differences within the cell. We then make recommendations to the battery manufacturers and USABC on how to improve the thermal design of the cell to increase its cycle life and safety.

Over the past several years, our testing has shown that the difference in efficiency over the full SOC range as compared to the usage SOC range has decreased for PHEV and EV cells. NREL typically discharges cells under a constant current from 100% to 0% SOC for comparison purposes against other cells. However, cells are not typically used over their full capacity range due to life cycle limitations of the cell. Thus, NREL additionally tests the cells over their usage range for the cell—for a PHEV and EV cell; the usage range is approximately 95% to 20% SOC. As would be expected, the cells are less efficient over the full SOC range as compared to the partial SOC range. In recent testing, however, the gap in efficiency has decreased, as shown in Figure III- 37. The cell was cycled over its full and usage range at 30°C and 0°C. As can be seen from the figure, the efficiencies for a given temperature are fairly well matched. Battery manufacturers use the data from the calorimeter to ensure that the cell has the desired efficiency over the usage range while making trade-offs on other aspects of the cell design, such as low temperature operation, safety, cost, and ease of manufacturing.

When testing a cell to size the thermal management system, it is imperative to test the cell according to how it will be used. Figure III- 38 shows a PHEV cell undergoing a US06 charge depletion cycle followed by a US06 charge-

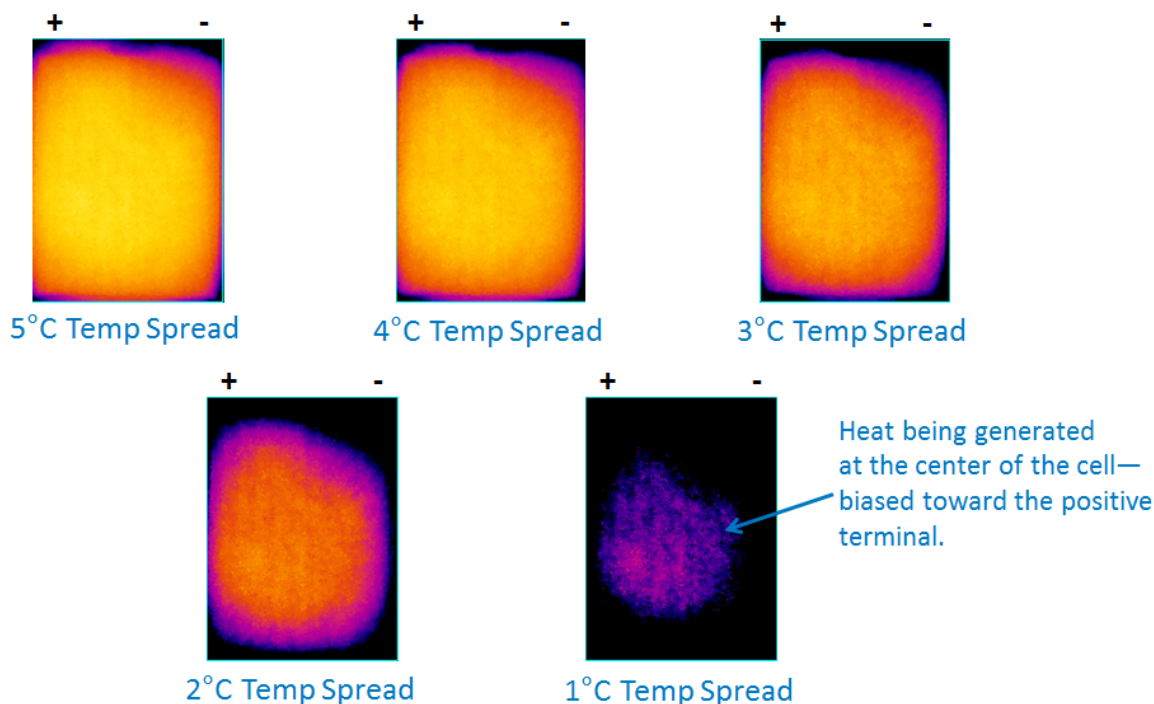


Figure III- 39: Infrared image of PHEV cell at the end of a 2C discharge

Figure III- 39 shows a PHEV cell at the end of a 2C discharge. Each IR image has a temperature spread associated with it—by decreasing the temperature spread from 5°C to 1°C, a visual reference can be used to determine where the heat is preferentially generated within the cell. For this cell, the heat generation is biased towards the left center of the cell underneath the positive terminal. The heating may be a result of the aluminum used for the positive terminal as compared to copper for the negative terminal. We are also assessing the uniformity of the cell temperature across the surface. When the cell temperature is uniform and consistent, all areas within the cell age at the same rate, leading to a better cycle life. NREL is working with battery developers to understand how temperature non-uniformities affect the efficiency and cost of the cell over its life.

Conclusions and Future Directions

NREL has thermally tested cells, modules, and/or packs from JCI, LG CPI, SK Innovations, Leyden, and Saft. It has provided critical data to the battery manufacturers and OEMs that can be used to improve the thermal design of the cell, module, pack, and their respective thermal management systems. The data included heat generation of cells under typical profiles for HEV, PHEV, EV, and 12 Volt Start/Stop applications, which is essential for designing the appropriately sized battery thermal management system. It was found that the majority of the cells tested had a thermal efficiency greater than 94% when cycled under a 2C constant current discharge. During the thermal imaging of the cells, NREL identified areas of thermal concern and helped the battery developers improve the thermal design of their cells.

In FY16, NREL will continue to thermally characterize cells, modules, packs for USABC, DOE, and US Drive partnership.

FY 2015 Publications/Presentations

1. 2010 DOE Annual Peer Review Meeting Presentation.
2. Quarterly meeting presentations to the USABC battery working group and manufacturer.
3. Presentation at the Global Automotive Management Council's Battery Congress, Michigan, June, 2015.

III.C Battery Analysis and Design Activities

III.C.1 Battery Multiscale Multidomain Framework & Modeling (NREL)

Objectives

- Develop a standard procedure for identifying model parameters for the multiscale multidomain (MSMD) battery model for simulating the performance of plug-in electric vehicle (PEV) batteries.
- Develop a MSMD parameter identification manual in support of DOE's Computer Aided Engineering for Electric Drive Batteries (CAEBAT) project.

Project Details

Brian Cunningham (DOE Program Manager)
DOE Agreement # 28883 Recipient: National Renewable Energy Laboratory

Gi-Heon Kim (NREL – PI)
15013 Denver West Parkway, M/S 1633
Golden, CO 80401
Phone: 303-275-4437
Email: gi-heon.kim@nrel.gov

Start Date: October 2014

Projected End Date: September 2015

Technical Barriers

- Lack of standard experimental procedure for extracting parameters for calibrating PEV battery models.
- Identification of a physics-based battery model is known to be difficult. This anticipated difficulty to the development of physics based constituent model comes from the fact that characterization of a battery is intrinsically solving an under-determined problem.

Technical Targets

- Develop calibrated and validated battery models for accelerating the development of PEV battery simulation tools.
- Support DOE's CAEBAT project by preparing a manuscript for 'MSMD Identification Manual'.

Accomplishments

- Integrated the C++ MSMD/GHMSMD particle domain model (PDM) and electrode domain model (EDM) with open-source optimization software
- Explored several numerical procedures for PDM/EDM identification using synthetic/experimental data
- Evaluated a modified galvanostatic intermittent titration test method for faster identification of solid state diffusion dynamics for MSMD-PDM multi-particle model
- Suggested a sequential optimization procedure to break the under-determined parameter estimation problem of the whole system into a sequence of fully determined fits to subsets of the parameters
- Prepared an initial draft of MSMD Identification Manual in support of CAEBAT project

Introduction

In support of US Department of Energy (DOE) CAEBAT project, National Renewable Energy Laboratory (NREL) developed the multi-scale multi-domain (MSMD) model, overcoming challenges in modeling the highly nonlinear multiscale response of battery systems. The MSMD provides high extent flexibility and multiphysics expandability through its modularized architecture, as well as computational efficiency to enable the model to run on standard desktop PCs by providing selective, finer meshes for low hierarchical subdomains. As part of the first phase of CAEBAT, NREL supported GM and ANSYS to incorporate MSMD in the battery simulation software in the commercial offering of ANSYS (Fluent 16).

The GH-MSMD, newly developed quasi-explicit nonlinear multiscale model framework, significantly improves computational speed of the model, while inheriting the modular architecture of the MSMD. However, acquisition of physics-based battery model parameters is known to be difficult. This difficulty comes from the fact that the characterization of a battery is intrinsically solving an under-determined problem. Physics-based models require component material properties and design parameters as model inputs. On the other hand, traditional battery characterization tests such as GITT or EIS use certain math models for quantifying property values from the measured data. Unfortunately, these circling-processes have been decoupled in practice. Model-based optimization has been limited by the lack of a fully-adaptive, fast-running, high-fidelity, flexible battery model. As part of this second phase of CAEBAT, NREL brings high fidelity fast-running models directly into battery system characterization step. For example, we directly use a high fidelity particle domain model, discrete diffusion particle model (DDPM), as a reference tool model for thermodynamic- kinetic- transport- electrical- and geometrical- characterizations of electrode particles.

Approach

The MSMD, a hierarchical multiscale modular framework, facilitates bottom-up identification. We suggest a sequential optimization procedure to break the under-determined parameter estimation problem of the whole system into a sequence of fully determined fits to subsets of the parameters. This sequential procedure is developed from the fact that the physicochemical processes in batteries occur in significant time scale segregation.

Results

NREL brings high fidelity fast-running models directly into battery system characterization step. NREL's baseline Multi-Scale Multi-Domain (MSMD) model has been implemented in an open-source programming language platform, C++, to expand access, and to increase flexibility. We suggested the standard model inputs and outputs, and the data structure. The MATLAB version codes were restructured and prototyped for porting, and the baseline MSMD has been ported into C++ language. The MSMD, a hierarchical multiscale modular framework, facilitates bottom-up identification. The MSMD particle-domain models (PDMs) solve lithium transport in solid electrode particles, interfacial reaction kinetics, and charge conservation at the interfaces. The electrode-domain models (EDMs) additionally consider polarization through electrolyte and composite matrices. In the extended cell-domain models (CDMs), additional polarization caused by non-uniform temperature and electric potential fields across cell volume is resolved.

MSMD: Expandable Multiscale Multiphysics Modular Framework

Physicochemical processes in Li batteries occur in intricate geometries over a wide range of time and length scales. As the size of the battery increases to meet the system demands of high-energy and high-power energy storage in electric vehicle applications, macroscopic design factors in combination with highly dynamic environmental conditions significantly influence the electrical, thermal, electrochemical, and mechanical responses of a battery system. Without better knowledge of the interplays among interdisciplinary multiphysics occurring across varied scales in the battery systems, it is costly to design long-lasting, high-performing, safe, large battery systems. NREL pioneered the multi-scale multi-domain (MSMD) model, overcoming challenges in modeling the highly nonlinear multiscale response of battery systems. The model resolves the battery geometry into three coupled computational domains. The MSMD provides high extent flexibility and multiphysics expandability through its modularized architecture (See Figure III- 40), as well as computational efficiency to enable the model to run on standard desktop PCs by providing selective, finer meshes for low hierarchical subdomains. Model domain separation for the physicochemical process interplay is carried out where the characteristic time or length scale is segregated. The MSMD particle-domain models (PDMs) solve collective response of electrically and ionically connected particle-batteries which are collocated in the electrode-domain. The electrode-domain models (EDMs) solve collective behavior of PD-batteries, considering polarization through electrolyte and composite matrices. The cell-domain models (CDMs) of the MSMD solves single- or multi-cell battery response by resolving collective behavior of paired plate batteries, considering polarization caused by non-uniform temperature and electric potential fields across cell volume.

MSMD – Bridging Scales

Extending scales, higher fidelity,
fully integrated system

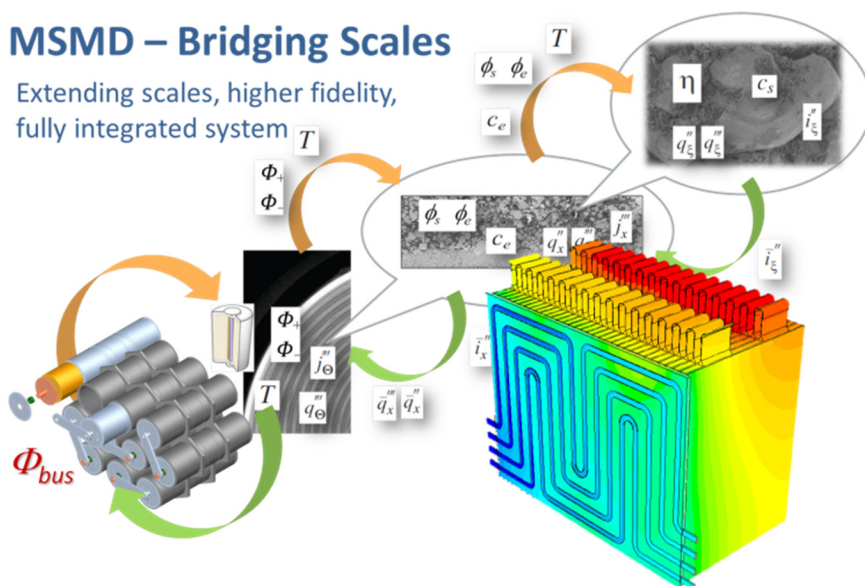


Figure III- 40: Modular Multiscale Model Framework of MSMD

electronically continuous, but ionically discrete. An arbitrary number of quantized discrete particles can be given as a user input. Thermodynamic, Kinetic, transport, electrical and geometrical model parameters of each discrete particle can be independently determined.

EDM solves electronic and ionic charge conservation respectively in composite electrodes and electrolyte, and species conservation in electrolyte. Assuming existence of a local in-plane ensemble average in a finite volume of cell-domain, one dimensional porous electrode model is chosen for a baseline EDM.

CDM solves for temperature and electronic current in current collectors and other passive pathways across cell dimensions. An orthotropic cell composite model is a baseline CDM for MSMD multiscale model. Battery cell-composite has intricate stratified structures, and the assembly units of paired electrode layers are stacked or wound to build prismatic or cylindrical cells. Macroscopic designs for electrically and thermally configuring cell components greatly affect the physicochemical processes occurring in a battery. Numerical complexity of a model can be significantly reduced by treating the cell-composite as a homogeneous orthotropic continuum. For example, the single potential-pair continuum (SPPC) model treats the stratified cell-composite as homogeneous continuum with orthotropic transport properties, and resolves temperature and a pair of current collector phase potentials in the volume of the continuum with distinguished in-plane and transverse conductivities for heat diffusion and electrical current conduction.

MSMD Inputs

MSMD (and GH-MSMD) accepts the two types of user-modifiable inputs; text-files and user-modifiable functions. Most of the model inputs are read in as text-files with the extension “inp”.

These inp-files are;

- To define battery
- To define usage
- To define model setup

Therefore, a user can choose materials, electrode designs, cell form-factors, battery use profiles, and submodel options for a MSMD battery simulation, by simply selecting a set of desired inp-files from a text-file database without recompiling the model code. Occasionally, a user may want to use custom functions for the material properties. Then, “PROFUNC.cpp” can be edited. The case requires re-compilation of the model code.

INP files: The standard input file structure facilitates modular multiscale multiphysics simulation (See Figure III- 41). These input files define a battery, a usage, and the numerics for model setup. The input file structure reflects the MSMD modularity. For example, if a user keeps the materials and the electrode design same and only wants to change the cell form factor, the “cdparm.inp” needs to be replaced. If a user changes

Baseline Sub-Models

PDM resolves lithium transport in solid electrode particles, interfacial reaction kinetics, and charge conservation at the interfaces. NREL has developed the discrete diffusion particle model (DDPM) as a baseline PDM for MSMD multiscale model, to better address the impacts of particulate morphology, size distribution, surface modification, contact resistances, mixture composition of active particles. A system of particles is considered

“edparm.inp” while keeping the others same, the electrode design of a battery is changed. “posptcltbl.inp” and “negptcltbl.inp” define the positive and negative active materials, respectively.

	PDM	EDM	CDM
Define Battery			
posptcltbl.inp, negptcltbl.inp	○	○	○
edparm.inp		○	○
cdparm.inp			○
Define Usage			
ELprofl.inp	○	○	○
Setup Model			
setup.inp	○	○	○

Figure III- 41: Standard MSMD input file structure

- ocp_func(xy, index)
- sgs_eff_func(sg_ref, Ea, T, Tref, vf)
- transferenceNumberFunc(ce, T)

Property Functions: A group of functions are used to define the physicochemical properties of battery materials. The list includes;

- De_eff_func(ce, Ea, T, Tref, vf, bex)
- Ds_func(Dsref, Eact, TT, Theta)
- dUdT_func(xy, index)
- dUdX_func(xy, index)
- kioref_func(ptclStruc ptcl, pk)
- kp_eff_func(ce, Ea, T, Tref, vf, bex, &kp_eff, &kpD_eff)

Experimental Activity

Test Cell Making: The following procedure is taking LMO and graphite as examples. Cathode slurry is prepared with a specific ratio using LMO, poly vinylidene fluoride (PVDF) as binder, and carbon black as conductive agents, in an n-methyl pyrrolidone (NMP) solvent. Anode slurry is prepared in a similar way. Upon uniform mixing they are spread onto a 15um thick current collecting aluminum foil. After drying and pressing, electrode pieces are punched from the coated foil in coin cell or pouch cell format. For coin cells, the electrodes are assembled with lithium foil as counter electrodes in a glove box. For pouch cells, half cells are prepared in a similar way. Additionally, paired cathode and anode are assembled with lithium foil as reference electrodes in a 3-electrode configuration. The electrolyte with 1.2M LiPF₆ is composed of ethylene carbonate (EC), diethyl carbonate (DEC) and dimethyl carbonate (DMC). Coating parameters like electrode dimension and solid loading level are measured and recorded. It should be noted that material properties including density, Brunauer-Emmett-Teller (BET) surface area and particle size distribution are also necessary for subsequent modeling, thus it is suggested to acquire them from vendors or manufacturers.

GITT Measurement: Coin cell tests are carried out with a battery tester. An environmental chamber maintains 20°C for at least 4 hours prior to tests. Coin cells are charged at 0.1C rate to higher voltage limit and kept under it until current dropped below 0.05C. In a time –effective manner, discharge is carried out in repeated 2-step segments: low c-rate discharge at 0.05C for 30s with 1 hour relaxation; high c-rate discharge at 0.1C for 1 hour with 4 hour relaxation. The segments are repeated until voltage reaches lower voltage limit. Open circuit potential (OCP) is recorded at the end of resting period in every low c-rate segments and GITT calculation uses the data in the same segments. The high c-rate discharge is used to reach certain state of charge stages faster.

EIS Measurement: Coin cells are charged at 0.1C rate under 20°C to corresponding voltage limit and kept at it until the current drops below 0.05C. After relaxation, the coin cells are discharged at 0.1C to reach 50% stage of charge. Four hours later, EIS tests from 1000 kHz to 0.005Hz with 5 mV amplitude are run on these cells.

Test Matrix

The list of required tests is suggested. MSMD model parameters are extracted from a defined test matrix, as shown in Table III- 15 below. The proposed tests are arranged in a consistent way that MSMD model framework is defined. With a bottom-up structure, parameters extracted from lower domain are independent of higher domain testing. Instead, the parameters are inputs to identify model parameters of higher domains.

Table III- 15: Suggested Test Matrix

Domain Level	Cell Samples	Test	Objectives
Material	Cathode active material	BET test Particle size analysis Density Test	Specific surface area Powder particle size distribution Ture and tape densities
	Anode active material	BET test Particle size analysis Density Test	Specific surface area Powder particle size distribution Ture and tape densities
Particle Domain	Cathode Half Cell	Formation cycle Constant-current discharge GITT EIS	Formation loss Crates performance OCP curve and diffusion Exchange current density and film resistance
	Anode Half Cell	Formation cycle Constant-current discharge GITT EIS	Formation loss Crates performance OCP curve and diffusion Exchange current density and film resistance
Electrode Domain	Three Electrode Cell	Formation cycle Constant-current discharge HPPC	Formation loss, negative and positive mass ratio Model calibration (constant load) Model calibration (dynamic load)
Cell Domain	Full Cell	Formation cycle Constant-current discharge HPPC	Model validation

Numerical Procedures

Method: Parameter estimation for battery identification is formulated here as a nonlinear least squares fitting problem of minimizing the least squares objective

$$F(p) = \sum_{i=1}^N |w_i (V^{\text{expt}}(t_i) - V^{\text{calc}}(t_i; p))|^2$$

with respect to the vector of parameter values p . Here, $V^{\text{expt}}(t_i)$ is the voltage recorded at different time points t_i during our experiment (CCD, GITT, etc), $V^{\text{calc}}(t;p)$ is the course of voltages calculated at the same times by MSMD, and w_i are weights associated with each data point. Note the explicit dependence on the parameter values p . Our goal is to find the values of p that minimize F . Note that it is likely true that for any given experimental device, there *is* a fixed value of p . However, because p is not directly measurable, we must rely on numerical procedures to find p , and thus we rely on what the data can tell us about p . And quite frequently the data does *not* indicate a single set of best p values. Our minimization is potentially an underdetermined problem.

That said, given a data set, and an initial guess for p , there are a variety of algorithms for minimizing $F(p)$. For our work we use the Levenberg-Marquardt algorithm as implemented in the FORTRAN code MINPACK (from Argonne National Laboratory) and “wrapped” to be accessible from python in the scipy numerical python library. This algorithm is a combination of steepest descent and Newton’s method, combining the robustness of the former with the efficiency of the latter. It is the “workhorse” method in this field. Analysis of the Jacobian matrix around the minimizer can provide estimates of confidence bounds on the estimated parameters, but we will not discuss this here. (Further details of the full probability distribution of the parameter values can be provided by Markov Chain Monte Carlo methods, especially in cases where the error cannot be assumed Gaussian. These methods are computationally expensive and will not be discussed further here, but we are actively pursuing this approach and connecting it to the traditional approaches as we move forward with our internal development.)

An important concept we recommend to overcome the underdetermined nature of the battery parameter estimation problem is the notion of *sequential optimization*. This simply means optimizing different sets of

parameters at a time. Smaller subsets of parameters are more completely determined by the data. Once fixed, these allow the next subset of parameters to be determined by (perhaps different portion of) the data. The justification of such an approach is *physical*, not mathematical. We describe a particular case (fitting the particle domain model) below in the Examples section.

Another approach, simple yet powerful, is *multi-start optimization*. This simply means re-running the fitting procedure from a variety of starting parameter sets p . You may *assume* there is a single best p but we have found that this procedure more often reveals that there are in fact many sets of parameters that can equally well describe the data. This is related to the sequential procedure. An “all-at-once” (as opposed to sequential) multi-start fit reveals the underdetermined problem that the sequential procedure is meant to allay. However, statistics is subtle; it can sometimes be naïve to assume that a fixed value obtained from one stage of sequential fitting is known with sufficient confidence to fix it once and for all. Often it is better to let all the parameters remain free and discover the “space” of optimal parameter sets. Then perhaps a targeted fit of one of them can determine at the same time the values of those with which it is correlated.

Fitting Parameters: Referring to Chapter 3 regarding the MSMD inputs, there are a large number of quantities in the various MSMD input files. These can be divided into categories according to domain (PD, ED, CD, etc.) and according to role (design parameter, material parameter, environmental parameter, etc.). For present purposes, we describe numerical fitting primarily at the particle domain level. Our goal here represents the “final stage” of the identification task and as such has several prerequisites, discussed in Chapter 5 regarding the MSMD “test matrix”. In particular, we assume here the geometry information (cell size) and property functions (e.g. “ocp_func”) have already been determined.

For this “final stage” of the MSMD battery identification task, we consider the following physical parameters;

- Reference exchange current density (“io_ref” in ptcltbl.inp). Assumed constant for each particle.
- Activation energy for exchange current density (“Eact_io” in ptcltbl.inp). Constant for each particle.
- Particle diffusion constant (“Ds_ref” in ptcltbl.inp). Assumed constant for each particle
- Activation energy for particle diffusion (“EactDs” in ptcltbl.inp). Constant for each particle.
- Particle radius r_i . (“ptclxs” in ptcltbl.inp). Different for each particle.
- Particle volume fraction f_i . (“ptclvf” in ptcltbl.inp). Different for each particle.
- Surface to volume ratio: In principle this is known, but it appears to be very imprecisely known, so we treat it as a “virtual” parameter and allow it to vary.

This problem also has several constraints. First the parameters are bound in physically realistic ranges (e.g., they are all positive). Second, the problem has two constraints relating particle radii r_i and particle volume fraction f_i :

$$\sum_{i=1}^n f_i = 1$$

$$\sum_{i=1}^n \frac{3}{r_i} f_i = s$$

The first simply says the volume fractions sum to one. The second expresses our desire to maintain the same particle surface to volume ratio. We are able to use the two constraints to eliminate two otherwise free radii or volume fractions from the fit. We have chosen to eliminate the volume fractions for the first two particles.

At the electrode domain level most parameters are design parameters, but there are also several internal parameters that we must determine through numerical fitting to data. These include;

- Bruggeman tortuosity exponent for electrolyte diffusion in positive electrode, negative electrode, and separator (“pos_bex”, “neg_bex”, and “sep_bex” in “edparm.inp”)
- Additional cell level ohmic resistance (“cel_Rohm” in “edparm.inp”)
- Lithium loss fraction during formation (“cel_formationloss” in “edparm.inp”)

Example: This example describes parameter identification for the cathode parameters of an experimental battery system of one of our industrial collaborators. For this study we seek to identify internal battery

parameters over two data sets. The first is approximately 50 hours of pulse charging, and the second is constant current discharge at 0.5, 0.1, 1, and 5 C rates. The parameters of interest to identify are;

- i_0 : exchange current density
- D_s : diffusivity
- R_i : particle sizes, $i=1..$ number of particles
- V_i : particle volume fractions
- E_{actio} : activation energy for exchange current density
- E_{actDs} : activation energy for diffusion coefficient

Surface to volume ratio: In principle this is known, but as above it appears to be very imprecisely known, so we treat it as a “virtual” parameter and allow it to vary. One prescription is to determine these parameters by the sequential method described above. Here we describe a complementary multi-start approach to exploring the whole probability distribution of the parameters at once, *without* resorting to expensive Monte Carlo methods. For this, we have performed not one but *many* Levenberg-Marquardt local fits of constant current discharge to *all* the parameters, each fit starting from a different set of randomly chosen initial parameter values. Almost all of the starting conditions result in about the same quality of fit, but these “optimal” parameter values vary, and in interesting ways that reveal how they are related. This fact illustrates precisely the indeterminacy we refer to above. The actual experimental battery presumably has specific values for all these parameters. But the combination of data plus the MSMD model cannot tell us these precise but hidden values. It can only tell us the set of values that is consistent with the data, and in this case it tells us that there is an interesting correlation structure, revealed by the multi-start approach. Figure III- 42 is a “pair plot”. It consists of a matrix of scatter plots. Each of these cells plots fitted values of one parameter (e.g., i_0) against another (e.g., D_s). The plot reveals that the 6 parameters we fit are by no means all free-variables with respect to optimization. In fact, it is likely that there are only two free variables: 1. one of V_4, V_5, V_7, V_8 , and V_9 . See caption for further discussion.

Conclusions and Future Directions

In support of DOE’s CAEBAT project, a document is prepared to help model users identify the model inputs for running the MSMD and the GH-MSMD model simulations. The current version draft manuscript suggests;

- Overview of the MSMD framework and the baseline submodels
- Review of conventional battery characterization test methods
- Standard input-files
 - To be commonly used in various existing and future submodel components, and
 - To be easily databased for various lithium-ion chemistries and battery designs
- Test cell making and experimental guides
- List of tests
- Numerical procedure

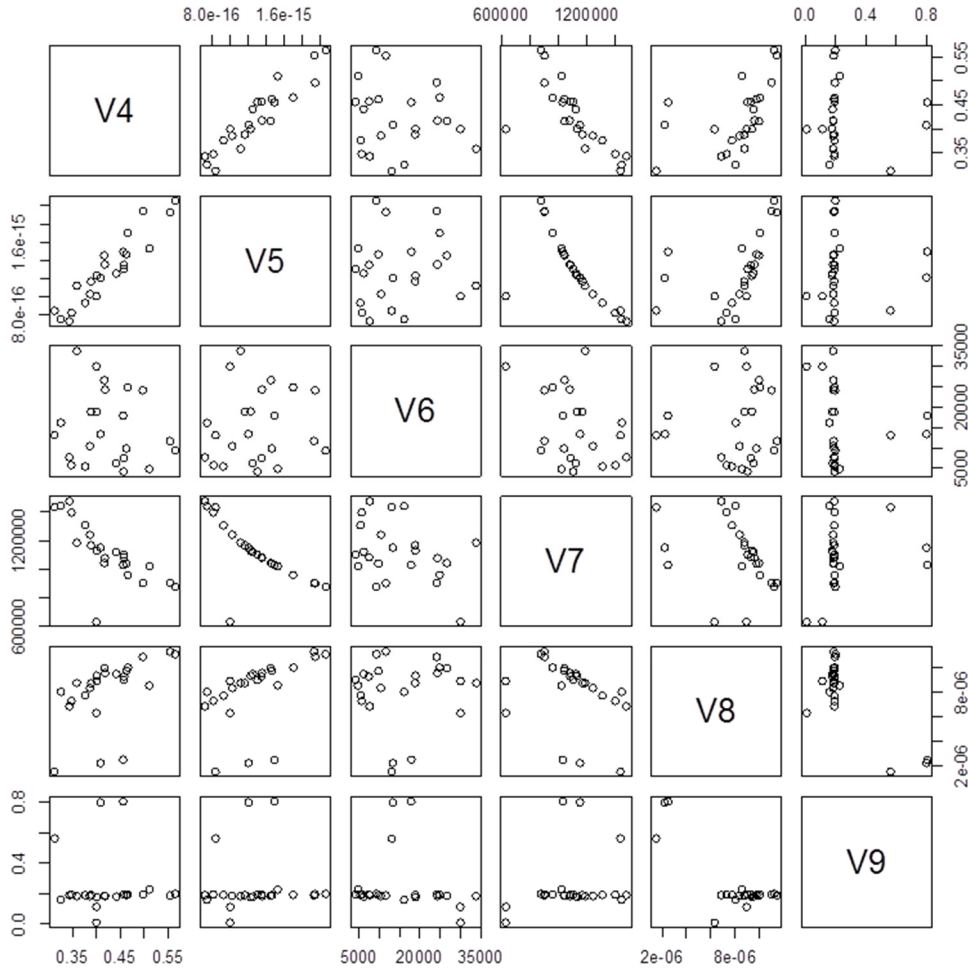


Figure III- 42: From left to right (top to bottom) the parameters summarized are: io , D_s , Eactio , surface area, radius 1, volume fraction 1. With respect to optimization there are only 2 or 3 free parameters: Cells labeled 4,5,7,8 are clearly correlated, so they represent only one actual choice by the optimizer. Except for outliers, V9 attains only one value. V6 appears uncorrelated with the other parameters

We will continue to develop sequential optimization procedure to break the under-determined parameter estimation problem of the whole system into a sequence of fully determined fits to subsets of the parameters. The procedure and the document will be updated for future publication. These developments will be performed under the third phase of CAEBAT project.

FY 2015 Publications/Presentations

1. Annual Milestone Reports, September, 2015

III.C.2 Computer Aided Engineering of Batteries – CAEBAT (NREL)

Objectives

The overall objective of the first phase of the Computer-Aided Engineering of Electric Drive Vehicle Batteries (CAEBAT) project is to develop electrochemical-thermal software tools to accelerate the design and simulate the performance, life, and safety of electric-drive vehicle (EDV) batteries. As part of the CAEBAT-1 effort, NREL's objectives are:

- Support the U.S. vehicle, battery, and software industry with cost-shared subcontracts to develop battery modeling tools to simulate and design cells and battery packs to accelerate development of improved batteries for hybrid, plug-in hybrid, and electric vehicles.
- Technically manage and monitor CAEBAT-1 subcontractors funded in 2011.
- Oversee completion of the General Motors (GM) subcontract to deliver validated advanced lithium-ion battery systems using GM's six-step model verification and validation approach.

Technical Barriers

- Cost, life (calendar and cycle), high performance at all temperatures, and safety are barriers for widespread adoption of lithium-ion batteries in EDVs.
- Existing design tools are not practical for realistic battery pack design and optimization.
- Various cell physics sub-models exist, but they have not been integrated in a single framework in commercial code.
- Current engineering workstations do not have the computational power required to simulate pack-level thermal response coupled with electrochemistry. System-level analysis or reduced order modeling (ROM) is required to simulate integrated pack-level physics. However, ROM approaches for battery packs are not well understood.

Technical Targets

- Develop suites of software tools that enable automobile manufacturers, battery developers, pack integrators, and other end-users to design and simulate the electrochemical and thermal performance of cells and battery packs to accelerate development of battery systems that meet the requirements of EDVs
- To be useful to automotive engineers, battery cell and pack design tools should have the following analytical capabilities:
 - Evaluate battery pack thermal management by predicting maximum intra- and inter-cell temperature difference under various drive-cycles
 - Ability to provide system simulations with ROM that allows for trade-off studies between the cooling cost and the battery pack warranty cost in the early stage of vehicle development.
 - Ability for a real-time system simulations that can lead to battery management system (BMS) development and enhancement.

Project Details

Brian Cunningham (DOE Program Manager)

DOE Agreement # 28883 Recipient:
National Renewable Energy Laboratory

Ahmad Pesaran (NREL – Project Coordinator)

15013 Denver West Parkway
Golden, CO 80401
Phone: 303-275-4441
Email: ahmad.pesaran@nrel.gov

Gi-Heon Kim (NREL Technical Monitor)

Email: gi-heon.kim@nrel.gov

Subcontractor: General Motors LLC

Taeyoung Han (Principal Investigator)

30500 Mound Road
Warren, MI 48090
Phone: (586) 986-1651
E-mail: taeyoung.han@gm.com

Partners:

ANSYS Inc. and ESim LLC

Start Date: June 2011

Projected End Date: February 2015

Accomplishments

- GM and its partners successfully completed their CAEBAT-1 subcontract by developing a validated battery simulation software and delivering all their reporting requirements.
- ANSYS officially released the public version of its battery 3D multi-physics simulation tool in December 2014 (Fluent Version 16).
- The ANSYS Battery Design Tool (ABDT) was developed utilizing the ANSYS Workbench Framework.
- A direct thermal ROM was developed and validated with full-field simulation.
- NREL developed a user defined function (UDF) for multiple particle/multiple active material models in support of the GM team.
- Semi-physics-based cycle life model was developed and validated with cycle life test.
- A battery pack-level model was validated compared to the full field simulation and the test data for a production-level battery pack, and comparisons are satisfactory.
- The three CAEBAT-1 subcontract teams (CD-adapco, EC Power, and GM) now have successfully completed their projects and released three different battery computer-aided design software tools to simulate the electrochemical-thermal performance of batteries.

Introduction

In April 2010, the DOE Vehicle Technologies Office (VTO) announced a new program activity called Computer-Aided Engineering of Electric Drive Vehicle Batteries (CAEBAT) to develop software tools for battery design, R&D, and manufacturing. The objective of CAEBAT is to incorporate existing and new models into battery design suites/tools with the goal of shortening design cycles and optimizing batteries (cells and packs) for improved performance, safety, long life, and low cost. The goal is to address the existing practices with which battery and pack developers operate: tediously experimenting with many different cell chemistries and geometries in an attempt to produce greater cell capacity, power, battery life, thermal performance and safety, and lower cost. By introducing battery simulation and design automation at an early stage in the battery design life cycle, it is possible to significantly reduce the product cycle time and cost, and thus significantly reduce the cost of the battery. When the project started three years ago, NREL had already developed an electrochemical-thermal model of lithium-ion cells with three-dimensional (3D) geometries. However, those tools were not integrated into a 3D computer-aided engineering (CAE) platform, which automotive engineers routinely use for other components. In many industries, including automotive and combustion engine development, CAE tools have been proven pathways to improve performance by resolving relevant physics in complex systems; shorten product development design cycles, thus reducing cost; and provide an efficient manner for evaluating parameters for robust design.

DOE VTO initiated the CAEBAT project to provide battery CAE tools to the industry. The goal of the CAEBAT activity is to “develop suites of software tools that enable automobile manufacturers, battery developers, pack integrators, and other end-users to simulate and design cells and battery packs in order to accelerate the development of energy storage systems that meet the requirements of the electric drive vehicle.” The involvement of industry (automakers, battery developers, and software producers) in the CAEBAT activity was sought by soliciting active participation of the industry in developing cell and pack software suites for the design of batteries through competitive procurements. To oversee the successful execution of the CAEBAT program, NREL was assigned to coordinate the industry and academic activities on Cell-Level Modeling and Pack-Level Modeling. To engage serious involvement of industry, NREL, with guidance from DOE, issued a Request for Proposals (RFP) in FY10 to seek development of cell and pack battery design tools for a period of three years with 50%–50% cost sharing. The CD-adapco, GM, and EC Power teams were selected for award in early 2011. The three subcontract teams started technical work in July 2011. CD-adapco and EC Power completed their subcontracts and released the battery CAE tools to the public in 2014 as reported in the DOE FY2014 Annual Progress Report for the Energy Storage R&D. CD-adapco’s battery simulation module in its STAR-CCM+ and EC Power’s AutoLion have been licensed by more than 50 organizations. The GM subcontract was extended into FY 2015; thus, this final report focuses solely on the progress by the GM team.

The principal objective of the GM team was to produce an efficient and flexible simulation tool that predicts multi-physics battery responses for battery pack thermal management and predicts an optimum cell energy capacity in terms of electrical performance, cooling requirements, life, safety, and cost. The GM team led the four-year CAEBAT project, which is sponsored by the Energy Storage Research and Development (R&D) activities of the VTO. The team is composed of GM researchers and engineers, ANSYS Inc. software developers, Professor Ralph E. White of the University of South Carolina and his ESim staff, and NREL. The team collaborated to develop a flexible modeling framework that supports multi-physics models and provides simulation process automation for robust engineering. The GM team's accomplishments included clarifying end-user requirements; physical validation of the models; cell aging and degradation models; and a new framework for multi-physics battery cell, module, and pack simulations. Many new capabilities and enhancements have been incorporated into ANSYS commercial software releases under the CAEBAT program. This is the last annual progress report for the CAEBAT-1 program.

Approach

The objective of GM's CAEBAT project was to develop a flexible, efficient software tool for multi-scale, multi-physics battery simulation based on the ANSYS Workbench framework. ANSYS is leveraging and enhancing its existing commercial products to provide both field-level (Fluent) and system-level (Simplorer) capabilities, including novel ROM methods and with other battery tools through the open architecture software interface.

Figure III- 43 shows the conceptual view of the ABDT Workbench infrastructure and architecture, which is the premise for ANSYS' software development. ABDT is the name adopted for the graphical user interface (GUI) layer that automates and customizes battery simulation workflow using ANSYS software products. In this vision, ABDT is the newly developed customization layer that ties the ANSYS building blocks together to provide a unified, intuitive simulation workflow. In software architecture terms, ABDT is a combination of an Addin, scripts, and templates. It was based initially on ANSYS Release 14.5, with updates to R15 and R16. The primary target for ABDT is automotive battery development or CAE engineers who are experts in neither battery physics nor simulation technologies. This community places a high value on process automation and ease of use. A secondary goal is to provide specialists with a convenient drill-through access to expert features such as electrochemistry sub-model details, numerical solution controls, and ROM algorithms. The essential role of the ABDT is to automate and integrate the ANSYS tools to make the various components emulate battery applications for cell and pack capabilities.

GM engineers generated the test database for validation of the nominal heat source model, as well as cell-level and pack-level electrical and thermal performance. ANSYS provided user-defined interfaces to utilize submodels developed by NREL that can represent multiple active materials and multiple particle sizes and shapes in the electrodes. ANSYS also created interfaces to enable these new tools to interface with current and future battery models developed by others. GM generated the test database for the physical validation of a 24-cell module and a production-intent battery pack including electrical and thermal performance. GM validated the tools, obtaining satisfactory agreement with the test data. GM also successfully demonstrated thermal runaway simulations for a battery pack having an internal short circuit. With the expected rapid deployment of these design tools to the industry, the project results will accomplish the ultimate goal of accelerating the pace of battery innovation and development for future EDVs.

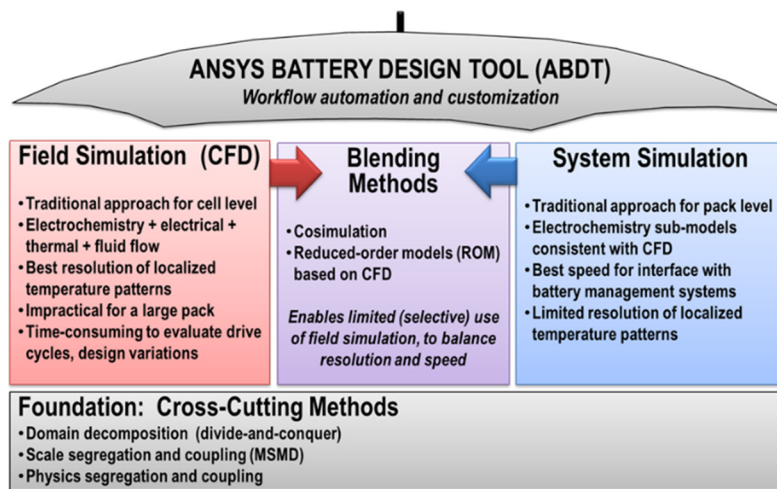


Figure III- 43: Battery simulation through ANSYS Battery Design Tool (ABDT)

thermal ROM are volumetric heat sources as a function of time, applied uniformly to certain regions of the battery cell, and the outputs are temperatures as a function of time at all points of the field-solver mesh. The technique used in this work is based on Krylov-projection [1].

Direct ROM Application and Results

A small battery-model case file is provided with the ABDT deliverable software. This case file includes two battery cells, with a liquid cooling fin between the battery cells that contains nine micro-channels. Nine input heat sources are defined, and for each of these, the volume of the associated zone is defined as an output parameter. A pictorial comparison of the temperature field for the 1.8-million cell discretization is shown in Figure III- 44. Typically, errors of less 1 K are obtained for batteries heated to a few hundreds of degrees, with only a handful of basis vectors. The ROMs generated by the Krylov method are particularly good for slowly varying inputs, and they always match the steady-state responses perfectly. For particularly rapidly varying inputs, larger discrepancies between the ROM and full-order models will be observed.

Similar results for a battery pack made up of 20 battery cells placed between air cooling channels are shown in Figure III- 45. In this case, a coarser discretization was used, so that in this example the order of the full model is about 417,000 elements.

ROM Summary

The system modeling with thermal Linear Time Variant (LTI) ROM for battery modules, under fixed mass flow rate cooling, approximates the battery module's volume averaged temperatures and the battery cell temperatures at specified locations of the battery cell quite well.

The Linear Parameter Varying (LPV) ROMs of mid/end cell units produced good approximations to temperature responses of the battery module. The amount of time it takes to generate the LPV training data is significantly reduced by the use of mid/end-cell units as compared to direct LPV approach. The divide-and-conquer approach to system modeling with mid/end cell LPV ROMs mimics well the thermal behavioral of the battery module under varying mass flow rate cooling scenarios and reduces the calculation time by orders of magnitude when compared to field simulations. The ECM is used in Simplorer to calculate the battery cell's voltage and heat generation. A careful cascade of the (tightly) coupled ECM and thermal ROMs was achieved in Simplorer. The direct thermal ROM can approximate the battery cell temperature field of a module with fixed coolant mass flow rate. The Krylov-projection method is an effective ROM method for thermal battery modeling. The most attractive feature of this method is the shorter and simpler ROM construction procedure compared to the black-box methods.

Results

The GM team continued developing and updating the cell- and pack-level battery simulation tools. New features were added to the ANSYS Fluent battery model that offer additional functionality and flexibility to the user.

Direct Thermal ROM Automation Tool

ROMs are typically faster to construct with a direct technique as the time-consuming step of computing the responses to a set of representative inputs is avoided or at least reduced. The inputs for a

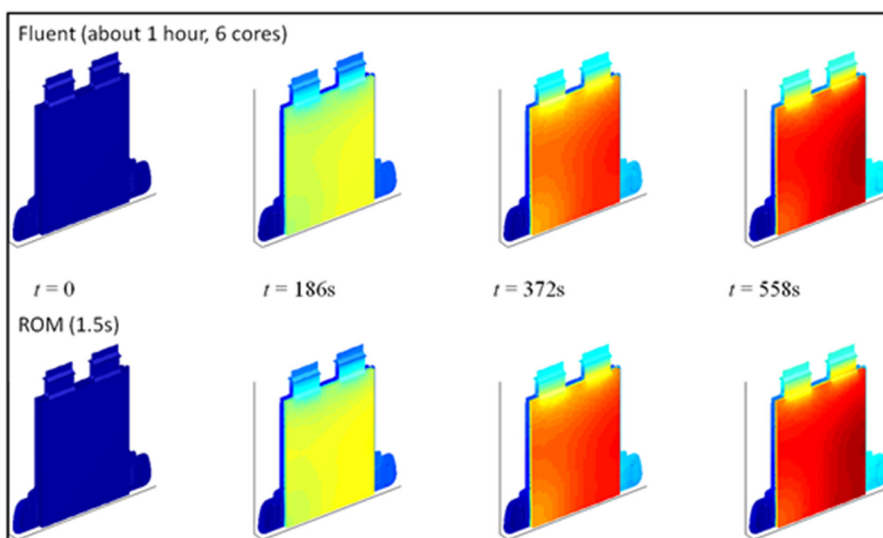


Figure III- 44: Comparison of transient simulation results (1.8 million unknowns)

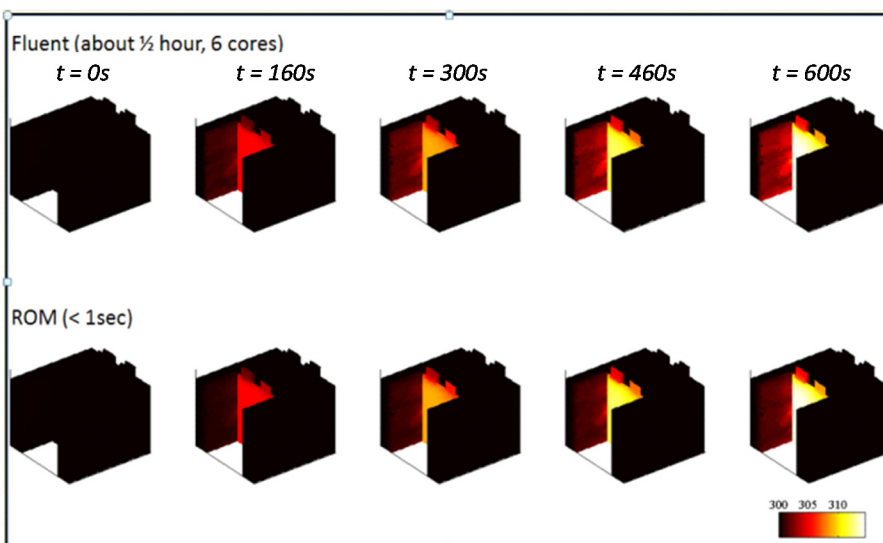


Figure III- 45: Comparison of transient simulation results (0.41 million unknowns)

Validation for Production Intent Battery Pack

The GM team has attempted to validate a battery pack that is planned to be implemented into a future GM hybrid vehicle. We cannot disclose the detail design of the production battery pack due to GM proprietary information. Therefore, the validation results for this battery pack are reported in a non-dimensional format only. The air-cooled battery pack consists of two modules with battery cells connected in series. The air-cooled battery pack is driven by an electric blower, and the air flow distribution at 24 cooling channels is non-uniform as shown in Figure III- 46. The heat transfer is enhanced by cooling design features in the gap between the cells. The test data available from the GM battery group are a part of the thermal durability test in a controlled thermal chamber. The chamber temperature varied while the battery pack ran with

pulsing current loads with different C-rates at a constant blower speed, as shown in Figure III- 47. The flow distribution and the heat transfer coefficients in the cooling channels are obtained from the field simulation with Fluent computational fluid dynamics package. The non-uniform flow information and the heat transfer coefficients are provided to the system simulation based on a Simplorer. The measured current profile and the chamber temperatures are specified as an input to the system simulation. The electrical sub model based on a 6 parameter ECM model is coupled with the thermal network model to predict the battery cell temperature response during the battery pack level test. Figure III- 48 and Figure III- 49 show the unit electrical and thermal models respectively. As indicated in Figure III- 48, the battery is represented by a 6P ECM model, and the empirical parameters used in model are in the form of a two-dimensional lookup table as a function of state of charge and temperature. At a given instance, each parameter is estimated based on current loading direction (charging or discharging), state of charge, and cell temperature. The value of the empirical parameters is calculated using the look-up table and bi-linear interpolation. The key thermal properties of the cell are obtained from cell level test data and also from a cell supplier.

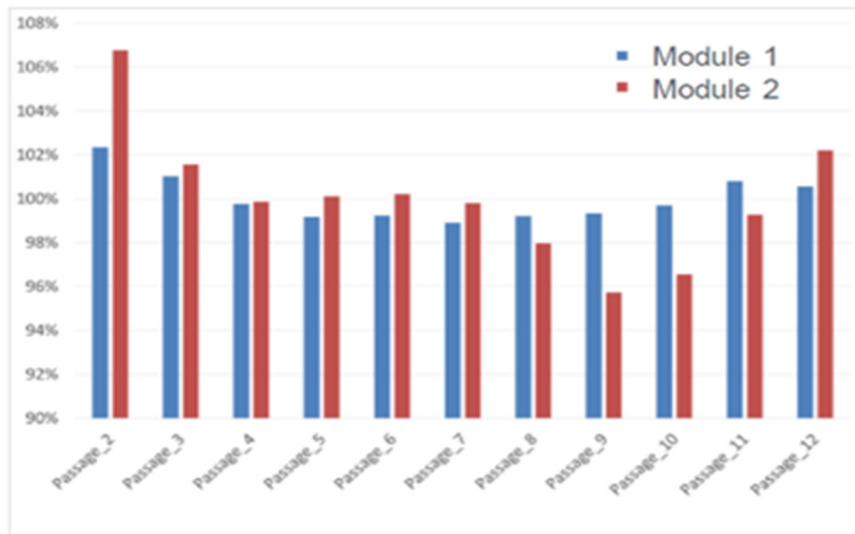


Figure III- 46: Flow distribution along the cooling channels

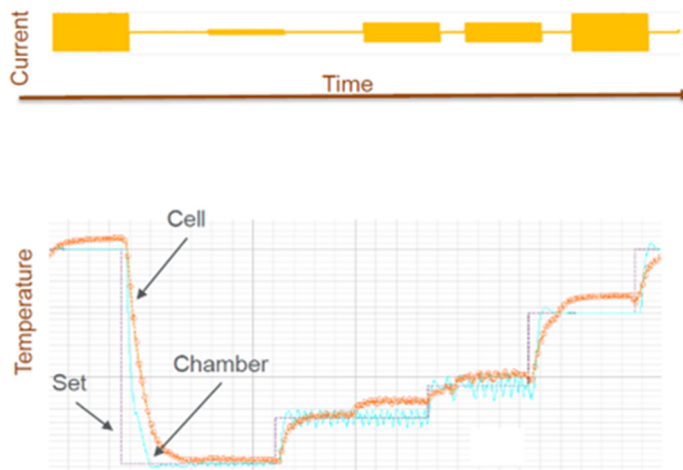


Figure III- 47: Pack level validation overview

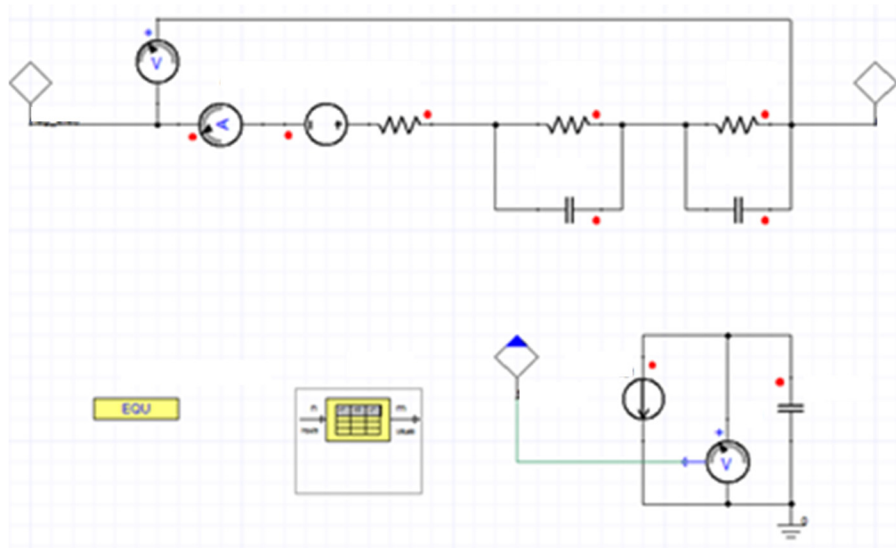


Figure III- 48: Electrical system model for a unit in a production-intent battery pack

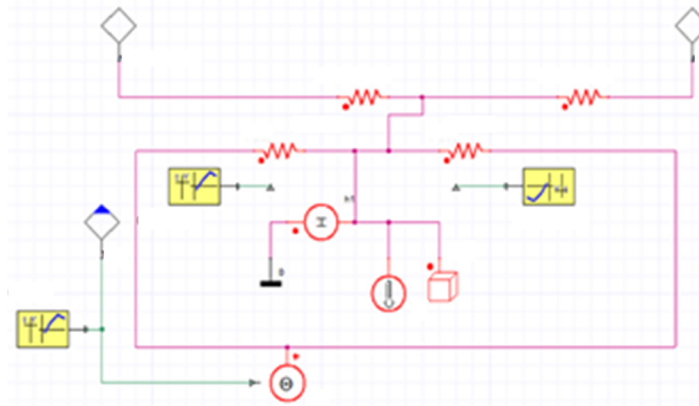


Figure III- 49: Thermal system model for a unit in a production-intent battery pack

Figure III- 50 summarizes the results and comparison of system modeling validation using the production-intent battery pack. The test data used for the validation were obtained from testing that involves different current loadings under different set temperatures. The validation result for the cell temperature prediction is shown in Figure III- 50. As shown in that figure, the system-level simulation predicted the cell temperature variation fairly well in comparison with the measured cell temperature. The comparison demonstrates that the system modeling is able to capture the transient response of the battery pack. Unlike the previous 24-cell module validation case reported in the previous section, the test data were not designed for a rigorous model validation; however, the available test data for the production-level battery pack helped us to complete the validation of the system-level simulation approach. As this is the first attempt for the production battery pack-level validation, GM will continue to gain further experience and will make use of these system simulations for future battery pack applications.

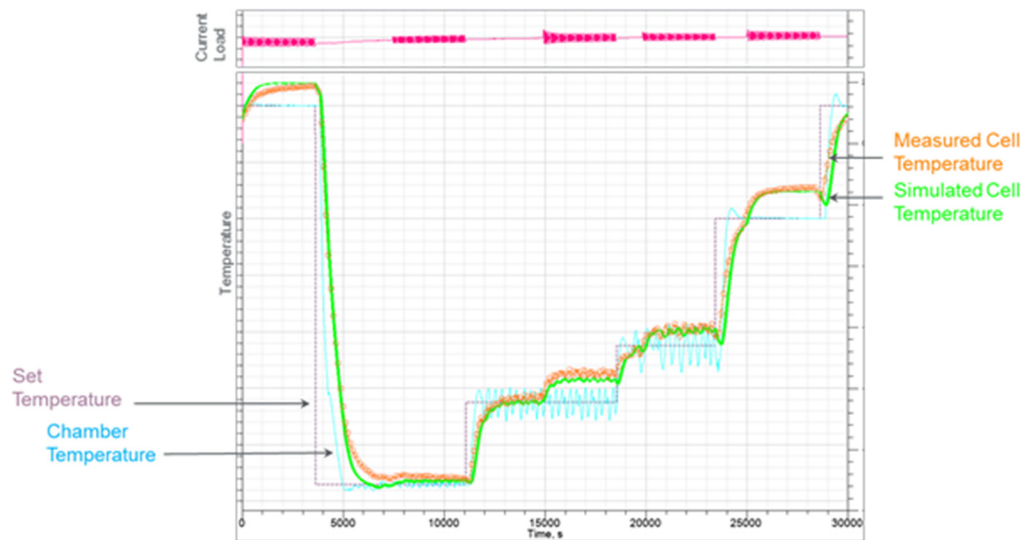


Figure III- 50: Thermal system model for a unit in a production-intent battery pack

Commercial Software Release

Many simulation tools and models developed under this project have been or are planned to be commercially released by ANSYS as integral feature enhancements to its existing, proven, commercial off-the-shelf products. The ADBT customization layer was delivered to NREL in source-code and executable forms with unlimited Government use rights, and is also being test-marketed by ANSYS to explore commercial viability, as discussed further below.

1. ANSYS Fluent Battery Module

The field-simulation battery module was first commercially released as a standard Fluent model with ANSYS R15 release in December 2013, and has subsequently been updated as follows:

ANSYS Fluent R15 (December 2013)

ANSYS Fluent R16 (January 2015)

ANSYS Fluent R17 (Planned for early 2016)

These capabilities were documented to commercial CAE standards in a new 112-page user-guide section delivered to every Fluent licensee, which includes two hands-on battery tutorials. Introductory user training materials were also developed and deployed to ANSYS' global technical-services organization.

2. Fluent-Simplorer Co-Simulation and ROM

The Fluent-Simplorer coupling capability was first commercially offered with ANSYS R14.0 in December 2011 and further refined and improved in the R14.5 release in November 2012. An example project distributed with the Simplorer software demonstrates a non-linear control system in Simplorer to control the coolant flow around a single cylindrical battery cell simulated in Fluent. Another new option, released with ANSYS R16.0 in 2015, provides the ability to import a Fluent LTI ROM and include it in the Simplorer system model as a Subcircuit.

3. ANSYS Battery Design Tool (ABDT)

ABDT has been distributed to (and evaluated by) the project team partners since May 2013 and has since been updated and extended many times. Although not yet an official ANSYS product, ABDT is available from ANSYS as a prototype, with customer training, support, and enhancement typically provided under an ad hoc services project.

4. Other Miscellaneous Code Features or Fixes

Thanks to the CAEBAT project, some new Simplorer scripting methods were added, and two new custom VHDL-AMS models for lookup of flow rates and drive cycles were developed. All commercial software enhancements were integrated into the ANSYS quality assurance process involving continuous regression testing to ISO 9001 standards, and a number of minor underlying code defects were identified and fixed in both Simplorer and Fluent.

5. Commercialization Activities

In addition to the contractually specified progress reports and annual merit review presentations, GM, ANSYS, ESim, and NREL authors on the project team have published a combined total of 11 technical papers in refereed journals and at technical conferences that document the R&D accomplishments. In addition, although not directly charged to the funded project, software commercialization efforts are an important part of the team's plans and the DOE vision for rapid transfer of the CAEBAT technology to the battery-design community. The following list briefly summarizes those uncharged activities during the project period, which are expected to continue in the future:

- Prominent outreach materials and resources were added to the automotive industry section of the ANSYS public website.
- In 2012, the project was featured in a GM-authored article in ANSYS Advantage, a marketing periodical with a global circulation of more than 50,000 CAE specialists (Figure III- 51). A second article focusing on system simulation is in press for 2015.
- GM and ANSYS presented CAEBAT progress at the ANSYS-sponsored Automotive Simulation World Congress in the United States (2012) and Asia (2014), respectively.
- On August 21, 2014, GM and ANSYS co-presented an SAE-sponsored webcast showcasing CAEBAT to a live audience of 199 people. Several hundred additional registrants could download the recording for the subsequent year from <http://www.sae.org/magazines/webcasts/>.
- In 2014, ANSYS conducted internal training of its 500-person global salesforce to promote the new capabilities, including exploration of new projects based on the ABDT prototype. A number of presales visits, presentations, and demonstrations to battery teams in industry have taken place.
- The ANSYS technical-support incident database confirms that more than a dozen customers in North America, East Asia, Europe, and India have already begun using the new battery features. These

existing licensees span from cell manufacturers to tier suppliers to automotive original equipment manufacturers.

- Most recently (January 2015), ANSYS presented CAEBAT and its potential for accelerating battery innovation to the European battery research community at the prominent AABC conference [2].

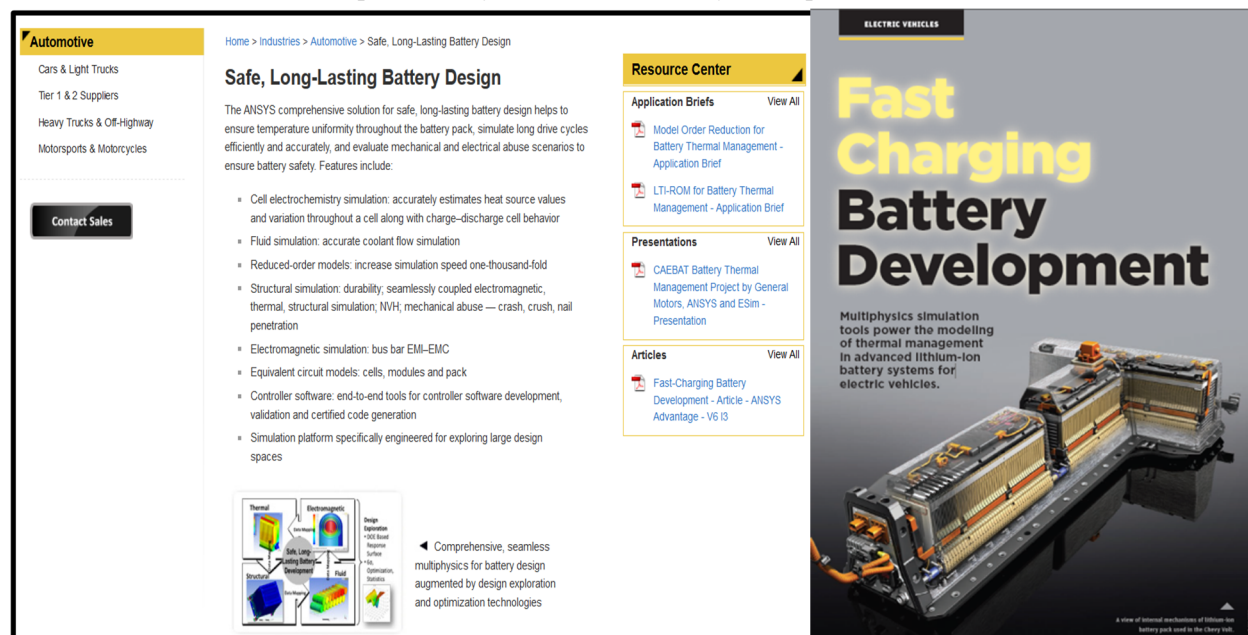


Figure III- 51: ANSYS website describes the battery simulation capabilities developed under the CAEBAT project

Conclusions and Future Directions

The three CAEBAT-1 subcontract teams (CD-adapco, EC Power, and GM) now have successfully completed their projects and released three different battery computer-aided design software tools to simulate the electrochemical-thermal performance of batteries. The GM team completed its project in FY2015 while the other two teams completed theirs in FY2014. The developed and publicly released tools are now in ANSYS Fluent Revision 16 and engineers use full simulation version for cell design and ROM version for back design.

As ANSYS leads the transfer of the newly developed technology to the industry, several logical continuation R&D activities can also be recommended to further increase the software’s capability and appeal.

- One clear example is to evolve the cell-aging models into general purpose, integrated features that would connect the deterministic, single-drive-cycle simulations currently emphasized in ABDT to the stochastic service-life prediction that is ultimately needed in design.
- Another would be to integrate a more sophisticated model to address particle morphology, size distribution, surface modification, contact resistances, and mixture composition of active particles.
- The structural analysis capabilities in the existing ANSYS family of commercial products, although automatically tied loosely to the new battery tools through Workbench, were not utilized significantly in this CAEBAT-1 project; a follow-on project in CAEBAT-2 and CAEBAT-3 has leveraged that investment by extending the ABDT concept to microstructural models of resolved electrodes and/or macroscopic mechanical battery abuse scenarios.

The MSMD is recognized as an effective model framework for modular architecture linking interdisciplinary battery physics across varied length and time scales. By implementing MSMD in Fluent, the team has overcome challenges in modeling the highly nonlinear multiscale response of battery systems. However, the inevitable nested iteration, ensuring self-consistency at each hierarchical level in the original MSMD, becomes a factor limiting computation speed. In a separate concurrent project in FY15 supported by DOE as part of CAEBAT-2, NREL developed a new quasi-explicit nonlinear multiscale multiphysics framework, the GH-MSMD (see Section III.C.7 of this report). The new framework uses time-scale separation and variable decomposition to eliminate several layers of nested iteration and still keeps the modular MSMD architecture that is critical to battery behavior simulations. Fast electronic charge balance is differentiated from the

processes related to slow ionic movements. During preliminary benchmark tests carried out at the electrode domain model (EDM) level, the GH-MSMD implementation demonstrated significant computational speed improvement compared to the original MSMD. One promising candidate to build on the accomplishments of this project is therefore to implement GH-MSMD into the commercially deployed ABDT tool, potentially increasing computational speed of the pack level simulation by a factor of 100. These latest developments will be carried into the third phase of CAEBAT to be started in FY16.

References

1. Grimme, E. J., “Krylov projection methods for model reduction,” Doctoral dissertation, University of Illinois at Urbana-Champaign, 1997.
2. “Battery Pack Simulation: Multiscale methods that achieve both speed and accuracy,” European Advanced Automotive & Stationary Battery Conference, 26–29, 2015, Mainz, Germany.

FY 2015 Publications/Presentations

1. Asgari, S., and Kaushik, S., “A linear parameter varying combined with divide-and-conquer approach to thermal system modeling of battery modules,” *SAE Int. J. Commer. Veh.* 15JAP-0010, 2015.

III.C.3 Open Architecture Software for CAEBAT (ORNL)

Objectives

- Develop and deploy a flexible and scalable computational framework that can integrate multiple physics models at various scales (battery pack, cell, electrodes, etc.), and provide a predictive modeling tool under the auspices of the CAEBAT program.
- Coordinate with partners across the program on requirements and design of the framework so as to preserve investment in existing models.
- Ultimately, the simulation capability will model coupled physical phenomena (charge and thermal transport; electrochemical reactions; mechanical stresses) across the porous 3D structure of the electrodes (cathodes and anodes) and the solid or liquid electrolyte system while including microscale effects through closures based on resolved quantities.
- Validate the simulation tool at the cell and pack level in order to provide design and analysis capability for next-generation batteries that exceed performance and safety requirements for transportation.

Project Details

Brian Cunningham (VTP Program Manager)

Subcontractor: ORNL

John A. Turner (Program Manager)

Computational Engineering and
Energy Sciences Group

Oak Ridge National Laboratory

Phone: 865-241-3943; Fax: 865-241-4811

E-mail: turnerja@ornl.gov

Collaborators: S. Allu, J. Billings, W. Elwasif,
S. Kalnaus, A. McCaskey, S. Pannala, S. Simunovic

Start Date: July 2010

End Date: September 2015

Technical Barriers

Given the complex requirements for development of electrical energy storage devices for future transportation needs, a predictive simulation capability which can accelerate design by considering performance and safety implications of different geometry, materials, and chemistry choices is required. This capability must leverage existing investments and integrate physics models across scales in order to (1) provide feedback to experiments by exploring the design space effectively, (2) optimize material components and geometry, and (3) address safety and durability in an integrated fashion.

Technical Targets

Develop computational framework that integrates both existing and new models developed by CAEBAT subcontractor teams that span the battery pack, modules, cells, etc. to provide an integrated design tool for battery manufacturers to optimize performance and safety in an accelerated fashion.

Accomplishments

- The Virtual Integrated Battery Environment (VIBE), which includes the CAEBAT Open Architecture Software (OAS) framework, standard interchangeable physics components, the Integrated Computational Environment (ICE), and support for standardized input (BatML) and Battery State, has been deployed through a new web site, <http://batterysim.org/>. Since its release, VIBE has been downloaded over 150 times by academic and industrial institutions around the world.
- Demonstration of cell, module, and pack simulation capabilities with automated mesh generation.
- Demonstration of two-way tight coupling between thermal and electrochemical components.
- Development of the AMPERES 3D electrochemistry capability, which is numerically stable up to extremely high discharge rates.

Introduction

Computational tools for the performance and safety analysis of battery systems are not currently predictive, in that they rely heavily on fitted parameters. While there is ongoing experimental research at various length

scales around the world, computational models are primarily developed for the lower-length scales (atomistic and mesoscopic), which do not scale to the system level. When this program started, models at the macroscopic or system level were typically based on electrical circuit models or simple 1D models, and there was no design tool for batteries that could leverage the significant investments in modeling efforts across DOE, industry, and academia. An open and flexible computational framework was developed that incorporated diverse existing capabilities as well as new capabilities developed by CAEBAT partners and now provides a foundation for design and rapid prototyping of batteries.

Approach

We have developed a flexible, robust, and computationally-scalable open-architecture framework that integrates multi-physics and multi-scale battery models. The physical phenomena of interest include charge and thermal transport, electrochemical reactions, and mechanical stresses. They operate and interact across the porous 3D structure of the electrodes (cathodes and anodes), the solid or liquid electrolyte system and the other battery components. The underlying lower-length processes are accounted for through closure equations and sub-models that are based on resolved quantities.

Results

Virtual Integrated Battery Environment (VIBE)

A hierarchical process to construct meshes for battery packs has been developed. In the automated script-based geometry and mesh construction procedure, a single prismatic cell is replicated to form a module which in turn is replicated to obtain a battery pack (Figure III- 52). This provides significant savings in time and effort in creating geometry for simulations.

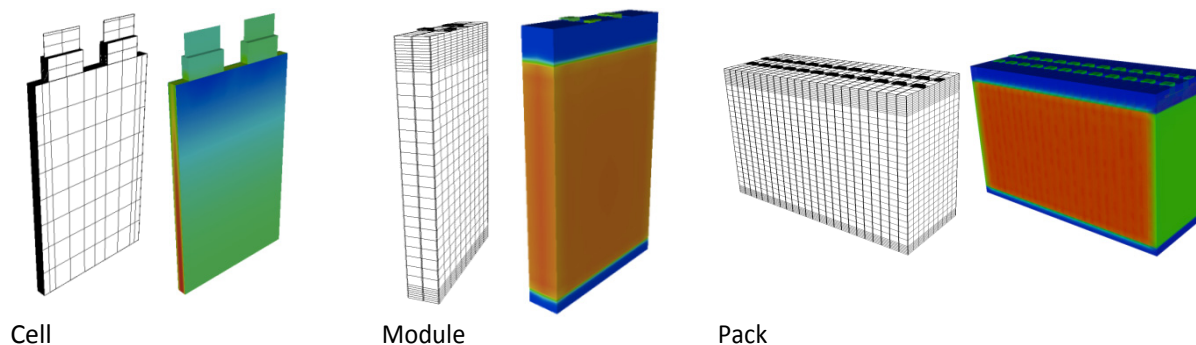


Figure III- 52: Automated mesh generation from cell to pack level with corresponding results of thermal solution

Mechanics simulations were performed with the goal of replicating the pinch test with a rigid sphere. Unlike other approaches for modeling battery response to an external load, where cell properties are homogenized over multiple domains, in this approach all layers are resolved. This allows application of failure criteria to each of the domains (electrode, current collector, separator, pouch material) independently, which in turn facilitates determination of the precise location of short circuits. Example results showing Von Mises stress on a deformed pouch cell mesh are shown in Figure III- 53.

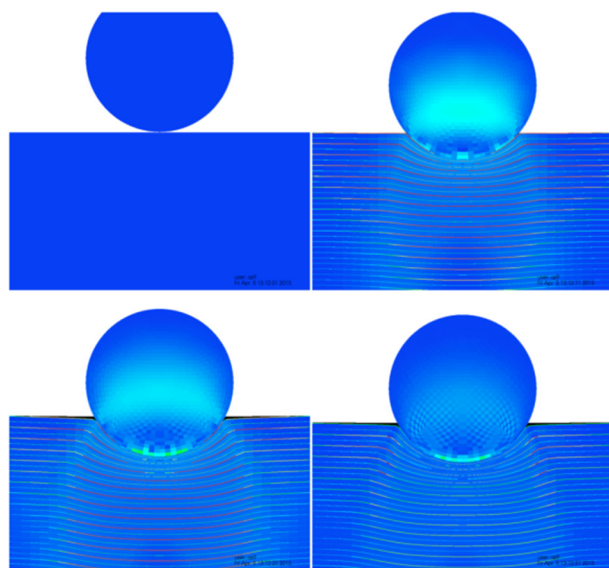


Figure III- 53: Von Mises stress distribution in different domains of a pouch cell under external mechanical loading

Battery Markup Language (BatML)

The objective of the Battery Markup Language (BatML) specification is to provide standardized format for definition of all the necessary information for modeling of battery performance. The main benefit of the standardized format is to enable easy method for exchange of battery model information between different programs. Large commercial simulation software packages already use eXtensible Markup Language (XML) and XML is a de-facto standard for data exchange on the Internet. XML can be tuned to the specifics of data that needs to be exchanged using XML Schemas. The schemas impose structures and controls that make data exchange much more efficient and robust. BatML is an XML variant that is tailored using BatML schema that include specifics of the battery information (hierarchical structure, physics, chemistry, etc.). BatML uses Material Markup Language (MatML) and Units Markup Language

(UnitsML) as its subsets. As an example, MatML is used in ANSYS for material model data, so that the data from ANSYS models can be easily exported into BatML format.

During FY2015, ORNL worked with BDS, ECPower and ANSYS developers and NREL colleagues to develop methods to convert data between different model types. The conversions were demonstrated on examples provided by the software vendors.

BatML has been documented on the project's web site <http://energy.ornl.gov/BatML>.

Specifics of the BatML schema have been documented at http://energy.ornl.gov/BatML/battery_ml.

At the same web site, we have implemented a program that validates the format of BatML documents. Users can upload BatML files to check if such files conform to the BatML schema specification. The program provides error report for non-compatible data that can be used for format debugging.

Battery State

The battery state file format was expanded by the addition of local state of charge as a variable in addition to local temperature, resistance, and heat source. This accomplishes the goal of including gradients in remaining capacity within the 3D domain of a cell (module, battery pack). When coupled with a thermal component, this allows modeling the influence of cooling strategies and temperature gradients on battery health. For example, module-level coupling allowed performing simulations of modules consisting of 4 pouch cells connected either in parallel or in series. Simulations of uneven cooling conditions on the module surface show that the potential difference in the cells on two sides can be as high as 2.5 mV. The results for a 4P module are shown in Figure III- 54.

Open Architecture Software (OAS)

OAS facilitates flexible coupling of physics components. Both loose and tight coupling of thermal and electrochemical components have been demonstrated. As one example, the well-known DualFoil pseudo-2D electrochemistry model (written in FORTRAN) has been coupled to the AMPERES 3D thermal model (written in C++) using OAS. Temperature-dependent diffusivities and Butler-Volmer kinetics provide feedback between physics components. Figure III- 55 shows results for discharge rates of 1C, 2C, and 3C for an unrolled Li-polymer cell for both loose and tight coupling. Improved accuracy is observed for higher discharge rates when using tight coupling, with rapid convergence of Picard iterations, typically <4 iterations. Other combinations of components that have been coupled include:

- DualFoil electrochemistry + AMPERES thermal
- DualFoil electrochemistry + AMPERES thermal + AMPERES electrical

- AutoLion¹⁰ (ECPower) + Dakota¹¹ (for optimization / parameter sweep)
- 1DElectrode electrochemistry (Sandia National Laboratories) + AMPERES thermal
- 1DElectrode electrochemistry + AMPERES thermal + AMPERES electrical
- AMPERES Newman-Tiedemann-Gu (NTG) electrochemistry + AMPERES thermal
- AMPERES NTG electrochemistry + AMPERES thermal + AMPERES electrical
- AMPERES 3D electrochemistry + LS-Dyna mechanics

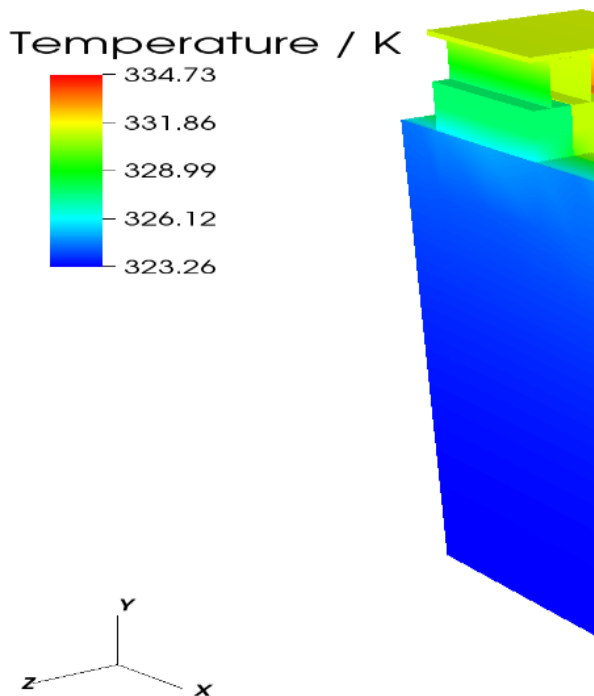


Figure III- 54: Temperature distribution in a module with asymmetric cooling

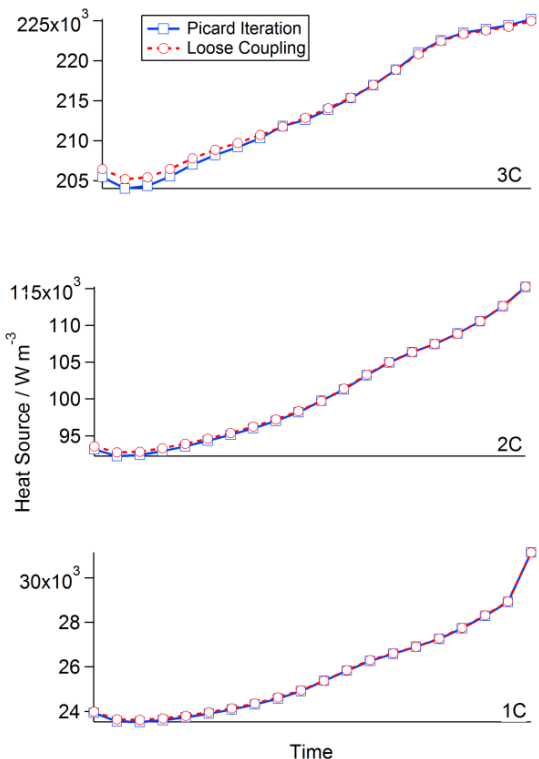


Figure III- 55: Calculated volumetric heat source using loosely and tightly coupled scenarios

Graphical User Interface and Integrated Workflow Environment. A customized version of the Eclipse Integrated Computational Environment (ICE)¹² was developed for simulation setup, launch and post-processing of simulations performed using VIBE/OAS. ICE currently allows:

- Editing of OAS input setup files
- Editing of BatML files
- Local and remote job launch
- Multi-file upload and download of VIBE data
- 3D visualization of output

A screen shot of the CAEBAT-ICE environment is shown in Figure III- 56. The tool facilitates model setup, with drop-down menus for model (component) selection, simulation control parameters and input of the material properties.

¹⁰ <http://ecpowergroup.com/autolion-2/>

¹¹ <https://dakota.sandia.gov/>

¹² <https://projects.eclipse.org/projects/technology.ice>

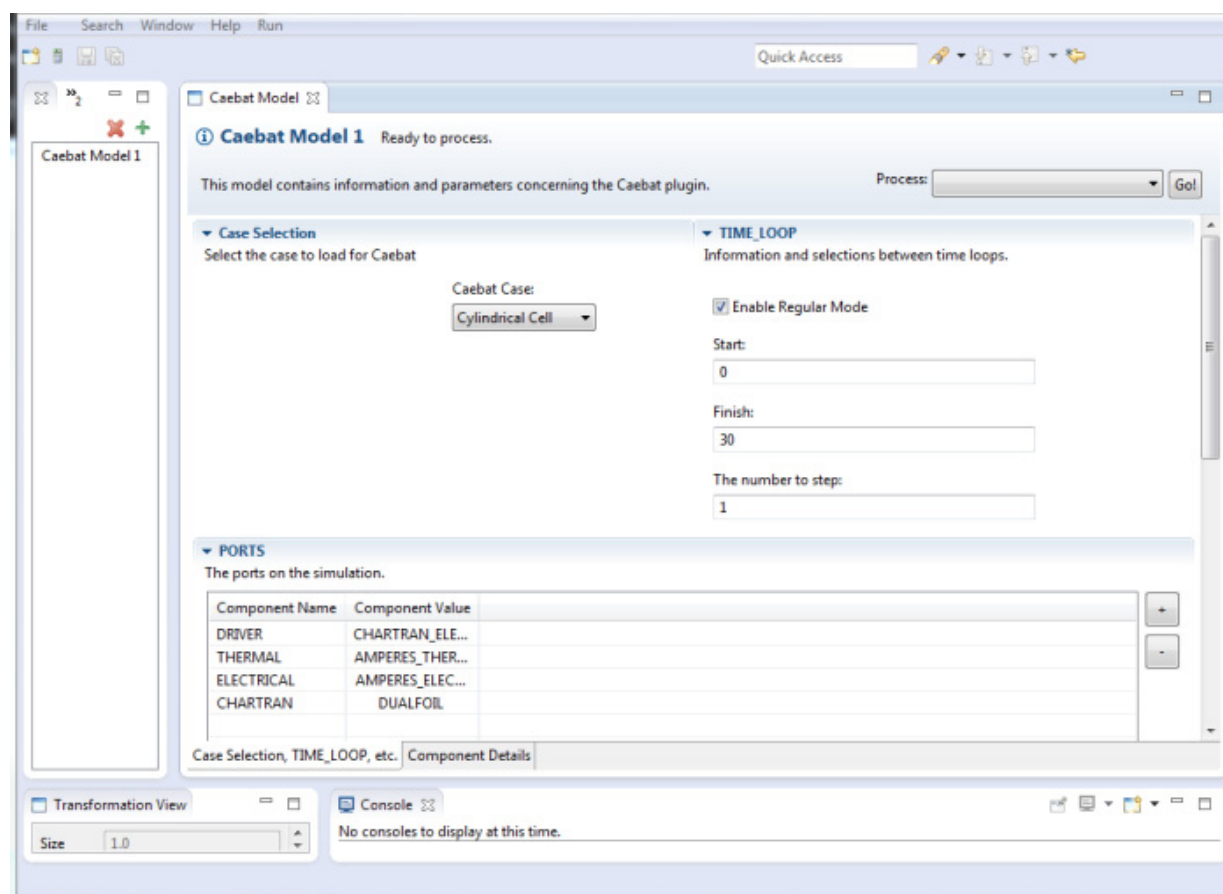


Figure III- 56: CAEBAT-ICE workflow environment for simulation setup, job launch and data post-processing

Conclusions and Future Directions

- The Virtual Integrated Battery Environment (VIBE), which includes the CAEBAT Open Architecture Software (OAS) framework, standard interchangeable physics components, the Integrated Computational Environment (ICE), and support for standardized input (BatML) and Battery State, has been deployed through a new web site, <http://batterysim.org/>. The software is packaged as a Virtual Machine for download, which allows distribution of a pre-configured, self-contained system that requires no installation in order to use. However, all necessary instructions and components are provided for users who wish to perform their own build, install, and configuration. Providing such flexibility appears to be desirable, because since its release, VIBE has been downloaded over 150 times by users around the world, including those from Apple to Lockheed Martin.
- VIBE provides cell to module to pack capabilities with automated mesh generation, two-way tight coupling between thermal and electrochemical components, and the AMPERES 3D electrochemistry capability, which is numerically stable up to extremely high discharge rates.
- Although this project has concluded, the strong interest in VIBE from the community indicates that support and improvements in coming years could be warranted. Specific areas of potential improvement include:
 - Investigation of container technologies such as Docker¹³ and Rocket¹⁴ for deployment, which would dramatically reduce the download size of VIBE.
 - Exploration of the cloud model.
 - Improvements to the ICE workflow and user interface capability.

¹³ <https://www.docker.com/>

¹⁴ <https://coreos.com/blog/rocket/>

- Documentation, user support, and outreach.
- BatML/Battery State revisions based on community feedback.
- Bug fixes and updates (as necessary)

FY 2015 Publications/Presentations

1. A.J. Stershic, S. Simunovic, J. Nanda, Modeling the evolution of lithium-ion particle contact distributions using a fabric tensor approach, *Journal of Power Sources*, Volume 297, 30 November 2015, Pages 540-550, ISSN 0378-7753, <http://dx.doi.org/10.1016/j.jpowsour.2015.07.088>.
2. S. Pannala, J. A. Turner, S. Allu, W. Elwasif, S. Kalnaus, S. Simunovic, A. Kumar, J. J. Billings, H. Wang, and J. Nanda, "Multiscale modeling and characterization for performance and safety of lithium-ion batteries," *J. Applied Physics* 118, 072017, Aug, **2015**, <http://dx.doi.org/10.1063/1.4927817>.
3. J. A. Turner, S. Allu, M. Berrill, W. Elwasif, S. Kalnaus, A. Kumar, D. Lebrun-Grandie, S. Pannala, S. Simunovic, "Safer Batteries Through Coupled Multiscale Modeling," *Procedia Computer Science* (51) **2015**, pp. 1168-1177, <http://dx.doi.org/10.1016/j.procs.2015.05.286>.
4. J. A. Turner, S. Allu, S. Kalnaus, A. Kumar, S. Pannala, S. Simunovic, H. Wang, "Simulation of Battery Mechanical Abuse and Thermal Runaway (AABC 2015)," *Advanced Automotive Battery Conference*, Detroit, Michigan, USA, June 15—19, **2015**.
5. J. A. Turner, S. Allu, W. Elwasif, S. Kalnaus, A. Kumar, D. Lebrun-Grandie, S. Pannala, S. Simunovic, S. Slattery, "Coupled multiscale safety simulations of Li-ion batteries." *2nd Frontiers in Computational Physics Conference: Energy Sciences*, Zurich, Switzerland, June 03—05, 2015.
6. J. A. Turner, S. Allu, M. Berrill, S. Kalnaus, A. Kumar, D. Lebrun-Grandie, S. Pannala, S. Simunovic, H. Wang, "Safer Batteries through Coupled Multiscale Modeling." *ICCS 2015 / 12th Intl Wkshp on Multiscale Modelling and Simulation*, Reykjavik, Iceland, June 01—04, **2015**.
7. S. Allu, S. Pannala, S. Kalnaus, A. Kumar, S. Simunovic, H. Wang, J. A. Turner, "Multiscale/Multiphysics Modeling for Performance and Safety of Lithium-Ion Batteries (Next Generation Batteries 2015)." *Next Generation Batteries 2015*, San Diego, California, USA, Apr, 21—22, **2015**.
8. M. A. Martin, C-F Chen, P. P. Mukherjee, S. Pannala, J-F Zietiker, J. A. Turner, and D. Ranjan, "Morphological Influence in Lithium-Ion Battery 3D Electrode Architectures," *J. Electrochem. Soc.* Mar, **2015** 162(6): A991-A1002; <http://dx.doi.org/10.1149/2.0631506jes>.
9. J. A. Turner, S. Allu, S. Kalnaus, A. Kumar, S. Pannala, S. Simunovic, H. Wang, "Advanced Crash Testing and Simulations for Automotive Batteries (32nd Intl. Battery Seminar)." *32nd International Battery Conference & Symposium*, Ft. Lauderdale, Florida, USA, March 09—12, **2015**.
10. S. Kalnaus, S. Pannala, S. Allu, W. Elwasif, S. Simunovic, J. J. Billings, A. Bennett, A. Kumar, J. A. Turner, "CAEBAT OAS/VIBE – Production Release v1.1," Mar, **2015**, <http://www.batterysim.org>.
11. J. A. Turner, S. Allu, S. B. Gorti, S. Kalnaus, A. Kumar, D. T. Lebrun-Grandie, S. Pannala, S. Simunovic, S. R. Slattery, H. Wang, "Crash Models for Automotive Batteries (DOT/NHTSA Project Report)," *ORNL Report TM-2015/366*, Feb, **2015**.
12. J. A. Turner, S. Allu, S. Kalnaus, A. Kumar, S. Pannala, S. Simunovic, H. Wang, "Li-ion Battery Safety Modeling (2015 SAE Gov/Ind Mtg)," *Society of Automotive Engineers 2015 Government/Industry Meeting*, Washington, District of Columbia, USA, January 21—23, **2015**.
13. J. A. Turner, S. Allu, W. Elwasif, S. Kalnaus, A. Kumar, S. Pannala, S. Simunovic, H. Wang, "Toward Predictive Crash Modeling of Automotive Batteries (Battery Safety 2014)," *Battery Safety 2014*, Washington, District of Columbia, USA, November 12—14, **2014**.
14. S. Allu, S. Pannala, J. Nanda, S. Simunovic, J. A. Turner, "A Generalized 3D Multiphysics Model for Li-Ion Intercalation Batteries," *ECS Meeting*, Oct, **2014**, <http://ma.ecsdl.org/content/MA2014-02/1/34.abstract>.
15. S. Simunovic, A. Stershic, S. Kalnaus, S. Allu, S. Pannala, J. A. Turner, "Mesoscale Models for Mechanics of Active Materials in Li-Ion Batteries," *ECS Meeting*, Oct, **2014**, <http://ma.ecsdl.org/content/MA2014-02/1/38.abstract>.

III.C.4 Coupling Mechanical with Electrochemical-Thermal Models Batteries under Abuse (NREL)

Objectives

- The main objective of this project is to develop mathematical models to couple the electrochemical-thermal (ECT) behavior of a lithium-ion (Li-ion) cell to its structural behavior after rapid mechanical deformation, with the eventual goal to predict the onset of a thermal runaway after a crash-induced crush.
- A second objective of this project is to develop validated codes to predict the combined structural, electrical, and thermal responses to a thermal ramp.

Technical Barriers

- Concerns regarding potential thermal event by Li-ion batteries in today's plug-in electric vehicles (PEVs) delaying faster adoption of PEVs.
- Poor availability of characterization data that identify mechanical limitations of Li-ion cells.
- Non-availability of a standard experimental approach that is widely accepted by the industry to characterize the mechanical response of a Li-ion cell and the resulting implications for battery safety.
- Limited understanding of physical phenomena that take place within a Li-ion cell just before and after a mechanical crush that result in the failure of the battery cell components.

Project Details

Brian Cunningham (DOE Program Manager)

DOE Agreement # 27041, Recipient:
National Renewable Energy Laboratory

Ahmad Pesaran (NREL – PI)

15013 Denver West Parkway, M/S 1633
Golden, CO 80401

Phone: 303-275-4441; Fax: 303-275-4415

Email: Ahmad.Pesaran@nrel.gov

<http://www.nrel.gov/vehiclesandfuels/energystorage/>

Subcontractors:

ANSYS

Massachusetts Institute of Technology

Start Date: October 2013

Projected End Date: March 2015

Technical Targets

The major technical targets for this effort include the:

- Creation of an experimentally validated mechanical deformation model for a Li-ion cell
- Development of a mechanism to understand the interactions among the mechanical effects and the chemical runaway reactions that occur within the cell
- Implementation of the coupling between the mechanical and ECT models on the ANSYS software platform for designing safer cells.

Accomplishments

- We developed a representative-sandwich (RS) model to predict the mechanical deformation of Li-ion cells under indentation tests.
- The team developed an analytical method to estimate through-thickness mechanical properties of battery cell components.
- The team proposed a couple of approaches to predict the mechanical-electrical-thermal response during a crush event.
- We conducted systematic case studies investigating the role of mechanical failure and electrical contact area on the subsequent electrical and thermal responses during a mechanical abuse.
- This report highlights the comparison of the simulation results to experimental data including results from the phenomenological models developed by our team members at Massachusetts Institute of Technology (MIT), the cell-level implementations by ANSYS, and the coupled models built at NREL using this information.

Introduction

The safety behavior of Li-ion batteries under external mechanical crush is of critical concern, especially during large-scale deployment. In this report, we present the mechanical response of Li-ion cells under different test conditions and examine the interaction between mechanical failure and electrical-thermal response by developing a simultaneously coupled mechanical-electrical-thermal model. This project as part of the CAEBAT-2 activity started in October 2013 with collaboration between NREL, MIT and ANSYS. The present work utilizes a single representative layer of electrodes (RS) to model the full pouch cell with explicit representations for each individual component, including the active material, current collector, separator, etc. Anisotropic constitutive material models are presented to describe the mechanical properties of the active materials and separator. The model accurately predicts the force-strain response and fracture of the battery structure, simulates the local failure of the separator layer, and captures the onset of the short circuit for the Li-ion battery cell under sphere indentation tests with three different diameters. Electrical-thermal responses to the three different indentation tests are elaborated and discussed. Numerical studies are presented to show the potential impact of the test conditions on the electrical-thermal behavior of the cell after the occurrence of the short circuit.

Approach

Our modeling approach builds upon the capabilities established during the last few years under CAEBAT-1. In this CAEBAT-2 project, NREL teamed with ANSYS to take advantage of the Multi-Scale Multi-Domain (MSMD) implementation of the ECT model for Li-ion batteries. The mechanical response is simulated using explicit methods available in the commercial finite-element software LS-DYNA. The material properties for the layers under various loads are measured by partner MIT in the Impact and Crash Laboratory.

Coupled Mechanical-Electrical-Thermal Model

We use solver modules available in LS-DYNA by default: solid mechanics solver, thermal solver, and electromagnetic (EM) solver. The basic equations for the three solvers are summarized below. The mechanical solver is used to solve for deformation and predict the failure of a structure suffering external or internal loading conditions. The explicit mechanical solver seeks a solution to the momentum conservation equation:

$$\sigma_{ij,j} + \rho f_i = \rho u_{i,tt} \quad (1)$$

where σ_{ij} denotes the components of stress, u_i denotes the components of displacement, ρ is the density, f_i is the body force density, and t is time. The comma on $\sigma_{ij,j}$ denotes covariant differentiation; similarly, $u_{i,tt}$ denotes acceleration. For a solid, the constituent (stress-strain) relationship can be written as follows:

$$\sigma_{ij} = C_{ijkl} \gamma_{kl} \quad (2)$$

where C_{ijkl} is the stiffness matrix, and the components of strain γ_{kl} are related to displacement by the following relationship:

$$\gamma_{kl} = \frac{1}{2} \left(\frac{\partial u_k}{\partial x_l} + \frac{\partial u_l}{\partial x_k} \right) \quad (3)$$

where x is the coordinate. And the indexes i, j, k , and l equal 1, 2, and 3 corresponding to x, y , and z directions. The LS-DYNA EM solver employs the eddy current approximation, which assumes a divergence-free current density and no charge accumulation. Two equations constituting the system response will be solved:

$$\nabla(\kappa \vec{\nabla} \varphi) = 0 \quad (4)$$

$$\kappa \frac{\partial \vec{A}}{\partial t} + \nabla \times \left(\frac{1}{\mu} \nabla \times \vec{A} \right) + \kappa \nabla \phi = \vec{j}_s \quad (5)$$

where the magnetic vector potential, \vec{A} , and electric scalar potential, ϕ , are two unknowns to be solved; κ is the electrical conductivity, μ is the magnetic permeability, and \vec{j}_s is the source current density. After solving the above two equations, the Lorentz force, $\vec{F}_{Lorentz}$, and Joule heating energy, E_{Joule} , can be computed as:

$$\vec{F}_{Lorentz} = \vec{j} \times \vec{B} \quad (6)$$

$$E_{Joule} = \frac{\vec{j} \cdot \vec{j}}{\kappa_s} \quad (7)$$

where J is the current density.

For the thermal solver, the governing equation of the conduction of heat in a three-dimensional solid is given by:

$$\rho c \frac{\partial T}{\partial t} = \frac{\partial}{\partial x_i} \left[k_{ij} \frac{\partial T}{\partial x_j} \right] + Q \quad (8)$$

where T is temperature, c is specific heat, k_{ij} is thermal conductivity, and Q indicates heat generation rate per unit volume, Ω .

In LS-DYNA, the mechanical, EM, and thermal solvers are fully coupled to each other. Figure III- 57 shows the interactions among the LS-DYNA mechanical, thermal, and EM solvers. The three solvers have distinct time steps, and generally the mechanical time step is a lot smaller than the EM and thermal time steps. At each mechanical time step, the EM and thermal field values are calculated by linear interpolation. At each EM time step, the EM solver and the mechanical solver interact, during which the EM solver communicates the Joule heating term, E_{Joule} , to the thermal solver while the thermal solver communicates the temperature to the EM solver.

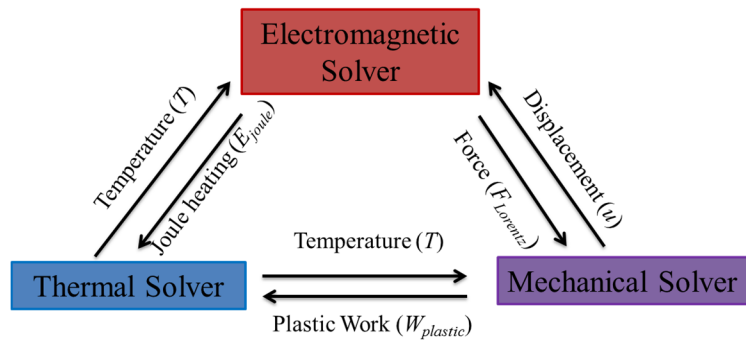


Figure III- 57: Interactions among the mechanical, EM, and thermal solvers for the simultaneously coupled modeling approach

At each EM time step, the EM solver communicates the Lorentz force described in Eq. (6) to the mechanical solver, which results in an extra force in the mechanical governing equation (Eq. (1)):

$$\sigma_{ij,j} + \rho f_i + F_{Lorentz} = \rho u_{i,t} \quad (9)$$

The mechanical solver returns the displacements and deformation of the structure to the EM solver. Similarly,

at each thermal time step the thermal solver communicates temperature to the mechanical solver while the mechanical solver communicates the value of the plastic work, $W_{plastic}$, to the thermal solver. The plastic work and Joule heating are the predominant sources of heat generation in our case, so Eq. (8) can be rewritten as follows:

$$\rho c \frac{\partial T}{\partial t} = \frac{\partial}{\partial x_i} \left[k_{ij} \frac{\partial T}{\partial x_j} \right] + \frac{\dot{W}_{plastic} + \dot{E}_{Joule}}{V} \quad (10)$$

where the dot indicates the time derivative, and V is the volume of the element. Note that there is no explicit representation of temperature in the governing equation for the mechanical and EM solvers. The material properties, such as conductivity, κ , and stiffness, C_{ijkl} , evolve as a function of the temperature. However, due to the limited availability of experimental data, in this work all the material properties are considered to be temperature independent throughout the analysis.

In typical electrochemical battery models, the magnetic field is not considered assuming $A = 0$ all over. Then the electrical potential can be obtained by solving the following two equations:

$$\vec{j} = -\kappa_s \vec{\nabla} \varphi \quad (11)$$

$$\vec{E} = -\vec{\nabla} \varphi \quad (12)$$

where \vec{E} is the electrical field. These are simplified versions of Eqs. (4) and (5). Contributions from the electrolyte to the short circuit are assumed to be negligible (κ_s is the solid-phase conductivity)—given that the difference between the electronic and ionic conductivities is four orders in magnitude or larger.

The goal of the model is to predict the initiation of the short circuit and its consequential evolution of the electrical properties (current and voltage) and temperature and, more importantly, the effect of external deformation on the electrical and thermal response of the cell. The information obtained from these simulations is extremely helpful for studying the electrochemical responses.

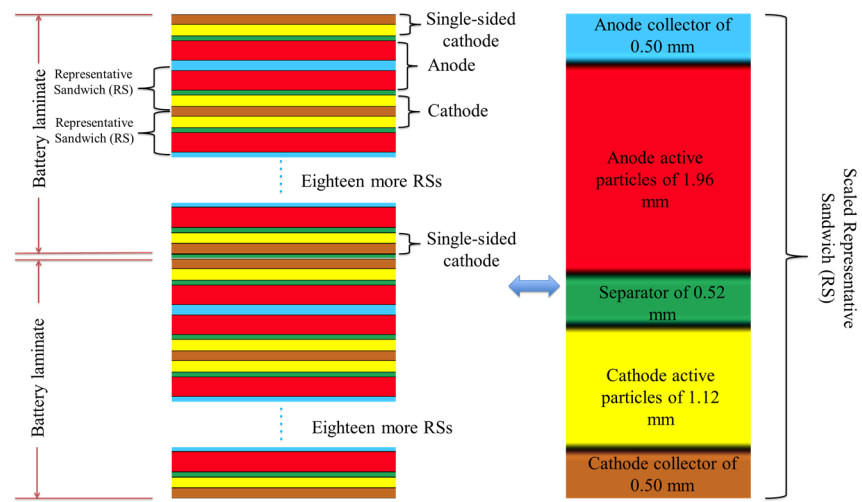
Numerical Implementation

The Li-ion battery studied in this work is a LiCoO₂ pouch cell that was previously characterized by MIT. The nominal capacity of the cell is 740 mAh with a nominal voltage of 3.7 V. To simulate the local damage and predict the short circuit, it is necessary to model each individual component (separators, collectors, and active materials) of the battery structure. In this work, a finite-element model was built to explicitly model each individual component without losing computational efficiency or accuracy. We use the electrical contact between the active materials following the failure of the separator as a criterion for the short circuit.

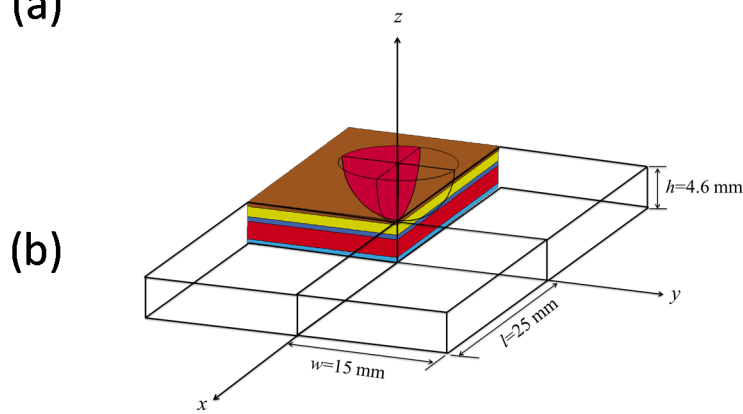
Representative Sandwich Model

The detailed stacking and dimensions of the studied pouch cell were reported by Sahraei et al. at MIT. It was found that the pouch cell was composed of two separate laminates; each can be considered a multilayered plate made from cathodes, anodes, and separators. A cross-sectional view is shown in Figure III- 58(a). A cathode and anode are each composed of collector and active layers. An RS is introduced to define the repeating layout, as shown in Figure III- 58(a). Each RS contains a cathode active material layer, a cathode current collector layer, an anode active material layer, an anode current collector layer, and one separator layer. The whole pouch cell contains approximately 165 layers, and it can be estimated to comprise of 40 representative sandwiches. The modeling of all 165 layers (the full pouch cell model) is computationally very costly. One simplifying approximation is to represent the 40 sandwiches as one single equivalent but with thicker RS (shown on the right side of Figure III- 58(a)), such that each layer has a proportionately larger thickness.

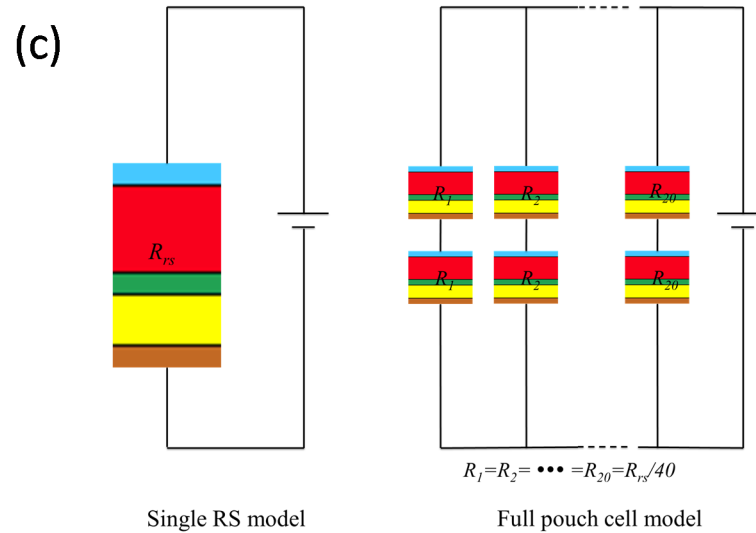
The schematic representation of an indentation model is shown in Figure III- 58(b). Due to symmetry, and to save computational time, we consider only one-quarter of the actual in-plane domain in our finite-element model. The geometry in our finite-element representation has a length, l , of 29.75 mm; a width, w , of 17 mm; and thickness, h , of 4.6 mm. The bottom surface (i.e., $z = 0$) of the battery models is constrained in the thickness direction (z -direction). The indentation tests were conducted with rigid spheres with diameters of 12.7 mm, 28.575 mm and 44.45 mm in three different test cases, respectively, moving downward in the z -direction at a constant speed to accomplish the loading process in 0.01 second. Although the loading speed is much higher than that in a typical quasi-static experiment, the simulations are still considered quasi-static because we were able to verify that the kinetic energy was less than 1% of the total energy.



(a)



(b)



(c)

Figure III- 58: (a) Cross-sectional view of a pouch cell and schematic of an RS: the pouch cell is represented by a single RS that explicitly represents the thickness proportions of each individual component. (b) Schematic and dimensions of the single RS indentation model: a quarter of the actual domain is utilized in the finite-element model based on symmetry. (c) Schematic of electrical connections for the single RS model and full pouch cell model: in this work, scaled electrical conductivity properties are utilized for each individual component of the single RS model to theoretically match the overall Joule heat

The battery model was meshed using solid elements, with 18 elements through the thickness (z -direction), 100 elements along the length (x -direction), and 60 elements through the width (y -direction), resulting in a total of 108,000 elements for the RS model. The indenter is modeled as a rigid sphere.

Constitutive Models for Battery Components

The development of an accurate constitutive model is essential to building a predictive model. Preliminary test results from MIT suggest that the electrodes and separator have significantly different tensile and compressive responses due to the presence of porous active materials. The separator is also known to be anisotropic under in-plane tensile loading conditions. Under this effort, MIT built an extensive experimental data set for the cell components (Figure III- 59) and developed anisotropic models.

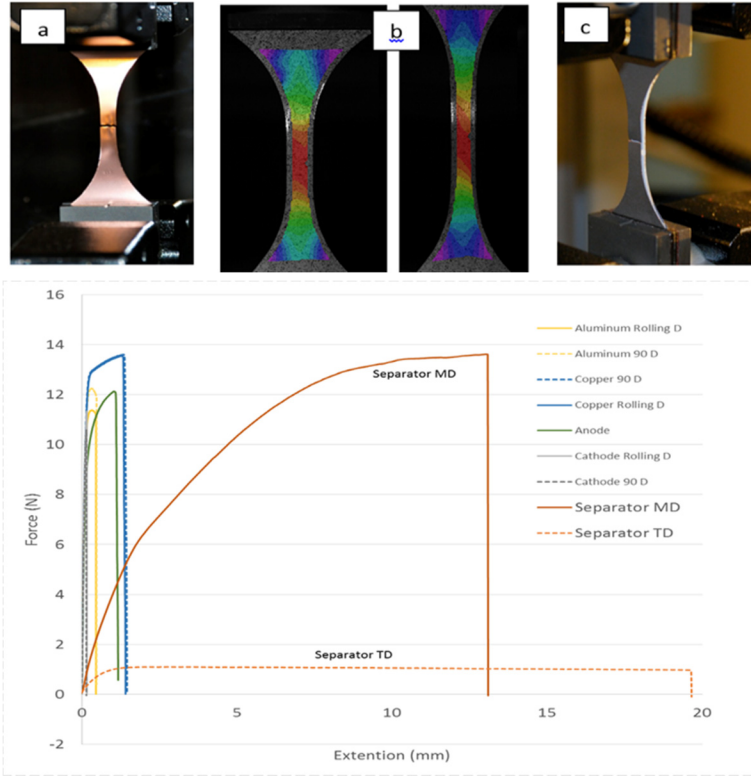


Figure III- 59: Experimental measurement of material properties

Electrical-Thermal Model

For the coupled simulations, a constant voltage of 3.7 V is applied between the top and bottom surfaces of the RS. The evolution of the voltage after the initiation of a short circuit is studied by calculating the internal voltage drop caused by the sudden decrease in resistance due to the short circuit. For thermal simulations, a default adiabatic boundary condition is used for the symmetrical surfaces ($x = 0, y = 0$). For the other four external surfaces ($x = -w, y = -l, z = 0$, and $z = h$), a convection boundary condition is defined to model the heat exchange between the surroundings and the battery cell:

$$q = k_{ij} \frac{\partial T}{\partial x_j} = h(T - T_{\infty}) \quad (13)$$

where q is the heat transferred per unit time and per unit area; h is the heat transfer coefficient, which in this work is defined as $15 \text{ W}/(\text{m}^2 \cdot \text{K})$; and T_{∞} is the temperature of the surroundings, which is considered constant at 298 K. An initial temperature of 298 K is applied to all the elements.

Mechanical and Electrical-Thermal Failure Criterion

The objective of this work is to predict the structure fracture-induced electrical short circuit of Li-ion batteries LIB under quasi-static indentation. Proper failure criteria and failure parameters should be implemented and defined to enable this capability. We used a maximum volume-strain failure criterion earlier to simulate the mechanical failure of the separator, and we carried out a parametric study on the maximum through-thickness volume-strain value of the separators using the single-RS model and found that when the failure strain equals 0.93 (which means that the thickness of the element is compressed to 7% of the initial thickness), the numerically predicted and the experimentally measured global failure strains match. In this work, the maximum tensile failure criterion implemented using the Honeycomb Model was utilized to simulate separator failure. The tensile failure strain of the separator varies a lot depending on the polymer component, manufacturing process, and specimen preparation.

We first conducted a mechanical-only simulation to correlate the mechanical indentation test results and recorded the critical global displacement, u_f , of the indenter at the moment of the cell fracture. Then we conducted the coupled simulation by applying exactly the amount of critical displacement, u_f , to the indenter and disabling mechanical failure criterion. Through this method we can obtain exactly the same deformed geometry at the instant of the cell fracture. The electrical contact is defined by a distance-based criterion, which means that the electrical contact initiates when the distance between two parts is below a certain threshold value, d_c . Once the mechanical failure criterion is satisfied, no more loading was added, which

corresponds to the test case in that the indenter will be held in place without further movement. No further deformation or relaxation occurred inside the pouch cell beyond the instant of the mechanical failure.

While existing models assume initiation of electrical contact following the mechanical failure of the separator layer, our approach calculates the current flow across the component layers that border the element subjected to the mechanical failure and utilizes the resultant voltage drop to determine the short resistance. This process allows us to introduce additional failure criteria based on the electrical and thermal properties of the different layers coming into contact across the instance of the mechanical failure. For instance, in this work, the criterion for the electrical failure is the instantaneous local current density exceeding a preset value, such as 0.01 C, which corresponds to a current density of 13.12 mA/mm² for a 740-mAh cell when the area of the elements subject to mechanical failure is 0.785 mm². Thermal failure is set to initiate when the temperature across the element in question exceeds the melting point of the corresponding material (e.g., 144°C or 417 K for the separator). However, mechanical failure sets in instantaneously compared to the thermal response, which is usually distributed throughout a span of several seconds. Accordingly, in this work we present our methodology for linking the mechanical-failure criterion to the follow-on electrical activity and discuss some preliminary thermal responses.

The numerical models were solved on a high-performance computing system equipped with a total of 31,104 Intel Xeon processors providing a total of approximately 608 TeraFLOPS or trillion floating-point calculations per second. The computational time for the mechanical-only simulation is 8 hours using 60 CPUs (central processing units), while the computational time for the coupled model was 16 hours, also using 60 CPUs.

Results

An efficient mechanical modeling strategy was established with the capability to predict the onset of the mechanical fracture and enable the coupled modeling of the electrical and thermal behavior. The mechanical model was validated through comparison of the numerically predicted and experimentally measured force and global-strain curves (see Figure III- 60). Utilizing the constitutive and failure models described in the previous section, the mechanical responses of the cell subjected to the indentation using the spherical indenters of three different diameters (12.7 mm, 28.575 mm, and 44.45 mm—named small punch, medium punch, and large punch, respectively) were simulated. Experimental indentation tests corresponding to these results on the pouch cell described above were conducted by MIT using the hemispherical punches at a loading rate of 1 mm/minute while monitoring the voltage simultaneously. A significant finding of the experimental results was the fact that the electrical short circuit detected from the drop in cell voltage coincided well with the drop in the load due to the mechanical failure.

Coupled Mechanical-Electrical-Thermal Simulation

In our work the global strain is defined as the applied displacement of the rigid sphere over the initial thickness of the RS model. The force is recorded as the reaction force of the rigid sphere in the through-thickness direction (z -direction). The maximum tensile failure strain of the separator is obtained through a parametric study comparing the numerical predicted force-strain curves to the experimental curves. Figure III- 60 (a) shows the parametric study of the mechanical responses for the small-punch indentation test obtained by varying the tensile failure strain of the separator. It is found that the numerically predicted global failure strain of the battery cell increases with the increase of the tensile failure strain for the separator layer. When the tensile failure strain of the separator equals 0.29, the numerical predicted and the experimentally measured global failure strain match.

Note that the failure strain value used for the indentation model is much lower than the experimental measured value in a uniaxial tensile test. This is because under a structure-level test some other local premature damage events—for example, cracking of electrodes—may cause earlier failure of the separator. The strain contour of the active materials at the instant before the fracture of the battery cell is shown in Figure III- 60 (a), from which we can see that the maximum tensile strain value of the active materials is about 0.2487, exceeding the experimental detected tensile failure strain of 0.03. This suggests that before the failure of the separator, the active material layers were very likely cracked.

The failure shape of the separator layer is also shown in Figure III- 60 (a). The crack initiated at exactly the center of the structure ($x=y=0$, Figure III- 58(b)) and propagated along the y -direction (machine direction). The cracking behavior is consistent with the characterized fracture image using X-ray CT scanning, which is likely

due to the anisotropic feature of the separator and the in-plane aspect ratio (length/width). The successful prediction of the cracking behavior further elaborates the significance of the presented single-RS model. Figure III- 60 (b) presents a comparison of the numerical and experimental results for the indentation tests using punches of three different diameters. The single-RS model predicts well the force-strain responses under all three indentation conditions, showing the suitability of the material models presented here in capturing the mechanical response of the pouch cell components and the viability of using the single-RS model to predict the global mechanical response of the full pouch cell. The latter observation is important when scaling these models to simulate the response of the multi-cell modules or battery packs. The single-RS model is capable of predicting the onset of failure within the pouch cell under indentation, and it enables a lumped representation of the cell with the ability to incorporate the mechanical properties of the individual cell components.

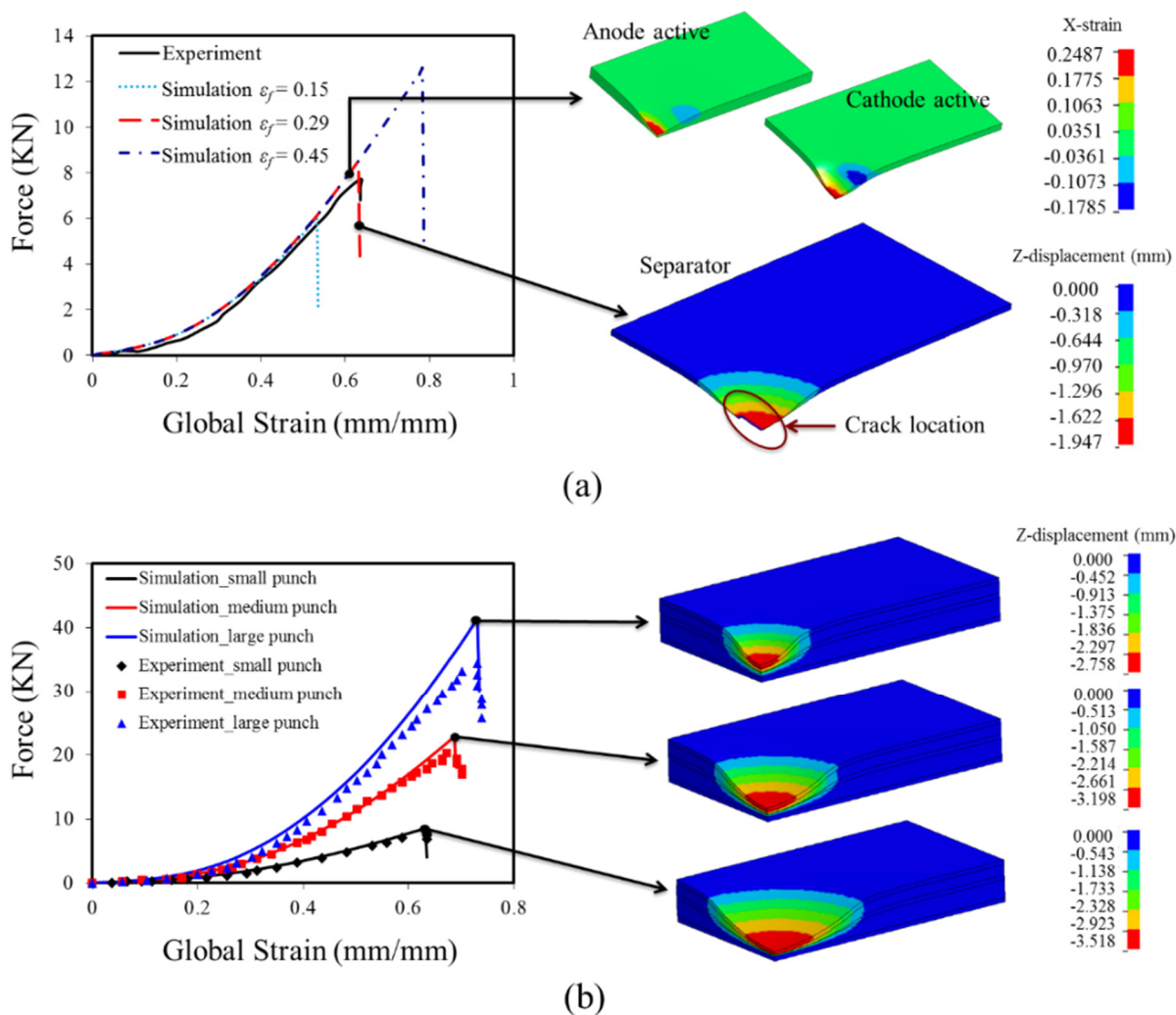


Figure III- 60: (a) Correlation of numerically predicted and experimentally measured force-strain curves for the small-punch indentation test and numerically predicted deformation of the separator and active materials at the instant of the cell fracture. The crack in the separator layer propagates along the y-direction, consistent with the experimental observation. (b) Comparison of the numerically predicted and experimentally measured force-strain responses for three different indentation tests and the numerically predicted deformation of the battery cell at the instant of the cell fracture. With an increase in indenter diameter, the maximum indentation depth at the moment of the fracture increases, indicating that the larger-punch test results in a delayed failure of the cell

Note that the onset of the cell fracture under different indentation conditions is predicted through parametric studies of tensile failure strain for the separator layer, shown in Figure III- 60 (a). The parametric study results in different tensile failure strain values for the three indentation conditions, which are 0.29 for the small punch, 0.17 for the medium punch, and 0.15 for the large punch. This is because the tensile strain of the separator is

related to the indenter diameter. A smaller indenter produces a sharp deformation and results in a relatively higher maximum tensile strain for the same indentation depth.

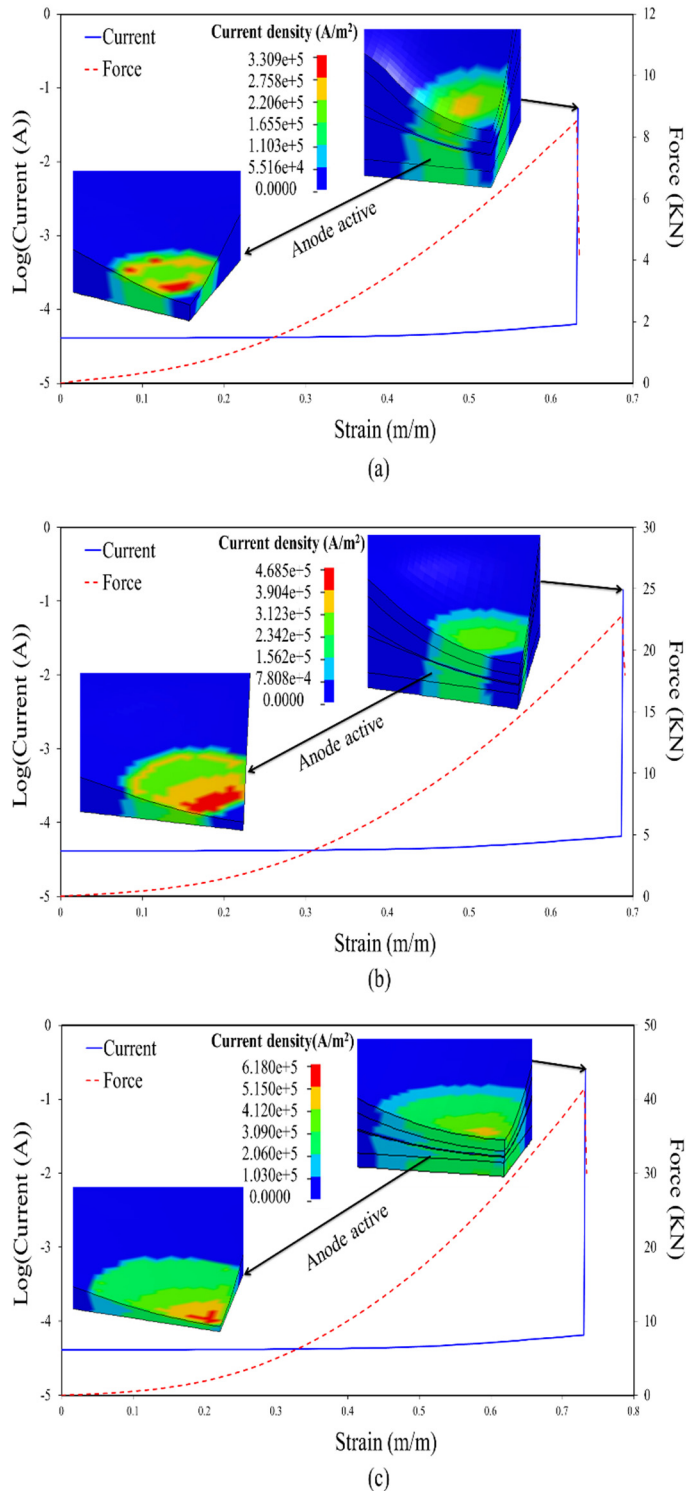


Figure III- 61: Evolution of average current (A) across the active material before and after short circuit at the electrical contact area, and isotropic-view of the current density (A/m²) distribution in the battery cell for the three different indentation tests: (a) small punch, (b) medium punch and (c) large punch

In the previous section, the single-RS model presented was correlated to the experimental results to predict the mechanical response and the onset of the structure fracture. The correlated models were then applied to simulate the mechanical-electrical-thermal responses of the battery cell during the indentation tests by incorporating the electrical-thermal model described earlier.

Prediction of Electrical Short Circuit

One main focus of this work is to predict the onset of the electrical short circuit during a mechanical crush. For the simultaneous coupled mechanical-electrical-thermal model, the distance-based criterion is utilized for the electrical contact initiation. Figure III- 60 (b) shows the overall displacement contour of the battery cell at the moment of the fracture, from which we identified that the maximum through-thickness displacement of the battery cell (loading distance of the indenter) is 2.758 mm, 3.198 mm, and 3.517 mm for the three indentation conditions. To predict the electrical short circuit, we assume the indenter stops moving once the structure fails, which means that there will be no further deformation after the mechanical failure of the battery cell. The critical distance, d_c , of the electrical short circuit of the LS-DYNA model is taken as the minimum thickness of the separator at the instant of the cell fracture (contour plots of Figure III- 60 (b)). Based on the electrical failure criteria, a current larger than 0.0074 A (0.01 C) will be sufficient to create a short circuit in the cell. The battery cell is considered electrically failed based on the detected current value at the moment of the cell fracture. Figure III- 61 shows the **evolution of the current** across the electrical contact area for the three different indentation tests. All three cases show the same electrical behavior during the test: there is a small increase in the current before the onset of the short circuit due to the thickness decreasing the induced decrease of the electrical resistance; a sharp increase in the current is detected at the moment of the failure due to the initiation of the short circuit, which corresponds to the

current density contour plot for the peak point (cell fracture and electrical failure). Note that the maximum concentration of the current density occurs in the anode active layer due to its relatively higher conductivity than the cathode active material.

Comparing the three different indentation tests, we found that there is an increase of the short-circuit area with the increase of indenter size, which is consistent with the mechanical deformation distribution (Figure III-60(b)) and illustrated in the current density contour plots (Figure III- 61) wherein the current density concentration area is larger for the indentation test with a larger indenter. The electrical contact area has a significant impact on the short-circuit behavior. The current at the moment of the short will be larger due to the relatively lower short resistance when there is a larger electrical contact area. This will then result in a faster voltage drop and a lower local maximum temperature. Note that the short-circuit behavior depends also on the electrical conductivities of the materials in contact.

Prediction of Thermal Ramp after Short Circuit

Understanding the voltage evolution behavior after the short circuit is of great significance, both for designing a safer battery as well as for the design of post-event containment measures. With the initiation of electrical contact, the voltage and resistance of the cell structure drops to very small values. Simultaneously, there is an evolution of the local cell temperature at the location of the short circuit. For the same cathode-anode short, as expected, the simulated voltage drop for the large-punch indentation test (largest electrical contact area) is faster than the other two tests. This result, when extrapolated, is useful in explaining why short circuits involving very small contact areas do not result in a thermal runaway. The voltage drop is so slow that any heat generated from such shorts is dissipated before a sufficient temperature rise can result in a runaway. On the other hand, when the contact area is exceedingly large, the energy content of the small format cell is released within milliseconds before the current density can rise to sufficiently large values to generate any heat; in contrast, a large-format cell will continue to have sufficient energy available across the same timescale and will generate sufficient heat to result in the follow-on reactions. The predicted temperature ramp is similar to the experimentally observed results reported by MIT. The change in the maximum surface temperature also matches the experimental results (10 K for the small-punch test, 50 K for the medium-punch test, and 40 K for the large punch) in a reasonable manner. In the experiments, the medium-punch test produces a higher temperature rise than the large punch test, which is likely due to the variation of the contact area at the moment of the short. At the moment of structural failure, the local deformation or damage event (e.g., cracking, fracture) is a very rapid process, which will result in significantly different contact areas at the instant of the short circuit. For the instant of the short circuit, a large contact area will produce a higher short-circuit current, a faster voltage drop, and a higher local temperature rise.

Conclusions and Future Directions

In collaboration with ANSYS and MIT, NREL developed a coupled mechanical-electrical-thermal model for predicting the mechanical-abuse-induced short-circuit behavior of Li-ion cells under different indentation test conditions. A Representative Sandwich model was used to enhance its accuracy in predicting the short-circuit location and temperature rise as well as to be compatible with the mechanical-electrical-thermal solvers.

The mechanical model successfully predicts the onset of the structure fracture and captures the local cracking behavior of the LIB under three different indentation conditions. The simultaneous coupled model accurately predicts the initiation of the short circuit due to the structural fracture and post-short thermal and electric responses through using a distance-based electrical contact criteria. It is identified that the maximum current density located in the anode active material and a larger indenter size creates a larger electrical contact area.

The simultaneously coupled modeling technique is useful in studying the safety behavior of Li-ion cells under mechanical abuse, especially when studying the interaction of the mechanical failure and short-circuit behavior. It is a helpful tool for evaluating the safety performance of a battery cell and designing more efficient and safer battery structures. Future work will focus on investigating more complicated crush conditions (multi-axial crush, impact, and battery module crush, etc.). Implementation of a methodology to transfer the mechanical simulation results to the battery models built in ANSYS Fluent are underway.

FY 2015 Publications/Presentations

1. “Coupled Mechanical-Electrochemical-Thermal Modeling For Accelerated Design of EV Batteries,” A. Pesaran, G-H. Kim, S. Santhanagopalan, *28th Electric Vehicle Symposium*, May 2015, Kintex, Korea.
2. “Coupled Mechanical-Electrical-Thermal Modeling for Lithium-ion Batteries,” C. Zhang, S. Santhanagopalan, M. Sprague, A. Pesaran, *Journal of Power Sources*, Vol. 290, p. 102–113, 2015.
3. “Damage of Cells and Battery Packs Due to Ground Impact,” Sahraei et al., *Journal of Power Sources*, Vol. 267, p. 78–97, 2014.
4. “Mechanical Electrochemical Thermal Simulation of Lithium Ion Batteries Subjected to Crush,” Pesaran et al., DOE VTO Annual Merit Review, Washington, D.C., June 9, 2015.
5. “A Representative Sandwich Model for Coupled Mechanical-Electrical-Thermal Simulation of Lithium-ion Battery Cell Under Quasi-Static Indentation Tests,” C. Zhang, S. Santhanagopalan, M. Sprague, A. Pesaran, *Journal of Power Sources*, Vol. 298, p. 309–321, 2015.
6. “Modeling of Cracks Developed in Lithium-ion Cells Under Mechanical Loading,” Sahraei et al., *RSC Advances*, Vol. 5, p. 80369–80380, 2015.

III.C.5 Mechanistic Modeling Framework for Predicting Extreme Battery Response (SNL)

Objectives

- Address root cause and implications of thermal runaway of Li-ion batteries by delivering a software architecture solution that can lead to the development of predictive mechanisms that are based on identification of species.

Technical Barriers

Key technical risks associated with the proposal involve the lack of mechanistic understanding of interfacial layers associated with electrodes in the Li-ion system.

Additionally, barriers involving the development of mechanistic understanding of degradation mechanisms and detailed kinetics of solid phase processes and liquid phase secondary reactions abound within the Li-ion battery community. We are developing software for these mechanisms to be addressed and then are making the software available as open source. Future collaborations using the software we hope will help to fill these gaps.

Additionally we have pursued upscaling of microstructure parameters to the macrohomogeneous scale. This approach addresses some of the uncertainty.

Technical Targets

- Implement 1DElectrode capability within CAEBAT and verify.
- Implement partially saturated porous flow and solid mechanics modeling within 1DElectrode.
- Develop consistent thermodynamic/transport models of the entire cell using CANTERA. Add partial saturation and solid mechanics models to CAEBAT. Build SEI Models that can predict the autocatalytic temperature behavior experimentally observed
- Implement upscaling ideas from microstructure models within CAEBAT using both averaged results and perhaps statistical distributions.
- Exercise new capability by developing new models for thermal runaway processes with 1DElectrode / CAEBAT

Accomplishments

- Linked 1DElectrode model into CAEBAT architecture, running thermal and electrical simulations using AMPERES/1DElectrode.
- Validated models against Dualfoil model within 1DElectrode/CAEBAT.
- 1DElectrode model improvements include real thermodynamics based chemistry, Stefan-Maxwell nondilute diffusion, and conservative enthalpy-based, multi-species energy conservation. This is new to battery modeling software.
- 1DElectrode model improvements include single-ion entropies and realistic electron entropies based on Seebeck coefficients. Combined, these additions allow for the correct treatment of distributed heat transfer in electrochemical systems when the thermal field is resolved across the battery.
- A formulation for the calculation of the solid-phase global stress and strain field has been written up and implemented. The change in the particle stress-free strains of the electrodes are partitioned

Project Details

Brian Cunningham (DOE Program Manager)

Tony Geller (Sandia Program Manager)

Sandia National Labs

Albuquerque, NM 87185-0836

Phone: 505-844-7795; Fax: 505-844-4523

E-mail: asgelle@sandia.gov

Harry Moffat (PI)

Phone: 505-844-6912; Fax: 505-844-9297

E-mail: hkmoffa@sandia.gov

Subcontractor:

S. Allu, Oak Ridge National Labs, TN

R. Kee, Colorado School of Mines, CO

Start Date: October 2013

Projected End Date: September 2015

between changing the porosity and between incorporated into the global stress-free strain field via a constitutive model. Testing is under way.

- A formulation for two-phase, multispecies electrochemical transport in porous electrodes has been developed, for subsequent implementation into 1Delectrode. It has not been completed yet.
- Successfully reconstructed 3D microscale digital models of Li-ion cathodes from FIB-SEM images and developed electrochemical transport models with Faradaic and Ohmic internal heat generation.
- Successfully simulated a 1C discharge rate in a cathode using the reconstructed 3D microscale model showing reasonable cell potential and Joule heating curves over full discharge cycle.

Introduction

We are expanding the functionality of the CAEBAT-I architecture developed at Oak Ridge National Laboratory by incorporating advanced speciation models. These models are built on the Cantera open-source software library for elementary thermodynamic, transport and kinetic processes. We will be implementing this modeling capability to address two key aspects of Li-Ion battery chemistry that will support the existing CAEBAT-I program.

- 1) Modeling the processes that transform chemical energy to thermal energy in abusive scenarios and the associated heat release for both normal operation and abusive conditions. In doing this, we focus on interactions between electrode-particle scale physics present within our Cantera-based approach and the cell-level physics already present within the CAEBAT framework. In follow on work, we will add models that can capture the autocatalytic temperature rise observed at elevated temperatures, fitting data from Sandia's BATLab program.
- 2) Modeling thermo-electro-mechanical interactions within porous materials that determine the heat, mass and electrical transport processes, addressing cell-level structural evolution under normal operation and abusive conditions. This includes modeling gasification mechanisms by adding partial saturated flow to battery models so that mechanisms for gasification may be envisioned and applied in at least a 1D context.

Our modular approach emphasizes hierarchical approaches to modeling the detailed chemistry system and onset of thermal abuse from a species-specific point of view. These represent a natural extension to the current CAEBAT architecture currently developed at ORNL. We also develop upscaling algorithms to bring information from subgrid variations in microstructure developed by Prof. Bob Kee at the Colorado School of Mines to the macrohomogeneous scale. This approach of incorporating detailed chemistry and fundamental processes into the CAEBAT OAS is based on the open-source program Cantera. Our first goal is to advance the state of the art in modeling chemical processes within the battery community using open software standards. Because the battery community has lacked such an infrastructure, fundamental quantitative comparisons of chemistry have not occurred to a significant extent within the community. We expect to emulate what has occurred within the combustion community with programs such as Chemkin, which brought together experimentalists and computational scientists to create an infrastructure, which was then used to quantitatively understand and predict mechanistic details.

Approach

We have had two complimentary goals within this project. The first goal is to advance the state of the art in modeling chemical processes within the battery community using open software standards. This is an important and often misunderstood goal. Because the battery community has lacked such an infrastructure, fundamental quantitative comparisons of chemistry have not occurred to a significant extent within the community. We hope to emulate what has occurred within the combustion community with programs such as Chemkin, which brought together experimentalists and computational scientists to create an infrastructure which was then used to elucidate mechanistic details.

The second goal of the project has been to start populating this infrastructure with models of various levels of fidelity that may address the thermal runaway process observed to occur within Li-ion batteries. Ideally this would involve understanding the formation of the SEI layer and its evolution as a function of temperature. Although the mechanistic details of this process as well as inputs for constitutive models that would make a model for this just are not available for engineering-level capabilities. We have proposed starting with those

models and then working to refine them using the experimental data from Sandia's BATLab program to interpret the thermal runaway process from an engineering perspective. Furthermore, we expand the engineering details into more sophisticated level that will track individual species in mechanisms that closely resembles the corrosion processes based on our current understanding of the stability of the passivating layers. This would necessarily involve determining the stability and thermodynamics of components of the SEI layer as a function of temperature and pressure.

An unappreciated feature of batteries is the need to understand the thermo-mechanical interactions of the porous materials as a function of the state of discharge and as a function of the number of cycles. We at Sandia have started to address this issue within our codes and would like to transfer some of the technology to the CAEBAT architecture with collaboration from ORNL. This involves solving the partially saturated flow equations, which are important for some battery systems, and represent failure mechanisms in others. And we had also proposed to include the poroelastic stress constitutive equations using the effective stress principles. This concept is essentially new to batteries, though we have extensively used it in other contexts with Sandia codes such as Goma, which can model the mechanical environments found in drying porous media or porous media in contact with continuum fluids that undergo external stresses.

The impact of this project will eventually be far-reaching as the technology is disseminated into the battery community. During this project, we have created infrastructure for the inclusion of detailed mechanistic models for thermochemical processes that are important to battery performance and safety. Additionally, the infrastructure for mechanistic understanding of thermal runaway processes in Li-ion batteries has been advanced. This capability can be linked to existing cell, module and pack-level capabilities being developed under CAEBAT-I.

Results

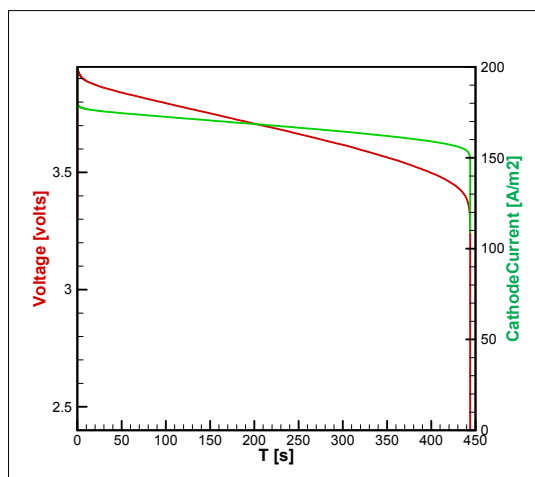


Figure III- 62: Comparisons of high current cantrilbat calculations against Mao et al., using the OCV fitting capability, the generalized Butler-Volmer implementation, and Surface Damkoeler limiter within Cantera

Model Development

We have expanded the list of electrode objects that can be used with `1DElectrode` to include diffusional objects with and without the total arbitrary Lagrangian Eulerian (TALE) capability.

For our thermal model, we have employed a total enthalpy formulation with additions for electrical potential energy that is conservative up to numerical round-off. All energy loss mechanisms are clearly delineated within this formulation, and analogies to the thermoelectric modeling equations are evident.

We have added the capability to employ arbitrary fitted OCV curves into the electrode object (which is the industry norm) in order to compare against dualfoil, which uses this method exclusively. In contrast, the default method for specification of the OCV within `1DElectrode` is to calculate the OCV from the specification of the electrochemical potentials of all of the species involved in the interfacial kinetics reaction,

and this is the method that will eventually lead to the greatest progress in understanding degradation methods. (Figure III- 62)

We have added to Cantera the ability to combine the concepts of a generalized Butler-Volmer formulation for charge-transfer reactions at interfaces with an affinity formulation, which is used extensively in the geochemistry community and which with the addition of the voltage-dependent modification of the activity energy can be made to look like a generalization of the B-V reaction. We have also added a Damkoeler limiter to Cantera that has been successful in resolving numerical difficulties in high-current simulations.

Comparison to High Discharge DualFoil Cases

In order to validate our thermal model we have carried out a validation exercise against dualfoil. We used the simulation of temperature rise problems from Mao et al. Figure III- 63 demonstrates that we can duplicate dualfoil calculations fairly well when the problem statement is specified. The work pointed out that additional numerical issues remain within our operator splitting approach that need to be worked out.

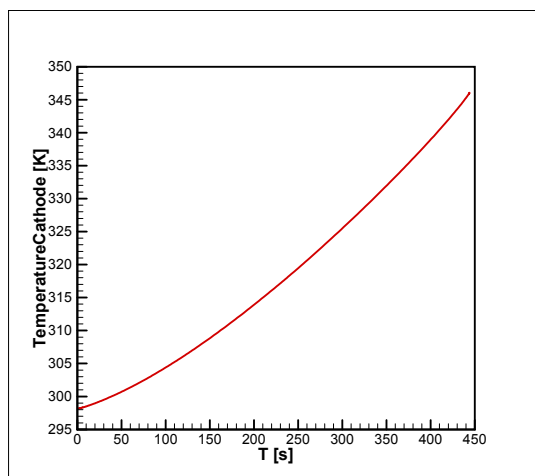


Figure III- 63: Corresponding Cathode Temperature vs. time. Temperatures were relatively flat across cell structure

CAEBAT development

One of the primary tasks has been to integrate the 1DElectrode model based on Cantera into Virtual Integrated Battery Environment (VIBE). We have successfully integrated this new software into the suite of components for modeling electro-chemistry inside VIBE. Below we show an existing example to demonstrate the capability to swap the dualfoil with the 1D electrode component and perform a coupled electrochemical, electrical and thermal simulation. In FY15, we have performed some detailed validation and comparison of the cell level simulations.

Example: Cylindrical Cell (Electrochemical-Electrical-Thermal)

This example contains the electro-chemistry, electrical and thermal transport components in a rolled cylindrical cell. Figure III- 64 shows the geometry and the finite element mesh used to resolve the geometry of the cylindrical cell and the current collectors. The top hierarchy model has 168 (56 each for the cell-sandwich and positive and negative current collectors) zones in 4 quadrants. The zones describe different current collector and cell sandwich regions. The simulation uses 56 concurrent 1D Electrode simulations for different cell-sandwich zones. Typical results are shown Figure III- 65. The maximum temperature occurs at the cell core as expected.

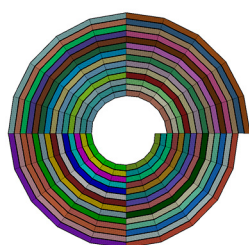
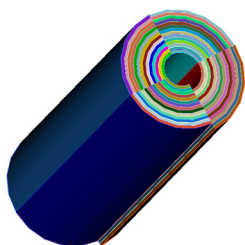


Figure III- 64: Geometry and mesh of the simulated cylindrical cell

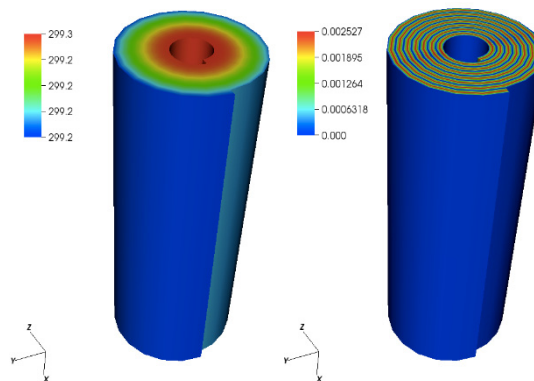


Figure III- 65: Sample results for cylindrical cell (temperature on the left and the electrical potential on the right)

Effective Properties from microscale electrode calculations

The CSM team has reconstructed Li-ion battery cathodes from Focused-Ion-Beam—Scanning Electron Microscope (FIB-SEM) experiments. The three-dimensional reconstructions form the geometrical basis for detailed transport and electrochemistry modeling. The models are implemented using User-Defined Function (UDF) interfaces to the ANSYS FLUENT software. An important aspect of the research is to upscale effective macroscopic properties from the detailed microscale reconstructions.

Effective mass density and specific heat capacity can be evaluated in a straightforward manner using volume-weighted averages of the intrinsic material properties. The effective thermal conductivity can be derived from modeling heat flux through a reconstructed microstructural cube (cf., Figure III- 66). Although the simulation

is geometrically complex, the thermal transport model is linear and easily accomplished with FLUENT. The effective conductivity is evaluated in terms of the modeled flux and the overall microscale cube dimensions.

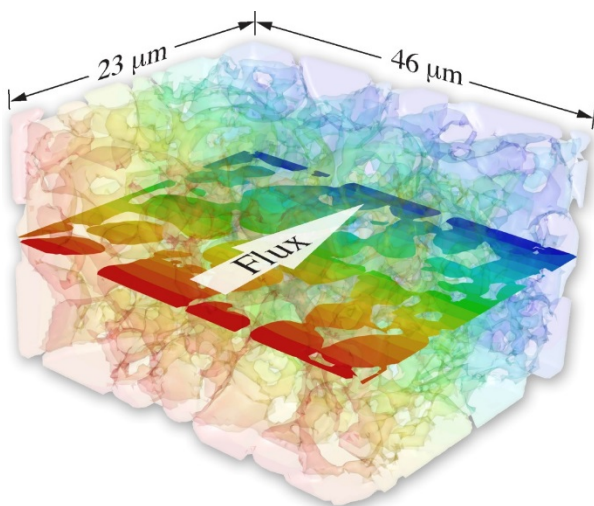


Figure III- 66: Simulated transport through a reconstructed composite cathode

Microstructurally derived effective properties can be used in modeling full cells. Figure III- 65 shows two illustrative results from modeling an 18650 cell with an internal short. The result on the left-hand side uses average isotropic properties that are derived from electrode microstructures and current-collection foils. The result on the right-hand side uses isotropic microstructurally derived electrode properties, but considers the inherent anisotropy associated with the current-collection foils and the jelly-roll architecture. The anisotropic result shows axial and circumferential heat spreading that is significantly elongated compared to the isotropic model.

Although evaluating effective properties from microscale reconstructions is relatively straightforward, evaluating effective heat-release rates is much more complicated. The local Faradaic

and Ohmic heat release rates can be modeled at the microscale, upscaling to a full cell is difficult. Because the heat-release rates depend strongly on local temperatures and charge/discharge rates, the boundary conditions for the microscale models must have some knowledge of the local conditions within the full cell. In other words, unlike the physical property evaluation, there is a strong coupling between the microscale and macroscale models. Clearly, modeling the microscale behavior within the full battery far exceeds any known computational resources.

Microstructurally Derived Heat-Generation Tables

A possible approach for upscaling microstructural heat release rates is being explored, but certainly not complete. Figure III- 67 illustrates the general tabular-based idea. The microscale thermal model can be run using a specified charge/discharge rate (C-rate), state of charge (SOC), and isothermal temperature and adiabatic boundary conditions. The result produces the net heat-release rate for the microcube. Such simulations can be precomputed and tabulated for ranges of temperature, SOC, and C-rate. Based on the local conditions, the macroscale model evaluates heat-release rates from the table.

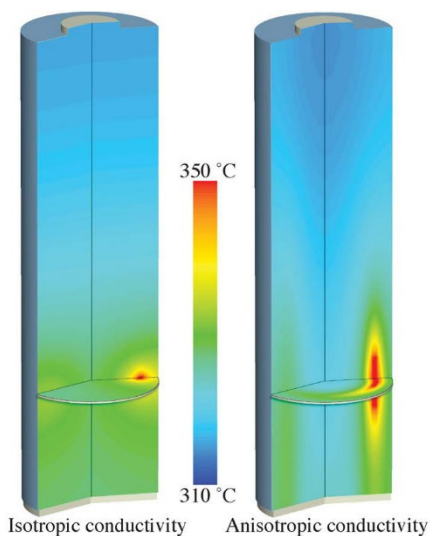


Figure III- 67: Simulated thermal response from an internal short in an 18650 cell

Although the tabular approach works in principle, its practicality is unclear. Simply populating the table from detailed three-dimensional microscale models is computationally intensive (taking time in the order of months). And, new tables would be needed for each battery electrode of interest. As battery technology evolves, manufacturers frequently implement new and improved architectures. So, the microscale modeling process must begin by developing the FIB-SEM or X-ray tomographic reconstructions. Then, the heat-release models must be run and tabulated. Deriving the needed physical properties is certainly realistic. However, the computational cost of developing the heat release tables is likely impractical.

As a practical matter, local heat-release models at the macroscale are more reasonably derived from local Newman-type models, such as the 1Delectrode model developed elsewhere in this project. Models of the three-dimensional microscale reconstructed electrodes would be used to assist calibrating and validating the 1Delectrode objects for particular battery and electrode architectures. (See Figure III- 68.)

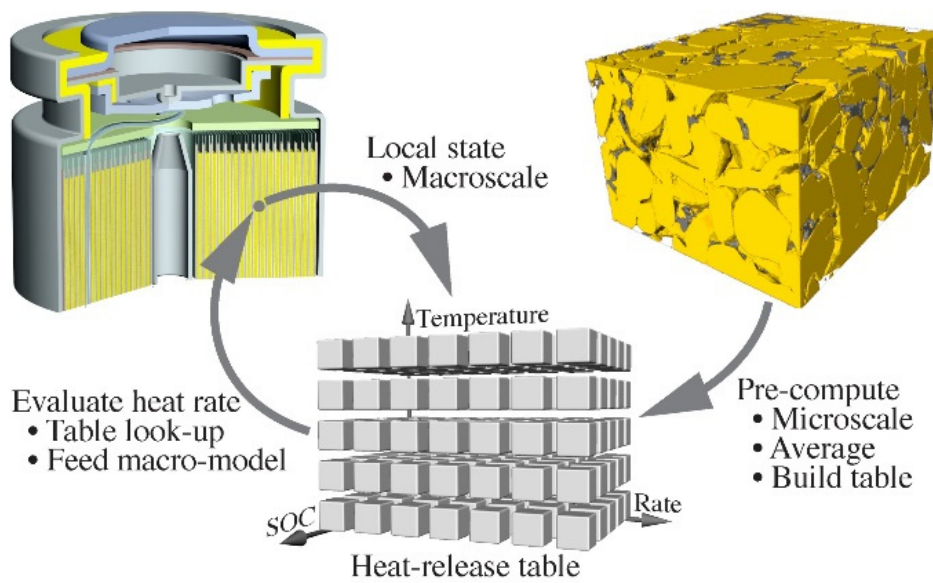


Figure III- 68: Methods of upscaling of heat generation tables are being evaluated

Conclusions and Future Directions

In addition to the partially saturated porous flow and solid mechanics modeling efforts planned, we have started to design new models for the SEI layers based on analogs to corrosion system, whose formulation reactions are thermodynamically reversible, so that they may be designed to dissipate under some conditions. Combining these models with traditional thermal models for thermal runaway, we will then attempt to fit these against Sandia's Batlab data.

FY 2015 Publications/Presentations

1. 2015 DOE Annual Peer Review Meeting Presentation
2. 89th Lithium Battery Technical/Safety Group Meeting, Sandia Labs, Sept 2014.
3. J. Hewson, H Moffat, V. Brunini, Mario Martinez, R. Muller, CantrilBat - 1D Modeling of Batteries, Sandia Report, Albuquerque, NM in prep (2016)

III.C.6 Efficient Safety and Degradation Modeling of Automotive Li-ion Cells and Pack (EC Power, Penn State U)

Objectives

- Develop an efficient & robust pack-level safety model.
- Develop abuse and refined life models.
- Perform life, abuse, and safety tests to acquire data for validation.
- Expand extensive materials database by characterizing and adding NCA material.
- Perform co-simulation of our software with structural mechanics software via the Open Architecture Standard (OAS).
- Support DOE CAEBAT activity.

Technical Barriers

Key barriers to more widespread adoption of hybrid and electric vehicles include challenges in the design of large-format Li-ion cells and packs related to performance, safety, life, and abuse. In the ongoing work of this project, we are developing and refining commercial physics-based software tool that is directly aimed at helping cell manufacturers and automakers overcome these design challenges and barriers through an accurate and fast computer aided engineering tool.

Technical Targets

- Develop and validate physics-based (non-empirical), predictive pack-level safety model.
- Develop and validate mechanism-based, fundamental models for accurately predicting degradation of Li-ion batteries.
- Develop and validate mechanism-based abuse models.
- Experimentally characterize NCA cathode material under automotive-relevant and wide ranging conditions (e.g. $-40^{\circ}\text{C} < T < 60^{\circ}\text{C}$).

Accomplishments

- Completed all multi-cell safety testing, generating data for model validation.
- Completed abuse testing, generating data for model validation.
- Approximately 60 cells successfully fabricated for life testing.
- Life testing for ageing model validation approximately 50% complete.
- Validation of safety, abuse, and life models is ongoing.
- Successfully completed implementation of new performance and ageing model including effects of active material swelling (e.g. to simulate life of materials such as Si).
- NCA cathode active material characterization ($-40^{\circ}\text{C} < T < 60^{\circ}\text{C}$) complete and implemented in commercial software database.

Project Details

Bruce Mixer (NETL Program Manager)
DE-EE0006425 Recipient: EC Power, LLC

Christian Shaffer (PI)
341 N. Science Park Rd.
State College, PA 16803
Phone: 814-861-6233; Fax: 814-861-6234
E-mail: ceshaffer@ecpowergroup.com

Subcontractor:
Penn State University, University Park, PA 16802

Start Date: October 2013
Projected End Date: September 2016

Introduction

The overarching objective of the ongoing work is to develop experimentally validated, robust, and easy-to-use computation models for Li-ion battery (a) pack-level safety and abuse simulation and (b) advanced and accurate degradation modeling. The commercial need for an efficient pack-level safety and abuse model is best highlighted by the recent Boeing 787 Li-ion battery pack fires, where there has been much debate as to the root cause of the fires, how the failure subsequently spread through the battery pack, and how to avoid such a

scenario in the future via enhanced design. The pack-level safety model addresses precisely this type of scenario, yielding great insight as to how an initially local safety-related event such as nail penetration or internal short spreads throughout the pack both thermally and electrically/electrochemically. In addition to pack safety simulation, our team is developing additional chemistry-specific life and abuse models for simulation of Li-ion battery life and overcharge, for example. The models developed are being extensively validated by generating in-house data from a variety of advanced diagnostics tests. Finally, the team is experimentally characterizing commercially widely-used NCA cathode material ($-40^{\circ}\text{C} < T < 60^{\circ}\text{C}$) and adding material to the previously developed extensive material database.

Approach

The EC Power-led team is working to develop physics-based Li-ion battery and pack design software, leveraging EC Power's demonstrated expertise in multi-physics modeling. This physics-based modeling approach results in a *predictive* design software focused on addressing life, safety, and performance barriers over automotive-relevant wide-ranging operating conditions (e.g. $-40^{\circ}\text{C} < T < 60^{\circ}\text{C}$), which will lead to more widespread adoption of Li-ion batteries in this application. To ensure model accuracy, we also leverage the expertise of the Penn State University team in materials characterization, safety, and life testing, in order to validate the software developed.

Results

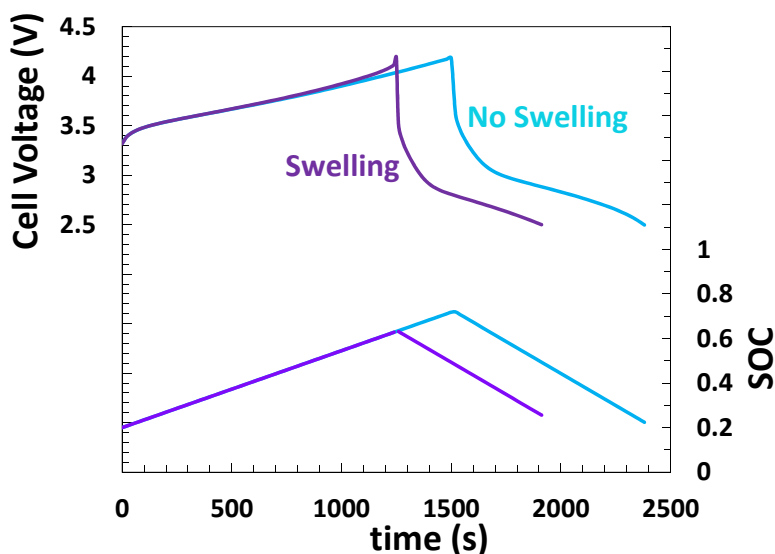


Figure III- 69: Charge voltage and SOC of Li-ion cell with Si alloy based anode with and without swelling effect accounted for in computational model

The work in the past year has focused largely on (a) refining our computational models for performance, life, and safety aspects of Li-ion batteries, (b) completing the characterization and subsequent implementation of NCA cathode material into the software materials database, and (c) carrying out a large number of tests to acquire data for life, safety, and abuse model validation.

Figure III- 69 gives an example of the refined models implemented. This figure shows the cell voltage and SOC versus time for Li-ion cell with silicon alloy based anode, with and without the swelling effect of the Si alloy

incorporated into the model. These results imply that including the swelling effect of the Silicon material has a significant impact on the performance of the cell. We have likewise incorporated the swelling effect into our life models in the past year. The big picture impact of this work is that the refined models will allow more accurate assessment and screening of novel electrode materials in a cost-effective software tool.

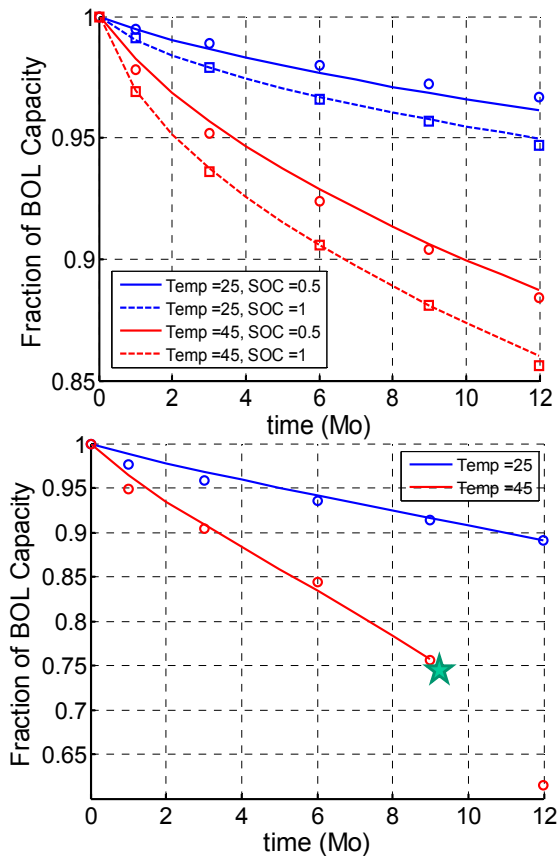


Figure III- 70: Calendar and cycle life ageing of 26650 LFP/Graphite cell with new ageing models (temperature in degrees Celsius); data taken from Delacourt et al., *Journal of the Electrochemical Society*, 159 (8) A1283-A1291 (2012)

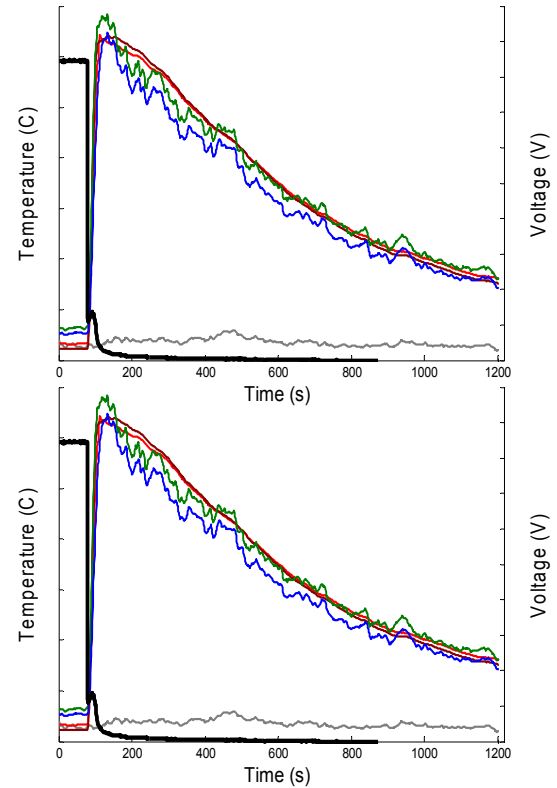


Figure III- 71: Nondimensional temperature and voltage data acquired from one single cell and one multi-cell nail penetration tests; data being used for validation of model

Figure III- 70 highlights a small portion of our life modeling efforts through this work. Figure III- 70(a) shows the calendar life, and Figure III- 70(b) the cycle life ageing of an LFP/graphite cell, as captured by the models implemented. Note that the physics-based models capture these battery life effects over a wide range of temperatures and states of charge. Our team is currently carrying out testing for additional Li-ion cells, and will validate all models in the coming year.

Figure III- 71 gives an example set of data from single cell and multiple cell nail penetration tests. In the past year, numerous repetitions of the nail penetration tests (both on the multi-cell and single-cell levels) have been performed to investigate reproducibility of the test data, which greatly enhances computational model validation. When the local temperature inside any cell reaches a dangerous level, thermal runaway will ensue, leading to a safety event such as fire or explosion. The predictive design software developed under this project allows users to quickly, cheaply, and safely iterate through various cell and pack designs to optimize safety before a cell is ever built, leading to a more refined and ultimately safer product. We expect this unprecedented capability of Li-ion battery cell and pack safety simulation will empower manufactures and automakers to reduce time and cost in developing safe Li-ion battery packs.

EC Power has completed the core of the software implementation of the models developed under this project, including those related to safety, abuse, and life. EC Power has additionally fully implemented NCA material into the software materials database. By working with our partners at Penn State, we have also completed safety and abuse testing. In 2016, the project will largely focus on completing the life testing and wrapping up validation of the models. The ultimate goal at the conclusion of the project is to have refined commercial Li-ion battery design software that cuts cost and time from the design phase of automotive Li-ion batteries and packs.

FY 2015 Publications/Presentations

1. 2015 DOE Annual Peer Review Meeting Presentation, June 9, 2015.
2. Hasan, M.F., Chen, C.F., Shaffer, C.E. and Mukherjee, P.P. (2015). "Analysis of the Implications of Rapid Charging on Lithium-Ion Battery Performance," *Journal of the Electrochemical Society*, 162(7), A1382-A1395.
3. Wang, Q., Shaffer, C.E. and Sinha, P.K. (2015). "Controlling factors of cell design on large-format Li-ion battery safety during nail penetration," *Front. Energy Res.*, 3:35.

III.C.7 Significant Enhancement of Computational Efficiency in Nonlinear Multiscale Battery Model for Computer-Aided Engineering (NREL)

Objectives

- The objective of the project is to develop a computational methodology for a significant enhancement in computation speed of nonlinear multiscale modeling of plug-in electric vehicle (PEV) batteries while maintaining or improving the solution accuracy from the most advanced state-of-the-art models.

Technical Barriers

- Lack of high-fidelity, fast-running battery simulation tools for battery design studies for PEVs.
- The inevitable nested iterations, ensuring self-consistency in the state-of-the-art multiscale multidomain (MSMD) model, become a factor limiting further improvement of computation speed.
- A traditional multiphysics approach, collapsing scales into a single, large, differential algebraic equation system, renders the system impractically large and stiff, sacrificing modularity.
- As soon as the reduced-order-model (ROM) basis is acquired in a reduced dimension space, physical interpretations are easily lost. The ROM basis is restricted to reuse in the system where its characteristics are evolving, such as battery aging.
- The ROM build process becomes computationally costly, with an increased number of parameters.
- Most state-of-the-art battery ROMs addressed coupling battery physics only within limited scales.
- The state-of-the-art ROMs suggested for battery models lose validity when severe nonlinearities arise.
- The model applicability can be limited for varied design, environment, and operation conditions.

Technical Targets

- Develop very fast, accurate electrochemical-thermal models for accelerating development of PEV batteries.
- Improve computation speed of state-of-the-art nonlinear multiscale battery model by a factor of 100 while maintaining its solution accuracy.
- Develop a new multiscale coupling method using time-scale separation and variable decomposition to eliminate several layers of nested iteration while still keeping the modular framework architecture that is critical to battery behavior simulations.
- Establish a new technique to identify a low-order state variable model (SVM) that is adaptive to system evolution.
- Construct an application programming interface for multiphysics integration of NREL's custom model library in a commercial software environment.

Accomplishments

- Developed GH-MSMD, a new quasi-explicit, modular, extendable, tightly coupled, nonlinear framework in both the C++ and MATLAB platforms.
- Demonstrated that the new GH-MSMD speeds up computations by 1,000 times.
- Demonstrated implementation of GH-MSMD cell-domain model (CDM) in ANSYS/Fluent.

Project Details

Brian Cunningham (DOE Program Manager)
DOE Agreement # 27042 Recipient:
National Renewable Energy Laboratory

Gi-Heon Kim (NREL – PI)
15013 Denver West Parkway, M/S 1633
Golden, CO 80401
Phone: 303-275-4437; Fax 303-275-4415
Email: gi-heon.kim@nrel.gov

Subcontractors:
ANSYS

Start Date: October 2013
Projected End Date: December 2015

- Built a custom graphical user interface (GUI) in ANSYS/Fluent for GH-MSMD simulation pre-processing.
- Compared options for an adaptive time-stepping algorithm in GH-MSMD versus the existing recursive method.
- Constructed the MSMD standard input file structure, facilitating its multiscale simulation.
- Refined the numerical method for the final version of the adaptive SVM (A-SVM) model.
- Validated and benchmarked A-SVM against other electrode domain model (EDM) MSMD models in MATLAB.
- Demonstrated that the A-SVM achieved 50x speed-up with accuracy better than 15 mV.
- Developed a new time-domain ROM, Error-corrected Time-domain Series solution (ETS) for the solid-phase diffusion equation.
- Evaluated the computational speed and the solution accuracy of the ETS.
- Performed the first demonstration of wall-clock speed-up for POD/DEIM method for prototype electrolyte equation.
- Initiated the MSMD integration with vehicle simulator software.

Introduction

NREL pioneered the multiscale multidomain (MSMD) model, overcoming challenges in modeling the highly nonlinear multiscale response of battery systems. The MSMD provides high extent flexibility and multiphysics expandability through its modularized architecture, as well as computational efficiency. However, further improvement of computational speed of the model is greatly desired to promote the application of the high fidelity multiphysics model in various battery engineering problems. In this project, we significantly improve the computation speed and stability of multiscale model framework by eliminating several layers of nested iterations through innovative multiscale coupling methodology, while still keeping the modular framework architecture, and provide a new reduced order model (ROM) that is adaptive to system evolution and identifiable with fewer compound parameters.

Approach

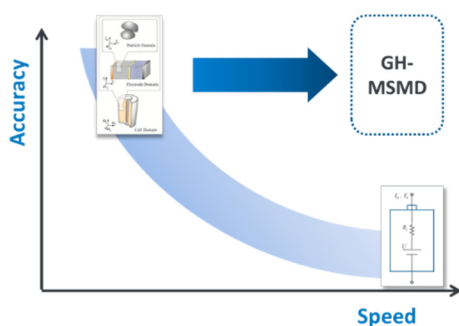


Figure III- 72: GH-MSMD significantly improves the computational speed of nonlinear multiscale battery model without compromising accuracy

invested in advance to find a reduced order basis in a much lower dimension than that of the full ordinary differential equation systems derived from spatial discretization of the partial differential equation systems. The ROM basis is typically restricted to reuse in the system where its characteristics are evolving, such as the battery aging process. In this project, we developed the A-SVM, a new ROM that adapts to system evolution and is identifiable with fewer compound parameters. For enhancing usability of the model, we constructed the MSMD-Fluent application programming interface for multiphysics integration of NREL's custom model library in a commercial software environment – ANSYS/Fluent.

Results

We have achieved the following progress:

Framework & Component: The project target is achieved through parallel and complementary efforts in framework efficiency improvement and component efficiency improvement. We developed a new quasi-explicit nonlinear multiscale model framework, GH-MSMD, using time-scale separation, variable decomposition, and partial linearization procedures (Figure III- 72). GH-MSMD eliminates several layers of nested iteration, significantly improves the speed and stability of the original MSMD, and retains the modular framework architecture that is critical to battery behavior simulations. We also develop advanced ROMs for the component models. Computational time is often

New Model Speeds Up Computations by 1,000 times

Last year, NREL met the 100-fold computational speed-enhancement target for its multiscale multiphysics battery model (MSMD) one year ahead of schedule. In FY15, we significantly exceeded the projected target by further improving the code structure and by extending the model to a larger scale. Figure III- 73 presents the comparison of the electrical and thermal response of a battery for a mid-size sedan plug-in hybrid electric vehicle (PHEV10) on the US06 20-minute driving power profile. While the model outputs are shown to be very close to each other, the new quasi-explicit, modular, extendable, tightly coupled, nonlinear MSMD framework, GH-MSMD, demonstrates that the most efficient electrode-scale battery-cell model option can run a 1,200-second driving profile simulation in only 0.74 seconds using a personal computer—an approximate 1,000-fold improvement over previous capabilities. In contrast, the original MSMD runs the same simulation in 654 seconds. When the model is extended to its full-scale, three-dimensional, larger cell domain, the speed-enhancement factor reaches 1,000 to 10,000, depending on the choice of sub-model.

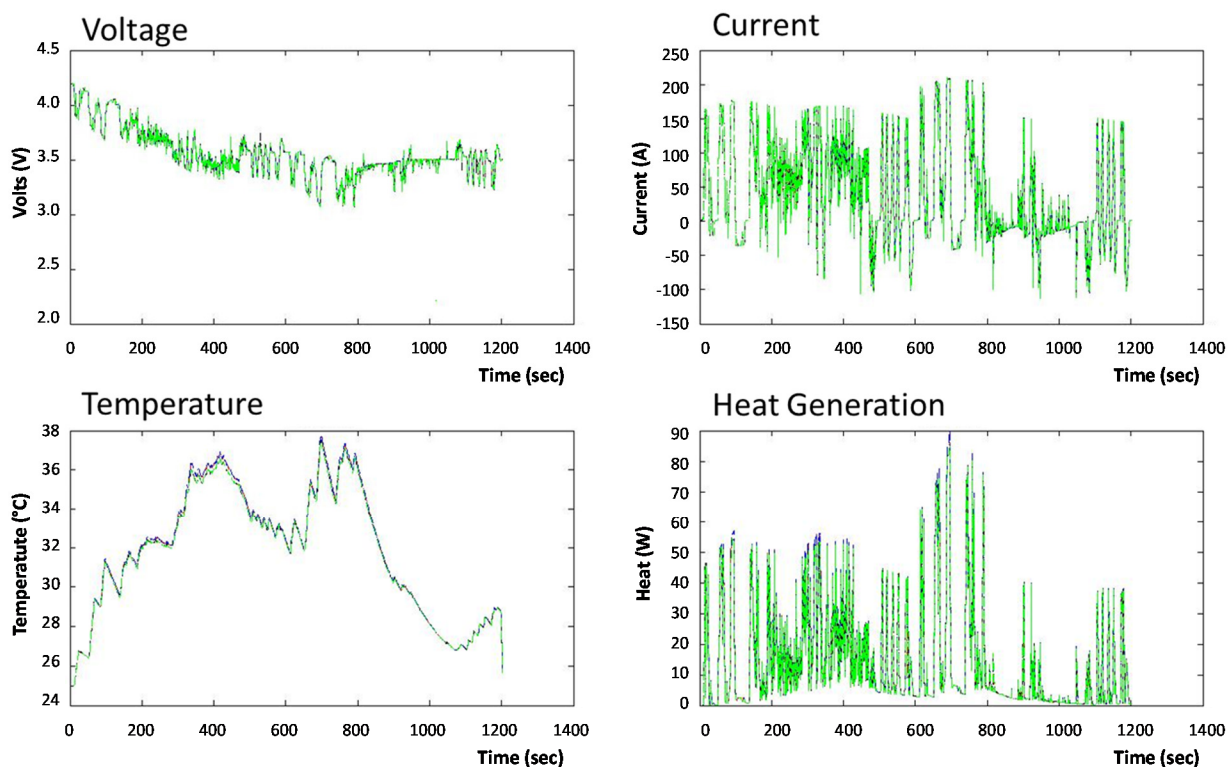


Figure III- 73: Comparison of electrical and thermal response of a battery for a mid-size sedan plug-in hybrid electric vehicle (PHEV10) on the US06 20-minute driving power profile from the GH-MSMD and the original MSMD

Figure III- 74 compares the model solution variables in each computational domain and the coupling variables exchanged between the adjacent length scale domains in MSMD (left) and in GH-MSMD (right). Even though the solution algorithms are significantly different between the two, the model structures are similar. This comparison signifies the modularity of model framework that the GH-MSMD inherited from the MSMD. The new GH-MSMD framework retains the flexibility needed for application to various lithium battery chemistries and designs. It still integrates a sophisticated particle model to address particulate morphology, size distribution, surface modification, contact resistances, and mixture composition of active particles. The model simulates all major cell form factors with variable electrode compositions and designs.

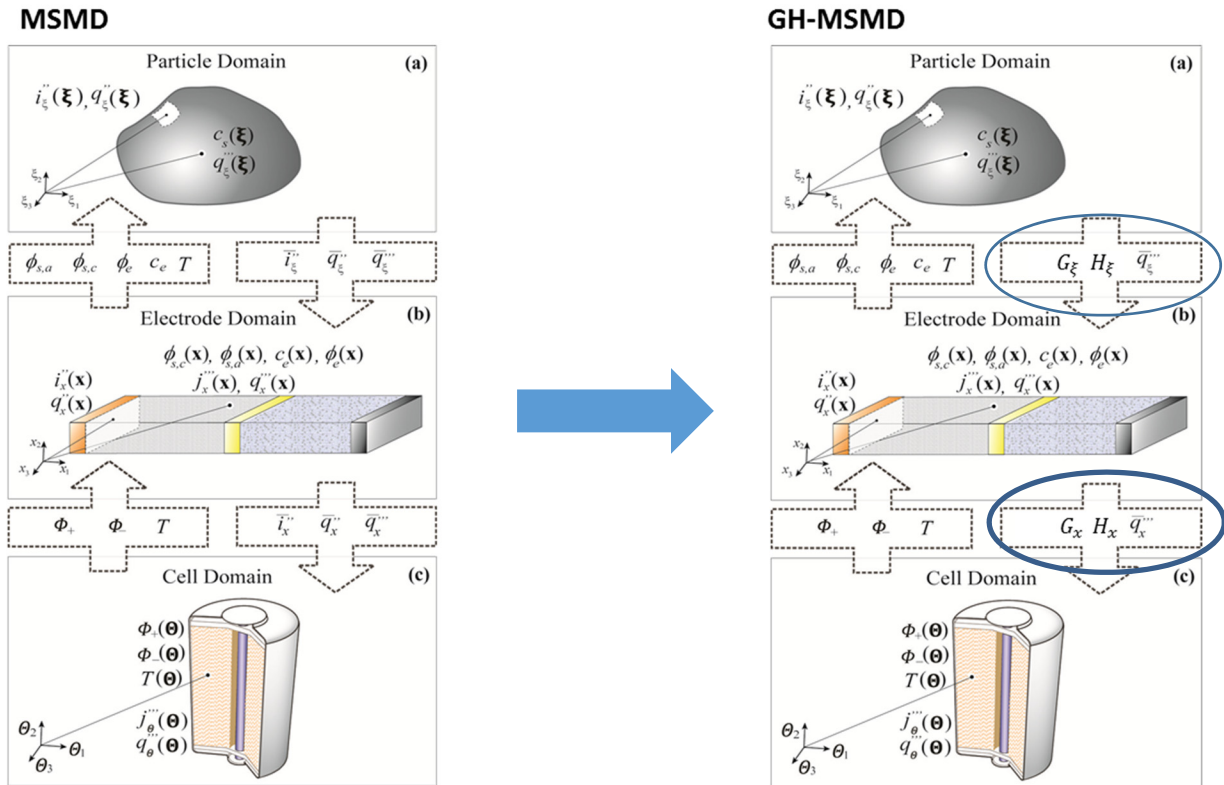


Figure III- 74: Comparison of the original MSMD and the GH-MSMD framework structure and main changes in the GH-MSMD

Reduced Order Electrochemical Model Becomes Adaptive

NREL developed an accurate, computationally efficient realization of the Newman electrochemical model that runs 100 to 1,000 times faster than typical numerical solutions in modern commercial software. Although spectral model order-reduction techniques are available to achieve speed enhancement, previous efforts that applied these methods to the Newman model required a cumbersome preprocessing step to identify a model versus a few selected parameters of interest. To overcome this limitation, NREL eliminated the preprocessing step so that a simulation could run immediately, and NREL fully populated the ROM so that it is extendable to all possible lithium-ion porous electrode designs and states of health. This achievement will enable the rapid optimization of lithium-ion cell chemistries and the use of the model for aging studies. The new A-SVM was validated and benchmarked against other EDM MSMD models (two MSMD-EDMs and two GH-MSMD-EDMs) in MATLAB. The compared MSMD EDM combinations are edLPD/pdPLLM, edPLM/edLPD, edSEG/pdPLM, and edSEG/pdSEG. Figure III- 75 presents the model output comparisons for a 5C and 10C pulse profile and constant current discharge in 1, 2, 5, and 10C. Accuracy is generally greater than 99%, and the speed-up factor of A-SVM against the highest-order segregated solver option is about 50. The unconditional stability of A-SVM enables a large time-step size, and additional speed-up is expected in practical situations. A-SVM shares the common input and output file structure with the MSMD/GH-MSMD.

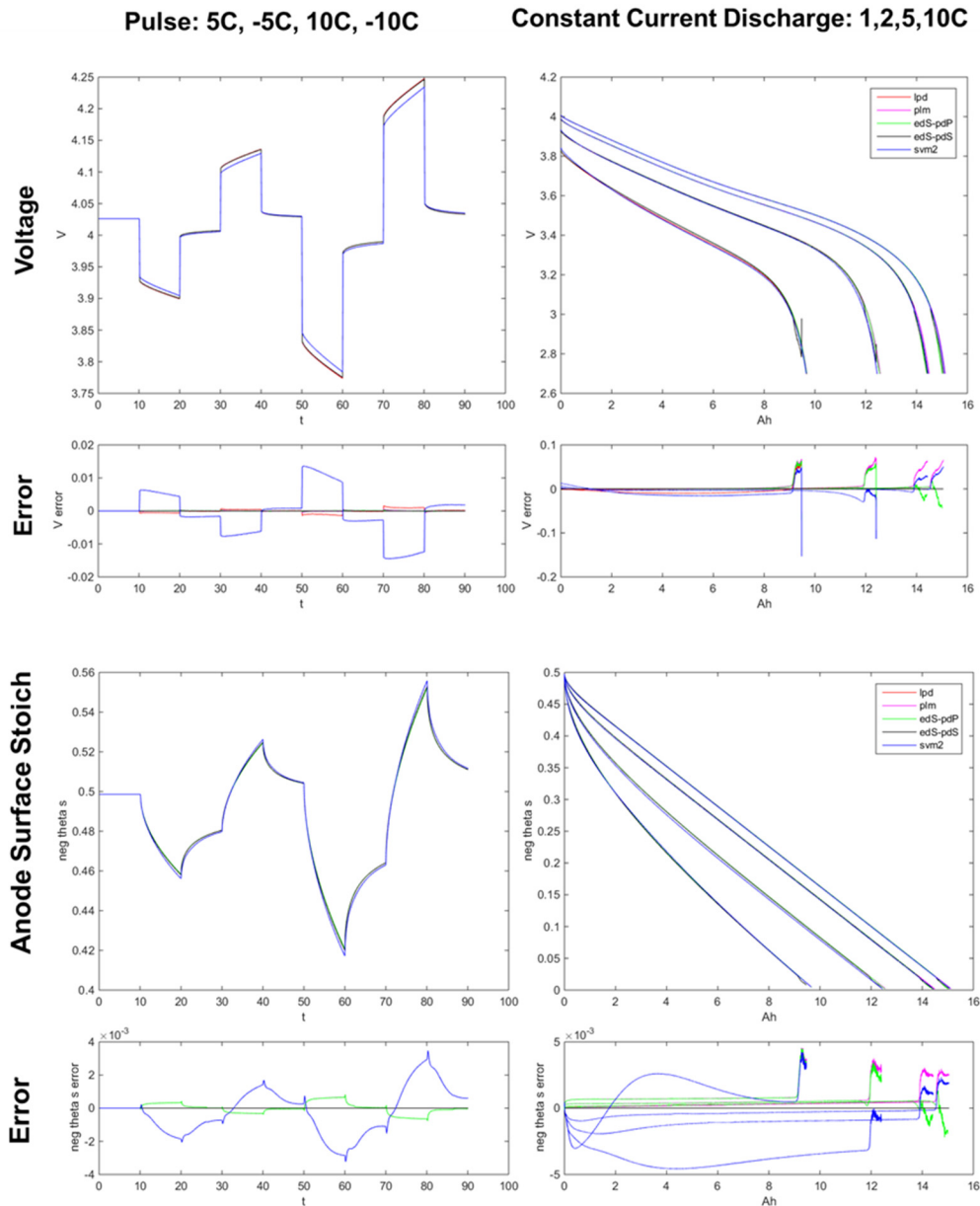


Figure III- 75: A-SVM verification and benchmark results against various MSMD/GH-MSMD models

Efforts to Promote Industry Access to New Models

The successful development of GH-MSMD is expected to shift the paradigm in using a model for electric-drive vehicle battery system design and evaluation, potentially revolutionizing the standard development process for the entire industry. NREL’s GH-MSMD baseline model codes are developed on both the MATLAB and C++ platforms. These NREL custom models are to be available to external users in future. For now, it is desired to implement GH-MSMD in commercial computer-aided engineering software to make it available immediately to a large number of users in the electric vehicle industry. To facilitate that, NREL developed a manual procedure for GH-MSMD implementation in ANSYS Fluent and built a GUI using scheme programming and the user codes. Figure III- 76 is a screen image of NREL’s custom GUI of GH-MSMD. The current GUI is similar to that in the ANSYS/Fluent MSMD Battery Module. The customized GUI enables us to practice and test GH-MSMD implementation into Fluent. Unique features could be added for the GH-MSMD methodology to link different domain levels and improve simulation efficiency. NREL’s implementation of the GH-MSMD CDM in Fluent has been verified by comparing the model outputs against commercially available existing MSMD model option in Fluent. The results are shown in Figure III- 77.

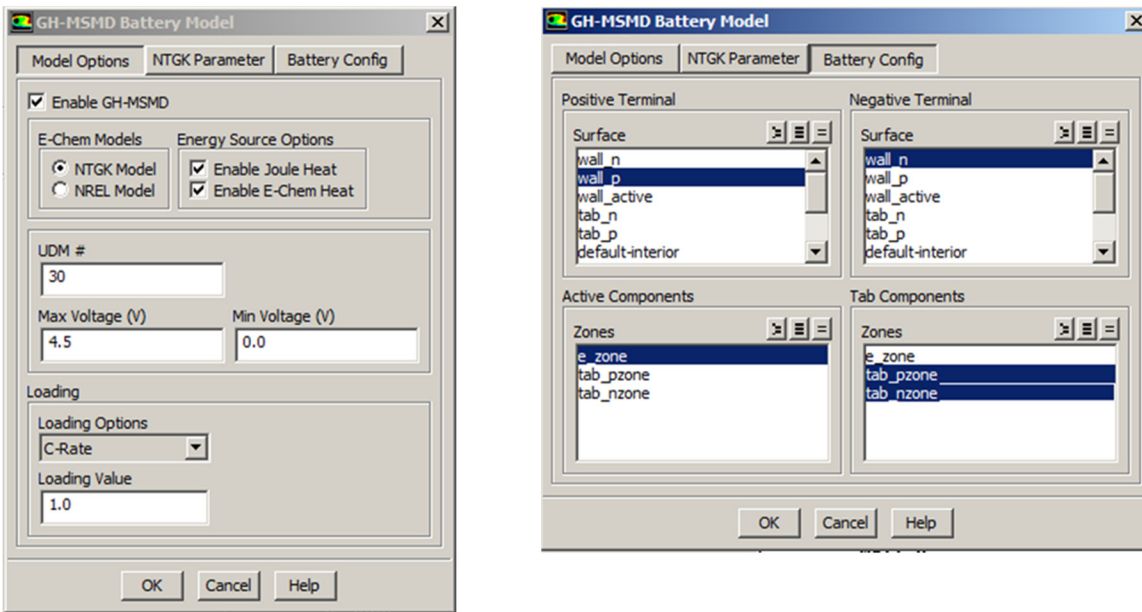


Figure III- 76: Custom GUI of GH-MSMD set up in ANSYS/Fluent

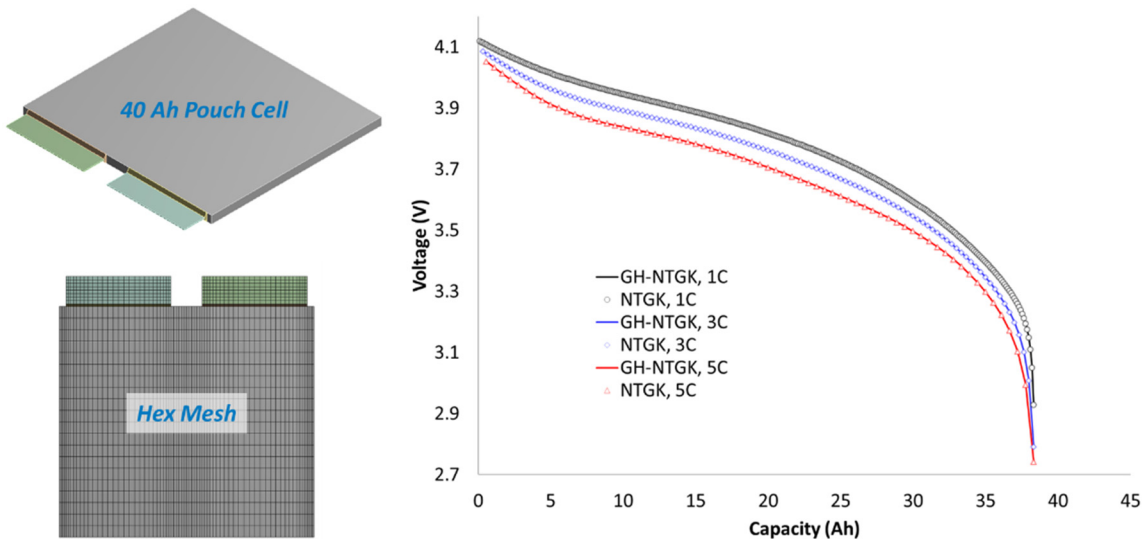


Figure III- 77: NREL’s custom implementation of GH-MSMD in Fluent is verified. Solid lines are the cell voltage response of NREL custom GH-MSMD model simulations, and the symbols are corresponding outputs from the Fluent MSMD Battery Simulation Module

Conclusions and Future Directions

We successfully accomplished the project goal and improved the computation speed of state-of-the-art nonlinear multiscale battery model by a factor of 100 while maintaining accuracy. The new GH-MSMD demonstrates a 1,000-fold speed up compared with the original MSMD during vehicle driving profile benchmark simulation tests. The remaining challenges and the future directions that we expect to address in the third phase of the CAEBAT project are identified below.

Remaining Challenges

- GH-MSMD demonstrates a significant speed up. The remaining challenge, however, is to enhance the applicability of the new model to various battery engineering problems.

- To address varied problems in the industry, interdisciplinary constituent models relating material/ design/ process/ operational parameters with physicochemical parameters of the GH- baseline models are needed.
- Electrochemical Impedance Spectroscopy is a frequently used method for battery characterization and diagnostics. Since the current GH-MSMD has been developed in time-domain, it is difficult to utilize the information produced in frequency domain.
- The modular architecture of GH-MSMD facilitates participation of external expertise across the battery community. Independently developed submodels can be plugged in the framework to extend the simulation capability. However, unlike the original MSMD, the GH-MSMD protocol is not intuitively understandable.
- Identification of a physics-based battery model is known to be difficult. This anticipated difficulty for development of a physics-based constituent model comes from the fact that characterization of a battery is intrinsically solving an under-determined problem.

Future Direction

- There are strong industry needs to use purely predictive physics-based models for design, evaluation, and control of batteries and systems. In the pursuit of such models, we will develop physics-based interdisciplinary constituent models working in the GH-MSMD framework.
- A frequency-domain GH-MSMD model will be developed from the identical governing equation sets used in the time-domain model, running with the standard input files.
- We will summarize the GH-MSMD principles and implementation and publicize them to encourage contributions from outside experts.
- We will develop sequential optimization procedures to address the under-determined parameter estimation problem of the whole system into a sequence of fully determined fits to subsets of the parameters and advanced model-based battery characterization.

FY 2015 Publications/Presentations

1. G.-H. Kim et al., “Significant Enhancement of Computational Efficiency in Nonlinear Multiscale Battery Model for Computer Aided Engineering,” DOE Annual Merit Review, June, 2015, Washington DC.
2. Annual Milestone Reports, September 2015.
3. G.-H. Kim, C. Yang, A. Pesaran, “Integrated Multiscale Multiphysics Modeling of Dynamic Short Circuit Behavior in Large Lithium-ion Batteries,” 228th Electrochemical Society Meeting, October, 2015, Phoenix, AZ.
4. C. Yang, G.-H. Kim, M. Keyser, A. Pesaran, “Numerically Characterizing Nail Penetration Testing for Safety Evaluation of Li-Ion Cells,” 228th Electrochemical Society Meeting, October, 2015, Phoenix, AZ.

III.C.8 Crash Propagation in Automotive Batteries: Simulations and Validation (NREL)

Objectives

- The objective of this work is to build simulation tools with adequate fidelity on commercial software platforms that the industry can use to simulate the electrical, thermal, and mechanical responses of a lithium-ion battery subjected to a sudden mechanical impact, such as a crash, focusing largely on the module- to pack-level phenomena.

Technical Barriers

- Concerns regarding potential thermal event by lithium-ion batteries in today's plug-in electric vehicles (PEVs) could delay increased adoption of PEVs.
- Insufficient characterization of battery safety for a vehicle subjected to crash. Recently, several experimental investigations were conducted by regulatory agencies and original equipment manufacturers (OEMs); but there is no systematic understanding of the propagation of failure from when an individual cell within a battery pack fails, to whether or not the mechanical crash will be followed by thermal events.
- Criteria relating design of cells (e.g., format, packaging, chemistry) to performance at the module level are difficult to build due to a limited understanding of complex interactions among different physical phenomena occurring during the crash. This leads to overdesigning for safety of battery packs and heavier and more expensive systems.
- Limited experimental studies on the modes of propagation, as well as the arbitrary nature of the test conditions, limit the understanding of how failure at the individual cell level translates to implications for the safety of the module or the pack.

Project Details

Brian Cunningham (DOE Program Manager)
DOE Agreement # 27041 Recipient:
 National Renewable Energy Laboratory

Shriram Santhanagopalan (NREL – PI)
 15013 Denver West Parkway, M/S 1633
 Golden, CO 80401
 Phone: 303-275-3944; Fax: 303-275-4415
 Email: Shriram.Santhanagopalan@nrel.gov
www.nrel.gov/transportation/energystorage/

NREL Collaborators:
 Chao Zhang, Michael A. Sprague

Subcontractor:
 Ford Motor Company

Start Date: December 2013

Projected End Date: December 2015

Technical Targets

- Develop mechanical models that can be coupled with thermal and electrochemical aspects of failure propagation in lithium-ion batteries. The emphasis is on single-cell to multi-cell propagation.
- Develop simulation capabilities in this area for individual cells and cell strings that show good agreement with experimental data for coordinates of the origin of failure and maximum surface temperature.
- Validate simulation capability to facilitate safer, less expensive, and lighter PEV battery designs.

Accomplishments

- We have developed the first-ever simulation tool that includes physics-based models for mechanical, electrochemical and thermal response of a multi-cell unit.
- Several test cases were simulated to demonstrate versatility of the models from the single-cell case and cell strings to modules in different configurations.
- Experimental validation of mechanical models across these geometries was demonstrated and summarized in this report.
 - For the single-cell and cell-string levels, the models capture the force response to within 15-20% accuracy and predict the location for the origin of failure based on the deformation data from the experiments.

- At the module level, there is some discrepancy due to spacing between the cells in the test article that we are addressing now.
- The cells within packaging volume of a module experienced about 60% less force under identical impact test conditions: so the packaging on the test articles is robust. However, under slow-crush simulations, we found that the maximum deformation of the cell strings with packaging is about twice that from cell strings without packaging.
- Thus, we have identified a sweet spot between balancing damage prevention during an impact test and forced deformation during a slow crush. This information will provide insight to pack assemblers to help design better modules by providing sufficient spacing between cells within the modules/cell-strings. An alternate approach is to design packaging material with better elastic properties while maintaining adequate failure strength.

Introduction

This effort builds upon our work in FY14 to develop a simulation tool that captures the propagation of thermal events following mechanical impact from a single cell across a multi-cell module. Ford Motor Company is our partner in this project, providing insight on packaging of cells in modules and overseeing crush testing. In the previous year's report, we demonstrated simulation capabilities across multiple form factors for individual cells (e.g., prismatic vs pouch cells, wound vs stacked, cylindrical vs prismatic). These models are chemistry agnostic, and leverage the battery module available from ANSYS based on previous work under the first phase of Computer-Aided Engineering for Electric-Driven Vehicle Batteries (CAEBAT) project.

Approach

The key distinguishing feature of our current approach is that our mathematical treatment of batteries accounts for the energetics that follow a mechanical deformation. Previously reported battery crash simulations treated batteries as passive materials similar to air-bags or structural elements of the vehicle. These models considered the mechanical aspects only, and did not capture the electrochemical effects. On the other hand, the state-of-the-art electrochemical-thermal models assumed that the contributions from the mechanical constraints imposed on the cells were limited. Physical deformation of the cells due to thermal/electrochemical events was not considered. In the present work, we present a new approach that combines the effect of deformation or mechanical failure of the different components in a battery with electrochemical models to simulate the thermal propagation response.

Geometry and Meshing

The models implement realistic geometries from computer-aided design (CAD) images for the actual test article hardware. We integrate the mechanical response from explicit simulations performed in LS-DYNA to the battery-abuse models available in ANSYS to perform different case studies of interest. One of the key challenges in simulating performance of large battery modules in three dimensions is the mathematical complexity and computational demand which scales with the size and shape of the different features associated with the geometry. In our case, in the geometry for the 20-cell module shown in Figure III- 78, for example, there were more than 800 individual parts that must be meshed to adequate detail before any simulation effort begins. Identification of the critical components that contribute to the propagation events and subsequent defeaturing of the geometry was streamlined as the first step towards extending the coupled thermal/mechanical simulation capability to CAD geometries reflective of actual hardware. This was accomplished using a shell script to identify contact faces that must be retained to capture the physics adequately. We are still evaluating the limits of the current approach and making refinements to the scalability with the size of the geometry.

Mechanical Models

We implemented the anisotropic material properties of the active materials and separator into the LS-Dyna Honeycomb Model. The model enables different tensile and compressive stress-strain responses and tensile-strain-based failure criteria. The LS-Dyna damage model is used together with the other models to describe damage of current collectors. The model parameters were calibrated using quasi-static cylindrical indentation test data. Figure III- 79 shows an example of calibration of the component properties in the mechanical models.

Electrochemical-Thermal Models

The results from the mechanical simulations (such as deformation or localized resistance values) are fed as input into the thermal/electrochemical simulations. Under the scope of this phase of the project, a one-way coupling is implemented; the contributions of the thermal or reaction parameters to the change in mechanical properties are not

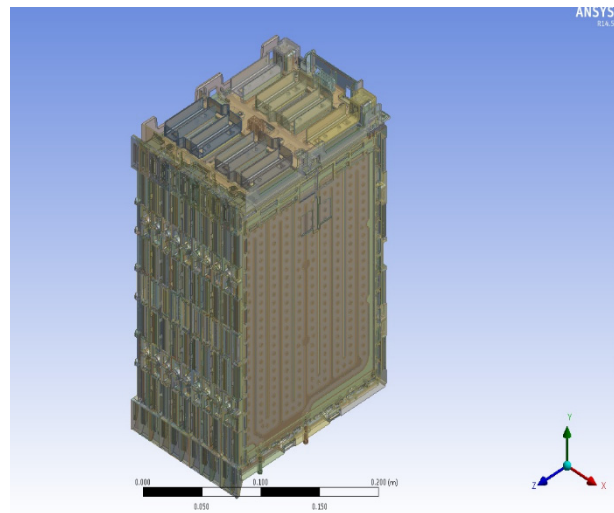


Figure III- 78: CAD image of a 20 cell module complete with packaging and heat-exchange fins (geometry courtesy of Ford): the hardware uses the same 15 Ah cells and has more than 800 small parts meshing of which results in more than 16 million elements, making it challenging to run efficient simulations

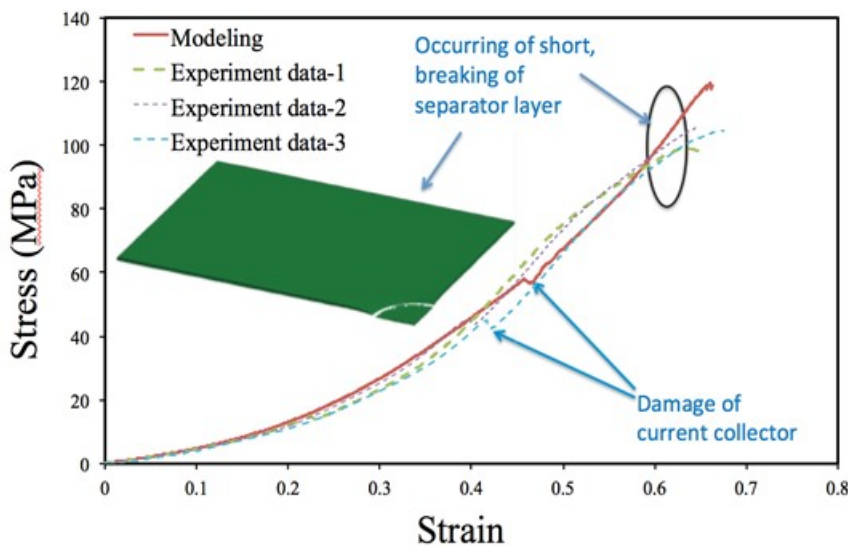


Figure III- 79: Illustration of obtaining parameters in the constitutive models by calibration against component-level test data. This information is then used as input to the cell-level and larger scale simulations

results, or in the absence of that, from test data at a lower-length scale. In this sense, the models at the different domains are fairly independent of each other. This is in line with the modular framework implemented across all of NREL’s battery simulation tools. It enables the end user to exercise some flexibility in the choice of models for the different domains; at the same time, it enables practical use of models at a given domain of interest without the need to build the entire suite. Table III- 16 describes the inputs and outputs across the different domains.

accounted for. This approach is valid for the impact (e.g., drop-test-type scenario) loading studied in our experimental test matrix. The results of the slow-crush simulations are less accurate because the one-way coupling methodology limits the validity to very slow (quasi-static) simulation cases.

One feature worth mentioning in our approach to modeling cells, strings and modules is that the input for any of these domains can be obtained from simulation

Table III- 16: Sample list of parameters and variables exchanged across the different domains

Scope	Cell-Level	Cell-Strings	Module-Level
Input	<ul style="list-style-type: none"> Electrical, thermal, and mechanical data on cell components Cell assembly information 	<ul style="list-style-type: none"> Mechanical models for individual cells Heat-generation model for the cell under short-circuit 	<ul style="list-style-type: none"> Mechanical models for individual cells Heat-generation model for the cell under short-circuit Properties of packaging material, module configuration
Output	<ul style="list-style-type: none"> Constitutive mechanical models representative of the cell-level response 	<ul style="list-style-type: none"> Origin and propagation of electrical/thermal phenomena, when multiple short-circuit events occur across the string during crush 	<ul style="list-style-type: none"> Origin and propagation of electrical/thermal phenomena under crush Identification of weak spots on the module to monitor /take preventive measures

Results

Simulations were performed at the cell, string and module levels. Validation hardware was assembled accordingly for each level. The following section summarizes a few test cases and examples of key observations.

Cell-Level Simulations

Cell-level mechanical simulations predict no breach of the packaging; this is in line with the experimental observations. The strain-based failure criterion we use, together with the lumped representation of the individual layers, does not adequately capture the dynamic effects or internal pressure events. (See Figure III-80.) The maximum force during the impact test is captured to within 20% of the experimental value in the simulation results. There is a rebounding of the thickness of the lumped separator layer from 0.076 mm to 0.096 mm, corresponding to recovery of the voltage drop observed experimentally.

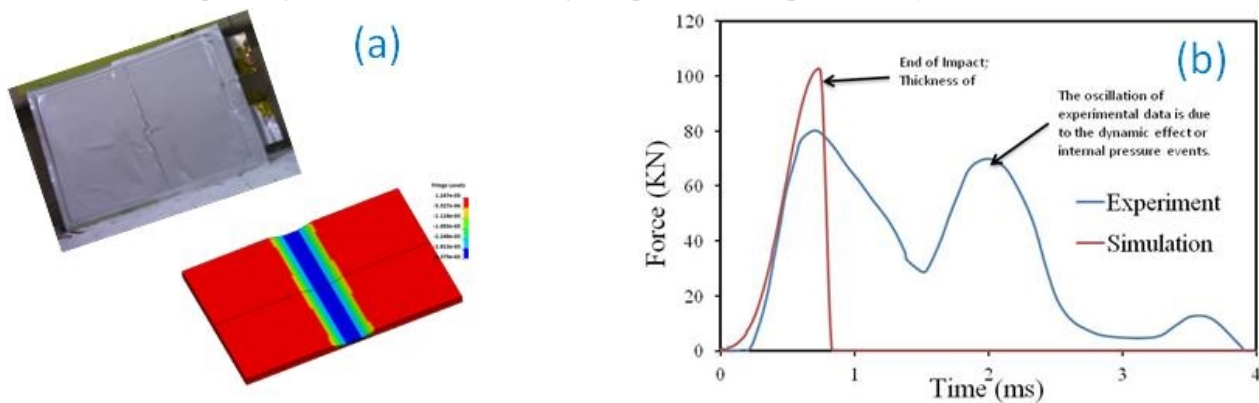


Figure III- 80: a) Comparison of experimental and simulated geometry showing no breach of packaging material under the impact load conditions tested; the model results for this test case compare well with the EUCAR-2 response observed in the tests. b) A detailed comparison of the force vs time shows that the test data suffer from oscillations of the indenter upon impact. The simulation results do not capture this because the models do not account for factors such as elasticity of the indenter material and fixtures to hold the cell

Four repeats under identical test conditions showed different voltage drops from the initial 4.15 V (80% state of charge, SOC). High-speed video results indicated the source of variability to be different contact times between the impact load and the cells. Different contact times were simulated to compare with the experimental results. Resistance of the short varies with the duration of contact. This metric is predictive and it can be used as an indicator of the remaining energy in the battery at any given time after the crash. This result has significant implications toward safety assessment of battery packs after crash. Figure III- 81 shows a comparison of the voltage drop and temperature rise as a function of contact duration between the indenter and the cell.

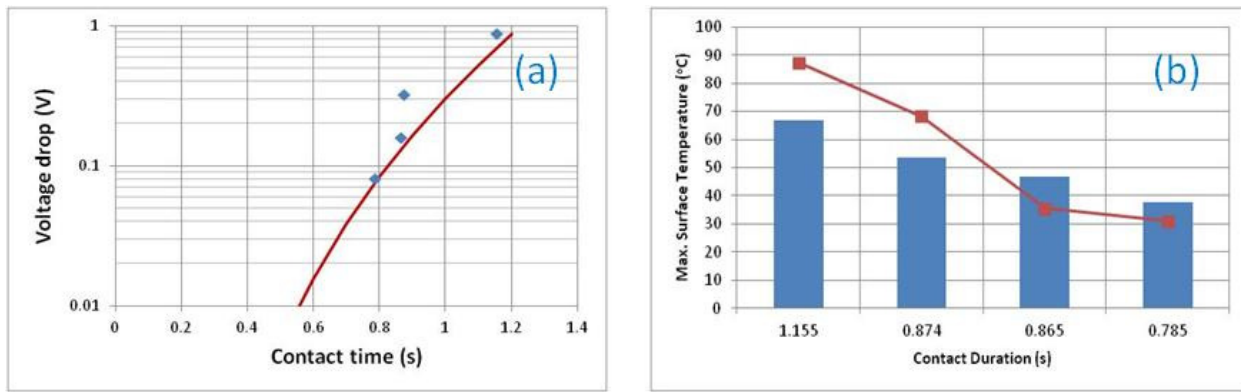


Figure III- 81: Electrical and thermal responses of the cell: a) Model predictions (solid line) vs experimental data from high-speed imagery (dots), b) Comparison of the experimentally observed maxima for the surface temperatures (dots) against the model predictions (bars). In general, the experimental results are consistent with the simulation: the initial voltage drop varies directly as a function of contact time with the load and the maximum temperature decreases with a decrease in the contact duration

Simulation of Cell Strings

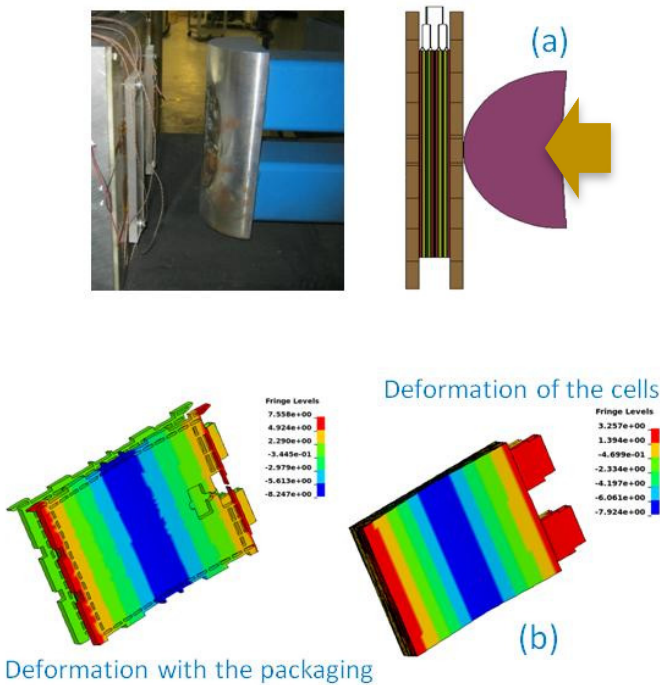


Figure III- 82: (a) Experimental test set up for X-plane crush of a cell string and (b) Sample simulation results comparing deformation with and without the packaging

For the cell-string crush, the 1S5P test configuration was used. A hemi-cylindrical indenter was used, as specified in the USABC test procedure. The simulation results for the x-plane crush are shown in this report (see Figure III- 82). The mechanical response of the cell string to the crush along the x-plane captured the test results for maximum deformation both along the axis of indentation and along the edges of the test structure, accurate to within 15%. With packaging, the deformation was twice that for the cells-only simulation case, indicating that the mechanical properties of the string packaging induce significant deformation under slow-crush conditions.

These results counter the benefits of having a robust packaging system under an impact (sudden-drop) test. The cells within the packaging likely have some buffer space to accommodate such conditions. More work is under way in this area to investigate the effect of spacing among cells in the string.

Previous models assuming constant resistance throughout the short circuit predict propagation along the current collectors 25 seconds into the short. Evolution of resistance with mechanical deformation predicts localized thermal events within the first few seconds of impact.

Module-Level Simulations

Two different sets of simulations were set up with the impactor approaching from the x- and z-planes (see Figure III- 83). The impact was simulated as a drop of a pre-determined mass from a height of 2 m (impact velocity of 6.26 m/s). Based on the experimental test plan previously developed from Ford, the loads on the impactors were set to 22 kg for the x-plane and 14 kg for the z-plane.

For the impact along the x-plane, the cell frame considerably reduces the propagation of mechanical damage across multiple cells. The maximum deflection of the end plate is limited to less than 2 mm, which is a

reduction of more than 15% in the maximum deformation for identical test cases with and without the cell frame. Structural damage is concentrated along the edges of the structure, particularly near the holes on the frame. The maximum strain (0.0829, front panel) is far less than the failure strain of steel. For the z-plane, the evolution of damage to the structure is strictly confined to the holes. These results are quite similar to those for the x-plane simulations. The inner frame acts as a shock absorber and takes in much of the deformation; also, as noted under the test conditions, the mass of the impactor also influenced the maximum deflection to some extent. Regardless, the overall damage observed in this case is lower than x-plane impact; the maximum plastic strain (0.395) is higher due to the structural design of the inner frame. The indenter reaches zero velocity after impact along the x-plane in about 50% of the time compared to the impact along the z-plane, due to a larger contact area. In a previous report, we discussed the thermal response of the module under the two cases: the temperature rise for the x-plane impact was much higher compared to the z-plane, primarily due to the presence of the spacing between the cells and the end frames along this direction.

The test articles were also instrumented with shunts to monitor the currents across the cells. The test setup will then enable us to monitor the propagation of failure across different cells within the module. Comparison against experimental results is under way.

Conclusions and Future Directions

Under this project, NREL developed the first-ever coupled mechanical-electrochemical-thermal model for batteries after a crush. We presented several examples of simulation results showing crash propagation response of automotive batteries alongside experimental validation. The effort over the last two years has enabled us to identify critical gaps in test data available and to quantitatively interpret the experimental results.

A good example is the test case showing the effect of duration of contact between the cells and the indenter. Previously, the variability among the test results could not be traced back to sensitivity of individual testing parameters without trial and error. Insights such as the ones described in this report help minimize such iterations and improve the quality of test results, as well as maximizing the value gained from the limited test data available. The validation of the electrical signals as a function of time is under way for the cell strings and modules. These results will provide additional insights on preventive measures and trade-off between designing efficient and light battery modules while addressing safety concerns. The experimental results reported here point to key differences in the damage intensity and duration of impact between the drop test and the slow crush: for the same peak force (~80 kN), the slow crush was more damaging than the drop test, which is a relatively fast crush test. The implications of these results for the safety of the battery are yet to be assessed. The swelling of the cells under slow-crush tests (versus no swelling during the drop test) points towards the need for strain-rate-dependent models and incorporating pressure build-up into the mechanical-abuse models. We will continue improving the fidelity of the model to simulate different experimental conditions and use the lessons learned in the next phase of CAEBAT project.

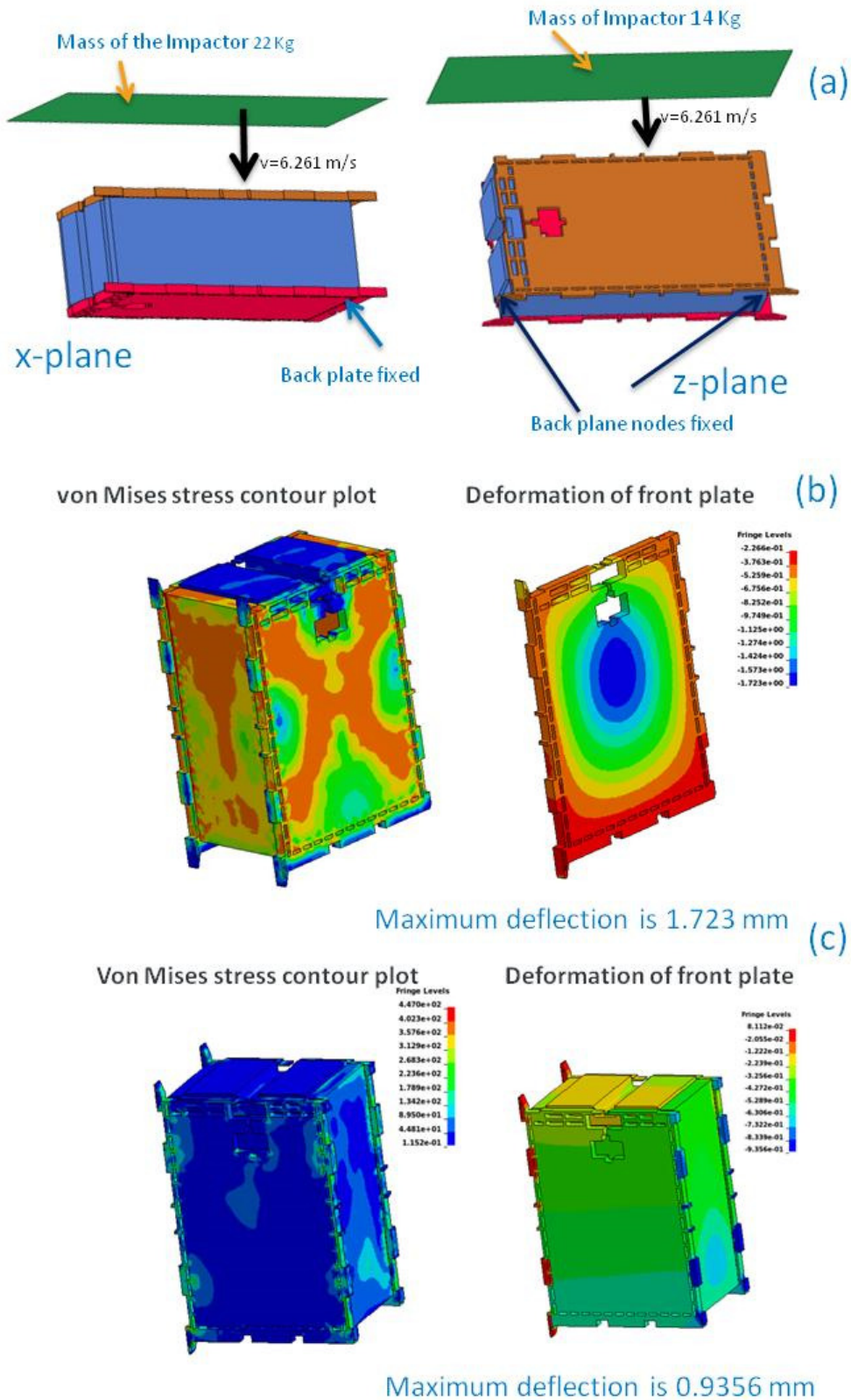


Figure III- 83: a) Simulation conditions for the module showing the different orientations of the test article subjected to crush; b) Sample simulation results for impact along the x-plane; (c) Sample simulation results for impact along the z-plane

FY 2015 Publications/Presentations

1. “Coupled Mechanical-Electrical-Thermal Modeling for Lithium-ion Batteries,” C. Zhang, S. Santhanagopalan, M. Sprague, A. Pesaran, J. Power Sources, vol. 290, pp. 102–113, 2015.
2. “Crash Propagation in Automotive Batteries: Simulations and Validation (NREL),” S. the Battery Show, Novi, MI, Sept. 2015.
3. “A Representative Sandwich Model for Coupled Mechanical-Electrical-Thermal Simulation of Lithium-Ion Battery Cell under Quasi-Static Indentation Tests,” C. Zhang, S. Santhanagopalan, M. Sprague, A. Pesaran, J. Power Sources, vol. 298, pp. 309–321, 2015.